INVESTIGATIONS ON THE NATURAL RADIOACTIVITY AND GAMMA ATTENUATION PROPERTIES OF BUILDING MATERIALS

Thesis submitted to the
University of Calicut in partial fulfillment of the requirements for
the award of the degree of

DOCTOR OF PHILOSOPHY IN PHYSICS

by

VISHNU C V

DEPARTMENT OF PHYSICS
UNIVERSITY OF CALICUT
KERALA, INDIA- 673635

JUNE 2024

INVESTIGATIONS ON THE NATURAL RADIOACTIVITY AND GAMMA ATTENUATION PROPERTIES OF BUILDING MATERIALS.

Ph.D. Thesis in Physics

Author:

Vishnu C V
Department of Physics
University of Calicut
Calicut University (P.O)
673635, Kerala, India
Email: venuvishnu24@gmail.com

Under the guidance of

Dr. Antony Joseph
Senior Professor (retd.)
Department of Physics
University of Calicut
Calicut University (P.O)
673635, Kerala, India
Email: aj@uoc.ac.in

Dr. Antony Joseph
Senior Professor
Department of Physics
University of Calicut

Calicut University (P.O)
673635, Kerala, India
+919446164109 (M)
Email: aj@uoc.ac.in

CERTIFICATE

Certified that the work presented in the thesis, entitled **"INVESTIGATIONS ON THE NATURAL RADIOACTIVITY AND GAMMA ATTENUATION PROPERTIES OF BUILDING MATERIALS"** is based on the authentic record of research carried out by Mr. VISHNU C V under my guidance in Department of Physics, University of Calicut, Calicut University (P.O), Kerala-673635 and this work has not been included in any other thesis submitted previously for the award of any degree.

Calicut University
21/06/2024

Dr. Antony Joseph

Dr. Antony Joseph
Senior Professor
Department of Physics
University of Calicut

Calicut University (P.O)
673635, Kerala, India
+919446164109 (M)
Email: aj@uoc.ac.in

CERTIFICATE

Certified that the work presented in the thesis, entitled **"INVESTIGATIONS ON THE NATURAL RADIOACTIVITY AND GAMMA ATTENUATION PROPERTIES OF BUILDING MATERIALS"** is based on the authentic record of research carried out by Mr. VISHNU C V under my guidance in Department of Physics, University of Calicut, Calicut University (P.O), Kerala-673635 and this work has not been included in any other thesis submitted previously for the award of any degree. Also, certified that the corrections suggested by the adjudicators have been incorporated in this revised thesis.

Calicut University
21/01/2025

Dr. Antony Joseph

DECLARATION

Certified that the work presented in this thesis, entitled **"INVESTIGATIONS ON THE NATURAL RADIOACTIVITY AND GAMMA ATTENUATION PROPERTIES OF BUILDING MATERIALS."** is based on the original research work done by me under the supervision and guidance of Dr. Antony Joseph, Senior Professor, Department of Physics, University of Calicut, Calicut university (P.O), Kerala-673635 and has not been included in any other thesis submitted previously for the award of any degree. The contents of the thesis have undergone plagiarism check using iThenticate software at C.H.M.K Library, University of Calicut, and Similarity index found within the permissible limit. I also declare that the thesis is free from AI generated contents.

Calicut university
21/06/2024

Vishnu C V

UNIVERSITY OF CALICUT

CERTIFICATE ON PLAGIARISM CHECK

1.	Name of the Research Scholar	VISHNU C V	
2.	Title of thesis / dissertation	INVESTIGATIONS ON THE NATURAL RADIOACTIVITY AND GAMMA ATTENUATION PROPERTIES OF BUILDING MATERIALS.	
3.	Name of the Supervisor	Dr. ANTONY JOSEPH	
4.	Department/Institution	Department of Physics University of Calicut	
5.	Similar content (%) identified	Non Core **Introduction/ Theoretical overview/Review of literature/ Materials & Methods/ Methodology**	Core **Analysis/Result/Discussion/ Summary/Conclusion/ Recommendations**
		4	5
	Acceptable maximum limit (%)	10	10
6.	Software used	Ithenticate	
7.	Date of verification	21-06-24	

**Report on plagiarism check, specifying included/excluded items with % of similarity to beattached.*

Checked by (with name , designation & signature) Dr. Nasirudheen. T
Assistant Librarian
University of Calicut, Kerala.

Name and signature of the Researcher VISHNU C V

Name and signature of the Supervisor. Dr. Antony Joseph

U.H. MOHAMMED KOYA LIBRARY
P.O. CALICUT UNIVERSITY
UNIVERSITY OF CALICUT

The Doctoral Committee* has verified the report on plagiarism check with the contents of the thesis, as summarized above and appropriate measures have been taken to ensure originality of the Research accomplished herein.

Name & Signature of the HoD/HoI (Chairperson of the Doctoral Committee)

Dr. MOHAMED SHAHIN THAYYIL
Professor & Head, Department of Physics
University of Calicut, Kerala (INDIA) - 673635

**In case of languages like Malayalam, Tamil etc..on which no software is available for plagiarism check, a manual check shall be made by the Doctoral Committee, for which an undertaking/certificate has to be attached.*

ACKNOWLEDGEMENT

The journey of completing my Ph.D. has been both challenging and rewarding, and I am deeply grateful for the support and encouragement I have received from various quarters. This thesis would not have been possible without the guidance, assistance, and love of several individuals who have contributed to my academic and personal growth.

First and foremost, I would like to express my profound gratitude to my esteemed guide, Dr. Antony Joseph. Your invaluable insights, constant encouragement, and unwavering support have been the backbone of this research. Your patience and dedication have inspired me to persevere through the toughest times. Thank you for believing in me and for being an exceptional mentor.

To my beloved wife, Anju, words cannot fully capture how much your love and support have meant to me throughout this journey. You have been my rock, my confidante, and my source of motivation. Your understanding, sacrifices, and constant encouragement have enabled me to pursue and achieve this milestone. I am forever grateful for your presence in my life.

My heartfelt thanks go to my parents, ACHA and AMMA, and my grandparents. Your unwavering faith in me, your endless encouragement, and your unconditional love have been my greatest source of strength. Your guidance and blessings have shaped me into the person I am today. I owe my success to the values and work ethic you have instilled in me. I would like to extend my deepest appreciation to my sister, Vandhana. Your support, encouragement, and belief in my abilities have been a constant source of motivation. Thank you for always being there for me, for your kind words during tough times, and for celebrating my achievements with genuine joy. Your love and encouragement have been indispensable.

A special thanks to my father-in-law, my mother-in-law and my sisters-in-law, Vava. Your kindness, support, and encouragement have been a tremendous source of comfort and strength. Thank you for welcoming me into your family, for your

unwavering belief in my capabilities, and for your constant support throughout this journey.

A special thanks to my roommates to my friends Rajeshettan, Aravindettan, Shinojettan, Manu Philip, Anu Sebastin, Aneesh, Rajeesh, Binil, Sudhish, Akhil, Vishnu Mohan, Vinoy, Riyas, Irfan, Nikhil Krishna, Noble, Manu dev and all my Hostel inmates. Your companionship and understanding have provided me with a home away from home. Thank you for the countless late-night conversations, the shared laughter, and your support in balancing the pressures of academic life with moments of relaxation and joy. Your friendship was a vital part of my journey. Your support, whether through thoughtful advice, a listening ear, or simply being there for me, has been invaluable. You have shared in my struggles and celebrated my achievements, making this journey even more meaningful.

A special thanks to my researchmates, Seban, Prasanthettan, Vidhya chechi, Nitu, Bintu, Shan, Shabeer, Jemshihas, Sravandas, Nicemon thomas. Vinodettan, Binesh, Sanila, Anjana, Ummukulsu, Parvathy, Vineetha miss, Hajara, Salma, Ramsiya and all my colleagues. Your camaraderie and collaborative spirit have made this academic journey enriching and enjoyable. Thank you for the stimulating discussions, the shared experiments, and the mutual support that has helped us navigate the challenges of research together. Your friendship and contributions have been vital to this work.

I am deeply grateful to my research collaborators, Vineethkumar, Shimod, Neeraja and Prakash sir. Your expertise, collaboration, and shared commitment to our research goals have been instrumental in the success of this work. Thank you for your insights, your willingness to share knowledge, and for making our joint efforts both productive and enjoyable.

I am grateful to the Head of the department, all previous HOD'S and teachers, whose wisdom and dedication have played a crucial role in my academic journey. Your teachings have not only imparted knowledge but have also inspired a passion for learning and discovery. Thank you for laying the foundation that has allowed me to pursue my research with confidence and curiosity.

I am also deeply grateful to the office staff at the Department of physics and Directorate of research, University of Calicut. Your administrative support, efficiency, and willingness to assist have ensured that the non-academic aspects of this journey ran smoothly. Your behind-the-scenes work has been instrumental in the completion of this thesis.

I would like to acknowledge the financial support from E-grants, Kerala State. This funding has been crucial in enabling my research, providing the necessary resources and support to pursue and complete my studies. I am thankful for the opportunities and support that this grant has provided.

Finally, I thank ALMIGHTY for His blessings and guidance throughout this journey. Your grace has given me the strength and perseverance to overcome challenges and achieve my goals. Thank you for providing me with the wisdom and courage needed to complete this work.

Vishnu C V

Dedication

To my father and mother,
For your unwavering support, encouragement, and love. This work is a testament to your belief in me and the values you've instilled in me.
Thank you for everything…

CONTENT

No.	*Tittle*	*Page No.*
1.0	**Introduction**	1
1.1	Fundamentals of Radiation	3
1.2	Natural Radioactivity	4
1.3	Significance of Natural Radioactivity Measurements	5
1.4	Primordial Radioactive Nuclides	7
1.5	Cosmogenic Radioactive Nuclides	11
1.6	Background Radiation	12
1.7	Terrestrial sources of natural radioactivity	13
1.8	Extraterrestrial sources of natural radioactivity	15
1.9	The distribution of primordial radionuclides in rocks and soils	16
1.9.1	The distribution of sedimentary rocks	16
1.9.2	The distribution of metamorphic rocks	18
1.9.3	The distribution of igneous rocks	18
1.10	Mineral deposition in the Rock and Soil samples	20
1.10.1	Mineral's deposition in the Rock samples	20
1.10.2	Mineral's deposition in the Soil samples	21
1.11	Technologically enhanced natural radionuclides	24
1.12	Radiogenic Heat Production and Heat flow	24
1.13	Interaction Mechanisms of Gamma Rays	26
1.13.1	Photoelectric effect	28
1.13.2	Compton effect	29
1.13.3	Pair Production	30
1.12.4	Photodisintegration	33
1.14	Photon Attenuation and Absorption	33
1.15	Gamma-ray shielding	34
1.16	Different Types of Shielding Materials	38
1.17	Motivation of this research	45

1.18	Objectives of the Work	47
1.19	Reference	49
2.0	**Literature and Backgrounds**	53
2.1	Radiation exposure pathways	55
2.2	Rock - Soil Samples Global analysis	56
2.3	Natural radioactivity measurements in India	59
2.4	Radiation shielding Materials	65
2.4.1	Concrete composites	66
2.4.2	Glass composites	67
2.4.3	Polymer composites	70
2.4.4	Epoxy-resin composites	75
2.5	Reference	78
3.0	**Experimental Techniques**	85
3.1	Introduction	87
3.2	Gamma-Ray Spectroscopy	87
3.2.1	Micro-R survey meter	88
3.2.2	NaI (Tl) scintillation detector	89
3.2.3	HPGe (High-Purity Germanium) detector	91
3.2.4	Energy, Resolution and Efficiency Calibration of the detector	95
3.2.5	Activity Measurement	98
3.3	Inductively Coupled Plasma-Mass Spectrometer (ICP-MS)	98
3.4	X-ray Diffractometer (XRD)	100
3.5	Energy Dispersive X-ray Fluorescence (EDXRF)	104
3.6	Field Emission Scanning Electron Microscopy (FESEM) and Energy Dispersive X-ray Analysis (EDAX)	107
3.7	Reference	110
4.0	**Theoretical Background**	111
4.1	Radiological parameters	113
4.1.1	Radium Equivalent Activity (Ra_{eq})	114
4.1.2	External And Internal Hazard Indices (H_{ex} and H_{in})	114

4.1.3	Indoor and Outdoor Absorbed Gamma Dose Rate (D_{in} and D_{out})	114
4.1.4	Annual Effective Dose Equivalents (AED)	114
4.1.5	External (γ-radioactivity) level index I_{γ}	115
4.1.6	Excess Lifetime Cancer Risk (ELCR)	116
4.1.7	Alpha Index(I_{α})	116
4.2	Radiogenic Heat Production and Heat Flow	117
4.2.1	Radiogenic Heat Production (RHP)	118
4.2.2	Heat Flow	119
4.3	Gamma-ray Attenuation	120
4.3.1	Bethe formula (or Bethe-Bloch formula):	121
4.3.2	Radiation Transport Equation	122
4.3.3	Linear Attenuation Coefficient (LAC)	122
4.3.4	The Mass Attenuation Coefficient (MAC)	123
4.3.5	Half-Value Layer (HVL) and Tenth-Value Layer (TVL)	123
4.3.6	Mean Free Path (MFP)	124
4.3.7	Effective Atomic Number (Z_{eff}) Effective Electron Density (N_{eff})	124
4.3.8	Effective Conductivity (C_{eff})	125
4.3.9	The Exposure Build-Up Factor	125
4.3.10	Fast Neutron Removal Cross Section (FNRCS)	127
4.4	Shielding Design Principles	128
4.5	Reference	130
5.0	**Radiological Impact of Natural Radioactivity and Heat Production in Populated Areas of Kerala**	135
5.1	Introduction	137
5.2	Thrissur- Palakkad highway zone (Kuthiran Hills, Western Ghats of Kerala)- Region I.	140
5.2.1	Sample collection and preparation	140
5.2.2	Geology of the Sampling area	140
5.2.3	Activity concentrations in rock samples	144
5.2.4	Radiological parameters of the rock samples	148

5.2.5	Mineralogical composition analysis of rock samples by XRD	156
5.2.6	Elemental concentration of radionuclides and Radiogenic Heat Production (RHP) in Kuthiran Hills.	158
5.2.7	Correlation between radionuclides and Radiogenic Heat Production (RHP) for studied region.	163
5.2.8	Conclusion	166
5.3	Urban regions along the National Highway (NH-66) in Kerala, India Region II.	167
5.3.1	Geology of the study area	168
5.3.2	Lithology of study area.	170
5.3.3	Activity concentration in NH-66 study sites.	172
5.3.4	Radiological Parameters	177
5.3.5	XRD analysis and Mineral compositions	182
5.3.6	Physico-chemical properties of soils	184
5.3.7	Elemental concentration of radionuclides and Radiogenic Heat Production (RHP) in NH-66 Zone.	186
5.3.8	Correlation between radionuclides and Radiogenic Heat Production (RHP) for studied region.	191
5.3.9	Conclusion	194
5.4	Athirappilly Waterfalls (Athirappilly Hills, part of Western Ghats in Kerala)- Region III.	194
5.4.1	About the study region	194
5.4.2	Mineralogy and Rock systems	195
5.4.3	Sample Collection and Preparation	198
5.4.4	Activity concentrations of radionuclides	200
5.4.5	Radiological Parameters	203
5.4.6	Pearson correlation analysis	209
5.4.7	Elemental concentration of radionuclides and Radiogenic Heat Production (RHP) in Athirappilly region.	211
5.4.8	Correlation between radionuclides and Radiogenic Heat Production (RHP) for studied region.	213

5.5	Comparison with Similar Studies	221
5.6	Chapter Conclusion	222
5.7	Reference	225
6.0	**Evaluation of gamma radiation shielding properties of concrete reinforced with naturally available additives.**	233
6.1	Introduction	235
6.2	Materials and Mixture Design	237
6.3	Results and discussion	238
6.4	Linear- Mass attenuation coefficients	241
6.5	Half Value Layer, Tenth Value Layer and Mean Free Path	248
6.6	Effective atomic number and electron density	253
6.7	Built-up Factors	255
6.8	Fast neutron removal cross section	263
6.8	Conclusion	264
6.9	Reference	266
7.0	**Gamma shielding analysis on Natural Rubber composites fortified with Barium tungstate oxide ($BaWO_4$).**	269
7.1	Introduction	271
7.2	Materials and Methods	274
7.2.1	Preparation of NR composites	275
7.2.2	Cure Characteristics Measurements	278
7.2.3	Density Measurement	279
7.2.4	Radiation shielding measurements.	279
7.2.5	Phy-X/PSD software analysis	280
7.3	Results and Discussion	281
7.3.1	Cure characteristics of the sample	281
7.3.2	Chemical Analysis and elemental distribution	283
7.4	Gamma-ray shielding properties.	285
7.4.1	Linear Attenuation Coefficient	285
7.4.2	Mass Attenuation Coefficient	289
7.4.3	Half-Value Layer (HVL) and Tenth-Value Layer (TVL)	292

7.4.4	Mean Free Path (MFP)	295
7.4.5	Atomic Cross-Section (ACS) and Electronic Cross-Section (ECS)	297
7.4.6	Effective atomic number (Z_{eff}) and Effective electron density (N_{eff})	299
7.4.7	Built-up Factors	301
7.5	Effective Conductivity (C_{eff}) and Fast neutron removal cross-section (FNRCS)	309
7.6	Conclusion	312
7.7	Reference	313
8.0	**Evaluation of the gamma radiation shielding characteristics of Epoxy wall paint modified with micro sized Bi_2O_3 and WO_3.**	317
8.1	Introduction	319
8.2	Fabrication of the samples and determination of their intrinsic charatertiscs	320
8.3	Gamma-ray attenuation in samples.	322
8.3.1	Theoretical prediction of gamma-ray attenuation in samples.	323
8.3.2	Gamma-ray shielding properties.	323
8.3.3	Linear attenuation coefficient.	324
8.3.4	Mass attenuation coefficient.	328
8.3.5	Half-Value Layer (HVL)	333
8.3.6	Mean Free Path (MFP)	335
8.3.7	Effective atomic number (Z_{eff}) and Effective electron density (N_{eff})	336
8.3.8	Built-up Factors	338
8.3.9	Effective Conductivity (C_{eff}) and Fast neutron removal cross-section (FNRCS)	344
8.4	Conclusion	345
8.5	Reference	346
9.0	**Summary and Conclusion**	349
10.0	**Recommendation**	355
	Appendix	357

LIST OF TABLES

Table No.	*Tittle*	*Page No.*
1.1	Isotopes with Specific isotopic heat production (mW/kg)	25
5.1	Sampling locations of Kuthiran hills in the present study.	142
5.2	Activity concentrations of ^{226}Ra, ^{232}Th and ^{40}K in the study area.	144
5.3	Statistical distribution of the three isotopes in the study area	147
5.4	Radiological hazard indices related to the rock samples in the study area.	149
5.5	Correlation matrix between the radionuclides and radiological parameters.	156
5.6	The elemental concentrations, Radiogenic Heat Production (RHP) and Heat flow (H_f) of the rock samples	159
5.7	The activity concentrations for the three radionuclides measured from study area.	174
5.8	Statistical parameters of the activity concentration (Bq/kg) in samples.	175
5.9	The radiological health hazard indices of the surface soil sample.	177
5.10	The physico-chemical properties of soils.	184
5.11	Correlation matrix between the radionuclides and physico-chemical parameters.	185
5.12	The elemental concentrations, Radiogenic Heat Production (RHP) and Heat flow (H_f) of the soil samples.	187
5.13	The sampling locations of Athirappilly waterfalls in the present study.	198
5.14	The activity concentrations of radionuclides ^{226}Ra, ^{232}Th, and ^{40}K rock samples in the study region.	200
5.15	Statistical distribution of the three isotopes in the study area	202
5.16	The radiological health hazard indices of the rock samples.	204
5.17	Correlation matrix between the radionuclides and radiological parameters.	212
5.18	The elemental concentrations, Radiogenic Heat Production (RHP) and Heat flow (H_f) of the rock samples	213

5.19	Comparison of the activity concentration of radionuclides in samples of present study with those measured different environs of the world.	221
6.1	Details about the concrete sample moulded along with density.	238
6.2	Qualitative elemental chemical composition (in weight.%.) of the fabricated concretes.	240
6.3	Experimental and theoretical values of LAC for the fabricated concretes.	242
6.4	Experimental and theoretical values of MAC for the fabricated concretes.	245
6.5	Experimental values of HVL and TVL for the selected Energies.	248
6.6	Experimental values of MFP for the selected Energies.	252
6.7	Equivalent atomic numbers of the pure concrete and 20% additives added composites for various energy values ranging from 0.015 to 15 MeV.	256
6.8	G-P energy absorption and exposure build-up factor parameters of the CSZ20 for various energy values ranging from 0.015 to 15 MeV.	258
6.9	G-P energy absorption and exposure build-up factor parameters of the CSN20 for various energy values ranging from 0.015 to 15 MeV.	259
7.1	Components of natural rubber (NR) composites, their contents, function, and suppliers.	275
7.2	Cure characteristics of the samples.	283
7.3	The weight fractions of the elements for the samples.	284
7.4	Experimental, XCOM, and Phy-X values of LAC for NR+$BaWO_4$ composites.	285
7.5	Comparison of the linear attenuation coefficients between the different rubber shields of gamma-rays at 0.662 MeV.	288
7.6	Mass attenuation μ/ρ (cm^2/gm) results for experimental, XCOM, and Phy-X of NR+$BaWO_4$ composites.	290
7.7	G-P energy absorption and exposure build-up factor parameters of the $BaWO_4$ (10 phr) for various energy values ranging from 0.015 to 15 MeV.	301
7.8	G-P energy absorption and exposure build-up factor parameters of the $BaWO_4$ (100 phr) for various energy values ranging from	302

	0.015 to 15 MeV.	
7.9	Equivalent atomic numbers of the $BaWO_4$ doped polymer composites for various energy values ranging from 0.015 to 15 MeV.	304
7.10	R values of the $BaWO_4$ doped polymer composites for various energy values ranging from 0.015 to 15 MeV.	305
8.1	The fabricated samples' nominal compositions and codes.	321
8.2	Examination of the theoretically (Phy-X/PSD) computed LAC of the samples with the experimental values recorded at various γ-ray photon energies.	325
8.3	Examination of the theoretically (Phy-X/PSD) computed MAC of the samples with the experimental values recorded at various γ-ray photon energies.	328
8.4	Comparison of the mass attenuation coefficients between the different shields of gamma-rays at 0.662 MeV(^{137}Cs)	332
8.5	Theoretically (Phy-X/PSD) computed HVL (cm) of the samples with the experimental values recorded at various γ-ray photon energies.	333
8.6	Theoretically (Phy-X/PSD) computed MFP (cm) of the samples with the experimental values recorded at various γ-ray photon energies.	335
8.7	Equivalent atomic numbers (Z_{eq}) of the composites for numerous gamma ray energy levels ranging between 0.015 to 15 MeV (by Phy-X/PSD software).	338
8.8	G-P energy absorption and exposure build-up factor parameters of the WPB4 for various energy values ranging from 0.015 to 15 MeV.	339
8.9	G-P energy absorption and exposure build-up factor parameters of the WPW4 for various energy values ranging from 0.015 to 15 MeV.	340
9.1	Comparison of linear attenuation coefficients for different shields in the present study of gamma rays at 0.662 MeV energy.	353

LIST OF FIGURES

Figure No.	*Tittle*	*Page No.*
1.1	Illustration of the varying penetrating powers of different types of ionizing radiation.	3
1.2	Uranium series (4n+2 series)	9
1.3	Thorium series (4n series)	9
1.4	Actinium series (4n+3 series)	10
1.5	Schematic of the photoelectric effect.	29
1.6	Compton scattering with a free electron.	30
1.7	Pair production interaction.	31
1.8	The three interaction processes for different absorber materials and gamma-ray energies.	32
3.1	Micro-R survey metre.	88
3.2	NaI (Tl) scintillation detector	89
3.3	Block diagram of NaI (Tl) scintillation detector.	90
3.4	HPGe Detector.	92
3.5	Block diagram of HPGe detector	93
3.6	The energy calibration graph.	97
3.7	Efficiency calibration graph.	97
3.8	X-ray diffractometer	100
3.9	Visualization of X-ray diffraction.	101
3.10	X-ray diffractometer components:	102
3.11	XEPOS ED-XRF spectrometer	104
3.12	Components of ED-XRF spectrometer	106
3.13	Field Emission Scanning Electron Microscope (FE-SEM)	108
5.1	The sampling stations of Kuthiran region, Kerala.	141
5.2	Geological formation and rock constituent of the sampling stations.	143
5.3	Contour distributions of radionuclides ^{226}Ra, ^{232}Th and ^{40}K in the study area.	146

5.4	The frequency distribution of the activity concentration of ^{226}Ra, ^{232}Th and ^{40}K.	148
5.5	Calculated values of radium equivalent indices rock the samples.	150
5.6	Calculated values of ambient gamma radiation dose rates (D_{out}) rock the samples.	150
5.7	Correlation between absorbed dose rate and the activity concentrations.	151
5.8	Calculated values of annual effective dose rates (AED) rock the samples.	152
5.9	The distribution of the hazard indices (H_{int} and H_{ext}) in the study area.	153
5.10	The distribution of the Excess Lifetime Cancer Risk (ELCR) in the study area.	154
5.11	The distribution of gamma index and Alpha index in the study	155
5.12	XRD spectra of rock samples of the same grain size of ≤100 μm collected from four sites of the study area.	157
5.13	The elemental concentrations of ^{238}U (in ppm).	160
5.14	The elemental concentrations of ^{232}Th in ppm.	160
5.15	The elemental concentrations of ^{40}K (in %)	161
5.16	The contour representation of Radiogenic heat and Heat flow of the study region.	162
5.17	Radiogenic Heat Production in Kuthiran study region.	163
5.18	Correlation between radionuclides for studied region.	164
5.19	Correlation between concentration of radionuclides and Radiogenic Heat Production (RHP) and for studied region.	165
5.20	Correlation between concentration of HF and RHP and for studied region.	166
5.21	Map indicating the positions of the sampling sites- NH 66 region	169
5.22	The geological map of the research region.	170
5.23	Contour distribution of the three radionuclides in the study area.	173
5.24	Distribution of the three radionuclides in the study area.	175
5.25	The frequency distribution of the activity concentration of	176

	^{226}Ra, ^{232}Th and ^{40}K.	
5.26	Distribution of the Raeq parameter in the study area.	178
5.27	Distribution of the Dout parameter in the study area.	178
5.28	The correlation between the activity concentrations and absorbed dose rates.	179
5.29	The distribution of the annual effective dose equivalent (AED) values.	180
5.30	The distribution of the hazard indices (H_{int} and H_{ext}) in the study area.	181
5.31	The distribution of the Excess Lifetime Cancer Risk (ELCR) in the study area.	182
5.32	The XRD pattern of soil samples collected from Azhinjillam sampling site (sample S-21).	183
5.33	Ternary diagram showing the proportion of clay, silt, and sand of the sampling area.	185
5.34	The elemental concentrations of ^{238}U (in ppm).	188
5.35	The elemental concentrations of ^{232}Th (in ppm).	189
5.36	The elemental concentrations of ^{40}K (in %).	189
5.37	The contour representation of Radiogenic heat and Heat flow of the study region.	190
5.38	Radiogenic Heat Production in NH-66 highway study region.	190
5.39	Correlation between radionuclides for studied region.	191
5.40	Correlation between concentration of radionuclides and Radiogenic Heat Production (RHP) and for studied region.	192
5.41	Correlation between concentration of heat flow and Radiogenic Heat Production (RHP) and for studied region.	193
5.42	Geological map depicting a portion of the study region.	197
5.43	The positioning of sedimentary rock sampling sites within Thrissur district, Kerala.	199
5.44	Activity concentration of the three radionuclides in rock samples in the study area.	201
5.45	The frequency distribution of the activity concentration of ^{226}Ra, ^{232}Th and ^{40}K.	203
5.46	Distribution of the Ra_{eq} parameter in the study area.	205

5.47	Distribution of the D_{out} parameter in the study area.	206
5.48	The correlation between the activity concentrations and absorbed dose rates.	207
5.49	The distribution of the annual effective dose equivalent (AED) values.	208
5.50	The distribution of the hazard indices (H_{int} and H_{ext}) in the study area.	208
5.51	The distribution of the Excess Lifetime Cancer Risk (ELCR) in the study area.	209
5.52	XRD spectra of rock samples of the Athirappilly region of grain size of ≤100 μm	210
5.53	The elemental concentrations of ^{238}U (in ppm).	214
5.54	The elemental concentrations of ^{232}Th (in ppm).	215
5.55	The elemental concentrations of ^{40}K (in %).	215
5.56	The condor representation of Radiogenic heat and Heat flow of the study region.	216
5.57	Radiogenic Heat Production in Athirappilly study region.	217
5.58	Correlation between radionuclides for studied region.	218
5.59	Correlation between concentration of radionuclides and RHP and for studied region.	219
5.60	Correlation between concentration of HF and RHP and for studied region.	220
6.1	Moulded concrete sample of size 10 × 10 × 10 cm^3 (a) and sem images of the moulded concretes with addition of aggregates (b-f).	239
6.2	Density of moulded concrete samples.	240
6.3	The gamma ray spectrum obtained from CSC20 sample.	241
6.4	The experimental results of LAC for moulded samples in selected energies.	243
6.5	Computational and experimental results of LAC by of the moulded concretes with respect to energy.	244
6.6	The experimental results of MAC for moulded samples in selected energies.	246
6.7	Computational and experimental results of MAC of the moulded concretes with respect to energy.	247

6.8	Computational and experimental results of HVL of the moulded concretes with respect to energy.	249
6.9	Computational and experimental results TVL of the moulded concretes with respect to energy.	251
6.10	Computational and experimental results of MFP of the moulded concretes with respect to energy.	253
6.11	Variation of Z_{eff} of the moulded concretes with respect to energy.	254
6.12	Variation of N_{eff} of the moulded concretes with respect to energy.	255
6.13	Variation of atomic numbers (Z_{eq}) of the cement samples with photon energy.	257
6.14	Variation of EABF for concrete and concrete modified with coconut shell powder for different mean free path.	260
6.15	Variation of EABF for concrete modified with Zirconium and Neodymium for different mean free path.	260
6.16	Variation of EABF for concrete modified with Perlite and vermiculite for different mean free path.	261
6.17	Variation of EBF for concrete and concrete modified with coconut shell powder for different mean free path.	262
6.18	Variation of EBF for concrete modified with perlite and vermiculite for different mean free path.	262
6.19	Variation of EBF for concrete modified with Zirconium and Neodymium for different mean free path.	263
6.20	Fast effective removal cross-section (Σ_R) values of the concrete samples.	264
7.1	Diagram with a short description of the experiment setting.	274
7.2	HEXA PLAST Two Roll Mill.	276
7.3	Compression mould hot press.	277
7.4	Density kit with balance	279
7.5	The schematic diagram of the gamma-ray attenuation experimental setup using NaI (Tl) Detector.	280
7.6	The fabricated flexible NR composites with NRBW nanoparticles.	281
7.7	The relationship between torque and vulcanization time on	282

	metal oxide-NR composites	
7.8	Density of the moulded rubber samples.	284
7.9	The experimental LAC value of the NR composites for 662 keV, 1173 keV, and 1332 keV gamma rays.	287
7.10	The linear attenuation coefficient of the studied NR-$BaWO_4$ composites across a continuous energy range.	287
7.11	The experimental MAC value of the NR composites for 662 keV, 1173 keV, and 1332 keV gamma rays.	291
7.12	The mass attenuation coefficient of the studied NR-$BaWO_4$ composites across a continuous energy range.	292
7.13	The experimental HVL value of the NR composites for 662 keV, 1173 keV, and 1332 keV gamma rays.	293
7.14	Half value layer (HVL) as a function of photon energy and $BaWO_4$-content of the samples.	294
7.15	The experimental TVL value of the NR composites for 662 keV, 1173 keV, and 1332 keV gamma rays	294
7.16	Tenth value layer (TVL) as a function of photon energy and $BaWO_4$-content of the samples.	295
7.17	The experimental MFP value of the NR composites for 662 keV, 1173 keV, and 1332 keV gamma rays	296
7.18	Mean free path (MFP) as a function of photon energy and $BaWO_4$-content of the samples.	296
7.19	Atomic cross section (ACS) as a function of photon energy and $BaWO_4$-content of the samples.	298
7.20	Electronic cross section (ECS) as a function of photon energy and $BaWO_4$-content of the samples.	298
7.21	Effective atomic number (Z_{eff}) as a function of photon energy and $BaWO_4$-content of the samples.	299
7.22	Effective electron density (N_{eff})as a function of photon energy and $BaWO_4$-content of the samples.	300
7.23	Equivalent atomic number (Z_{eq})as a function of photon energy and $BaWO_4$-content of the samples.	306
7.24	R values as a function of photon energy for $BaWO_4$-incorparated NR samples	306
7.25	Exposure build-up factors (EABF) against photon energies at	307

	various mfp.	
7.26	Exposure build-up factors (EBF) against photon energies at various mfp.	308
7.27	Conductivity C_{eff} as a function of photon energy and $BaWO_4$-content of the samples.	310
7.28	Fast neutron removal cross-sections of the investigated sample.	311
8.1	FESEM images of composite with of Bismuth and Tungsten oxides.	321
8.2	Schematic design of radiation shielding experimental setup.	322
8.3	Energy spectra of gamma rays obtained from ^{137}Cs source, which attenuated by composites in different concentrations.	324
8.4	The Experimental values of LAC as a function of photon energy for wall paint reinforced with micro WO_3.	326
8.5	The Experimental values of LAC as a function of photon energy for wall paint reinforced with micro Bi_2O_3.	326
8.6	The LAC as a function of photon energy for wall paint reinforced with micro WO_3.	327
8.7	The LAC as a function of photon energy for wall paint reinforced with micro Bi_2O_3.	327
8.8	The Experimental values of MAC as a function of photon energy for wall paint reinforced with micro WO_3.	329
8.9	The Experimental values of MAC as a function of photon energy for wall paint reinforced with micro Bi_2O_3.	330
8.10	The MAC as a function of photon energy for wall paint reinforced with micro Bi_2O_3.	330
8.11	The MAC as a function of photon energy for wall paint reinforced with micro WO_3.	331
8.12	The experimental and theoretical values of HVL as a function of photon energy for wall paint reinforced with micro Bi_2O_3 and WO_3.	334
8.13	MFP as a function of photon energy for wall paint reinforced with micro Bi_2O_3 and WO_3.	336
8.14	Z_{eff} as a function of photon energy for wall paint reinforced with micro Bi_2O_3 and WO_3.	337
8.15	N_{eff} as a function of photon energy for wall paint reinforced	337

	with micro Bi_2O_3 and WO_3.	
8.16	Energy build-up factors (EBF) against photon energies at various mean free paths of wall paint composites with 5% to 20% loading of Bi_2O_3.	341
8.17	Energy build-up factors (EBF) against photon energies at various mean free paths of wall paint composites with 5% to 20% loading of WO_3.	341
8.18	Energy absorption build-up factors (EABF) against photon energies at various mean free paths of wall paint composites with 5% to 20% loading of Bi_2O_3.	342
8.19	Energy absorption build-up factors (EABF) against photon energies at various mean free paths of wall paint composites with 5% to 20% loading of WO_3	342
8.20	The variability in effective conductivity (C_{eff}) in paint samples	344
8.21	The effective removal cross-section values of the fabricated wall paint samples.	345

PUBLICATIONS

As First author

1. Vishnu C V and Antony Joseph, Determination of natural radioactivity, hazard parameters and physico-chemical properties of soils from Palakkad-Thrissur district, Kerala, India. *Materials Today: Proceedings*, 55(2022), 127–134. https://doi.org/10.1016/j.matpr.2021.12.548.

2. Vishnu C V and Antony Joseph. Evaluation of Natural Radioactivity Levels and Exhalation rate of ^{222}Rn and ^{220}Rn in the Soil Samples from the Kuthiran Hills, Kerala, India. *Journal of Nuclear Physics, Material Sciences, Radiation and Applications*, 9(2), (2022) 229–239. https://doi.org/10.15415/jnp.2022.92034.

3. Vishnu, C. V., Antony Joseph., Anju, K. (2023). Evaluation of the gamma radiation shielding characteristics of epoxy wall paint modified with micro sized Bi_2O_3 and WO_3. *Materials Today: Proceedings*, *xxxx.* https://doi.org/10.1016/j.matpr.2023.03.309.

4. Vishnu C. V and Antony Joseph. Gamma-ray shielding analysis on natural rubber composites fortified with barium tungstate ($BaWO_4$). *Radiation Physics and Chemistry*, *216* (October 2024), 111389. https://doi.org/10.1016/j.radphyschem.2023.111389.

5. Vishnu C V. Antony Joseph, Vineethkumar V and Shimod K P, The dissemination of naturally occurring radionuclides in soil samples from urban regions along the National Highway in Kerala, India. (Accepted in the Journal of Discover applied Physics).

6. Vishnu C. V and Antony Joseph, Assessment of natural radioactivity and monitoring of radiological hazards in construction materials from Kerala, India. Indian Journal of Pure & Applied Physics. Vol. 62, August 2024, pp. 700-711. DOI: 10.56042/ijpap.v62i8.7746

Conference Proceedings

1. Vishnu C V and Antony Joseph, Assessment of environmental radioactivity levels and associated radiogenic heat production in rock samples at locations spread along Thrissur-Palakkad highway region, Kerala, India. Proceedings of the DAE Symp. on Nucl. Phys. 65 (2021).

2. Vishnu C V, Antony Joseph, T A Sajith, and Sabu Thomas, Design of Flexible Gamma Ray Shielding Material Composite of Natural Rubber with Coconut Shell/Clay Powder. Proceedings of the DAE Symp. on Nucl. Phys. 64 (2019).

3. Vishnu C V and Antony Joseph, Gamma ray attenuation studies of cement pastes modified with naturally available additives. Proceedings of the DAE Symp. on Nucl. Phys. V. 63 (2018).

As a Co-author

1. P.V. Thulasi, Antony Joseph, K.M. Varier, Somashekarappa H.M., Vinayak Anand Kamat, **Vishnu C.V.**, Coherent scattering cross sections of some rare earth compounds at small angles below 10° for 59.54 keV gamma rays. Radiation Physics and Chemistry, Vol. 202, 2023,110539, ISSN 0969-806X, https://doi.org/10.1016/j.radphyschem.2022.110539.

2. Nafeesa Baby, T., Vineethkumar, V., Shimod, K., **Vishnu C.V**, and Jayadevan, S. (2022). Heavy metal contamination in water sources of Thaliparamba municipality, Kerala, India. Radiation Protection and Environment, 45(1), 54. https://doi.org/10.4103/rpe.rpe_25_21.

3. Shimod, K. P., Vineethkumar, V., Prasad, T. K., Jayapal, G., and **Vishnu, C. V.** (2022). Radiological threat to the human in the context of alarming urbanization: a geographical enquiry on concentration of radionuclides in building materials used in Kannur district, Kerala, India. Journal of Radioanalytical and Nuclear Chemistry, 331(10), 4323–4333. https://doi.org/10.1007/s10967-022-08488-7.

4. Vinodkumar, T.; Vineethkumar, V.; **Vishnu C. V**.; Sayooj, V. V.; Prakash, V., Assessment of heavy metal enrichment and contamination in the wetlands of Kannur district, Kerala. Radiation Protection and Environment 44(3&4):p 152-160, Jul–Dec 2021. | DOI: 10.4103/rpe.rpe_22_21.

Papers Presented on National / International Conferences (oral/poster)

1. Vishnu C V. and Antony Joseph, The Gamma ray attenuation studies on concrete reinforced with coconut Shells, in the 62nd DAE-BRNS symposium on Nuclear Physics held at Thapar institute of Engineering and Technology, Patiala, Punjab Dec.15,2017.

2. Vishnu C V and Antony Joseph, Gamma Ray Attenuation Studies of Cement Pastes Modified with Naturally Available Additives, in the 63rd DAE-BRNS symposium held on Nuclear Physics. BARC Mumbai, Maharashtra. Dec.6, 2018.

3. Vishnu C V. and Antony Joseph, Utilization of Perlite and Vermiculite in Cement composites for gamma ray shielding applications, in the 31st Kerala Science Congress, held at Fathima College, Kollam, Kerala. Jan.13, 2019.

4. Vishnu C V, Antony Joseph, Sabu Thomas and Sajith T S, Design of Flexible Gamma Ray Shielding Material Composite of Natural Rubber with Coconut Shell/Clay Powder, in 64th DAE-BRNS symposium on Nuclear Physics Lucknow, Uttar Pradesh, Dec.13, 2019.

5. Vishnu C V., Antony Joseph, Sabu Thomas and Sajith T S, Influence of coconut shell powder contents on mechanical and gamma ray attenuation properties on natural rubber composites, In the International conference on Theoretical and experimental Physics (ICTEP-2020), held at Farook college, Kerala on January 13, 2020.

6. Vishnu C V. and Antony Joseph, Determination of Natural Radioactivity, Hazard Parameters and Physico-Chemical Properties of Soils from Palakkad-Thrissur District, Kerala, India., in the 9th National Conference on Condensed Matter Physics and Applications (CMPA-2021). Department Of Physics, Manipal Institute of Technology, Manipal, Karnataka, Dec 27, 2021.

7. Vishnu C V. and Antony Joseph, Evaluation of Natural Radioactivity Levels and Exhalation rate of ^{222}Rn and ^{220}Rn in the soil samples from the Kuthiran Hills, Kerala, India, in the Online International Conference on Recent Trends in Nuclear Physics. Chitkara University, Dharamshala, Himachal Pradesh. Oct 13-16, 2022.

8. Vishnu C V. and Antony Joseph, Assessment of Environmental radioactivity levels and associated radiogenic heat production in rock samples at locations spread along Thrissur-Palakkad highway region, Kerala, India., Held on the 65th DAE-BRNS symposium on Nuclear Physics, DAE Convention Centre, Anushaktinagar, Mumbai, Maharashtra. Dec. 18-23, 2022.

9. Vishnu C V. and Antony Joseph, Assessment of natural radioactivity levels in rocks of Kuthiran Tunnel and hills, Kerala, India. in the 34th Kerala Science Congress, KSCSTE, Thiruvananthapuram, Kerala, Dec.27-29, 2022.

10. Vishnu C V., Antony Joseph, Vineethkumar V and Shimod K P., Radiological assessment of urban soil in the National highway zone (NH-66) corridor of Kerala state, India., in the 23rd National Symposium on Radiation Physics (NSRP), Mysuru University January 19-21, 2023.

ABBREVIATIONS

PET	-	Positron emission tomography
PE	-	Photoelectric effect
$A_{Ra,}$ A_{Th}, A_K	-	Activity concentrations of Radium, Thorium and Potassium
C_U, C_{Th}, C_K	-	Elemental concentrations of Radium, Thorium and Potassium
BDL	-	Beyond detectable limit
MDA	-	Minimum Detectable activity
Ra_{eq}	-	Radium equivalent
AED	-	Annual effective dose equivalents
AED_{ind}	-	Indoor Annual Effective Dose Equivalents
AED_{out}	-	Outdoor Annual effective dose equivalents
ELCR	-	Excess lifetime cancer risk
$ELCR_{ind}$	-	Indoor Excess lifetime cancer risk
$ELCR_{out}$	-	Outdoor Excess lifetime cancer risk
H_{int}	-	Internal Hazard index
H_{ext}	-	External Hazard Index
D_{ind}	-	Indoor absorbed dose rate
D_{out}	-	Outdoor absorbed dose rate
I_α	-	Alpha index
$I\gamma$	-	Gamma index
AGDE	-	Annual Gonadal dose equivalent
DL	-	Duration of Lifetime
RHP	-	Radiogenic Heat Production
H_f	-	Heat Flow
MNT	-	Mannuthy
VGY	-	Vengassery

MUD	-	Mudicode
PNY	-	Pananchery PNY
PTK	-	Pattikadu
CHM	-	Chuvannamannu
VKP	-	Vazhukumpara
KDT	-	Kuthiran Temple
IMB	-	Irumbupalam Bridge
VMP	-	Vaniyampara
KTN	-	Kuthiran tunnel
KNB	-	Kannanbra
KGP	-	Kurangupara
PVC	-	Poovanchira
PTP	-	Pattathipara (PTP)
GPS	-	Geographical positioning system
UNSCEAR	-	United Nations Scientific Committee on the Effects of Atomic Radiation
ICRP	-	International Commission on Radiological Protection
EC	-	European Commission
TENORM	-	Technologically Enhanced Natural Radioactive Materials
NORM	-	Naturally Occurring Radioactive Materials
HBRA	-	High Background Radiation Areas.
LBRA	-	Low Background Radiation Areas.
ppm	-	parts per million
MAC	-	Mass attenuation coefficient
LAC	-	Linear attenuation coefficient
HVL	-	Half Value Layer
TVL	-	Tenth Value Layer
MFP	-	Mean Free Path

ACS	-	Atomic cross section
ECS	-	Electronic cross section
Neff	-	Effective atomic density
Zeff	-	Effective atomic number
G-P	-	Geometric Progression
EBF	-	Exposure build-up factor
EABF	-	Exposure absorption build-up factor
Ceff	-	Effective conductivity
FNRC	-	Fast Neutron Removal Cross Section
XRD	-	Xray diffraction.
XRF	-	Xray fluorescence.
SEM	-	Field Emission Scanning Electron Microscopy
EDAX	-	Energy Dispersive X-ray Analysis
PSD	-	Photon Shielding and Dosimetry
CS	-	Ordinary concrete
CSC10	-	Ordinary concrete+10% Coconut shell powder
CSC20	-	Ordinary concrete+20% Coconut shell powder
CSP10	-	Ordinary concrete+10% Perlite
CSP20	-	Ordinary concrete+20% Perlite
CSV10	-	Ordinary concrete+10% Vermiculite
CSV20	-	Ordinary concrete+20% Vermiculite
CSZ10	-	Ordinary concrete+10% Zirconium Oxide
CSZ20	-	Ordinary concrete+20% Zirconium Oxide
CSN10	-	Ordinary concrete+10% Neodymium Oxide
CSN20	-	Ordinary concrete+10% Neodymium Oxide
phr	-	parts per hundred
TMQ	-	2,2,5 4-Trimethyl-1,2 Dihydroquinoline

CBS	-	N-Cyclohexyl-2-benzothiazole sulfonamide.
EMFC	-	Electro Magnetic Force Compensation.
Pure NR	-	Pure Natural rubber
NRBW10	-	Natural rubber with 10 phr Barium Tungstate.
NRBW20	-	Natural rubber with 20 phr Barium Tungstate.
NRBW40	-	Natural rubber with 40 phr Barium Tungstate.
NRBW80	-	Natural rubber with 80 phr Barium Tungstate.
NRBW100	-	Natural rubber with 100 phr Barium Tungstate.
WP	-	Pure Wall paint
WPB1	-	Wall paint with 5% Bi_2O_3
WPB2	-	Wall paint with 10% Bi_2O_3
WPB3	-	Wall paint with 15% Bi_2O_3
WPB4	-	Wall paint with 20% Bi_2O_3
WPW1	-	Wall paint with 5% WO_3
WPW2	-	Wall paint with 10% WO_3
WPW3	-	Wall paint with 15% WO_3
WPW4	-	Wall paint with 20% WO_3

INVESTIGATIONS ON THE NATURAL RADIOACTIVITY AND GAMMA ATTENUATION PROPERTIES OF BUILDING MATERIALS

Abstract

Natural radioactivity refers to the spontaneous decay of unstable atomic nuclei found in nature, releasing energy in the form of radiation. This phenomenon is primarily associated with naturally occurring radionuclides such as uranium (^{238}U), thorium (^{232}Th), and potassium (^{40}K). These radionuclides are ubiquitous in the Earth's crust, present in varying concentrations in rocks, soil, water, and even in the human body. The radiations emitted include alpha particles, beta particles, and gamma rays, with gamma rays being the most penetrating and potentially harmful to living organisms. Studying natural radioactivity is crucial for understanding the radiation levels in different environments, which can vary significantly based on the geological and geographical factors. By measuring and analysing natural radioactivity, scientists can assess potential radiological hazards, ensuring that environments remain safe for human in habitation and associated activities. Radiogenic heat is the thermal energy produced by the natural decay of the radioactive isotopes within the Earth's interior. The primary contributors to this heat generation are long-lived radionuclides. As these isotopes decay, they release particles and energy, a portion of which is converted into heat. The distribution of radiogenic heat-producing elements within the lithosphere is crucial for understanding crustal temperature distribution and the mechanical strength of the lithosphere. Combined determinations of surface heat flow and radiogenic heat production (RHP) provide basic information about the thermal field and the structure of the Earth's lithosphere.

The medical and nuclear power, research fields are well known for their increased dependency on ionizing radiation for their essential services. As well as the hazards and risks posed by radiation. Significant chromosomal abnormalities and carcinogenic effects may be caused by high doses of radiation. Radiation damage is

dependent on an organ's sensitivity, as well as the quantity and type of radiation received. Gamma rays, a form of electromagnetic radiation with high energy and deep penetration capabilities, can cause serious health effects, including DNA damage and cancer. Therefore, shielding against gamma rays is essential in various settings. Gamma ray shielding involves using materials that can absorb or attenuate gamma radiation, protecting people and sensitive equipment from the exposure. Effective gamma ray shielding materials include lead, concrete, polymers, glasses, and specialized composites containing high-density elements such as bismuth (Bi), tungsten (W), and certain metal oxides. Recent research focuses on developing innovative shielding materials that not only provide superior radiation protection but also maintain desirable mechanical and physical properties.

On the basis of these motivations, the major objectives of this thesis are detailed below.

- The first objective is the comprehensive measurement of natural radioactivity, focusing on rock and soil samples from specified regions. This includes analyzing radiogenic heat production and associated radiological parameters, such as radium equivalent activity, external hazard index, and annual effective dose, to assess the potential health risks and ensure the public safety.
- The second objective is the development of optimized gamma ray shielding materials with characteristics such as low cost, high flexibility, and at the same time sufficient hardness and durability. Different compositions of shielding materials, particularly epoxy-based coatings, are evaluated for their effectiveness in attenuating gamma radiation.
- The third objective involves utilizing numerical simulation techniques to predict the gamma attenuation properties of various shielding composites and validating the results through experimental observations to ensure accuracy and reliability.

This thesis is an attempt to accomplish the set of objectives mentioned above. The thesis comprised of seven chapters. Chapter 1 provides an overview of natural radioactivity, gamma radiation interactions with matter, and materials used for radiation shielding. Chapter 2 offers a review of existing literature, discussing the previous studies and the current state of knowledge in these fields. Chapter 3 details the experimental techniques and methodologies employed in this research. Chapter 4 delves into the theoretical framework underpinning the study. Chapters 5 to 8 present the results and discussions, focusing on the measurement of natural radioactivity in soil and rock samples and the development and characterization of gamma ray shielding materials. Finally, Chapter 9 provides the general conclusion and offers recommendations for future research which are led to practical applications.

The results presented in this thesis are obtained from the first-time measurements in many unexplored areas in the state of Kerala, India. Nationally and internationally, the present results are significant as they contribute to the attempts initiated to map the natural radiation levels globally.

നിർമ്മാണ സാമഗ്രികളുടെ പ്രകൃതിദത്ത റേഡിയോ ആക്റ്റിവിറ്റി, ഗാമ ശോഷണ കഴിവുകൾ എന്നിവയെക്കുറിച്ചുള്ള അന്വേഷണങ്ങൾ

സംഗ്രഹം

പ്രകൃതിയിൽ കാണപ്പെടുന്ന അസ്ഥിര ആറ്റോമിക് അണുകേന്ദ്രങ്ങളുടെ സ്വതസിദ്ധമായ ക്ഷയം, വികിരണത്തിന്റെ രൂപത്തിൽ ഊർജ്ജം പുറത്തുവിടുന്നതിനെയാണ് സ്വാഭാവിക റേഡിയോ ആക്ടിവിറ്റിയെന്ന പറയുന്നത്. ഈ പ്രതിഭാസം പ്രാഥമികമായി യുറേനിയം-238, തോറിയം-232, പൊട്ടാസ്യം-40 തുടങ്ങിയ പ്രകൃതിദത്തമായ റേഡിയോ അണുകേന്ദ്രങ്ങളുമായി ബന്ധപ്പെട്ടിരിക്കുന്നു. ഈ റേഡിയോ അണുകേന്ദ്രങ്ങൾ ഭൂമിയുടെ പുറംതോടിൽ സർവ്വവ്യാപിയാണ്. പാറകൾ, മണ്ണ്, വെള്ളം, കൂടാതെ മനുഷ്യശരീരത്തിൽ പോലും വ്യത്യസ്ത സാന്ദ്രതകളിൽ കാണപ്പെടുന്നു. പുറത്തുവിടുന്ന വികിരണങ്ങളിൽ ആൽഫ കിരണങ്ങൾ, ബീറ്റാ കിരണങ്ങൾ, ഗാമാ കിരണങ്ങൾ എന്നിവ ഉൾപ്പെടുന്നു, ജീവജാലങ്ങളിൽ ഏറെ തുളച്ചു കയറുന്നതും ദോഷകരവുമായ കിരണങ്ങൾ ആണ് ഗാമ കിരണങ്ങൾ. ഭൂമിശാസ്ത്രപരമായ ഘടകങ്ങളെ അടിസ്ഥാനമാക്കി ഏറെ വ്യത്യാസപ്പെട്ടിരിക്കാവുന്ന വിവിധ പരിതസ്ഥിതികളിലെ വികിരണതോത് മനസ്സിലാക്കുന്നതിന് പ്രകൃതിദത്ത റേഡിയോ ആക്ടിവിറ്റി പഠിക്കുന്നത് നിർണായകമാണ്.

പ്രകൃതിദത്ത റേഡിയോ ആക്ടിവിറ്റി അളക്കുന്നതിലൂടെയും വിശകലനം ചെയ്യുന്നതിലൂടെയും, ശാസ്ത്രജ്ഞർക്ക് കിരണവീജ്ഞാനം അപകടസാധ്യതകൾ വിലയിരുത്താനും കഴിയും, ആവാസവ്യവസ്ഥയിലും അനുബന്ധ പ്രവർത്തനങ്ങളിലും ചുറ്റുപാടുകൾ മനുഷ്യർക്ക് സുരക്ഷിതമായി തുടരുന്നുവെന്ന് ഉറപ്പാക്കുകയും ചെയ്യുന്നു. ഭൂമിയുടെ അന്തർഭാഗത്തുള്ള റേഡിയോ ആക്ടീവ് ഐസോടോപ്പുകളുടെ സ്വാഭാവിക ക്ഷയം മൂലം ഉണ്ടാകുന്ന താപ ഊർജ്ജമാണ് റേഡിയോജനിക് ഹീറ്റ്. ഈ താപ ഉൽപാദനത്തിന്റെ പ്രാഥമിക സംഭാവന ദീർഘകാല റേഡിയോ അണുകേന്ദ്രങ്ങളാണ്. ഈ ഐസോടോപ്പുകൾ ക്ഷയിക്കുമ്പോൾ, അവ കണങ്ങളും ഊർജ്ജവും പുറത്തുവിടുന്നു, അതിന്റെ ഒരു ഭാഗം താപമായി മാറുന്നു. ശിലാമണ്ഡലത്തിനുള്ളിലെ റേഡിയോജനിക് താപം ഉൽപ്പാദിപ്പിക്കുന്ന മൂലകങ്ങളുടെ വിതരണം, പുറംതോടിന്റെ താപനില വിതരണവും ശിലാമണ്ഡലത്തിന്റെ യാന്ത്രികമായ ശക്തിയും മനസ്സിലാക്കാൻ നിർണായകമാണ്. ഉപരിതല താപ പ്രവാഹത്തിന്റെയും റേഡിയോജനിക് താപ പ്രവാഹത്തിന്റെയും (RHP) സംയോജിത നിർണ്ണയം താപ മണ്ഡലത്തെക്കുറിച്ചും ഭൂമിയുടെ ശിലാമണ്ഡലത്തിന്റെ ഘടനയെക്കുറിച്ചും അടിസ്ഥാന വിവരങ്ങൾ നൽകുന്നു.

വൈദ്യശാസ്ത്രം, അണുശക്തി എന്നീ ഗവേഷണ മേഖലകൾ അവയുടെ അവശ്യ സേവനങ്ങൾക്കായി അയോണൈസിംഗ് വികിരണത്തെ കൂടുതലായി ഉപയോഗപ്പെടുത്തുന്നു. എന്നിരുന്നാലും ഉയർന്ന ഊർജ്ജവും കൂടിയ അളവിലുള്ള, ആഴത്തിലുള്ള നുഴഞ്ഞുകയറ്റ ശേഷിയുള്ള വൈദ്യുതകാന്തിക വികിരണത്തിന്റെ ഒരു രൂപമായ ഗാമ വികിരണം ക്രോമാസോം അസാധാരണത്വം, ഡി എൻ എ കേടുപാടുകൾ, അർബുദം, എന്നിവ ഉൾപ്പെടെ ഗുരുതരമായ ആരോഗ്യ പ്രത്യാഘാതങ്ങൾ ഉണ്ടാക്കും ആയതിനാൽ, വിവിധ ക്രമീകരണങ്ങളിൽ ഗാമാ കിരണങ്ങൾക്കെതിരായ സംരക്ഷണം അത്യാവശ്യമാണ്. ഗാമാ വികിരണം ആഗിരണം ചെയ്യാനോ, ദുർബലമാക്കാനോ കഴിയുന്ന പദാർത്ഥങ്ങളാൽ നിർമ്മിക്കുന്ന ഗാമാ കിരണ കവചം, ആളുകളെയും സെൻസിറ്റീവ് ഉപകരണങ്ങളെയും വികിരണ സമ്പർക്കത്തിൽ നിന്ന് സംരക്ഷിക്കുന്നു.

ഈയം, കോൺക്രീറ്റ്, രാസസംയുക്തങ്ങൾ, ഗ്ലാസുകൾ, ബിസ്മത്ത് (Bi), ടങ്സ്റ്റൺ (W), ചില ലോഹ ഓക്സൈഡുകൾ തുടങ്ങിയ ഉയർന്ന സാന്ദ്രത മൂലകങ്ങൾ അടങ്ങിയ പ്രത്യേക

സംയുക്തങ്ങൾ ഫലപ്രദമായ കിരണ കവച സാമഗ്രികളിൽ ഉൾപ്പെടുത്തുന്നു. മികച്ച വികിരണ സംരക്ഷണം മാത്രമല്ല, അഭികാമ്യമായ ഭൗതിക യാന്ത്രിക കഴിവുകൾ നിലനിർത്തുകയും ചെയ്യുന്ന നൂതനമായ കവച സാമഗ്രികൾ വികസിപ്പിക്കുന്നതിൽ സമീപകാല ഗവേഷണങ്ങൾ ശ്രദ്ധ കേന്ദ്രീകരിക്കപ്പെടുന്നുണ്ട്. ഈ പ്രചോദനങ്ങളുടെ അടിസ്ഥാനത്തിൽ, ഈ പ്രബന്ധത്തിന്റെ പ്രധാന ലക്ഷ്യങ്ങൾ താഴെ വിശദമായി പ്രതിപാദിക്കുന്നു.

- നിർദ്ദിഷ്ട പ്രദേശങ്ങളിൽ നിന്നുള്ള പാറയുടെയും മണ്ണിന്റെയും സാമ്പിളുകളിൽ ശ്രദ്ധ കേന്ദ്രീകരിച്ച് പ്രകൃതിദത്ത റേഡിയോ ആക്ടിവിറ്റിയുടെ സമഗ്രമായ അളവെടുപ്പാണ് ആദ്യ ലക്ഷ്യം. ആരോഗ്യപരമായ അപകടസാധ്യതകൾ വിലയിരുത്തുന്നതിനും പൊതു സുരക്ഷ ഉറപ്പാക്കുന്നതിനുമായി റേഡിയോജനിക് താപ ഉൽപാദനവും അനുബന്ധ കിരണവീര്യജ്ഞാന അളവുകോലുകളുമായ റേഡിയം തുല്യമായ പ്രവർത്തനം, ബാഹ്യ അപകട സൂചിക, ഫലപ്രദമായ വാർഷിക തോത് എന്നിവ വിശകലനം ചെയ്യുന്നത് ഇതിൽ ഉൾപ്പെടുന്നു.
- കുറഞ്ഞ ചെലവ്, ഉയർന്ന വഴക്കം, അതേ സമയം മതിയായ കാഠിന്യം, ഈട് എന്നിവ പോലുള്ള സവിശേഷതകളുള്ള ഉത്തമീകരിക്കുന്ന ഗാമാ കിരണ കവചങ്ങളുടെ വികസനമാണ് രണ്ടാമത്തെ ലക്ഷ്യം. കവചങ്ങളുടെ വ്യത്യസ്ത ഘടനകൾ, പ്രത്യേകിച്ച് പശിമയുള്ള കവചങ്ങൾ, ഫലപ്രദമായ രീതിയിൽ ഗാമാ വികിരണം കുറയ്ക്കുന്നതിനായി പ്രയോജനപ്പെടുത്തുന്നു.
- മൂന്നാമത്തെ ലക്ഷ്യം, വിവിധ കവച സംയുക്തങ്ങളുടെ ഗാമാ ശോഷണ കഴിവ് പ്രവചിക്കാൻ സംഖ്യാ സിമുലേഷൻ സാങ്കേതികത്വം ഉപയോഗപ്പെടുത്തുകയും കൃത്യതയും വിശ്വാസ്യതയും ഉറപ്പുവരുത്തുന്നതിനായി പരീക്ഷണ നിരീക്ഷണങ്ങളിലൂടെ ഫലങ്ങൾ സാധൂകരിക്കുകയും ചെയ്യുന്നു.

ഈ പ്രബന്ധം മുകളിൽ സൂചിപ്പിച്ച ഒരു കൂട്ടം ലക്ഷ്യങ്ങൾ സാക്ഷാത്കരിക്കാനുള്ള ശ്രമമാണ്, പ്രബന്ധത്തിൽ ഒൻപത് അധ്യായങ്ങൾ ഉൾക്കൊള്ളുന്നു.

അദ്ധ്യായം 1 സ്വാഭാവിക റേഡിയോ ആക്ടിവിറ്റി, ദ്രവ്യവുമായുള്ള ഗാമാ റേഡിയേഷൻ ഇടപെടലുകൾ, വികിരണങ്ങളുടെ കവചനിർമ്മാണത്തിനായി ഉപയോഗിക്കുന്ന വസ്തുക്കൾ എന്നിവയുടെ ഒരു അവലോകനം നൽകുന്നു. അധ്യായം 2 നിലവിലുള്ള ഗവേഷണത്തിന്റെ അവലോകനം വാഗ്ദാനം ചെയ്യുന്നു, മുൻ പഠനങ്ങളും ഈ മേഖലകളിലെ അറിവിന്റെ നിലവിലെ അവസ്ഥയും ചർച്ചചെയ്യുന്നു.അധ്യായം 3 ഈ ഗവേഷണത്തിൽ ഉപയോഗിച്ചിരിക്കുന്ന പരീക്ഷണാത്മക സാങ്കേതികതകളും രീതിശാസ്ത്രങ്ങളും വിശദീകരിക്കുന്നു. അധ്യായം 4 പഠനത്തിന് അടിവരയിടുന്ന സൈദ്ധാന്തിക ചട്ടക്കൂട് പരിശോധിക്കുന്നു. 5 മുതൽ 8 വരെയുള്ള അധ്യായങ്ങൾ ഫലങ്ങളും ചർച്ചകളും അവതരിപ്പിക്കുന്നു, മണ്ണിന്റെയും പാറയുടെയും സാമ്പിളുകളിലെ സ്വാഭാവിക റേഡിയോ ആക്റ്റിവിറ്റി അളക്കുന്നതിലും ഗാമാ വികിരണ കവച സാമഗ്രികളുടെ വികസനത്തിലും സ്വഭാവത്തിലും ശ്രദ്ധ കേന്ദ്രീകരിക്കുന്നു. അവസാനമായി, അധ്യായം 9 പൊതുവായ നിഗമനം നൽകുകയും പ്രായോഗിക പ്രയോഗങ്ങളിലേക്ക് നയിക്കുന്ന ഭാവി ഗവേഷണത്തിനുള്ള ശുപാർശകൾ വാഗ്ദാനം ചെയ്യുന്നു.

ഈ ഗവേഷണ പ്രബന്ധത്തിൽ അവതരിപ്പിച്ച ഫലങ്ങൾ, ഇന്ത്യയിലെ കേരളത്തിലെ പര്യവേക്ഷണം ചെയ്യപ്പെടാത്ത പല പ്രദേശങ്ങളിലും ആദ്യമായി നടത്തിയ പരീക്ഷണ നീരീക്ഷണങ്ങളിൽ നിന്നാണ് ലഭിച്ചത്. ദേശീയമായും അന്തർദേശീയമായും, ആഗോളതലത്തിൽ പ്രകൃതിദത്ത വികിരണത്തിന്റെ തോത് മാപ്പ് ചെയ്യുന്നതിനുള്ള ശ്രമങ്ങൾക്ക് സംഭാവന നൽകുന്നതിനാൽ നിലവിലെ ഫലങ്ങൾ പ്രാധാന്യമർഹിക്കുന്നു.

PREFACE

Natural radioactivity is a ubiquitous phenomenon that originates from the spontaneous decay of unstable atomic nuclei found in nature. This process releases energy in the form of radiation, which includes alpha particles, beta particles, and gamma rays. Among these, gamma rays are the most penetrating and pose potential health risks to living organisms. The radionuclides primarily responsible for natural radioactivity include Radium-226 (^{226}Ra), Thorium-232 (^{232}Th), and Potassium-40 (^{40}K). These elements are pervasive in the Earth's crust, varying in concentration across different geological and geographical regions. Understanding and analysing these variations is critical for evaluating environmental radiation levels and their potential radiological hazards. The insights derived from such studies enable us to take appropriate precautions to safeguard human health and ensure that environments remain safe for habitation and activities.

One significant aspect of natural radioactivity is radiogenic heat, which is the thermal energy produced as a result of radioactive decay. The long-lived radionuclides in the Earth's crust and mantle contribute substantially to this heat generation. The distribution of radiogenic heat-producing elements influences surface heat flow and crustal temperature distribution, making it a subject of interest for geophysicists and environmental scientists. An in-depth understanding of this phenomenon not only enriches our knowledge of Earth's thermal history but also has implications for geological and geothermal studies.

Despite the indispensable role of radiation in various fields, excess exposure to ionizing radiation poses serious health risks, the most significant being cancer. In regions like Kerala, India, the incidence of cancer is alarmingly high and increasing year by year. While lifestyle factors undoubtedly contribute to this trend, the role of environmental radioactivity must be quantified and understood. This is particularly important as individuals spend a considerable amount of time indoors, where radiations from building materials—floors, walls, and roofs—can contribute significantly to daily radiation exposure through ingestion and inhalation. This

highlights the importance of assessing radiation levels in building materials, which, in Kerala, predominantly consist of rocks, laterite, and bricks sourced from local geological formations. In the initial phase of this research, we focused on evaluating the natural radioactivity in raw materials such as rocks and soils from previously unexplored geological regions in Kerala, specifically in Thrissur, Palakkad, Malappuram, and Kozhikode districts.

While the harmful effects of ionizing radiation are well-documented, its beneficial applications in fields such as medicine, energy, and industrial processes cannot be overlooked. Radiation is indispensable in medical diagnosis and treatment, power generation, non-destructive testing, and scanning. This necessitates the development of effective shielding materials to ensure safety in various radiation-related applications. Shielding materials must be optimized for specific requirements based on the type and energy of radiation involved. With this motivation, the latter part of our research focused on the development of innovative radiation shielding materials. We explored materials based on concrete, epoxy paints, and rubber, incorporating special additives to enhance their gamma-ray attenuation properties.

The primary objectives of this research were designed to address both these critical areas. The first objective was to conduct a comprehensive study of natural radioactivity levels in selected regions of Kerala. This included analysing the activity concentrations of ^{226}Ra,^{232}Th and ^{40}K in rock and soil samples and evaluating associated radiological parameters such as radium equivalent activity, annual effective dose, absorbed dose rate, and hazard indices. Furthermore, the study extended to quantifying radiogenic heat production and heat flow to gain insights into the thermal implications of natural radioactivity. The second objective was the development and evaluation of gamma-ray shielding materials. This involved the fabrication of concrete bricks, epoxy paint composites, and natural rubber composites, each modified with additives to optimize their shielding effectiveness. The performance of these materials was analyzed using both experimental techniques and numerical simulations.

This thesis is structured into nine chapters, each building upon the preceding one to provide a coherent narrative of the research undertaken:

Chapter 1: Introduction- This chapter provides an overview of natural radioactivity, including the mechanisms by which gamma radiation interacts with matter. It also introduces the significance of radiation shielding and the materials commonly used for this purpose. The chapter establishes the context and motivation for the research and outlines the key objectives.

Chapter 2: Literature Review- A comprehensive review of existing literature is presented in this chapter, focusing on natural radioactivity measurements in rocks and soils, with particular emphasis on studies conducted in Kerala and other parts of the world. Additionally, the chapter explores previous research on gamma-ray shielding materials, highlighting the current status of developments in this field and identifying research gaps addressed in the present study.

Chapter 3: Methodology and Experimental Techniques- This chapter details the experimental techniques and methodologies employed in the research. It includes descriptions of gamma-ray spectroscopy, sample preparation, and measurement protocols. Theoretical backgrounds for radiological and shielding parameter calculations are also discussed, providing a solid foundation for the subsequent chapters.

Chapter 4: Radiological Parameters and Gamma Attenuation- The various radiological parameters used to assess radiation hazards are discussed in this chapter. These include radium equivalent activity, external and internal hazard indices, and the absorbed dose rate. Additionally, the chapter introduces gamma attenuation parameters crucial for evaluating the effectiveness of shielding materials, such as linear and mass attenuation coefficients.

Chapter 5: Measurement of Natural Radioactivity and Radiogenic heat- This chapter presents the results of gamma-ray spectroscopy measurements carried out to estimate the activity concentrations of ^{226}Ra,^{232}Th and ^{40}K in samples collected from

various locations in Kerala. Specific sites include regions near the Thrissur-Palakkad highway, urban areas along NH-66, and the Athirappilly-Vazhachal Waterfalls. Radiological parameters are analysed to assess potential health risks, and radiogenic heat production is evaluated to understand its implications for surface heat flow.

Chapter 6: Development of Concrete-Based Shielding Materials- The development of concrete bricks reinforced with additives such as coconut shell powder, perlite, vermiculite, and oxides of zirconium and neodymium is discussed in this chapter. The gamma-ray attenuation properties of these materials are evaluated, and the results are compared with conventional concrete.

Chapter 7: Natural Rubber Composites for Radiation Shielding- The fabrication of natural rubber composites fortified with barium tungstate is described in this chapter. The shielding effectiveness of these composites is evaluated through experimental measurements and simulations, demonstrating their potential for use in various radiation protection applications.

Chapter 8: Epoxy Paint Composites for Gamma Shielding- This chapter focuses on the development of epoxy wall paint composites modified with oxides of bismuth and tungsten. The fabrication process, gamma attenuation measurements, and comparative analysis with standard paints are presented in detail.

Chapter 9: Conclusion and Future Scope- The final chapter summarizes the key findings of the research, highlighting the contributions to the understanding of natural radioactivity and the development of gamma-ray shielding materials. The chapter also discusses the implications of the results and outlines future directions for research in this field.

The research presented in this thesis is an endeavour to address critical issues related to environmental radioactivity and radiation protection. By combining extensive field measurements with innovative material development, this work contributes to both scientific understanding and practical applications in radiation physics. It is my hope that the findings and methodologies documented here will serve as a valuable resource

for researchers, educators, and professionals in related fields, fostering further advancements in this important area of study.

CHAPTER 1
INTRODUCTION

Contents	
1.1	*Fundamentals of Radiation*
1.2	*Natural Radioactivity*
1.3	*Significance of Natural Radioactivity Measurements*
1.4	*Primordial Radioactive Nuclides*
1.5	*Cosmogenic Radioactive Nuclides*
1.6	*Background radiation*
1.7	*Terrestrial sources of natural radioactivity*
1.8	*Extraterrestrial sources of natural radioactivity*
1.9	*The distribution of primordial radionuclides in rocks and soils*
1.10	*Minerals deposition in the Rock and Soil samples*
1.11	*Technologically enhanced natural radionuclides*
1.12	*Radiogenic Heat Production and Heat flow*
1.13	*Interaction Mechanisms of Gamma Rays*
1.14	*Photon Attenuation and Absorption*
1.15	*Gamma-ray shielding*
1.16	*Different Types of Shielding Materials*
1.17	*Motivation of this research*
1.18	*Objectives of the Work*
	Reference

Abstract: *This study delves into the core principles of natural radioactivity, examining how gamma radiation interacts with various materials and the methods used for gamma-ray shielding. The research aims to deepen our understanding of these fundamental concepts to improve radiation protection strategies. The chapter begins with a brief overview of natural radioactivity, followed by an exploration of the mechanisms through which gamma rays interact with matter. It also covers various techniques and materials used in gamma-ray shielding. The latter part of the chapter articulates the motivation for this research and specifies the objectives intended to be achieved. By addressing these aspects, the study seeks to contribute to the development of more effective radiation shielding solutions.*

1.1 Fundamentals of Radiation

Radiation is a form of energy which can be particle type or electromagnetic type. Some of these are ionising and others are non-ionizing. It has always been a part of our environment and surrounds us constantly. In the universe, radioactive materials and radiation are natural components of our world, and life has evolved in the midst of the significant levels of ionizing radiations. Generally, when we talk about radiation, we associate it with artificial radioactive elements being used in the medical field, nuclear weapons and reactors. However, radiation is also found in soil, rock, the air we breathe, the water we drink, and the food we eat. These are called natural radiations. Even the human body contains some radioactive materials. Electromagnetic radiation includes Radio waves, Microwaves, Visible light, X-rays, and Gamma rays (γ), while particle radiation consists of Protons, Alpha particles (α), Beta particles (β), Neutron radiation, Heavy ions etc[1]. Ionizing radiation has the ability to alter the structure of atoms in the medium through which it passes. In living organisms, it leads to health risks such as tissue and DNA damage. On the other hand, non-ionizing radiation lacks the energy required to remove electrons from atoms but can cause atomic and molecular excitations.

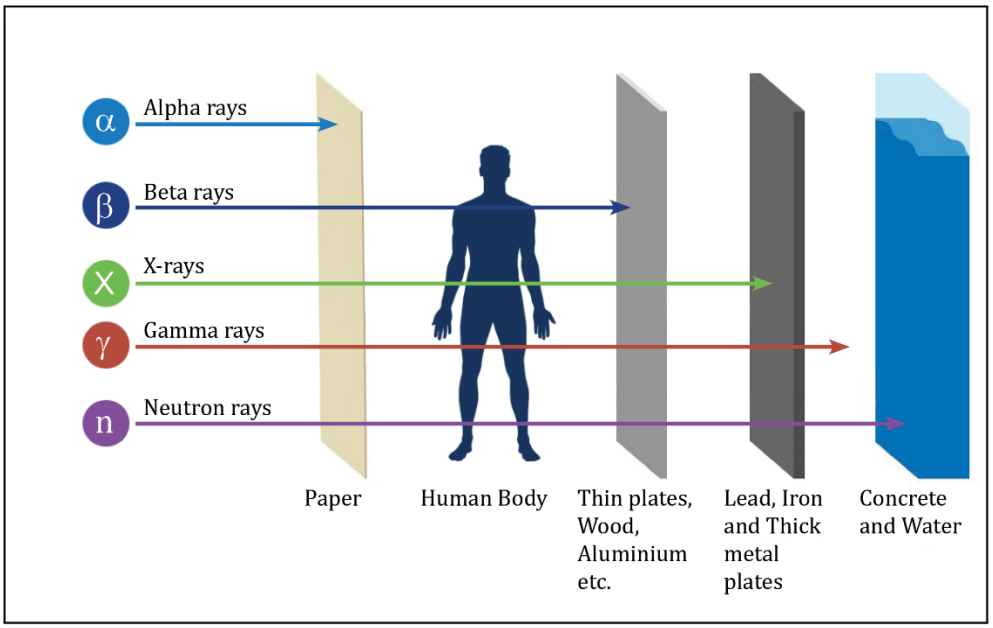

Figure 1.1: Illustration of the varying penetrating power of different types of ionizing radiations.

Natural radiation has played a crucial role in the evolution of life. All living organisms are continuously exposed to ionizing radiation, which has always existed naturally. When the Earth was formed around four billion years ago, it contained numerous radioactive isotopes, some with short half-lives and others with very long half-lives. These natural radioactive materials are present in rocks, soil, air, food, and drinking water. Consequently, the natural environment is a significant source of radiation exposure for humans. The ionizing radiations from these natural sources that we are constantly exposed to, is known as natural background radiations. In addition to this background radiation, with the terrestrial origin there are another background radiation having extra-terrestrial origin, commonly called cosmic rays.
According to the United Nations Scientific Committee on the Effects of Atomic Radiation (UNSCEAR) [2], each person on Earth is exposed to an average annual radiation dose of about 2.4 mSv from both cosmic sources and the Earth's crust. Additional sources of radiation are artificial, stemming from medical applications, the nuclear industry, like non-destructive testing and nuclear explosions. Collectively these are called man-made radiations. Soil has always been crucial for human health, providing resources for shelter and food production. However, the mineral, chemical, and biological components of soil can be harmful to health, due to their intake through ingestion, inhalation, and thermal absorption. For instance, it is a known fact that cancers can be caused by inhaling radon gas, which is produced by the radioactive decay chain of Uranium in soil minerals.

1.2 Natural Radioactivity

Natural radioactivity refers to the phenomenon where certain elements spontaneously undergo radioactive decay, emitting radiations in the form of Alpha particles, Beta particles, gamma rays, and sometimes neutrons and heavy ions. This process is entirely natural and has been occurring since the formation of the Earth and the universe. It is distinct from artificial or human-made sources of radioactivity. Radioactive materials are naturally found in various substances on Earth, including rocks, minerals, and even living organisms. Some common naturally occurring radioactive elements include isotopes of Uranium, Thorium, and

Potassium. These radioactive elements can be present in the Earth's crust, and their decay products can emit radiations, which can have both beneficial and harmful effects. Benefits of natural radioactivity include its use in geology for dating rocks and determining Earth's age (radiometric dating) and its application in medical imaging (diognosis) and cancer treatment (radiotherapy). However, excessive exposure to natural sources of radioactivity, such as radon gas in homes or prolonged exposure to radioactive minerals, can pose health risks and increase the likelihood of radiation-induced diseases, such as cancer.

1.3 Significance of Natural Radioactivity Measurements

Natural radioactivity has been extensively used in geophysics to study the Earth's interior. The distribution of radioactive isotopes like Uranium, Thorium, and Potassium in rocks and minerals provides information on the Earth's composition and age. The use of natural radioactivity in medicine has become widespread. Radioactive isotopes are employed in various medical imaging techniques, such as Positron Emission Tomography (PET) and nuclear medicine, for diagnosis and treatment of diseases. Understanding natural radioactivity is crucial for developing guidelines and practices for radiation protection. This includes setting safety standards, monitoring radiation exposure, and implementing measures to minimize the risks associated with natural and artificial sources of radiation [3], [4]

Natural radioactivity plays a role in cosmic ray research. High-energy particles from space can induce nuclear reactions and generate secondary particles when interacting with the Earth's atmosphere. This field of study has implications for astrophysics and our understanding of the universe. Thus, the study of natural radioactivity has been foundational in advancing our understanding of nuclear physics, the structure of matter, and it has led to numerous practical applications in various scientific and technological fields.

The measurement of natural radioactivity is essential for various reasons, including environmental monitoring, public health and safety, scientific research, and industrial applications. Here are some of the key reasons why natural radioactivity measurements are necessary:

1. Radiation Protection: Monitoring natural radioactivity helps assess and mitigate the potential health risks associated with exposure to ionizing radiation. This includes setting safety standards for radiation levels in workplaces, homes, and the environment to protect individuals from harmful radiation exposure.
2. Health Effects Assessment: Understanding the levels of natural radioactivity in various environments allows for the assessment of potential health effects on people who live or work in those areas. It helps identify areas with elevated radiation levels that can be linked to increased cancer risks or other health issues.
3. Environmental Impact: Natural radioactivity measurements are crucial for assessing the impact of radioactive substances on the environment. This includes monitoring radioisotope concentrations in soil, water, air, and wildlife, to ensure ecological balance and to prevent contamination.
4. Geological and Geophysical Studies: Radioactive decay processes are used in geology to date rocks and minerals through radiometric dating. This helps determine the Earth's age, understand geological processes, and assess the potential for mineral resources.
5. Nuclear Energy and Industry: In nuclear power plants and various industrial processes, natural radioactivity measurements are essential for monitoring radiation levels, ensuring worker safety, and preventing accidental releases of radioactive materials.
6. Medical Applications: In the medical field, the use of naturally occurring radioactive materials, such as radionuclides in diagnostic imaging and therapy, relies on accurate measurements to deliver effective treatments and minimize patient exposure.
7. Scientific Research: Natural radioactivity measurements are a fundamental tool in scientific research across various disciplines, including nuclear physics, astrophysics, and environmental science. Researchers use these measurements to understand the fundamental properties of matter and the universe.
8. Emergency Preparedness: Monitoring natural radioactivity is crucial in preparing for and responding to radiological emergencies, such as nuclear accidents or incidents involving the transportation of radioactive materials.

9. Regulatory Compliance: Many countries have regulations and guidelines that require the monitoring and reporting of natural radioactivity levels in specific industries and environments. Compliance with these regulations is essential for ensuring safety and environmental protection.
10. Public Awareness: Providing information about natural radioactivity levels in a particular area can raise public awareness about potential radiation risks, helping individuals make informed decisions about their activities and exposure.
In summary, natural radioactivity measurements play a vital role in safeguarding public health, protecting the environment, advancing scientific knowledge, and supporting various industrial and medical applications. These measurements enable us to understand, control, and manage the impact of natural radioactivity on society. To protect against the harmful effects of natural radioactivity, regulatory agencies and organizations set guidelines and safety measures to minimize exposure to ionizing radiation and ensure the safe use of radioactive materials. The primary sources of natural radioactivity include Primordial Radioactive Nuclides and cosmogenic radioactive nuclides.

1.4. Primordial Radioactive Nuclides

Primordial nuclides are naturally occurring radioactive isotopes that have existed since the formation of the Earth and are found in various minerals and materials. These nuclides have long half-lives and are part of the Earth's natural radioactivity. They play a significant role in shaping the composition of the Earth's crust and in contributing to the background radiation that we are exposed to [5]–[7]. Some of the key radioactive primordial nuclides relevant to the present study are given below:
1. Uranium-238 (^{238}U): This isotope has a half-life of about 4.5 billion years and is part of the decay series known as the Uranium series or Radium series. It decays into various daughter isotopes. This decay series begins with Uranium-238 and ends at Lead-206 (^{206}Pb) with the emission of eight Alpha and six Beta particles. Uranium-238 (^{238}U) and its decay products are major contributors to background radiation. It is found in varying concentrations in different environmental materials, primarily in soil and rocks. ^{238}U is the most abundant isotope (99.28%) of natural Uranium and is

the parent of a series of 15 radionuclides. It enters the human body through the food chain and atmospheric dust particles. On average, 5 Bq of Uranium is found in the annual dietary intake from areas with normal background levels. ^{238}U decays to Radium-226 (^{226}Ra), a significant Alpha emitter with a half-life of 1620 years. ^{226}Ra and its daughters are a substantial component of natural radiation exposure.

2. Uranium-235 (^{235}U): This isotope has a half-life of about 700 million years and is significant because it can undergo nuclear fission, releasing a substantial amount of energy. U-235 is used as fuel in nuclear reactors and has applications in nuclear weapons. It begins with Uranium-235 and ends with the radioactive isotope of Lead -207 (^{207}Pb), with the emission of seven Alpha and four Beta particles.

3. Thorium-232 (^{232}Th): With a half-life of about 14 billion years, the starting isotope of this Thorium series. Decays end at Lead-208 (^{208}Pb) with the emission of six Alpha and four Beta particles. Thorium-232 (^{232}Th) and its decay products are also major sources of terrestrial radiation. It is widespread in varying concentrations in soil and rocks and is the only long-lived radionuclide in its decay chain. Thorium-232's specific activity is 2.97 Bq/g, compared to 8.9 Bq/g for Uranium-238. Thorium-232 decays to Radium-228 through Alpha emission. Radium-228 (^{228}Ra) is a notable Beta emitter with a half-life of 5.76 years. It is more concentrated in plants and animals compared to its parent ^{232}Th and plays a significant role in dose estimation for regions with Monazite deposits.

4. Potassium-40 (^{40}K): This isotope has a half-life of about 1.3 billion years and is found in all Potassium-bearing materials. It contributes to the radiation dose received by humans through both external exposure and internal ingestion.

5. Radium-226 (^{226}Ra): With a half-life of about 1,600 years, Radium-226 (^{226}Ra) is part of the Uranium series and decays into Radon gas (^{222}Rn). The other two prominent isotopes of radon are thoron and actinon (^{220}Rn and ^{219}Rn).

6. Polonium-210 (^{210}Po): This isotope has a relatively short half-life of about 138 days and is present as a decay product of radon (^{222}Rn). It is known for its high radioactivity and its association with certain cases of environmental and occupational exposure.

7. Lead-210 (^{210}Pb): This isotope is part of the decay chain of radon-222 (^{222}Rn). It

decays into stable lead-206 and is often used in dating sediments and in determining sediment accumulation rates.

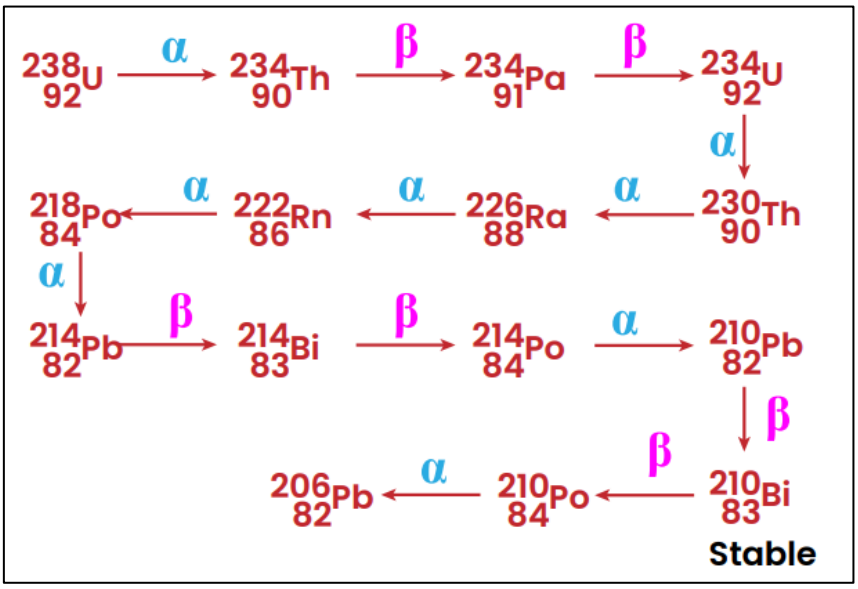

Figure 1.2: Uranium-series (4n + 2 series)

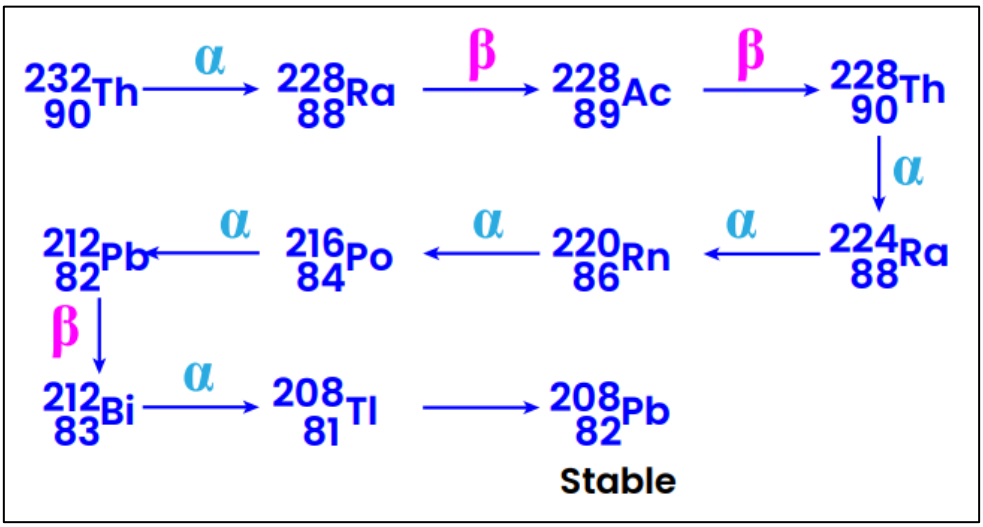

Figure 1.3: Thorium series (4n series)

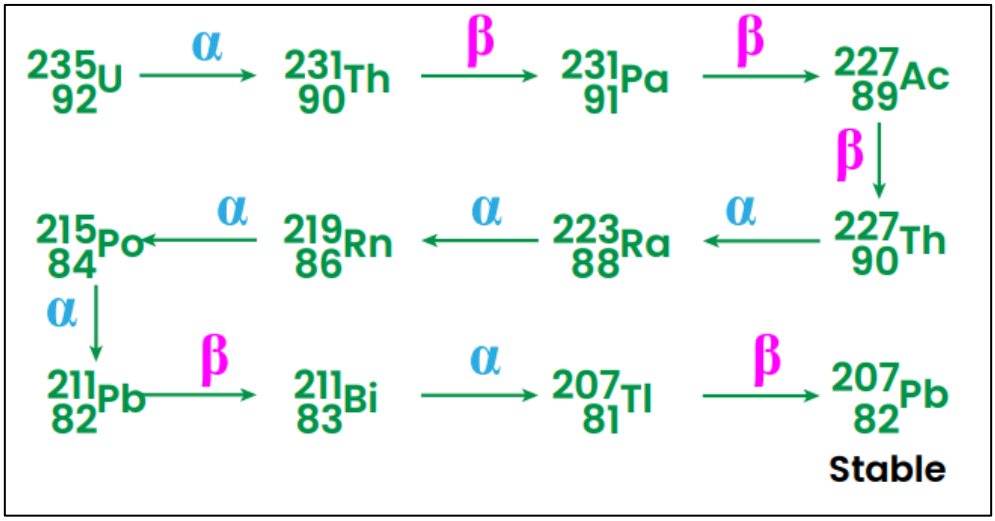

Figure 1.4: Actinium series (4n + 3 series)

Radon gas (^{222}Rn) is a colourless, odourless, and tasteless radioactive noble gas that is naturally present in the environment [6], [8]. It is a decay product of Uranium-238 (^{238}U) in the decay series known as the Uranium decay chain. Radon is formed as U-238 undergoes a series of radioactive decays, eventually leading to the formation of radon gas.

Radon itself is radioactive and undergoes Alpha decay. It emits Alpha particles (Helium nuclei) during the decay, transforming into other radioactive isotopes, known as radon decay products or radon daughters. Radon is a health hazard because its decay products are solid particles that can attach to dust and other airborne particles [9], [10]. When inhaled, these particles can become lodged in the respiratory tract and emit Alpha particles, potentially damaging lung tissue and increasing the risk of lung cancer. Radon exposure is considered the second leading cause of lung cancer after smoking. Radon can migrate from the ground into buildings through cracks in foundations, gaps around pipes, and other openings. Because buildings can trap radon indoors, radon levels can become elevated in enclosed spaces. Radon levels can vary widely depending on the location and geology. To assess radon exposure, measurements can be taken using specialized devices. If elevated radon levels are detected in homes or workplaces, mitigation measures such as sealing cracks, improving ventilation, and installing radon mitigation systems can be implemented to reduce indoor radon concentrations. Radon levels can vary significantly from one geographic region to another. Areas

with certain types of soil and rock formations are more likely to have elevated radon concentrations. Geological factors, such as soil permeability and Uranium content, play a role in radon generation. Many countries have established guidelines and regulations to address radon exposure in residential and occupational settings. These guidelines help protect individuals from excessive radon exposure. Public awareness campaigns and educational efforts aim to inform people about the risks of radon exposure and encourage actions to reduce exposure, particularly in homes and workplaces. Reducing radon exposure is crucial for minimizing the associated health risks. Regular testing of indoor radon levels and taking appropriate measures to mitigate Radon infiltration can help protect individuals from the harmful effects of this radioactive gas.

These primodial nuclides are found in varying concentrations in rocks, minerals, soil, water etc. Their presence and decay contribute to the natural background radiation that always surrounds us. Even though exposure to these radioactive elements is generally low and not a significant health concern in normal conditions, so surveys are always important in a place like Kerala, where we have places with very high background radiations. It is important to understand their presence, behaviour, and potential health implications, in certain contexts such as mining, construction, and nuclear industry operations.

1.5 Cosmogenic Radioactive Nuclides

Radioactive cosmogenic nuclides are isotopes that are produced in the upper atmosphere and at the Earth's surface their takes place interactions between high-energy cosmic rays and stable target nuclei. These interactions result in the transformation of stable atoms into radioactive isotopes. These nuclides have relatively short half-lives compared to the primordial nuclides mentioned earlier. Because they are continuously produced and decay, they serve as valuable tools for various scientific applications, particularly in fields such as geology, archaeology, and environmental studies. The significant radioactive cosmogenic nuclides are:

- Carbon-14 (^{14}C): Carbon-14 is perhaps the most well-known radioactive cosmogenic nuclide. It is produced in the upper atmosphere when Nitrogen-14

(^{14}N) is bombarded by cosmic rays. ^{14}C is incorporated into carbon dioxide, which is then taken up by plants and consumed by animals, making it part of the food chain. Because of this, living organisms maintain a consistent ^{14}C to ^{12}C ratio while they are alive. When an organism dies, it stops exchanging carbon with the environment, and the ^{14}C in its tissues begins to decay. By measuring the remaining ^{14}C content in organic materials, scientists can determine the age of ancient objects and fossils through a process known as radiocarbon dating.

- Beryllium-10 (^{10}Be): Beryllium-10 is produced in the atmosphere when Oxygen and Nitrogen are bombarded by cosmic rays. It is also generated in minerals near the Earth's surface when they are exposed to cosmic rays. ^{10}Be has a relatively long half-life of around 1.39 million years. It is often used in studies related to surface exposure dating, erosion rates, and glacial history.
- Chlorine-36 (^{36}Cl): Chlorine-36 is produced in the atmosphere by the interaction of cosmic rays with Argon and Potassium. It can also be formed in minerals at the Earth's surface. With a half-life of about 301,000 years, ^{36}Cl is used to estimate the exposure history of rock surfaces and to determine the age of groundwater.
- Aluminium-26 (^{26}Al): Aluminium-26 is produced by cosmic ray interactions with Silicon and Oxygen in minerals near the Earth's surface. It has a relatively short half-life of about 717,000 years. It is used in studies of exposure ages, meteorite chronology, and in understanding sediment transport.

These cosmogenic nuclides provide valuable insights into Earth's processes and history. By measuring their concentrations in various materials, scientists can gain information on the surface exposure ages, erosion rates, glacial retreat, volcanic activity, and other geologic phenomena. They also contribute to our understanding of cosmic ray interactions, the Earth's magnetic field, and the dynamic interactions between the Earth and the outer space.

1.6 Background Radiation:

Earth is constantly bombarded by cosmic rays, which produce secondary radiation upon interaction with the atmosphere. This background radiation contributes to

natural radioactivity. Background radiation refers to the ionizing radiation that is present in the environment from natural and man-made sources. This radiation is constantly around us and comes from various sources, including cosmic rays from space, radioactive materials in the Earth's crust, and even human activities. Background radiation is typically at low levels and is generally not harmful in everyday situations. It contributes to the baseline radiation exposure that everyone experiences. Background radiation is typically measured in units such as micro sieverts per hour (μSv/h) or millisieverts per year (mSv/y). The level of background radiation varies depending on factors like geographical location, altitude, local geology, and lifestyle[11], [12].

While background radiation is an unavoidable part of our environment, It is important to manage and minimize unnecessary exposure, especially in occupations or situations where radiation levels are high. Monitoring and understanding background radiation contributes to our overall attempts to mitigate radiation levels and thereby achieving radiation safety and health.

1.7. Terrestrial sources of natural radioactivity

Natural radioactive elements are the primary sources of radioactivity in the environment. As mentioned earlier, there are four important decay series, each led by a specific radioactive isotope. These series include the Uranium-series headed by ^{238}U, the Thorium series headed by ^{232}Th, the Actinium series headed by ^{235}U, and the Neptunium series led by ^{241}Pu, which has a shorter half-life of 14 years. These naturally occurring radioactive elements fall into two categories: those that exist individually and those that are part of the Uranium (^{238}U), Thorium (^{232}Th), and Actinium (^{235}U) series. Among these, the Uranium and Thorium series are particularly significant as they contribute a substantial amount of ionizing radiation to the environment.

Potassium-40 (^{40}K) is the most prevalent individually occurring radionuclide, with a half-life of 1.3×10^9 years. It is widely distributed in soil and rocks. Its decay occurs through two modes: Beta emission to form ^{40}Ca or K-electron capture to form Argon-40 (^{40}Ar). The resulting excited ^{40}Ar subsequently emits gamma radiation. The average concentration of ^{40}K is approximately 1.8 mg/kg in Earth, with a

specific activity of about 400 Bq/kg. The abundance of ^{40}K is 0.012% of total Potassium, meaning that 1 kg of soil contains around 2.36 mg of radioactive Potassium-40, significantly contributing to gamma radiation in the environment.

Terrestrial materials with radioactivity refer to naturally occurring substances, such as rocks, minerals, soil, and water, that contain varying levels of radioactive elements and isotopes. These materials contribute to the natural background radiation that surrounds us. Major terrestrial materials exhibiting radioactivity are:

- Granite and other rocks: Some types of rocks, including granite, contain higher concentrations of radioactive elements like Uranium, Thorium, and their decay products. These elements contribute to the radioactivity of the rocks and the soil derived from them.
- Minerals: Certain minerals are known for their radioactivity. For instance, Monazite, a mineral containing Thorium and rare earth elements, can be significantly radioactive. Uraninite, also known as pitchblende, is a mineral that contains high concentrations of Uranium.
- Soil: The radioactivity of soil is influenced by the geological composition of the area. Areas with underlying rocks rich in radioactive elements will have soil with higher levels of radioactivity.
- Water: Groundwater can contain trace amounts of radioactive isotopes, particularly radionuclides from the Uranium and Thorium decay series. Radon gas can also dissolve in water, contributing to its radioactivity.
- Construction Materials: Some construction materials, such as concrete, bricks, and tiles, can contain naturally occurring radioactive materials. The aggregates used in these materials might have elevated levels of radioactivity due to their geological origin.
- Gemstones: Certain gemstones, such as Zircon, can contain radioactive elements. This radioactivity can be detected using specialized instruments.
- Fertilizers and agricultural products: Some fertilizers, particularly those derived from phosphate rock, can contain elevated levels of radionuclides like Uranium and Thorium. These elements can eventually end up in agricultural products.

- Caves and underground spaces: Underground spaces, including caves, can sometimes have elevated radon levels due to the emanation of radon gas from the surrounding rocks.

The main radioactive isotopes in crustal granitic rocks are ^{232}Th, ^{235}U, ^{238}U and ^{40}K, all of which have different isotopic abundance, decay constants, and half-lives. It is important to note that while these materials contain radioactivity, the levels are usually low and hence not a significant health concern in normal conditions. However, in certain cases, prolonged exposure to elevated levels of radioactivity from these materials can pose health risks, especially in confined spaces or poorly ventilated areas. Regulatory agencies and health organizations provide guidelines and recommendations to manage potential risks associated with radioactivity in terrestrial materials.

Biological Sources

Biological sources of radiation refer to natural sources of ionizing radiation that originate from living organisms or biological materials. These sources contribute to the background radiation exposure that individuals experience. While the levels of radiation from biological sources are generally low and not a significant health concern, they are part of the overall radiation environment. Certain living organisms, such as bananas and certain types of plants, contain trace amounts of radioactive isotopes, particularly ^{40}K.

Regulatory bodies and health organizations establish safety limits to ensure that the radiation exposure from these sources remains within safe levels. Understanding the contributions of these sources to background radiation exposure helps provide a comprehensive view of our radiation environment and informs radiation safety practices.

1.8. Extraterrestrial sources of natural radioactivity

Extraterrestrial sources of natural radioactivity refer to radioactive materials and particles that originate from sources beyond the Earth, such as outer space, cosmic rays, and meteorites. These sources contribute to the overall background radiation that reaches the Earth's surface and can have interesting implications for our

understanding of both terrestrial and cosmic processes. The major examples of extraterrestrial sources of natural radioactivity are: solar and galatic cosmic rays, meteorites, which are fragments of asteroids or other celestial bodies, nuclear reactions in space, interstellar dust and solar neutrinos

These extraterrestrial sources of natural radioactivity are a reminder that the Earth is constantly interacting with the cosmos, and the radiation environment on our planet is shaped by both terrestrial and cosmic processes. Studying these sources helps us understand the broader context of radiation exposure and the connections between Earth and the universe.

1.9. The distribution of primordial radionuclides in rocks and soils

The distribution of primordial radionuclides in rocks is primarily influenced by the underlying geological conditions. The concentrations of Potassium, Uranium, and Thorium are determined by their physical and chemical behaviour during rock-forming processes. These processes include crystal fractionation in igneous rocks, metamorphic and hydrothermal activities, as well as erosion and depositional mechanisms in the formation of sedimentary rocks. ^{40}K is a natural isotope of Potassium and is the most prevalent naturally occurring radioactive element. It is uniformly mixed with Potassium, accounting for approximately 0.0118% by mass. Potassium, an alkali metal easily oxidized, shares similar chemical behaviour with sodium, constituting essential components of alkali feldspars and feldspathoids. Natural Potassium has three isotopes, with ^{40}K being the only unstable one. The abundance of natural Potassium varies from 0.3% to 4.5% in different rock types, with lower concentrations observed in certain basalts and sands compared to granites and other basalts.

1.9.1. Distribution of sedimentary rocks

Sedimentary rocks are formed through the accumulation and cementation of sediments over time. This includes the processes of weathering, erosion, transportation, deposition, and lithification. Weathering breaks down existing rocks into sediment particles, which are then transported by agents like water, wind, or ice.

Deposition occurs when these particles settle and accumulate in a new location. Over time, compaction and cementation turn the accumulated sediments into solid rock. Uranium and Thorium content in sedimentary rocks are generally lower when compared to those in igneous rocks. However, phosphates and organic matter in sedimentary rocks can concentrate Uranium. They form at or near the Earth's surface through the accumulation and consolidation of sedimentary materials. Sedimentary rocks cover a wide range of rock types, each with unique characteristics. Sedimentary rocks often have a layered or stratified appearance due to the sequential deposition of different sedimentary materials. Grain size and sorting can vary within sedimentary rocks, influencing their texture. There are three main categories of sedimentary rocks: clastic (detrital), chemical, and organic. Clastic sedimentary rocks formed from the accumulation of mineral and rock fragments (clasts) produced by the weathering of pre-existing rocks. Sandstone, shale, and conglomerate aree belongs to these types of rocks. Chemical sedimentary are rocks formed by the precipitation of minerals from a solution. Limestone, gypsum, and halite belongs to these categories. Organic sedimentary rocks are composed of the remains of once-living organisms. Coal (from plant material) and certain types of limestone (from marine organisms) are belonging to these categories.

Sedimentary rocks frequently contain fossils, which are the preserved remains or traces of ancient organisms. Fossils are especially common in rocks formed in aquatic environments, such as marine or lake sediments. The colour of sedimentary rocks varies based on the mineral composition and the environment of formation. Red or brown colours often indicate the presence of Iron oxides, while white or gray colour may suggest a predominance of quartz or calcium carbonate. Sedimentary rocks play a crucial role in preserving Earth's history and are valuable for understanding past environments, climate conditions, and the evolution of life on Earth. The distribution of primordial radionuclides in sedimentary rocks is influenced by the composition of the original sediments and subsequent diagenetic processes. The absolute Potassium content depends on the proportions of Feldspars, Mica, and Clay mineral aggregates, which can be determined from the composition

of the source rock and its proximity. Uranium and Thorium exhibit strong lithophile characteristics.

Uranium commonly appears in various forms such as Oxides, Hydroxides, Phosphates, Carbonates, Sulphates, Arsenates, Vanadates, Molybdonates, and Silicates, often having affinities with hydrocarbon complexes. Thorium tends to form ions with Chloride, Fluoride, Nitrate, Sulphate, Carbonate, and Hydroxide, with possible complexes like Silicate, Phosphate, and organic compounds, making Thorium mobile under specific pH conditions.

In most regions of the Earth, natural radioactivity remains within narrow limits, but in some areas, deviations from normal levels occur due to abnormally high concentrations of minerals containing primordial radionuclides in the rock. Uranium, a universally present element in two radioactive decay series (^{235}U and ^{238}U), occurs naturally in low levels in all rocks, soil, and water. Uranium concentrations are higher in phosphate, igneous, and granite rocks, while sedimentary rocks like limestone typically have lower concentrations. The measurement of natural radioactivity in rocks is crucial for Thorium and Uranium prospecting.

1.9.2. Distribution Metamorphic rocks

Metamorphic rocks result from the alteration of pre-existing rocks due to heat and pressure. Uranium and Thorium tend to be more concentrated in metamorphic rocks than in sedimentary rocks, as the processes of metamorphism can lead to the concentration of these elements in minerals like Zircon and Monazite. The distribution of primordial radionuclides in metamorphic rocks is dependent on the mineralogical changes that occur during metamorphism.

1.9.3. Igneous rocks

Igneous rocks form from the solidification of molten magma or lava. Uranium and Thorium are often more concentrated in igneous rocks, especially in granitic rocks. Granite is known for having higher Uranium and Thorium content compared to

other rock types. Granitic rocks, commonly referred to as granite, are a type of igneous rock that forms from the slow crystallization of magma beneath the Earth's surface. Granite is a widely recognized and utilized rock in various applications due to its durability, aesthetic appeal, and diverse range of uses. Some key characteristics of granitic rocks are:

Granitic rocks are primarily composed of three main minerals: Quartz, Feldspar (both Orthoclase and Plagioclase), and Mica (usually Biotite or Muscovite). These minerals give granite its distinctive appearance. Granites typically have a coarse-grained texture, meaning that individual mineral crystals are easily visible to the naked eye. The interlocking nature of these crystals contributes to the rock's strength and durability.

The magma that gives rise to granite is often derived from the partial melting of continental crust. Granite comes in a variety of colours, reflecting the diverse mineral composition. Common colours include pink, gray, white, and variations of these hues. The specific minerals present contribute to the rock's coloration. Due to its durability and aesthetic qualities, granite is widely used as a dimension stone in construction. It is often employed as countertops, flooring, exterior cladding, monuments, and other architectural features. Granitic rocks, especially those with higher concentrations of Uranium and Thorium, can exhibit elevated levels of natural radioactivity. This is because these rocks may contain the primordial radionuclides ^{238}U, ^{232}Th and ^{40}K. Granitic rocks are found in various geological settings, but they are particularly abundant in continental crust. Large granite batholiths and plutons are common features in mountainous regions. Granite is an intrusive igneous rock, meaning it forms from the cooling of magma beneath the Earth's surface. When granite is exposed at the surface, it is usually the result of erosion that removed overlying rocks. Overall, granitic rocks are a significant component of the Earth's crust, and their characteristics make them valuable in both geological studies and a wide range of human applications. Potassium-40 is abundant in many igneous rocks, as Potassium is a common element in the Earth's

crust. Potassium-rich minerals like feldspar contribute to the overall radioactivity of these rocks.

In summary, the concentration and distribution of primordial radionuclides in rocks are influenced by the geological processes that lead to the formation of sedimentary, metamorphic, and igneous rocks. The mineral composition, geological history, and the specific conditions under which these rocks are formed play a key role in determining the levels of natural radioactivity in each rock type.

1.10 Mineral deposition in Rock and soil samples

The gamma-ray spectrometric approach may identify Potassium alteration, which is commonly linked with hydrothermal ore deposits. The method is also utilized in the exploration of Uranium and Thorium, heat flow research, and environmental mapping, such as the delineation of surface drainage features.

1.10.1 Mineral deposition in Rock samples

The common radioactive minerals are Uraninite (oxide of U, Pb, Ra+ Th, rare earths), Monazite (ThO_2 + rare earth phosphate), Thorianite [$(Th, U)O_2$], Rubidium (^{87}Rb) in granite-pegmatite, Feldspar, Muscovite [$H_2KAl(SiO_4)_3$], Alunite [$K_2A_{16}(OH)_{12}(SiO_4)$], Carnallite ($MgCl_2.6H_2O$) and Sylvite (KCl) in acid igneous rocks. Potassic Feldspars and Micas are the major hosts of Potassium in rocks. Orthoclase Microcline ($KAlSi_3O_8$) with an approximate 13% and Biotite and Muscovite with 8% are examples of Potassic Feldspars and Micas, respectively.

Thorium (about 12 ppm) is a small component of the Earth's crust. Monazite and Zircon ($ZrSiO_4$) are the main Thorium-bearing minerals; they are resilient to the effects of weathering and can form vast dunes. Thorium can be preserved in Fe or Ti Oxides/Hydroxides and clays because of the mineral breakdown during weathering. Uranium is a radioactive element having a low abundance on average (approximately 3 ppm) in the Earth's crust. It was found in rocks as the oxide and silicate minerals Uraninite and Uranothorite ($ThSiO_4$+U); and as trace amounts in other minerals or along grain boundaries as Uranium oxides or Silicates. In rocks

and soils, the distribution of radioelements as studied by further examination by [13] revealed that Potassium (2.35%), an alkali element with simple chemistry, was a significant part of the Earth's crust.

1.10.2 Mineral deposition in Soil samples

The composition of soil has a significant impact on natural radioactivity. Different soil types contain varying concentrations of radioactive elements, and the composition influences the retention, mobility, and distribution of these elements. Other than mineral composition, there are other key factors that are related to the soil radioactivity are:

Clay and Sandy Soils

Clay and sandy soils are two distinct types of soil with different properties, and these differences can impact various aspects, including natural radioactivity. Clay soils have fine particles with sizes less than 0.002 mm. The small particle size provides a larger surface area for interactions with minerals and organic matter. Clay soils have high water retention capacity due to their fine texture. They can hold onto water for more extended periods, influencing the movement of water-soluble elements, including certain radionuclides. Clay soils have a higher nutrient retention capacity, which can affect the availability and mobility of radionuclides in the soil. Nutrients and radionuclides may compete for binding sites on clay particles.

Clay soils generally have a higher Cation Exchange Capacity (CEC), which refers to their ability to hold and exchange cations (positively charged ions). This can influence the retention of radionuclides in the soil. Clay soils often exhibit higher natural radioactivity levels compared to sandy soils. This is partly due to the higher concentrations of minerals containing Uranium, Thorium, and Potassium in clay-rich materials.

Sandy soils have larger particles with sizes ranging from 0.05 to 2.0 mm. This results in a coarser texture and a lower surface area compared to clay soils. Sandy soils have excellent drainage capabilities. Water passes through them more easily, which can impact the leaching and migration of radionuclides. Sandy soils may experience nutrient leaching more than clay soils due to their low nutrient retention

capacity. This characteristic can affect the movement of certain radionuclides as well. Sandy soils generally have a lower CEC compared to clay soils. This can influence the adsorption and retention of radionuclides in the soil. Sandy soils often exhibit lower natural radioactivity levels compared to clay soils. The lower concentrations of Uranium, Thorium, and Potassium-containing minerals contribute to reduced radioactivity.

pH Levels

pH levels, representing the acidity or alkalinity of soil, are important factors that can influence natural radioactivity in the soil. The pH of the soil may influence the availability and mobility of certain radionuclides. Changes in pH can affect the solubility of minerals and impact the leaching or retention of radioactive elements. Some radionuclides are associated with specific minerals, and changes in pH can influence the dissolution or precipitation of these minerals, impacting the availability of radioactive elements[14]. Soil pH levels are critical factors that can influence the geochemical and biological processes governing the behaviour of radionuclides in the soil. Understanding the relationship between pH and natural radioactivity is essential for assessing environmental impact, managing potential health risks, and interpreting radioactivity measurements in various soil types.

Anthropogenic Influences

Anthropogenic influences can significantly alter the natural radioactivity of soils, introducing additional radionuclides beyond those naturally occurring. Above-ground nuclear testing, conducted in the mid-20th century, released significant amounts of artificial radionuclides, such as Cesium-137 and Strontium-90, into the atmosphere. These radionuclides eventually settle onto the soil, contributing to anthropogenic radioactivity. Accidents involving nuclear facilities, such as the Chernobyl disaster in 1986 and the Fukushima Daiichi nuclear disaster in 2011, released substantial amounts of radioactive materials into the environment. These incidents contribute to elevated levels of anthropogenic radionuclides in affected soils. Improper disposal of radioactive waste from nuclear power plants, medical facilities, or industrial processes can lead to localized contamination of soil with artificial radionuclides. Containment failures or leaks from storage facilities are also

potential sources of soil contamination.

Certain industrial activities, such as mining and processing of minerals, can release naturally occurring radionuclides from geological materials into the environment. Additionally, industrial processes may generate waste containing radioactive materials, impacting nearby soil. Applications involving the use of radioactive materials in various industries, research, and medical practices can lead to localized soil contamination. Accidental spills or improper disposal of radioactive sources contribute to anthropogenic radioactivity.

The production and use of phosphate fertilizers can introduce elevated levels of radionuclides, particularly Uranium and Thorium, into the soil. Phosphate rock, a raw material for fertilizer production, often contains these radioactive elements. Coal contains trace amounts of radioactive elements, and the combustion of coal in power plants releases ash that may contain concentrated radionuclides. This ash, if not properly managed, can contribute to anthropogenic radioactivity in the surrounding soil. Certain metal smelting processes may release radioactive materials into the environment. Tailings from mining and smelting activities can contribute to soil contamination with both natural and anthropogenic radionuclides.

Military operations, including the testing and use of munitions containing depleted Uranium, can result in localized soil contamination with anthropogenic radionuclides. Managing and mitigating the impact of these human activities on soil radioactivity is essential for environmental protection and the well-being of both ecosystems and human populations.

Geological Characteristics

The geological history of an area contributes to the types of minerals present in the soil. Regions with specific geological formations may have distinctive natural radioactivity signatures. Geological characteristics play a crucial role in influencing the natural radioactivity of soils. The composition and geological history of an area contribute to the types and concentrations of radioactive elements present in the soil. The weathering of geological materials releases radionuclides into the soil. Over time, physical and chemical weathering breaks down rocks, contributing to the accumulation of radioactive elements in soils. Specific geological formations, such

as ore deposits, may contain elevated concentrations of radioactive minerals. Mining activities in these formations can release these minerals, affecting soil radioactivity.

In natural radioactivity measurements, researchers consider these factors to obtain accurate assessments of soil radioactivity. Understanding the relationship between soil composition and radioactivity is essential for environmental monitoring, assessing potential health risks, and interpreting data in various scientific fields.

1.11 Technologically Enhanced Natural Radionuclides

It is important to note that natural radioactivity is ubiquitous and has been a part of Earth's environment since its formation. While some of these sources can pose health risks, they also have important applications in various fields, including medicine, archaeology, and geology. Technologically Enhanced Natural Radioactive Materials (TENORM) refer to naturally occurring radioactive materials that have been concentrated or otherwise altered by human activities, leading to higher levels of radioactivity than typically found in their natural state. These materials can be generated as byproducts of various industrial processes, such as mining, mineral extraction, oil and gas production, and certain manufacturing activities. Major technological process that generates/enhance natural radionuclides are Uranium and Thorium Mining, Phosphate Industry, Oil and Gas Production, Coal Combustion, Rare Earth Element Extraction, Building Materials, Water Treatment Residues, Metal Production and Scrap Metal Recycling.

It is worth noting that while TENORM can have elevated levels of radioactivity compared to their natural state, the extent of risk and regulatory control depends on factors such as the specific materials involved, the concentrations of radionuclides, the exposure pathways, and the disposal methods. Regulatory agencies monitor and manage TENORM to ensure public and environmental safety.

1.12 Radiogenic Heat Production and heat flow

Geothermal energy is produced by the Earth's internal heat. It provides dependable heat with minimal greenhouse gas emissions. This energy source is reliable and can lessen the reliance on imported fuels for electricity generation. It is also renewable

due to its reliance on an almost inexhaustible resource [15]. Furthermore, geothermal energy offers significant environmental benefits, as its emissions are free from chemical pollutants and waste, consisting mainly of water that is reinjected underground. The Earth's internal heat comes from several sources, with two primary origins. One is the gradual cooling of the Earth since its formation, a time when internal temperatures were significantly higher than they are today. Another significant source of the Earth's internal heat is the decay of long-lived radioactive isotopes. This is the primary contributor to the Earth's internal heat, driving all geodynamic processes [15]. The Earth continuously loses heat from its interior at a rate far greater than the energy lost through other means, such as changes in the Earth's rotation or energy released through geothermal flux, amounting to approximately 4.4×10^{3} W, or 1.4×10^{21} Jyr^{-1}.

Geophysical methods are essential in geothermal exploration. These surveys aim to indirectly obtain physical parameters of geothermal systems from shallow depths. Techniques used in geothermal energy exploration include measuring subsurface (shallow) temperatures [15]–[20].

The primary isotopes meeting these criteria are ^{238}U, ^{235}U, ^{232}Th, and ^{40}K. Among these, ^{235}U has a shorter half-life than ^{238}U and releases more energy during decay [21], [22] shown in Table 1.1

Table 1.1: Isotopes with Specific isotopic heat production (mW/kg)

Isotope	**Isotopic abundance (wt%)**	**$\tau_{1/2}$ (Ma)**	**Decay constant, λ ($year^{-1}$)**	**Specific isotopic heat production (mW/kg)**
^{238}U	99.28	4470	1.551×10^{-10}	94.65
^{235}U	0.71	704	9.85×10^{-10}	568.72
^{232}Th	100	14000	4.95×10^{-11}	26.38
^{40}K	0.0119	1250	5.54×10^{-10}	29.17

Combining the measurement and analysis of radionuclide contributions to geothermal heat production can enhance the accurate assessment of potential geothermal resource areas. This approach aids in identifying sites for future detailed investigations and possible exploitation. The heat generated by radioactive decay in

rocks is crucial for understanding the Earth's thermal history and interpreting continental heat flux data. Energy released by short-lived radioactive isotopes may have contributed to the Earth's initial heating, but these isotopes were consumed relatively early. In contrast, heat generated by long-lived isotopes has been a significant source throughout most of Earth's history. For isotopes to be a substantial heat source, they must have a half-life comparable to the Earth's age, their decay energy must be fully converted to heat, and they must be sufficiently abundant.

Heat can be transported by conduction, convection, and radiation. Conduction and convection require a material medium, whereas radiation can occur through space or a vacuum. Conduction is the primary heat transport mechanism in solid materials but is relatively inefficient. When molecules can move freely, as in fluids or gases, convection becomes more important. Although the mantle, is solid concerning the rapid passage of seismic waves, its high temperature allows it to behave as a viscous fluid over long periods [21]. Therefore, convection is also a dominant form of heat transport in the fluid core.

1.13 Interaction Mechanisms of Gamma Rays

Einstein showed that a photon feels the pull of gravity as if it were a particle even though it has no rest mass. Photons are fundamental to physics because they transmit the electromagnetic force; two electric charges are believed to interact by "exchanging" photons (photons are emitted by one charge and absorbed by the other).

Gamma radiation refers to high-energy electromagnetic radiation. Gamma rays are a form of ionizing radiation that possess extremely short wavelengths and high frequencies. They are typically emitted during nuclear reactions, radioactive decay, or particle interactions. When gamma beams encounter matter, they undergo various interactions that can be categorized into three essential processes: the photoelectric effect, Compton scattering, and pair production. These processes involve the transfer of energy from the gamma-ray photon to electrons. The dominance of each process depends on the energy of the gamma rays and the characteristics of the material being interacted with.

At low energies and with high atomic-number materials, the photoelectric effect is the dominant interaction. In this process, the gamma-ray photon transfers its energy completely to an electron, causing its ejection from the atom. In the mid-energy range and with low-atomic number materials, Compton scattering becomes the most significant interaction. Here, the gamma-ray collides with an electron, transferring a fraction of its energy and changing direction. The scattered gamma rays retain a lower energy level. At high photon energies, pair production becomes more effective than other types of gamma interactions. Pair production occurs when the energy of the gamma-ray is transformed into the mass of an electron-positron pair, typically in the presence of a nucleus' electric field.

Understanding these interactions is crucial as the dominance of each process depends on the energy of the gamma rays and the material composition. This knowledge is valuable for various applications, such as radiation detection, medical imaging and therapy, and nuclear physics research. Photon interaction with matter is a fundamental concept in physics and plays a crucial role in understanding a wide range of phenomena, from the behaviour of light and electromagnetic radiation to the operation of various technologies and even the structure of the universe. Photons originate in interesting ways; they simply appear when it is necessary to carry off excess energy (such as bremsstrahlung production, in radioactive transformation, or in nuclear interactions). The dichotomy of being both a wave and a particle is intriguing, but both properties are required to explain photon interactions in media. The origin and appearance of interference and diffraction phenomena are clearly wave properties, and its absorption to deposit energy and impart momentum requires a particle description as so effectively as deduced by Einstein (photoelectric effect) and Compton (in explaining photon scattering). It is difficult to accept that both could exist simultaneously, yet both properties are required to completely describe photons. Neither the wave nor the particle theory is wholly correct all the time, but both, as defined by Bohr, are “complementary” to each other.

The principal modes by which photons interact with matter to be attenuated and to deposit energy are by the photoelectric effect, the Compton effect, and pair production [3]. Photons also undergo Rayleigh scattering, Bragg scattering,

photodisintegration, and nuclear resonance scattering; however, these result in negligible attenuation or energy deposition and can generally be ignored for purposes of radiation protection.

1.13.1 Photoelectric effect

A low-energy photon can, by a process known as the photoelectric effect, collide with a bound orbital electron and eject it from the atom. The electron is ejected with an energy equal to that of the incoming photon, hυ, minus the binding energy of the electron in its orbit, an energy that is required to free an electron from the atom. The interaction must occur with a bound electron since the entire atom is necessary to conserve momentum, and it often occurs with one of the inner-shell electrons (Shown in Figure 1.5). Since a vacancy is created in the electron shell, a characteristic X-ray, typically from filling the K shell, will also be emitted.

The kinetic energy of the ejected electron is almost always absorbed in the medium where photoelectric absorption occurs. Characteristic X-rays that are produced are also very likely to be absorbed in the medium, typically by another photoelectric interaction or by the ejection and absorption of Auger electrons.

The photoelectric absorption coefficient τ is a function of the atomic number Z of the absorbing material (generally related to the density of the absorbing medium) and the energy of the radiation as follows[3].

$$\tau \approx \text{Constant} \times \frac{Z^5}{E^3}$$

It is evident that photoelectric absorption is most pronounced in high-Z materials and for low-energy photons (less than 0.5 MeV). In a high-Z material such as lead, L X-rays and M X-rays can also be prominent emissions from target atoms, and these will either be absorbed in the absorbing medium or will contribute to the photon fluence.

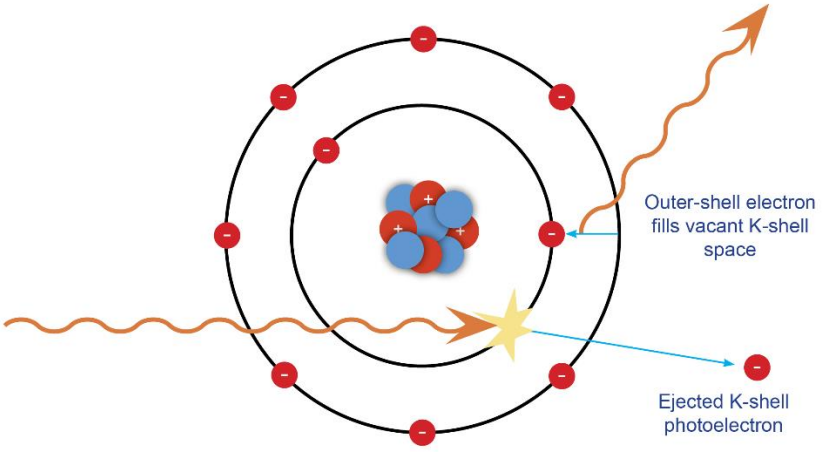

Figure 1.5: Schematic of the photoelectric effect.

1.13.2 Compton effect

Compton scattering interactions are especially important for gamma rays of medium energy (0.5–1.0 MeV), and, for low-Z materials such as tissues, can be the dominant interaction mechanism down to 0.1 MeV. Compton scattering involves a collision between a photon and a "free" or very loosely bound electron in which a part of the energy of the photon is imparted to the electron, as shown in Figure 1.6. Both energy and momentum are conserved in the collision.

The Compton-scattered photon emerges from the collision in a new direction and with reduced energy and increased wavelength[3]. The change in wavelength

$$\lambda' - \lambda = \frac{h}{m_0 c}(1 - \cos\theta) = 2.4264 \times 10^{-10}(1 - \cos\theta)$$

It is notable that the change in wavelength (and decrease in energy) of the photon is determined only by the scattering angle. The term h/m_0c, often called the Compton wavelength, has the value 2.4264×10^{-10} cm.

Energy transfer to the recoiling electron is the most important consequence of Compton interactions since it will be absorbed locally to produce radiation dose. This is a variable quantity and can range from zero up to a maximum value for electrons ejected in the forward direction. The fraction of the photon energy hm that is transferred to the Compton electron is shown in Figure 1.6.

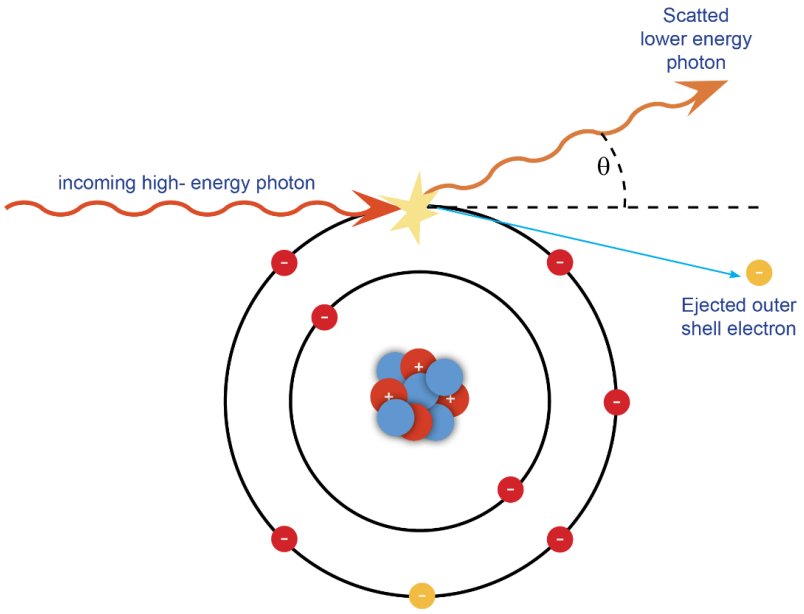

Figure 1.6: Compton scattering with a free electron.

The Compton interaction coefficient σ consists of two components,

$$\sigma = \sigma_a + \sigma_s$$

where σ is the total Compton interaction coefficient, σ_a is the Compton absorption coefficient for photon energy lost by collisions with electrons, and σ_s is the loss of energy due to the scattering of photons out of the beam. The Compton interaction coefficient is determined by electron density (τ) which is directly related to Z and inversely proportional to E as follows.

$$\tau \approx \text{Constant} \times \frac{Z}{E}$$

For photons with energies above 100 keV, Compton interactions in soft tissue (low-Z material) are much more important than either the photoelectric or pair production interactions.

1.13.3 Pair Production

When a high-energy (>1.022 MeV) photon interacts with the strong electromagnetic field surrounding a nucleus shown in Figure 1.7, its energy can be converted into a pair of electron masses, one of which is negatively charged (the electron) and the other, called the positron, is positively charged. Pair production can also occur in the field of an electron yielding a triplet consisting of a positron, a negatron, and the

recoiling electron. Pair production interactions are also accompanied by the emission of two annihilation photons of 0.511 MeV each, which are also shown in Figure 1.7.

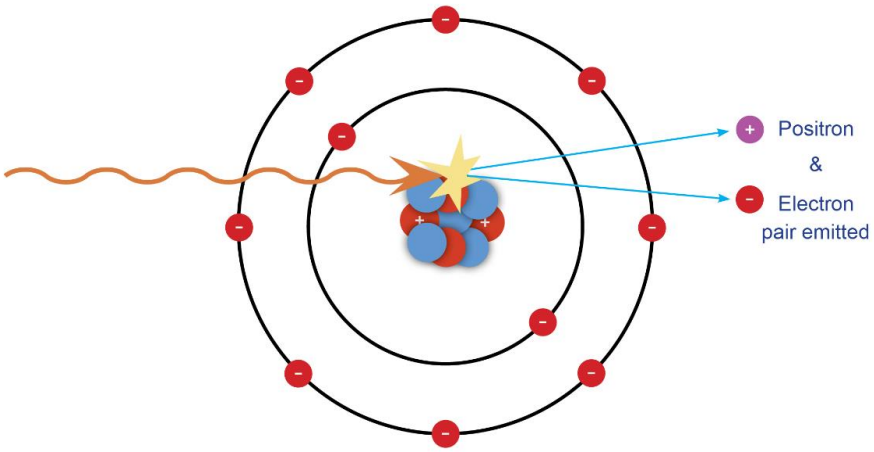

Figure 1.7: Pair production interaction.

Pair production is a classic example of Einstein's special theory of relativity in which the pure energy of the photon is converted into two electron masses, and since energy is conserved the positron and electron share the energy left over (hν – 1.022) after the electron masses have been formed. This remaining energy appears as kinetic energy of the e^+ and e^- pair but is not shared equally. The positively charged nucleus repels the positively charged positron which provides an extra "kick" while the electron is attracted and thus slowed down with a decrease in its kinetic energy. Because of these circumstances, the positron should receive a maximum of about 0.0075Z more kinetic energy than the average electron energy. The slight difference in energy shared by the positron and the electron in pair production interactions is of little consequence to radiation dosimetry or detection since the available energy, hν – 1.022 MeV, will be absorbed in the medium with the same average result regardless of how it is shared.

The positron will exist as a separate particle if it has momentum and kinetic energy. However, when it has been fully absorbed, being antimatter in a matter world, it will interact with a negatively charged electron forming for a moment a "neutral particle" of "positronium" which then vanishes yielding two 0.511 MeV photons, i.e., mass becomes energy. The absorption of high-energy photons thus yields a complex

pattern of energy emission and absorption in which the pure energy of the photon produces an electron and a positron which deposit hν – 1.022 MeV of kinetic energy along a path of ionization, followed in turn by positron annihilation with a free electron to convert mass back into energy. The absorption of a high-energy photon by pair production thus yields two new photons of 0.511 MeV which may or may not interact in the medium and an intermediate pair of electron masses which almost certainly do.

The pair production interaction coefficient κ is proportional to the square of the atomic number Z for photons with energy greater than 2 × 0.511 MeV (the energy required to form an electron–positron pair) and has the following relationship:

$$\kappa \approx \text{Constant} \times Z^2 (E\text{-}1.022)$$

The absorption coefficient increases rapidly with energy above the 1.022 MeV threshold and varies approximately as Z^2. The significance of the three processes mentioned above varies depending on the absorber material and the energy of gamma rays, as depicted in Figure 1.8.

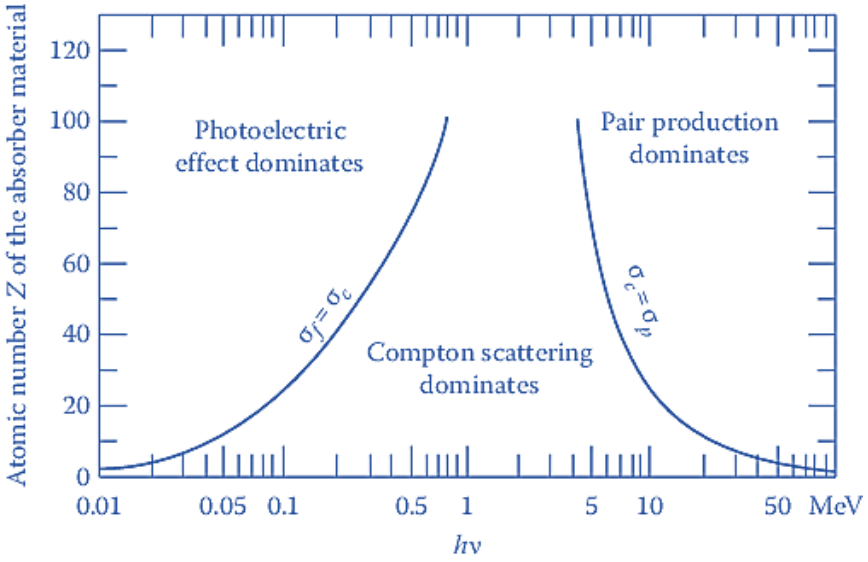

Figure 1.8: The three interaction processes for different absorber materials and gamma-ray energies.

On the left side of the graph, there is a line indicating the energy values where photoelectric absorption and Compton scattering have equal probabilities, varying with the atomic number of the absorber. Conversely, on the right side, another line marks photon energy values where Compton scattering, and pair production are equally probable. This graphical representation divides the plot into three distinct areas, each corresponding to the predominance of photoelectric absorption, Compton scattering, or pair production processes, respectively.

1.13.4 Photodisintegration

Photodisintegration interactions can also deplete a beam of photons if the photon energy is sufficiently large. From a practical standpoint, photodisintegration can generally be neglected in calculating the energy removed from a photon beam; however, such reactions are quite sharp at 1.66 MeV for ^{9}Be (γ, n) interactions and 2.225 MeV for ^{2}H (γ,n) interactions. Except for these two light elements, photodisintegration reactions require photon energies of 8 MeV or more. For photon energies above 20 MeV, the cross-sections for photodisintegration are sufficiently large and must be accounted for in shield designs. Large neutron fields are created at these energies and these neutrons will be mixed with many unabsorbed photons, both of which must be considered in radiation dosimetry and shield designs, at particularly in medical fields.

1.14 Photon Attenuation and Absorption

Photon interactions with matter are very different from those of charged particles. When X-rays or gamma rays traverse through matter, some are absorbed, some pass through without interaction, and some are scattered as lower energy photons in directions that are quite different from that of primary beam.

The attenuation of a photon beam by an absorber is characterized as occurring in "good geometry" or "poor geometry,". Good geometry exists when every photon that interacts is either absorbed or scattered out of the primary beam such that it will not impact a small receptor some distance away.

When good geometry exists only those photons that have passed through the absorber without any kind of interaction will reach the detector, and each one of these photons will have all its original energy. This situation exists when the primary

photons are confined to a narrow beam and the detector is small and sufficiently far away that scattered photons have a sufficiently large angle with the original narrowly focused beam that they truly leave the beam and do not reach the detector. Because of this condition, this geometry is also characterized as "narrow beam" geometry. Readings taken with and without the absorber in place will yield the fraction of photons removed from the narrow beam, by whatever process.

In poor geometry or "broad-beam geometry", a significant fraction of the scattered photons will also reach the receptor of interest in addition to those transmitted without interaction. Poor geometry exists in most practical conditions. Such conditions often exist when tissue is exposed or a shield is used to attenuate a photon, and each scattered photon will be degraded in energy according to the angle through which it is scattered. The photons reaching a receptor will then have a complex energy spectrum, including scattered photons of many energies and un-scattered photons originally present in the primary beam. The pattern of energy deposition in the detector will be equally complex and governed by the energy distribution and the exact geometrical arrangement used. The amount of energy deposited in an absorber or a detector under such conditions is very difficult to determine analytically.

1.15 Gamma-ray shielding

Gamma-ray shielding refers to the process of using specialized materials or structures to protect against the harmful effects of gamma radiation. Gamma rays are highly energetic electromagnetic waves or photons that can penetrate matter and potentially cause damage to living organisms and sensitive equipment. Gamma-ray shielding works by reducing the intensity of gamma radiation as it passes through a shielding material. The shielding material is selected based on its ability to absorb or scatter gamma rays, thereby effectively reducing their energy and preventing them from reaching the target area.

Gamma-ray shielding is essential for various applications incluing those in industries that involve the use of radioactive materials or exposure to sources of ionizing radiation, particularly gamma radiation [23]. Gamma rays are high-energy electromagnetic waves emitted during the radioactive decay of certain atomic nuclei

or generated in processes like nuclear reactions. They can penetrate most materials, including human tissue, making them potentially harmful to living organisms and sensitive equipment. The need for gamma-ray shielding arises due to several important reasons:

1. **Radiation Protection:** The primary reason for gamma-ray shielding is to protect humans and the environment from the harmful effects of ionizing radiation. Exposure to high levels of gamma radiation can damage or kill living cells, increasing the risk of cancer and other health issues. Shielding materials absorb and scatter gamma rays, reducing their intensity and the associated health risks for individuals working or living in proximity to radiation sources.

2. **Occupational Safety:** Many industries, such as nuclear power plants, medical facilities, research laboratories, and industrial processes, use or produce radioactive materials that emit gamma rays. Workers in these industries are at risk of exposure to high levels of radiation if proper shielding measures are not in place. Adequate gamma-ray shielding ensures the safety of workers and minimizes their exposure to harmful radiation.

3. **Medical Applications:** In medical settings, gamma-ray shielding is crucial to protect both patients and medical staff. Medical procedures that involve the use of radioactive isotopes for diagnostic imaging or cancer treatment emit gamma radiation. Shielding ensures that the radiation is confined to the targeted area, minimizing the dose to surrounding healthy tissues and reducing the potential for secondary health effects.

4. **Nuclear Industry:** Nuclear reactors, nuclear waste storage facilities, and spent fuel pools emit gamma radiation as part of their normal operation. Proper shielding is essential to prevent radiation leaks and protect the surrounding environment from contamination and radiation hazards.

5. **Space Exploration:** During space missions, astronauts are exposed to higher levels of cosmic radiation, including gamma rays, due to the lack of Earth's protective atmosphere. Designing spacecraft with effective gamma-ray shielding

is crucial to ensure the safety and health of astronauts during extended space travel.

6. **Security and Defence:** In some cases, gamma radiation sources can be used for nefarious purposes, such as in radiological weapons ("dirty bombs"). Shielding materials can help mitigate the impact of such devices by reducing the dispersion of radioactive materials and the spread of contamination.

7. **Sensitive Equipment:** Some scientific instruments and electronic devices are highly sensitive to radiation and can be damaged or malfunction if exposed to gamma rays. Shielding helps preserve the integrity and functionality of these instruments.

Gamma-ray shielding is achieved using dense materials that are capable of attenuating (reducing the intensity of) gamma radiation through processes like absorption and scattering. Common shielding materials include Lead, concrete, steel, and various types of high-density polymers. The thickness and type of shielding required depend on factors such as the energy and intensity of the gamma radiation, the distance from the source, and the level of protection needed.

The basic working of gamma-ray shielding involves the interaction of gamma rays with the shielding material to reduce their intensity and prevent them from reaching the target area. Here's a step-by-step explanation of the process:

1. Gamma Radiation Source: Gamma rays are emitted from various sources, such as nuclear reactions, radioactive decay, or high-energy particle interactions. These gamma rays are highly energetic electromagnetic waves with no charge and can penetrate matter.

2. Shielding Material Selection: The appropriate shielding material is selected based on the specific requirements of the application, including the energy and intensity of the gamma radiation. Materials with high density and high atomic number, such as lead, concrete, or steel, are commonly chosen as shielding materials.

3. Attenuation of Gamma Rays: The combined effects of absorption, scattering, and pair production lead to a reduction in the intensity of gamma radiation as it passes through the shielding material. The more interactions that occur, the greater the

attenuation of the gamma rays.

4. Shielding Effectiveness: The effectiveness of gamma-ray shielding depends on factors such as the thickness and composition of the shielding material, the energy of the gamma radiation, and the distance between the radiation source and the protected area. Thicker shielding materials and materials with high-density and high-atomic number properties provide greater attenuation.

By utilizing appropriate shielding materials and optimizing the thickness and composition, gamma-ray shielding can effectively reduce the intensity of gamma radiation, minimizing the risk of exposure and providing protection to individuals, equipment, and the environment.

To effectively shield against gamma radiation, gamma-ray shielding material must meet certain requirements. These requirements ensure that the material provides adequate protection and minimizes the risk of exposure. Key requirements for a gamma-ray shielding material are:

1. Attenuation Capability: The primary requirement of a gamma-ray shielding material is its ability to attenuate or reduce the intensity of gamma rays. The material should have a high linear attenuation coefficient, which measures how effectively it absorbs and scatters gamma radiation. The higher the attenuation capability, the better the shielding material.

2. High Density: Gamma rays are high-energy photons that can penetrate matter. Therefore, the shielding material should have a high density to effectively absorb and scatter the gamma rays. High-density materials have a greater number of atoms per unit volume, increasing the chances of interaction with gamma radiation.

3. High Atomic Number: Materials with a high atomic number tend to have a greater probability of interacting with gamma rays. Elements such as Lead (Pb), Tungsten (W), and Bismuth (Bi) have high atomic numbers and are commonly used in gamma-ray shielding.

4. Thickness: The thickness of the shielding material is an important factor in determining its effectiveness. Gamma rays lose their intensity exponentially as they pass through matter, so a thicker material provides more opportunities for interaction and absorption. The required thickness of the shielding material depends on the

energy and intensity of the gamma radiation.

5. Stability: The shielding material should be stable and not undergo significant degradation or deterioration when exposed to gamma radiation over time. Stability ensures that the shielding material remains effective and does not release any harmful by-products that could pose additional risks.

6. Non-Toxicity: The shielding material should be non-toxic to ensure the safety of individuals who handle. Approach to it. This is especially important in applications where the shielding material is used near humans, such as medical facilities. Non-toxic materials, such as borated polyethylene, are preferred in such cases.

7. Cost and Availability: The cost and availability of the shielding material are practical considerations. The material should be cost-effective and readily accessible in order to be feasible for use in various applications. Common materials like lead and concrete are often chosen for their affordability and widespread availability.

8. Structural Integrity: In certain applications, such as shielding for infrastructure or equipment, the material should possess sufficient structural integrity. It should be able to withstand the physical stresses and strains placed upon it without compromising its shielding capabilities.

9. Regulatory Compliance: The shielding material must comply with relevant regulations and standards regarding radiation protection. These regulations may specify requirements for maximum exposure limits, acceptable attenuation levels, and other safety guidelines. Adhering to these regulations ensures that the shielding material provides the necessary protection in each application.

1.16 Different Types of Shielding Materials

It is important to note that the specific requirements for a gamma-ray shielding material can vary depending on the intended use, energy levels of the gamma radiation, and the desired level of protection. Different applications may require different combinations of materials and thicknesses to meet their specific shielding requirements.

Gamma-ray shielding materials are designed to protect individuals and sensitive equipment from the harmful effects of gamma radiation. Gamma rays are highly

energetic electromagnetic waves or photons that are emitted during certain nuclear reactions, radioactive decay, and high-energy particle interactions. Shielding materials work by absorbing or attenuating the gamma rays, reducing their intensity, and preventing them from reaching their target. Several types of materials can effectively shield against gamma radiation. The choice of shielding material depends on factors such as the energy and intensity of the gamma rays, the duration of exposure, and the specific application. Here are some commonly used gamma-ray shielding materials:

1. Lead: Lead (Pb) is widely recognized as one of the most effective materials for Gamma-ray attenuation. It possesses several properties that make it an ideal choice for shielding against Gamma radiation. Here are some key points about lead's role in Gamma-ray attenuation. First is high atomic numbers. Lead has a high atomic number (82), which means it contains many protons in its nucleus. The high atomic number results in a greater probability of interaction between the gamma rays and the lead atoms, leading to effective attenuation. Lead is a dense material with a density of 11.34 grams per cubic centimeter. The density contributes to its attenuation capability by providing a larger number of atoms per unit volume for gamma rays to interact with, thereby increasing the likelihood of absorption or scattering. Lead attenuates gamma rays through several interaction mechanisms, including the photoelectric effect, Compton scattering, and pair production. The probability of these interactions occurring is proportional to the atomic number and density of the material, making lead highly effective in attenuating gamma rays.

Lead offers exceptional shielding effectiveness against gamma rays, especially in the energy range typically encountered in medical and industrial applications. It can significantly reduce the intensity of gamma radiation by absorbing and scattering the photons, preventing them from passing through the shielding material. When designing lead shielding for gamma-ray attenuation, the thickness and configuration of the lead are important factors. Increasing the thickness of the lead barrier increases the attenuation level since more interactions occur. However, there may be practical limitations due to weight, space, and cost considerations. While lead is highly effective for gamma-ray attenuation, it is essential to consider radiation safety

measures during the design, installation, and maintenance of lead shielding. Proper handling, containment, and monitoring procedures should be followed to protect individuals from radiation exposure.

2. Concrete: Concrete is commonly used as a shielding material for gamma-ray attenuation due to its availability, cost-effectiveness, and inherent radiation shielding properties. Concrete is a composite material composed of cement, aggregates (such as sand and gravel), and water. The specific composition and proportions may vary depending on the desired strength and other engineering requirements. The presence of heavy aggregates, such as dense minerals or metals, in the concrete mixture enhances its gamma-ray attenuation capabilities. The density of concrete plays a crucial role in gamma-ray attenuation. Higher density concrete, achieved through the use of heavier aggregates or additives, provides better shielding as it increases the number of atoms per unit volume, thereby increasing the probability of interaction with gamma rays.

The probability of these interactions occurring is influenced by the atomic composition and density of the materials within the concrete. The interaction mechanisms result in the absorption, deflection, and degradation of gamma rays, effectively reducing their intensity. The thickness of the concrete shielding determines its effectiveness in attenuating gamma rays. Increasing the thickness increases the number of interactions between the gamma rays and the shielding material, leading to higher attenuation. However, the attenuation capability may saturate at a certain thickness due to the limitations of the concrete's composition and the energy of the gamma radiation. When designing concrete shielding for gamma-ray attenuation, factors such as the energy and intensity of the radiation, the required shielding level, and space constraints should be considered. Computational modelling or empirical data can be utilized to determine the appropriate concrete thickness and configuration to achieve the desired attenuation. Concrete shielding for gamma-ray attenuation should comply with applicable regulatory standards and guidelines, such as those set by radiation protection agencies or organizations. These standards define the acceptable levels of radiation exposure and specify the minimum requirements for shielding materials in different applications. It is

important to note that the attenuation capabilities of concrete may vary depending on the energy spectrum of the gamma radiation. For higher energy gamma rays, additional shielding measures or materials with higher atomic number may be necessary. Consulting with radiation shielding experts and following industry best practices are recommended to ensure effective gamma-ray attenuation when using concrete as a shielding material.

3. Steel: Steel is another material commonly used for gamma-ray shielding. Steel is an alloy primarily composed of iron and carbon, along with small amounts of other elements such as manganese, chromium, and nickel. The composition of the alloy can vary, and different types of steel may have varying levels of attenuation effectiveness. It is especially useful in applications that require structural integrity along with radiation protection. The high density and atomic number of steels make it an effective shield against gamma radiation. The density of steel typically ranges from 7.75 to 8.05 grams per cubic centimetre, which provides a sufficient number of atoms per unit volume for gamma-ray interactions. Steel shielding is commonly used in nuclear reactors, research facilities, and radioactive material transportation. In addition to its gamma-ray attenuation properties, steel is often chosen as a shielding material due to its structural strength. Steel can provide both radiation protection and structural integrity, making it suitable for applications where both aspects are important, such as in radiation therapy rooms or nuclear facilities. Steel offers good shielding effectiveness against gamma rays, especially in the lower to medium energy range. It can significantly reduce the intensity of gamma radiation by absorbing and scattering the photons, preventing them from passing through the shielding material.

4. Tungsten: Tungsten (W) is a highly effective material for gamma-ray attenuation due to its unique properties. Tungsten has a high atomic number (74), which means it contains a large number of protons in its nucleus. This high atomic number results in a greater probability of interaction between gamma rays and Tungsten atoms, leading to effective attenuation. Tungsten is a dense material with a density of approximately 19.3 grams per cubic centimetre. The high density contributes to its attenuation capabilities by providing a large number of atoms per unit volume for

gamma rays to interact with, increasing the likelihood of absorption or scattering. The probability of these interactions occurring is proportional to the atomic number and density of the material, making Tungsten highly effective in attenuating gamma rays. Tungsten offers excellent shielding effectiveness against gamma rays, especially in the higher energy range. It can significantly reduce the intensity of gamma radiation by absorbing and scattering the photons, preventing them from passing through the shielding material. Increasing the thickness of the Tungsten barrier increases the attenuation level as more interactions occur. However, practical considerations such as weight, space limitations, and cost may impose restrictions on the thickness of the Tungsten shielding.

Tungsten is also used in the form of Tungsten alloys, such as Tungsten-copper or Tungsten-nickel-iron, for gamma-ray shielding. These alloys provide a balance between Tungsten's attenuation capabilities and the desirable properties of other metals, such as thermal conductivity or mechanical strength. It is important to note that Tungsten is a dense and heavy material, which can make it challenging to work with in some applications. Its high cost is also a factor to consider. Therefore, a thorough assessment of the specific requirements, radiation characteristics, and application constraints should be carried out to determine the suitability of Tungsten for gamma-ray attenuation. Consulting with radiation shielding experts and considering relevant standards and guidelines is recommended for effective design and implementation.

5. Bismuth: Bismuth is a low-toxicity, high-density metal that is increasingly being used as a gamma-ray shielding material, especially in medical and dental applications. Bismuth-based alloys, such as Bismuth-lead or Bismuth-tin, provide effective shielding while reducing the overall weight of the shielding material. Bismuth (Bi) is a highly effective material for gamma-ray attenuation due to its unique properties. Bismuth has a high atomic number (83), which means it contains a large number of protons in its nucleus. This high atomic number results in a greater probability of interaction between gamma rays and Bismuth atoms, leading to effective attenuation. Bismuth is a dense material with a density of approximately 9.8 grams per cubic centimetre. The high density contributes to its attenuation

capabilities by providing a large number of atoms per unit volume for gamma rays to interact with, increasing the likelihood of absorption or scattering. When designing Bismuth shielding for gamma-ray attenuation, the thickness and configuration of the Bismuth are important factors. Increasing the thickness of the Bismuth barrier increases the attenuation level as more interactions occur. However, practical considerations such as weight, space limitations, and cost may impose restrictions on the thickness of the Bismuth shielding. Bismuth is also widely used as a radiopaque contrast agent in medical imaging procedures. Its high atomic number makes it highly visible on X-ray and other imaging modalities, aiding in the visualization of anatomical structures and the detection of abnormalities. When considering Bismuth for gamma-ray attenuation, a comprehensive evaluation of the specific requirements, radiation characteristics, and application constraints should be performed. Consulting with radiation shielding experts and adhering to relevant standards and guidelines is recommended for effective design and implementation.

6. Polymer composites: Polymer composites can be effectively used for Gamma-ray attenuation due to their unique combination of properties. Gamma rays are high-energy electromagnetic waves, and they require materials with high atomic number elements and density to attenuate them. Polymer composites can be reinforced with high atomic number fillers such as lead, Tungsten, Bismuth, or Barium sulphate [24]–[29]. These fillers have a high electron density, which increases the probability of interaction between the gamma rays and the composite material, leading to attenuation. The concentration of filler materials in the polymer matrix plays a crucial role in Gamma-ray attenuation. Higher filler concentrations result in increased attenuation due to the increased number of atoms available for interaction with the gamma rays.

The size and distribution of the filler particles within the polymer matrix also affect the attenuation properties. Smaller particle sizes and uniform distribution promote better interactions with gamma rays, leading to improved attenuation. The choice of polymer matrix is essential as it provides structural integrity and helps disperse the filler particles. Common polymer matrices used for Gamma-ray attenuation include epoxy resins, Polyethylene, and Polystyrene [30]. The thickness of the polymer

composite is a critical factor in Gamma-ray attenuation. Thicker materials provide increased shielding by allowing more interactions between the gamma rays and the composite. However, the attenuation capability may saturate at a certain thickness due to the inherent properties of the composite. When designing polymer composites for Gamma-ray attenuation, it is crucial to test their performance under relevant conditions. Certification bodies and regulatory agencies may have specific standards and guidelines for evaluating the effectiveness of such materials in attenuating gamma rays. It is important to note that the design and selection of polymer composites for Gamma-ray attenuation should be performed by experts in radiation shielding and material engineering. The specific requirements, radiation source characteristics, and application constraints should be carefully considered to ensure the desired level of attenuation is achieved.

7. Glass: Glass can provide some level of gamma-ray attenuation, but its effectiveness depends on various factors. The composition of glass plays a crucial role in its gamma-ray attenuation capabilities. Certain types of glass, such as Lead glass or Borosilicate glass, contain heavy elements like lead or boron, which have high atomic numbers. These heavy elements enhance the attenuation properties of the glass by increasing the probability of interaction with gamma rays. The atomic number and density of the elements present in the glass determine its ability to attenuate gamma rays. Glass containing higher atomic number elements and denser materials can effectively attenuate gamma radiation by promoting interactions such as the photoelectric effect and Compton scattering. Increasing the thickness of the glass increases the number of interactions between gamma rays and the glass material, leading to higher attenuation. However, there may be practical limitations to consider, such as weight and space constraints.

The effectiveness of glass for gamma-ray attenuation can vary depending on the energy range of the gamma radiation. Different types of glass may have different optimal energy ranges for attenuation. It is important to consider the energy spectrum of the gamma rays and select the appropriate glass type accordingly. When using glass for gamma-ray attenuation, the design of the shielding system is crucial. Factors such as the required shielding level, geometry, and configuration of the glass

panels should be carefully considered. Multiple layers or combinations of glass with other shielding materials may be necessary to achieve the desired attenuation. Glass has certain limitations for gamma-ray attenuation compared to other materials like Lead or Tungsten. It may not be as effective in attenuating higher energy gamma rays due to its atomic composition. Additionally, glass may have limitations in terms of temperature resistance, mechanical strength, and cost-effectiveness. It is important to consult with radiation shielding experts and follow relevant standards and guidelines when using glass for gamma-ray attenuation. They can provide guidance on the appropriate glass type, thickness, and configuration based on the specific requirements and radiation characteristics.

1.17 Motivation of this research

Natural radioactivity in building materials poses a significant health risk due to prolonged exposure to radiation. Understanding the levels of natural radioactivity in these materials is crucial for ensuring safe living and working environments. Moreover, as the construction industry continuously seeks materials that are not only cost-effective but also safe, there is a growing need to evaluate and enhance the gamma attenuation properties of these materials.

In some of the earlier studies, environmental radioactivity had been measured at specific locations in India, particularly in Kerala, including some coastal areas and the Western Ghats. Though many places had been covered under such studies, there are still certain hilly regions and densely populated cities which had not yet been explored. Nowadays, the number of cancer patients are increasing alarmingly. So, it is a need of the hour and a social responsibility to carry out studies like this, concentrating at places which are frequently used by people for travel and stay. In our country, there are attempts to conduct a national-wide survey of environmental radioactivity. The present data will surely contribute to it and that is the relevance of the present study. Investigating both the natural radioactivity levels in building materials and their gamma attenuation capabilities, this research aims to contribute to the development of safer building practices and materials.

The presence of natural radioactivity in the environment, particularly in densely

populated areas, raises significant public health concerns. Rock and soil, the primary components of the Earth's crust, naturally contain radioactive elements such as Uranium, Thorium, and Potassium. When these materials are present in residential and commercial areas, they can contribute to the background radiation levels, potentially increasing the risk of radiation-related health issues among the inhabitants. Therefore, it is imperative to measure and monitor the radioactivity levels in these areas to assess the potential health risks and ensure the safety of the population.

Accurate measurement of radioactivity in rock and soil samples from populated areas allows for the evaluation of associated radiological parameters such as Radium equivalent activity, external hazard index, and annual effective dose. These parameters provide a comprehensive understanding of the radiation exposure levels and help in developing guidelines and regulations to mitigate the risks. By conducting thorough investigations and analyses, this research aims to identify areas with elevated radioactivity levels and propose effective measures to reduce radiation exposure, thereby enhancing public health and safety. The outcomes of this study will not only contribute to the scientific understanding of environmental radioactivity but also support policymakers in making informed decisions regarding land use and construction practices in populated regions.

In an era where radiation technology is extensively used in medical, industrial, and scientific fields, ensuring adequate protection from gamma radiation has become a critical concern. Traditional shielding materials, such as lead, though effective, pose several drawbacks, including high cost, significant weight, and environmental toxicity. These limitations necessitate the development of innovative shielding materials that are not only cost effective and environment friendly but also exhibit properties such as flexibility, hardness, and ease of application. Epoxy coatings, known for their versatility and durability, present a promising solution in this regard. The development of low-cost, hard, flexible and epoxy-based gamma shielding materials could revolutionize the field of radiation protection. These materials would provide a lightweight and environmentally friendly alternative to conventional shielding materials. By incorporating effective gamma attenuation properties into

concrete, natural rubber, epoxy coatings, we aimed to create a material that offers robust protection while being easy to manufacture and apply. The success of this initiative could lead to significant advancements in radiation safety, reducing exposure risks and enhancing the overall safety of environments where gamma radiation is prevalent.

1.18 Objectives of the Work

The entire research work presented in this thesis is founded on the motivations outlined above. Accordingly, the major objectives of the thesis work are as listed below:

- **Comprehensive measurement of natural radioactivity**:
  - Conduct extensive measurements of natural radioactivity levels in specific sites in the state of Kerala, India: Thrissur-Palakkad highway zone (Kuthiran Hills, part of the Western Ghats in Kerala), Urban regions along National Highway 66 (NH-66) in Kerala and Athirappilly Waterfalls (Athirappilly Hills, part of the Western Ghats in Kerala), focusing on rock and soil samples.
  - Analyse the radiogenic heat production and associated radiological parameters, such as Radium equivalent activity, annual effective dose, absorbed dose rate and hazard indices.
  - Identify the primary sources and levels of radiation exposure in these regions to assess the potential health risks and ensure public safety.
- **Development of optimized gamma-ray shielding materials**:
  - Design and develop gamma-ray shielding materials with optimized characteristics, such as low cost, high flexibility, and sufficient hardness.
  - Evaluate different compositions of shielding materials, particularly epoxy-based coatings, to determine their effectiveness in attenuating gamma radiation.

- Identify the most practical and efficient compositions for various applications, including medical, industrial, and personal protective equipment.

➢ **Numerical simulation of attenuation properties**:

- Utilize numerical simulation techniques to predict the gamma attenuation properties of the developed shielding composites.
- Validate the simulation results through experimental measurements to ensure accuracy and reliability.
- Use the simulation data to refine the design and development process of shielding materials, aiming to enhance their performance and applicability in real-world scenarios.

Brief outline of the thesis chapters

This thesis is structured to comprehensively explore the motivations and objectives driving the research on natural radioactivity and gamma-ray shielding materials. It is present in 9 Chapters. Chapter 2 provides a review of the existing literature, laying the groundwork by discussing previous studies and the current state of knowledge in the fields of natural radioactivity and radiation shielding. Chapter 3 details the experimental techniques and methodologies employed in this work. Here describing the procedures for measuring radioactivity in soil and rock samples, as well as the development and testing of gamma-ray shielding materials.

Chapter 4 delves into the theoretical framework based on which underpinning the study, offers a detailed explanation of the principles and models used to analyse the data. The results and discussion, divided into two major sections: first, Chapter 5 focuses on the measurement of natural radioactivity levels of soil and rock samples, associated radiological parameters, radiogenic heat production and heat flow arises in the study regions. While the second section (chapter 6-8) discusses the development, characterization and key finding of gamma-ray shielding materials. This chapter synthesizes the findings, comparing them with theoretical predictions and existing literature.

Finally, Chapter 9 provides general conclusions drawn from the research, summarizing the key findings and their implications. Also, offers recommendations

for future research and practical applications, suggesting ways to enhance the safety and effectiveness of materials used in radiation shielding and the monitoring of natural radioactivity in populated areas.

1.19 Reference

[1] G. R. Gilmore and J. Wiley, *Practical Gamma-ray Spectrometry*, 2nd Edition. 2011.

[2] UNSCEAR, *Sources, Effects and Risks of Ionizing Radiation*, vol. 120, no. 1. 2008.

[3] G. F. Knoll, *Radiation Detection and Measurement*, 3rd ed. John Wiley & Sons, Inc, 2000.

[4] Nicholas Tsoulfanidis, "MEASUREMENT AND DETECTION OF RADIATION," *Theor. Opt.*, pp. 273–287, 2004, doi: 10.1002/3527604294.ch14.

[5] R. Ravisankar *et al.*, "Multivariate statistical analysis of radiological data of building materials used in tiruvannamalai, tamilnadu, india," *Appl. Radiat. Isot.*, vol. 85, pp. 114–127, Feb. 2014, doi: 10.1016/j.apradiso.2013.12.005.

[6] B. G. Jagadeesha and Y. Narayana, "Effect of Grain Size on Radon Exhalation Rate in the Soils of Hassan District of Southern India," *Radiochemistry*, vol. 60, no. 3, pp. 328–333, 2018, doi: 10.1134/S1066362218030177.

[7] M. M. Prakash, C. S. Kaliprasad, and Y. Narayana, "Studies on natural radioactivity in rocks of Coorg district, Karnataka state, India," *J. Radiat. Res. Appl. Sci.*, vol. 10, no. 2, pp. 128–134, 2017, doi: 10.1016/j.jrras.2017.02.003.

[8] A. K. Mahur, R. Kumar, R. G. Sonkawade, D. Sengupta, and R. Prasad, "Measurement of natural radioactivity and radon exhalation rate from rock samples of Jaduguda Uranium mines and its radiological implications," *Nucl. Instruments Methods Phys. Res. Sect. B Beam Interact. with Mater. Atoms*, vol. 266, no. 8, pp. 1591–1597, Apr. 2008, doi: 10.1016/j.nimb.2008.01.056.

[9] P. M. Raste *et al.*, "A study on natural radioactivity and potential of 222Rn, 220Rn exhalation from Deccan table land of Kolhapur district, Maharashtra, India," *J. Radioanal. Nucl. Chem.*, vol. 326, no. 2, pp. 1333–1341, 2020, doi: 10.1007/s10967-020-07384-2.

[10] C. S. Kaliprasad, P. R. Vinutha, and Y. Narayana, "Natural Radionuclides and Radon Exhalation Rate in the Soils of Cauvery River Basin," *Air, Soil Water Res.*, vol. 10, 2017, doi: 10.1177/1178622117746948.

[11] S. Monica, A. Visnu Prasad, S. Soniya, and P. Jojo, "Estimation of indoor and outdoor effective doses and lifetime cancer risk from gamma dose rates along the coastal regions of Kollam district, Kerala," *Radiat. Prot. Environ.*, vol. 39, no. 1, p. 38, 2016, doi: 10.4103/0972-0464.185180.

[12] M. Ramsiya, A. Joseph, K. P. Eappen, and A. K. Visnuprasad, "Activity concentrations of radionuclides in soil samples along the coastal areas of Kerala, India and the assessment of radiation hazard indices," *J. Radioanal. Nucl. Chem.*, vol. 320, no. 2, pp. 291–298, 2019, doi: 10.1007/s10967-019-06481-1.

[13] ICRP, "Recommendations of the International Commission on Radiological Protection.," 1991.

[14] H. A. M. Al-Trabulsy, A. E. M. Khater, and F. I. Habbani, "Heavy elements concentrations, physiochemical characteristics and natural radionuclides levels along the Saudi coastline of the Gulf of Aqaba," *Arab. J. Chem.*, vol. 6, no. 2, pp. 183–189, 2013, doi: 10.1016/j.arabjc.2010.10.001.

[15] E. O. Joshua and O. O. Alabi, "Pattern of Radiogenic Heat Production in Rock Samples of Southwestern Nigeria," *J. Earth Sci. Geotech. Eng.*, vol. 2, no. 2, pp. 25–38, 2012.

[16] T. Ramingwong, S. Lertsrimongkol, P. Asnachinda, and S. Praserdvigai, "Update On Thailand Geothermal Energy Research and Development," vol. 2, pp. 377–386, 2000.

[17] X. Li, L. Cai, S. Liu, and X. Li, "Thermal Properties of Evaporitic Rocks and their Geothermal Effects on the Kuqa Foreland Basin, Northwest China," *Geothermics*, vol. 88, no. May, p. 101898, 2020, doi: 10.1016/j.geothermics.2020.101898.

[18] T. Farag, N. Soliman, A. El Shayat, and H. Mizunaga, "Comparison among the natural radioactivity levels, the radiogenic heat production, and the land surface temperature in arid environments: A case study of the El Gilf El Kiber area, Egypt," *J. African Earth Sci.*, vol. 172, p. 103959, 2020. doi: 10.1016/j.jafrearsci.2020.103959.

[19] T. A. Adagunodo, O. G. Bayowa, A. I. Ojoawo, M. R. Usikalu, and M. Omeje, "Radiogenic Heat Model in the southern axis of Ogbomoso, SW Nigeria," *J. Phys. Conf. Ser.*, vol. 1299, no. 1, 2019, doi: 10.1088/1742-6596/1299/1/012074.

[20] S. O. Asere, and Sedara, "Determination of Natural Radioactivity Concentration and Radiogenic Heat Production in Selected Quarry Sites in Ondo State, Nigeria," *NIPES J. Sci. Technol. Res.*, vol. 2, no. 3, p. 256, Aug. 2020, doi: 10.37933/nipes/2.3.2020.26.

[21] E. O. Joshua, O. A. Ehinola, M. A. Akpanowo, and O. A. Oyebanjo, "Radiogenic heat production in crustal rock samples of Southeastern Nigeria," *Eur. J. Sci. Res.*, vol. 23, no. 2, pp. 305–316, 2008.

[22] D. Liao, D. Feng, J. Luo, and X. Yun, "Relationship between radiogenic heat production in granitic rocks and emplacement age," *Energy Geosci.*, vol. 4, no. 4, p. 100157, 2023, doi: 10.1016/j.engeos.2023.100157.

[23] I. Akkurt, H. Akyıldırım, B. Mavi, S. Kilincarslan, and C. Basyigit, "Annals of Nuclear Energy Photon attenuation coefficients of concrete includes barite in different rate," *Ann. Nucl. Energy*, vol. 37, no. 7, pp. 910–914, 2010, doi: 10.1016/j.anucene.2010.04.001.

[24] A. A. El-Maaref, B. M. Alotaibi, N. Alharbi, A. F. A. El-Rehim, and K. S. Shaaban, "Effect of Fe2O3 as an Aggregate Replacement on Mechanical, and Gamma/ Neutron Radiation Shielding Properties of Phosphoaluminate Glasses," *J. Inorg. Organomet. Polym. Mater.*, vol. 32, no. 8, pp. 3117–3127, 2022, doi: 10.1007/s10904-022-02345-6.

[25] N. Plangpleng *et al.*, "Flexible gamma-ray shielding based on natural Rubber/BaSO4 nanocomposites," *Radiat. Phys. Chem.*, vol. 199, Oct. 2022, doi: 10.1016/j.radphyschem.2022.110311.

[26] W. Poltabtim, E. Wimolmala, and K. Saenboonruang, "Properties of lead-free gamma-ray shielding materials from metal oxide/EPDM rubber composites," *Radiat.*

Phys. Chem., vol. 153, pp. 1–9, 2018, doi: 10.1016/j.radphyschem.2018.08.036.

[27] R. El-Mallawany, M. I. Sayyed, M. G. Dong, and Y. S. Rammah, "Simulation of radiation shielding properties of glasses contain PbO," *Radiat. Phys. Chem.*, vol. 151, no. June, pp. 239–252, 2018, doi: 10.1016/j.radphyschem.2018.06.035.

[28] A. Kozlovskiy, D. B. Borgekov, D. I. Shlimas, and V. Zdorovets, "Study of the efficiency of increasing the Bi2O3 concentration on the optical, radiation shielding and strength characteristics of 0.5TeO2-(0.5-x)WO3-xBi2O3 glasses," *Opt. Mater. (Amst).*, vol. 120, no. May, p. 111494, 2021, doi: 10.1016/j.optmat.2021.111494.

[29] A. Obeid, M. Roumie, M. S. Badawi, and R. Awad, "Evaluation of the Effect of Different Nano-Size of WO3 on the Structural and Mechanical Properties of HDPE," *J. Inorg. Organomet. Polym. Mater.*, vol. 32, no. 4, pp. 1506–1519, 2022, doi: 10.1007/s10904-021-02219-3.

[30] N. Kucuk, M. Cakir, and N. A. Isitman, "Mass attenuation coefficients, effective atomic numbers and effective electron densities for some polymers," *Radiat. Prot. Dosimetry*, vol. 153, no. 1, pp. 127–134, 2013, doi: 10.1093/rpd/ncs091.

CHAPTER 2

LITERATURE AND BACKGROUNDS

Content	
2.1	*Radiation exposure pathways*
2.2	*Rock - Soil Samples Global analysis*
2.3	*Natural radioactivity measurements in India*
2.4	*Radiation shielding Materials.*
2.5	*Reference*

Abstract: *This review explores current research on natural radioactivity measurements and materials used for gamma radiation shielding. It highlights the importance of accurate radioactivity monitoring for environmental and health safety and discusses advancements in shielding materials, including concrete, glass, polymer, and epoxy-resin composites.*

2.1 Radiation exposure pathways

Radiation exposure to human beings can either be internal or external. Internal exposure is usually because of inhalation of radon, thoron, and their progenies, or ingestion of foods and/or drinks contaminated with the radionuclides. Ingestion mainly occurs when the radionuclides present in the environment enter the food chain. The contamination may also occur directly where the radionuclides are deposited on the above-ground parts of the plants. Also, indirect contamination takes place when the radionuclides are taken from the soil by the root system of plants through the sorption process[1].

Radioactive elements found in the crust and mantle are widespread and their abundance can contribute to the levels of background radiation in earth's environment. Natural radioactivity investigations are essential for comprehending human exposure to natural radiation. About 96% of the total radiation dose to people is from natural sources, while 4% is from man-made sources. The radionuclides ^{226}Ra, ^{232}Th and ^{40}K are a constant and inescapable feature of life on Earth because these radionuclides exist everywhere: in soils, rocks, water, plants, building materials, air and the human body. The decay products of the ^{226}Ra and ^{232}Th series exist in the Earth's crust in parts per million (ppm) level. ^{40}K is a single natural radionuclide and makes up 0.0118% of the total Potassium present in the crust. ^{226}Ra, ^{232}Th, and ^{40}K concentrations in the soil vary because their concentration level depends on the soil and the nature of the rocks. Sediments are considered an essential environmental material for building materials, streets and playgrounds. The presence of naturally decaying radionuclides in these materials leads to indoor exposure.

Radon and thoron gases emanate from the soil in form of soil gas and can enter and attain high concentration levels in indoor air. The radon isotopes are carcinogenic and are responsible for the largest fraction of cancer cases among non-smokers. Radon is considered as the second most important cause of lung cancer after smoking in many countries [2]–[6], as declared by WHO, (2011) [5]. While most inhaled dose has previously been attributed to radon (^{222}Rn), more recent studies

show that thoron (^{220}Rn) is of concern particularly in dwellings where the main building material is soil. In China for instance, residential dwellings constructed using soil and earth-dug cave dwellings with elevated thoron concentration in some cases as high as 1,860 Bq m^{-3} have been reported by Tokonami *et al*., 2005 [7]. Radon concentration depends on the type of building materials, humidity, place, and time, inflow of soil gas from the ground and ventilation of the house. Thoron on the other hand varies significantly due to its short half-life[8]. The levels of the isotopes have also been reported to vary seasonally with the highest levels being reported in winter, and lowest being reported in summer. In winter, doors and windows remain closed almost throughout the period resulting to poor ventilation. In summer, however, the doors and windows remain open most of the time enhancing air exchange between the inside and the outside. Studies done in Garhwal Himalaya reported higher radon and thoron levels in mud houses as compared to wooden houses[9]. Thoron progeny measured as Equilibrium Equivalent Thoron Concentration (EETC) levels in the same study were reported to be higher in mud-built houses and lowest in cemented houses[10]–[13]. The isotopes by itself are not responsible for the dose to the respiratory tract that is said to cause cancer but rather their progeny. Unlike the Radon isotopes, the progenies, (^{210}Pb and ^{210}Po) are short-lived charged particles and may become attached to aerosol, dust, smoke, and moisture particles. When inhaled in free or attached form, the progeny can lodge itself in the lungs. Consequently, upon decay, they deposit energetic Alpha particles on the cells of the mucous membranes, bronchi and other pulmonary tissues which may damage the bronchial epithelial cells thereby increasing the risk of lung cancer [14].

2.2 Rock - Soil Samples Global analysis

All rocks and soils contain some amounts of primordial radionuclides whose levels depend on the geology of the given area. Areas with extremely high concentration levels of the radionuclides are regarded to as High Background Radiation Areas (HBRA). Some of the high background radiation areas in the world include Guarapari in Brazil, Ramsar in Iran, Paralana in Austria, Yangjiang in China and

Karunagappally in India. Several studies have been carried out across the world. Recently, researchers have developed great interest in Thoron and the daughter products which have been ignored for a long time.

Akingboye et al., 2021 carried out detailed real-time in situ gamma-ray spectrometric measurements to determine the radionuclides concentration, mobilization, Radiogenic Heat Production (RHP) rate (first report for the area) and environmental radiation risk to humans. of the Basement Complex rocks in Akungba- Akoko, southwestern Nigeria [15]. The results of this study were integrated with previous data on the petrography and geochemistry of these rocks, for detailed interpretation. The results of average elemental and activity concentrations for Akungba-Akoko rocks, were 2.66%, 3.16 ppm and 13.98 ppm, and 831.35, 39.01 and 56.77 $Bqkg^{-1}$ for ^{40}K, ^{238}U and ^{232}Th, respectively. They found that due to the high gamma radiation from the pegmatitic and biotite-rich rocks in the studied area, their high usage should be reduced. Hence, periodic monitoring of the study area is advised.

In 2021, Selin Özden and Serpil Aközcan were examined the activity concentration of natural ^{226}Ra, ^{232}Th, and ^{40}K radionuclides in some sediments samples from 30 locations selected locations in Aliaga Bay of Izmir district, Turkey. The activity concentration was measured by a gamma-ray spectrometry using a high-purity germanium HPGe gamma-ray detector[16]. The activity concentrations of the sediment samples range from 23.5 ± 1.7 to 59.5 ± 1.6 Bq kg^{-1} for ^{226}Ra, 37.5 ± 0.9 to 64.4 ± 0.6 Bq kg^{-1} for ^{232}Th, and 354.7 ± 5.6 to 978.4 ± 5.8 Bq kg^{-1} for ^{40}K. Based on the obtained results, the radiological parameters were evaluated. The mean values for absorbed dose rate, annual effective dose equivalent, Radium equivalent activity, external hazard index, and excess lifetime cancer risk were determined and found as 81.64 nGy h^{-1}, 100.13 μSv y^{-1}, 173.31 Bq kg^{-1}, 0.47, and 0.40, respectively. The results obtained in this study were found to be above the global standard limit for most locations.

Mehboob et al., in 2020, measured the activity concentration of ^{235}U, ^{40}K, ^{238}U, ^{226}Ra, and ^{232}Th in phosphate rock found in the Kingdom of Saudi Arabia (from four

places namely Al-Jalamid, Turaif, UmmWu'al, and As-Sanam) by the HPGe gamma-ray spectrometry[17]. The average activity concentration of ^{235}U, ^{238}U, ^{226}Ra, ^{232}Th, and ^{40}K has been measured as (10.34±1.49 Bq kg^{-1}, 260.99±19.68 Bq kg^{-1}, 242.33±2.74 Bq kg^{-1}, 3.42±0.94 Bq kg^{-1}, and 47.50±3.03 Bq kg^{-1}) for Al-Jalamid phosphate rock ores, respectively; (46.10±2.61 Bq kg^{-1},1028.31±36.88 Bq kg^{-1}, 989.98±6.41 Bq kg^{-1}, 13.75±1.68 Bq kg^{-1}, and 51.93±3.82 Bq kg^{-1}) for Turaif phosphate rock ores, respectively; (63.60±3.33 Bq kg^{-1}, 1353.25±41.58 Bq kg^{-1}, 1304.29±7.70 Bq kg^{-1}, 13.45±1.64 Bq kg^{-1}, and 40.26±3.67 Bq kg^{-1}) for UmmWu'al phosphate rock ores, respectively; and (13.83±1.59 Bq kg^{-1}, 318.72±21.78 Bq kg^{-1}, 350.50±3.14 Bq kg^{-1}, 5.01±1.13 Bq kg^{-1}, and 42.15±3.02 Bq kg^{-1}) for As-Sanam phosphate mines, respectively. The elemental analysis of phosphate rock has been carried out using the wavelength dispersion of the X-ray fluorescence technique and the composition analysis has been carried out by the X-ray diffraction technique.

Amini Birami et al., in 2019, investigated the distribution and possible radiological hazards of natural radionuclides in the rock and soil samples from a region in Northern Iran to quantify radionuclide variations on the basis of mineralogical composition and physicochemical properties, respectively[18]. They found average activity concentration of ^{226}Ra, ^{232}Th and ^{40}K was 2495 ± 6788 Bqkg^{-1}, 33 ± 28 Bq kg^{-1} and 822 ± 125 Bq kg^{-1}, respectively for the case of analyzed soil samples. In the case of rock samples, average activity concentration was found to be 47 ± 25 Bqkg^{-1}, 59 ± 32 Bq kg^{-1} and 800 ± 240 Bq kg^{-1}, respectively for ^{226}Ra, ^{232}Th and ^{40}K. They concluded that the ^{40}K-bearing feldspars and ^{226}Ra-rich carbonates are the main radiation contributors in that study area. Also, the highest activity concentrations and radiological hazard indices were related to Arud granitic body and Ramsar's soil.

Soil samples from vegetable farmland in densely populated wards of Nepal were analyzed for natural radionuclide levels, employing a NaI (Tl) 3"× 3" gamma detector. The study aimed to evaluate the causes of radiation risk, attributing it to soil contamination resulting from the rapid urbanization and concretization that

followed the earthquake in 2015. The activity concentration of ^{226}Ra, ^{232}Th and ^{40}K and the ranges observed are 2.08±0.08–33.67±1.35 Bq kg^{-1}, 17.22±0.19–119.94±1.38 Bq kg^{-1}, and 11.20 ± 0.32–748.83±21.72 Bq kg^{-1}, respectively.

Azeem et al., in 2024 focused on measuring the levels of naturally occurring radioactivity in the soil of Swabi, Khyber Pakhtunkhwa, Pakistan, as well as the associated health hazard [19]. Thirty (30) soil samples were collected from various locations and analyzed for ^{226}Ra, ^{232}Th and ^{40}K radioactivity levels using a High Purity Germanium detector (HPGe) gamma-ray spectrometer with a photo-peak efficiency of approximately 52.3%. The average values obtained for these radionuclides are 35.6 ± 5.7 Bq kg^{-1}, 47 ± 12.5 Bq kg^{-1}, and 877 ± 153 Bq kg^{-1}, respectively.

2.3 Natural radioactivity measurements in India

Yadav et al., in 2020, conducted a study at the Singrauli coal mine environment in Singrauli coalfield, India. The activity concentrations of Thorium (^{232}Th), Uranium (^{238}U), and Potassium (^{40}K) in rock samples were analyzed by gamma spectrometry using a p-type high-purity germanium (HPGe) detector with a carbon fiber window[20]. The average activity concentrations ^{232}Th, ^{238}U, and ^{40}K were 77.6 ± 38.2, 122.6 ± 46.1, and 843.5 ± 26.0 Bq kg^{-1}, respectively. The average activity ratio of ^{232}Th/^{238}U in various types of rocks was 1.8 ± 0.5 Bq kg^{-1}. The Radium equivalent activity (Ra_{eq}) for various types of rock samples varied from 132.8.1±2.8 to 382.9±6.2 Bq kg^{-1}, with an average value of 317.7±6.53 Bq kg^{-1}.

Srinivasa et al., in 2019, radionuclide activity concentrations in different types of rock samples in and around Hassan district were measured using gamma spectrometry-based high-purity Germanium detector[21]. The average activity concentration of ^{226}Ra, ^{232}Th, and ^{40}K radionuclides in rock samples varies from 29.4 ± 1.2 to 83.7 ± 1.7, 37.9 ± 1.2 to 198.4 ± 2.2, and 346.1 ± 9.0 to 1024.4 ± 19.4 Bq kg^{-1} with an average value of 50.9 ± 1.4, 79.6 ± 1.5, and 609.2 ± 12.8 Bq kg^{-1}, respectively. The study concludes that, from the radiological point of view, all the rock samples (Except granites, pegmatite-intruded pink granites) of the study area

are safe for construction purposes. The data obtained in this study will serve as baseline data for assessing the radiation exposure of the residents.

Rangaswamy et al., in 2016, studied the activity concentration of natural primordial radionuclides, (^{226}Ra, ^{232}Th, and ^{40}K) in different rock samples of Ramanagara and Tumkur districts, by using gamma-ray spectrometry[22]. The average activity concentration of ^{226}Ra, ^{232}Th, and ^{40}K in the collected rock samples was found to be 41.08 ± 2.12, 86.26 ± 2.94, and 869.29 ± 3.78 Bq/kg, respectively. They found the average absorbed dose rate in rock samples was found as 107.33 nGy/h and is slightly higher than the worldwide average value.

Eugin shaji et al., in 2016, measured activity concentration of natural radionuclides such as ^{226}Ra, ^{238}U, ^{232}Th and ^{40}K in rock and the surrounding soil samples were collected from 20 different locations in the lower hills of Western Ghats, Kanyakumari district. The measurements were carried out using a 3"×3" NaI gamma spectrometry [23]. Gamma spectrometric analyses were performed and the mean activity concentrations obtained for each of the radionuclides expressed in Bq/kg are 19.0, 7.59, 20.35 and 192.52 for ^{226}Ra, ^{238}U, ^{232}Th and ^{40}K for soil samples and 18.51, 6.41, 20.43 and 199.89 Bq/kg for ^{226}Ra, ^{238}U, ^{232}Th and ^{40}K for rock samples respectively.

In 2016, Senthilkumar R. D. and Narayanaswamy R., were measured the radioactivity concentration of radionuclides in the soil sample from twenty-two sampling sites across the polluted area of Tamilnadu [24]. They found the activity concentration of ^{238}U, ^{232}Th, and ^{40}K range from 20.28 to 24.72 Bq/kg, 37.3 to 43.2 Bq/kg, and 220.9 to 270.3 Bq/kg, respectively. The Pearson correlation analysis and cluster analysis are employed to analyse the data and identify the existing relationships between the radiological hazard parameters with the natural radionuclides.

In the year 2015, Manigandan P. K. and Chandar Shekar B. were investigated naturally occurring radionuclides in soil samples collected from a tropical rainforest in the Western Ghats, India in the year of 2015[25]. For comparison, a number of soil samples from nearby meadows (open grassland) from Nilgiri district were also

studied using NaI (Tl) gamma-ray spectrometry. Average ^{238}U, ^{232}Th and ^{40}K activity concentrations in the meadow and forest soil samples were found to be 36.3 ± 17.3, 107.8 ± 50.4, 231.9 ± 84.3 Bq/kg and 26.3 ± 9.1, 53.6 ± 10.4, 204.1 ± 30.4 Bq/kg, respectively. They concluded, variations in the activity levels in the forest soil samples were within the activity values measured around the world, but this was not the case for the meadow soil samples.

Mohapatra et al., in 2015, measured radioactivity was estimated in surface soil samples collected around a natural high background radiation area (HBRA) at Odisha, India by using n-type high purity Germanium (HPGe) detector having 50 % relative efficiency with high resolution[26]. The average concentration distribution of ^{238}U, ^{226}Ra, ^{232}Th, ^{40}K and ^{137}Cs in soil samples is found to be 89.0 ± 80.2, 58.6 ± 42.3, 471.0 ± 437.7, 379.5 ± 206.9 and 0.3 ± 0.3 Bq/kg, respectively. They found, the study area was enriched with Monazite and Zircon which is in the form of daughters of deposits of ^{232}Th to the total dose rate was higher than the other radionuclides.

In another study, Shanthi et al., in 2010, measured concentration of natural radionuclides (^{226}Ra, ^{232}Th and ^{40}K) in the soil samples were determined for 28 locations in Kanyakumari district of southwest India by means of gamma spectroscopy with NaI (Tl) detector[27]. The areas where the samples collected from locations are categorized as HBRA and low background radiation areas (LBRAs). The mean activities of the studied HBRA region are 31±9, 206±27 and 1590±490 Bq/kg, respectively, for ^{226}Ra, ^{232}Th and ^{40}K for. For the LBRA samples, the activity concentrations are 8±5, 22±20 and 295±84 Bq/kg, respectively, for ^{226}Ra, ^{232}Th and ^{40}K.

Jogha singh et al., in 2009, determined the natural radionuclide (^{226}Ra, ^{232}Th, and ^{40}K) contents in soil samples from 26 locations around the Upper Siwaliks of Kala Amb, Nahan and Morni Hills, Northern India, using high-resolution gamma-ray spectrometric analysis[28]. It was observed that the concentration of natural radionuclides viz., ^{226}Ra, ^{232}Th and ^{40}K, in the soil varies from 28.3 ± 0.5 to 81.0 ±1.7 Bq/kg, 61.2 ± 1.3 to 140.3 ± 2.6 Bq/kg and 363.4 ± 4.9 to 1002.2 ± 11.2 Bq/kg

respectively.

Ravisankar et al., in 2012, focused on determining the activity concentrations of ^{238}U, ^{232}Th and ^{40}K in soil samples collected from different locations of Yelagri Hills, Tamil Nadu using gamma-ray spectrometry [29]. The radio activities of 25 samples have been measured with a NaI(Tl) detector. The radioactivity concentrations of ^{238}U, ^{232}Th and ^{40}K ranged from 2.17 to 53.23,13.54 to 89.89 and from 625.09 to 2207.3 Bq/kg, respectively. The measured activity concentrations for these radio nuclides were compared with world average activity of soil. The average activity concentration of ^{232}Th in the present study is1.19 times higher than world median value while the activity of ^{238}U and ^{40}K is found to be lower.

Khawlany et al., in 2018, measured activity concentrations of radionuclides ^{226}Ra, ^{232}Th and ^{40}K in soil samples collected from different locations of Aurangabad were determined using gamma-ray spectrometry system NaI (Tl) detector[30]. The aim of this study is to determine the level of natural radioactivity and associated radiological hazard caused by natural radioactivity in soil samples. The activity concentrations of natural radionuclides were found to vary from 7.425 to 12.862 Bq/kg with an average value of 9.189 Bq/kg for ^{226}Ra, from 18.898 to 21.316 Bq/kg with an average value of 20.176 Bq/kg for ^{232}Th, and from 60.508 to 120.142 Bq/kg with an average value of 94.464 Bq/kg for ^{40}K. The results were comparable to reported data worldwide and samples studied exhibit radiation well within the permissible limit and have normal levels of natural background radiation.

Satyanarayana et al., 2023, collected soil samples from various locations in the Visakhapatnam district in Andhra Pradesh, India [31]. The measurement of specific activity of ^{226}Ra, ^{232}Th and ^{40}K radionuclides is carried out with the help of HPGe based gamma spectrometer system. Activity concentration of radionuclides in the samples ^{226}Ra, ^{232}Th, and ^{40}K ranged from 20 ± 2 to 91 ± 2 Bq/kg, 45 ± 3 to 365 ± 3 Bq/kg, and 400 ± 9 to 607 ± 8 Bq/kg, and the respective mean values are 53.36 Bq/kg, 203.74 Bq/kg and 479.19 Bq/kg. The measured mean value of the absorbed dose rate is 171.41 nGy/h, which was beyond the worldwide mean outdoor value of 60 nGy/h. Thus, the annual effective dose estimated from the above value is 1.04

$mSvy^{-1}$. The correlation was done among the measured ^{226}Ra, ^{232}Th, and ^{40}K activity concentrations.

Activity concentrations of ^{226}Ra, ^{232}Th, and ^{40}K were measured by Yadav et al. in 2023 in soil samples from several areas of Garhwal Himalaya, Northern India, by gamma-ray spectrometry[9]. In this region, which extends around the Himalayan Main Central Thrust, a tectonic line that separates several geological provinces, background levels of natural terrestrial radiation were assessed. The maximum levels of Radium, 285 Bq/kg and 136 Bq/kg, respectively, were found in the Budhakedar and Uttarkashi regions, exceeding the world average value of 35 Bq/kg. The mean radiation levels were found to be different between the areas, which reflects the geological diversity in the region.

Recently in 2024, Mitra et al., aimed to measure the natural background radiation level and the associated gamma radiation dose in air in the Beldih apatite mine region of Purulia district, India [32]. This study is primarily focused on the determination of ^{238}U, ^{232}Th and ^{40}K activities in the sub-surface soil of the study area. The measurements were carried out using a High Purity Germanium (HPGe) detector-based gamma-ray spectrometer. (^{238}U, ^{232}Th and ^{40}K) are found to be widely distributed. The average concentrations of ^{238}U, ^{232}Th and ^{40}K in the area under investigation are found to be 2102.49 ± 20.58 Bq kg^{-1}, 135.60 ± 8.86 Bq kg^{-1}, and 279.34 ± 5.52 Bq kg^{-1}, respectively. The occurrence of Uranium mineralization in the area is indicated by the high levels of ^{238}U content in the area. The values of different hazard indices and dosages that are found in the present work are mostly beyond the safety levels for radiation exposure.

The activity concentration of primordial radionuclides, ^{226}Ra, ^{232}Th and ^{40}K in soil samples of Ramanagara and Tumkur districts were determined by gamma spectrometry using HPGe detector[22]. The average activity concentrations of ^{226}Ra, ^{232}Th and ^{40}K were found to be 33.78 ± 1.99, 77.44 ± 2.37 and 791.58 ± 5.78 Bq/kg respectively. The radiological hazard indices of the natural radioactivity have been calculated and compared with the internationally approved values. The concentration of these radionuclides with different size and depth of the soil samples

was studied.

Rangaswamy & Sannappa, in 2022 investigated the activities ^{226}Ra, ^{232}Th and ^{40}K in soil samples of Chikkamagaluru district, Karnataka, using γ-ray spectrometry [33]. The average activity of ^{226}Ra, ^{232}Th and ^{40}K were found to vary from 15.2 ± 0.6 to 58 ± 1.2 Bq kg^{-1}, 14 ± 0.6 to 86.2 ± 1.7 Bq kg^{-1}, and 224.5 ± 5.5 to 1650 ± 20.3 Bq kg^{-1} with a mean value of 36.93 ± 1.0, 51.6 ± 1.3 and 566.97 ± 11.0 Bq kg^{-1}. The average activity concentrations are slightly higher than world average value. The average annual effective dose is more than the Indian average value of 0.084 mSv y^{-1}. The average values of all the radiological hazards are less than the criterion limit.

Suresh et al., 2022, estimated the natural radioactivity and their associated radiological hazards in soil samples of Uttara Kannada district having different geological conditions [34]. The ^{226}Ra, ^{232}Th and ^{40}K activities were estimated using HPGe detector-based gamma-ray spectrometer. The average ^{226}Ra, ^{232}Th and ^{40}K activity concentrations are 36.13 ± 0.96, 48.47 ± 1.26 and 415.76 ± 6.83 Bq kg^{-1} respectively. The mean annual effective dose equivalent value was found to be 0.40 mSv y^{-1} and is less than the ICRP proposed value of 1 mSv y^{-1}. The radiological hazard indices were computed and compared with internationally agreed values.

Zubair & Shafiqullah, 2020 evaluated the activity concentrations of natural radionuclides ^{226}Ra, ^{232}Th and ^{40}K in soil samples collected from Sijua Dhanbad, India were measured by using a gamma-ray spectrometer with a NaI(Tl) detector [35]. The average activity concentration of ^{226}Ra, ^{232}Th and ^{40}K was found as 60.3, 64.5 and 481.0 Bq/kg, respectively. Average radium equivalent activity, absorbed dose rate, outdoor dose, external hazard index and internal hazard index for the area under study is determined as 189.5 Bq/kg, 87.2 nGy/h, 0.4, 0.5 and 0.6 $mSvy^{-1}$, respectively. The annual effective dose to the public is found 0.4 $mSvy^{-1}$. This value lies well below the limit of 1 $mSvy^{-1}$. Measured values have found safe for the environment and public health of safety area.

Khyalia et al., 2024 carried out a detailed investigation of radionuclides (Ra, Th, and K) present in the soil around the reported Uranium deposit site in the Sikar district

of Rajasthan, India [36]. Measurements are carried out using the state-of-the-art gamma-ray spectroscopy (HPGe detector) technique. The specific activity of ^{226}Ra, ^{232}Th, and ^{40}K are found in the range of 9.5 ± 0.5–50.6 ± 1.0 Bq kg^{-1}, 11.0 ± 0.4–83.2 ± 1.5 Bq kg^{-1}, and 177 ± 13–753 ± 47 Bq kg^{-1} with the mean values of 17.8 ± 7.5 Bq kg^{-1}, 22.6 ± 13.4 Bq kg^{-1}, and 393 ± 76 Bq kg^{-1} respectively.

Srinivasa et al., 2019 natural primordial radionuclide activity concentrations in different types of rock samples in and around Hassan district were measured using gamma spectrometry-based high-purity Germanium detector[21]. The average activity concentration of ^{226}Ra, ^{232}Th, and ^{40}K radionuclides in rock samples varies from 29.4 ± 1.2 to 83.7 ± 1.7, 37.9 ± 1.2 to 198.4 ± 2.2, and 346.1 ± 9.0 to 1024.4 ± 19.4 Bq kg^{-1} with an average value of 50.9 ± 1.4, 79.6 ± 1.5, and 609.2 ± 12.8 Bq kg^{-1}, respectively. The study concludes that except granite rocks, all the rock samples analyzed are safe when used as construction materials and do not pose any significant radiation hazards.

2.4 Radiation shielding Materials.

Over the past century, ionizing radiation has been widely used in many aspects of society, including radiation medicine, the nuclear power industry, aerospace exploration industries, and nuclear research laboratories. The safety of workers, patients, and equipment has become a fundamental issue due to the hazards of working with radiation. High-energy radiation has strong penetrability and thus has hazardous effects on both equipment and the human body. Radiation shielding materials must be used to reduce the hazardous effects of radiation [37]. Radiation shields are used to contain radioactive sources and also serve as a medium for reducing the intensity or completely blocking the radiation. The result is that radiation shields are regarded as one of the most fundamental and crucial ideas in the field of radiation protection, or, to put it another way, the ability to control radiation of all types and sources by providing the right shield. The shielding depends mainly on the type of radiation falling on the material [38], [39]. It is technically and engineering-wise acceptable to use a radioactive source, provided that all necessary safety protocols, shielding mechanisms, and regulatory

requirements are strictly followed to ensure the safety of personnel and the environment. [40]. Sometimes Humans are vulnerable to radiation, hence shielding is essential to avoid threats to the individual. Many studies and experiments have been done to build shields to protect against extreme radiation that penetrates like gamma rays by measuring the attenuation coefficients of various materials and demonstrating the characteristics of its ability. To block this unwanted and harmful radiation to cells, this section shows some previous studies and research conducted on different materials used as shields against radiation.

2.4.1 Concrete composite

The shielding property of concrete is predominated by thickness and density, and denser concrete can deliver better shielding. Several studies have been conducted on improving concrete and mortar shielding capability against ionizing radiation. Akkurt and his colleagues (2010) experimented with barite-produced concrete [38]. Their findings were compared to the performance of a normal lead shielding material. 1 keV – 1 GeV linear attenuation coefficients were calculated and compared. At 662, 1173, and 1333 keV, a gamma spectrometer with a NaI (Tl) and MCA detector was used to make the measurements. The theoretically calculated results and the practically calculated results in the laboratory were in complete agreement. Nevertheless, the lead attenuation coefficient remained the highest among the other factors, while for the linear attenuation of barite, it was higher than that of barite concrete.

A group of heavy concrete samples were prepared by Al-ghamdi et al., (in 2022) containing varying concentrations of Tungsten oxide, and the mechanical and radiation shielding properties of the resulting samples was studied using theoretical and experimental technique [41]. The increase in the amount of WO_3 caused a reduction in the half value layer and an increase in the radiation protection efficiency for the prepared concretes.

Gouda et al., in 2023, explored the radiation protection properties of white mortars based on white cement as a binder and Bi_2O_3 micro and nanoparticles in proportions of 15 and 30% by weight as replacement sand[42].The experimental values of the

prepared mortars' Mass Attenuation Coefficients (MAC) match well with those determined theoretically from the XCOM database. Other shielding parameters, including Half Value Layer (HVL), Tenth Value Layer (TVL), Mean Free Path (MFP), Effective Electron Density (N_{eff}), Effective Atomic Number (Z_{eff}), Equivalent Atomic Number (Z_{eq}), and Exposure Buildup Factor (EBF), were also determined at different photon energies to provide more shielding information about the penetration of gamma radiation into the selected mortars. The obtained results indicated that the sample containing 30% by weight of nano Bi_2O_3 has the largest attenuation coefficient value.

Several studies focused on adding different materials with it to improve its performance, such as lime, gypsum, as well as some minerals. In 2023, Ahmed M. El-khatib et al., introduce a study of a new material by a mixture of bentonite clay as a matrix with cement, ball, kaolin and red clay as composite slabs to perform as a shielding material for radiation protection and improving the clay materials' properties [43]. They concluded formation of a clay mixture characterized by morphological properties, where the voids and the porosity were less than the one type of clay, in addition to that the attenuation properties of gamma rays became more efficient, the attenuation coefficients were calculated experimentally and compared them theoretically using the X-COM program and a great agreement between the experimental and theoretical was noticed.

2.4.2 Glass composite

Glasses have been explored as one such material which are chemically inert, thermally stable and most importantly can be transparent. Therefore, glasses can be employed in radiative environments for both dosimetric and shielding purposes. Gurinder Pal Singh et al., in 2020, proposed glass system WO_3-Al_2O_3-PbO-B_2O_3 can be found suitable to be used in radiation exposed environments. By using computer aided software Phy-X/PSD and to find the elastic parameters and hardness of these glasses so as to find their suitability as materials for gamma-ray shielding [44].

G. Lakshminarayana et al., in 2018, studied gamma radiation shielding parameters for six TeO_2-B_2O_3-Bi_2O_3-Ti_2O glasses, by using XCOM program[45]. First

evaluated the (μ/ρ) values within the energy range 0.015–10 MeV, and from them, the γ-ray shielding parameters such as Z_{eff}, N_{eff}, MFP, HVL, and exposure buildup factor (EBF) values using Geometric progression (G–P) fitting method are derived for their potential applications as γ-ray shielding materials.

Aboudeif et al, 2020, reported radiation protection characteristics of two prototyped oxide glasses with different compositions (PZCdO in pure form and doped with Thulium-PZCdO:Tm) against ionising radiation ranging from 0.015 to 15 MeV [46]. utilising Phy-X/PSD software. The outcomes of the simulation process demonstrate the relationship between the incident photon energy and the recorded values for the LAC and MAC. PZCdO doped with Tm shows better LAC and MAC outcomes than its pure form.

El-Maaref et al., 2022, recorded the impact of Fe_2O_3 on the mechanical and photon shielding characteristics of lead phosphor aluminate glasses. The shielding parameters were established using the Phy-X / PSD[47]. The mace attenuation coefficient is the highest in the sample with the maximum Fe_2O_3 content. The (Z_{eff}) and (N_{eff}) values decreased and then increased slowly at lower energy. Because of the Compton scattering interaction, the (Z_{eq}) value decreases as the energy and Fe_2O_3 content increase. The parameters' analysis revealed that the glasses under consideration are strong candidates for radiation shielding.

Kurtulus & Kavas, 2021, addressed the theoretical radiation shielding competencies and physical properties of Borotellurite (BT) glass system[48],. The intended BT glass systems had the following batch design: xB_2O_3 - $(100-x)TeO_2$ system (x: 5 to 25 mol% with a step of 5). Afterward, newly developed user-friendly Phy-X/PSD software was utilized for determining Linear Attenuation Coefficient (LAC) and Fast Neutrons Removal Cross-Section (FNRCS) parameters at Ba-133 radioactive source energies. The study signified that adding B_2O_3 in replacement for TeO_2 could diminish photon shielding competencies, but enhanced neutron attenuation characteristics.

Hegazy et. al., in 2021, investigated the capacity of Strontium bismo-borate glasses doped with different concentrations of Nd_2O_3 content with the form B_2O_3–Bi_2O_3–

SrO-Nd_2O3 as ionizing radiation and neutron shielding[49]. The newly developed Phy-X/PSD software and Geant4 simulation code were performed to achieve this goal by evaluating several parameters such as MAC, gamma photons dose rate, FNRCS, and scattering/absorption lengths and cross sections for thermal neutrons. Glasses with the highest concentration of Nd_2O_3 show the best thermal/fast neutron shielding capability among the investigated glasses. One can conclude that BBSN5.7 glass owns the best shielding capacity among all BBSN glasses due to the highest LAC values comparing to other selected ones.

Almisned et al., in 2023 reported the role of the chemical modifications on various gamma-ray attenuation properties of four different tellurite glasses reinforced through WO_3[50]. Based on the rise in density, it was determined that the maximum concentration of WO_3 also resulted in a significant change in the overall gamma-ray absorption properties, when all of the study's findings were examined. It was observed that the glass sample, in which TeO_2 and WO_3 were 40 mol%, had the highest density. Report that WO_3 incorporation is a functional component that may be employed in tellurium glasses and is a suitable material for circumstances in which gamma-ray absorption qualities must be enhanced.

Saudi and S. U. El-Kameesy in 2018, [51] investigated on detailed analysis of radiation-shielding properties of (70-x) B_2O_3–20ZnO–10Li_2O–xBaO where ($0 \leq x \leq 40$ mol%) glasses, where x = 0, 10, 20, 35 and 40 mol%. The gamma rays-shielding properties such as the mass attenuation coefficients and half-value layer (HVL) of glass samples have been experimentally determined, and a comparison with a theoretical approach making use of the XCom program has been performed. Moreover, the chemical durability and the effect of gamma irradiation dose on hardness are determined.

Alajerami et al., in 2021, explored a series of glass samples $20Na_2O \cdot 15CdO \cdot xBi_2O_3 \cdot (65–x)B_2O_3$ where (x = 0, 10, 20 and 30) were fabricated by the traditional melt-quench method. The structural, chemical stability and significant mechanical properties[52]. Based on the obtained results, the current glass samples appear excellent shielding features for electromagnetic and particulate

radiation nominate to utilize as structural shielding in different radiation facilities.

Saleh et al. in 2022, evaluated the nuclear radiation shielding for prepared ZnO-Li_2O-P_2O5 glass doped with various concentrations of Yb_2O_3[53]. The effect of Yb_2O_3 on the radiation shielding properties of gamma rays and fast neutron removal cross section were studied using XCOM and Phy-X/PSD software programs for photon energies from 0.015 up to 15 MeV. Moreover, the structural properties of the prepared samples using x-ray diffraction were evaluated.

2.4.3 Polymer composite

There is an increasing demand for developing new radiation shielding materials that can attenuate both gamma rays and neutrons whilst mitigating the disadvantages of traditional shielding materials. During the past decade, high-Z nano- and micro-materials dispersed in polymer matrices have shown enhanced ability in attenuating and absorbing high energy radiation [54]

CaO et. al in 2020, investigated the gamma-ray shielding performance, and the physical and mechanical properties of Poly Methyl Methacrylate (PMMA) composites embedded with 0-44.0 wt% Bismuth Trioxide (Bi_2O_3) fabricated by the fast ultraviolet (UV) curing method[55]. The results showed that the addition of Bi_2O_3 had significantly improved the gamma shielding ability of PMMA composites. Mass attenuation coefficient and half-value layer were examined using five gamma sources (Cs-137, Ba-133, Cd-109, Co-57, and Co-60). The high loading of Bi_2O_3 in the PMMA samples improved the micro-hardness to nearly seven times that of the pure PMMA. With these enhancements, it was demonstrated that PMMA/Bi_2O_3 composites are promising gamma shielding materials. Furthermore, fast UV curing exerts its great potential in significantly shortening the production cycle of shielding material to enable rapid manufacturing.

Polymers are widely used in many fields because of its various good prop er ties like soft ness, insulators, elasticity polymer materials are C-, H-, O-based and known as low-*Z* materials, that are not inflammable, having low weight, are less expensive, more stable on high temperature, and can be used at large scale. in polymer, natural

rubber (NR) acts as a matrix, as it is well established that NR contains various good properties such as elasticity, high elongation at break, tear resistance and high impact strength. It can bend and not break or crack easily. In addition, if natural rubber can be developed as a mass product for gamma radiation protection, it will benefit many government agencies and state enterprises gamma related. It is clear that, the radiation shielding parameters must be good or acceptable for use it in any application. Alternatively, nonlead Natural Rubber (NR) shielding with high atomic number filler particles such as iIon oxide (Fe_3O_4), Tungsten oxide (W_2O_3), Bismuth oxide (Bi_2O_3) was reported by many researchers. However, such materials are expensive, less flexible and high stiffness due to difficulty mixing the fillers into NR.

Alabsy and Elzaher, in 2023 aimed to evaluate the shielding performance of Ethylene Propylene Diene Monomer (EPDM) rubber composites filled with 200 phr of different metal oxides (either Al_2O_3, CuO, CdO, Gd_2O_3,or Bi_2O_3) as protective materials against gamma and neutron radiations. to explore their potential usage as radiation protective materials [56]. To this end, the linear attenuation coefficients (μ) of the suggested EPDM rubber composites were simulated using Geant4 simulation code. According to the obtained results, the investigated metal oxide/EPDM rubber composites can be employed as comfortable clothing and gloves designed for workers in radiation facilities.

Lim-Aroon et al., 2019, light-weighted, flexible, and lead-free X-ray/gamma-ray shielding natural rubber (NR) sponges were developed with the help of a blowing agent, namely Oxybis Benzene Sulfonyl Hydrazide (OBSH) (its contents varied from 0, 8 to 16 parts per hundred parts of rubber; phr), and an X-ray/gamma protective filler, namely Bismuth oxide (Bi_2O_3) (its content varied from 0, 100, 300, to 500 phr) in natural rubber (NR) composites [57]. overall properties investigated in this work suggested that the developed NR sponges could be used to attenuate X-rays and gamma rays efficiently with additional properties of being light-weighted and highly flexible, which are crucial for safety of radiation-related personnel and users.

Khatib et al., 2020, loaded Natural rubber (NR) with 30 phr of N220 black (critical concentration) as a conductive and reinforcing filler [40]. These rubber matrices are loaded with different concentrations of Pb powder (up to 100 phr) as filler. Gamma attenuation study was carried out using a 3″×3″ NaI (Tl) scintillation detector. The obtained results demonstrated that the composites of Pb/W/NR are the most promising alternative materials for γ-ray shielding applications. Also, introducing more contents of lead and waste rubber as fillers inside the composite will produce a good shielding material but on the other hand, this will affect the stability of the composite and much future work should be done to solve the problem of stability.

Plangpleng et al., 2022, developed natural rubber with $BaSO_4$ nanocomposites has great potential to be used as flexible shielding [58]. The advantages of NR with BaSO4 nanocomposites are flexible, lightweight, and lead-free. The shielding composites were successfully fabricated with various fillers loading of 10, 20, 30 and 50 parts per hundred rubbers (phr). The gamma-ray shielding properties were measured with ^{57}Co (122.06 keV) and ^{133}Ba (356.02 keV) sources. Results indicated that additional filler concentrations into NR increased density, hardness (shore A), tensile modulus, tensile strength, and elongation at break of NR. Tensile properties and elongation at break of NR with $BaSO_4$ nanoparticles were slightly lower than the ordinary-sized $BaSO_4$. In comparison of shielding properties between NR with $BaSO_4$ nanoparticles and the ordinary-sized $BaSO_4$ showed that the NR with nanocomposites provided better gamma radiation shielding due to the large surface to volume area of nanocomposites.

Gamal et al., in 2023, prepared a new shielding material composite made from an NBR/SBR blend and loaded with black nanocarbon particles [59]. This blend will be the host matrix for a PbO filler. The effect of lead oxide concentration on both the mechanical and shielding properties of the prepared blend will be investigated. The optimum concentration of the lead filler will be determined. This developed material composite should have distinct physico mechanical and attenuation features, be lightweight, and have low expense allowing it to be used in the fabrication of radiation protection equipment used by medical, industrial, and military personnel.

In 2022, Sayyed et al., examined novel polymer composites for use in radiation protection applications. These prepared polymers are non-toxic compared with lead and show potential to be used as protective gear in different medical applications where low-energy photons are utilized [37]. They prepared silicon rubber (SR) with different concentrations of micro- and nano sized MgO. The results revealed that the LAC values for SR with nano-MgO are higher than those with micro-MgO. The difference between the LAC values of the micro- and nano-MgO polymers were greater at lower energies, and the advantage that nanoparticles have over microparticles was not as evident at higher energies.

Lim-Aroon et al., in 2019 developed light-weighted, flexible, and lead-free X-ray/gamma-ray shielding natural rubber (NR) sponges were with the help of a blowing agent, namely Oxybis Benzene Sulfonyl Hydrazide (OBSH) (its contents varied from 0, 8 to 16 parts per hundred parts of rubber; phr), and an X-ray/gamma protective filler, namely Bismuth oxide (Bi_2O_3) (its content varied from 0, 100, 300, to 500 phr) in natural rubber (NR) composites [57]. the overall properties investigated in this work suggested that the developed NR sponges could be used to attenuate X-rays and gamma rays efficiently with additional properties of being light-weighted and highly flexible, which are crucial for safety of radiation-related personnel and users.

Properties such as gamma shielding, cure characteristics, and mechanical properties of natural rubber (NR) system with addition of oxides such as: Iron (II, III) oxide (Fe_3O_4), Tungsten (III) oxide (W_2O_3), or Bismuth (III) oxide (Bi_2O_3) were studied by Toyen et al., in 2018, for potential replacement of flexible Lead (Pb), and introduced as gamma-shielding materials, to minimize risks caused by Pb [60]. Specifically, for NR with Bi_2O_3 composites, the mass attenuation coefficients (μm) are the highest amongst all the NR composites investigated and also higher than the value of μm of lead metal sheets, thereby showing great potential to replace lead-based gamma-shielding materials.

A novel composite based on ethylene-propylene-diene monomer (EPDM) rubber for gamma shielding were prepared by Huang et., in 2016, using carbon blacks (CB)

and ball milled $PbWO_4$ (PWO) powder as fillers [61]. The microstructure of ball milled PWO powder which has a uniform morphology in these composites and shielding tests were performed to determine mechanical and radiation attenuation properties, respectively. The results show these materials exhibit excellent mechanical and radiation-resistance properties.

Saeed and Abu-raia, used a Bismuth Tungsten oxide $Bi_2(WO_4)_3$ compound as a filler to inlay the silicone rubber SR composite because it collects between the properties of W and Bi [62]. The mechanical properties of the considered $SR/Bi_2(WO_4)_3$ composite were examined. The attenuation performance was tested using three different energies of gamma rays. Finally, the two best composites of $SR/Bi_2(WO_4)_3$ were chosen and the effect of gamma-ray irradiation on their mechanical properties was studied.

Kalkornsurapranee et al., in 2021, successfully prepared and developed, Flexible shielding materials based on natural rubber (NR) composites with different radiation shielding fillers including Barium carbonate ($BaCO_3$), Bismuth oxides (Bi_2O_3) and Barium sulphate ($BaSO_4$) Kalkornsurapranee et al., 2021. NR/Bi_2O_3 composite is the most suitable choice for preparing novel flexible radiation shielding materials. The study concludes that the NR with $BaCO_3$, Bi_2O_3, and $BaSO_4$ can be potential candidates for the application in lead-free flexible gamma and X-rays shielding materials.

Kalkornsuranee et al., 2022 aimed to compare the performance between natural rubber (NR) composites with Lead oxide (PbO) and Bismuth oxide (Bi_2O_3) as shielding fillers for gamma radiation shielding applications [64]. The results indicated that the composites based on NR with both shielding fillers (i.e. Bi_2O_3 and PbO) offered higher modulus, hardness, specific gravity, oil resistance, thermal stability and radiation shielding properties.

Alresheedi et al., in 2023 prepared silicone rubber composites with heavy metal oxide nanoparticles for gamma-ray shielding applications Alresheedi et al., 2023. Different heavy metal oxide nanoparticles were incorporated into the silicone rubber matrix, and the prepared composites were characterized for their thermal,

mechanical, and radiation shielding properties. Overall, this study provides valuable insight into the development of silicone rubber composites with heavy metal oxide nanoparticles for gamma-ray shielding applications. The prepared composites exhibited promising radiation shielding properties, indicating their potential use in various radiation shielding applications.

Kameesy et al., 2015 made an attempt has been devoted, to prepare the polymer composite for radiation shielding using silicone rubber as a polymer matrix and Bismuth (Bi) which has high effective atomic number as filler with different concentrations [66]. Then, the gamma-ray attenuation coefficients and the mechanical properties as a function of gamma-ray energy and filler concentrations were investigated.

M.Elsafi et. Al, in 2023, fabricated six silicone rubber composites embedded with TeO_2 and B_2O_3 were used as shielding flexible materials against ionizing radiation, where the attenuation coefficients were calculated at different energies of incident photons by experimental measurements and confirmed by theoretical techniques [67]. It was concluded that the enhancement of the linear attenuation coefficient values has a positive effect on the transmission rate, and radiation protection efficiency values where the half-value thickness and transmission rate were decreased accompanied by an increase in the efficiency.

2.4.4 Epoxy-resin composite

Karem G. Mahmoud et al., in 2023 synthesized a series of epoxy reinforced Bi_2O_3 compounds were using Polyepoxide resin and a solidifying agent at room temperature [68]. The density of the synthesized composites was enhanced from 1.103 to 1.20 g/cm^3 by raising the concentration of Bi_2O_3 composite from 0 wt.% to 10 wt.%. The ability of the synthesized composites to attenuate the low-photon energies was estimated using the Monte Carlo simulation N-Particle transport code in the gamma energy interval between 15 keV and 661 keV. The estimated results show that the linear attenuation values are enhanced by raising the Bi_2O_3 concentration in the synthesized composites. Furthermore, the Phy-X/PSD results for buildup factors show a decrease in their values with increasing Bi_2O_3

concentration.

Dong et al., 2023 developed boron rich slag/epoxy resin nuclear shielding composites with excellent thermal neutron protection performance [69]. Based on the radiation protection theory, Phy-X/PSD program, XCOM program, and ^{60}Co gamma-ray source were integrated to obtain the shielding parameters of boron rich slag/ epoxy resin composites at 0.015-15 MeV. The work is meaningful for the potential application of the boron rich slag in the nuclear shielding field.

Asgari et al., in 2021 doped by 10 mm and100 nm size of lead, Bismuth and Tungsten particles as filler with 30 and 60 weight percentages were prepared the elastomer composites [70]. To survey the shielding properties of the polymer composites using gamma-ray emitted from ^{152}Eu and ^{137}Cs sources. Also, the Monte Carlo simulation (MCs) method was used. The results showed a direct relationship between the linear attenuation coefficients of the absorbent and filler ratio. Also, the decrease in the particle size of the shielding material in each weight percentage improved the radiation shielding features. When the dimension of the particles was in the order of nano-size, more attenuation was achieved.

Mahmoud et al., 2023 examined the effect of halloysite nanoparticle weight% on the structural and gamma-ray shielding capabilities of epoxy resin composites [71]. Using MCNP code and XCOM theoretical programme, the linear attenuation coefficient of the newly developed epoxy resin reinforced with halloysite nanoparticles was simulated in the 15-2560 keV gamma photon energy interval. MCNP revealed that the addition of halloysite nanoparticles increases the linear attenuation coefficient of the fabricated composites by 43% (for gamma energy of 15 keV), 17% (for gamma energy of 662 keV) and 17% (for gamma energy of 1252 keV) when the halloysite nanoparticle concentration increased from 0 wt% to 40 wt%.

Karabul & İçelli, 2021 devoted to investigating the radiation shielding performance of Epoxy/Bi_2O_3 and Epoxy/WO_3 micro and nanostructured composites have been prepared by using direct pouring method [72]. The additive percentages have been varied from 0 to 30 % weight and 0 to 20 % weight for the micro and nanoparticles,

respectively. While radiation shielding abilities of the micro composites have been determined both experimentally and theoretically via MCNP6, the nanocomposites' radiation shielding performance has been evaluated by using experimental data. They concluded use of nanoparticles is more successful than the radiation attenuation micro-additive. Ultimately, it can be concluded, epoxy-based composites having the highest Bi_2O_3 and WO_3 micro and nanoparticle contents offer a convenient radiation shielding achievement for the low-energetic gamma-rays used in nuclear medicine.

Ghozza, in 2023 focused on the effect of the nickel doping ratio on γ-ray attenuation radiological parameters for five compounds of chemical compositions BaMn1-xNixO_3 (x=0.1,0.3,0.5,0, and 0.9), in energy range between 0.015 and 15 MeV utilizing Phy-X/PSD software [73] f. Finally, our measurements revealed that BaMn1-xNixO_3 had good γ- ray and neutron detection over a wide energy range. This could be advantageous for nuclear medicine sensors, detectors, and application.

Abbas et al., 2023 designed new composites of the main matrix of bentonite–gypsum was intercalated in various amounts with micro- and nanosized particles of Bismuth oxide (Bi_2O_3) as the filler with varying percentages (6, 13, and 20) in bulk and nanosized particles to produce new bentonite-based bulk and nanocomposite radiation shielding materials [43]. The experimental values of the mass attenuation coefficient were determined and compared with the theoretical XCOM ones, giving good comparability of the results. It was observed that the specimens with a higher weight percentage of Bi_2O_3 showed higher mass attenuation coefficients. Moreover, the specimens that contain nanoscale Bi_2O_3 have much higher mass attenuation coefficients compared with the same percentages of the main matrix and filler bulk Bi_2O_3, at the same photon energies.

2.5 Reference

[1] UNSCEAR, *Sources and Effects of Ionizing Radiation, United Nations Scientific Committee on the Effects of Atomic Radiation UNSCEAR 2000 Report to the General Assembly, with Scientific Annexes*, vol. I. 2000.

[2] K. N. Narasimhamurthy, G. V Ashok, N. Nagaiah, N. G. S. Prasad, and A. N. Prema, "Indoor 222 Rn exposure in selected schools and residential dwellings of Mandya , Karnataka," pp. 21–25, 2020, doi: 10.4103/rpe.RPE.

[3] P. Semwal *et al.*, "Measurement of ^{222}Rn and ^{220}Rn exhalation rate from soil samples of Kumaun Hills, India," *Acta Geophys.*, vol. 66, no. 5, pp. 1203–1211, 2018, doi: 10.1007/s11600-018-0124-3.

[4] Y. M. Atiah Al-Zahy and M. Mzahiwat, "Investigating the Level of Radon ^{222}Rn and Radium ^{226}Ra in Soil Samples Taken from Al-Amarah in the South of Iraq," *J. Phys. Conf. Ser.*, vol. 1829, no. 1, 2021, doi: 10.1088/1742-6596/1829/1/012028.

[5] E. E. Saleh, A. M. A. Al-Sobahi, and S. A. E. El-Fiki, "Assessment of radon exhalation rate, radon concentration and annual effective dose of some building materials samples used in Yemen," *Acta Geophys.*, vol. 69, no. 4, pp. 1325–1333, 2021, doi: 10.1007/s11600-021-00628-z.

[6] S. A. Mujahid, A. Rahim, S. Hussain, and M. Farooq, "Measurements of natural radioactivity and radon exhalation rates from different brands of cement used in PAKISTAN," vol. 130, no. 2, pp. 206–212, 2008.

[7] S. Tokonami, H. Yonehara, S. Akiba, M. V Thampi, and W. Zhuo, "Natural radiation levels in Tamil Nadu and Kerala , India," vol. 7, no. 04, pp. 554–559, 2005, doi: 10.1016/S1569-4860(04)07066-4.

[8] R. Bhaskaran *et al.*, "Hazard indices and annual effective dose due to terrestrial radioactivity in Northern Kerala, India," *J. Radioanal. Nucl. Chem.*, vol. 314, no. 3, pp. 2171–2179, 2017, doi: 10.1007/s10967-017-5583-5.

[9] M. Yadav, M. K. Jindal, P. Bossew, and R. C. Ramola, "Geological control of terrestrial background radiation in Garhwal Himalaya, India," *Environ. Geochem. Health*, vol. 45, no. 11, pp. 8379–8401, 2023, doi: 10.1007/s10653-023-01729-y.

[10] P. Bangotra *et al.*, "Assessment of annual effective dose from equilibrium equivalent concentration of ^{222}Rn and ^{220}Rn in northern zone of Punjab (India)," *Test Eng. Manag.*, vol. 83, no. April, pp. 9116–9121, 2020.

[11] R. C. Ramola, M. Yadav, and G. S. Gusain, "Distribution of natural radionuclide along Main Central Thrust in Garhwal Himalaya," *J. Radiat. Res. Appl. Sci.*, vol. 7, no. 4, pp. 614–619, 2014, doi: 10.1016/j.jrras.2014.10.002.

[12] O. Ndour *et al.*, "Assessment of natural radioactivity and its radiological hazards in several types of cement used in Senegal," *SN Appl. Sci.*, vol. 2, no. 12, pp. 1–8, 2020, doi: 10.1007/s42452-020-03904-7.

[13] S. Singh, N. J. Raju, and S. Nazneen, "Environmental risk of heavy metal pollution and contamination sources using multivariate analysis in the soils of Varanasi environs, India," *Environ. Monit. Assess.*, vol. 187, no. 6, pp. 1–12, 2015, doi: 10.1007/s10661-015-4577-4.

[14] C. Nyambura *et al.*, "Annual effective dose assessment due to radon and thoron progenies in dwellings of kilimambogo, Kenya," *Radiat. Prot. Dosimetry*, vol. 184, no. 3–4, pp. 430–434, 2019, doi: 10.1093/rpd/ncz090.

[15] A. S. Akingboye, A. C. Ogunyele, A. T. Jimoh, O. B. Adaramoye, A. O. Adeola, and T. Ajayi, "Radioactivity, radiogenic heat production and environmental radiation risk of the Basement Complex rocks of Akungba-Akoko, southwestern Nigeria: insights from in situ gamma-ray spectrometry," *Environ. Earth Sci.*, vol. 80, no. 6, pp. 1–24, 2021, doi: 10.1007/s12665-021-09516-7.

[16] S. Aközcan, F. Külahcı, O. Günay, and S. Özden, "Radiological risk from activity concentrations of natural radionuclides: Cumulative Hazard Index," *J. Radioanal. Nucl. Chem.*, vol. 327, no. 1, pp. 105–122, 2021, doi: 10.1007/s10967-020-07474-1.

[17] T. Alharbi, "Establishment of natural radioactivity baseline, mapping, and radiological hazard assessment in soils of Al-Qassim, Al-Ghat, Al-Zulfi, and Al-Majmaah," *Arab. J. Geosci.*, vol. 13, no. 11, 2020, doi: 10.1007/s12517-020-05420-9.

[18] F. Amini Birami, F. Moore, R. Faghihi, and B. Keshavarzi, "Distribution of natural radionuclides and assessment of the associated radiological hazards in the rock and soil samples from a high-level natural radiation area, Northern Iran," *J. Radioanal. Nucl. Chem.*, vol. 322, no. 3, pp. 2091–2103, 2019, doi: 10.1007/s10967-019-06912-z.

[19] U. Azeem *et al.*, "Radionuclide concentrations in agricultural soil and lifetime cancer risk due to gamma radioactivity in district Swabi, KPK, Pakistan," *Nucl. Eng. Technol.*, vol. 56, no. 1, pp. 207–215, 2024, doi: 10.1016/j.net.2023.09.026.

[20] A. K. Yadav, S. K. Sahoo, P. Lenka, A. V. Kumar, and R. M. Tripathi, "Assessment of Radionuclide Concentration and Radiation Dose in Rock in Singrauli Coalfield , India," vol. 24, no. 1, pp. 1–6, 2020, doi: 10.1061/(ASCE)HZ.2153-5515.0000458.

[21] E. Srinivasa, D. R. Rangaswamy, and J. Sannappa, "Assessment of radiological hazards and effective dose from natural radioactivity in rock samples of Hassan district, Karnataka, India," *Environ. Earth Sci.*, vol. 78, no. 14, Jul. 2019, doi: 10.1007/s12665-019-8465-z.

[22] D. R. Rangaswamy, M. C. Srilatha, C. Ningappa, E. Srinivasa, and J. Sannappa, "Measurement of natural radioactivity and radiation hazards assessment in rock samples of Ramanagara and Tumkur districts, Karnataka, India," *Environ. Earth Sci.*, vol. 75, no. 5, pp. 1–11, 2016, doi: 10.1007/s12665-015-5195-8.

[23] K. C. and F. K. M. Eugin shaji. J, "Analysis of radionuclide level in soil and rock powder samples and assessment of radiological risks," pp. 261–274, 2016.

[24] R. D. Senthilkumar and R. Narayanaswamy, "ScienceDirect Assessment of radiological hazards in the industrial effluent disposed soil with statistical analyses," *J. Radiat. Res. Appl. Sci.*, vol. 9, no. 4, pp. 449–456, 2016, doi: 10.1016/j.jrras.2016.07.002.

[25] P. K. Manigandan and B. Chandar Shekar, "Evaluation of radionuclides in the terrestrial environment of Western Ghats," *J. Radiat. Res. Appl. Sci.*, vol. 7, no. 3, pp. 310–316, 2014, doi: 10.1016/j.jrras.2014.04.001.

[26] S. Mohapatra *et al.*, "On the radiological assessment of natural and fallout

radioactivity in a natural high background radiation area at Odisha , India," pp. 2081–2092, 2015, doi: 10.1007/s10967-014-3814-6.

[27] G. Shanthi, "SIRJANA JOURNAL [ISSN : 2455-1058] VOLUME 54 ISSUE 2 PAGE NO : 42," vol. 54, no. 2, pp. 41–54.

[28] J. Singh, H. Singh, S. Singh, B. S. Bajwa, and R. G. Sonkawade, "Comparative study of natural radioactivity levels in soil samples from the Upper Siwaliks and Punjab, India using gamma-ray spectrometry," *J. Environ. Radioact.*, vol. 100, no. 1, pp. 94–98, 2009, doi: 10.1016/j.jenvrad.2008.09.011.

[29] R. Ravisankar *et al.*, "Natural radioactivity in soil samples of Yelagiri Hills, Tamil Nadu, India and the associated radiation hazards," *Radiat. Phys. Chem.*, vol. 81, no. 12, pp. 1789–1795, 2012, doi: 10.1016/j.radphyschem.2012.07.003.

[30] A. H. Al-Khawlany, A. R. Khan, and J. M. Pathan, "Determination of Natural Radioactivity Levels and Radiation Hazards for Soil Samples from Aurangabad Maharashtra-India.," *Academia.Edu*, no. Ii, 2018, [Online]. Available: https://www.academia.edu/download/56293446/paper_IJMMS.pdf.

[31] G. V. V Satyanarayana, N. S. Sivakumar, D. Vidyasagar, N. Murali, A. D. P. Rao, and P. V. L. Narayana, "Journal of the Indian Chemical Society Measurement of natural radioactivity and radiation hazard assessment in the soil samples of Visakhapatnam , Andhra Pradesh , India," *J. Indian Chem. Soc.*, vol. 100, no. 1, p. 100856, 2023, doi: 10.1016/j.jics.2022.100856.

[32] S. Mitra, N. Naskar, J. Mukherjee, S. Sutradhar, S. Lahiri, and C. Barman, "Assessment of NORMs (238U, 232Th, 40K) and radiation hazard indices in Beldih apatite mine region of Purulia district, West Bengal, India," *Environ. Geochem. Health*, vol. 46, no. 2, pp. 1–13, 2024, doi: 10.1007/s10653-023-01844-w.

[33] E. S. D. R. Rangaswamy and S. S. J. Sannappa, "Natural radioactivity levels and associated radiation hazards in soil samples of Chikkamagaluru district , Karnataka , India," *J. Radioanal. Nucl. Chem.*, vol. 331, no. 4, pp. 1899–1906, 2022, doi: 10.1007/s10967-021-08133-9.

[34] S. Suresh, D. R. Rangaswamy, J. Sannappa, S. Dongre, E. Srinivasa, and S. Rajesh, "Estimation of natural radioactivity and assessment of radiation hazard indices in soil samples of Uttara Kannada district, Karnataka, India," *J. Radioanal. Nucl. Chem.*, vol. 331, no. 4, pp. 1869–1879, 2022, doi: 10.1007/s10967-021-08145-5.

[35] M. Zubair and Shafiqullah, "Measurement of natural radioactivity in several sandy-loamy soil samples from Sijua, Dhanbad, India," *Heliyon*, vol. 6, no. 3, pp. 0–7, 2020, doi: 10.1016/j.heliyon.2020.e03430.

[36] B. Khyalia *et al.*, "Estimation of radionuclides in the soil samples from the Uranium mining zone of Sikar, Rajasthan, India," *J. Radioanal. Nucl. Chem.*, no. 0123456789, 2024, doi: 10.1007/s10967-024-09386-w.

[37] M. I. Sayyed, H. Al-Ghamdi, A. H. Almuqrin, S. Yasmin, and M. Elsafi, "A Study on the Gamma Radiation Protection Effectiveness of Nano/Micro-MgO-Reinforced Novel Silicon Rubber for Medical Applications," *Polymers (Basel).*, vol. 14, no. 14, 2022, doi: 10.3390/polym14142867.

[38] I. Akkurt, H. Akyıldırım, B. Mavi, S. Kilincarslan, and C. Basyigit, "Annals of Nuclear Energy Photon attenuation coefficients of concrete includes barite in

different rate," *Ann. Nucl. Energy*, vol. 37, no. 7, pp. 910–914, 2010, doi: 10.1016/j.anucene.2010.04.001.

[39] I. Akkurt and K. Günoğlu, "Natural radioactivity measurements and radiation dose estimation in some sedimentary rock samples in Turkey," *Sci. Technol. Nucl. Install.*, vol. 2014, 2014, doi: 10.1155/2014/950978.

[40] A. M. El-Khatib *et al.*, "Conductive natural and waste rubbers composites-loaded with lead powder as environmental flexible gamma radiation shielding material," *Mater. Res. Express*, vol. 7, no. 10, 2020, doi: 10.1088/2053-1591/abbf9f.

[41] H. Al-ghamdi, M. Elsafi, M. I. Sayyed, and A. H. Almuqrin, "Performance of newly developed concretes incorporating WO_3 and barite as radiation shielding material," *J. Mater. Res. Technol.*, vol. 19, pp. 4103–4114, 2022, doi: 10.1016/j.jmrt.2022.06.145.

[42] S. M. A.-B. andMahmoud T. A. Mona M. Gouda, AhmedM. El-Khatib , Mahmoud I. Abbas, "Gamma Attenuation Features of White Cement Mortars," vol. 16, p. 1580, 2023.

[43] M. I. Abbas *et al.*, "Investigation of Gamma-Ray Shielding Properties of Bismuth Oxide Nanoparticles with a Bentonite–Gypsum Matrix," *Materials (Basel).*, vol. 16, no. 5, 2023, doi: 10.3390/ma16052056.

[44] G. Pal *et al.*, "Analysis of enhancement in gamma-ray shielding proficiency by adding WO 3 in Al 2 O 3 -PbO-B 2 O 3 glasses using Phy-X / PSD," *J. Mater. Res. Technol.*, vol. 9, no. 6, pp. 14425–14442, 2020, doi: 10.1016/j.jmrt.2020.10.020.

[45] G. Lakshminarayana, A. Kumar, M. G. Dong, M. I. Sayyed, N. V. Long, and M. A. Mahdi, "Exploration of gamma radiation shielding features for titanate Bismuth borotellurite glasses using relevant software program and Monte Carlo simulation code," *J. Non. Cryst. Solids*, vol. 481, no. October, pp. 65–73, 2018, doi: 10.1016/j.jnoncrysol.2017.10.027.

[46] M. Aboudeif, "An evaluation of the radiation protection characteristics of prototyped oxide glasses utilising Phy-X/PSD software," 2020.

[47] A. A. El-Maaref, B. M. Alotaibi, N. Alharbi, A. F. A. El-Rehim, and K. S. Shaaban, "Effect of Fe2O3 as an Aggregate Replacement on Mechanical, and Gamma/ Neutron Radiation Shielding Properties of Phosphoaluminate Glasses," *J. Inorg. Organomet. Polym. Mater.*, vol. 32, no. 8, pp. 3117–3127, 2022, doi: 10.1007/s10904-022-02345-6.

[48] R. Kurtulus and T. Kavas, "Calculations on Linear Attenuation Coefficient and Fast Neutron Removal Cross-section for B2O3-TeO2 Glass System via Phy-X/PSD," *J. Turkish Chem. Soc. Sect. A Chem.*, vol. 1, no. 4, pp. 19–23, 2021.

[49] H. H. Hegazy *et al.*, "Nuclear shielding properties of B2O3–Bi2O3–SrO glasses modified with Nd2O3: Theoretical and simulation studies," *Ceram. Int.*, vol. 47, no. 2, pp. 2772–2780, 2021, doi: 10.1016/j.ceramint.2020.09.131.

[50] G. Almisned *et al.*, "The impact of chemical modifications on gamma-ray attenuation properties of some WO3-reinforced tellurite glasses," *Open Chem.*, vol. 21, no. 1, 2023, doi: 10.1515/chem-2022-0297.

[51] H. A. Saudi and S. U. El-Kameesy, "Investigation of modified zinc borate glasses

doped with BaO as a nuclear radiation-shielding material," *Radiat. Detect. Technol. Methods*, vol. 2, no. 2, pp. 1–7, 2018, doi: 10.1007/s41605-018-0075-x.

[52] Y. S. Alajerami, "Radiation Shielding Properties for NaO–CdO–Bi2O3–B2O3 Glasses Using XCOM, Phy-X/PSD and Srim Programs," *Glas. Phys. Chem.*, vol. 47, pp. S10–S20, 2021, doi: 10.1134/S1087659621070026.

[53] E. E. Saleh *et al.*, "Synthesis and Nuclear Radiation Shielding Ability of Li2O-ZnO-P2O5 Glasses: The Role of Yb2O3," *J. Electron. Mater.*, vol. 51, no. 12, pp. 7283–7296, 2022, doi: 10.1007/s11664-022-09979-9.

[54] P. Sikora *et al.*, "Rheological, Mechanical, Microstructural and Radiation Shielding Properties of Cement Pastes Containing Magnetite (Fe3O4) Nanoparticles," *Int. J. Concr. Struct. Mater.*, vol. 17, no. 1, 2023, doi: 10.1186/s40069-022-00568-y.

[55] D. Cao, G. Yang, M. Bourham, and D. Moneghan, "Gamma radiation shielding properties of poly (methyl methacrylate) / Bi2O3 composites," *Nucl. Eng. Technol.*, vol. 52, no. 11, pp. 2613–2619, 2020, doi: 10.1016/j.net.2020.04.026.

[56] M. T. Alabsy and M. A. Elzaher, "Radiation shielding performance of metal oxides/EPDM rubber composites using Geant4 simulation and computational study," *Sci. Rep.*, vol. 13, no. 1, pp. 1–13, 2023, doi: 10.1038/s41598-023-34615-9.

[57] P. Lim-Aroon, E. Wimolmala, N. Sombatsompop, and K. Saenboonruang, "Manufacturing process and properties of lead-free natural rubber sponge for use in X-ray and gamma-ray shielding applications," *IOP Conf. Ser. Mater. Sci. Eng.*, vol. 526, no. 1, 2019, doi: 10.1088/1757-899X/526/1/012015.

[58] N. Plangpleng *et al.*, "Flexible gamma-ray shielding based on natural Rubber/BaSO4 nanocomposites," *Radiat. Phys. Chem.*, vol. 199, Oct. 2022, doi: 10.1016/j.radphyschem.2022.110311.

[59] R. Gamal, E. Salama, H. Elshimy, D. E. El-nashar, and A. Bakry, "Gamma Attenuation and Mechanical Characteristics of a Lead / NBR / SBR Rubber Composite with Black Nanocarbon Reinforcement," 2023.

[60] D. Toyen, A. Rittirong, W. Poltabtim, and K. Saenboonruang, "Flexible, lead-free, gamma-shielding materials based on natural rubber/metal oxide composites," *Iran. Polym. J. (English Ed.*, vol. 27, no. 1, pp. 33–41, 2018, doi: 10.1007/s13726-017-0584-3.

[61] W. Huang, W. Yang, Q. Ma, J. Wu, J. Fan, and K. Zhang, "Preparation and characterization of γ-ray radiation shielding PbWO4/EPDM composite," *J. Radioanal. Nucl. Chem.*, vol. 309, no. 3, pp. 1097–1103, 2016, doi: 10.1007/s10967-016-4713-9.

[62] A. Saeed and W. A. Abu-raia, "Silicone rubber composite reinforced by Bismuth Tungsten oxide as an effective gamma-ray protective materials," *J. Polym. Res.*, vol. 29, no. 5, pp. 1–7, 2022, doi: 10.1007/s10965-022-03055-w.

[63] E. Kalkornsurapranee *et al.*, "Wearable and flexible radiation shielding natural rubber composites: Effect of different radiation shielding fillers," *Radiat. Phys. Chem.*, vol. 179, p. 109261, Feb. 2021, doi: 10.1016/J.RADPHYSCHEM.2020.109261.

[64] E. Kalkornsuranee *et al.*, "Mechanical and gamma radiation shielding properties of

natural rubber composites: effects of Bismuth oxide (Bi_2O_3) and lead oxide (PbO)," *Mater. Res. Innov.*, vol. 26, no. 1, pp. 8–15, 2022. doi: 10.1080/14328917.2020.1853383.

[65] M. T. Alresheedi, Mohamed Elsafi, Yosef T. Aladadi Abdullrahman Bin Ganam, M. I. Sayyed, Mohd Adzir Mahdi and Ahmad Fauzi Abas, "Assessment of Silicone Rubber / Lead Oxide Composites, Enriched with Bi_2O_3, WO_3, BaO, and SnO_2 Nanoparticles for Radiation Shielding Applications". Polymers 2023, 15, 2160. https://doi.org/ 10.3390/polym15092160.

[66] S. U. El Kameesy, D. E. El Nashar, M. A. A.- Leila, and M. Ahmed, "Influence of Bismuth Contents on Mechanical and Gamma-ray Attenuation Properties of Silicone Rubber Composite," *Int. J. Adv. Res. Influ.*, vol. 3, no. 6, pp. 1035–1039, 2015.

[67] M. Elsafi, N. Almousa, N. Al-Harbi, M. N. Almutiri, S. Yasmin, and M. I. Sayyed, "Ecofriendly and radiation shielding properties of newly developed epoxy with waste marble and WO3nanoparticles," *J. Mater. Res. Technol.*, vol. 22, pp. 269–277, 2023, doi: 10.1016/j.jmrt.2022.11.128.

[68] K. G. Mahmoud, M. I. Sayyed, A. H. Almuqrin, J. Arayro, and Y. Maghrbi, "Monte Carlo Investigation of Gamma Radiation Shielding Features for Bi2O3/Epoxy Composites," *Appl. Sci.*, vol. 13, no. 3, 2023, doi: 10.3390/app13031757.

[69] M. Dong, S. Zhou, H. Yang, and X. Xue, "Gamma-ray attenuation behaviors and mechanism of boron rich slag/ epoxy resin shielding composites," *Nucl. Eng. Technol.*, vol. 55, no. 7, pp. 2613–2620, 2023, doi: 10.1016/j.net.2023.04.041.

[70] M. Asgari, H. Afarideh, and H. Ghafoorifard, "Comparison of nano / micro lead , Bismuth and Tungsten on the gamma shielding properties of the fl exible composites against photon in wide energy range (40 keV e 662 keV)," *Nucl. Eng. Technol.*, vol. 53, no. 12, pp. 4142–4149, 2021, doi: 10.1016/j.net.2021.06.022.

[71] K. G. Mahmoud, M. I. Sayyed, S. Hashim, A. H. Almuqrin, and A. El-Soad A.M, "Impacts of halloysite clay nanoparticles on the structural and γ-ray shielding properties of the epoxy resin," *Nucl. Eng. Technol.*, vol. 55, no. 4, pp. 1585–1590, 2023, doi: 10.1016/j.net.2023.02.015.

[72] Y. Karabul and O. İçelli, "The assessment of usage of epoxy based micro and nano-structured composites enriched with Bi_2O_3 and WO_3 particles for radiation shielding," *Results Phys.*, vol. 26, 2021, doi: 10.1016/j.rinp.2021.104423.

[73] M. Ghozza, "Radiation Attenuation Properties of $BaMnO_3$ Doping Nickel Semiconductor Perovskite Using Phys-X/PSD Software," *Arab J. Nucl. Sci. Appl.*, vol. 0, no. 0, pp. 0–0, 2023, doi: 10.21608/ajnsa.2022.154447.1621.

CHAPTER 3

EXPERIMENTAL TECHNIQUES

Contents	
3.1	*Introduction*
3.2	*Gamma-Ray Spectroscopy*
3.3	*Inductively Coupled Plasma-Mass Spectrometer (ICP-MS)*
3.4	*X-ray Diffractometer (XRD)*
3.5	*Energy Dispersive X-ray Fluorescence (EDXRF)*
3.6	*Field Emission Scanning Electron Microscopy (FESEM) and Energy Dispersive X-ray Analysis (EDAX)*
3.7	*Reference*

Abstract: *This chapter provides an in-depth discussion of the instruments used in the current study, focusing on their key features and applications. Radionuclide enrichment, radiation levels, and trace element concentrations were measured using instruments.*

3.1 Introduction

This chapter includes a detailed discussion of the instruments utilised in the current study and their key aspects. Radionuclide enrichment, radiation levels, and trace element concentrations in the environment are all measured using proper instruments. The exposure rates in the environment were measured in the current study utilising a gamma radiation survey metre (UR-705). To detect and measure natural radionuclide gamma-ray radiation, a flat type NaI (TI) gamma-ray spectrometer and a high purity Germanium detector (HPGe) were utilised. The trace element concentrations were determined using an Inductively Coupled Plasma-Mass Spectrometer (ICP-MS). The presence of heavy minerals was determined using an X-ray Diffractometer (XRD), Energy Dispersive X-Ray Diffraction Fluorescence (EDXRF). Field and Emission Scanning Electron Microscopy (FESEM) and Energy Dispersive X-ray Analysis (EDAX). outlines the experimental techniques employed in this research, detailing the principles, methodologies, and applications of each technique. The chapter covers a range of analytical and detection methods essential for studying natural radioactivity and evaluating radiation shielding materials.

3.2 Gamma-Ray Spectroscopy

Gamma-ray spectrometry relies on the direct relationship between the energy of incoming gamma rays and the pulse amplitude generated at the detector's output. Once these pulses are amplified and digitized, their amplitudes are analyzed to produce an energy spectrum of the detected radiation. Because each radionuclide emits gamma rays at specific energies, the resulting gamma-ray spectra can be used to identify and measure the radionuclides present in a sample.

Nowadays, radiation and related studies have become very popular for scientists as it has started to be used in many different fields such as medical hospitals, energy power plants, agriculture, environmental issues, etc. In all fields, radiation measurement is an important issue as it needs to be known exact values of radiation, due to its possible especially health effects. For gamma-ray measurement, there are different types of detector system and NaI (Tl) scintillation detectors are one of the most widely used detector types for many years. This is because of its low cost,

resistant to thermal effects and weather conditions (especially when compared to HPGe detectors) and does not need extra cooling devices. Its high detection efficiency is also an advantage in comparison with HPGe type. On the other hand, HPGe type detector has higher resolution. The high absorption efficiency of NaI (Tl) detector is due to the presence of Tl (Thallium, Z = 53) element in its structure, and so a high photopeak to Compton ratio makes it also preferable detector type. In the detection process of gamma rays with NaI (Tl) detector, the physical interactions of gamma rays with the crystal of the detector are well-known.

3.2.1 Micro-R survey meter

Indoor and outdoor gamma radiation levels were measured in the specific locations using a Micro-R survey metre UR-705 procured from Nucleonix systems Pvt. Ltd. India. The picture of the Micro-R survey metre used in this investigation is shown in Figure 3.1.

Figure 3.1: Micro-R survey metre.

It is designed with an integrally linked 1"×1" NaI (Tl) Scintillator to a 1.5-inch Photomultiplier tube and can measure and show dose rates in the range of 0-10,000 μRh^{-1} or 0-100 $\mu Sv\ h^{-1}$ on a dot matrix LCD with auto-ranging capability. Its calibration accuracy is better than 15% (specified with a Cs-137 standard source) from 100 Rh^{-1} onwards, and within 20% up to 10000 μRh^{-1}. Dose rates close to the

natural background radiation level can be accurately assessed using this equipment. When low radiation levels are considered, it is beneficial in radiometric and environmental radiation monitoring[1].

The dosage rates were measured in the air at one metre above the ground, according to established protocol. Each selected residence received approximately 15 inside and outdoor readings. Using a conversion factor of 1 μR/h = 8.7 nGy/h, the gamma radiation level recorded in R h^{-1} was translated to absorbed dose (AD) in nGy/h[1].

3.2.2 NaI (Tl) scintillation detector

The NaI (Tl) scintillation detector is a commonly used type of radiation detector that is particularly effective in detecting and measuring gamma rays and X-rays [2]. It is based on the scintillation principle, where the interaction of radiation with a scintillating material produces flashes of light that can be detected and analysed. A gamma-ray spectrometer with a " 3×3 " NaI(Tl) scintillation detector, connected to a multichannel analyser (Easy-MCA-8K, ORTEC), was utilized for measuring the spectra of naturally occurring radionuclides. The NaI(Tl) system had the following specifications: a resolution (FWHM) of 60 keV at 1.33 MeV for ^{60}Co, and a relative efficiency of 7.5% at the same energy. The detector was positioned at the center of a two-layer chamber made of stainless steel (10 mm thick) and lead (30 mm thick), which shielded it from unwanted background radiation and minimized scattered radiation from the shield. The sample was placed on the detector for at least 10 hours. The spectra were then analysed using the MAESTRO software program (Version 7.01, ORTEC, Inc.).

Figure 3.2: NaI (Tl) scintillation detector

Here is a brief explanation of the working of the NaI (Tl) scintillation detector:

Gamma-ray Interaction: When a gamma-ray photon enters the NaI (Tl) crystal, it interacts with the material primarily through the photoelectric effect, Compton scattering, or pair production (depending on the energy of the gamma-ray). These interactions result in the transfer of energy from the gamma photon to the electrons in the crystal.

Scintillation Process: The transferred energy excites the electrons in the NaI(Tl) crystal. As these excited electrons return to their ground state, they release the excess energy in the form of visible light photons. This process of converting gamma-ray energy into visible light is called scintillation.

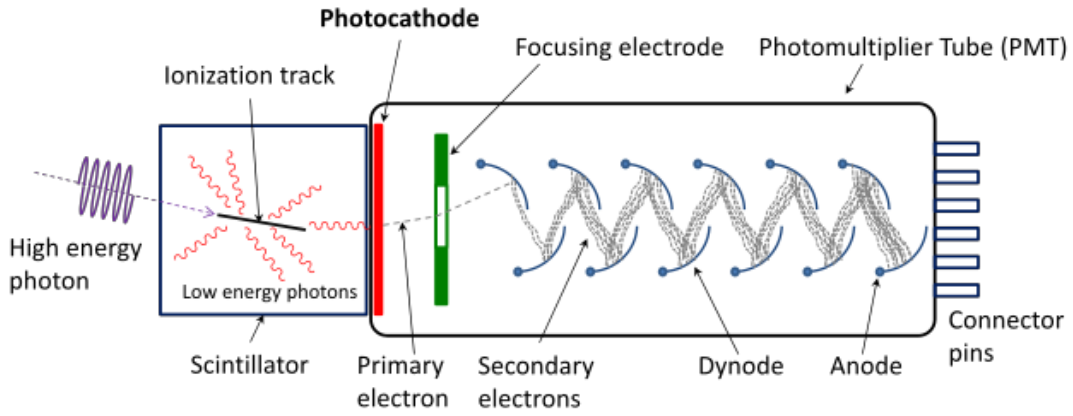

Figure 3.3: Block diagram of NaI (Tl) scintillation detector.

Thallium Doping: The Thallium doping in the NaI crystal plays a crucial role in the scintillation process. Thallium atoms create energy states within the band gap of the NaI crystal, allowing for more efficient conversion of the absorbed energy into visible light. This doping enhances the light output and shifts it to a wavelength (~415 nm) where it can be effectively detected by Photomultiplier Tubes (PMTs).

Light Collection: The visible light photons generated in the scintillation process are collected and directed towards a photomultiplier tube (PMT) or other light sensors. The efficiency of light collection can be improved by using reflective materials around the crystal and ensuring good optical coupling between the crystal and the

PMT.

Photomultiplier Tube (PMT): The PMT is a device that converts the collected light photons into an electrical signal. When the light photons strike the photocathode of the PMT, they release electrons via the photoelectric effect. These electrons are then multiplied through a series of dynodes in the PMT, resulting in a measurable electrical pulse.

Signal Processing: The electrical pulses generated by the PMT are proportional to the energy of the original gamma-ray photon. These pulses are amplified and digitized for further analysis. The amplitude of each pulse corresponds to the energy of the detected gamma-ray photon.

Energy Spectrum Analysis: The digitized pulses are sorted and counted to create an energy spectrum. Peaks in the spectrum correspond to the specific energies of gamma rays emitted by the radionuclides present in the sample. By analyzing these peaks, one can identify and quantify the radionuclides.

Spectrum Analysis: The processed signals from multiple scintillation events are analyzed to create a gamma-ray energy spectrum. The spectrum provides information about the energies and intensities of the detected gamma rays, enabling the identification of specific radioactive isotopes and their activities[3].

NaI(Tl) scintillation detectors offer a good balance between sensitivity, energy resolution, and cost-effectiveness, which makes them widely used in various applications such as environmental monitoring, nuclear medicine, and radiation detection in industries.

3.2.3 HPGe (High-Purity Germanium) detector

HPGe (High-Purity Germanium) detector is a type of radiation detector that is commonly used in various applications, particularly in gamma-ray spectroscopy. It is highly sensitive and offers excellent energy resolution, making it well-suited for precise measurements of gamma rays. Germanium detectors are widely used for gamma-ray spectroscopy. The main advantage of HPGe detector, for gamma-ray

measurement, is its superior energy resolution. The resolution depends on the number of single carriers which are generated during particle interaction with the detector material. On the other hand, this detector has two main disadvantages. First, the efficiency of it is lower that of NaI(TI) because of their smaller size and lower Z. Detection efficiency of a NaI (TI) detector system depends on different parameters.

Figure 3.4: HPGe Detector.

Second, it is necessary to cool it down to very low temperature by utilized liquid nitrogen. This makes HPGe detector more expensive to purchase and to maintain than NaI(TI).

The HPGe detector is constructed using a high-purity germanium crystal, which is carefully grown and processed to achieve a low level of impurities. The purity of the germanium crystal is crucial as impurities can introduce electronic noise and hinder the detector's performance. When gamma rays interact with the germanium crystal of the HPGe detector, they undergo various processes such as photoelectric absorption, Compton scattering, and pair production. These interactions result in the generation of charge carriers (electron-hole pairs) within the crystal. To detect these charge carriers, the HPGe detector is typically operated in a reverse-biased mode, creating an electric field within the crystal. The charge carriers generated by gamma-ray interactions drift under the influence of this electric field towards the detector's electrodes. The electrodes of the HPGe detector collect and measure the

charges produced by the gamma-ray interactions. The resulting electrical signals are amplified and processed to determine the energy and intensity of the incident gamma rays[2], [3]. The primary advantage of the HPGe detector is its excellent energy resolution, which allows for precise identification and quantification of gamma rays of different energies. This high energy resolution is due to the low electronic noise and the ability of the germanium crystal to accurately capture and measure the charge carriers. HPGe detectors are commonly used in scientific research, nuclear power plants, environmental monitoring, and various other applications where precise gamma-ray spectroscopy is required. However, they are relatively expensive and require careful handling, as the germanium crystal is fragile and sensitive to moisture and other contaminants.

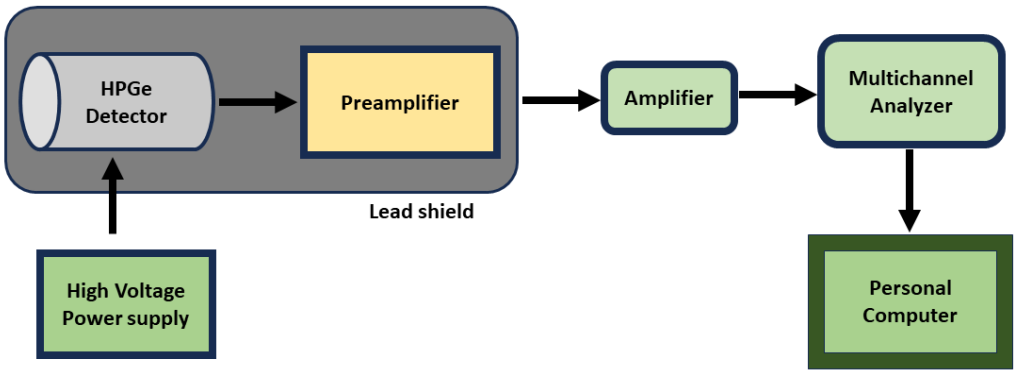

Figure 3.5: Block diagram of HPGe detector

The working of an HPGe (High-Purity Germanium) detector involves several steps that enable it to detect and measure gamma radiation with high precision. Here is a brief explanation of the working principle:

1. Germanium Crystal: The heart of an HPGe detector is a high-purity germanium crystal. This crystal is carefully grown and processed to have a low concentration of impurities. The purity of the germanium crystal is crucial as it affects the detector's energy resolution and sensitivity.

2. Reverse Biasing: The germanium crystal is operated in a reverse-biased mode, meaning a voltage is applied to create an electric field within the crystal. This electric field allows for the efficient collection of charge carriers generated by the interaction of gamma rays with the crystal.

3. Gamma-ray Interaction: When gamma rays interact with the germanium crystal, several processes can occur, including photoelectric absorption, Compton scattering, and pair production. These interactions result in the generation of electron-hole pairs within the crystal lattice.

4. Charge Collection: The electron-hole pairs created by gamma-ray interactions are drifted towards the electrodes of the HPGe detector under the influence of the electric field. The positive holes move towards the negatively biased electrode (n-type contact), while the electrons move towards the positively biased electrode (p-type contact).

5. Signal Amplification: The charge carriers collected by the electrodes create a small electrical signal. This signal is typically very weak, so it needs to be amplified for further processing. The detector system includes a preamplifier that amplifies the electrical signal while minimizing electronic noise.

6. Pulse Processing: The amplified electrical signal is then processed by various electronics within the detector system. This processing includes shaping the signal, further amplification, and converting it into a digital form for analysis and storage.

7. Energy Determination: The energy of the incident gamma-ray is determined based on the amplitude of the processed electrical signal. The high energy resolution of the HPGe detector allows for precise energy determination, enabling the identification and quantification of gamma rays with different energies.

8. Spectrum Analysis: The processed signals from multiple gamma-ray interactions are analyzed to create a gamma-ray energy spectrum. The spectrum provides information about the energies and intensities of the

detected gamma rays, allowing for the identification of specific radioactive isotopes and their activities.

The working of an HPGe detector requires careful handling and environmental control. The detector is typically operated at cryogenic temperatures using liquid nitrogen or a cryocooler to reduce the thermal noise and improve energy resolution. The shielding around the detector helps minimize background radiation and electronic noise, further enhancing the detector's performance. Overall, the HPGe detector's high sensitivity and excellent energy resolution make it a valuable tool in various fields, including nuclear physics, environmental monitoring, and radioactive waste management.

This study employed a p-type, closed-end coaxial HPGe detector (model GR4020, Canberra) coupled with a 16 K multichannel analyzer (Canberra Industries, Inc., USA) for spectral measurements. The HPGe detector, configured vertically and cooled with liquid nitrogen, had specific performance specifications: it achieved resolutions (FWHM) of 1333 keV at ≤2.000 keV and 122.0 keV at ≤ 0.925 keV, with a relative efficiency of 40%. To minimize background radiation to less than 1%, the detector was housed within a four-layered lead shield, each layer being 10 cm thick.

3.2.4 Energy, Resolution and Efficiency Calibration of the detector

Equation (3.1) shows the energy resolution, R, which is defined as the detector's ability to resolve little alterations in the energy of incident photons. (FWHM) is the full width at half maximum and it is known as the width of the distribution at half of the level of the peak and where Hc represents the peak centroid channel number,

$$R = \frac{\text{FWHM}}{\text{Hc}} \times 100 \qquad (3.1)$$

Efficiency is a crucial parameter for NaI(TI) and HPGe detectors, encompassing several components: absolute efficiency, intrinsic efficiency, and intrinsic photopeak efficiency[3], [4]. For any gamma radiation detector, the absolute efficiency, Ɛ is formally defined by the following ratio:

$$\varepsilon = \frac{\text{Number of gamma rays detected}}{\text{Number of gamma rays emitted by the source}} = \frac{N_d}{N_s} \qquad (3.2)$$

The intrinsic photopeak efficiency ε_p focuses solely on the full energy peak region of interest, making it a valuable measure as it excludes areas of the spectrum that may be affected by scattering from surrounding objects or electrical noise[4]. Equation (3.3) defines intrinsic photopeak efficiency:

$$\varepsilon_p = \frac{C_p}{N_\gamma} \qquad (3.3)$$

where C_p is the number of counts in the photopeak corresponding to energy Eγ per unit time, and Nγ is the total number of gamma rays emitted by the source per unit time.

Before acquiring data from the samples, the energy calibration of the HPGe detector (gamma-ray energy as a function of channel number) was conducted using standard gamma-ray sources ^{60}Co, ^{137}Cs, ^{22}Na, and ^{133}Ba. The HPGe detector was connected to the DSPEC hardware unit, which supplies high voltage (HV) to the detector and provides the working voltage for the preamplifier and the multichannel analyzer (MCA). The MCA operates based on instructions from the MAESTRO-32 software installed on a PC. Figure 3.6 shows the energy calibration graph obtained.

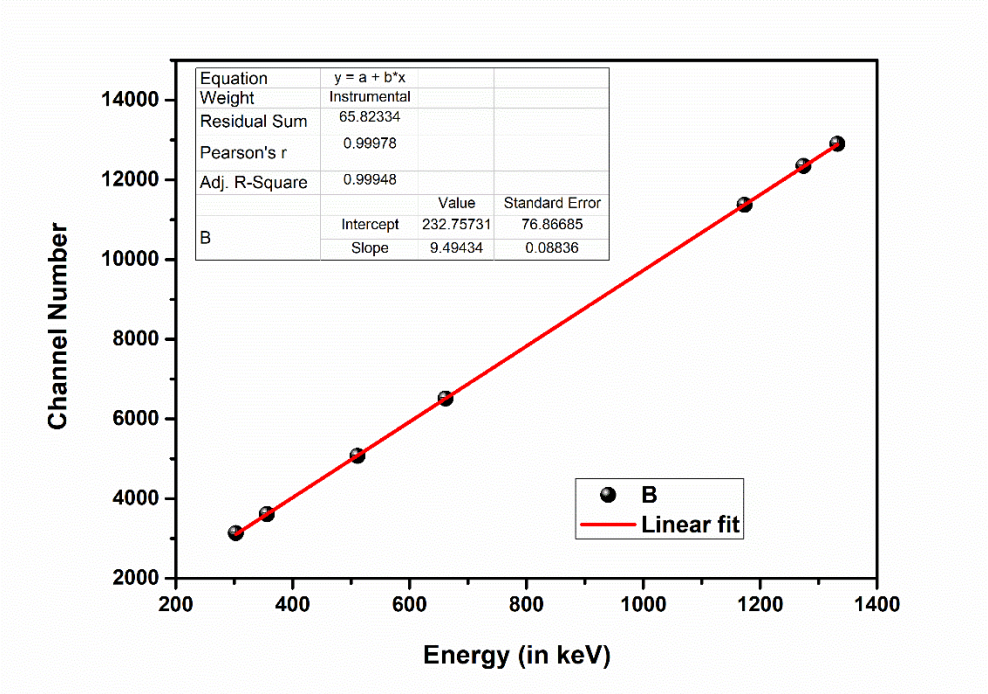

Figure 3.6: The energy calibration graph.

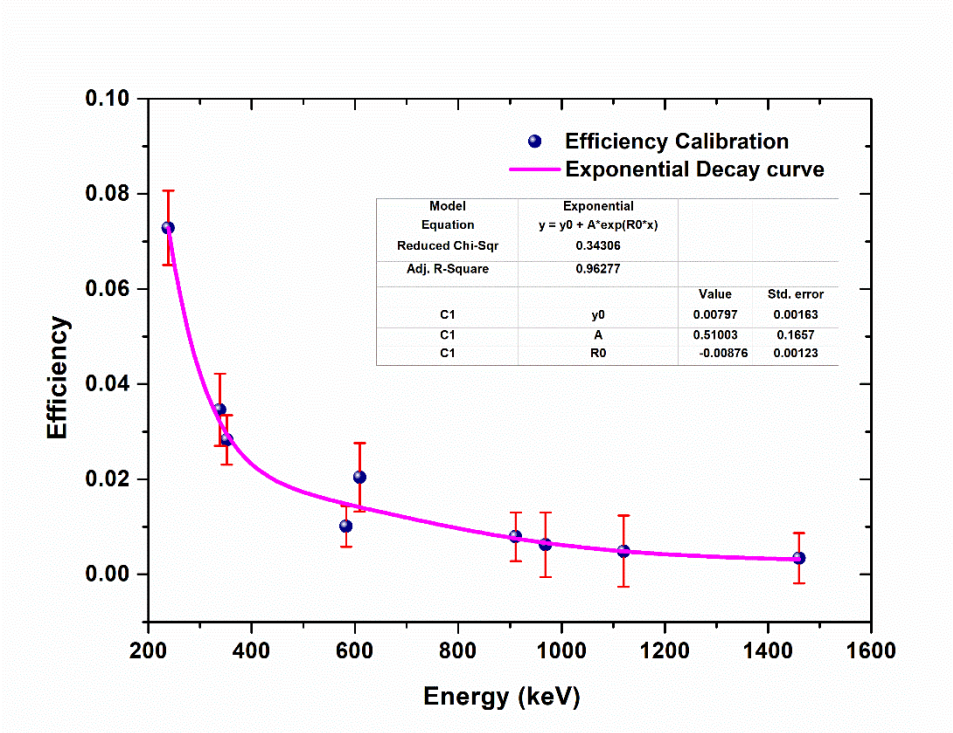

Figure 3.7: Efficiency calibration graph.

The spectrum was acquired and analyzed using a 16K multichannel analyzer (Multiport, CANBERRA) along with GENIE 2000 software (Mirion Technologies, Canberra, USA). Detector efficiency calibration was conducted using quality assurance reference materials from the International Atomic Energy Agency (IAEA), including RG U-238, RG Th-232, RG K-1, and SOIL-6. Both the standard source materials and samples were placed in containers of identical size and type to maintain consistent detection geometry. Standard techniques were then used to analyse the samples.

3.2.5 Activity Measurement

The activity of ^{40}K was evaluated from the 1461 keV photo peak. The gamma-ray transitions used to estimate the concentration of the assigned nuclides in the series were as follows: ^{226}Ra (186.1 keV), ^{214}Pb (295.1and 352.0 keV), ^{214}Bi (609.3, 1120.3 and 1765 keV) for Uranium series; ^{208}Tl (583.0 and 860.6 keV), ^{214}Pb (238.6 keV), ^{212}Bi (288.07, 727.33 and 1620.50 keV) and ^{228}Ac (338.5 and 911.2 keV) for Thorium series, after subtracting the background counts and applying the Compton correction. The Minimum Detection Levels (MDL) for the gamma spectrometry system used in the present study were 0.9, 1.2, and 4.06 Bq/kg for ^{226}Ra, ^{232}Th, and ^{40}K, respectively at 95% confidence level.

The activity concentration (Specific activity) in the sample is then calculated using the equation [5]

$$A = \frac{C_t}{P_\gamma \eta m} (Bqkg^{-1}) \qquad (3.4)$$

where C_t is the counts per second above background, P_γ is the absolute gamma-ray transition probability, η is the photo peak efficiency (%) of the detector and m is the mass of the sample in kg.

3.3 Inductively Coupled Plasma-Mass Spectrometer (ICP-MS)

An Inductively Coupled Plasma-Mass Spectrometer (ICP-MS) is an analytical instrument that combines two powerful techniques: Inductively Coupled Plasma (ICP) and Mass Spectrometry (MS). It is widely used for the elemental analysis of

samples across various fields, including environmental monitoring, geology, pharmaceuticals, and forensic science. Here's a brief explanation of the working principle of an ICP-MS:

1. Inductively Coupled Plasma (ICP): The ICP serves as the ionization source in the ICP-MS. It is a high-temperature plasma generated by an argon gas flow passing through a radiofrequency (RF) coil. The RF coil induces a strong electromagnetic field that ionizes the argon gas, creating a plasma composed of high-energy ions, electrons, and excited atoms.

2. Sample Introduction: The sample to be analyzed is typically introduced into the ICP as an aerosol or a solution via a nebulizer, which breaks it down into small droplets. The aerosol is then transported into the ICP by a carrier gas, typically argon or helium.

3. Ionization and Atomization: As the sample enters the ICP, the high temperature of the plasma vaporizes and atomizes the sample constituents. The atoms and ions within the plasma are in an excited state.

4. Ion Extraction and Separation: A series of skimmer cones and lenses are used to extract and focus the ions from the plasma into a vacuum chamber. These components ensure efficient ion transfer and separate the ions from the neutral particles and background gases present in the plasma.

5. Mass Separation: Inside the vacuum chamber, the ions are introduced into a mass spectrometer, which separates and analyzes them based on their mass-to-charge ratio (m/z). The mass spectrometer typically consists of an ion lens system, an analyzer, and a detector.

6. Mass Analysis and Detection: The ion lens system focuses and accelerates the ions into the analyzer, which can be a quadrupole, magnetic sector, or time-of-flight (TOF) analyzer. The analyzer selectively filters ions based on their m/z values, allowing only specific ions to reach the detector. The detector measures the number of ions detected for each mass, generating a mass spectrum.

7. Data Analysis: The mass spectrum obtained from the ICP-MS analysis represents the elemental composition of the sample. The intensities of the peaks in the spectrum correspond to the relative abundances of the ions detected, providing quantitative and qualitative information about the elements present in the sample.

ICP-MS offers high sensitivity, wide dynamic range, and the ability to analyze a broad range of elements, including both major and trace elements. It is capable of detecting elements at extremely low concentrations, often down to parts per trillion (ppt) or lower. The instrument's versatility and analytical power make it an essential tool for a wide range of scientific and industrial applications.

3.4 X-ray Diffractometer (XRD)

An X-ray Diffractometer (XRD) is a scientific instrument used to analyse crystalline materials. It is an indispensable tool for characterizing thin films and powder samples of electro ceramic materials. It utilizes the principle of X-ray diffraction to determine the atomic and molecular structure of a sample.

Figure 3.8: X-ray diffractometer

The diffraction of X-rays from crystalline materials arises from two fundamental principles. The first principle is that elastic (Thomson) scattering of photons allows atomic planes to be treated as mirrors, invoking the laws of specular reflectance. The second principle is that the wavelength of X-rays (0.15 – 0.5 nm) is comparable to the interatomic distances in crystals, leading to constructive and destructive interference phenomena.

X-ray diffraction is best visualized as shown in Figure 3.9, where an X-ray beam with a wavelength λ is incident at an angle θ onto a series of atomic planes with spacing d. The X-ray beam scatters off the planes at an angle θ equal to the incident angle relative to the crystalline plane. The relative phase shifts between X-rays scattered from the first and second planes are represented by the distance marked in orange in Figure 3.9.

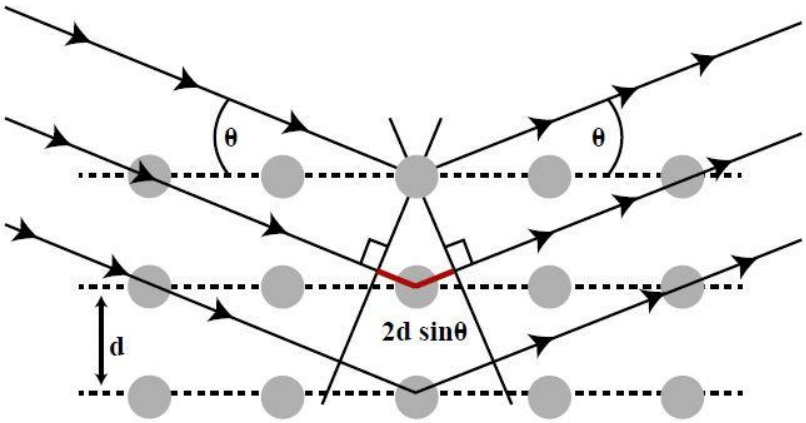

Figure 3.9: Visualization of X-ray diffraction.

Geometric considerations show that constructive interference occurs at certain angles θ_B depending on the interplanar spacing d, as described by the Bragg Equation[6]:

$$n\lambda = 2d_{hkl} \sin \theta_B$$

In this equation, θ_B is the Bragg angle, and d_{hkl} refers to the interplanar spacing corresponding to the Miller indices of the crystallographic plane. The integer n is the

order of the diffraction maxima, with n = 1 being the first order, n = 2 being the second order, and so on. The Bragg Equation relates the angular position of diffracted X-rays to the lattice spacing and is fundamental to all X-ray diffraction (XRD) measurements.

An X-ray diffractometer is composed of five key components: the X-ray source, the detector, the incident (or primary beam) optics, the receiving (or diffracted beam) optics, and the goniometer, as illustrated in Figure 2. The entire diffractometer setup is housed within a radiation enclosure and is operated via computer control.

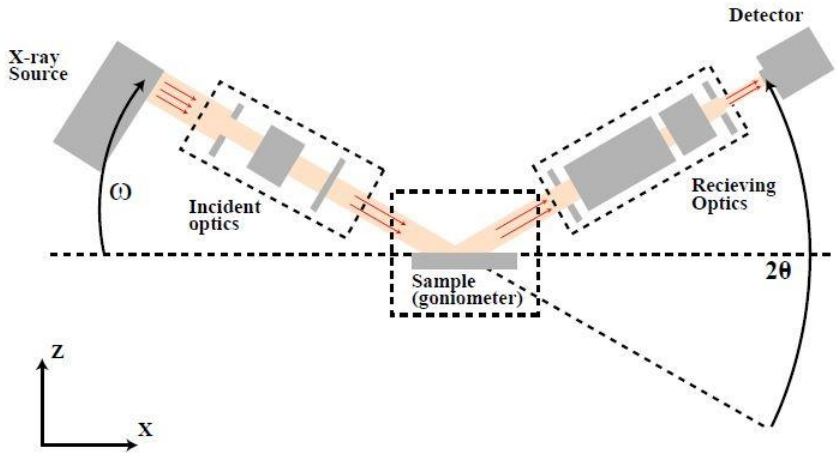

Figure 3.10: X-ray diffractometer components:

Here's a brief explanation of the XRD and its working principle:

1. X-ray Source: The XRD instrument consists of an X-ray source, typically an X-ray tube, that emits X-rays with a specific wavelength. The most commonly used X-ray source in XRD is copper (Cu) K_α radiation, which has a wavelength of 1.5406 Å (angstroms).

2. Sample Preparation: The sample of interest, usually a crystalline material, is prepared and mounted onto a sample holder. The sample must be finely ground and evenly dispersed to ensure a representative measurement.

3. Incident X-ray Beam: The X-ray beam is directed onto the sample at a specific angle. The incident X-rays interact with the atoms in the crystal

lattice of the sample.

4. Diffraction: When the X-rays encounter the crystal lattice, they undergo a phenomenon called diffraction. The X-rays interact with the electrons in the atoms of the crystal, causing constructive interference and producing a diffraction pattern.

5. Detector: A detector, such as a scintillation counter or a solid-state detector, is positioned opposite the sample to capture the diffracted X-rays. The detector records the intensity and position of the diffracted X-ray beams.

6. Data Collection: The sample and detector are rotated together, collecting a series of diffraction patterns as the angle of incidence changes. The diffraction patterns are recorded as a function of the angle of diffraction.

7. Data Analysis: The recorded diffraction patterns are processed using mathematical algorithms to extract the structural information of the sample. The diffraction pattern is converted into a diffraction pattern plot, known as a diffraction pattern or X-ray diffraction (XRD) pattern.

8. Structure Determination: The XRD pattern contains distinctive peaks that correspond to the atomic arrangements within the crystal lattice of the sample. The position, intensity, and shape of the peaks are analyzed to determine the crystal structure, lattice parameters, and other structural properties of the sample.

X-ray diffraction provides valuable information about the crystal structure, phase identification, crystal orientation, and lattice imperfections of materials. It is widely used in various scientific and industrial applications, including material science, geology, chemistry, and pharmaceuticals.

For this study, a Rigaku Miniflex 600 X-ray diffractometer operating at 40 kV and 15 mA with a Cu-Kα monochromator (wavelength of 1.541 Å) was utilized. Scans were conducted continuously from 3° to 90° with a step size of 0.020° and a scan speed of 10°/minute to gather intensity data. The resulting analysis is presented

graphically, displaying peaks where % intensity is plotted on the Y-axis against 2θ values on the X-axis. Each peak's 2θ value and corresponding intensity are specific to the crystal structure under investigation. The XRD pattern was analyzed using PDXL software. By comparing the experimentally obtained diffraction pattern of the samples with the standard powder diffraction data file from the Cambridge Crystallographic Data Centre (CCDC) database, the unique powder patterns were matched to identify and characterize the crystal structures [7].

3.5 Energy Dispersive X-ray Fluorescence (EDXRF)

X-ray fluorescence (XRF) is a well-established analytical method used for both qualitative and quantitative analysis of samples. It allows for the simultaneous detection of numerous elements in solid or liquid states with high sensitivity. XRF is commonly applied in various interdisciplinary fields such as environmental science, material science, biomedicine, and archaeology [8]–[11].

Figure 3.11 shows XEPOS ED-XRF spectrometer, with an X-ray source of 50-W Pd end-window X-ray tube. Co/Pd binary alloy bremsstrahlung targets produced continuous X-rays of maximum energy of 50 keV for atomic excitation [12].

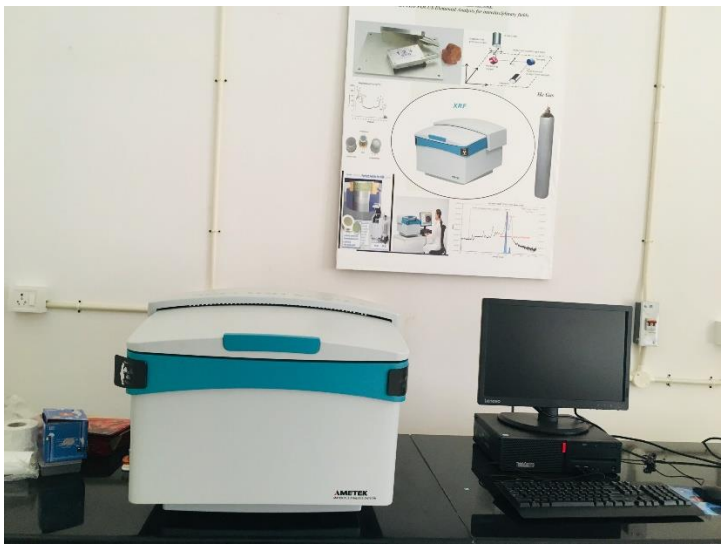

Figure 3.11: XEPOS ED-XRF spectrometer

The technique operates on the principle that individual atoms, when excited by an external energy source, emit X-ray photons with characteristic energies or

wavelengths. By counting the number of photons of each energy emitted from the sample, the elements present can be identified and quantified [8], [9].

Analysing process and working principle of EDXRF:

X-Ray Fluorescence (XRF) is an effective method for analysing trace elements in solid, liquid, and thin-film samples. The sensitivity of XRF depends on the energy of the incident radiation, the instrument's geometry, and the detector's efficiency. The fundamental principle of XRF analysis is the measurement of the energy or wavelength and intensity of the characteristic X-ray photons emitted from a sample. Since these characteristic X-rays provide a unique signature for each element, the recorded spectrum can be used to identify and quantify the elements in the sample. There are two main types of XRF spectrometers: Wavelength Dispersive (WD) and Energy Dispersive (ED). In Wavelength Dispersive X-Ray Fluorescence (WDXRF), a spectrum of wavelength versus intensity is obtained using a Bragg single-crystal dispersion medium, which diffracts X-rays based on their wavelength. These X-rays are then counted by a proportional or scintillation counter. Energy-Dispersive X-Ray Fluorescence (EDXRF) uses a solid-state detector and a multichannel analyser (MCA). The detector captures photon counts, and the MCA sorts them by energy to produce an energy versus intensity spectrum. While WDXRF offers better resolution, its additional optical components like rotating crystals and collimators reduce efficiency and increase costs. EDXRF, on the other hand, is more cost-effective and capable of analysing most elements in the periodic table simultaneously.

When a primary X-ray from an X-ray tube or radioactive source strikes a sample, it can either be absorbed by the atom or scattered by the material. The process where an X-ray is absorbed by transferring all its energy to an innermost electron is known as the "photoelectric effect." If the primary X-ray has sufficient energy, it ejects electrons from the inner shell, creating vacancies and leading to an unstable atomic state. As the atom returns to a stable state, electrons from the outer shells move to fill the vacancies in the inner shells, emitting electromagnetic radiation equal to the energy difference between the two levels specific to the excited element. This

emitted radiation serves as a unique signature of the element. This process of emission of characteristic X-rays is known as X-ray fluorescence (XRF). In addition to this radiative process, a competing non-radiative process called Auger electron emission can also occur. The probabilities of X-ray emission and Auger emission are dependent on the atomic number (Z) of the element, with Auger yield being higher for light elements and fluorescence yield being higher for heavy elements.

XRF detection predominantly involves the innermost K and L shells. The characteristic X-rays are labelled K, L, M, or N, corresponding to the shells from which they originate. Transitions between these energy levels are also denoted with Greek letters such as α, β, or γ to indicate the origin of the X-ray from transitions of electrons from higher to lower energy levels. A K_α X-ray is produced from an electron transition from the L to the K shell, while a K_β X-ray is produced from an electron transition from the M to the K shell, and so on. When the K-shell $1s_{1/2}$ is excited, electron transitions can occur between the subshells $2P_{3/2}$ or $2P_{1/2}$ of the L shell, resulting in $K_{\alpha 1}$ and $K_{\alpha 2}$ emissions, respectively. Similarly, $K_{\beta 1}$ corresponds to transitions from the subshells of the M shell.

The detection system measures the energies and intensities of these emission lines. Elements in a sample are identified by their specific spectral line energies or wavelengths for qualitative analysis, while the intensities of these lines are related to the concentrations of the elements, enabling quantitative analysis. A schematic diagram of the XRF setup is shown in Figure 3.12.

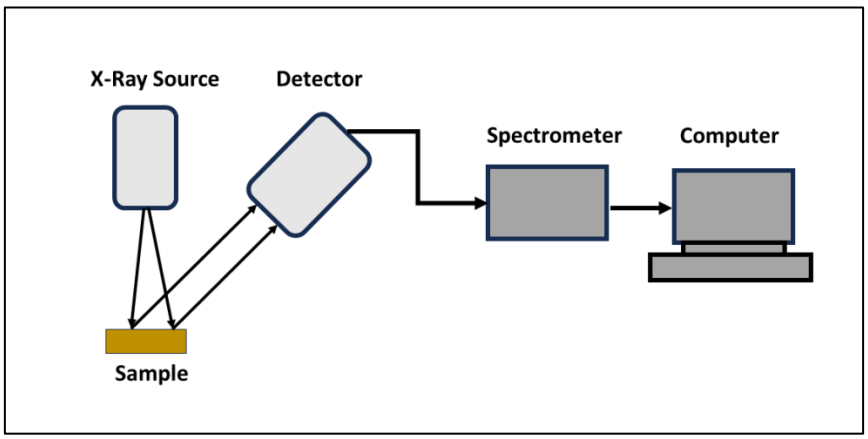

Figure 3.12: Components of ED-XRF spectrometer

Typically, light, and medium-mass elements (Z = 20-50) are identified by their K X-rays, whereas heavy elements are identified by their L X-rays due to lower detector efficiency for K X-rays of heavy elements. The spectral data is converted into elemental concentrations using advanced software based on fundamental parameter methods or empirical quantification methods. XRF is widely used to determine the elemental composition of materials because it is a fast and non-destructive technique. It is highly recommended for analytical applications and industrial production due to its efficiency. XRF enables non-destructive analysis of various sample types at a low cost and with a broad elemental range. Portable, handheld EDXRF instruments offer ease of operation and enhanced accessibility. Additionally, the maintenance cost is significantly lower compared to other nuclear analytical techniques. EDXRF is a widely used technique for elemental analysis in various industries, including environmental monitoring, mining, metallurgy, pharmaceuticals, and art conservation. It offers advantages such as non-destructive analysis, multi-elemental detection, and relatively simple sample preparation.

3.6 Field Emission Scanning Electron Microscopy (FESEM) and Energy Dispersive X-ray Analysis (EDAX)

FESEM-EDAX is a combination of two powerful analytical techniques used in material science and engineering for the detailed characterization of materials. Let's break down what each acronym stands for and their roles:

FESEM (Field Emission Scanning Electron Microscopy)

Field Emission Scanning Electron Microscopy (FESEM) is an advanced form of Scanning Electron Microscopy (SEM). It uses a field emission gun as the electron source, which provides a very fine electron beam. This results in:

High Resolution: FESEM can achieve resolutions on the order of nanometers, allowing for the detailed imaging of surface structures.

Surface Topography: It provides detailed images of the surface morphology of a sample.

High Depth of Field: Produces three-dimensional-like images with a high depth of field.

EDAX (Energy Dispersive X-ray Analysis)

Energy Dispersive X-ray Analysis (EDAX) is a technique used in conjunction with electron microscopes (like FESEM) to provide elemental composition information:

Elemental Analysis: EDAX detects X-rays emitted from the sample during electron beam interaction. Each element emits X-rays at characteristic energies, allowing for qualitative and quantitative analysis of the sample's elemental composition.

Mapping and Line Scans: EDAX can create elemental maps and line scans that show the distribution of elements across the sample surface.

Figure 3.13 represents the FE-SEM Microscope (Adopted from CISF, University of Calicut, Kerala.)

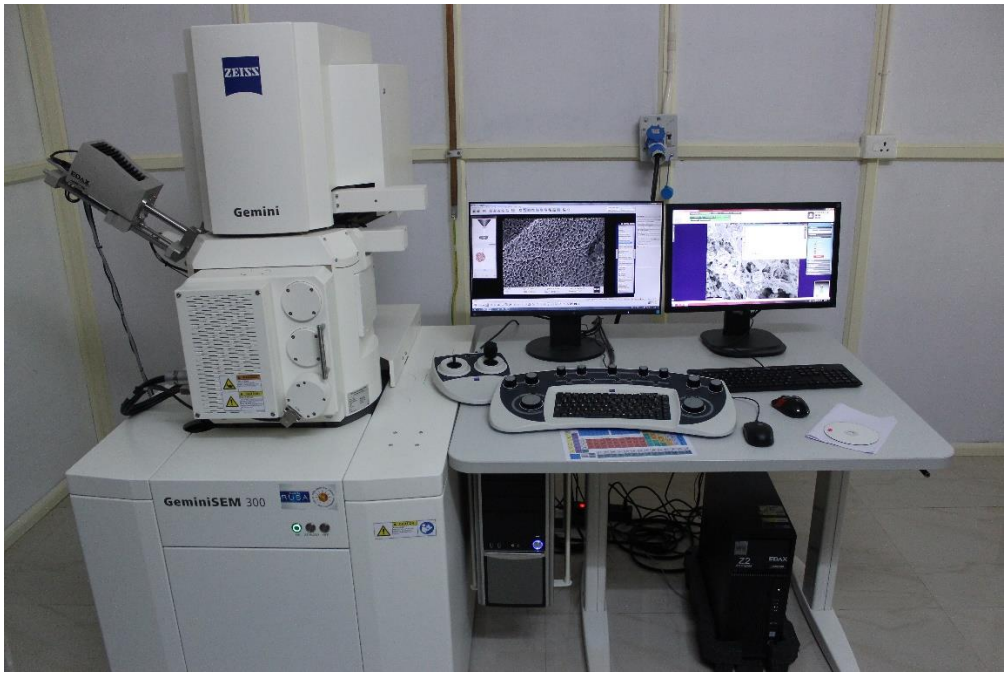

Figure 3.13: Field Emission Scanning Electron Microscope (FE-SEM)

Technical Specifications ZEISS Gemini SEM 300.

- Resolution: 0.6 nm at 30 kV (STEM) ,0.7 nm at 15 kv ,1.2 nm at 1 kv, 1.1 nm at1kV TD
- Inlens BSE Resolution: 1.2 nm at 1 kV
- Resolution in Variable Pressure mode (30 Pa) : 1.4 nm at 3 kV and 1.0 nm at 15 kV
- Acceleration Voltage: 0.02 - 30 kV
- Probe Current: 3 pA - 20 nA (100 nA configuration also available)
- Magnification: 12 – 2,000,000

Applications

- **Materials Science:** Characterization of metals, ceramics, and composites.
- **Nanotechnology:** Imaging and analysis of nanostructures and nanomaterials.
- **Biology and Medicine:** Detailed examination of biological specimens and medical implants.
- **Semiconductor Industry:** Analysis of thin films, coatings, and semiconductor devices.

3.7 Reference

[1] K. N. Mahamood and V. Prakash, "Radon , Thoron and their progeny distribution and estimation of annual effective dose and excess lifetime cancer risk in Panathady , kasaragod district , kerala," pp. 1–9, 2019, doi: 10.1093/rpd/ncz255.

[2] G. F. Knoll, *Radiation Detection and Measurement*, 3rd ed. John Wiley & Sons, Inc, 2000.

[3] G. R. Gilmore and J. Wiley, *Practical Gamma-ray Spectrometry*, 2nd Editio. 2011.

[4] H. M. QADR, "Comparison of Energy Resolution and Efficiency of NaI(TI) and HPGe Detector using Gamma-ray Spectroscopy," *J. Phys. Chem. Funct. Mater.*, vol. 3, no. 1, pp. 24–27, 2020, [Online]. Available: https://dergipark.org.tr/en/pub/jphcfum/issue/54729/727617.

[5] A. J. Vishnu C V, "Determination of natural radioactivity, hazard parameters and physico-chemical properties of soils from Palakkad-Thrissur district, Kerala, India," *Mater. Today Proc.*, vol. 55, pp. 127–134, 2022, doi: 10.1016/j.matpr.2021.12.548.

[6] G. F. Harrington and J. Santiso, "Back - to - Basics tutorial : X - ray diffraction of thin films," *J. Electroceramics*, pp. 141–163, 2021, doi: 10.1007/s10832-021-00263-6.

[7] B.D. Cullity S.R. Stock, *Elements of X-Ray Diffraction*, Third. Pearson New International Edition.

[8] A. Khuder, M. K. Sawan, J. Karjou, and A. K. Razouk, "Spectrochimica Acta Part B Determination of trace elements in Syrian medicinal plants and their infusions by energy dispersive X-ray fl uorescence and total re fl ection X-ray fl uorescence spectrometry," vol. 64, pp. 721–725, 2009, doi: 10.1016/j.sab.2009.05.020.

[9] T. D. T. Oyedotun, "X-ray fluorescence (XRF) in the investigation of the composition of earth materials : a review and an overview," *Geol. Ecol. Landscapes*, vol. 9508, pp. 1–7, 2018, doi: 10.1080/24749508.2018.1452459.

[10] C. I. Cristache, N. Engineering, O. G. Duliu, C. Ricman, and M. Toma, "Determination of elemental content in geological samples," no. June 2014, 2008.

[11] J. F. Boyle, "Rapid elemental analysis of sediment samples by isotope source XRF," pp. 213–221, 2000.

[12] S. Ibrahim *et al.*, "Trace elemental fingerprinting of Ayurvedic formulation Nishakatakadi using XRF and NAA," *J. Radioanal. Nucl. Chem.*, vol. 328, no. 1, pp. 435–446, 2021, doi: 10.1007/s10967-021-07659-2.

CHAPTER 4

THEORETICAL BACKGROUND

Contents	
4.1	*Radiological parameters*
4.2	*Radiogenic heat production and Heat Flow*
4.3	*Gamma-ray Attenuation*
4.4	*Shielding Design Principles*
4.4	*References*

Abstract: This chapter outlines the theoretical background of various radiological parameters and indices used to assess radiation exposure and safety. Additionally, it covers the concepts of radiogenic heat production, heat flow, and neutron removal cross sections, providing a comprehensive foundation for understanding radiation measurement and shielding effectiveness.

4.1 Radiological parameters

The potential radiological hazards associated with the studied materials were assessed by calculating various radiological parameters. These parameters included Radium Equivalent Activity (Ra_{eq}), criteria formula(CF), Gamma Absorbed Dose Rate (D_{out}), Annual Effective Dose Equivalent (AED), Representative Level Index (RLI), Annual Gonadal Dose Equivalent (AGDE), Excess Lifetime Cancer Risk (ELCR), Activity Utilization Index (AUI), Internal Hazard Index (H_{int}), External Hazard Index (H_{ext}), Gamma Index (Iγ), and Alpha Index (I_{α}).These parameters were utilized to quantify the potential risk by determining the amount of radiation emitted by the primordial radionuclides, namely ^{226}Ra, ^{232}Th, and ^{40}K, present in the building materials. In all these calculations, A_{Ra}, A_{Th} and A_K are the activity concentrations of ^{226}Ra, ^{232}Th and ^{40}K, respectively in $Bqkg^{-1}$[1]–[3].

4.1.1 Radium Equivalent Activity (Ra_{eq})

The distribution of natural radionuclides in the samples under investigation is not uniform. Therefore, a common radiological index has been introduced to evaluate the actual activity level of ^{226}Ra, ^{232}Th and ^{40}K in the samples and the radiation hazards associated with these radionuclides. This index is usually known as Radium equivalent activity ($Bqkg^{-1}$) and it is given by

$$Ra_{eq} = A_{Ra} + 1.43A_{Th} + 0.077A_K \qquad (4.1)$$

It is a measure used in radiological assessments to quantify the combined radioactivity from various radionuclides present in a material. It is a way to express the potential radiation hazard of a substance due to the presence of different radioactive isotopes. By calculating the Radium equivalent activity, one can determine if the material complies with safety standards and regulations regarding radiation exposure.The maximum value of Ra_{eq} in a sample must be less than 370 Bq kg^{-1}, to make sure of its safe limit of radiation [4].

Based on models suggested by Krisiuk et al., (1971) and Stranden (1976), a value of 1.5 mGy was obtained by Krieger (1981) when evaluating the annual external radiation dose inside dwellings constructed of building materials with a Ra_{eq} value

of 370 Bq/kg.

4.1.2 External And Internal Hazard Indices (H_{ex} and H_{in})

Natural radionuclides in soil, rocks, sediments, and other environmental constituents produce external radiation, to which all human beings are exposed. External and internal exposures are the major ways of radiation hazard threat to the inhabitants. Radiation exposure threat to respiratory organs may be as a result of increase above the safe limit of internal exposure to radionuclide [7]. The external and internal radiological hazards from the rocks of the study area were quantified by the external and internal hazard indices (H_{ex} and H_{in}), which are estimated by the following equations [8]

$$H_{ext} = (A_{Ra}/370) + (A_{Th}/259) + (A_K/4810) \quad (4.2)$$

$$H_{int} = (A_{Ra}/185) + (A_{Th}/259) + (A_K/4810) \quad (4.3)$$

The values of H_{ext} and H_{int} must be less than unity (< 1) for the radiation hazard to be negligible.

4.1.3 Indoor and Outdoor Absorbed Gamma Dose Rate (D_{in} and D_{out})

Gamma radiation effects are usually expressed in terms of the absorbed dose rate in air, which emanate from radioactive sources in the rock outcrops and soils in the study area. This quantity is used to measure the radiation exposure to human body due to the concentrations of ^{238}U, ^{232}Th and ^{40}K in the environmental materials [4]. The absorbed gamma dose rate (D_{out}) 1m above the ground surface can be estimated from the concentration of radionuclides in the samples. D_{out} and D_{ind} was computed using the following equation,

$$D_{out}\,(nGyh^{-1}) = 0.462A_{Ra} + 0.621A_{Th} + 0.0417A_K \quad (4.4)$$

$$D_{ind}\,(nGyh^{-1}) = 0.92A_{Ra} + 1.1A_{Th} + 0.081A_K \quad (4.5)$$

4.1.4 Annual Effective Dose Equivalents (AED)

The annual effective dose equivalent or AED is an important quantity used when

assessing the radiation effects arising from building materials like bricks, soils, concrete, granite gravels, stones and rocks. The annual effective dose equivalent (AED) is estimated by employing a conversion factor of 0.7 $SvGy^{-1}$. Commonly, adults spend about 80% of their time indoors, while the remaining 20% of their time is spent outdoors. Therefore, the indoor and outdoor occupancy factors are 0.8 and 0.2, respectively [4], [9].The outdoor and indoor annual effective doses (AED_{out}) were calculated using the following equation

$$AED_{out}\ (\mu Sv\ y^{-1}) = D_{out}\ (nGy\ h^{-1}) \times 8760\ \ (h\ y^{-1}) \times 0.2 \times 0.7\ \ (SvGy^{-1}) \times 10^{-3} \quad (4.6)$$

$$AED_{ind}\ (\mu Sv\ y^{-1}) = D_{out}\ (nGy\ h^{-1}) \times 8760\ \ (h\ y^{-1}) \times 0.8 \times 0.7\ \ (SvGy^{-1}) \times 10^{-3} \quad (4.7)$$

4.1.5 External (γ-radioactivity) level index I_γ

The European Commission (EC) suggested that gamma index (Iγ) could be used to examine if the materials meet the limits of dose criteria. In this study, gamma index (Iγ) is used to estimate the level of gamma radiation hazard related to the natural radionuclides in selected rock outcrops of the study area. I_γ must be less than one for radiation hazard to be insignificant and for the safe use of materials in the construction of engineering structures. The gamma index, I_γ is also known as the representative level index and is calculated from the following relation is calculated using the following equation [10].

$$I_\gamma = (A_{Ra}/300) + (A_{Th}/200) + (A_K/3000) \leq 1 \quad (4.8)$$

The OECD group of experts suggested some criteria for a definition of different levels of to be, $I_\gamma = 1$ as an upper limit, $I_\gamma \leq 1$ corresponds to 0.3 mSv y^{-1} and $I_\gamma \leq 3$, corresponds to 1 mSv y^{-1} [10-11].

Concerning different building materials, the ranges of Iγ are:

- Materials used in bulk amounts like bricks: $I_\gamma \leq 0.5$ to $I_\gamma \leq 1$.
- Superficial and other materials: $I_\gamma \leq 0.2$ to $I_\gamma \leq 6$.

4.1.6 Excess Lifetime Cancer Risk (ELCR)

The excess lifetime cancer risk is the possibility or threat to an individual for developing a cancerous cell as a result of exposure to toxic and harmful substances from various exposure pathways over time. According to the guidelines issued by the UNSCEAR, excess lifetime cancer risks (ELCR) can be calculated using the following equation,

$$ELCR_{out} = AED_{out} \times \text{Average duration of life (DL)} \times \text{Risk factor (RF)} \quad (4.9)$$

$$ELCR_{ind} = AED_{ind} \times \text{Average duration of life (DL)} \times \text{Risk factor (RF)} \quad (4.10)$$

where DL is life expectancy (70 years) and RF (1/Sv) is a fatal risk factor per Sievert, which is equal to 0.057 [12-14].

4.1.7 Alpha Index(I_α)

The Alpha index was developed as an assessment of the excess Alpha radiation exposure caused by inhalation originating from building materials. The Alpha index(I_α) is determined by the following formula.

$$\mathbf{I_\alpha} = \frac{A_{Ra}}{200\ \text{Bq/kg}} \quad (4.11)$$

where A_{Ra} is the ^{226}Ra activity concentration (Bq/kg) in the building materials. When the ^{226}Ra activity concentration of a building material exceeds a value of 200 Bq kg^{-1}, it is possible that the radon gassing from this material could cause an indoor radon concentration in excess of 200 Bqm^{-3}. In contrast, when the ^{226}Ra activity concentration is below 100 Bq/kg, it is unlikely that the radon exhalation from the building materials could cause indoor radon concentrations in excess of exceeding 200 Bqm^{-3} [16]. The recommended exemption level and recommended upper level for the ^{226}Ra activity concentration in building materials are 100 Bq/kg and 200 Bq/kg, respectively, in building materials as suggested by the Authorities in Denmark, Finland, Iceland, Norway and Sweden[16]. This upper level agrees with the action level given by the ICRP in Publication 65 (1994) and by the European Commission (EC, 1990).

4.2 Radiogenic Heat Production and Heat Flow

The radiogenic heat production rate is a fundamental property that quantifies the amount of heat released over a given time and volume within rock due to the decay of unstable radiogenic isotopes[12], [18]. These isotopes, including ^{238}U, ^{235}U, ^{232}Th, and ^{40}K, play a significant role in generating heat within the Earth. They possess half-lives comparable to the age of the Earth and remain abundant in the Earth's crust, serving as a vital radiation source. The connection between observed heat flow and heat production from radioactive isotopes within local rocks was first identified by J. Jolly in 1909. The natural abundance of radioactive elements in the Earth's crust contributes significantly to surface heat flow, which represents the rate of heat emanating from the Earth's interior[19]. These radioactive elements in the Earth's crust and mantle have significant applications in geophysics and geochemistry. Their decay generates heat within the Earth's crust, a crucial aspect of geothermal studies[20].

Radiogenic heat production is a vital factor in the study of geophysical properties, although it is not currently a widely recognized property. According to Kukkonen and Clauser (1994), this heat production is utilized to predict and explain temperature variations in deep drilling and temperature distribution modeling. Radiogenic heat production constitutes a smaller portion of surface heat flow in cratons and sedimentary basins. The Earth's continental crust has higher radiogenic heat production compared to the mantle, which contributes at most 1-2 mW/m^2 to the total heat flow. According to Waples (2002), the Earth's surface experiences approximately 65 mW/m^2 of heat flow, while the mantle's contribution in continental areas is approximately 20 mW/m^2, with the difference being attributed to the radioactive heat generation in crustal rocks. The primary source of crustal heat is the decay of radioactive isotopes, which, depending on geographic location, can account for up to 98% of heat generation. Other contributions, such as cosmic neutrino interactions with the Earth's mass and gravitational distortion, are likely to be negligible. The presence of natural radioactive elements in the Earth's crust can significantly influence surface heat flow depending on the geological characteristics

of the region.

Measuring the concentration of radioactive elements is the subject of numerous studies due to its critical role in modeling the thermal properties of the lithosphere. The isotopes ^{232}Th, ^{40}K, and ^{238}U are the primary contributors to terrestrial heat flow. Determining the concentration of these radioactive elements is crucial for understanding the composition of the Earth's mantle and crust. As radioactive nuclides decay, their mass is converted into the kinetic energy of emitted particles and gamma radiation, which is absorbed by rocks and ultimately transformed into heat. Studying radiogenic heat production helps identify anomalously high thermal conditions in various regions.

Several mathematical techniques can be employed to ascertain the concentrations of heat-producing elements, with gamma-ray spectrometry being the sole method that allows simultaneous determination of U, Th, and K concentrations, typically providing sufficient accuracy for most rock types. Understanding the heat generated by radioactive decay in rocks is crucial for comprehending the Earth's heat release and interpreting continental heat flux data.

4.2.1 Radiogenic Heat Production (RHP)

The main interior sources of heat in Earth are the heat content of the primitive Earth, directly after the formation due to the gravitational shrinkage and that do to the decay of unstable radioactive isotopes. The radiogenic decay of the unstable isotopes of Uranium (^{238}U, ^{235}U), Thorium (^{232}Th) and Potassium (^{40}K) deliver the largest content of the internal source of heat. These radionuclides are enriched in the Earth’s crust and mantle [21], [22]. RHP studies have been widely applied in sedimentary, metamorphic, and igneous terrains.

Here we consider the heat production in rock sample due to the decay of the radioactive isotopes of U, Th, and K. It is defined as the quantity of heat produced by radioactivity in unit volume of the rock per unit time and is expressed in μWm^{-3}. The quantity of the produced heat can be evaluated from the relations [20], [23], [24],

$$1 \text{ ppm U} = 12.35 \text{ Bq kg}^{-1} \text{ of } ^{238}\text{U} \quad (4.12)$$

$$1 \text{ ppm Th} = 4.06 \text{ Bq kg}^{-1} \text{ of } ^{232}\text{Th} \quad (4.13)$$

$$1\% \text{ K} = 313 \text{ Bq kg}^{-1} \text{ of } ^{40}\text{K} \quad (4.14)$$

$$\text{RHP } (\mu\text{Wm}^{-3}) = \rho\,(9.52\, C_U + 2.56\, C_{Th} + 3.48\, C_K)\, 10^{-2} \quad (4.15)$$

where ρ is the dry density of rock (kgm^{-3}) and C_U, C_{Th} are the concentrations of U and Th in ppm and C_K that of K in % respectively. The constants 9.52, 2.56 and 3.48 are the radiogenic heat generation rate per unit mass of respectively [20]. The significance of the equation (4.18) is that it enables the estimates of the magnitudes of energy emitted during the decay of the radionuclides of the radioactive elements [10]. The decay process produces Alpha, Beta and gamma radiation. A physical check on the equation shows variation in RHP contributions among the three main radio active elements of U, Th, and K. The various constants of 0.0952 (Uranium), 0.0256 (Thorium), and 0.0348 (Potassium) shows the dominance of Uranium radio elements in terms of RHP contribution, followed by Th, and lastly K radioelement which provides the least contribution. The amount of RHP generated over a given geographical location depends on the quantity of U, Th, and K contents of the underlying lithology [1,32]. However, the concentrations of these radioelements varies significantly according to rock type, composition, and its formation mechanism [1]. This implies that the rock density, rock type and the radio-element's composition influence the amount of RHP to be generated. Rock formation processes such as sedimentation, metamorphism, and magmatic differentiation controls the amount of radio-active minerals to be found in a rock, and consequently the amount of RHP to be generated [12], [25]. Granitic rocks tend to record high RHP values due to the high concentration of U, Th, and K formed during the late stage of magmatic differentiation.

4.2.2 Heat Flow

The amount of heat that flows per second across a square meter of surface was H_f calculated using Equation (4.17) as introduced by Turcotte & Schubert and later used for river sediment samples by Asere and colleagues [26], [27]as;

$$H_f\ (mWm^{-2}) = \frac{RHP}{S}\ (Mm + Cr) \qquad (4.16)$$

where RHP is the heat production due to radioactive decay in the rock, Mm + Cr is the mass of mantle plus crust, given as 4×10^{24} kg and S is the total surface area of the earth, given as 5.1×10^{14} m^2.

Based on geochemical studies, the core can't contain a significant fraction of the heat-producing elements. Hence, the mass of the mantle is used instead of the Earth. According to Turcotte & Schubert, the mean H_f for all continents is 65±1.6 mWm^{-2} with 37 mWm^{-2} as the fraction attributed to the decay of ^{238}Ra, ^{232}Th and ^{40}K. The remaining 28 mW m^{-2} was attributed to basal heating of the continental lithosphere by mantle convection. Determination of heat flow by Fourier's law is beyond the scope of this work which requires further studies. The negative sign is needed to account for the direction of the heat flow; if temperature increases in the downward direction of the z-axis, the flow of heat from high to low temperature is upward.

4.3 Gamma-ray Attenuation

A gamma-ray may interact in any of the three main ways mentioned earlier when it travels through matter (though for pair production, it must have an energy higher than 1.022 MeV). Figure 1.8 (from Chapter 1) shows the importance of the three interactions (photoelectric, Compton, and pair production) as the energy of the gamma-ray and Z of the target material change.

It is observed that the interaction of the photoelectric effect is predominant for gamma rays of low energy. For intermediate energies, the interaction of the Compton effect predominates, and for high energies pair production is the dominant interaction. Similarly, the atomic number Z of the absorber material can also decide which interaction is going to be dominant at given energies. Taking a photon of 10 MeV for example, if it is travelling through carbon (Z = 6) the main mechanism of interaction will be the Compton effect. Whereas if the same photon was travelling through iodine (Z = 53) it will interact mostly through pair production.

4.3.1 Bethe formula (or **Bethe-Bloch formula**):

Describes the energy loss of charged particles as they travel through matter. It is particularly important for understanding the interactions between high-energy charged particles (such as protons, electrons, or ions) and the atomic electrons of a material. The formula is fundamental in the study of particle physics, radiation protection, and cosmic ray interactions.

$$\frac{dE}{dx} = \frac{-4\pi NAZ^2e^4}{m_e v^2} \ln\left(\frac{m_e v^2}{I}\right) \qquad (4.17)$$

where, $\frac{dE}{dx}$ is the rate of energy loss of the particle per unit distance (MeV/cm or GeV/m), N is the number of atoms per unit volume, A is the atomic mass of the material, Z is the atomic number, e is the charge of the electron, m_e is the electron mass, v is the velocity of the incoming particle, and I is the mean excitation potential of the material (in eV). When a charged particle, like an electron or proton, passes through matter, it loses energy mainly through interactions with the electrons of the atoms in the material. This energy loss occurs primarily by two processes: ionization- the charged particle ionizes atoms, knocking electrons out of their orbitals and by excitation: the charged particle excites atoms to higher energy states without ionizing them. The Bethe formula describes the rate of energy loss per unit length due to these processes as a function of the particle's velocity and the material's properties. The rate at which a charged particle loses energy depends on the nature material through which it is passes and the particle's velocity. The energy loss decreases as the particle's velocity increases. The logarithmic term describes how the energy loss changes as the particle's velocity increases. It reflects the behaviour of the ionization process. The energy loss is proportional to the square of the atomic number Z of the material. This means that heavier atoms (i.e., higher Z) cause more energy loss per unit length compared to lighter atoms. This is why high-Z materials like lead are particularly effective in shielding against high-energy particles. The energy loss is inversely proportional to the square of the particle's velocity v. This implies that faster particles (those with higher energy) lose less

energy per unit distance because they interact less frequently with the material's electrons.

Mean excitation potential is the average energy needed to excite an electron in the material. It varies with the material and is typically in the range of 10–100 eV. A lower value of I results in higher energy loss since the logarithmic term becomes larger. The formula can be used to estimate the range of a charged particle in a given material. By integrating the stopping power over the distance, the particle travels, one can estimate the total energy loss and determine the depth at which the particle comes to rest.

4.3.2 Radiation Transport Equation

This a fundamental equation in radiation physics that describes the distribution and propagation of radiation (e.g., photons, neutrons) as it interacts with a medium. It is used in diverse applications such as nuclear reactor design, medical physics, astrophysics, and shielding calculations. This equation provides a framework for modelling how radiation is absorbed, scattered, and emitted within a given material.

The radiation transport equation can be expressed as

$$\frac{\partial \Psi(r,\hat{\Omega},E,t)}{\partial x} + \hat{\Omega}\,.\nabla\Psi = \frac{\sigma_t(E)}{4\pi}\int_{4\pi}\int_0^{\infty} \psi(\mathrm{r},\hat{\Omega},\mathrm{E}',\mathrm{t})\,\sigma_s\,(\mathrm{E},\mathrm{E}')\mathrm{dE}\,\mathrm{d}\hat{\Omega}, + \mathrm{Q}(\mathrm{r},\hat{\Omega},\mathrm{E},\mathrm{t}) \quad (4.18)$$

Here, $\Psi(r,\hat{\Omega},E,t)$ is the radiation intensity at position r in the direction $\hat{\Omega}$ for energy E and time t, $\sigma_t(E)$ is the macroscopic total cross-section**,** describing the probability per unit path length that a particle will interact with the medium (includes both absorption and scattering), $\sigma_s(\mathrm{E},\mathrm{E}')$ is the scattering cross-section and $\mathrm{Q}(\mathrm{r},\hat{\Omega},\mathrm{E},\mathrm{t})$ is the source term**,** representing the rate of production of particles (e.g., from a radiation source or nuclear reaction).

4.3.3 Linear Attenuation Coefficient (LAC)

The total probability of interaction, also known as the linear attenuation coefficient μ, is equal to the sum of the probabilities, or cross sections, for each interaction. The

approach followed for calculating the gamma-ray shielding parameters is based on a specific theoretical framework. It relies on two fundamental coefficients: The linear attenuation coefficient, is a measure of the likelihood of radiation interacting with matter over a particular distance or path length (cm^{-1}) is equal to the sum of the probabilities, or cross sections, for each interaction.

$$\mu = \tau + \sigma + \kappa \qquad (4.19)$$

where τ, σ and κ are the cross sections for the photoelectric effect, the Compton effect, and pair production respectively. The use of the linear attenuation coefficient is constrained by the fact that it varies with the density of the absorber.

$$\mu = \frac{1}{x}\ln\left(\frac{I_0}{I}\right) \qquad (4.20)$$

where, I_0 and I are the incident and transmitted intensities of gamma-rays respectively and x is the thickness of the composites(cm).

4.3.4 The Mass Attenuation Coefficient (MAC)

A more favourable parameter is the mass attenuation coefficient (μm), which normalizes the linear attenuation coefficient by the density of the absorber material. The mass attenuation coefficient μ_m (MAC) was obtained by dividing the linear attenuation coefficient μ by the density ρ (g/cm^3) of the composite as given in Equation 4.21 [28].

$$MAC = \mu/\rho \qquad (4.21)$$

The mixture rule is employed to determine the total mass attenuation coefficient (MAC) value for compounds and mixtures that consist of multiple elements [29]

$$(\mu_m)_{composite} = \sum_i w_i\,(\mu_m)_i \qquad (4.22)$$

where, w_i is the weight fraction of each element in composites, $(\mu_m)_i$ is the mass attenuation coefficient for individual element in composites.

4.3.5 Half-Value Layer (HVL) and Tenth-Value Layer (TVL)

The half-value layer (HVL) is a metric that quantifies the thickness of a

homogeneous absorbing substance capable of reducing a narrow beam intensity to half of its initial value. Similarly, the tenth-value layer (TVL) pertains to the thickness of the shielding material at which the intensity of incoming radiation decreases to one-tenth of its original value. These quantities can be computed using the formulas [30], [31] given in equations (4.24) and (4.25)

$$HVL = \frac{0.693}{\mu} \qquad (4.23)$$

$$TVL = \frac{2.303}{\mu} \qquad (4.24)$$

4.3.6 Mean Free Path (MFP)

The mean free Path (λ), also referred to as the relaxation length, represents the average distance between two consecutive interactions of photons with matter. It is denoted by the following expression [32],

$$MFP = \frac{1}{\mu} \qquad (4.25)$$

4.3.7 Effective Atomic Number (Z_{eff}) Effective Electron Density (N_{eff})

To determine these parameters, knowledge of the values of atomic cross section (ACS, σ_{at}) and electron cross section (ECS, σ_{ec}) are necessary. ACS represents the likelihood of interaction between radiation and an individual atom within the unit volume of a composite material. The total atomic cross-section (σ_{at}) can be determined using the mass attenuation coefficient value, using the following relation [30],

$$ACS = \frac{(\mu_m)_{composite}}{N_A \sum w_i A_i} \qquad (4.26)$$

in which, N_A represents the Avogadro's number and A_i is the atomic weight of the i^{th} constituent element of the composite. The Electron Cross Section (ECS) represents the likelihood of interaction per electron within a unit volume of the composite material, and it can be estimated using equation (4.27)[32].

$$ECS = \frac{1}{N_A} \sum_i^n \frac{f_i A_i}{Z_i} (\mu_m)_i \qquad (4.27)$$

Here, f_i represents the number of atoms of element i relative to the total number of atoms of all elements in the composite and while Z_i stands for the atomic number of the i^{th} element in the composites [33].

The total atomic cross-section and total electronic cross-section are associated with the effective atomic number (Z_{eff}) of the composite, through formula [31], [34],

$$Z_{eff} = \frac{ACS}{ECS} \qquad (4.28)$$

The effective electron density (N_{eff}) indicates the quantity of electrons per unit mass of the material [35]. Its relationship with the effective atomic number (Z_{eff}) is formulated as follows [30], [31], [36],

$$N_{eff} = N_A Z_{eff} \qquad (4.29)$$

4.3.8 Effective Conductivity (C_{eff})

Effective conductivity (C_{eff}), which quantifies the number of unbound electrons within the material's unit volume that interact with gamma-ray energy. C_{eff} exhibits a direct correlation with the material's density, the effective electron density (N_{eff}), and the temperature prevailing in the environment where the interaction takes place. This relationship is given by Equation (4.30)

$$C_{eff} = \left(\frac{N_{eff}\, e^2 \tau}{m_e}\right) 10^3 \qquad (4.30)$$

where e (in C) and m_e (in kg) are quantities representing the charge of the electron and the mass of the electron. τ (s) gives the relaxation time of the electron on the Fermi surface and can be calculated by the equation (4.30).

4.3.9 The Exposure Build-Up Factor

The Lambert-Beer law does not account for beam divergence and the multiple scattering of gamma rays (which are due to the large thickness of the interacting medium). For the law to be valid, certain conditions need to be met:

i. The gamma rays need to be monoenergetic.
ii. The interacting medium must be thin.

iii. The gamma rays need to be collimated into a narrow beam (narrow beam geometry).

In place of meeting these difficult conditions, a simple multiplicative correction has been introduced, and the law is modified to:

$$(t)=BI_0\, e^{-\mu t} \qquad (4.31)$$

where B is the correction factor and It is known as the build-up factor. B is always greater than or equal to unity, depending on the type of gamma-ray detector used and the specific geometry of the experiment (B =1 when the three conditions above are met).

The exposure build-up factor is an important parameter for radiation shielding and measurement. It is defined as the ratio of a quantity at a point due to the total number of particles to that same quantity at that same point due to uncollided particles only.

To calculate the build-up factors, accounting for multiple scattering, the Geometric Progression (G-P) fitting method was employed, as follows [35], [37], [38]:

Calculation of the G-P fitting coefficients (a, b, c, d and X_k)

$$P = \frac{P_1(\log Z_2 - \log Z_{eq}) + P_2\,(\log Z_{eq} - \log Z_1)}{(\log Z_2 - \log Z_1)} \qquad (4.32)$$

where P_1 and P_2 denotes the G-P fitting coefficients corresponding to the Z_1 and Z_2, respectively.

First, the equivalent atomic number (Z_{eq}) calculated using the relation[39]

$$Z_{eq} = \frac{Z_1(\log R_2 - \log R) + Z_2\,(\log R - \log R_1)}{(\log R_2 - \log R_1)} \qquad (4.33)$$

where R is the ratio of Compton partial cross section to total cross section, Z_1 and Z_2 are the atomic numbers of the elements corresponding to the ratios R_1 and R_2, respectively [34], [40].

Exposure build-up factor (EBF) is given by

$$\mathrm{EBF}\,(\mathrm{E},\mathrm{X}) = \begin{cases} 1 + \frac{(\mathrm{b}-1)(\mathrm{K}^{\mathrm{X}}-1)}{\mathrm{K}-1}, & \text{for } \mathrm{K} \neq 1 \\ 1 + (\mathrm{b}-1)\,\mathrm{X}, & \text{for } \mathrm{K} = 1 \end{cases} \qquad (4.34)$$

In this equation, B is the value of the build-up factor at 1 MFP and the K (E, X) can be calculated for the different penetration depths (X) using the following equation [31], [34], [41], [42]:

$$\mathrm{K}\,(\mathrm{E},\mathrm{X}) = \mathrm{cX}^{\mathrm{a}} + \mathrm{d}\,\frac{\tanh\left((\mathrm{X}/\mathrm{X}_{\mathrm{K}})-2\right)-\tanh\,(-2)}{1-\tanh\,(-2)} \text{ for } \quad \mathrm{X} \leq 40 \text{ mfp} \qquad (4.35)$$

Where, E is incident photon energy and x is the mfp.

4.3.10 Fast Neutron Removal Cross Section (FNRCS)

A neutron is also an uncharged particle and one of the most dangerous radiation types, and thus, it is more difficult to shield in comparison with the other radiation types. This may be due to the differences of its interaction with matter. The main interaction processes of neutron with a matter may be via (n,p) reaction and hydrogenous materials are generally preferred to shield neutron. The neutron attenuation properties are expressed as effective removal cross-section (Σ_R, cm^{-1}). The fast (or fission energy) neutron attenuation is called the fast neutron effective removal cross section (FNRCS) plays an important role to express for neutron shielding properties. As it serves well for situations when there is not sufficient hydrogen in the material, it is worth calculating the removal cross sections of different materials. The removal cross section is defined as the probability of a first collision which removes that neutron from its uncollided fast group.

In essence, Σ_R serves as a measure of the probability of fast neutron removal during its traversal through the material [43], [44]. The FNRC is remains consistent within the energy range of 2 to 12 MeV [45]–[47]. It signifies the likelihood that a fast or fission energy neutron, in its initial collision, will be separated from the group of non-collided, penetrating neutrons [44]. It was computed with equation.

$$(\Sigma_R)_g = \rho \sum w_i \left(\frac{\Sigma R}{\rho}\right)_i \qquad (4.36)$$

where, ρ, w_i, and $\left(\frac{\Sigma R}{\rho}\right)_i$ is the density of material, weight fraction, and mass removal cross section of the i^{th} element in the compound. Σ_R of the samples in this study were calculated using equation 4.36 [45]. Generally, Σ_R/ρ is a function of atomic number according to the equations [45],

$$\frac{\Sigma R}{\rho} = 0.19Z^{-0.743} \text{ For } Z \leq 8 \qquad (4.37)$$

and

$$\frac{\Sigma R}{\rho} = 0.125Z^{-0.565} \text{ For } Z > 8 \qquad (4.38)$$

Mean free path (MFP), half-value layer (HVL) and tenth value layer (TVL) for fast neutron can be derived in a similar way as for photons.

4.4 Shielding Design Principles

Designing an effective radiation shielding system involves optimizing material selection, thickness, radiation type, energy range, and shield geometry to ensure safety.

1. **Material Selection**: High-Z, high-density materials like lead, tungsten, and concrete are effective for gamma and X-rays due to their higher interaction cross-sections. Neutron shielding uses low-Z, hydrogen-rich materials like polyethylene, while alpha and beta particles are blocked by lightweight materials like plastic or aluminum.
2. **Radiation Type and Energy**: Shielding is tailored to radiation type and energy. High-energy photons need denser or thicker shields, while low-energy radiation requires lighter materials.
3. **Shield Thickness**: Thickness is determined by attenuation needs and radiation energy. Calculations consider intensity reduction factors, source strength, and safety margins.
4. **Layered Shields**: Combining different materials enhances shielding efficiency, e.g., lead for gamma rays and polyethylene for neutrons, thereby optimizing the attenuation.

5. **Shield Geometry**: Proper shape and placement ensure full coverage of radiation paths. Design must address directionality, avoid gaps, and minimize material usage.
6. **Practical Considerations**: Cost, structural integrity, and radiation-induced damage influence material choice. Long-term stability under varying conditions is crucial.

In conclusion, radiation shielding design balances material properties, thickness, and practicality to ensure safety, optimize costs, and meet application-specific requirements.

4.5 Reference

[1] S. Suresh, D. R. Rangaswamy, J. Sannappa, S. Dongre, E. Srinivasa, and S. Rajesh, "Estimation of natural radioactivity and assessment of radiation hazard indices in soil samples of Uttara Kannada district, Karnataka, India," *J. Radioanal. Nucl. Chem.*, vol. 331, no. 4, pp. 1869–1879, 2022, doi: 10.1007/s10967-021-08145-5.

[2] M. Imani *et al.*, "Natural radioactivity and radiological risks of common building materials used in Semnan Province dwellings, Iran," *Environ. Sci. Pollut. Res.*, vol. 28, no. 30, pp. 41492–41503, 2021, doi: 10.1007/s11356-021-13469-6.

[3] V. S. A. Chandrasekaran and S. M. A. Tamilarasi, "Assessment of natural radiation hazards and function of heat production rate in lake sediments of Puliyanthangal Lake surrounding the Ranipet industrial area , Tamil Nadu," *J. Radioanal. Nucl. Chem.*, vol. 331, no. 3, pp. 1495–1505, 2022, doi: 10.1007/s10967-022-08207-2.

[4] UNSCEAR, *Sources and Effects of Ionizing Radiation, United Nations Scientific Committee on the Effects of Atomic Radiation UNSCEAR 2000 Report to the General Assembly, with Scientific Annexes*, vol. I. 2000.

[5] M. S. Hamideen, "Correlations study between environmental radioactivity concentrations and some health risk indicators of soil samples in Amman city , Jordan," *Int. J. Environ. Anal. Chem.*, vol. 00, no. 00, pp. 1–11, 2020, doi: 10.1080/03067319.2020.1722812.

[6] R. Ravisankar *et al.*, "Multivariate statistical analysis of radiological data of building materials used in tiruvannamalai, tamilnadu, india," *Appl. Radiat. Isot.*, vol. 85, pp. 114–127, 2014, doi: 10.1016/j.apradiso.2013.12.005.

[7] M. Tufail, Nasim-Akhtar, Sabiha-Javied, and T. Hamid, "Natural radioactivity hazards of building bricks fabricated from saline soil of two districts of Pakistan," *J. Radiol. Prot.*, vol. 27, no. 4, pp. 481–492, 2007, doi: 10.1088/0952-4746/27/4/009.

[8] D. R. Rangaswamy, M. C. Srilatha, C. Ningappa, E. Srinivasa, and J. Sannappa, "Measurement of natural radioactivity and radiation hazards assessment in rock samples of Ramanagara and Tumkur districts, Karnataka, India," *Environ. Earth Sci.*, vol. 75, no. 5, pp. 1–11, 2016, doi: 10.1007/s12665-015-5195-8.

[9] E. Srinivasa, D. R. Rangaswamy, and J. Sannappa, "Assessment of radiological hazards and effective dose from natural radioactivity in rock samples of Hassan district, Karnataka, India," *Environ. Earth Sci.*, vol. 78, no. 14, Jul. 2019, doi: 10.1007/s12665-019-8465-z.

[10] EC, "Radiation Protection 112: Radiological protection principles concerning the natural radioactivity of building materials," *Eur. Comm.*, pp. 1–16, 1999, [Online]. Available: https://ec.europa.eu/energy/sites/ener/files/documents/112.pdf.

[11] ICRP, "Recommendations of the International Commission on Radiological Protection.," 1991.

[12] M. A. Adabanija, O. N. Anie, and M. A. Oladunjoye, "Radioactivity and gamma-ray spectrometry of basement rocks in Okene area, southwestern Nigeria," *NRIAG J. Astron. Geophys.*, vol. 9, no. 1, pp. 71–84, 202.

doi: 10.1080/20909977.2020.1711695.

[13] Y. Raghu, R. Ravisankar, A. Chandrasekaran, P. Vijayagopal, and B. Venkatraman, "Assessment of natural radioactivity and radiological hazards in building materials used in the Tiruvannamalai District, Tamilnadu, India, using a statistical approach," *J. Taibah Univ. Sci.*, vol. 11, no. 4, pp. 523–533, 2017. doi: 10.1016/j.jtusci.2015.08.004.

[14] Y. Raghu, R. Ravisankar, A. Chandrasekaran, P. Vijayagopal, and B. Venkatraman, "Assessment of natural radioactivity and radiological hazards in brick samples used in Tiruvannamalali District, Tamilnadu, India, with a statistical approach," *Health Phys.*, vol. 111, no. 3, pp. 265–280, 2016, doi: 10.1097/HP.0000000000000530.

[15] V. Ramasamy *et al.*, "Natural radioactivity measurements in beach-rock samples of south-east coast of Tamilnadu, India," *Radiat. Prot. Dosimetry*, vol. 111, no. 2, pp. 229–235, 2004, doi: 10.1093/rpd/nch328.

[16] G. Saxebøl, H. M. Olerud, O. Hjardemaal, W. Leitz, A. Servomaa, and T. Walderhaug, *Nordic guidance levels for patient doses in diagnostic radiology*, vol. 80, no. 1–3. 1998.

[17] S. Righi and L. Bruzzi, "Natural radioactivity and radon exhalation in building materials used in Italian dwellings," vol. 88, pp. 158–170, 2006, doi: 10.1016/j.jenvrad.2006.01.009.

[18] M. Elsadek M. Sabra, A. L. Abdeldayem, M. A. S. Youssef, A. A. Masoud, and S. A. Mansour, "Determination of the radiation dose rate and radiogenic heat production of North Gabal Abu Hibban area, central Eastern Desert, Egypt," *NRIAG J. Astron. Geophys.*, vol. 8, no. 1, pp. 103–111, 2019. doi: 10.1080/20909977.2019.1617556.

[19] C. E. Pereira, V. K. Vaidyan, A. Sunil, S. Ben Byju, R. Maria, and P. J. Jojo, "Radiological assessment of cement and clay based building materials from southern coastal region of Kerala," vol. 49, no. June, pp. 372–376, 2011.

[20] Rybach, "Author Index," *Am. J. Occup. Ther.*, vol. 52, no. 10, pp. 932–935, 1998, doi: 10.5014/ajot.52.10.932.

[21] M. A. Shaheen, "Distribution of Radioactive Elements and Their Relation to the Radiogenic Heat Production at Jabal Kharazah Area, North Eastern Desert, Egypt," *J. Geosci. Environ. Prot.*, vol. 08, no. 04, pp. 155–168, 2020. doi: 10.4236/gep.2020.84011.

[22] C. Jaupart, S. Labrosse, F. Lucazeau, and J. C. Mareschal, "Temperatures, Heat, and Energy in the Mantle of the Earth," *Treatise Geophys. Second Ed.*, vol. 7, pp. 223–270, 2015, doi: 10.1016/B978-0-444-53802-4.00126-3.

[23] N. Maden and E. Akaryali, "A review for genesis of continental arc magmas: U, Th, K and radiogenic heat production data from the Gümüşhane Pluton in the Eastern Pontides (NE Türkiye)," *Tectonophysics*, vol. 664, pp. 225–243, 2015, doi: 10.1016/j.tecto.2015.09.023.

[24] T. Farag, N. Soliman, A. El Shayat, and H. Mizunaga, "Comparison among the natural radioactivity levels, the radiogenic heat production, and the land surface

temperature in arid environments: A case study of the El Gilf El Kiber area, Egypt," *J. African Earth Sci.*, vol. 172, p. 103959, 2020. doi: 10.1016/j.jafrearsci.2020.103959.

[25] L. Scharfenberg, A. Regelous, and H. De Wall, "Radiogenic heat production of variscan granites from the Western Bohemian Massif, Germany," *J. Geosci. (Czech Republic)*, vol. 64, no. 4, pp. 251–269, 2019, doi: 10.3190/jgeosci.293.

[26] S. O. Asere, and Sedara, "Determination of Natural Radioactivity Concentration and Radiogenic Heat Production in Selected Quarry Sites in Ondo State, Nigeria," *NIPES J. Sci. Technol. Res.*, vol. 2, no. 3, p. 256, Aug. 2020. doi: 10.37933/nipes/2.3.2020.26.

[27] Turcotte D. L. & Schubert G., *T URCOTTE , D. L. & S CHUBERT , G. 2002. Geodynamics , 2nd ed. xv + 456 pp. Cambridge, New York, Melbourne: Cambridge University ISBN 0 521 66186 2; 0 521 66624 4 (pb).*, vol. 139, no. 6. 2002.

[28] C. V. Vishnu, A. Joseph, and K. Anju, "Evaluation of the gamma radiation shielding characteristics of epoxy wall paint modified with micro sized Bi_2O_3 and WO_3," *Mater. Today Proc.*, no. xxxx, 2023, doi: 10.1016/j.matpr.2023.03.309.

[29] F. Özpolat, B. Alım, E. Şakar, M. Büyükyıldız, and M. Kurudirek, "Phy-X/ZeXTRa: a software for robust calculation of effective atomic numbers for photon, electron, proton, alpha particle, and carbon ion interactions," *Radiat. Environ. Biophys.*, vol. 59, no. 2, pp. 321–329, 2020, doi: 10.1007/s00411-019-00829-7.

[30] C. V. More, Z. Alsayed, M. S. Badawi, A. A. Thabet, and P. P. Pawar, *Polymeric composite materials for radiation shielding: a review*, vol. 19, no. 3. Springer International Publishing, 2021.

[31] M. Büyükyıldız, M. A. Taşdelen, Y. Karabul, M. Çağlar, O. İçelli, and E. Boydaş, "Measurement of photon interaction parameters of high-performance polymers and their composites," *Radiat. Eff. Defects Solids*, vol. 173, no. 5–6, pp. 474–488, 2018, doi: 10.1080/10420150.2018.1477155.

[32] O. Kilicoglu *et al.*, "Micro Pb filled polymer composites: Theoretical, experimental and simulation results for γ-ray shielding performance," *Radiat. Phys. Chem.*, vol. 194, no. February, 2022, doi: 10.1016/j.radphyschem.2022.110039.

[33] S. Intom *et al.*, "Mechanical and radiation shielding properties of flexible material based on natural rubber/ Bi_2O_3 composites," *Radiat. Phys. Chem.*, p. 108772, 2020, doi: 10.1016/j.radphyschem.2020.108772.

[34] E. Şakar, Ö. F. Özpolat, B. Alım, M. I. Sayyed, and M. Kurudirek, "Phy-X / PSD: Development of a user friendly online software for calculation of parameters relevant to radiation shielding and dosimetry," *Radiat. Phys. Chem.*, vol. 166, no. September 2019, 2020, doi: 10.1016/j.radphyschem.2019.108496.

[35] Ş. Erdem, "Determination of photon-shielding features and build-up factors of nickel – silver alloys," vol. 172, no. February, 2020. doi: 10.1016/j.radphyschem.2020.108778.

[36] M. Büyükyıldız, A. D. Kılıç, and D. Yılmaz, "White and some colored marbles as alternative radiation shielding materials for applications," *Radiat. Eff. Defects Solids*,

vol. 175, no. 7–8, pp. 657–671, 2020, doi: 10.1080/10420150.2020.1737695.

[37] M. I. Sayyed, "Half value layer, mean free path and exposure buildup factor for tellurite glasses with different oxide compositions," *J. Alloys Compd.*, vol. 695, pp. 3191–3197, Feb. 2017, doi: 10.1016/j.jallcom.2016.11.318.

[38] M. R. Ambika *et al.*, "Preparation and characterisation of Isophthalic-Bi_2O_3 polymer composite gamma radiation shields," *Radiat. Phys. Chem.*, vol. 130, no. March 2016, pp. 351–358, 2017, doi: 10.1016/j.radphyschem.2016.09.022.

[39] S. Prabhu, S. G. Bubbly, and S. B. Gudennavar, "Synthetic polymer hydrogels as potential tissue phantoms in radiation therapy and dosimetry," *Biomed. Phys. Eng. Express*, vol. 6, no. 5, 2020, doi: 10.1088/2057-1976/aba209.

[40] M. Kamislioglu, "An investigation into gamma radiation shielding parameters of the (Al:Si) and (Al+Na):Si-doped international simple glasses (ISG) used in nuclear waste management, deploying Phy-X/PSD and SRIM software," *J. Mater. Sci. Mater. Electron.*, vol. 32, no. 9, pp. 12690–12704, 2021, doi: 10.1007/s10854-021-05904-8.

[41] P. Limarun, T. Markpin, N. Sombatsompop, E. Wimolmala, and K. Saenboonruang, "Cellular Bi_2O_3/natural rubber composites for light-weight and lead-free gamma-shielding materials and their properties under gamma irradiation," *J. Cell. Plast.*, vol. 58, no. 2, pp. 285–303, 2022, doi: 10.1177/0021955X21997353.

[42] M. Kurudirek, M. Aygun, and S. Z. Erzeneoğlu, "Chemical composition, effective atomic number and electron density study of trommel sieve waste (TSW), Portland cement, lime, pointing and their admixtures with TSW in different proportions," *Appl. Radiat. Isot.*, vol. 68, no. 6, pp. 1006–1011, 2010. doi: 10.1016/j.apradiso.2009.12.039.

[43] Y. Al-Hadeethi and M. I. Sayyed, "Radiation attenuation properties of Bi_2O_3–Na_2O–V_2O_5– TiO_2–TeO_2 glass system using Phy-X / PSD software," *Ceram. Int.*, vol. 46, no. 4, pp. 4795–4800, 2020, doi: 10.1016/j.ceramint.2019.10.212.

[44] M. R. Kaçal, F. Akman, and M. I. Sayyed, "Evaluation of gamma-ray and neutron attenuation properties of some polymers," *Nucl. Eng. Technol.*, vol. 51, no. 3, pp. 818–824, 2019, doi: 10.1016/j.net.2018.11.011.

[45] H. H. Hegazy *et al.*, "Nuclear shielding properties of B_2O_3–Bi_2O_3–SrO glasses modified with Nd_2O_3: Theoretical and simulation studies," *Ceram. Int.*, vol. 47, no. 2, pp. 2772–2780, 2021, doi: 10.1016/j.ceramint.2020.09.131.

[46] W. Ramadan, K. Sakr, M. Sayed, N. Maziad, and N. El-Faramawy, "Anisotropic thermal, physical and neutron attenuation studies of borated acrylamide composites," *Radiat. Phys. Chem.*, vol. 172, no. November 2019, p. 108745, 2020, doi: 10.1016/j.radphyschem.2020.108745.

[47] K. Mariselvam, "Physical, optical and radiation shielding features of Yb^{3+} ions doped H_3BO_3 - Bi_2O_3 - $BaCO_3$ - CaF_2 - ZnO glasses," *Optik (Stuttg).*, vol. 230, no. January, 2021, doi: 10.1016/j.ijleo.2021.166319.

CHAPTER 5

RESULTS AND DISCUSSION

Radiological Impact of Natural Radioactivity and Heat Production in Populated Areas of Kerala.

Content	
5.1	*Introduction*
5.2	*Thrissur- Palakkad highway zone (Kuthiran Hills, Western Ghats of Kerala).*
5.3	*Urban regions along the National Highway in Kerala, India*
5.4	*Athirappilly Waterfalls (Athirappilly Hills, part of Western Ghats in Kerala).*
5.5	*Comparison with Similar Studies*
5.6	*Chapter Conclusion*

Abstract: *In this chapter, critically evaluates the natural radioactivity, associated radiological parameters and radiogenic heat production of rock and soil sample collected from various locations in the state of Kerala, India. Gamma-ray dose and hazard parameters based on the activity concentrations of the natural radionuclides* ^{238}U, ^{232}Th, *and* ^{40}K. *Additionally, X-ray diffraction (XRD) was used to analyze the composition of the samples, providing detailed information on their atomic structure and composition.*

Sampling locations- Kuthiran tunnel, Athirappilly waterfalls and NH-66 highway Malappuram-Kozhikode and samples in the typical container bottle.

5.1 Introduction

Low-level ionizing radiation is ubiquitously present, with all living organisms being subject to exposure. Soil, as the topmost layer of Earth's crust, plays a fundamental role in maintaining natural ecosystems and the biosphere. In its natural state, it serves as a significant source of outdoor radiation exposure to the population by facilitating the release of radionuclides into the surrounding environment [1]. Soil plays a decisive role as a resource for human populations, being used for agriculture, construction, and climate regulation. It is both a continuous source of radionuclide radiation and a transporter of radioactive materials to organisms. The accumulation of the naturally occurring radionuclides at a place is affected by a number of factors, such as nature and geometry of strata, minerals containing trace amounts of radionuclides (e.g. Ilmenite, rutile, Zircon, and Monazite), and moisture, etc. [2]–[4]. ^{226}Ra, ^{232}Th, and ^{40}K are the most found radionuclides in rocks. Thorium element is 3–4 times more abundant than Uranium in crustal rocks because it is less susceptible to mobilization in the supergene environment. The amount of Thorium also varies from place to place in Monazite from placer deposits. It mainly depends upon the type of rock from which the Monazite forms. Monazite is usually seen in the high or intermediate rank of metamorphic rocks, generally formed from argillaceous sediments. Many characteristics of Monazite show that it is formed in metamorphic rock. The range of Thorium present in metamorphic rock depends upon the grade of metamorphism. ^{232}Th is a precursor of the natural mass number 4n decay series that finishes at stable ^{208}Pb.

The gamma-ray spectrometric measurements as a means for geological mapping have been reported in many locations of the world to assess the radionuclide concentrations in crustal formations [5]–[7] in geothermal fields [8], [9], along geologically altered zones [10], in volcanic areas [11], [12], and active mining sites [13]. Most of the Potassium is present in K feldspar and micas, while Uranium and Thorium are largely present in minerals such as Zircon, allanite, sphene, Monazite, apatite etc. [14]. These minerals are more abundant in granitoid rocks, which therefore, account for bulk of the heat production in the continental crust gamma-ray spectrometry is the only one technique that enables simultaneous determination of U, Th and K, and its accuracy is generally sufficient for these purposes.

Radiogenic heat generation, a petrophysical property independent of temperature and pressure, arises from the decay of naturally occurring radioactive elements in the Earth's crust. Akkurt et al. (2022) demonstrated that almost all energy released during this decay is converted into heat within the rocks [15]. In 1998, Rybach suggested that radioactive heat production is a thermal, scalar, and isotropic property of rock, reliant on its chemical composition rather than in-situ conditions [16], [17]. Consequently, the radiogenic heat released at a given depth is determined by the amount of radioactive elements present, regardless of pressure and temperature [18]. Following planetary accretion, geochemical differentiation led to an iron-rich core constituting 32% of Earth's mass, with silicate-rich mantle and crust layers above. The distribution of heat-producing elements (U, Th, K) in the Earth's interior is shaped by continental differentiation settings [19]. The radioactive heat production rate (RHP) quantifies heat released per unit volume of rock from decaying unstable radiogenic isotopes [20]–[22]. This rate is determined by the rock's lithological and geochemical characteristics, with granitic rocks playing a pivotal role in Earth's geodynamic evolution and thermal regime. Granite intrusions are crucial to continental crust formation, and understanding RHP in granite intrusions of varying ages is vital for thermal modeling of the continental lithosphere. Assuming radioactive elements are concentrated in the upper crust's granitic rocks, with an average thickness of 10-20 km [23]–[25], the mean RHP in the crust is about 71.0 mW/m^3. Granite's radioactive decay significantly contributes to continental surface heat flow, providing approximately 65 mW/m^3, with 40% attributed to crustal RHP and 60% to mantle RHP [26]. The primary source of crustal heat is radioactive decay, generating up to 98% depending on geographic location, while contributions from cosmic neutrino interaction and gravitational distortion are minimal. The presence of natural radioactive elements in the crust can significantly influence surface heat flow, contingent on regional geology. Measuring the elemental concentrations of radioactive elements is essential for modeling lithospheric thermal evaluation. Isotopes like ^{238}U, ^{232}T and ^{40}K hare major contributors to terrestrial heat flow, with their concentrations providing insights into the mantle and crust [17]. Gamma-ray spectrometry, enabling simultaneous determination of U, Th, and K, is a precise method for measuring these concentrations. Heat from radioactive decay in rocks is fundamental to understanding Earth's heat liberation and interpreting continental heat flux data. This method aids in characterizing lithological and rock

alterations [27], [28], determining Uranium migration in crustal formations [29], and estimating crustal radiogenic heat production [30]–[32]. Long-lived radioactive isotopes, particularly U, Th, and K, produce most of the crustal heat [14], with their decay continuing as Earth's primary heat source. These elements contribute to about 70% of the total surface heat flow in the continental crust, offering a comprehensive thermal account of radioelement contributions [33]–[35]. Radiogenic heat-producing rocks provide insights into lithospheric heat flux and help understand the thermal evolution of Earth and potential geothermal energy sources. Numerous studies have examined radioactive heat production in rock samples from India and elsewhere [4], [21], [36]–[44].

In the present study, gamma-ray spectroscopy was employed to estimate the concentrations of Uranium, Thorium, and Potassium in samples collected from various locations in the state of Kerala, India. The specific sites include:

- Thrissur-Palakkad highway zone (Kuthiran Hills, part of the Western Ghats in Kerala, Region I).
- Urban regions along National Highway 66 (NH-66) in Kerala (Region II)
- Athirappilly Waterfalls (Athirappilly Hills, part of the Western Ghats in Kerala, Region III).

Gamma-ray dose and hazard parameters based on the activity concentrations of the natural radionuclides ^{238}U, ^{232}Th, and ^{40}K. Additionally, X-ray diffraction (XRD) was used to analyze the composition of the samples, providing detailed information on their atomic structure and composition.

Approximately 2–3 kg of samples was collected from the fresh outcrops of intrusive bodies in each location. The collected samples were crushed into powder form, pulverized and separately sieved with a 125 μm mesh sieve. The samples were then electrically oven-dried at a temperature of 110°C for 10 hours and allowed to cool. Then samples were weighed and transferred into separate plastic containers and sealed tightly with polyvinyl chloride insulation tape and epoxy resin to prevent ^{222}Rn escape. The sealed samples were allowed to attain secular equilibrium by keeping it undisturbed for 28 days before they were taken to the laboratory for gamma spectrometric analysis.

5.2. Thrissur- Palakkad highway zone (Kuthiran Hills, Western Ghats of Kerala)- Region I.

5.2.1 Sample collection and preparation

In order to get a representative coverage of the geological formations, 60 rock samples were collected from 15 locations by covering 25 km, namely Mannuthy (MNT), Vengassery (VGY), Mudicode (MUD), Pananchery (PNY), Pattikadu (PTK), Chuvannamannu (CHM), Vazhukumpara (VKP), Kuthiran Temple (KDT), Irumbupalam Bridge (IMB), Vaniyampara (VMP), Kuthiran tunnel (KTN), Kannanbra (KNB), Poovanchira (PVC), Kurangupara (KGP) and Pattathipara (PTP). At each sampling site, a geographical positioning system (GPS) is employed to record the geographical coordinates. Rock samples from these collection sites were selected not only because of their massive occurrence/abundance and their high usage as construction aggregates.

5.2.2. Geology of the Sampling area

Western Ghats (also known as Sahyadri) is a mountain range that runs parallel to the western coast of the Indian peninsula, located in India. The range starts near the border of Gujarat and Maharashtra and runs through the states of Maharashtra, Goa, Karnataka, Kerala and Tamilnadu ending at Kanyakumari at the tip of India. Sample collecting locations (sampling station) in Thrissur district, which is coming under the western ghats, lies between North latitudes 10°32'10" and 10°35'17" and East longitudes 76°15'58" and 76°25'53". A location map is shown in Figure 5.1 and geographical location data is given in Table 5.1. It is bounded northeast by Palakkad district. The average annual rainfall of the studied area ranges between 2310.1 and 3955.3 mm, with a mean yearly rainfall of 3198.1 mm. The vegetation here is of the rain forest type, with evergreen and broad-leaved trees. The maximum temperature ranges from 29.3 to 44.2°C whereas the minimum from 22.1 to 24.9°C. High temperature and heavy rainfall lead to creation of a lateritic type of soil from these rocks of Archean metamorphic complex.

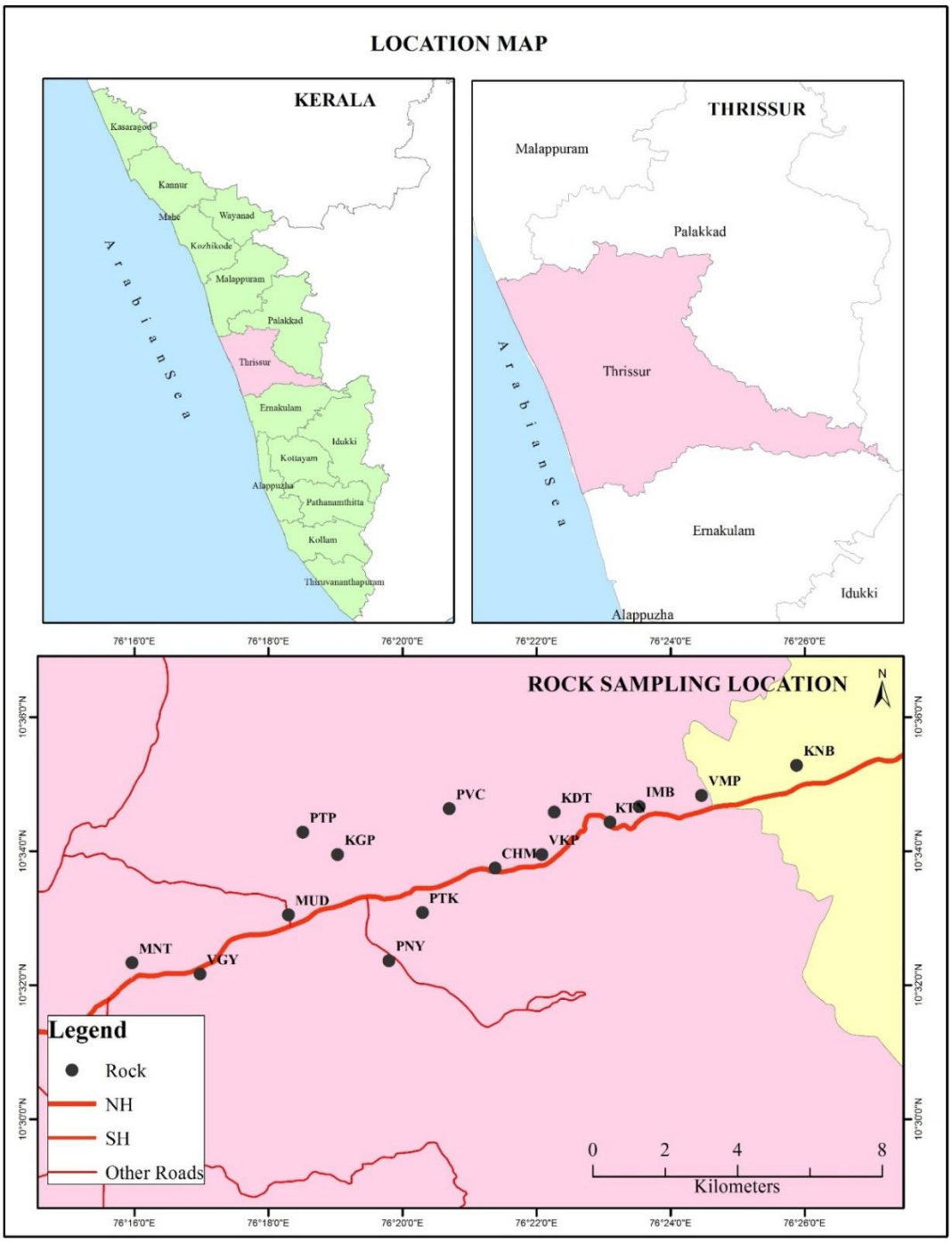

Figure 5.1: The sampling stations of Kuthiran region, Kerala.

Table 5.1: Sampling locations of Kuthiran hills in the present study.

Place Name	Place Code	North	East
Mannuthy	MNT	10°32’20”	76°15’58”
Vengassery	VGY	10°32’10”	76°16’59”
Mudicode	MUD	10°33’03”	76°18’18”
Pananchery	PNY	10°32’22”	76°19’48”
Pattikadu	PTK	10°33’05”	76°20’18”
Chuvannamannu	CHM	10°33’45”	76°21’23”
Vazhukumpara	VKP	10°33’57”	76°22’05”
Kuthiran Temple	KDT	10°34’35”	76°22’46”
Kuthiran Tunnel	KTN	10°34’26”	76°23’06”
Irumbupalam Bridge	IMB	10°34’40”	76°23’32”
Vaniyampara	VMP	10°34’50”	76°24’28’’
Kannanbra	KNB	10°35’17”	76°25’53’’
Poovanchira	PVC	10°34’38”	76°20’42”
Kurangupara	KGP	10°33’57”	76°19’02”
Pattathipara	PTP	10°34’17”	76°18’31”

Rock types in Thrissur district can be broadly divided into four categories - (i) Charnockite belt, which is widespread and most prominent in the district; (ii) Gneissic belt represented by Biotite gneiss, Hornblende-biotite gneiss, and Quartzo-feldspathic gneiss, (iii) Granitic gneiss restricted to the southeastern part and (iv) the Quaternaries of the coastal tract. The dominant rock types in the study area are

charnockites and a variant of it called Migmatitic rocks. Figure 5.2 shows the map of geological formation and rock constituents of the sampling stations.

The Charnockite rocks are composed of coarse-grained, massive fine-grained, and gneissic fine-grained varieties. These rocks are generally low-lying outcrops, with smooth rounded boulders and few low-lying hills, forming oval to subcircular and elongated bodies [45]**.** Charnockites and associated gneiss constitute the most extensive hard rock formations in Kerala, occupying more than 45 per cent of the total geographical area [46]–[49]. The available information indicates that the deposits of Monazite in the coastal areas of Kerala and Tamil Nadu are formed due to the weathering of these rocks in Western Ghats and are transported and deposited in the southern coastal areas through the drainage system including rivers, back waters etc. [48]–[51]**.**

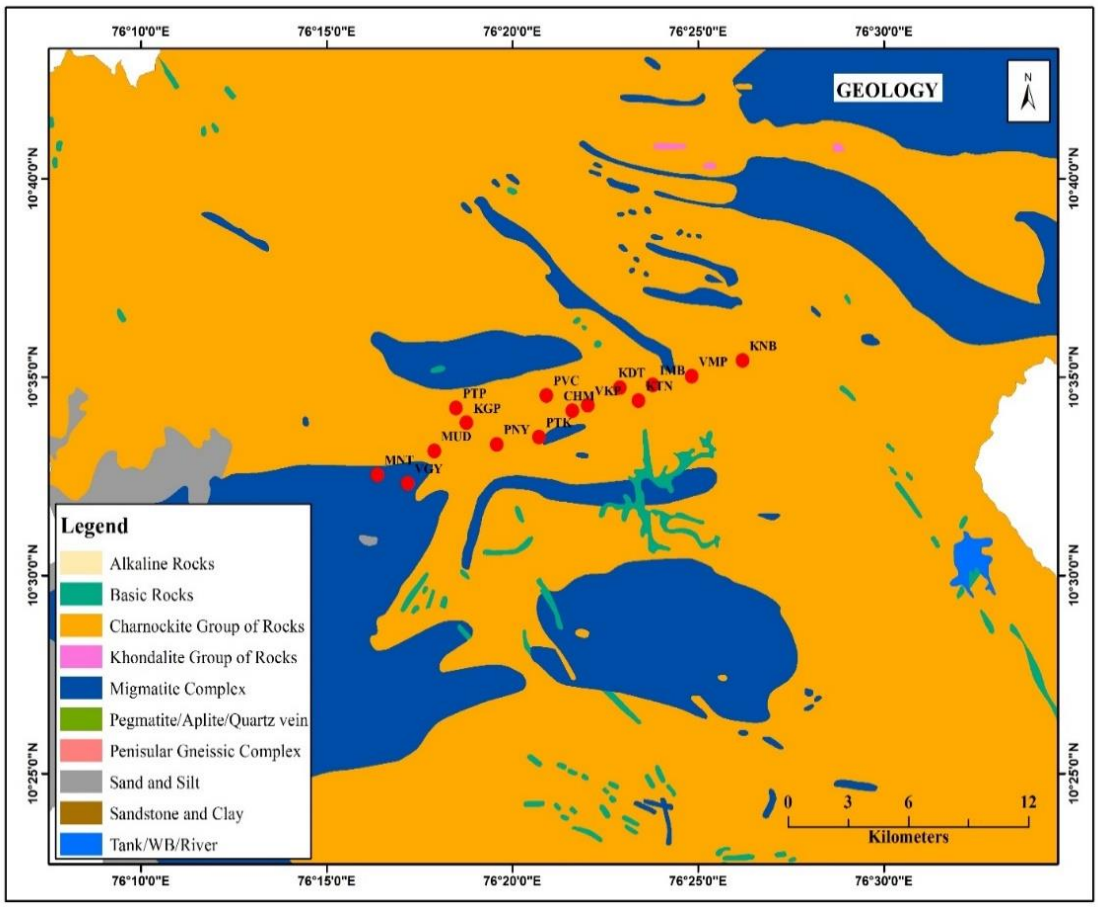

Figure 5.2: Geological formation and rock constituents of the sampling stations.

5.2.3. Activity concentrations in rock samples

Natural radioactivity concentrations of ^{226}Ra, ^{232}Th and ^{40}K estimated in the collected rock samples from the study area are given in Table 5.2. The variation of the activity concentration in the rock samples collected from different sites are due to the mineral content present in different rock types. The variation is shown in Figure 5.2. The activity concentrations of radionuclides in the rock samples ranged from 16.44 to 88.33 Bq/kg with average of 59.28 Bq/kg for ^{226}Ra, 67.42 to 174.3 Bq/kg with an average of 120.09 Bq/kg for ^{232}Th, and 739 to 1064 Bq/kg with a mean of 916.33 Bq/kg for ^{40}K.

Table 5.2 Activity concentrations of ^{226}Ra, ^{232}Th and ^{40}K in the study area.

Place Name	Place Code	Activity Concentration of rock samples		
		^{226}Ra (Bq/kg)	^{232}Th (Bq/kg)	^{40}K (Bq/kg)
Mannuthy	MNT	16.44±2.54	67.42±1.5	816±20
Vengassery	VGY	28.14±3.35	96.23±2.63	739±18
Mudicode	MUD	33.56±2.54	118.4±2.5	866±20
Pananchery	PNY	37.24±1.91	110.2±2.5	1050±24
Pattikadu	PTK	74.21±2.51	120.9±1.8	997±22
Chuvannamannu	CHM	58.28±3.64	109. 6±2.72	890±20
Vazhukumpara	VKP	52.45±2.53	72.8±1.41	980±22
Kuthiran Temple	KDT	68.81±2.61	101.2±2.62	820±16
Kuthiran Tunnel	KTN	86.29±3.53	148.4±1.19	1012±22
Irumbupalam Bridge	IMB	80.34± 3.65	81.23±2.52	940±23
Vaniyampara	VMP	58.24±3.51	127.1±2.4	860±21
Kannanbra	KNB	73.62±2.42	174.3±3.3	917±20
Poovanchira	PVC	54.13±2.51	86.2±2.4	922±23
Kurangupara	KGP	79.18±3.55	138.9±1.94	852±20
Pattathipara	PTP	88.33±4.72	168.4±2.6	1064±21
Average		59.28±2.57	120.09±3.74	916.33±20.81
Standard deviation		21.54	31.89	92.24
World average		32	45	412

Corresponding to ^{226}Ra, ^{232}Th and ^{40}K, the observed highest values of radioactivity concentrations are 88.33±0.72 Bq/kg (PTP), 174.3±1.3 Bq/kg (KNB) and 1064±24 Bq/kg (PNY) while the lowest values are 16.44±0.54 Bq/kg (MNT), 67.41±0.5 Bq/kg (MNT) and 739±18 Bq/kg (VGY), respectively. The order of average radioactivity concentrations of radionuclides recorded from these samples is as follows: $^{40}K > ^{232}Th > ^{226}Ra$. The measured average concentrations ^{226}Ra, ^{232}Th and ^{40}K are significantly higher than the worldwide average values of 32, 45 and 412 $Bqkg^{-1}$, respectively. The spatial variations in the activity concentrations of these radionuclides in the rock samples is due to the variation in the chemical composition of the geological formations. The contour distribution of radionuclides in the study is shown in Figure 5.3.

The studied locations have a variety of rock systems like hornblende-biotite gneisses, migmatite gneisses, granite gneisses and mylonites gneisses. Relatively higher activity concentrations of ^{226}Ra, ^{232}Th, and ^{40}K in rock samples were observed at Kurangupara (KGP), Pattathipara (PTP), Vaniyampara (VMP), Kannanbra (KNB), Irumbupalam (IMB) and at Kuthiran tunnel (KTN). It may be due to the fact that these regions are attributed to having gneiss, green granites, charnockite, loamy soils, layey soils and altered gray granites types of rocks having higher concentrations ^{226}Ra, ^{232}Th, and ^{40}K, respectively. The spatial distribution of the radionuclides across the rock outcrops. This reveals a dominance of ^{232}Th and ^{226}Ra due to silicates and Monazite contents in rocks.

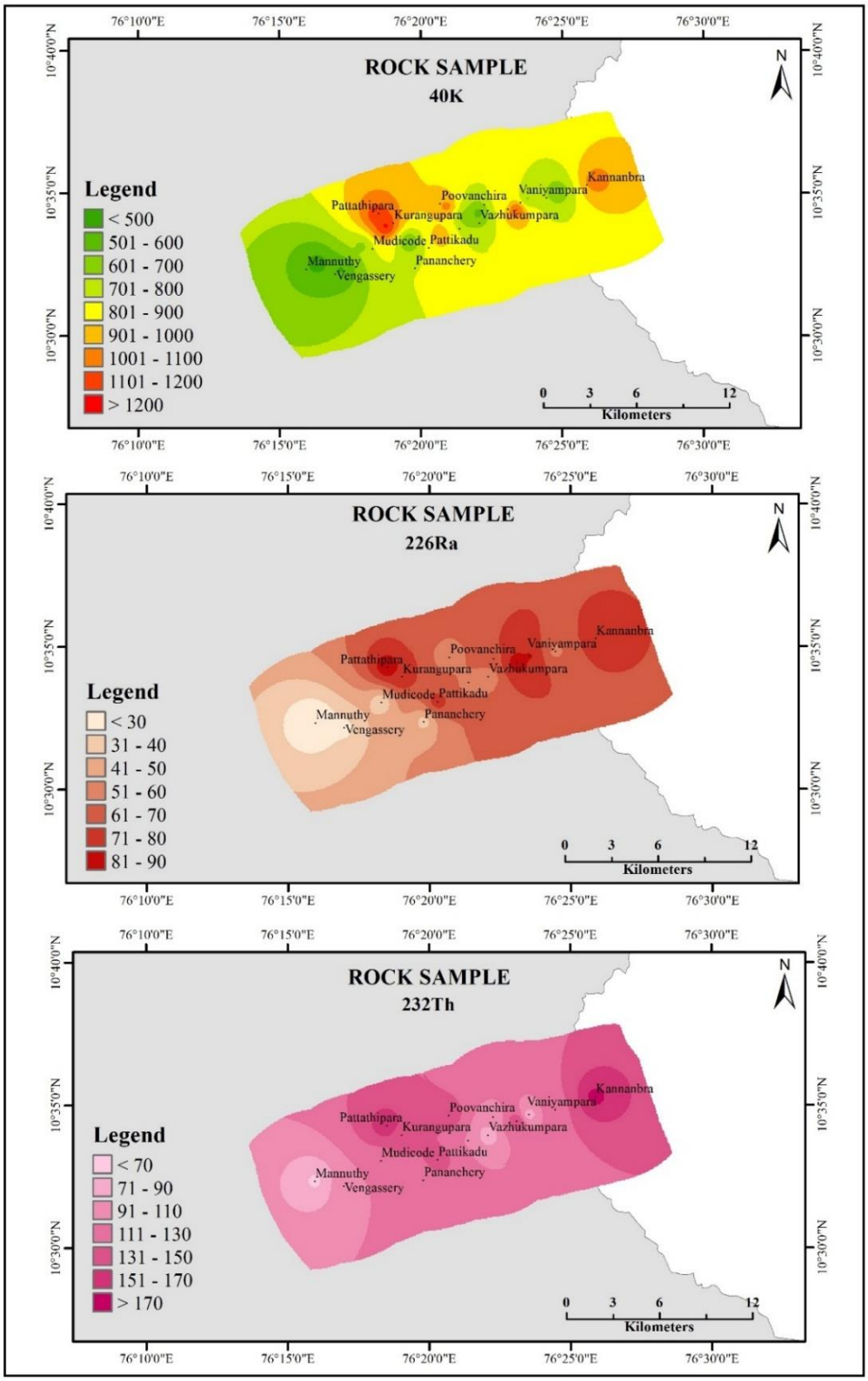

Figure 5.3: Contour distributions of radionuclides ^{226} Ra, ^{232}Th and ^{40} K in the study area.

Table 5.3 shows the basic statistical parameters such as minimum, maximum, mean, standard deviation, variance, skewness, and kurtosis, which are calculated to assess the characteristics of the radionuclides in the rock samples. Arithmetic mean and standard deviation are used to describe the variation of the data.

Table 5.3: Statistical distribution of the three isotopes in the study area.

Parameter	**^{226}Ra**	**^{232}Th**	**^{40}K**
Minimum	16.44	67.44	739
Maximum	88.33	174.30	1084
Mean	59.28	120.09	916.33
Median	58.28	120.09	917
Standard Deviation	21.54	31.89	92.24
Variance	497.13	1089.92	9115.52
Kurtosis	-0.80	-0.90	-0.51
Skewness	-0.51	-0.01	0.07

The frequency distribution of the activity concentration of ^{226}Ra, ^{232}Th and ^{40}K of rock samples is shown in Figure 5.4. The standard deviation values of ^{226}Ra, ^{232}Th and ^{40}K are found to be lower than the mean value and it indicates a high degree of uniformity among the samples. Skewness data describes the degree of asymmetry of a distribution around its mean. The skewness values of ^{226}Ra, ^{232}Th and ^{40}K from the present study are -0.51, -0.01 and 0.07, respectively. Positive skewness values indicate that the distribution of radionuclides is asymmetric, with a tail extending towards more positive values. Kurtosis is a measure of the peakedness of the probability distribution of a real-valued random variable. The kurtosis values of ^{226}Ra, ^{232}Th and ^{40}K from the present study were, -0.80, -0.90 and -0.51, respectively. The negative kurtosis values observed for all the radionuclides indicates a flat distribution.

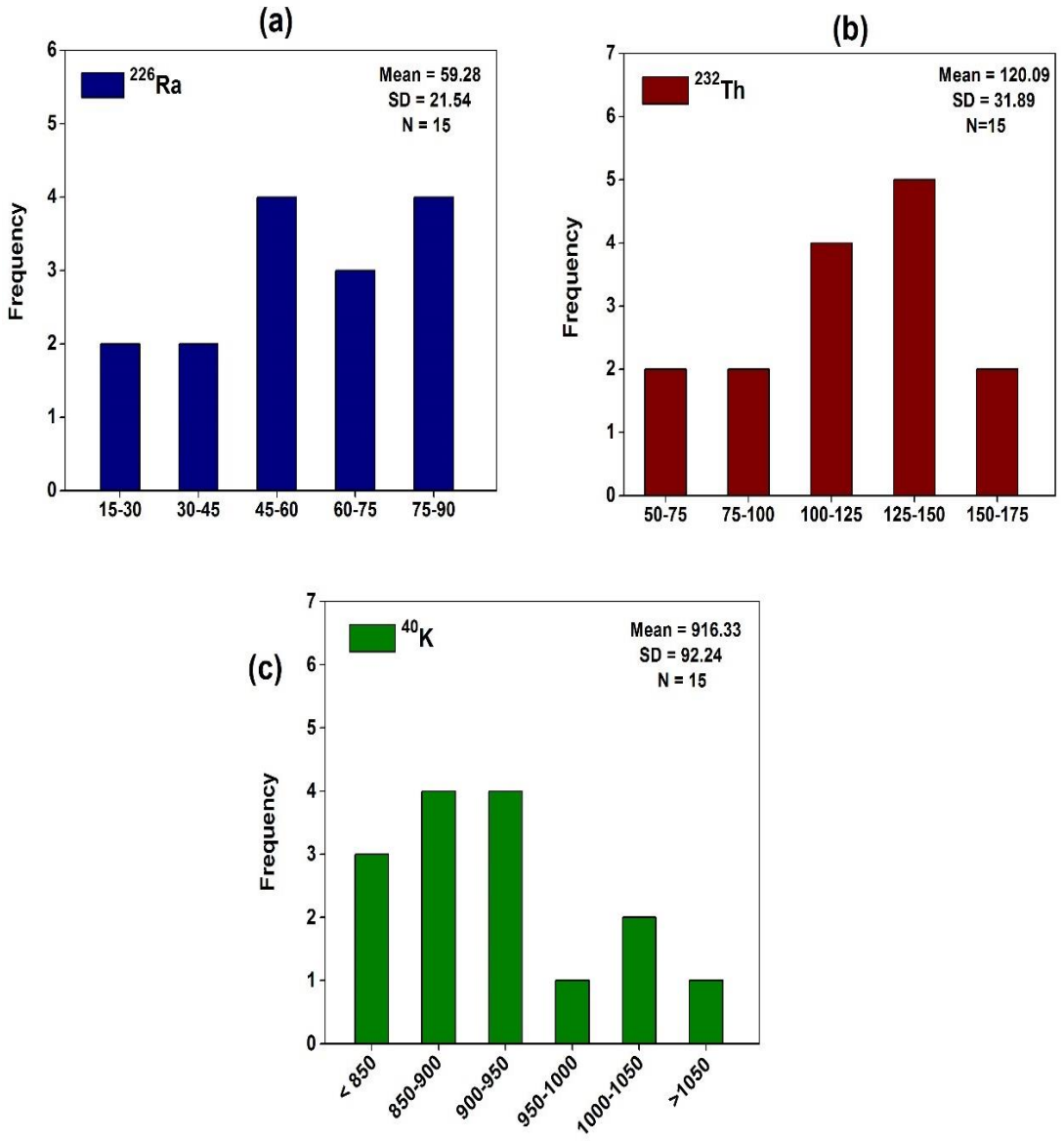

Figure 5.4: The frequency distribution of the activity concentration of ^{226}Ra, ^{232}Th and ^{40}K.

5.2.4 Radiological parameters of the rock samples

The computed radiological hazard indices related to the rock samples are summarized in Table 5.4.

Table 5.4 Radiological hazard indices related to the rock samples in the study area.

Sample Code	Ra_{eq} (Bq/kg)	D_{out} (nGy/h)	AED_{ind} (mSv/y)	AED_{out} (mSv/y)	H_{int}	H_{ext}	$ELCR_{ind}$ ($\times10^{-3}$)	$ELCR_{out}$ ($\times10^{-3}$)	I_γ	I_α
MNT	175.68	82.34	0.76	0.10	0.52	0.47	3.04	0.40	0.66	0.08
VGY	222.65	101.94	0.94	0.13	0.68	0.60	3.75	0.50	0.82	0.14
MUD	269.55	123.13	1.13	0.15	0.82	0.73	4.53	0.60	0.99	0.17
PNY	275.68	127.55	1.18	0.16	0.85	0.74	4.71	0.62	1.03	0.19
PTK	352.47	160.96	1.49	0.20	1.15	0.95	5.95	0.79	1.28	0.37
CHM	283.54	130.24	1.21	0.16	0.92	0.77	4.82	0.64	1.04	0.29
VKP	232.01	109.07	1.02	0.13	0.77	0.63	4.07	0.53	0.87	0.26
KDT	276.67	127.11	1.18	0.16	0.93	0.75	4.72	0.62	1.01	0.34
KTN	376.43	171.70	1.59	0.21	1.25	1.02	6.35	0.84	1.37	0.43
IMB	268.88	125.38	1.17	0.15	0.94	0.73	4.69	0.61	0.99	0.40
VMP	306.21	139.54	1.29	0.17	0.98	0.83	5.15	0.68	1.12	0.29
KNB	393.48	177.53	1.64	0.22	1.26	1.06	6.53	0.87	1.42	0.37
PVC	334.19	151.76	1.40	0.19	1.05	0.90	5.58	0.74	1.22	0.27
KGP	343.41	156.01	1.45	0.19	1.14	0.93	5.77	0.76	1.24	0.40
PTP	412.75	187.79	1.74	0.23	1.35	1.11	6.94	0.92	1.50	0.44
Mean	301.57	130.24	1.28	0.17	0.98	0.81	5.12	0.68	1.10	0.30
S D	64.53	28.50	0.26	0.04	0.22	0.17	1.05	0.14	0.23	0.11
World Limit	370	59	0.07	0.40	1	1	1.45	0.29	1	1

The calculated Radium equivalent indices, Ra_{eq} for the rock samples are presented in Table 5.4. It is found to vary from 175.68 to 412.75 Bq/kg, with a mean value of 301.57 Bq/kg and a standard deviation of 64.53. The mean Radium equivalent activity at all samples was found to be lower than the world limiting value of 370 Bq/kg (except in sample from Pattathipara (PTP)). For Pattathipara (PTP), the value of Radium equivalent was found to be 412.75 Bq/kg.

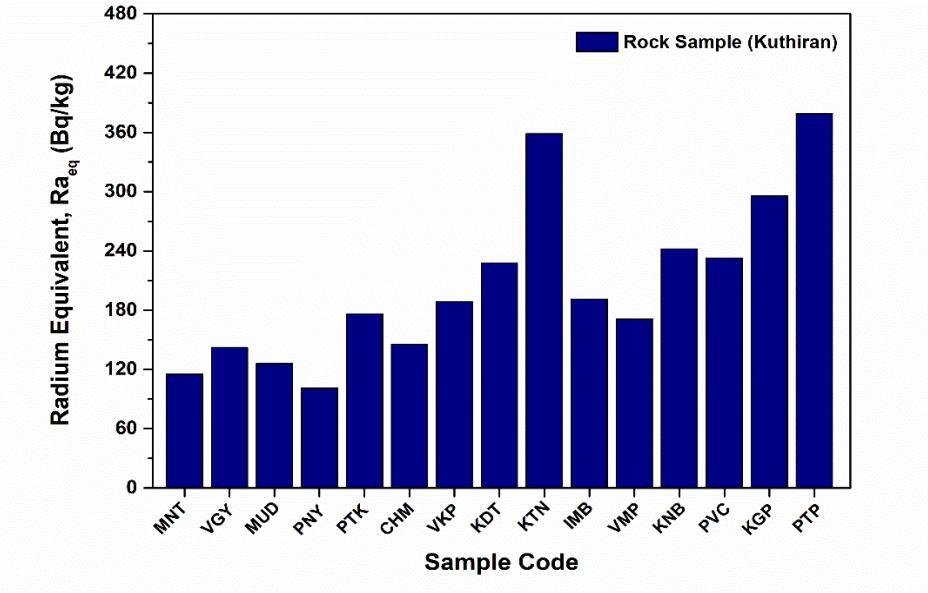

Figure 5.5: Calculated values of Radium equivalent indices of the rock samples.

The estimated average ambient absorbed gamma radiation dose rates (D_{out}), in air at approximately 1 m above the earth surface at different sampling locations in the study area are as shown in Table 5.4 (column 2) and Figure 5.6. The corresponding values vary from 82.34 (MNT) to 187.79 $nGyh^{-1}$ (PTP) with a mean value of 130.24 $nGyh^{-1}$. The estimated mean value of the absorbed dose rates of the rock samples were found to be higher than the world limit value of 59 $nGyh^{-1}$ (outdoor) as per UNSCEAR report, but within the world permissible range of 10 to 200 $nGyh^{-1}$ [52].

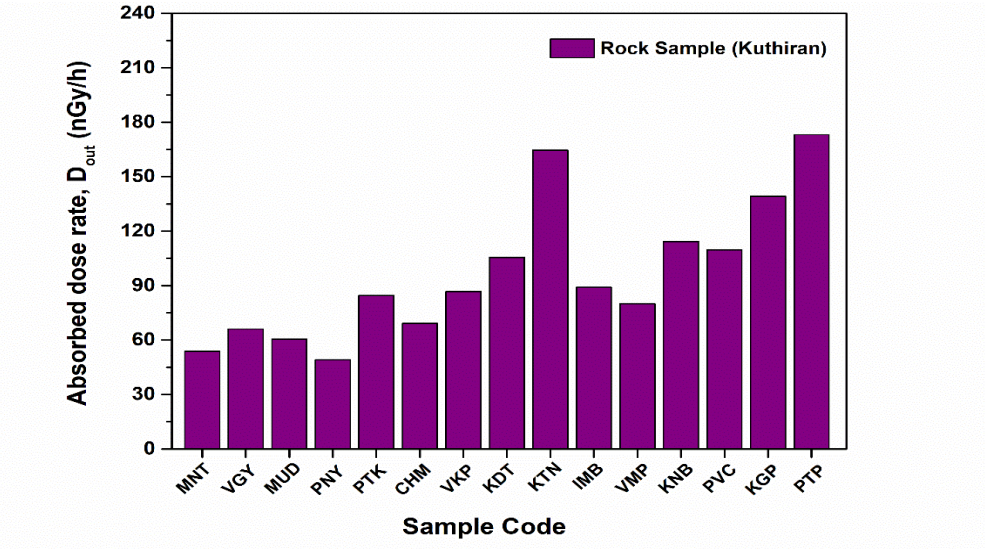

Figure 5.6: Calculated values of ambient gamma radiation dose rates (D_{out}) of the rock samples.

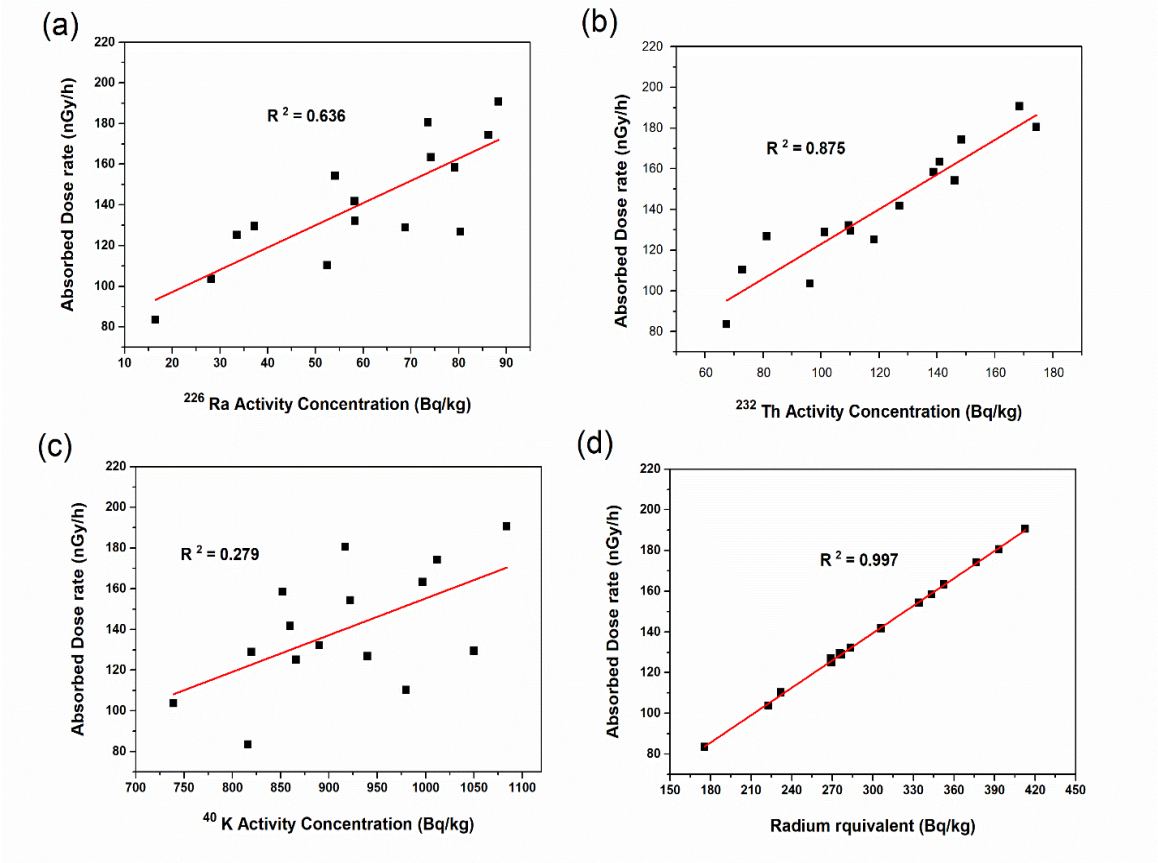

Figure 5.7: Correlation between absorbed dose rate with the activity concentrations(a-c) and Radium equivalent vs absorbed dose rate (d).

Figure 5.7 (a-c) illustrates the correlation between activity concentrations and absorbed dose rates (D_{out}) in the rock samples. The regression analysis showed a linear and positive relationship. Specifically, a positive correlation coefficient (R^2) of 0.87 was observed between D_{out} and ^{232}Th concentration. But, the correlations between D_{out} and ^{226}Ra as well as ^{40}K were not found to be significant. However, shows a clear positive correlation between absorbed dose rate and Radium equivalent.

The gamma radiation levels in the rocks are influenced by their mineralogical compositions and the activity concentrations of radionuclides present in the geological materials. The average values of the annual effective dose rates (AED_{out}) for the rock samples were lower than the worldwide limit of 0.40 mSv/y.

According to Table 5.4 and Figure 5.8, the calculated annual indoor effective dose

rates range from 0.76 mSv/y (MNT) to 1.74 mSv/y (PTP), with an average of 1.28 mSv/y. These values indicate that the average AED_{out} from the rock samples is higher than the world limit of 0.070 mSv/y.

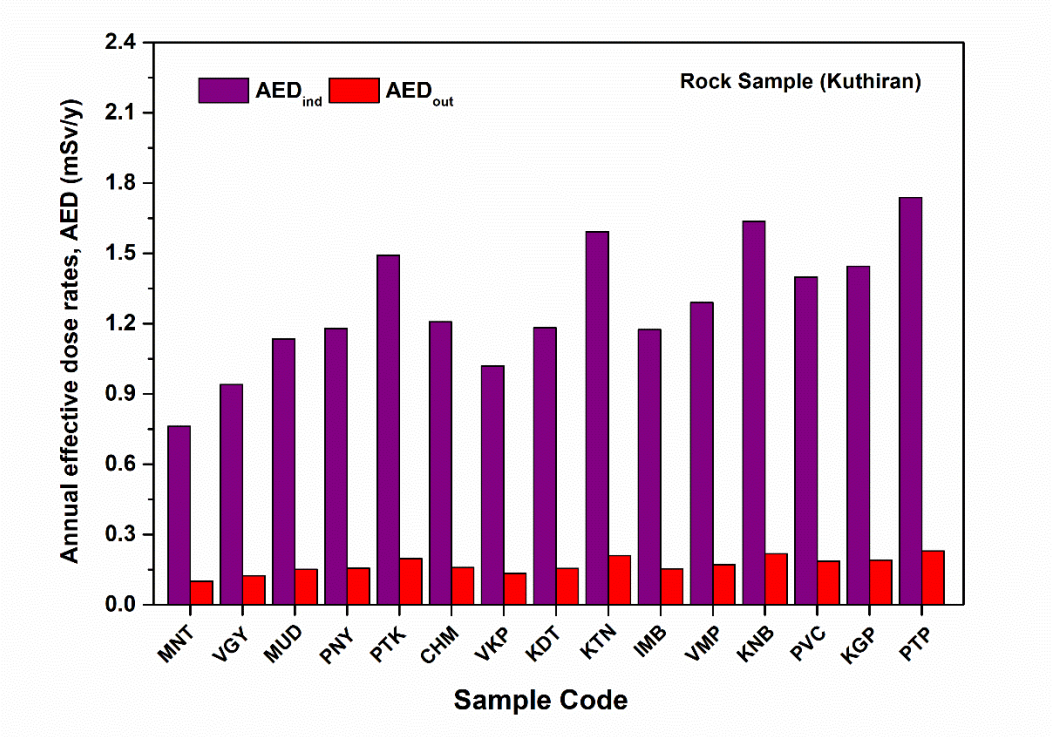

Figure 5.8: Calculated values of annual effective dose rates (AED) rock the samples.

The external and internal hazard index values of rock samples range from 0.50 (MNT) to 1.11 mSv/y (PTP) and 0.54 (MNT) to 1.35 mSv/y (PTP) with mean values of 0.81 and 0.98 mSv/y respectively, is shown in Figure 5.9 (Table 5.4). However, rock samples from Pattathipara (PTP), Kuthiran Tunnel (KTN), Kannanbra (KNB), and Pattikadu (PTK) shows relatively higher index values (>1 mSv/y) but the overall mean of external and internal hazard index values of all the rock samples shows below the recommended level of 1 (Table 5.4).

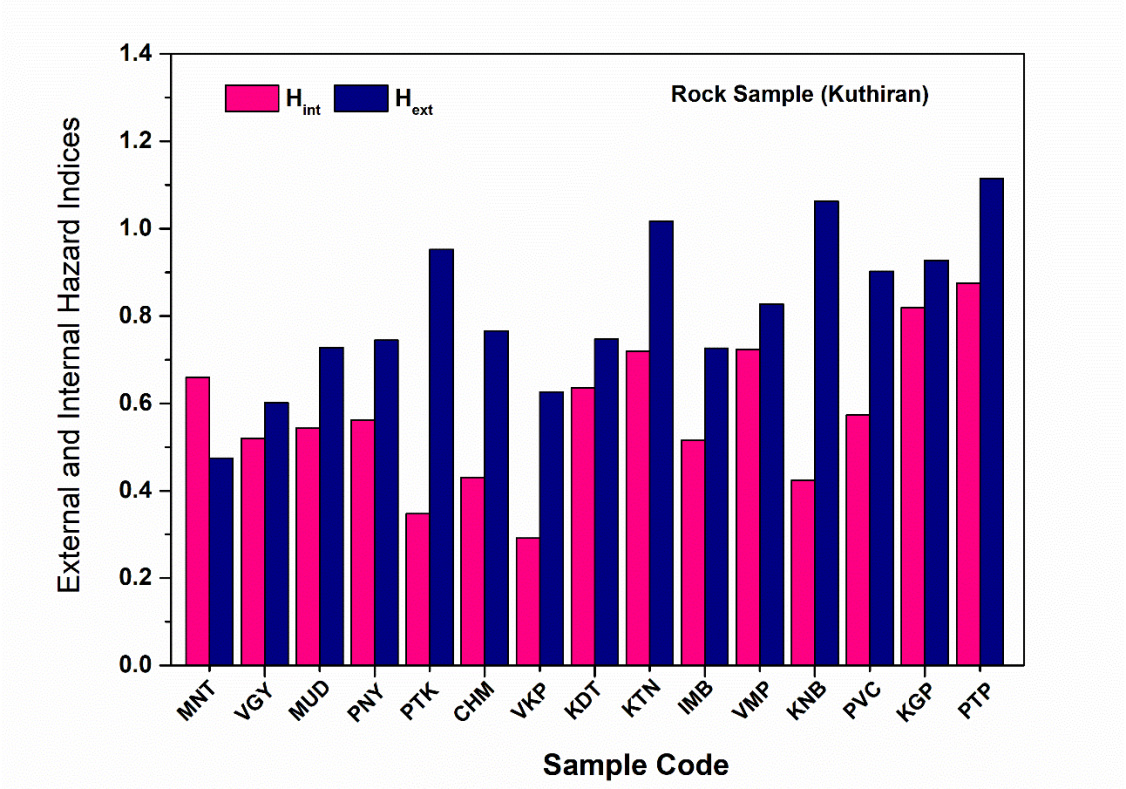

Figure 5.9: The distribution of the hazard indices (H_{int} and H_{ext}) in the study area.

Therefore, we conclude that there is no significant radiological risk from external and internal exposure for people residing in and around the study area. As a result, these geological materials can be safely utilized for building construction. The threat of radiation hazard to respiratory organs, indicated by an elevated H_{int} value exceeding safe limits[53], is not observed. This suggests that the use of rocks from the study area will not result in elevated risks of respiratory disease such as asthma, or external diseases like skin cancer, erythema, and cataracts.

The distribution of the excess lifetime cancer risk (ELCR) data in the study area is shown graphical form in Figure 5.10. The estimated values of $ELCR_{ind}$ vary between 3.04×10^{-3} and 6.94×10^{-3}, with an average value of 5.11×10^{-3}. The average value $ELCR_{ind}$ is higher than the world limit value of 1.45×10^{-3}, recommended by [54]. The estimated values of $ELCR_{out}$ vary between 0.40×10^{-3} and 0.92×10^{-3}, with an average value of 0.68×10^{-3}. The average value $ELCR_{out}$ is higher than the world limiting value of 0.29×10^{-3}, recommended by [54].

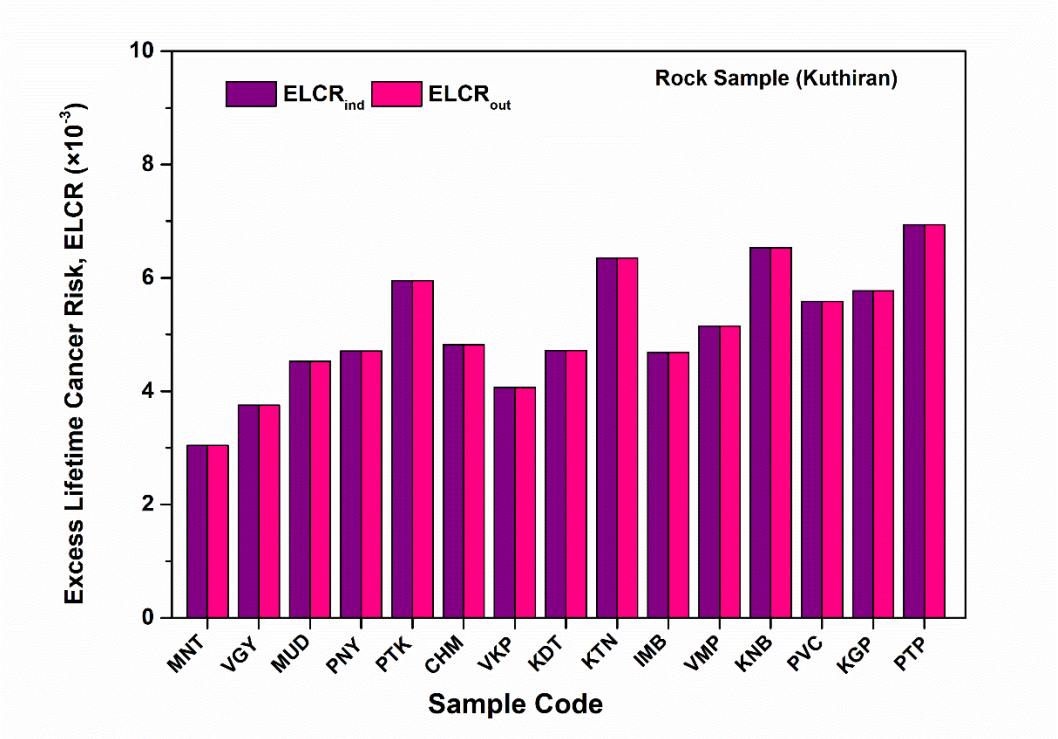

Figure 5.10: The distribution of the excess lifetime cancer risk (ELCR) in the study area.

The distribution of gamma index and Alpha index in the study are as shown in Figure 5.11. The gamma index (I_γ) takes into consideration the suitability of the materials used for building construction. For suitability of rock or stone used in construction applications, the I_γ should be less than 1 [54]. The estimated gamma index values of the rock samples in the present study range from 0.66 (MNT) to 1.50 (PTP), with a mean of 1.10 (given in Table 5.4). The value of $I_\gamma \leq 0.5$ corresponds to a dose rate limit of 0.3 mSv y^{-1}, whereas $0.5 \leq I_\gamma \leq 1$ corresponds to a dose rate limit of 1 mSv y^{-1} [55].

The gamma radiation index (I_γ) values obtained from rock samples at Pattathipara (PTP), Kuthiran Tunnel (KTN), and Kurangupara (KGP) slightly exceed the permissible limit of unity and the recommended value of 1 mSv/y for annual effective dose rates.

Furthermore, most of the rock samples in the study area (7 out of 15) exceed the permissible limit of unity and the recommended value of 1 mSv/y for annual effective dose rates. However, the radiological risks to the general public from the

rock outcrops and residual soils in the study area are considered insignificant at present. It should be noted, though, that prolonged exposure to excessive radiation doses from these sources could pose radiological threats in the future.

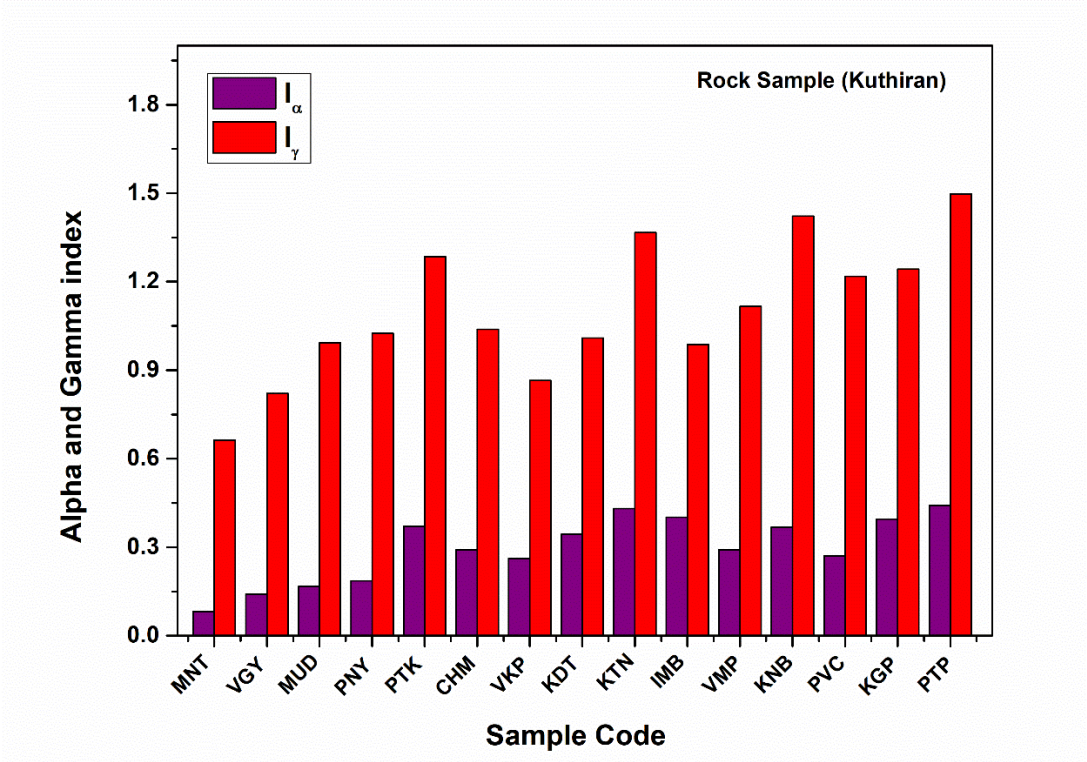

Figure 5.11: The distribution of gamma index and Alpha index in the study

The gamma index, $I_\gamma \leq 2$, corresponds to an annual effective dose rate standard of 0.3 mSv/y, while $2 \leq I_\gamma \leq 6$ corresponds to a criterion of 1 mSv/y. Areas where $I_\gamma > 6$ indicate annual effective dose rates above 1 mSv/y, which exceeds the recommended level and poses a risk to people living in the vicinity of the rocks [55]. The estimated Alpha index values of the rock samples in the present study range from 0.08 (MNT) to 0.44 (PTP), with a mean of 0.30 (given in Table 5.4). so, estimated mean Alpha index is less than the world limit of 1.

Table 5.5 shows a weak correlation between ^{226}Ra and ^{232}Th (R = 0.59), ^{226}Ra and ^{40}K (R^2 = 0.49), and between ^{232}Th and ^{40}K (R= 0.36).

Table 5.5: Correlation matrix between the radionuclides and radiological parameters.

Variables	^{226}Ra	^{232}Th	^{40}K	Ra_{eq}	D_{out}	I_{α}	I_{γ}	AED	ELCR	H_{ext}	H_{int}
^{226}Ra	1										
^{232}Th	0.59	1									
^{40}K	0.49	0.36	1								
Ra_{eq}	0.96	0.85	0.76	1							
D_{out}	0.96	0.84	0.79	0.94	1						
I_{α}	0.92	0.89	0.74	0.92	0.86	1					
I_{γ}	0.91	0.82	0.78	0.94	0.86	0.86	1				
AED	0.91	0.84	0.84	0.76	0.91	0.84	0.86	1			
ELCR	0.92	0.84	0.79	0.81	0.66	0.88	0.88	0.88	1		
H_{ext}	0.92	0.83	0.77	0.86	0.64	0.81	0.81	0.94	0.84	1	
H_{int}	0.92	0.94	0.76	0.87	0.66	0.82	0.78	0.96	0.88	0.91	1

The Pearson correlation analysis is a statistical method used to measure the strength and direction of relationships between radioactive variables. Correlation can be classified into positive and negative types. The correlation coefficient (denoted by "R") ranges from -1 to +1, where a value closer to +1 indicates a strong positive linear relationship between variables. Conversely, a low R value indicates a weak linear relationship, and an R value close to zero suggests no linear relationship[74].

In this study, a weak correlation coefficient was observed between Uranium (^{238}U) and Thorium (^{232}Th). This correlation suggests that the origin of ^{40}K differs significantly from the origin of the other radionuclides, ^{238}U and ^{232}Th, although they may share similar controlling factors or sources. Additionally, the correlation coefficients (R) of radiological parameters such as Radium equivalent activity, absorbed dose rate, annual effective dose equivalent, internal hazard index, external hazard index, and excess lifetime cancer risk indicate a strong correlation with the activity of ^{238}U in the rocks.

5.2.5. Mineralogical composition analysis of rock samples by XRD

The results of the XRD analysis of the rock samples collected from four locations in the study area (namely Poovanchira, Kuthiran tunnel, Kannanbra and Pattathipara) are presented in Figure 5.12 (a-d). The major components found in all the rock ores are Monazite (Ce, La,T)PO_4, Limonite ($FeO(OH).nH_2O$), Zirconium orthosilicate

($ZrSiO_4$) and Zeolite ($NaAlSiO_4$). In addition to this traces of quartz (SiO_2), Titanium dioxide (TiO_2), Chromium oxides (Cr_2O_3), Iron Oxides (Fe_2O_3), Phosphorus oxide (P_2O_5) and calcite ($CaCO_3$) have also been seen in the collected rock samples. The peaks corresponding to ores observed at different 2θ angles for some of the selected rock samples in the study are shown here in Figure 5.12 (a-d).

Monazite is significant due to its composition of light rare earth elements (REE), Thorium, and Uranium [76]. In the studied stream sediments, Monazite mineral grains are typically subhedral, occasionally euhedral, flattened, or broken, sometimes displaying pitted surfaces. Zircon, on the other hand, appears mostly as euhedral to subhedral grains, ranging from fine to very fine sizes, often with prismatic to elongated shapes and a good adamantine luster.

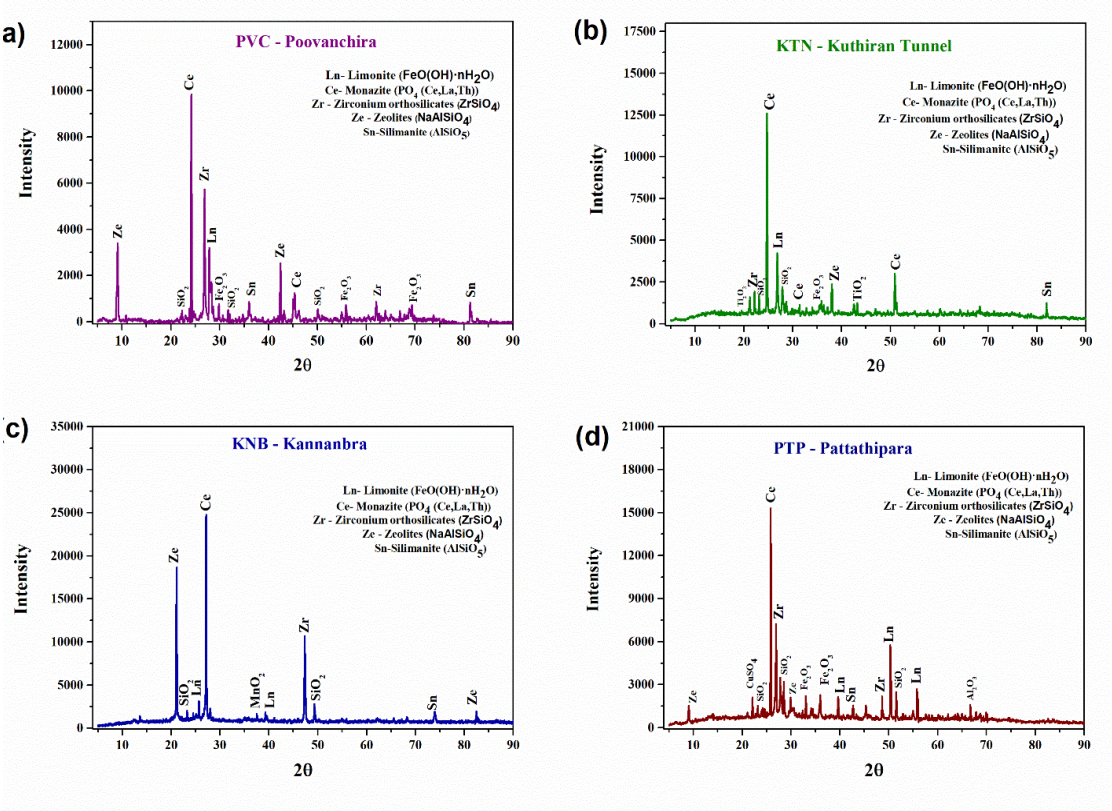

Figure 5.12: XRD pattern of rock samples of the same grain size of ≤100 µm collected from four sites of the study area.

The presence of Monazite and Zircon deposits in these rocks is crucial in terms of radioactivity. The Thorium content in Monazite placer deposits varies depending on the type of rock from which the Monazite originates. Rocks that are more plutonic in

nature tend to have higher percentages of Thorium content [46], [47], [49], [56].

The study indicates that the elevated activity levels of ^{232}Th and ^{226}Ra in the region result from minerals such as Monazite, Zirconium orthosilicate ($ZrSiO_4$), and zeolite ($NaAlSiO_4$) that have weathered from the rock formations. Radionuclides present in the rock samples are directly associated with minerals like Zircon, Monazite, thorite, uranothorite, iron oxides, and fluorite. Zircon usually contains Uranium and Thorium concentrations ranging from 0.01 to 0.19 and 1 to 2%, respectively [57]. Uranium in iron oxides is first trapped by adsorption. The high Uranium content in the mineralized rock is attributed to the ability of iron oxide in them to adsorb Uranium [58]. The studied locations consist of a variety of rock systems and these rocks contain varying number of primordial radionuclides. The obtained data indicates that the major oxides present in the samples are SiO_2, Al_2O_3, MgO, Fe_2O_3, CaO, P_2O_5, K_2O, and TiO_2. The rock samples analyzed showed a higher concentration of SiO_2 compared to other components. Al_2O_3 was also prominent composite, with concentrations ranging from 6.72% to 18.71% and averaging 12.42%. This average is significantly higher than the crustal average value of 4.72%, suggesting that a substantial amount of Aluminium oxide may have originated from the weathering of silicate-rich rocks containing feldspar and mica. Additionally, the presence of abundant oxides of various elements in the rocks from the study area indicates that the natural radionuclides present in these rocks with varying concentrations can be attributed to these oxide forms of elements.

5.2.6 Elemental concentration of radionuclides and Radiogenic Heat Production (RHP) in Kuthiran Hills.

The elemental concentrations of ^{238}U in ppm, ^{232}Th in ppm and ^{40}K in % and radiogenic heat production (RHP) in μWm^{-3} of the rock samples collected from Kuthiran hills, Kerala were calculated and tabulated in Table 5.5

Table 5.6: The elemental concentrations, radiogenic heat production (RHP) and Heat flow (H_f) of the rock samples

Place Name	Place Code	Concentration of radionuclides			RHP ($\mu W/m^3$)	H_f ($\mu W/m^2$)
		^{238}U (ppm)	^{232}Th (ppm)	^{40}K (%)		
Mannuthy	MNT	1.33	16.61	2.61	1.44	13.54
Vengassery	VGY	2.28	23.70	2.36	2.10	19.05
Mudicode	MUD	2.72	29.16	2.77	2.84	23.16
Pananchery	PNY	3.02	27.14	3.35	2.66	23.13
Pattikadu	PTK	6.01	34.70	3.19	3.80	33.04
Chuvannamannu	CHM	4.72	27.00	2.84	3.16	26.07
Vazhukumpara	VKP	4.25	17.93	3.13	2.39	20.49
Kuthiran Temple	KDT	5.57	24.93	2.62	2.93	26.50
Kuthiran Tunnel	KTN	6.99	36.55	3.23	4.65	36.03
Irumbupalam Bridge	IMB	6.51	20.01	3.00	2.97	26.03
Vaniyampara	VMP	4.72	31.31	2.75	3.52	28.30
Kannanbra	KNB	5.96	42.93	2.93	4.79	37.16
Poovanchira	PVC	4.38	36.01	2.95	3.70	30.30
Kurangupara	KGP	6.41	34.21	2.72	4.24	33.23
Pattathipara	PTP	7.15	41.50	3.46	4.96	39.45

The elemental concentrations of ^{238}U in ppm, ^{232}Th in ppm and ^{40}K in % shown in Figure 5.13, 5.14 and 5.15 respectively. The elemental concentration of Uranium varies from 1.32 to 7.11 ppm with an average of 4.77 ppm. The highest elemental concentration of $_{238}U$ was observed in Pattathipara (7.11 ppm). Very low elemental concentration was observed in Mannuthy (MNT) (1.32 ppm).

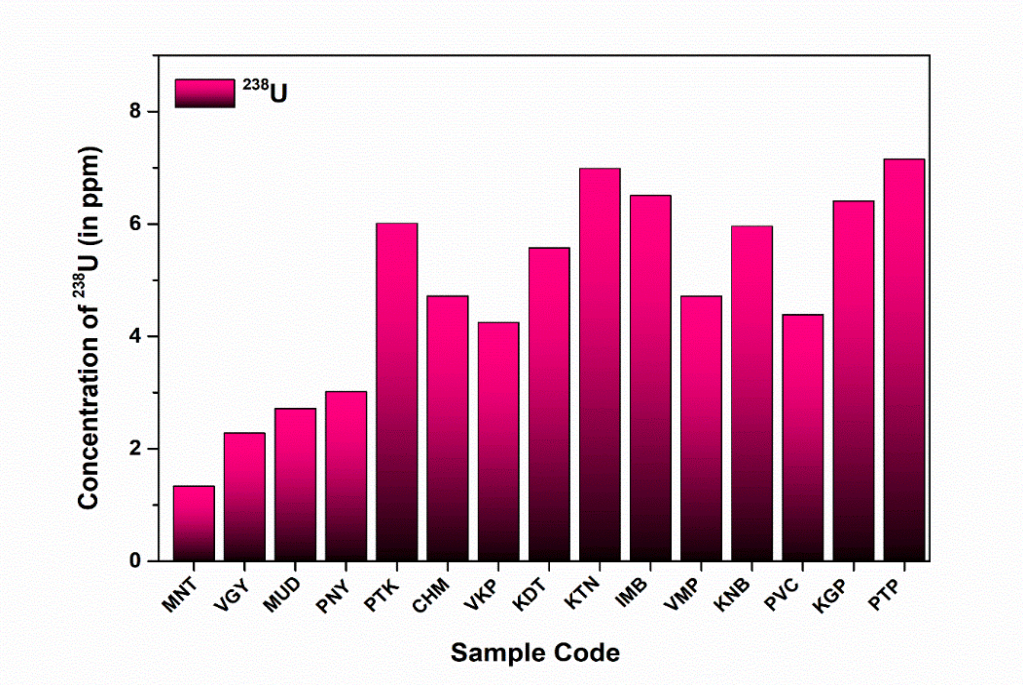

Figure 5.13: The elemental concentrations of ^{238}U (in ppm).

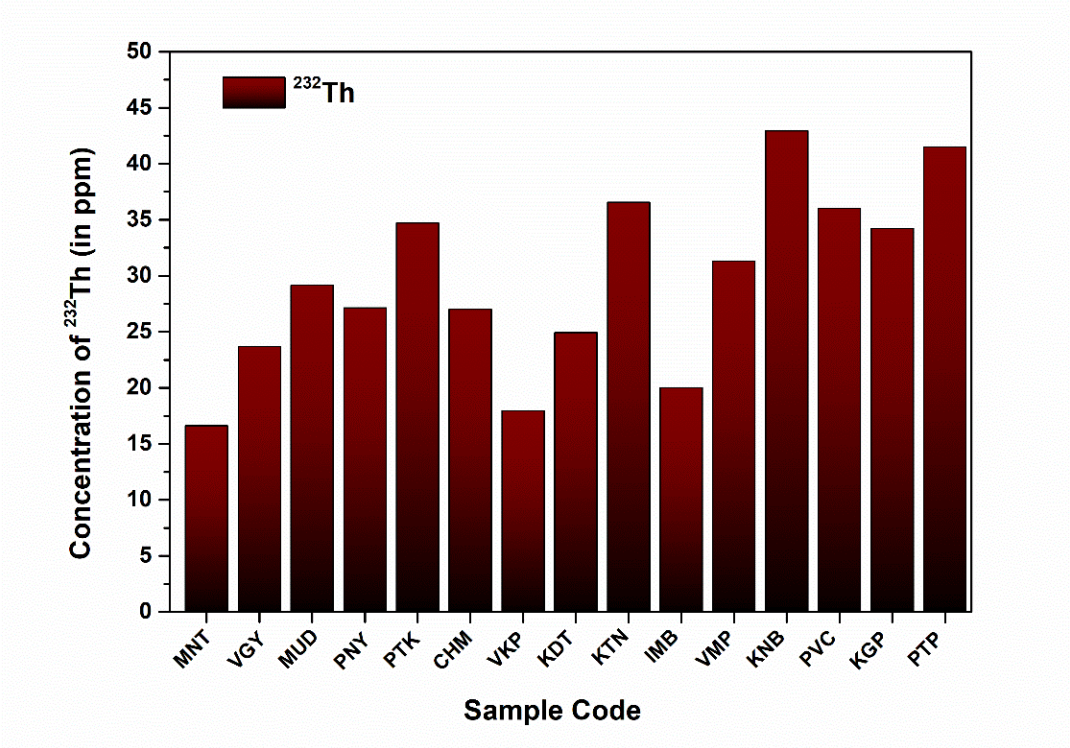

Figure 5.14: The elemental concentrations of ^{232}Th in ppm.

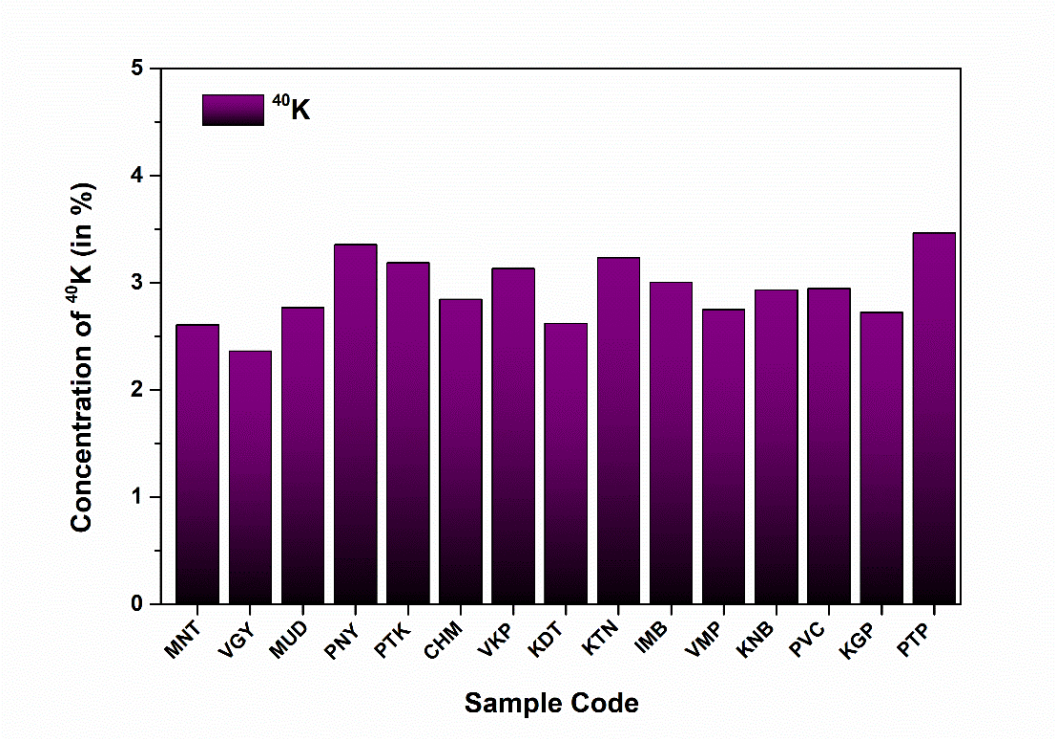

Figure 5.15: The elemental concentrations of ^{40}K (in %)

The elemental concentration of ^{232}Th ranged from 16.40 ppm to 42.41 ppm with an average of 29.22 ppm. The highest was observed in Kannanbra (42.41 ppm). The other locations also have a higher amount of concentration. Very low elemental concentration was observed in Mannuthy (16.40 ppm). The elemental concentration of ^{40}K ranged from 2.44% to 3.57% with an average of 3.02%. The highest elemental concentration of ^{40}K was observed in Pattathipara (3.57 %). Very low elemental concentration was observed in Vengassery (2.44 %). Figure 5.16 represents the contour representation of Radiogenic heat and Heat flow of the study region.

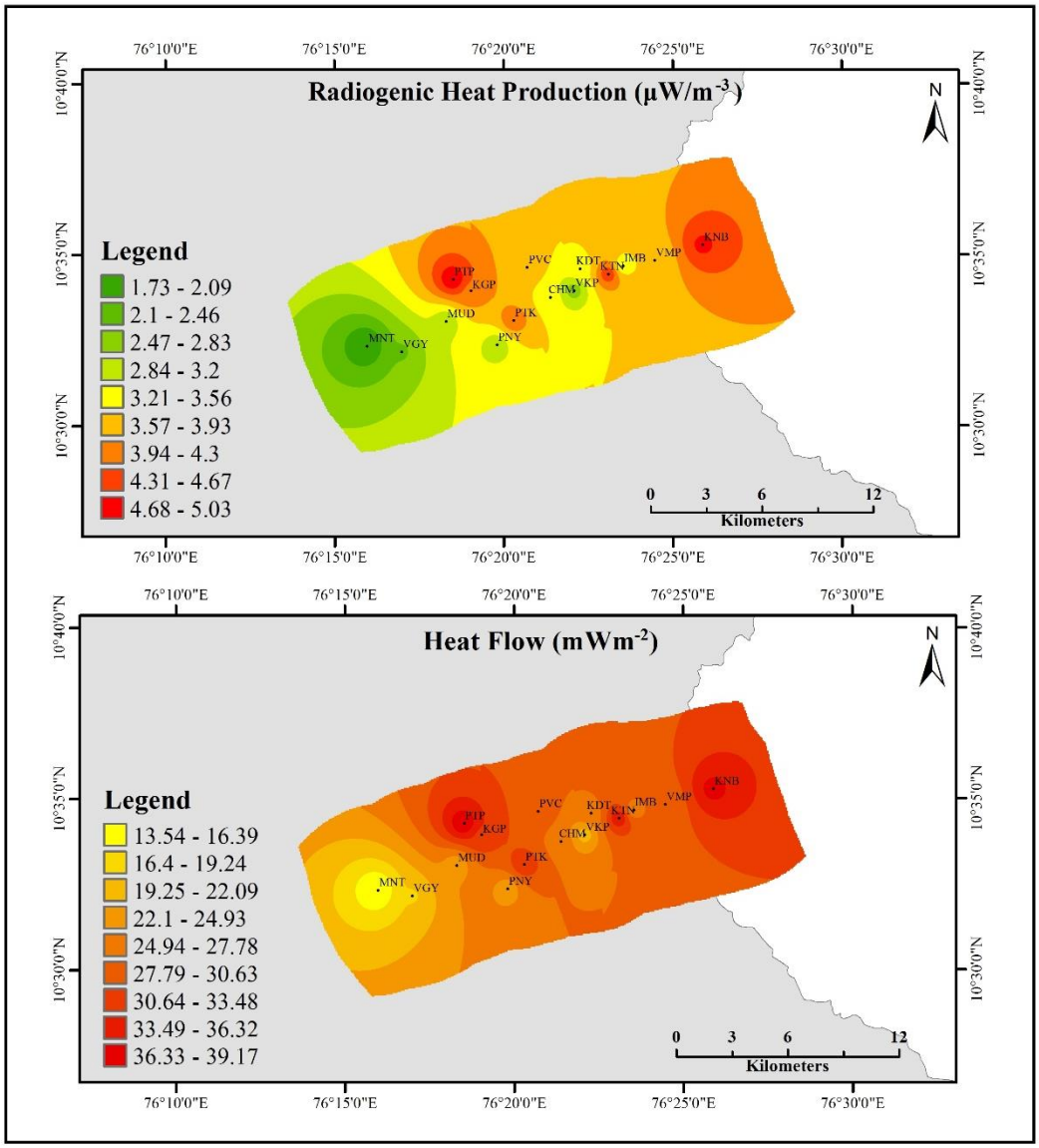

Figure 5.16: The contour representation of Radiogenic heat and Heat flow of the study region.

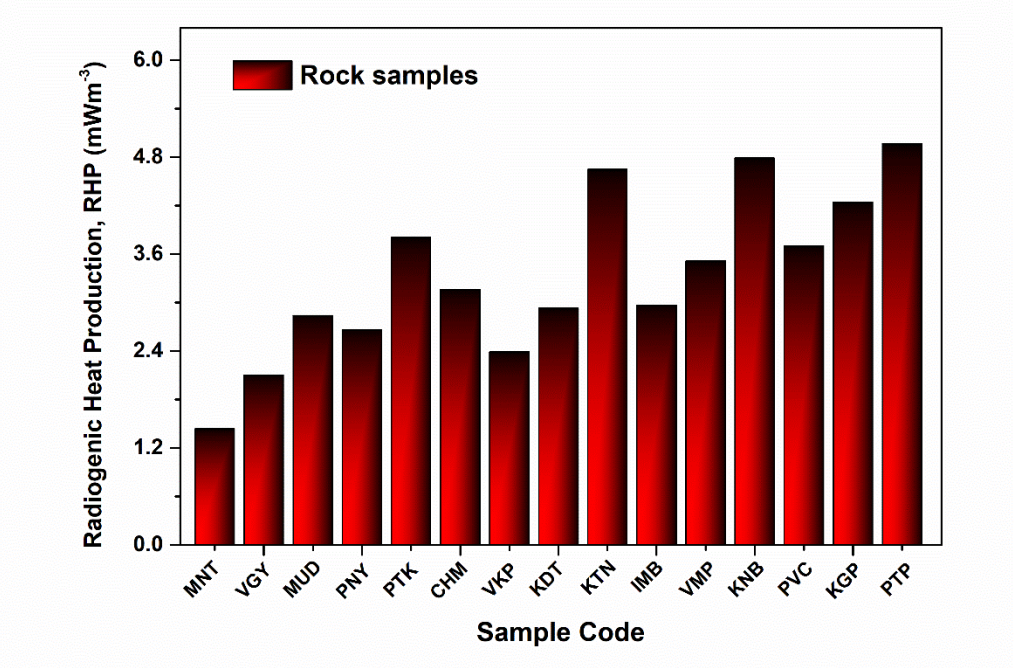

Figure 5.17: Radiogenic heat production in Kuthiran study region.

The highest radiogenic heat production in the rock samples collected in zone-1 was found in Pattathipara (4.96 μW/m^3). The other locations Kurangupara (4.24 μW/m^3), Kannanbra (4.79 μW/m^3), Kuthiran Tunnel (4.65μW/m^3), Pattikadu (3.80 μW/m^3) and Poovanchira (3.70 μW/m^3), show higher radiogenic heat production. But some locations show lower radiogenic heat production, which are, Mannuthy (1.44 μW/m^3) and Vengassery (2.10 μW/m^3) as shown in Figure 5.17 The weighted mean of Radiogenic Heat Production (RHP) was 3.34 μWm^{-3}, which exceeds the Earth's crust average ranging between 0.8 and 1.2 μWm^{-3}. This higher value is attributed to the substantial presence of gneiss rocks observed across all the profiles studied.

5.2.7 Correlation between radionuclides and Radiogenic Heat Production (RHP) for studied region.

In order to determine the existing ratio between the elemental concentrations of ^{238}U, ^{232}Th and ^{40}K in the rock samples, correlations between them were drawn using origin. Figure 5.18 (a - c) show the correlations between the elemental concentrations of ^{238}U, ^{232}Th and ^{40}K, respectively, with a trend line drawn among the data points.

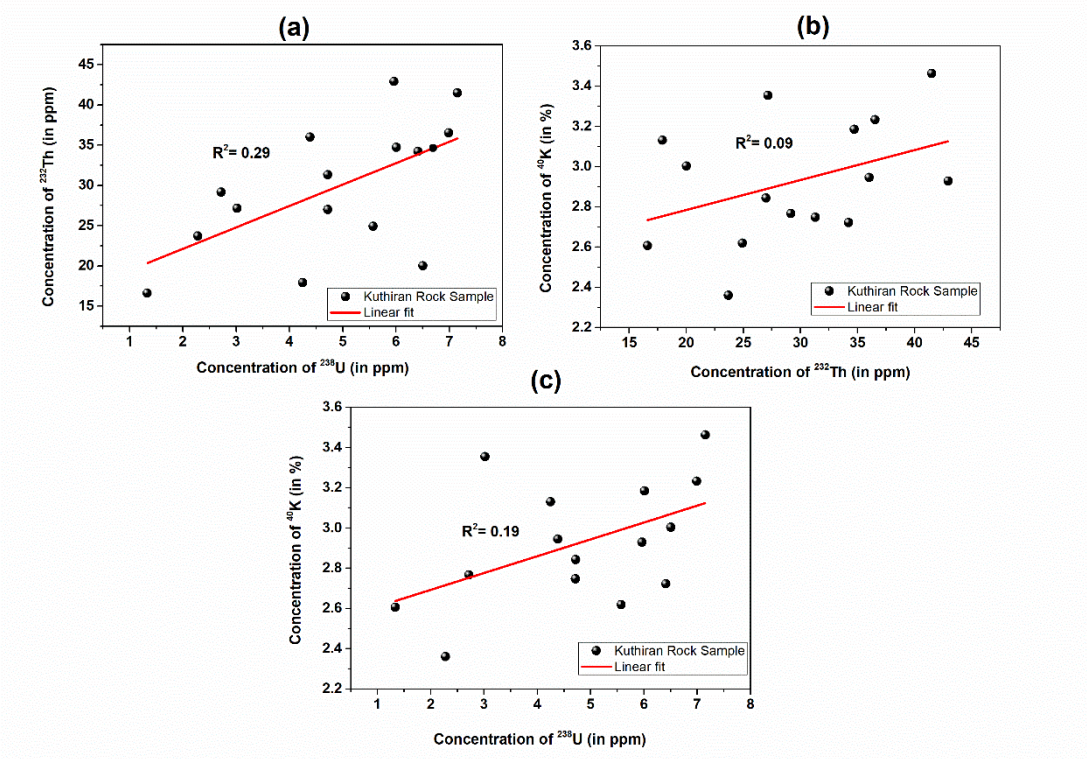

Figure 5.18: Correlation between radionuclides for studied region.

It appears that there is a weak correlation between ^{232}Th and ^{238}U, with a correlation coefficient (R^2) of 0.29. Similarly, in Figure 5.18 (b), the slope is 0.09 with an intercept of 0.1679%, whereas in Figure 5.18 (c), the slope and intercept are 0.19 and 0.5435%, respectively. However, as argued later in this paper, the most notable observation is the lack of consistent correlations observed among ^{238}U, ^{232}Th, and ^{40}K.

Now figure 5.19 (a-c) shows correlations among radiogenic heat and ^{238}U, ^{232}Th, and ^{40}K. From 5.19 (a), it is found that radiogenic heat produced in the study area has a low dependence with ^{40}K concentration (R^2 = 0.19). Also, it is observed that from 6.6 (b-c), ^{238}U concentration is the dominant producer of RHP, having R^2 = 0.84 and ^{238}Th concentration has moderate correlation with RHP (R^2 = 0.69).

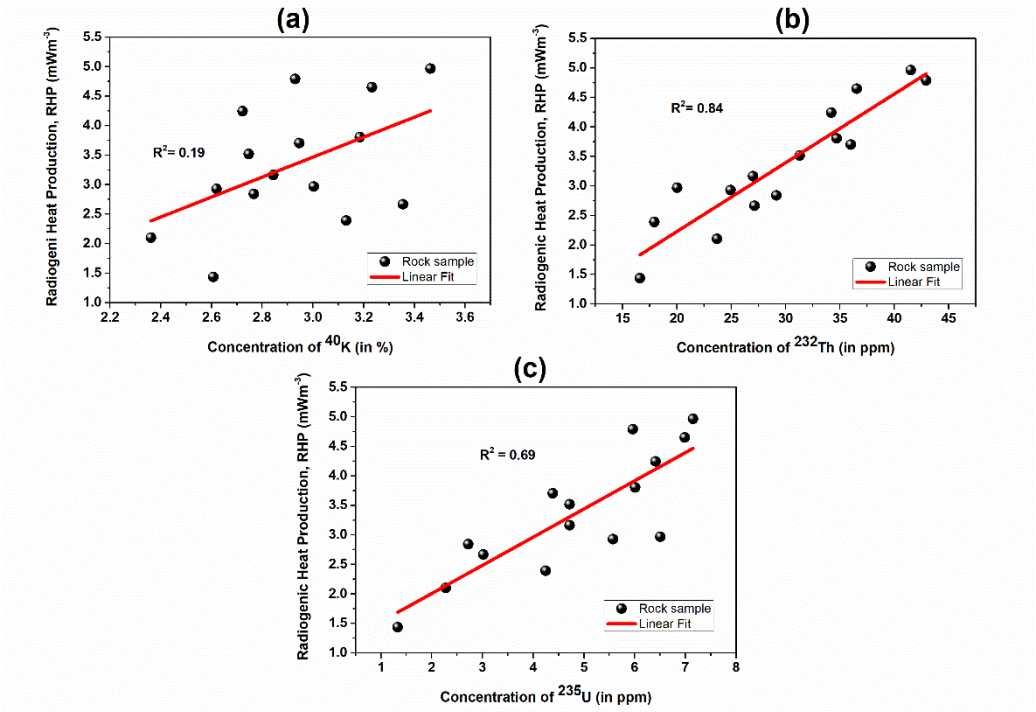

Figure 5.19: Correlation between concentration of radionuclides and Radiogenic Heat Production (RHP) and for studied region.

To determine H_f in the sampled points due to the decay of ^{238}U, ^{232}Th and ^{40}K, H_f was modeled from the values of RHP. The H_f in the samples due to the decay of ^{238}U, ^{232}Th and ^{40}K varied from (13.54 ± 1.0 – 39.45 ± 4.0) mWm^{-2} with average of 27.69± 1.8 mW m^{-2}. This average H_f is slightly higher than 21 mWm^{-2} reported by Asere and colleagues for quarry sites in Ondo State, Nigeria but less than the global value of 37 mWm^{-2} stated by Turcotte & Schubert for inactive regions[26], [39]. Katumwehe and colleagues reported H_f for North Uganda Terrane of between 58-65 mWm^{-2}, while reported 34-70 mWm^{-2} for the Tanzanian craton[59]. In comparison, the maximum H_f value 80 mWm^{-2} obtained in their study maybe be an outlier, not true value for the North Uganda terrane and is beyond the scope of this work. This requires further investigation using another method. Figure 5.20 shows the plot of the total RHP against H_f with significantly strong correlation coefficient of $R^2 = 0.98$. As expected, RHP in the samples produced a significantly greater effect on H_f. The H_f values reflect the high RHP due to decay of ^{238}U, ^{232}Th and ^{40}K in the study area, indicating feasibility for geothermal exploration. This agrees with the findings of Turcotte & Schubert for stable continental areas, where the H_f had a strong

correlation with the surface RHP. Hence, this research shows that the study area is in more thermally quiescent regions.

Figure 5.20 illustrates a plot of total RHP and H_f producing a linear distribution segment with strong correlation coefficient of R^2 = 0.98. The linear regression through the data points gives a slope of 7.02 and vertical axis intercept of 4.23 mW m^{-2}.

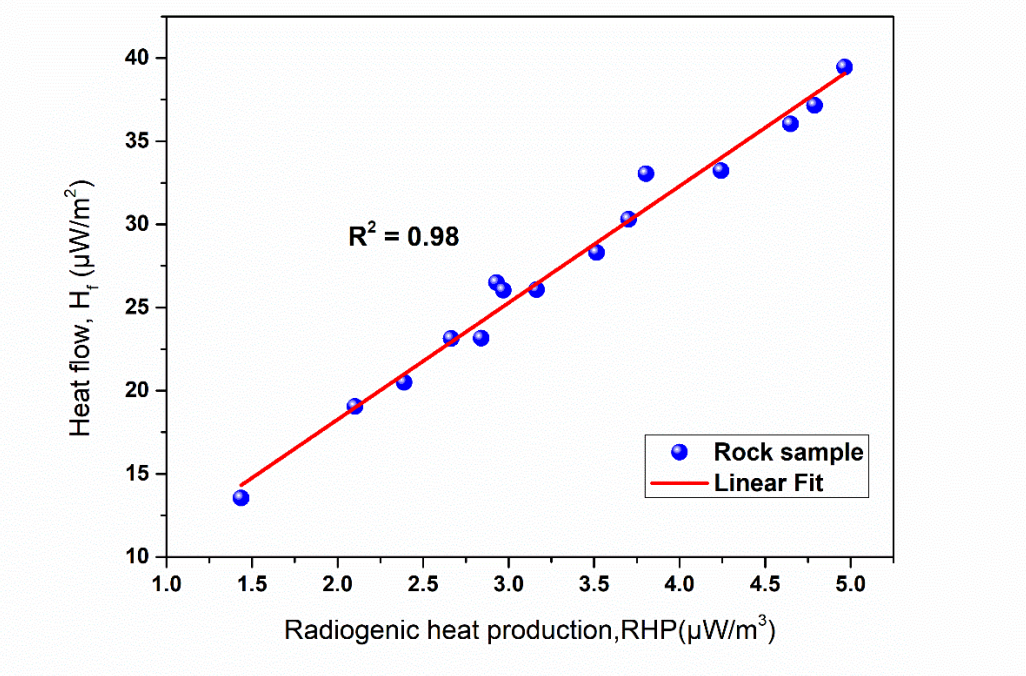

Figure 5.20: Correlation between concentration of HF and RHP and for studied region.

5.2.8 Conclusion:

The assessment of rock samples, radiological risks, radiogenic heat production, and heat flow in the Thrissur-Palakkad highway region of Kerala state had been conducted using ground radiometric data. The goal was to provide insights useful for geothermal modeling. The study demonstrates that radiometric data can reliably compute heat generation values through numerical approaches. Key findings from this study include:

Average activity concentrations of basement rocks are 59.28 Bq/kg for ^{226}Ra, 120.09 Bq/kg for ^{232}Th and 916.33 Bq/kg for ^{40}K. Elemental analysis conducted in this

study serves as an indicator to identifying mineralogical composition, types of radioisotopes, and activity levels in the collected samples, which are predominantly natural in origin. XRD analysis reveals major mineral types such as ilmenite, Zircon, rutile, and Monazite in the investigated samples. Charnockite rocks in the study area exhibit activity values above the global crustal average. Radiological hazard parameters due to gamma radiation, including an average Ra_{eq} of 301.57 Bq/kg (is below the global limit of 370 Bq/kg) and average absorbed doses of 130.24 nGy/h (above the global permissible limit of 59 nGy/h), suggest a radiologically safe environment (Table 5.4). Other estimated radiological parameters such as AED_{out} AED_{ind}, H_{ext}, H_{int} indices, I_{γ}, and I_{α} compared favorably with the recommended upper global permissible limit, indicating safety from a radiological perspective. The estimated $ELCR_{out}$ (average of 0.68×10^{-3}) exceeds the global permissible limit of 0.29×10^{-3}, indicating a potential higher risk for radiological exposure in the studied sample, albeit still within acceptable levels. In conclusion, this study underscores that exposure to natural radionuclides in the studied rock samples poses no significant health risks to the farmers and residents of the investigated regions.

In the Thrissur-Palakkad highway region, the observed rates of radiogenic heat production (RHP) for the studied rocks range from 1.44 to 4.96 μWm^{-3}, with an average of 3.34 μWm^{-3}, which exceeds the global average range of 0.8–1.2 μWm^{-3} for such measurements. Notably, charnockite rocks exhibit RHP values above the world crustal average.

5.3. Urban regions along the National Highway (NH-66) in Kerala, India Region II.

The significance of measuring natural radioactivity amidst the ongoing expansion of National Highway 66 (NH-66) in Kerala lies on its utility for impact assessment. As the highway project advances, evaluating natural radioactivity levels in the area provides essential insights into the background radiation. This data aids in identifying variations or abnormalities in radiation levels attributed to geological formations, construction materials, or human activities linked to the expansion. Moreover, investigating natural radioactivity near construction sites offers valuable

information on the potential radiation exposure risks for workers, nearby residents and others supporting the environment. This proactive monitoring approach is needed for upholding safety standards and regulatory compliance, particularly considering the sensitivity of radiation-related concerns and their potential long-term effects on public health and environmental integrity. Consequently, integrating natural radioactivity measurements with the NH 66 expansion project adds a novel dimension to its environmental impact evaluation and safety protocols. Typically, conventional sampling methods focus on surface-level measurements, potentially overlooking the intricacies of subsurface geological formations and their impact on natural radioactivity. Sampling at greater depths, however, allows researchers to access soil and rock layers with potentially higher concentrations of radioactive elements, facilitating a more comprehensive understanding of the overall radiation landscape. This depth-specific analysis can uncover variations in radioactivity levels and shed light on the geological processes shaping the distribution of radioactive materials. Furthermore, sampling at such depths enables exploration of potential pathways for the migration of radioactive contaminants and their long-term effects on groundwater quality and ecosystem health. Hence, the novelty of sampling at depths of 12-16 meters lies in its potential to enrich the accuracy and depth of knowledge concerning natural radioactivity near the NH-66 expansion, thereby guiding more precise and effective mitigation strategies to bring down the radiation-related risks to human health and to the environment.

5.3.1 Geology of the study area

The precise positions of the soil sampling stations were recorded using a Global Positioning System (GPS), as illustrated in Figure. 5.21.

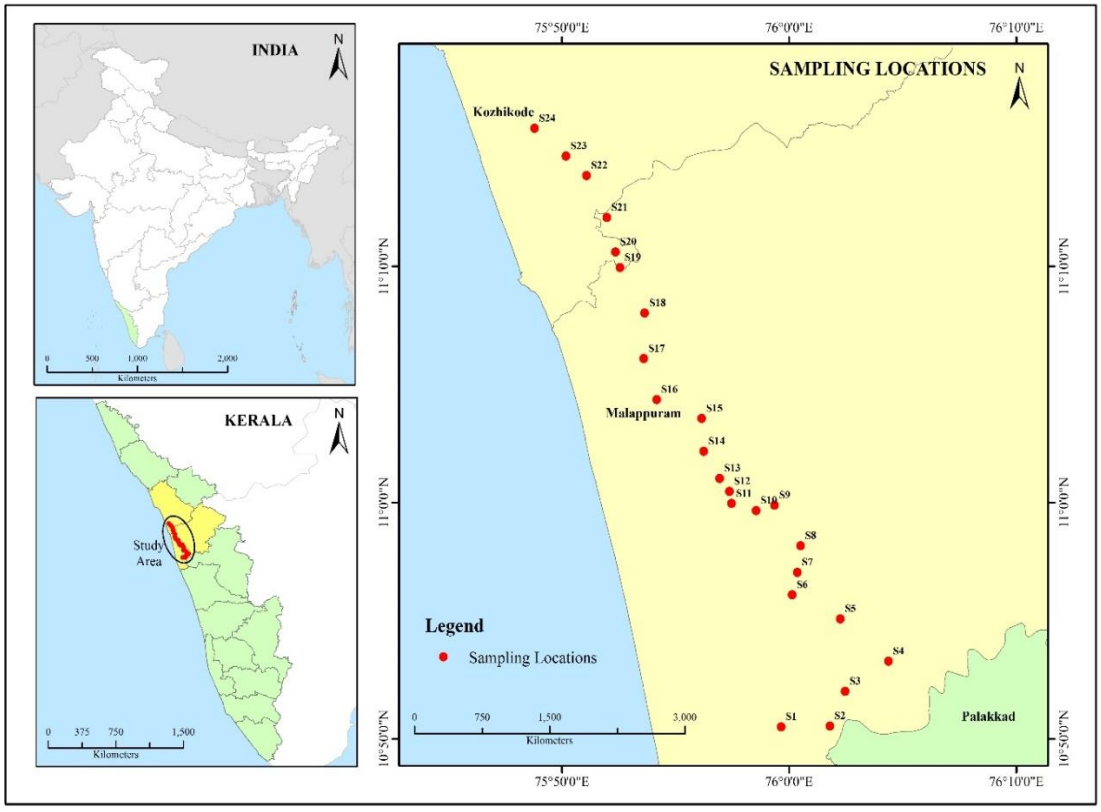

Figure 5.21: Map indicating the positions of the sampling locations.

The study area under investigation is a section of NH-66, located between the head quarters of Kozhikode and Malappuram districts of Kerala state, India. It is situated within the geographical coordinates of longitude 75°59′E–76°05′E and latitude 10°46′N–11°16′N. A comprehensive set of 120 soil samples were gathered from the study area, specifically targeting 24 significant sites, distributed over a distance spanning 78 kilometres. Currently, the land acquisition and the contracting process for the expansion of the national highway are progressing rapidly in Kerala. Construction of new bypass roads near the sampling sites has already been commenced. National Highway 66 (NH-66) runs along the western coast of India, stretching from Panvel, south of Mumbai, to Kanyakumari in Tamil Nadu. This major highway passes through the states of Maharashtra, Goa, Karnataka, Kerala, and Tamil Nadu. In Kerala, NH-66 follows the alignment of NH-17 and incorporates a substantial segment of NH-47. Efforts to expand NH-66 into a six-lane highway are currently underway in various states. However, in Kerala, progress has been

impeded by land conflicts along the highway route, resulting in construction delays or, in some cases, partial suspensions of construction activities.

Due to the high population density and land value in Kerala, the national highway is being widened to 45 meters with six lanes. These measurements serve to establish the dose rate required for implementing preventive measures when the radiation dosage exceeds acceptable limits. The data gathered will be employed to establish a foundational map for the area. This map can be utilized to monitor alterations in the background radiation levels caused by changes in highway terrain, new developments, urban expansion along the highway or other human-induced factors influencing the radiation background levels.

5.3.2 Lithology of study area.

Figure 5.22 shows the geological map of the research region. The map is drawn by the Kerala State Land Use Board, which operates a Natural Resource Data Bank.

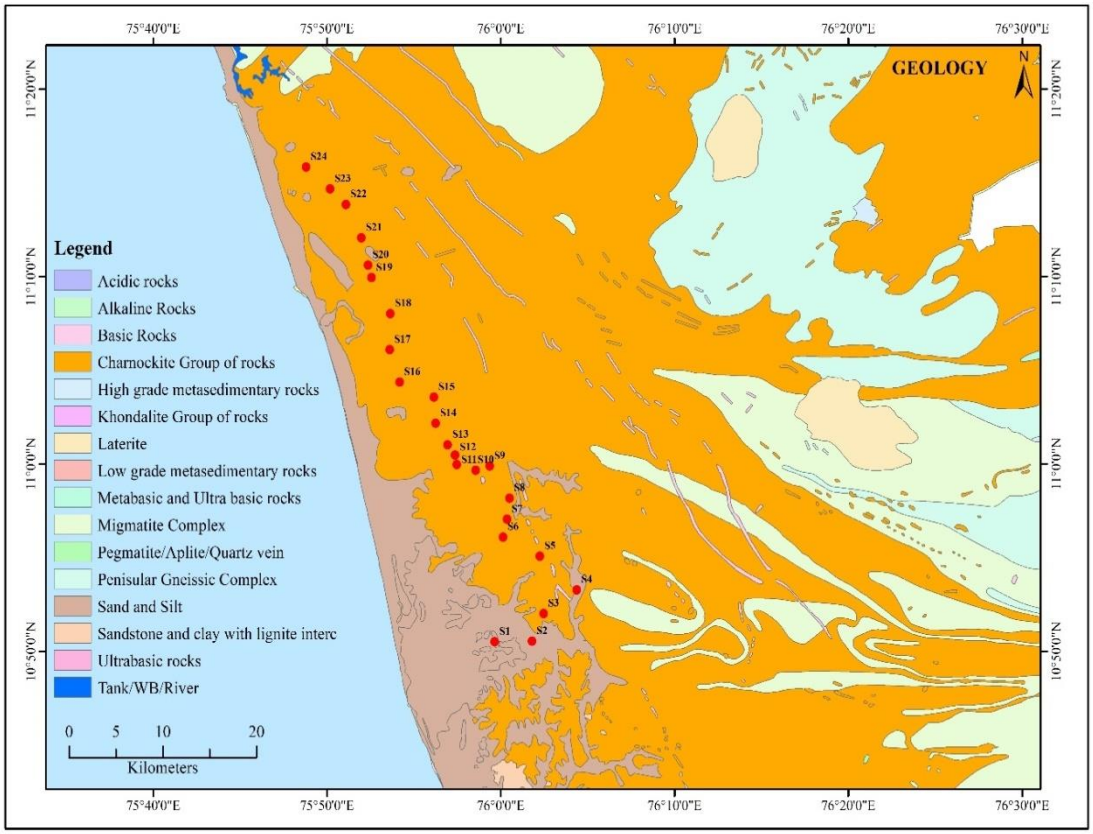

Figure 5.22: The geological map of the research region.

The Western Ghat mobile belt covers various lithologies of the Western Ghat Supergroup, including charnockite, Khondalite, and migmatite. The district boasts a wealth of minerals, including gemstones, bauxite, graphite, apatite, Vermiculite, and magnetite. The crust of the region comprises rare earth elements, often found in conjunction with Uranium (U) and Thorium (Th) within minerals such as Monazite, samarskite, fergusonite, and allanite [60]. These minerals were abundantly present in Precambrian pegmatites and played a significant role in the creation of notable Monazite placers [49], [61]–[63]. The sampling locations were selected based on a preliminary investigation, which involved using a gamma survey monitor to detect radiation levels above 0.10 Svh^{-1}. From north to south, the geomorphic topography transitions from mountains to hills, plains, and platforms. Hills and mountains of various types cover more than 65 percent of the total area. The soil types include latosol, mountain lateritic red earth, and paddy soil. Intrusive rocks, which cover a significant portion of the sample region are the most common parent rocks for soil formation. Additionally, limestone and sand shale are prevalent in the study area. The categorization of lithology in Malappuram district into two groups based on the presence of Monazite, namely the Charnockite and Khondalite groups of rocks, is related to the geological characteristics of the region [64]. It suggests that the occurrence of Monazite is likely to be particularly high in metamorphosed Charnockite rocks.

Charnockite is a type of granulite rock that is commonly found in the southern part of India, including the Malappuram district in the state of Kerala. Charnockites are characterized by their coarse-grained, reddish, or brownish appearance, and they are composed mainly of minerals such as orthopyroxene, quartz, and feldspar. Monazite, a rare earth mineral, is often found associated with charnockite rocks in this region. Monazite contains valuable elements like Thorium and rare earth elements, making it of economic interest. The presence of Monazite in the charnockite rocks can have economic implications, as it has been a source of Thorium and rare earth element extraction in the past. Khondalite are typically

composed of alternating layers of quartz, feldspar, and other minerals such as garnet and sillimanite. Like charnockites, Khondalite rocks in this region may also contain Monazite, which can have economic importance due to its rare earth element content.

The presence of Monazite in both the Charnockite and Khondalite groups of rocks in the Malappuram district can be significant not only for geological studies but also for the potential extraction of valuable minerals. However, the mining and extraction of these minerals must adhere to environmental regulations and sustainable practices to mitigate potential negative impacts on the environment and local communities. Additionally, it is essential to note that geological conditions and mineral deposits may change over time, so up-to-date surveys and assessments are necessary for accurate information on the region's geology and mineral resources.

The Charnockite group of rocks and the Biotite Gneiss group are extensively distributed in the Western Ghats region, specifically in the southern part of Palakkad, which encompasses the central portion of Kerala state [65], [66]. The presence of Monazite in these formations has been already confirmed by previous studies [46], [49], [61], [67]–[69].

5.3.3 Activity concentration in NH-66 study sites.

The soil samples were coded as S_1 to S_{24} given in Table 5.7. Table 5.7 also presents the measured concentrations of natural radioactivity, specifically, ^{226}Ra, ^{232}Th, and ^{40}K in the soil samples collected from the study area. The specific activity of these radionuclides in the soil samples ranged from 15.33 ± 0.74 to 87.47 ± 6.35 Bqkg^{-1} for ^{226}Ra, 17.98 ± 0.86 to 132.87 ± 7.41 Bqkg^{-1} for ^{232}Th, and 336.48 ± 10.12 to 1478.36 ± 22.31 Bqkg^{-1} for ^{40}K.

On average, the activity concentrations (with standard variation) were found to be 39.88 ± 6.20 Bqkg^{-1} for ^{226}Ra, 61.19 ± 4.32 Bqkg^{-1} for ^{232}Th, and 815.51 ± 18 Bqkg^{-1} for ^{40}K in the soil samples from the study area. Distribution of the three radionuclides in the study area is shown in Figure 5.23 and 5.24 Notably, the highest

concentrations of Radium, Thorium, and Potassium were observed in sampling site S-22, which can be attributed to the presence of granitic rock with high radioactivity.

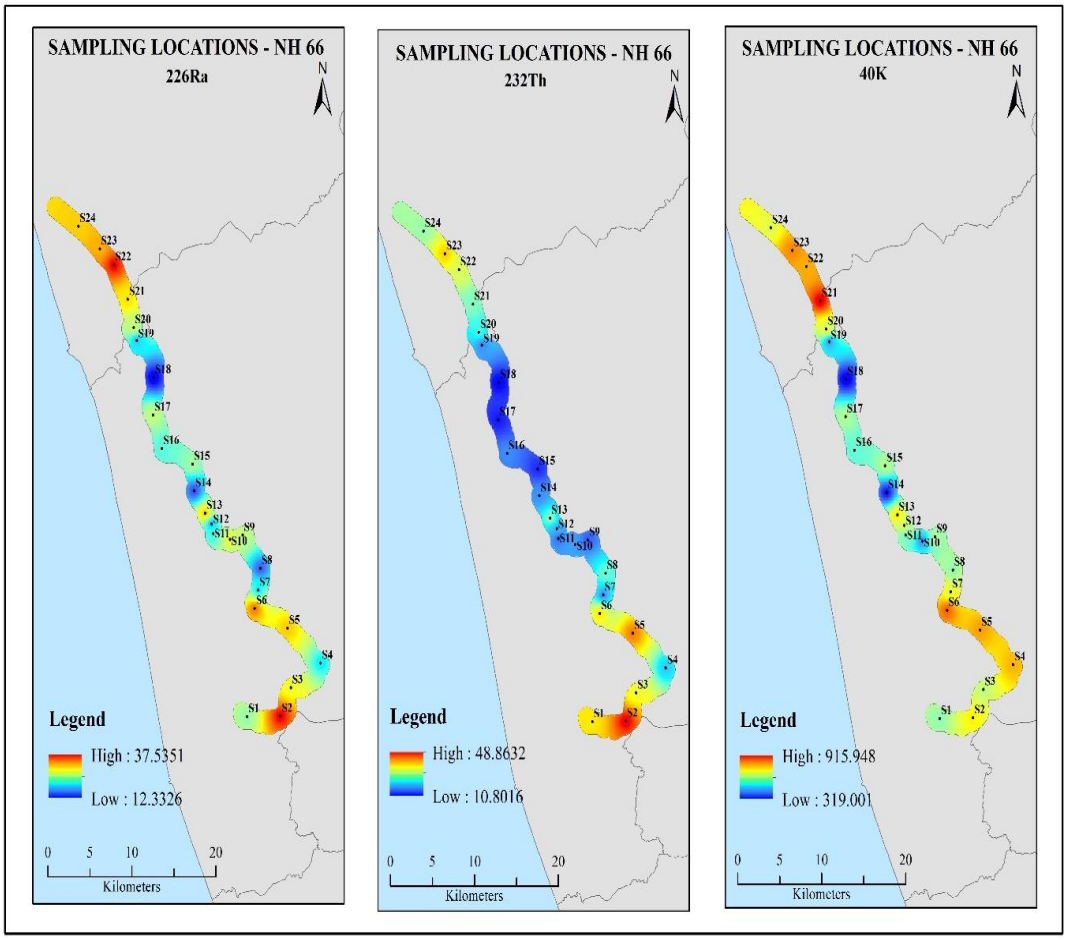

Figure 5.23: Contour distribution of the three radionuclides in the study area.

The activity concentrations of terrestrial radionuclides in soil are widely recognized to vary based on the geological composition of the region and the types of rocks involved in the soil formation. Additionally, factors such as soil type, geochemical structure, and human activities can also influence the levels of naturally occurring radionuclides in soil [52], [70].

Table 5.7: Activity concentrations of the three radionuclides measured from the study area.

Longitude	Latitude	Places	Code	Activity concentrations (Bq/kg)		
				^{226}Ra	^{232}Th	^{40}K
75.9943	10.8420	Ayankalam	S1	43.9±2.1	96.98±5.6	984.34±22
76.0300	10.8425	Kuttippuram	S2	57.54±2.6	68.87±3.2	715.25±20
76.0411	10.8670	Moodal	S3	28.42±2.2	34.46±2.1	628.21±18
76.0729	10.8882	Valanchery	S4	80.8±5.6	120.98±5.8	1172.68±12
76.0376	10.9181	Vattappara	S5	63.01±3.8	92.98±5.1	1090.35±23
76.0023	10.9351	Vettichira	S6	74.06±4.3	86.97±3.2	915.66±20
76.0060	10.9508	Puthananthani	S7	30.9±2.9	58.3±2.2	684.36±15
76.0085	10.9696	Randathani	S8	35.9±2.6	46.83±3.4	714.12±16
75.9894	10.9982	Kottakkal	S9	26.01±1.8	35.24±2.8	610.88±15
75.9759	10.9944	Edarikode	S10	68.33±3.1	88.94±5.4	1041.92±22
75.9579	10.9995	Kozhichena	S11	21.5±2.8	26.46±2.3	558.17±16
75.9563	11.0080	Pookiparambu	S12	19.27±2.4	29.87±2.5	664.37±12
75.9492	11.0171	Venniyoor	S13	31.01±2.8	27.49±2.1	728.48±20
75.9375	11.0362	Kakkad	S14	15.33±1.8	28.3±2.4	336.48±11
75.9359	11.0594	Kolappuram	S15	24.61±2.2	42.44±3.2	620.15±18
75.9030	11.0727	Thalappara	S16	22.23±2.1	17.98±1.8	554.1±15
75.8935	11.1016	Padikkal	S17	36.01±2.8	51.83±3.5	614.24±16
75.8942	11.1336	Thenhipalam	S18	42.33±2.6	100.8±6.6	1218.94±22
75.8761	11.1658	Idimuzhikkal	S19	29.48±3.1	57.98±2.5	658.24±18
75.8727	11.1767	Ramanattukara	S20	66.12±4.8	104.87±6.1	1084.68±22
75.8664	11.2010	Azhinjillam	S21	70.01±5.1	96.95±5.8	916.28±20
75.8516	11.2306	Panthiramkavu	S22	87.47±5.4	132.87±6.6	1478.36±22
75.8364	11.2444	Iringallor	S23	42.01±2.5	78.34±5.6	910.38±21
75.8134	11.2639	Thondayad	S24	30.77±2.6	27.87±2.6	671.25±22
Avearge				43.63	64.78	815.5
World permissible limit				35	30	340
Standard deviation				21.08	33.34	259.79

Basic statistical measures were employed to describe the properties of the radionuclides, encompassing average activity concentration, minimum, maximum, median and standard deviation. The statistical attributes of the soil sample data are summarized in Table 5.8 and Figure 5.25.

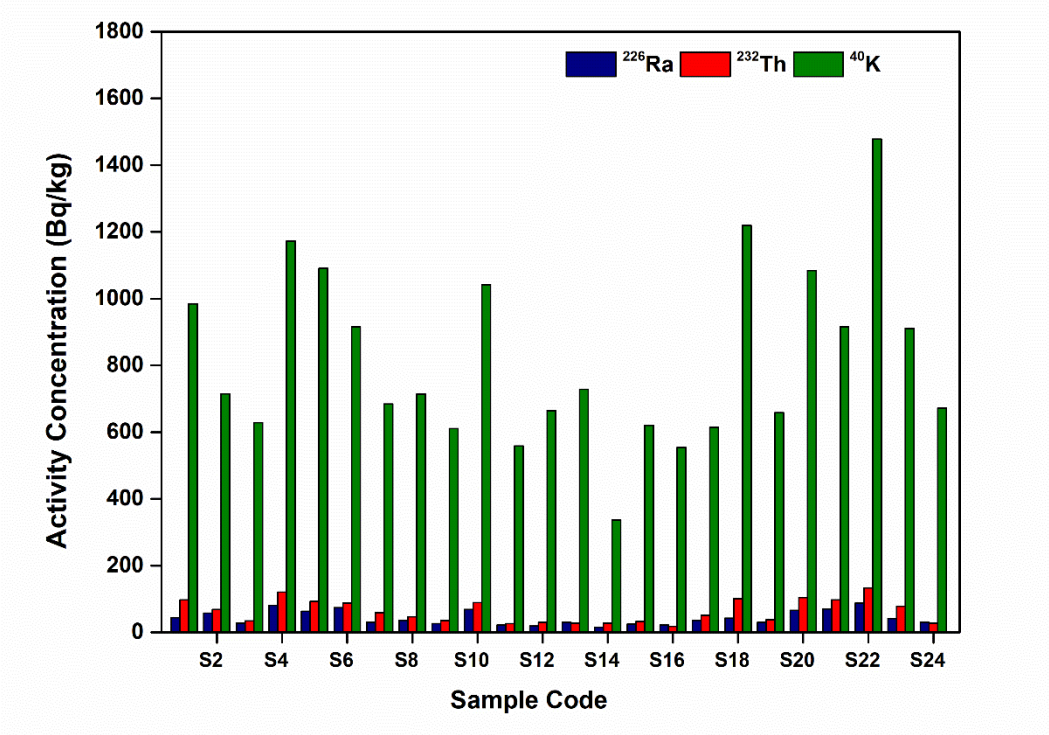

Figure. 5.24: Distribution of the three radionuclides in the study area.

Table 5.8: Statistical parameters of the activity concentration (Bq/kg) in samples.

Parameters	**^{226}Ra**	**^{232}Th**	**^{40}K**
Minimum	15.33	17.98	336.48
Maximum	87.47	132.87	1478.36
Mean	43.63	64.78	815.50
Median	35.96	58.14	714.69
Std Dev	21.08	33.34	259.79
Kurtosis	-0.91	-1.12	0.21
Variance	463.70	1159.70	70425.61
Skewness	0.64	0.36	0.69

The standard deviation values for ^{226}Ra, ^{232}Th, and ^{40}K are lower than their respective mean values, suggesting a high degree of uniformity among the samples in terms of their concentrations. The skewness values of ^{226}Ra, ^{232}Th and ^{40}K from the present study are 0.64, 0.36 and 0.69, respectively. Positive skewness values

indicate that the distribution of radionuclides are asymmetric, with a tail extending towards more positive values.

Kurtosis is a measure of the peakedness of the probability distribution of a real-valued random variable. The kurtosis values of ^{226}Ra, ^{232}Th and ^{40}K from the present study are, -0.91, -1.12 and 0.21, respectively. Negative kurtosis for ^{226}Ra and ^{232}Th indicates that a distribution has lighter tails and a flatter peak compared to a normal distribution. This implies that the data is more spread out and less concentrated around the mean. In the context of the concentration of various radionuclides in the soil samples, observing negative kurtoses for the radionuclides suggests that these two radionuclides exhibit extreme variations in concentration. Instead, their concentrations are relatively evenly distributed across the samples.

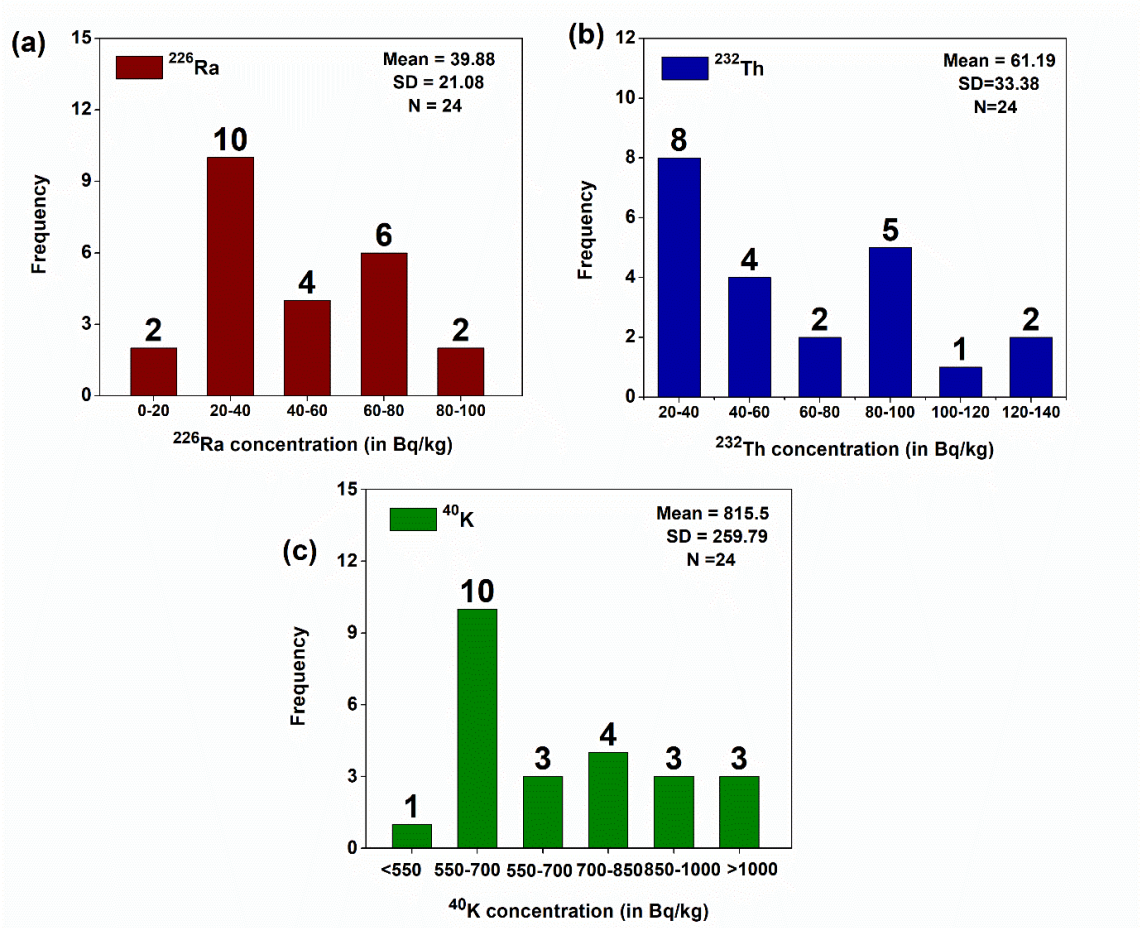

Figure 5.25: The frequency distribution of the activity concentration of ^{226}Ra, ^{232}Th and ^{40}K.

5.3.4 Radiological Parameters

The values of the Radium equivalent (Ra_{eq}) absorbed dose rate (D_{out}), annual effective dose rate (AED), hazard indices (H_{int} and H_{ext}), excess lifetime cancer risk (ELCR) and Alpha-gamma index (I_α and I_γ) obtained are shown in Table 5.9.

Table 5.9: The radiological health hazard indices of the surface soil samples.

Sample Code	Ra_{eq} (Bq/kg)	D_{out} (nGy/h)	AED_{ind} (mSv/y)	AED_{out} (mSv/y)	H_{ind}	H_{ext}	$ELCR_{ind}$ ($\times10^{-3}$)	$ELCR_{out}$ ($\times10^{-3}$)	I_γ	I_α
S1	258.38	119.90	0.59	0.15	0.70	0.82	2.35	0.59	0.96	0.22
S2	211.10	98.01	0.48	0.12	0.57	0.73	1.92	0.48	0.77	0.29
S3	126.07	60.14	0.30	0.07	0.34	0.42	1.18	0.29	0.48	0.14
S4	344.10	159.30	0.78	0.20	0.93	1.15	3.12	0.78	1.27	0.40
S5	279.93	130.74	0.64	0.16	0.76	0.93	2.56	0.64	1.04	0.32
S6	268.93	124.93	0.61	0.15	0.73	0.93	2.45	0.61	0.99	0.37
S7	166.96	78.03	0.38	0.10	0.45	0.53	1.53	0.38	0.62	0.15
S8	157.85	74.65	0.37	0.09	0.43	0.52	1.46	0.37	0.59	0.18
S9	123.44	58.78	0.29	0.07	0.33	0.40	1.15	0.29	0.47	0.13
S10	275.74	128.74	0.63	0.16	0.74	0.93	2.52	0.63	1.02	0.34
S11	102.32	49.19	0.24	0.06	0.28	0.33	0.96	0.24	0.39	0.11
S12	113.14	54.65	0.27	0.07	0.31	0.36	1.07	0.27	0.44	0.10
S13	126.41	61.31	0.30	0.08	0.34	0.43	1.20	0.30	0.48	0.16
S14	81.71	38.21	0.19	0.05	0.22	0.26	0.75	0.19	0.30	0.08
S15	133.05	62.86	0.31	0.08	0.36	0.43	1.23	0.31	0.50	0.12
S16	90.61	44.24	0.22	0.05	0.24	0.30	0.87	0.22	0.35	0.11
S17	157.42	73.56	0.36	0.09	0.43	0.52	1.44	0.36	0.58	0.18
S18	280.33	131.27	0.64	0.16	0.76	0.87	2.57	0.64	1.05	0.21
S19	163.08	76.09	0.37	0.09	0.44	0.52	1.49	0.37	0.61	0.15
S20	299.60	139.12	0.68	0.17	0.81	0.99	2.72	0.68	1.11	0.33
S21	279.20	129.11	0.63	0.16	0.75	0.94	2.53	0.63	1.02	0.35
S22	391.31	182.31	0.89	0.22	1.06	1.29	3.57	0.89	1.45	0.44
S23	224.14	104.69	0.51	0.13	0.61	0.72	2.05	0.51	0.84	0.21
S24	122.31	59.04	0.29	0.07	0.33	0.41	1.16	0.29	0.47	0.15
Mean	199.04	93.28	0.45	0.12	0.53	0.65	1.82	0.45	0.74	0.22
World Limit	370	59	0.07	0.40	1	1	1.45	0.29	1	1

Figures 5.26 and 5.27 illustrate the distribution of the radiological parameters Ra_{eq} and D_{out}. The estimated Radium equivalent activity (Ra_{eq}) in the study area ranged from 81.71 to 391.31 Bq/kg, with an average value of 199.04 Bq/kg, which is below the criterion limit of 370 Bq/kg. The absorbed dose rate (D_{out}) values ranged from 38.21 to 182.31 nGy/h, with an average of 93.29 nGy/h. This average value is higher than the worldwide average outdoor absorbed gamma dose rate of 59 nGy/h.

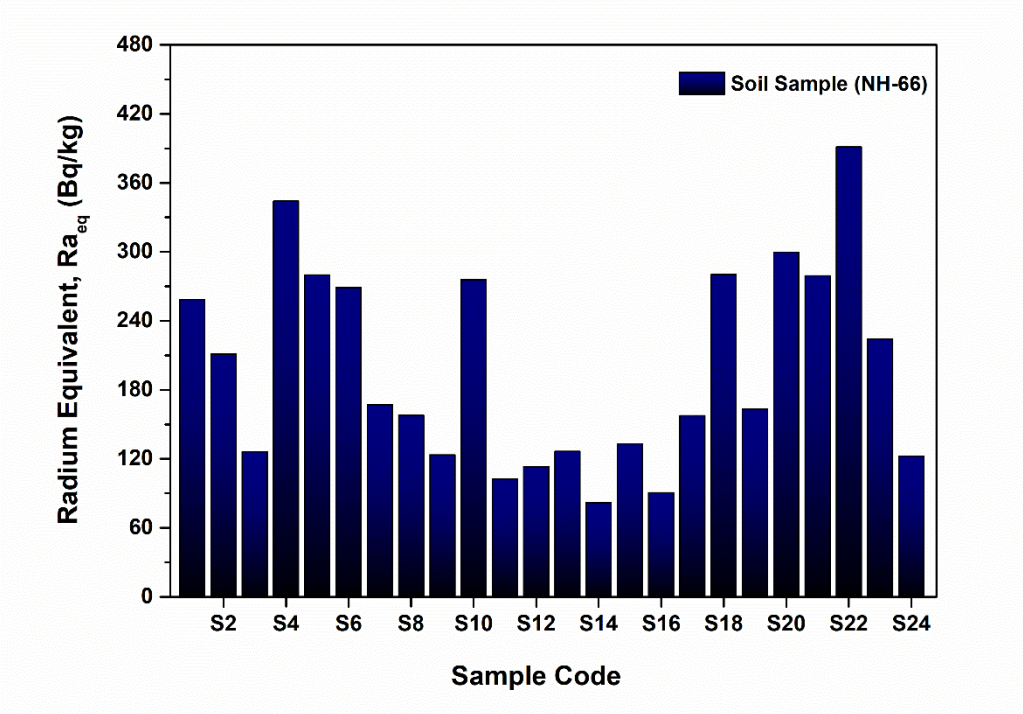

Figure 5.26: Distribution of the Ra_{eq} parameter in the study area.

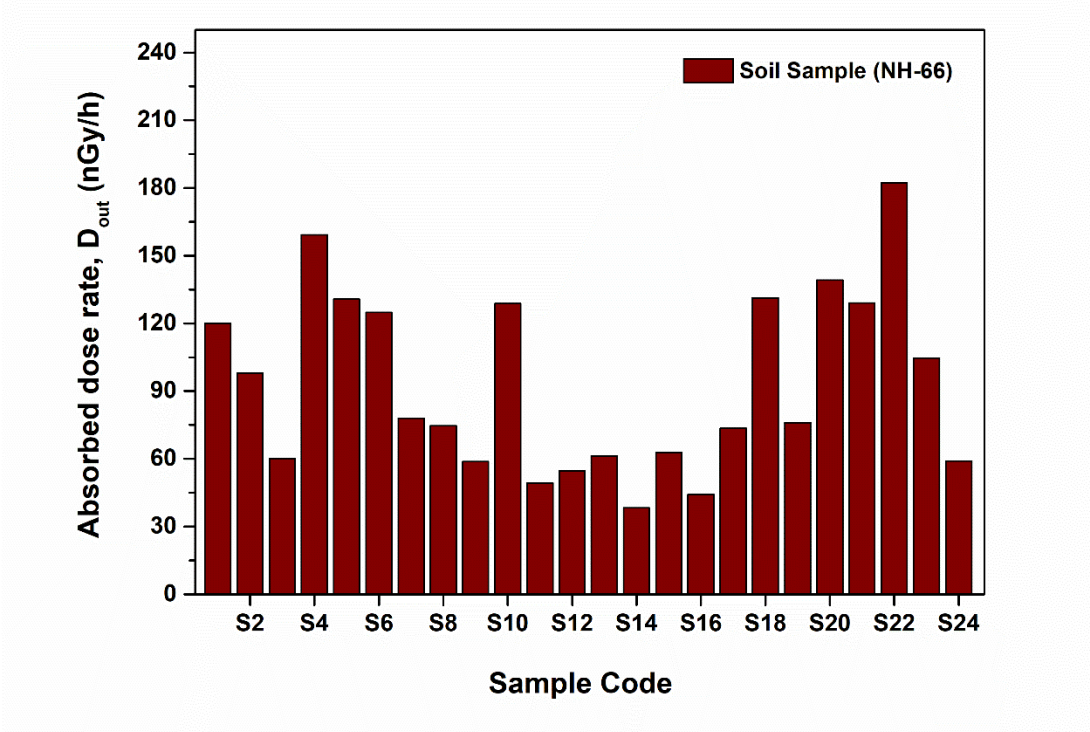

Figure 5.27: Distribution of the D_{out} parameter in the study area.

The correlation between the activity concentrations and absorbed dose rates D_{out} in

the soil samples is shown in Figure. 5.28 (a-d). Here, the regression was found to be linear and positive. A positive correlation coefficient (R^2) of 0.87, 0.97 and 0.90 between D_{out} and concentrations of ^{226}Ra, ^{232}Th and ^{40}K respectively was observed. Also, the correlation between D_{out} and Ra_{eq} is always prominent.

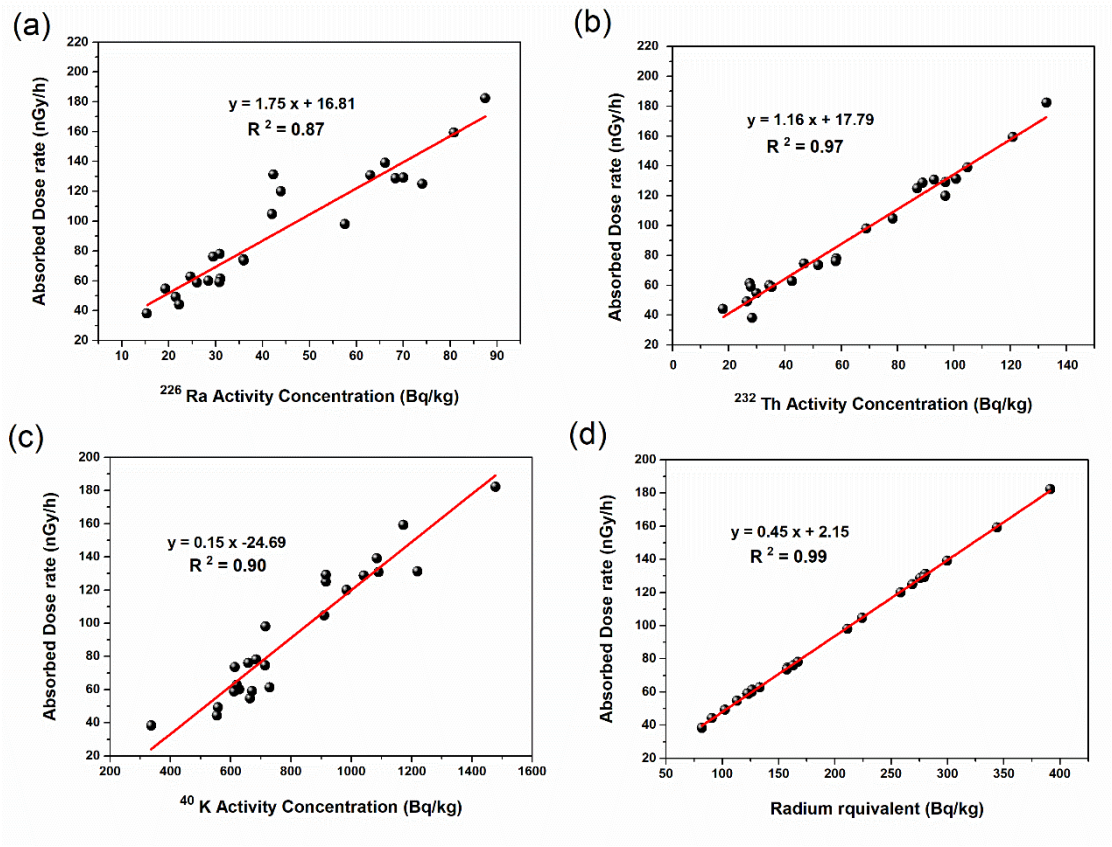

Figure 5.28: The correlation between the activity concentrations and absorbed dose rates.

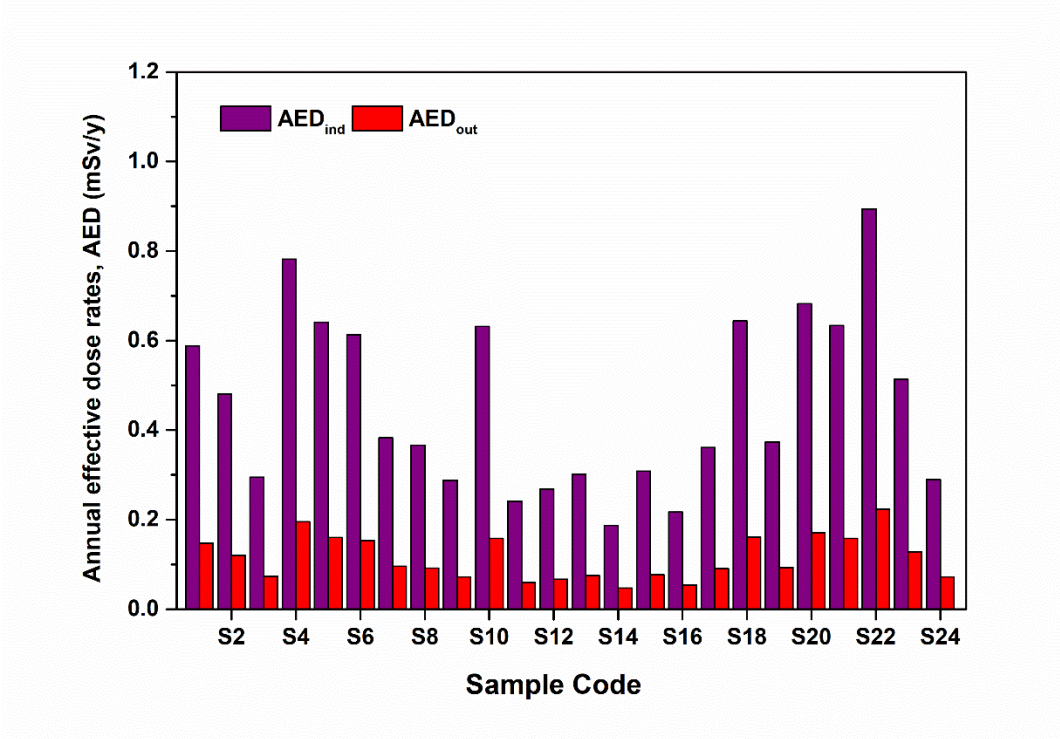

Figure 5.29: The distribution of the annual effective dose equivalent (AED) values.

Figure 5.29 illustrates the distribution of the annual effective dose equivalent (AED) values. The indoor annual effective dose equivalent (AED) values varied from 0.19 to 0.89 $mSvy^{-1}$, with an average of 0.46 $mSvy^{-1}$, which is slightly higher than the global average value of 0.07 $mSvy^{-1}$[52], [71]. In terms of outdoor annual effective dose equivalent (AED), values ranged from 0.05 to 0.22 mSv/y, averaging 0.11 mSv/y, which is lower than the global average value of 0.40 mSv/y. Figure 5.30 illustrates the distribution of the hazard indices (H_{int} and H_{ext}) in the study area. The calculated internal radiation hazard index (H_{int}) for the soil samples ranged from 0.22 to 1.06, with an average value of 0.53 and a geometric mean value of 0.65.These values, being less than 1, indicate that according to the report of Radiation Protection [55], there is no significant internal threat if construction materials are made from the soil of selected area of Malappuram district. Figure 5.30 illustrates the distribution of the hazard indices (H_{int} and H_{ext}) in the study area. The external hazard index (H_{ext}) due to ^{226}Ra, ^{232}Th, and ^{40}K in the soil of the study region ranged from 0.26 to 1.29, with a mean value of 0.65.

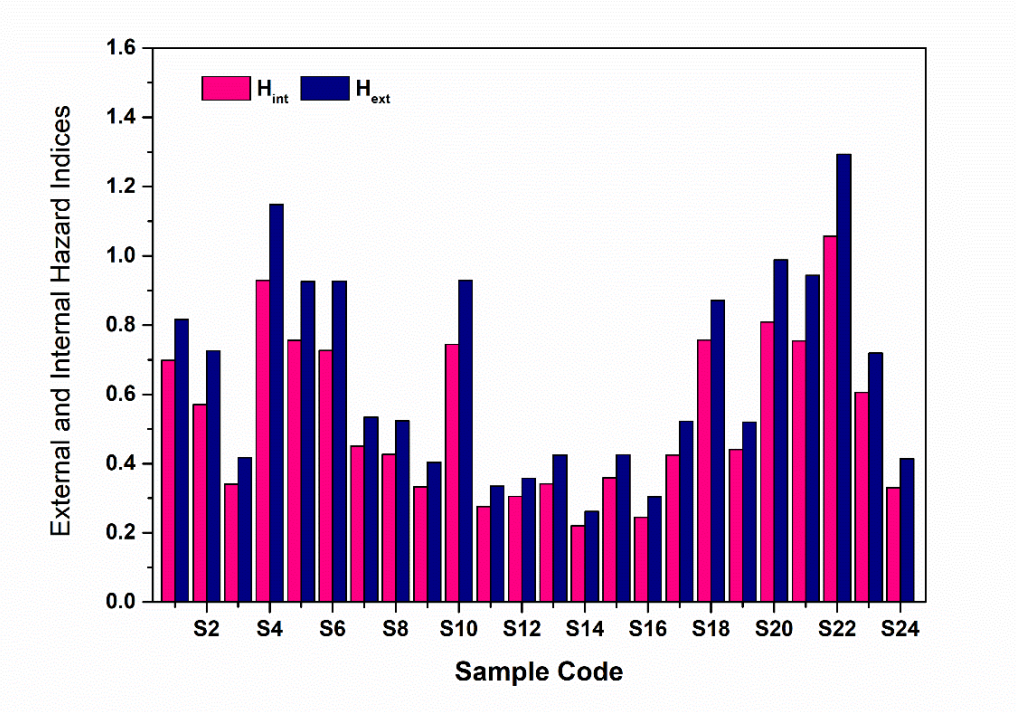

Figure 5.30: The distribution of the hazard indices (H_{int} and H_{ext}) in the study area.

The internal hazard index for all examined sites is determined to be less than 1.0 (except S-22), indicating that all values are below the recommended threshold (1.0). Consequently, it can be inferred from these findings that the naturally occurring radionuclides existing in the soil of the study region do not pose a notable internal radiation risk.

The overall radiological risk associated with the soil, considering the presence of ^{226}Ra, ^{232}Th, and ^{40}K, is assessed by the gamma index. In the soil samples, the gamma index ranged from 0.30 to 1.45, with an average value of 0.75. According to the European Commission's guidelines, a gamma index value of 1.0 is recommended to ensure minimal radiation hazards for the population, corresponding to an effective dose of 300 Sv/y. In the research region (except S-4, S-20 and S-22), the gamma index values are near to 1.0 or less than that, indicating that the soil poses no significant radiation concerns and is considered safe for the people.

Figure 5.31 illustrates the distribution of the excess lifetime cancer risk (ELCR) in the study area. The indoor excess lifetime cancer risk in the soil ranged from 0.75

$\times 10^{-3}$ to 3.57×10^{-3}, with a mean value of 1.83×10^{-3}. However, the global average value is 1.45×10^{-3}, indicating that the cancer risk in the study area is slightly higher than the global average.

The outdoor excess lifetime cancer risk in the soil ranged from 0.19×10^{-3} to 0.89×10^{-3}, with a mean value of 0.45×10^{-3}. So, comparing with the global average value is 0.29×10^{-3}, this indicating that the cancer risk in the study area is slightly higher than the global average[72]. Additionally, the excess lifetime cancer risk (ELCR) was estimated to quantify the risk of developing fatal cancer. The obtained values of ELCR exceeded acceptable limits in the study regions, indicating health risks to the residents of these areas [72].

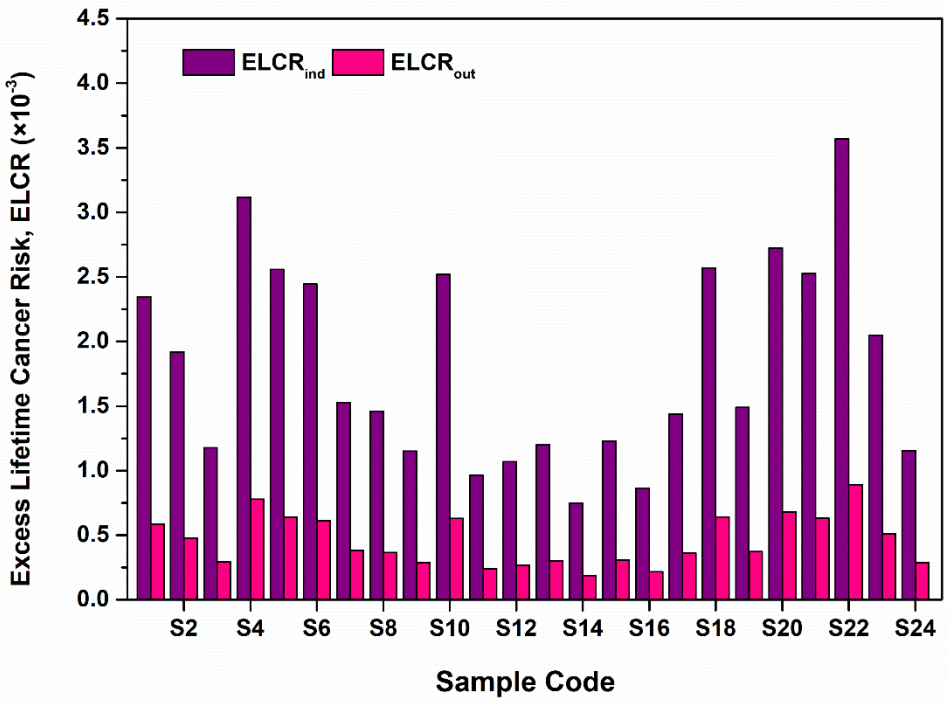

Figure 5.31: The distribution of the excess lifetime cancer risk (ELCR) in the study area.

5.3.5 XRD analysis and Mineral compositions

The mineralogical compositions of the soil samples were identified through X-ray diffraction analysis, and Figure 5.32 displays the results for one of the study areas (Azhinjillam).

The analysis revealed the presence of heavy minerals in the soil samples collected, indicating an enrichment of heavy minerals such as radioactive Monazites, Zircons, limonite, rutile, zeolites, and silimanite. Monazite minerals contain varying amounts of Thorium, Uranium, and rare earth oxides, which contribute to the elevated levels of natural radioactivity observed in the study area. Monazite, a rare mineral composed of Thorium oxide (7-10%), Uranium oxide (less than 0.5%), and rare earth oxides, is well-known for its significant contribution to the heightened natural radioactivity in this region [49], [67]. It is widely recognized that soil deposits containing Monazite and Zirconium play a significant role in the radioactivity levels in certain areas of Kerala and Tamil Nadu [49], [65]–[68], [73], [74]. The concentration of Thorium in Monazite placer deposits indeed varies depending on the type of rock from which the Monazite is derived.

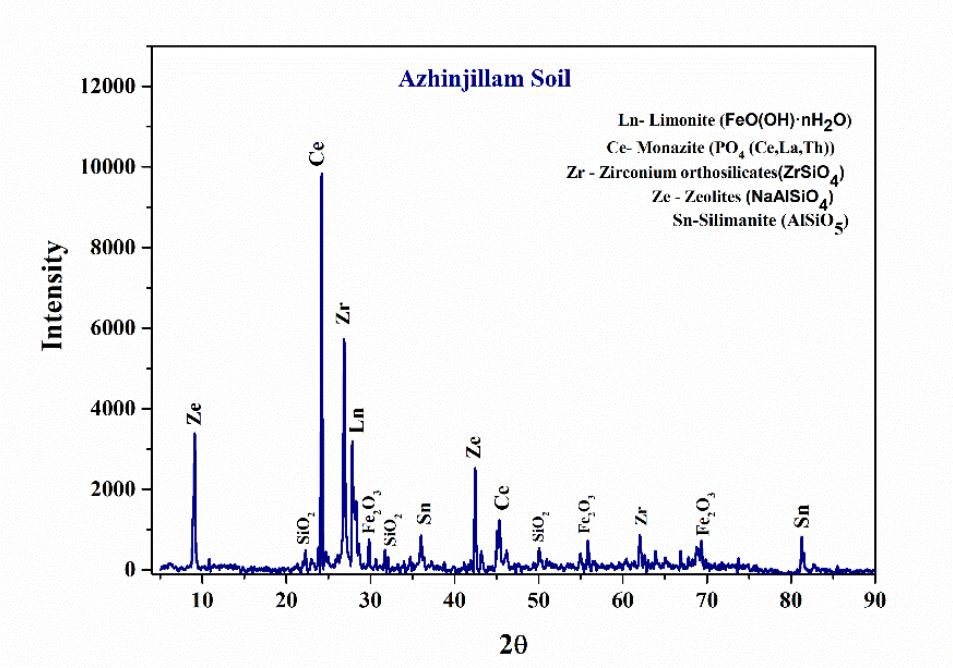

Figure 5.32: The XRD pattern of soil samples collected from Azhinjillam sampling site (sample S-21).

Monazite is typically found in association with various types of geological formations, and the Thorium content in Monazite can vary significantly based on its geological source. Different rock types and geological processes can lead to variations in the Thorium concentration within Monazite deposits, which in turn

affects the level of natural radioactivity in the surrounding soil and environment. This variation in Thorium concentration is an important consideration in assessing and managing the radiological impact of Monazite-rich deposits in specific locations [75].

5.3.6. Physico-chemical properties of soils

Table 5.10 presents a summary of the physical and chemical characteristics of the investigated soil samples. The pH values, which ranged from 6.18 to 9.08 with an average of 7.49, indicate that the soil samples are mildly alkaline. Electrical conductivity (EC), which measures the ability of a solution to conduct electric current, reflecting the level of dissolved salts, ranged from 37.70 to 253.70 scm^{-1} with an average of 100.73 scm^{-1}. Salinity values ranged from 12.38 to 54.12 ppm, with an average of 28.29 ppm.

Table 5.10: The physico-chemical properties of soils.

Characteristic	Minimum	Maximum	Mean	Std. Dev.
pH	6.18	9.08	7.49	0.76
Salinity	12.38	54.12	28.29	12.33
EC	37.70	253.70	100.73	57.61
% Clay	12.06	55.58	34.14	10.67
% Sand	19.65	62.25	39.28	11.41
% Silt	12.27	52.36	26.58	11.44

The soil samples exhibited significant variation in clay content and soil texture, as illustrated in the Ternary diagram shown in Figure 5.33.

The proportions of clay, silt, and sand in the study area are represented in the diagram. The texture of soil refers to the relative proportions of clay, silt, and sand, which influence various soil properties. Clay, with its large surface area, has a high capacity to absorb metals. Sand particles, found in sandy soils, enhance water permeability. Silt particles have intermediate granulometry and contribute to the overall soil texture. The determination of soil texture was carried out using

densitometry. The majority of the samples were categorized as clay, while the urban and industrial soil samples exhibited a range of textures from clayey to loamy sand. The texture of urban and industrial soils is significantly influenced by industrialization, urbanization, transportation, and particle mixing. The correlation coefficients (R) between natural radioactivity levels observed in the sediments and physico-chemical parameters are presented in Table 5.11.

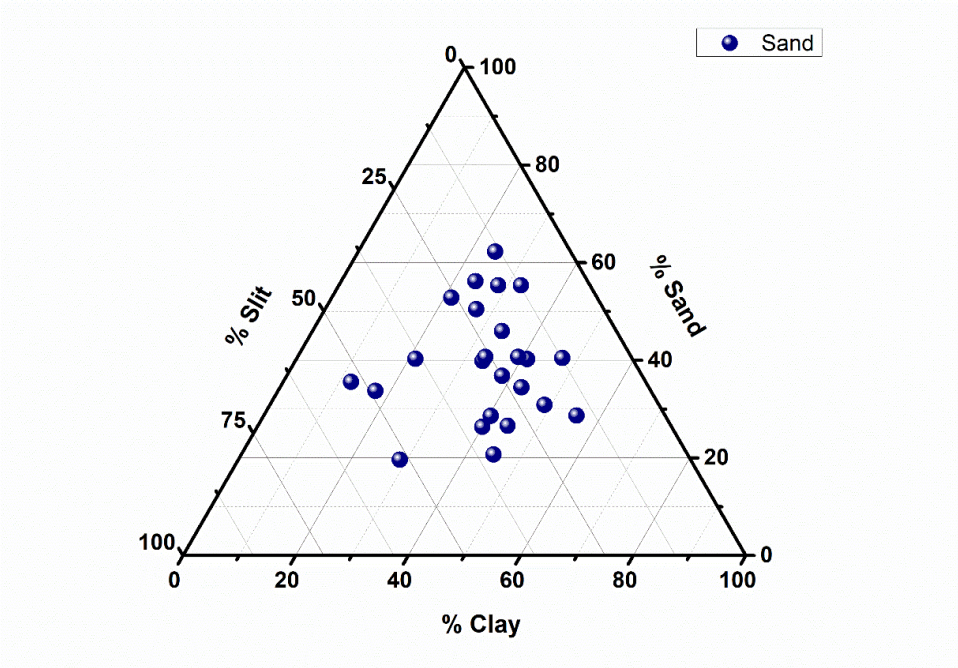

Figure 5.33: Ternary diagram showing the proportion of clay, silt, and sand of the sampling area.

Table 5.11: Correlation matrix between the radionuclides and physico-chemical parameters.

	^{226}Ra	^{232}Th	^{40}K	Ra_{eq}	D_{out}	pH	Salinity	EC	%Clay	%Sand	%Silt
^{226}Ra	1.00										
^{232}Th	0.91	1.00									
^{40}K	0.84	0.93	1.00								
Ra_{eq}	0.94	0.99	0.95	1.00							
D_{out}	0.93	0.99	0.95	1.00	1.00						
pH	0.68	0.68	0.65	0.69	0.69	1.00					
Salinity	0.42	0.34	0.37	0.38	0.38	0.35	1.00				
EC	0.16	0.17	0.19	0.17	0.17	-0.19	-0.04	1.00			
%Clay	-0.02	0.07	0.12	0.06	0.06	-0.04	-0.42	-0.26	-0.47		
%Sand	0.21	0.14	0.17	0.17	0.16	0.32	0.32	0.38	-0.47	1.00	
%Silt	-0.19	-0.19	-0.26	-0.22	-0.22	-0.28	0.06	-0.08	-0.47	-0.56	1.00

A Pearson correlation analysis was conducted to explore the relationships among radionuclide concentrations, radiological parameters, and physico-chemical properties in the sediment samples. This statistical method allows scientists to quantitatively assess the strength and direction of linear relationships between these variables. A positive correlation coefficient indicates a direct linear relationship, suggesting that as one variable increases, the other tends to increase as well. Conversely, a negative correlation coefficient signifies an inverse linear relationship, where an increase in one variable corresponds to a decrease in the other. A correlation coefficient near zero indicates a weak or negligible linear relationship between the variables. The Pearson correlation coefficient ranges from -1 to +1, where +1 denotes a perfect positive correlation, -1 represents a perfect negative correlation, and 0 indicates no linear correlation. In this study, the concentrations of natural Uranium and Thorium isotopes demonstrated a robust positive relationship, with correlation coefficients surpassing 0.9. Likewise, there was a positive correlation between ^{40}K and the concentrations of Uranium and Thorium (with correlation coefficients of 0.843 and 0.925, respectively). Furthermore, ^{226}Ra, ^{232}Th, and ^{40}K demonstrated a significant relationship with soil pH and a moderate association with soil electrical conductivity (EC). Consequently, the absorbed dose rate resulting from natural radionuclides in the soil is minimally influenced by soil conductivity and texture.

5.3.7 Elemental concentration of radionuclides and Radiogenic Heat Production (RHP) in NH-66 Zone.

The elemental concentrations of ^{238}U in ppm, ^{232}Th in ppm and ^{40}K in % and radiogenic heat production (RHP) in μWm^{-3} of the rock samples collected from NH-66 highway zone, Kerala were calculated and tabulated in Table 5.12. The elemental concentrations of ^{238}U in ppm, ^{232}Th in ppm and ^{40}K in % shown in Figure 5.34, 5.35 and 5.37 respectively.

Table 5.12: The elemental concentrations, radiogenic heat production (RHP) and Heat flow (H_f) of the soil samples.

Place Name	Place Code	Concentration of radionuclides			RHP ($\mu W/m^3$)	H_f ($\mu W/m^2$)
		^{238}U (ppm)	^{232}Th(ppm)	^{40}K (%)		
Ayankalam	S1	3.55	23.89	3.14	1.10	24.67
Kuttippuram	S2	4.66	16.96	2.29	0.86	17.92
Moodal	S3	2.30	8.49	2.01	0.44	15.74
Valanchery	S4	6.54	29.80	3.75	1.45	29.38
Vattappara	S5	5.10	22.90	3.48	1.13	27.32
Vettichira	S6	6.00	21.42	2.93	1.09	22.94
Puthananthani	S7	2.50	14.36	2.19	0.68	17.15
Randathani	S8	2.91	11.53	2.28	0.59	17.89
Kottakkal	S9	2.11	8.68	1.95	0.44	15.31
Edarikode	S10	5.53	21.91	3.33	1.10	26.11
Kozhichena	S11	1.74	6.52	1.78	0.35	13.99
Pookiparambu	S12	1.56	7.36	2.12	0.38	16.65
Venniyoor	S13	2.51	6.77	2.33	0.39	18.25
Kakkad	S14	1.24	6.97	1.08	0.33	8.43
Kolappuram	S15	1.99	10.45	1.98	0.51	15.54
Thalappara	S16	1.80	4.43	1.77	0.27	13.88
Padikkal	S17	2.92	12.77	1.96	0.63	15.39
Thenhipalam	S18	3.43	24.83	3.89	1.15	30.54
Idimuzhikkal	S19	2.39	14.28	2.10	0.67	16.49
Ramanattukara	S20	5.35	25.83	3.47	1.25	27.18
Azhinjillam	S21	5.67	23.88	2.93	1.17	22.96
Panthiramkavu	S22	7.08	32.73	4.72	1.60	37.04
Iringallor	S23	3.40	19.30	2.91	0.92	22.81
Thondayad	S24	2.49	6.86	2.14	0.39	16.82

The elemental concentration of Uranium varies from 1.24 to 7.08 ppm with an average of 3.53 ppm. The highest elemental concentration of ^{238}U was observed in Panthiramkavu (7.08 ppm). Very low elemental concentration was observed in Kakkad (1.24 ppm).

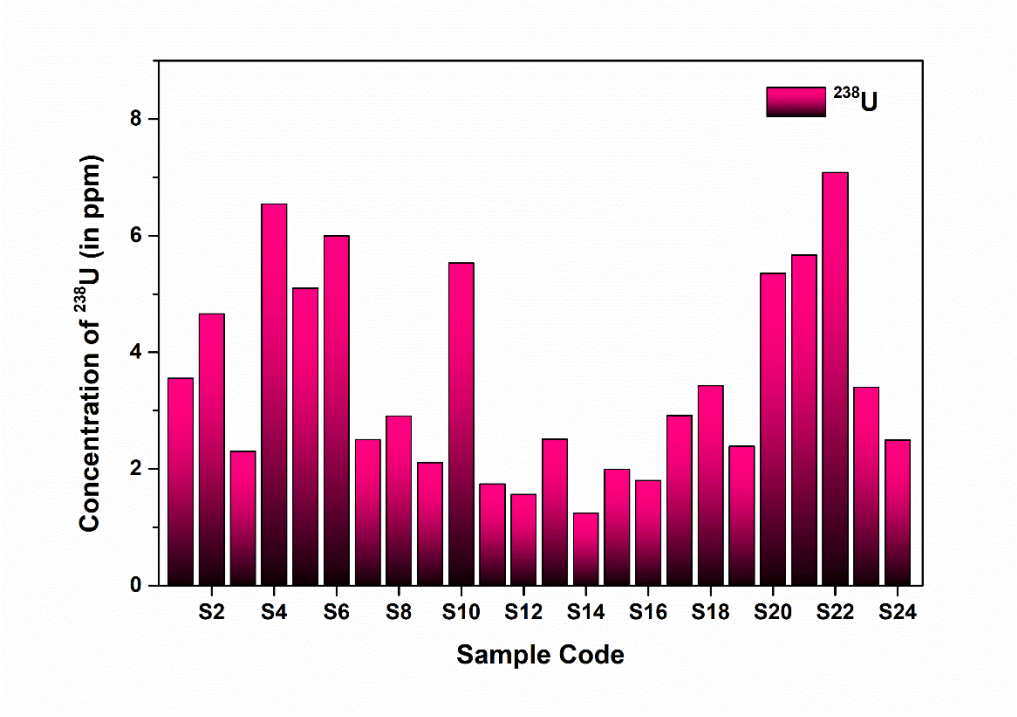

Figure 5.34: The elemental concentrations of ^{238}U (in ppm).

The elemental concentration of ^{232}Th ranged from 4.43 ppm to 32.73 ppm with an average of 15.95 ppm. The highest was observed in Panthiramkavu (32.73 ppm). The other locations also have some higher amount of concentration. Very low elemental concentration was observed in Thalappara (4.43 ppm).

The elemental concentration of ^{40}K ranged from 1.08% to 4.72% with an average of 2.61%. The highest elemental concentration of ^{40}K was observed in Panthiramkavu (4.72 %). Very low elemental concentration was observed in Kakkad (2.44 %). Figure 5.37 represents the condour representation of Radiogenic heat and Heat flow of the study region.

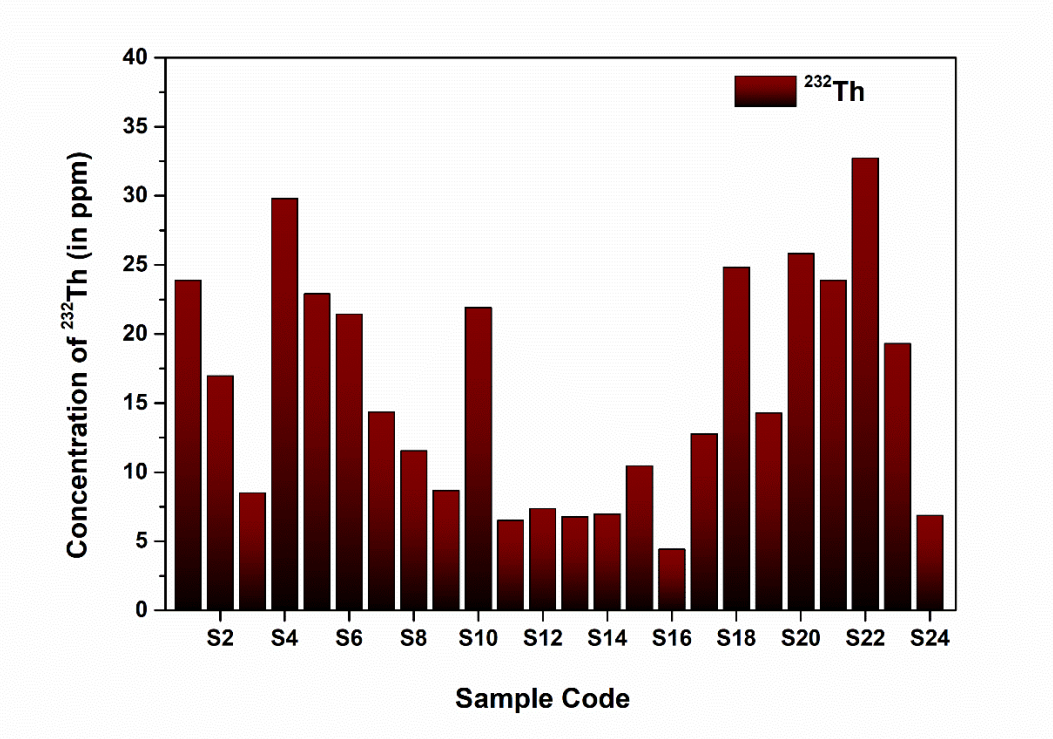

Figure 5.35: The elemental concentrations of ^{232}Th (in ppm).

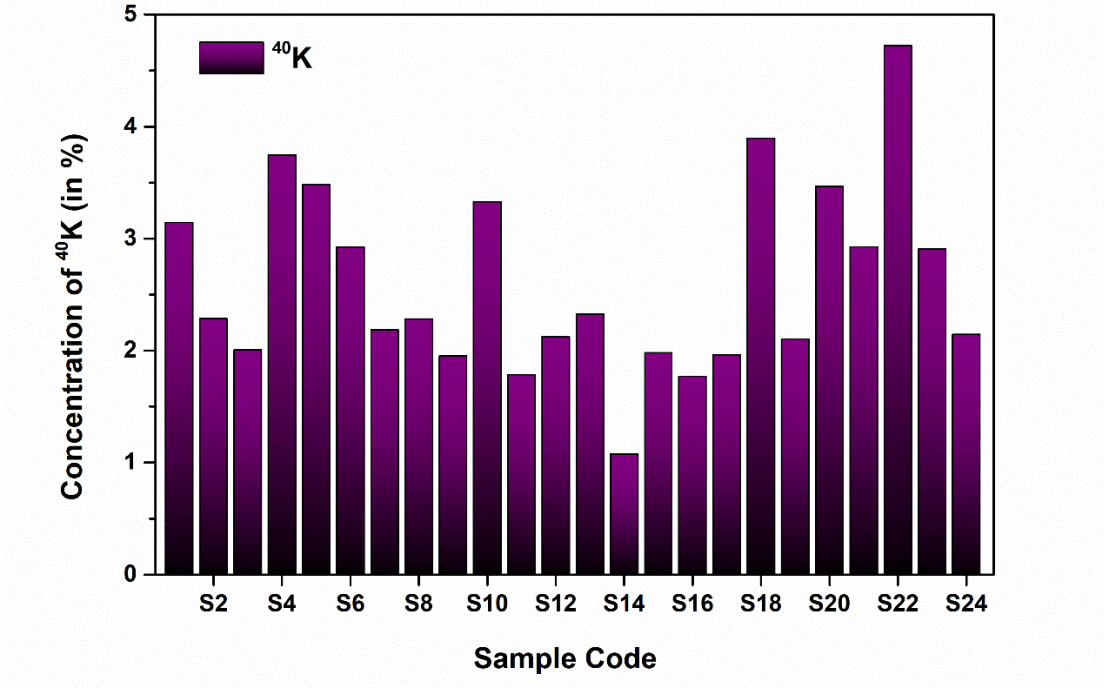

Figure 5.36: The elemental concentrations of ^{40}K (in %).

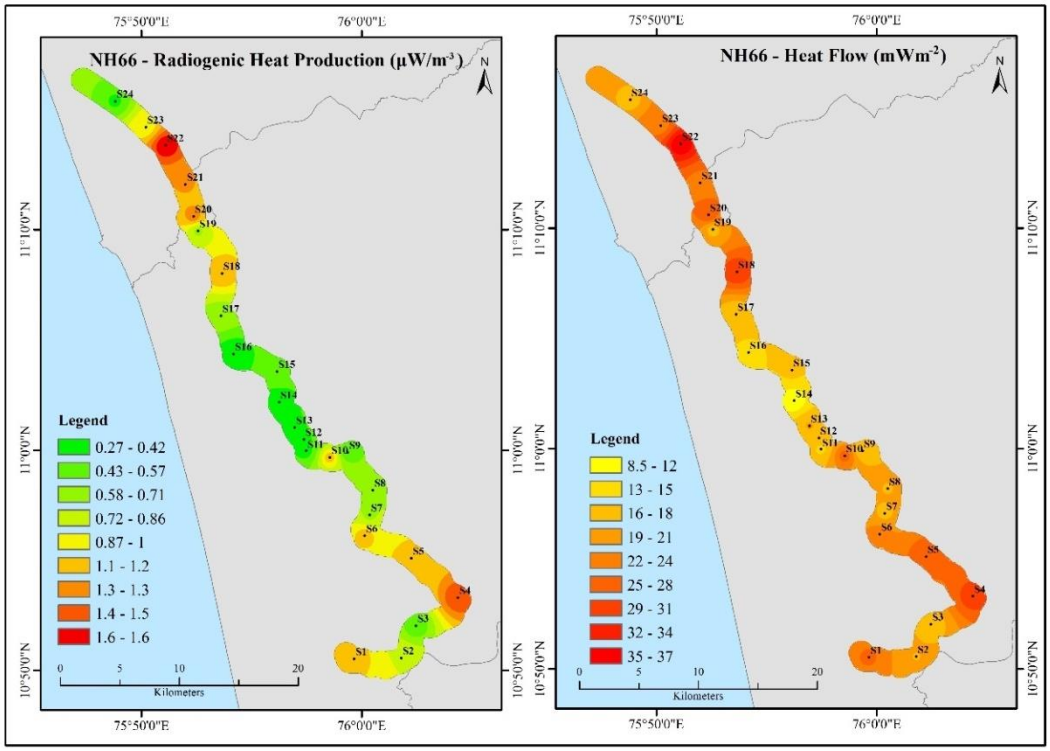

Figure 5.37: The contour representation of Radiogenic heat and Heat flow of the study region.

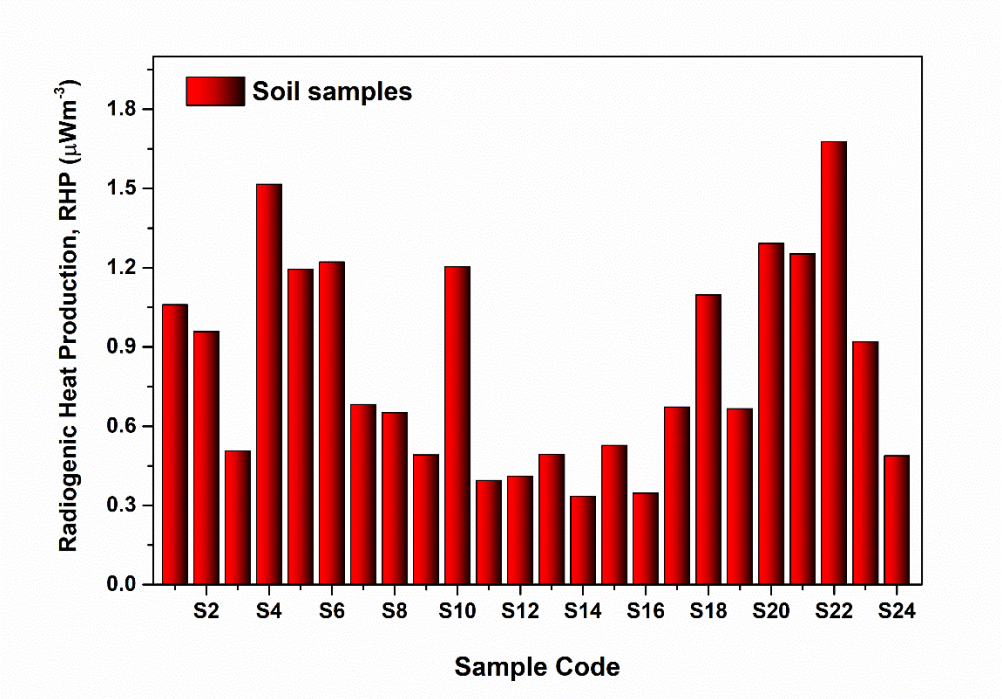

Figure 5.38: Radiogenic heat production in NH-66 highway study region.

The radiogenic heat production in the soil samples collected in zone-2 was found to varied from 0.27 to 1.60 μW/m^3 with an average of 0.79 μW/m^3 shown in Figure 5.38. RHP value is found to be highest in Panthiramkavu (1.60 μW/m^3) and samples from Thalappara shown lower radiogenic heat production, which is, 0.27 μW/m^3). The RHP weighted mean 0.79 μW/m^3 compared to the earth's crust mean between 0.8 and 1.2 μW/m^3 was lower due to significant presence of gneiss rocks and soil in all the studied profiles.

5.3.8 Correlation between radionuclides and Radiogenic Heat Production (RHP) for studied region.

In order to determine the existing ratio between the elemental concentrations of ^{238}U, ^{232}Th and ^{40}K in the rock samples, correlations between them were drawn using origin. Figure 5.39 (a-c) show the correlations between the elemental concentrations of ^{238}U, ^{232}Th and ^{40}K, respectively, with a trend line drawn among the data points.

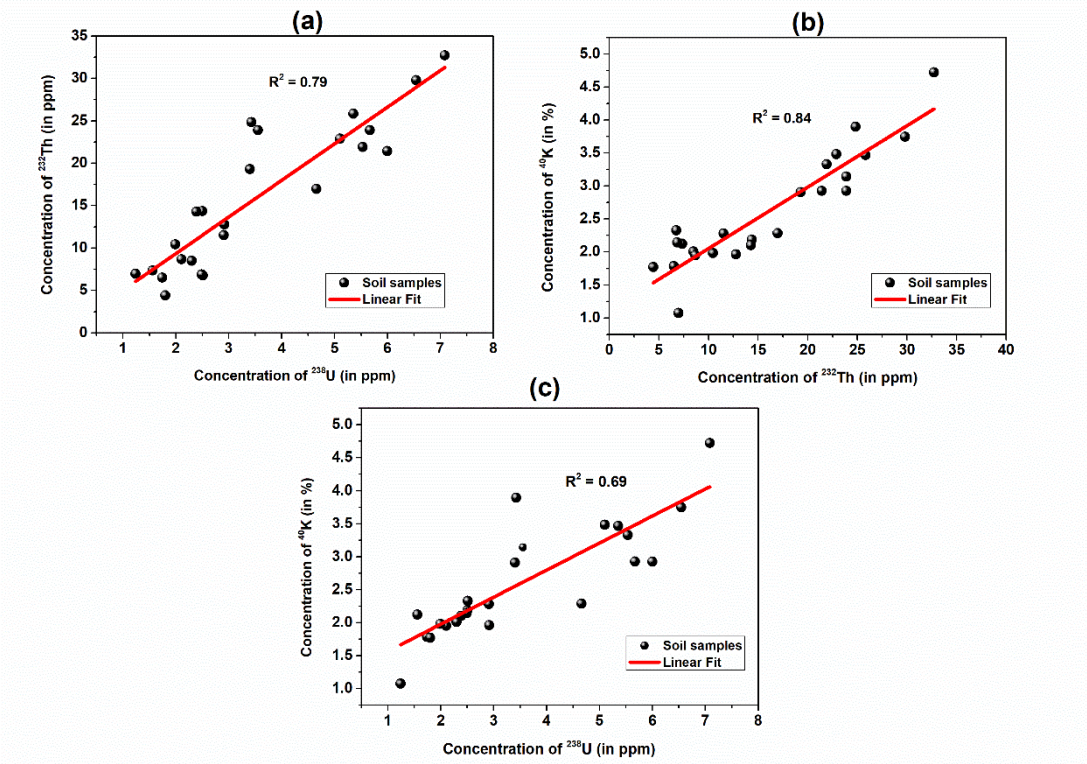

Figure 5.39: Correlation between radionuclides for studied region.

In Figure 5.39 (a – c), linear and positive correlations were found. It can be seen that there is a good correlation between ^{232}Th and ^{238}U with correlation coefficient of (R^2 = 0.79). The relation shows a slope of 3.689 with intercept 13.69 ppm. Similarly, Figure 5.39 (b) show a positive correlation coefficient of (R^2 = 0.84) slope of 0.02922 with intercept of 0.1679% while Figure 5.39 (c) has R^2 = 0.69 and 0.5435% as slope and intercept, respectively. However, as is argued later in this paper, the most striking fact that there is consistent correlations were observed between ^{40}K and ^{232}Th, and between ^{40}K and ^{238}U with weak correlation coefficients of (R^2 = 0.84) and (R^2 = 0.69), respectively.

Now Figure 5.40 (a-c) shows correlations among radiogenic heat and ^{238}U ^{232}Th, and ^{40}K. From 5.40 (a), it is found that radiogenic heat produced in the study area have a low dependence with ^{40}K concentration (R^2 = 0.19). Also, it is observed that, ^{238}U concentration is the dominant producer of RHP, having R^2 = 0.84 and ^{238}Th concentration have moderate correlation with RHP (R^2 = 0.69).

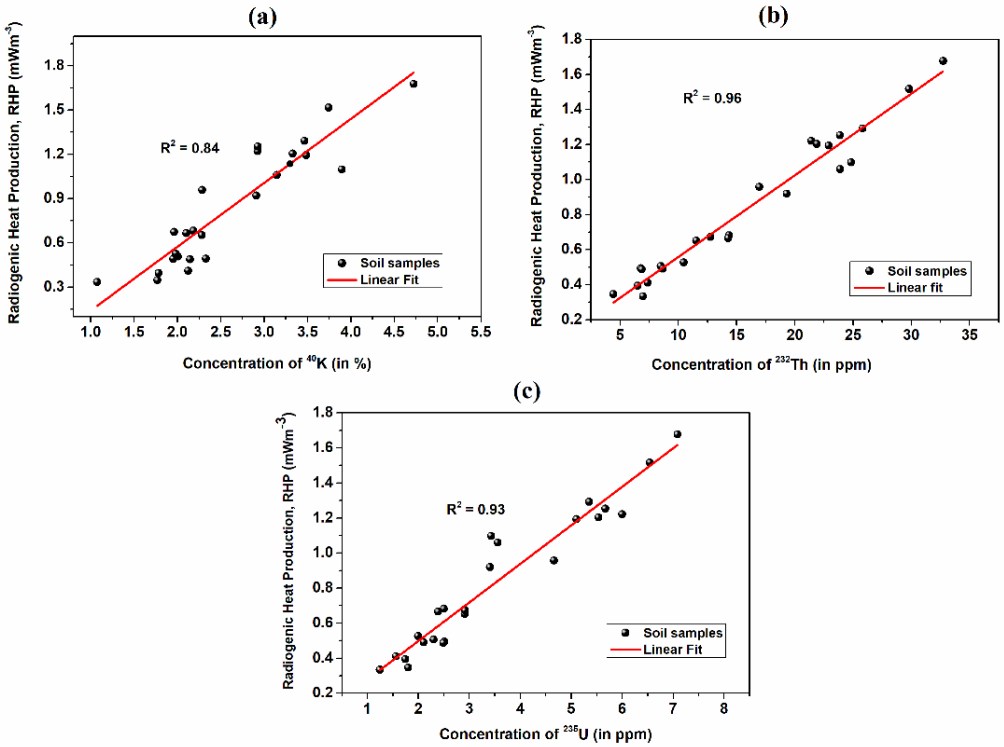

Figure 5.40: Correlation between concentration of radionuclides and Radiogenic Heat Production (RHP) and for studied region.

The value H_f in the sampled points due to the decay of ^{238}U, ^{232}Th and ^{40}K as determined from the values of RHP. The H_f in the samples due to the decay of ^{238}U, ^{232}Th and ^{40}K varied from (8.43± 1.0 – 37.04 ± 4.0) mWm^{-2} with average of 20.43± 1.8 mWm^{-2}. This average H_f is slightly higher than 21.6 mWm^{-2} reported by Asere and colleagues for quarry sites in Ondo State, Nigeria but less than the global value of 37 mWm^{-2} stated by Turcotte & Schubert for inactive regions[26], [39].

Figure 5.41 illustrates a plot of total RHP and H_f producing a linear distribution segment with strong correlation coefficient of R^2 = 0.85. The linear regression through the data points gives a slope of 15.64 and vertical axis intercept of 8.11 mW m^{-2}. As expected, RHP in the samples produced a significantly greater effect on H_f. The H_f values reflect the high RHP due to decay of ^{238}U, ^{232}Th and ^{40}K in the study area, indicating feasibility for geothermal exploration. This agrees with the findings of Turcotte & Schubert for stable continental areas, where the H_f had a strong correlation with the surface RHP. Hence, this research shows that the study area is in more thermally quiescent regions.

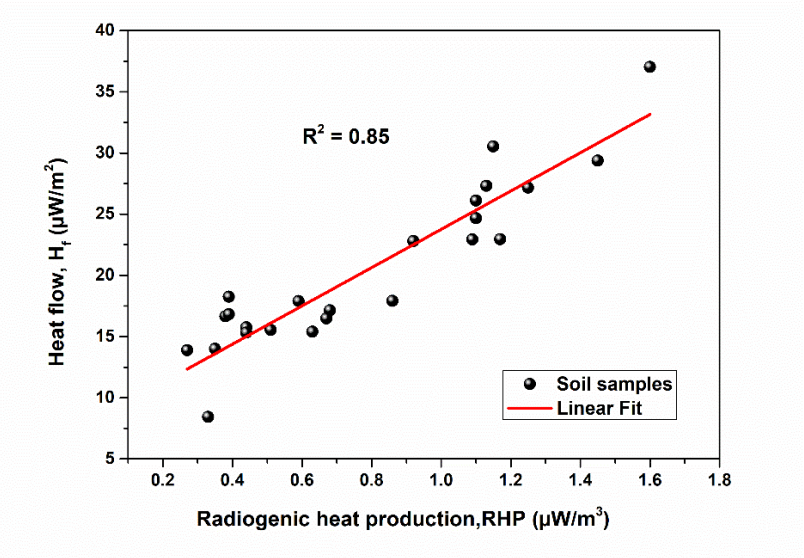

Figure 5.41: Correlation between concentration of heat flow and Radiogenic Heat Production (RHP) and for studied region.

5.3.9. Conclusion

In this study, gamma-ray spectrometry was utilized to measure the concentrations of naturally occurring radionuclides (^{226}Ra, ^{232}Th, and ^{40}K) at 24 soil sampling sites located along National Highway along the NH-66 in Kerala state, India. These sampling sites spanned 78 km between the Kozhikode and Malappuram districts. The results revealed that in urban soil, the activity concentrations of natural radionuclides followed the order of ^{40}K > ^{232}Th > ^{226}Ra. The calculated radiological hazard parameters were found to be either equal to or lower than the global average or the relevant safety criteria. Furthermore, the fundamental physico-chemical properties of the soil, including its texture (represented by the proportions of sand, silt, and clay), pH, electrical conductivity, and salinity, were assessed. The results of the multivariate statistical analysis revealed that the natural radioactivity and radiological attributes in the study area had a negligible influence on the physico-chemical parameters of the soil. All the computed values for the radioactive indices were below the global average thresholds set by radiation monitoring organizations. The overall average elemental and activity concentrations of basement rocks are 3.53 ppm, 15.95 ppm and 2.61% for ^{226}Ra, ^{232}Th and ^{40}K, respectively. The observed RHP rates for the studied rocks are in the mean value of 0.27 to 1.60 W/m^3, with average of 0.79 W/m^3 which is above the world average 0.8–1.2 W/m^3.

5.4. Athirappilly Waterfalls (Athirappilly Hills, part of Western Ghats in Kerala)- Region III.

5.4.1 About the study region

Athirappilly and Vazhachal Falls are two magnificent waterfalls located in the Indian state of Kerala. These waterfalls are nestled in the verdant Western Ghats, a UNESCO World Heritage Site renowned for its biodiversity and natural beauty. Let's explore the geography of Athirappilly and Vazhachal Falls in more detail. Athirappilly Falls, often referred to as the "Niagara of India," is situated on the Chalakudy River. It is located about 63 kilometers (39 miles) northeast of Kochi, one of Kerala's major cities. The falls originate from the Anamudi mountain range,

which is the highest peak in South India. The Chalakudy River, originating from the Anamudi, cascades down a rocky terrain to form the breathtaking Athirappilly Falls. The falls plunge from a height of approximately 24 meters (80 feet) and span a width of 140 meters (460 feet), holds the distinction of being the largest waterfall in Kerala. Situated just a brief drive away from Athirapilly is the Vazhachal Falls, nestled amidst lush green forests. These forests are not only a scenic marvel but also serve as habitats for numerous endangered and endemic species of flora and fauna.

Vazhachal Falls is situated a short distance downstream from Athirappilly Falls. It is also a part of the Chalakudy River and is located in the Athirappilly Panchayat. Vazhachal Falls is slightly smaller than Athirappilly Falls, with a height of around 15 meters (50 feet). However, it compensates for its size with its picturesque beauty and lush surroundings. The falls are surrounded by dense tropical forests, making it a haven for biodiversity. The region surrounding Athirappilly and Vazhachal Falls is known for its rich biodiversity and tropical rainforests. These falls are located in the Sholayar Range, which is part of the Western Ghats. The Western Ghats are a mountain range that runs parallel to the western coast of India, stretching over six states. They are recognized as one of the world's eight "hottest hotspots" of biological diversity and are home to numerous endemic species. In recent years, there have been debates regarding the development of hydroelectric projects in the region, raising concerns about the potential impact on the delicate ecosystem. Efforts are being made by various stakeholders to strike a balance between development and conservation, ensuring the sustainable management of these natural wonders for future generations to enjoy.

5.4.2. Mineralogy and Rock systems

Athirappilly and Vazhachal Falls, located in the Western Ghats of Kerala, India, are known for their natural beauty and lush surroundings. While the falls themselves are primarily composed of flowing water and rocky terrain, the region surrounding them exhibits interesting rock systems and a diverse array of minerals. Geologically, the Athirappilly-Vazhachal region falls within the Western Ghats, which is characterized by ancient rock formations. The Western Ghats are composed of

several rock types, including granites, gneisses, charnockites, and schists. These rocks have undergone millions of years of geological processes, including weathering, erosion, and metamorphism, resulting in their current composition and structure. Figure 5.42 showing the map of geological formation and rock constituent of the sampling stations.

Granite is a prevalent rock type in the Athirappilly-Vazhachal area. It is an igneous rock formed from the slow cooling and solidification of molten magma beneath the Earth's surface. Granite is characterized by its coarse-grained texture and is primarily composed of minerals such as quartz, feldspar, and mica. It often appears in shades of gray, pink, or white. The durability and resistance of granite make it an essential component of the rocky terrain surrounding the waterfalls. Gneiss is a metamorphic rock commonly found in the Western Ghats, including the Athirappilly-Vazhachal region. It is formed from the recrystallization of pre-existing rocks, such as granite, under high pressure and temperature. Gneiss exhibits a banded or layered appearance due to the segregation of different mineral layers during metamorphism. It can display a variety of colours, including gray, pink, and green. The presence of gneiss adds to the geological diversity and aesthetic appeal of the area. Charnockite is another rock type found in the Athirappilly-Vazhachal region. It is a type of granitic rock composed mainly of orthopyroxene, quartz, and feldspar. Charnockite is known for its characteristic reddish-brown colour, imparted by the presence of iron oxide minerals. This rock type contributes to the unique visual appeal of the area's landscape. Schist: Schist is a metamorphic rock that can also be found in the region surrounding the waterfalls. It is formed through the metamorphosis of pre-existing rocks, such as shale or clay. Schist exhibits a foliated texture, with its minerals aligned in distinct layers or bands. The minerals in schist can vary, but common ones include mica, quartz, and feldspar. Schist adds further geological interest and texture to the rocky formations around Athirappilly and Vazhachal.

These rock types play a crucial role in the formation and stability of the Athirappilly and Vazhachal Falls. The granite, gneiss, charnockite, and schist in the area contribute to the rocky cliffs, channels, and cascades that shape the waterfalls' appearance. The interplay between the different rock types creates a visually

captivating and dynamic landscape. The specific combination of rock types in the Athirappilly-Vazhachal area contributes to its unique geological and scenic features, attracting visitors from far and wide to witness the beauty of these waterfalls.

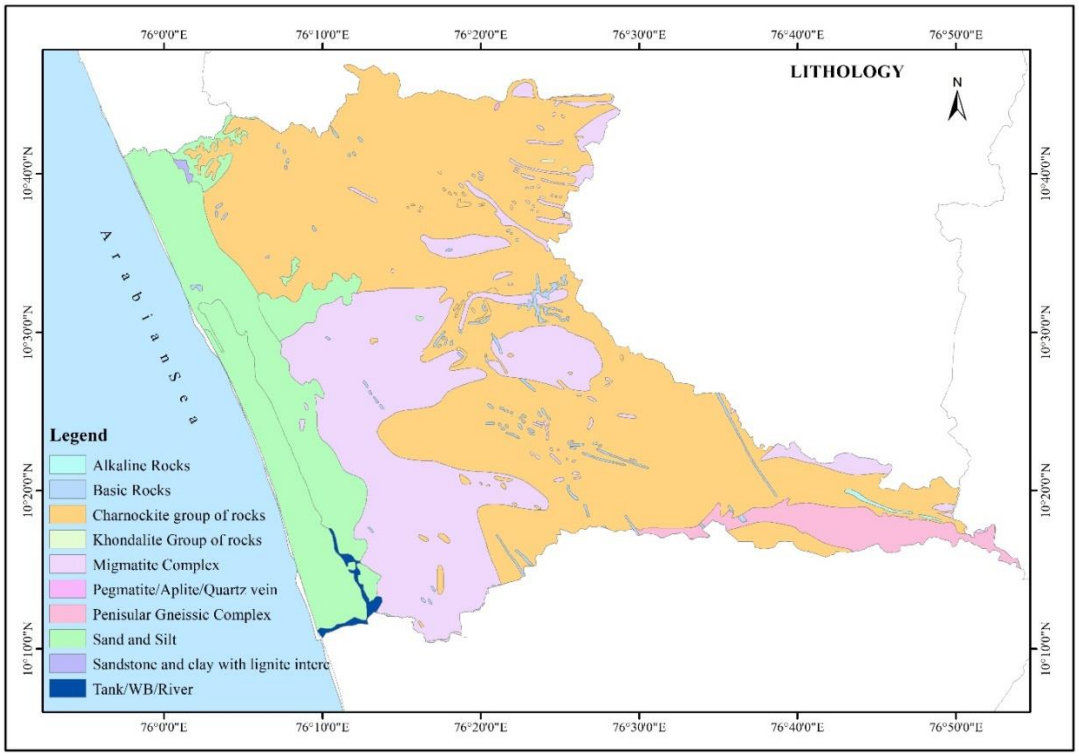

Figure 5.42: Geological map depicting a portion of the study region.

The Western Ghats are known for their mineral wealth, and the Athirappilly-Vazhachal region is no exception. While the exact mineral composition of the area may vary, certain minerals are commonly found in the region's rocks. Quartz, for example, is a prevalent mineral found in granite and gneiss. It is a crystalline form of silica and often appears as clear or white crystals. Quartz is valued for its various industrial applications, including in the production of glass and electronic devices. Feldspar is another common mineral found in the rocks of the Athirappilly-Vazhachal region. It is a group of rock-forming minerals that constitute a significant portion of granite and gneiss. Feldspar minerals have diverse colours and are used in the production of ceramics, glass, and other industrial products. Mica, a group of sheet silicate minerals, is also present in the region. It is known for its excellent heat and electrical insulation properties. Mica minerals, such as muscovite and biotite,

often occur as thin flakes or sheets within the granite and gneiss rocks. It is worth noting that while the Athirappilly-Vazhachal region exhibits interesting rock systems and minerals, the focus of attraction in the area is primarily the waterfalls themselves. The geological and mineralogical aspects mentioned contribute to the overall landscape and provide a context for understanding the natural processes that have shaped the region over millions of years.

5.4.3. Sample Collection and Preparation

The sampling locations were meticulously recorded using GPS and documented in Table 5.13.

Table 5.13: The sampling locations of Athirappilly waterfalls in the present study.

Places	Type of Rock	Sample Code	Longitude	Latitude
Thumboormuzhi	Dolerite	T1	76.4614	10.2956
	Dolerite	T2	76.4489	10.2948
	Dolerite	T3	76.4363	10.2939
	Charnockite	T4	76.4238	10.2931
	Quartzite	T5	76.4113	10.2923
	Quartzite	T6	76.3988	10.2915
	Quartzite	T7	76.3862	10.2906
	Charnockite	T8	76.3737	10.2898
	Charnockite	T9	76.3612	10.2890
Athirappilly Waterfalls	Dolerite	A1	76.5650	10.2922
	Quartzite	A2	76.5648	10.2920
	Quartzite	A3	76.5645	10.2918
	Dolerite	A4	76.5642	10.2915
	Charnockite	A5	76.5639	10.2913
	Quartzite	A6	76.5636	10.2911
	Dolerite	A7	76.5633	10.2908
	Charnockite	A8	76.5631	10.2906
	Charnockite	A9	76.5628	10.2904
Vazhachal Waterfalls	Quartzite	V1	76.5917	10.3019
	Dolerite	V2	76.5913	10.3016
	Dolerite	V3	76.5910	10.3013
	Charnockite	V4	76.5907	10.3010
	Charnockite	V5	76.5904	10.3007
	Dolerite	V6	76.5900	10.3004
	Quartzite	V7	76.5897	10.3001
	Charnockite	V8	76.5894	10.2999
	Quartzite	V9	76.5891	10.2996

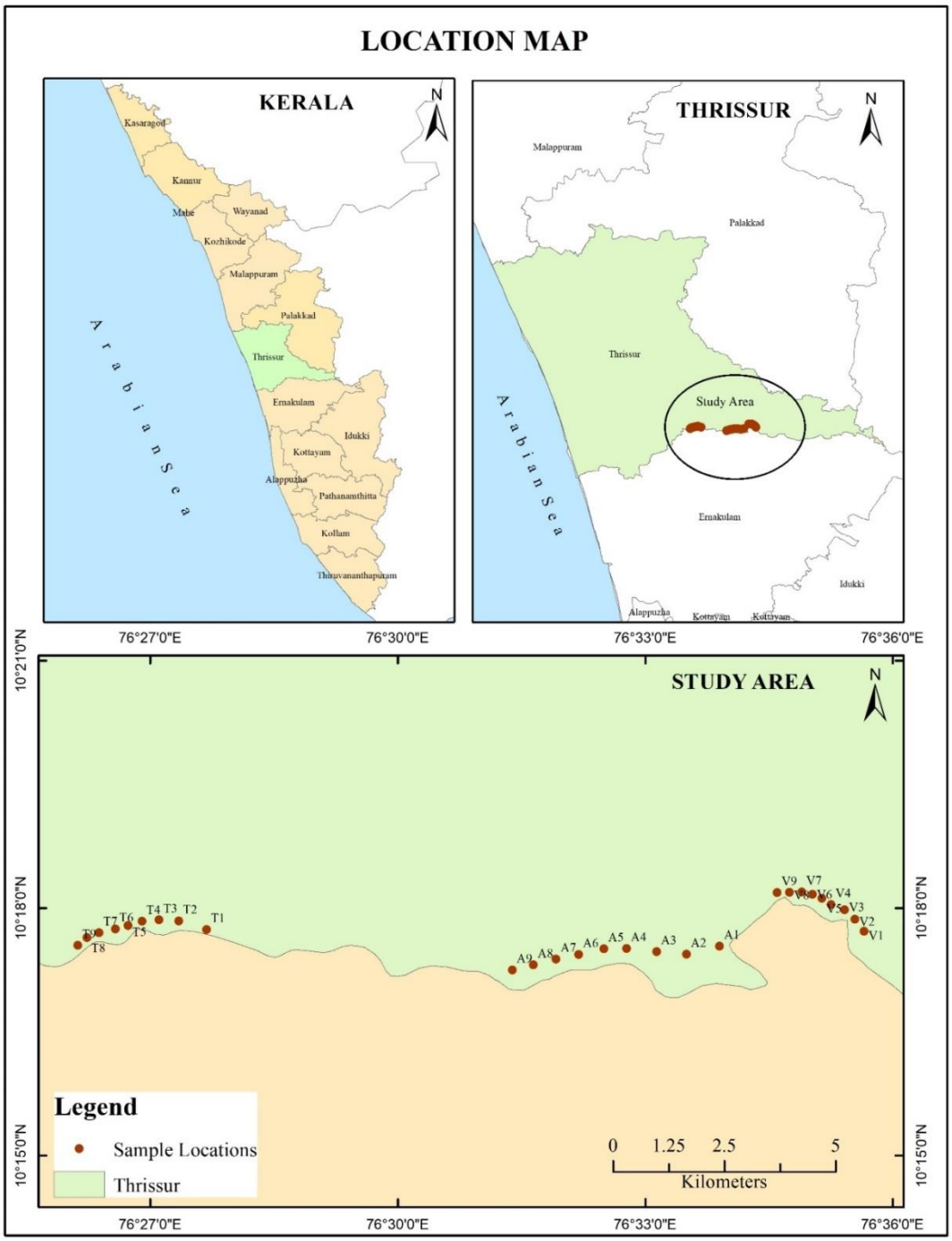

Figure 5.43: The positioning of sedimentary rock sampling sites within Thrissur district, Kerala.

The precise positions of the soil sampling stations were recorded using a Global Positioning System (GPS), as illustrated in Figure. 5.43. Dolerite, Charnockite and Quartzite types of samples were collected from each sampling locations. Preparing samples for spectrometry analysis involved several steps. Samples were randomly

gathered from specified zones within the study area and subjected to gamma spectrometry for radionuclide activity concentration determination.

5.4.4. Activity concentrations of radionuclides

The activity of ^{226}Ra, ^{232}Th and ^{40}K of the rock samples is shown in Table 5.14.

Table 5.14: The activity concentrations of radionuclides ^{226}Ra, ^{232}Th, and ^{40}K of rock samples in the study region.

Types of rocks	Sample Code	Activity Concentration (Bq/kg)		
		^{226}Ra	^{232}Th	^{40}K
Dolerite	T1	51.68±3.6	80.34±5.4	1008.39±21
Dolerite	T2	32.92±2.4	73.12±5.8	714.08±18
Dolerite	T3	41.25±3.1	76.84±5.4	648.21±16
Charnockite	T4	47.42±3.4	70.28±3.6	782.52±19
Quartzite	T5	28.36±1.8	33.66±2.1	677.06±18
Quartzite	T6	36.84±2.6	41.85±3.4	816.35±22
Quartzite	T7	22.68±1.9	28.72±1.9	572.67±18
Charnockite	T8	55.71±3.1	81.09±6.6	825.36±22
Charnockite	T9	57.34±3.3	88.38±6.8	1072.48±20
Dolerite	A1	42.36±2.8	53.02±3.3	942.38±21
Quartzite	A2	61.25±2.9	94.52±5.9	928.11±22
Quartzite	A3	33.51±2.1	41.32±3.4	835.82±19
Dolerite	A4	48.25±3.5	62.36±4.2	973.65±20
Charnockite	A5	73.64±3.8	98.94±5.9	1142.84±24
Quartzite	A6	82.38±4.2	118.68±6.8	932.45±22
Dolerite	A7	96.42±4.4	102.26±6.1	1034.32±20
Charnockite	A8	81.81±4.1	111.42±6.4	1246.24±23
Charnockite	A9	54.26±3.2	81.23±6.1	981.25±22
Quartzite	V1	16.81±1.9	21.38±2.6	465.18±18
Dolerite	V2	26.83±2.8	54.17±3.6	514.63±16
Dolerite	V3	72.25±3.6	104.24±7.3	866.38±16
Charnockite	V4	90.25±5.2	75.61±4.1	1190.34±22
Charnockite	V5	66.18±3.8	78.34±4.3	1153.52±22
Dolerite	V6	67.33±3.2	106.31±6.4	1040.24±24
Quartzite	V7	91.68±4.5	134.36±7.1	708.36±18
Charnockite	V8	79.65±3.6	128.25±7.1	1026.35±24
Quartzite	V9	19.05±2.3	62.64±3.8	547.2±18
Average		54.74	77.90	875.79
World limit		33	45	420
Standard Deviation		23.52	30.01	215.51

The activity concentration ^{226}Ra was found to vary from 16.81 ± 2.18 to 96.42 ± 6.34 Bq/kg and for ^{232}Th concentration ranged from 21.38 ± 2.15 Bq/kg to 134.36 ± 6.88 Bq/kg. The activity of ^{40}K varies from 465.18 ± 12 Bq/kg to 1246.24 ± 18 Bq/kg. In this study, the minimum detection limits for ^{226}Ra, ^{232}Th, and ^{40}K were determined to be 1.03 Bq/kg, 3.23 Bq/kg, and 6.06 Bq/kg, respectively. The mean activity concentrations of these natural radionuclides were found to be 54.74 Bq/kg for ^{226}Ra, 77.91 Bq/kg for ^{232}Th, and 875.79 Bq/kg for ^{40}K. These values exceed the world average concentrations of 33 Bq/kg for ^{226}Ra, 45 Bq/kg for ^{232}Th, and 420 Bq/kg for ^{40}K. Figure 5.44 illustrates that the activity concentrations in the rock samples originate predominantly from natural sources.

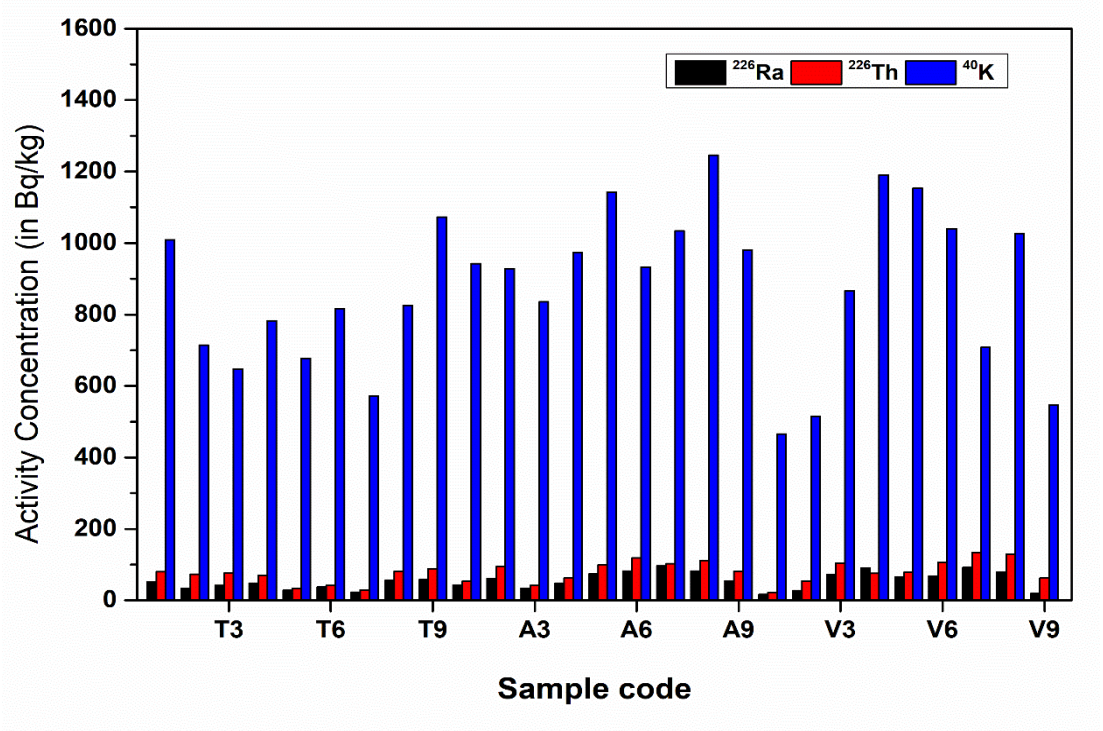

Figure 5.44: Activity concentration of the three radionuclides in rock samples in the study area.

Table 5.15 presents essential statistical parameters including minimum, maximum, mean, standard deviation, variance, skewness, and kurtosis. Figure 5.45 shows the frequency distribution of soil samples. These parameters were computed to evaluate the characteristics of radionuclides in the rock samples. The arithmetic mean and standard deviation are employed to describe the variability within the data set.

Table 5.15 Statistical distribution of the three isotopes in the study area

Parameter	**^{226}Ra**	**^{232}Th**	**^{40}K**
Minimum	16.81	21.38	465.18
Maximum	96.42	134.36	1246.24
Mean	54.74	77.90	875.79
Median	54.26	78.34	928.11
Std Dev	23.08	29.45	211.49
Kurtosis	-1.06	-0.60	-0.80
Variance	553.32	900.45	46446.67
Skewness	0.11	-0.05	-0.26

The standard deviation values of ^{226}Ra, ^{232}Th, and ^{40}K are lower than their respective mean values, indicating a high degree of uniformity among the samples. Skewness measures the asymmetry of a distribution around the mean. In this study, the skewness values for ^{226}Ra, ^{232}Th, and ^{40}K are 0.11, -0.05, and -0.26, respectively. Positive skewness suggests that the distribution of radionuclides is skewed to the right, with a tail extending towards higher values. Negative skewness indicates that the distribution is skewed to the left, with a longer or fatter tail on the lower values side.

Kurtosis quantifies the peakedness of a probability distribution for a random variable. In this study, the kurtosis values for ^{226}Ra, ^{232}Th, and ^{40}K were -1.06, -0.60, and -0.80, respectively. These negative kurtosis values indicate a flat distribution where the tails of the distribution are lighter and the peak is flatter compared to a normal distribution. This implies that the data for these radionuclides are more evenly spread out and less concentrated around the mean. The negative kurtosis values observed across all radionuclides in the rock samples suggest that none of them exhibit extreme variations in concentration; instead, their concentrations are relatively uniform across the samples.

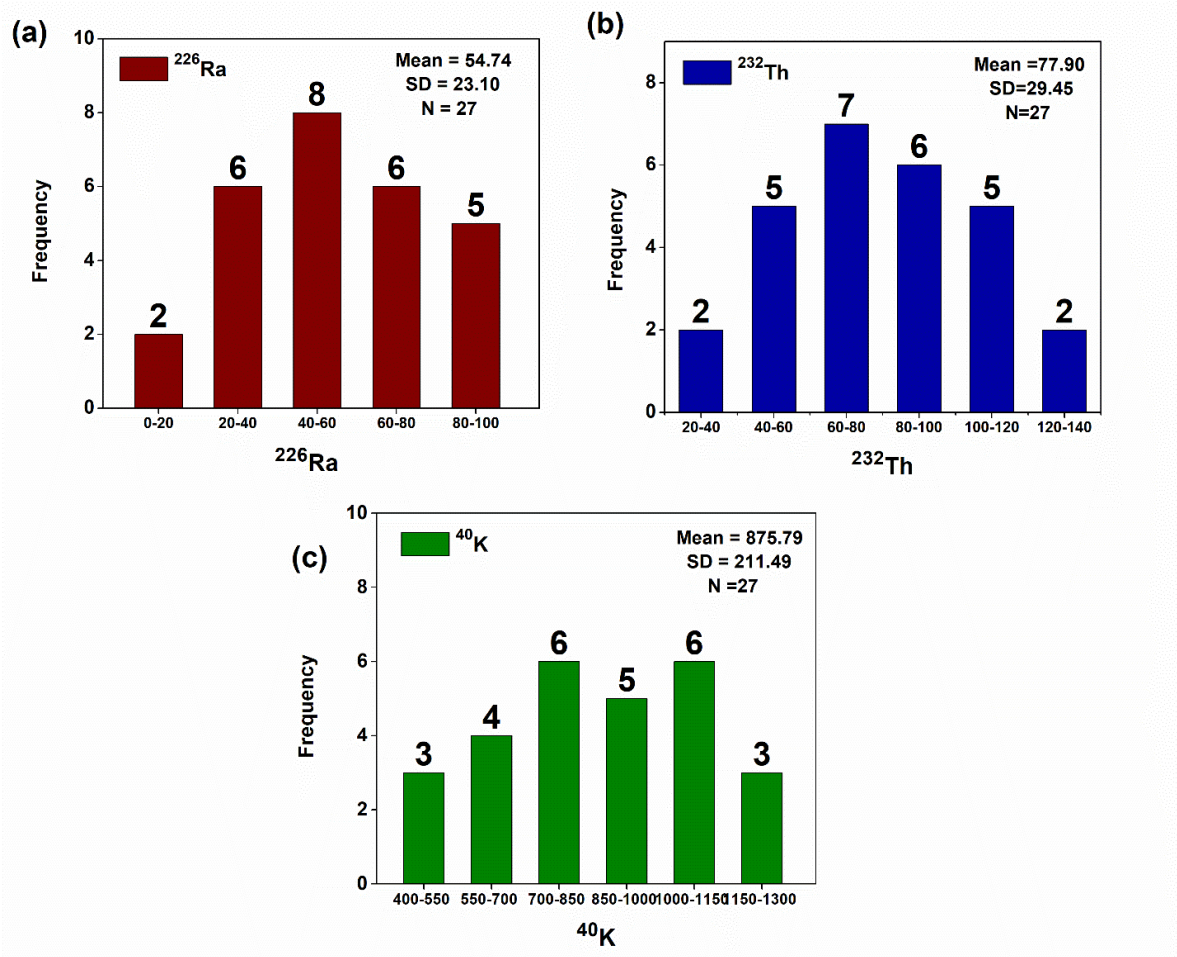

Figure 5.45: The frequency distribution of the activity concentration of ^{226}Ra, ^{232}Th and ^{40}K.

5.4.5 Radiological Parameters

The computed radiological hazard indices related to the rock the samples are summarized in Table 5.16. The calculated Radium equivalent indices, Ra_{eq} for the rock samples are presented in Table 5.16. It is found to vary from 83.20 to 342.08 Bq/kg, with a mean value of 233.58 Bq/kg and a standard deviation of 74.49. The mean Radium equivalent activity at all samples was found to be lower than the world limiting value of 370 Bq/kg. Ra_{eq} due to gamma radiation generated from ^{226}Ra, ^{232}Th, and ^{40}K in Thumboormuzhi region it is varied from 107.85 to 266.30 Bq/kg with an average of 196.72 Bq/kg. In Athirappilly, D_{out} varied from 156.96 to 337.10 Bq/kg with an average of 262.26 Bq/kg. In the case of Vazhachal region, values varied from 83.20 to 342.08 Bq/kg with an average of 244.76 Bq/kg. These

values are lower than the world's average value (370 Bq/kg; UNSCEAR 2000) in all three regions. Figure 5.46 and 5.47 illustrates the distribution of the radiological parameters Ra_{eq} and D_{out}.

Table 5.16: The radiological health hazard indices of the rock samples.

Sample Code	Ra_{eq} (Bq/kg)	D_{out} ($nGyh^{-1}$)	AED_{ind} ($mSvy^{-1}$)	AED_{out} ($mSvy^{-1}$)	H_{int}	H_{ext}	$ELCR_{ind}$ ($\times10^{-3}$)	$ELCR_{out}$ ($\times10^{-3}$)	I_γ	I_α
T1	244.21	217.30	0.56	0.14	0.66	0.80	2.27	0.57	0.91	0.34
T2	192.47	168.34	0.44	0.11	0.52	0.61	1.77	0.44	0.71	0.22
T3	201.04	174.78	0.45	0.11	0.54	0.65	1.84	0.46	0.74	0.28
T4	208.17	184.08	0.48	0.12	0.56	0.69	1.92	0.48	0.77	0.32
T5	128.63	117.76	0.30	0.08	0.35	0.42	1.22	0.30	0.49	0.19
T6	159.54	145.81	0.37	0.09	0.43	0.53	1.51	0.38	0.60	0.25
T7	107.85	98.67	0.25	0.06	0.29	0.35	1.02	0.26	0.41	0.15
T8	235.22	207.06	0.54	0.13	0.64	0.79	2.16	0.54	0.87	0.37
T9	266.30	236.52	0.61	0.15	0.72	0.87	2.47	0.62	0.99	0.38
A1	190.74	173.34	0.45	0.11	0.52	0.63	1.80	0.45	0.72	0.28
A2	267.88	235.22	0.61	0.15	0.72	0.89	2.46	0.62	0.99	0.41
A3	156.96	143.73	0.37	0.09	0.42	0.51	1.49	0.37	0.60	0.22
A4	212.40	191.56	0.49	0.12	0.57	0.70	1.99	0.50	0.80	0.32
A5	303.12	268.81	0.69	0.17	0.82	1.02	2.80	0.70	1.12	0.49
A6	323.89	281.59	0.73	0.18	0.87	1.10	2.95	0.74	1.18	0.55
A7	322.29	284.66	0.73	0.18	0.87	1.13	2.96	0.74	1.18	0.64
A8	337.10	298.40	0.77	0.19	0.91	1.13	3.11	0.78	1.25	0.55
A9	245.98	218.46	0.56	0.14	0.66	0.81	2.28	0.57	0.91	0.36
V1	83.20	76.52	0.20	0.05	0.22	0.27	0.79	0.20	0.32	0.11
V2	143.92	125.80	0.33	0.08	0.39	0.46	1.32	0.33	0.53	0.18
V3	288.02	251.05	0.65	0.16	0.78	0.97	2.63	0.66	1.05	0.48
V4	290.03	262.26	0.67	0.17	0.78	1.03	2.71	0.68	1.08	0.60
V5	267.03	240.15	0.62	0.15	0.72	0.90	2.49	0.62	1.00	0.44
V6	299.45	262.83	0.68	0.17	0.81	0.99	2.75	0.69	1.10	0.45
V7	338.36	289.31	0.75	0.19	0.91	1.16	3.04	0.76	1.21	0.61
V8	342.08	297.18	0.77	0.19	0.92	1.14	3.12	0.78	1.25	0.53
V9	150.76	130.59	0.34	0.09	0.41	0.46	1.38	0.35	0.56	0.13
Mean	233.59	206.73	0.54	0.14	0.63	0.78	2.16	0.54	0.86	0.36
World Limit	370	59	0.07	0.40	1	1	1.45	0.29	1	1

The values of D_{out} due to gamma radiation generated from ^{226}Ra, ^{232}Th, and ^{40}K varied from 76.52 to 298.40 nGy/h with an average of 206.73 nGy/h is shown in (Table 5.16). In Thumboormuzhi region it is varied from 98.67 to 236.52 nGy/h with an average of 172.23 nGy/h. In Athirappilly, Dout varied from 143.73 to 298.40 nGy/h with an average of 232.86 nGy/h. In the case of Vazhachal region, values varied from 76.52 to 297.18 nGy/h with an average of 215.08 nGy/h. These values are greater than the world's average value (59 nGy/h; UNSCEAR 2000) in all three regions.

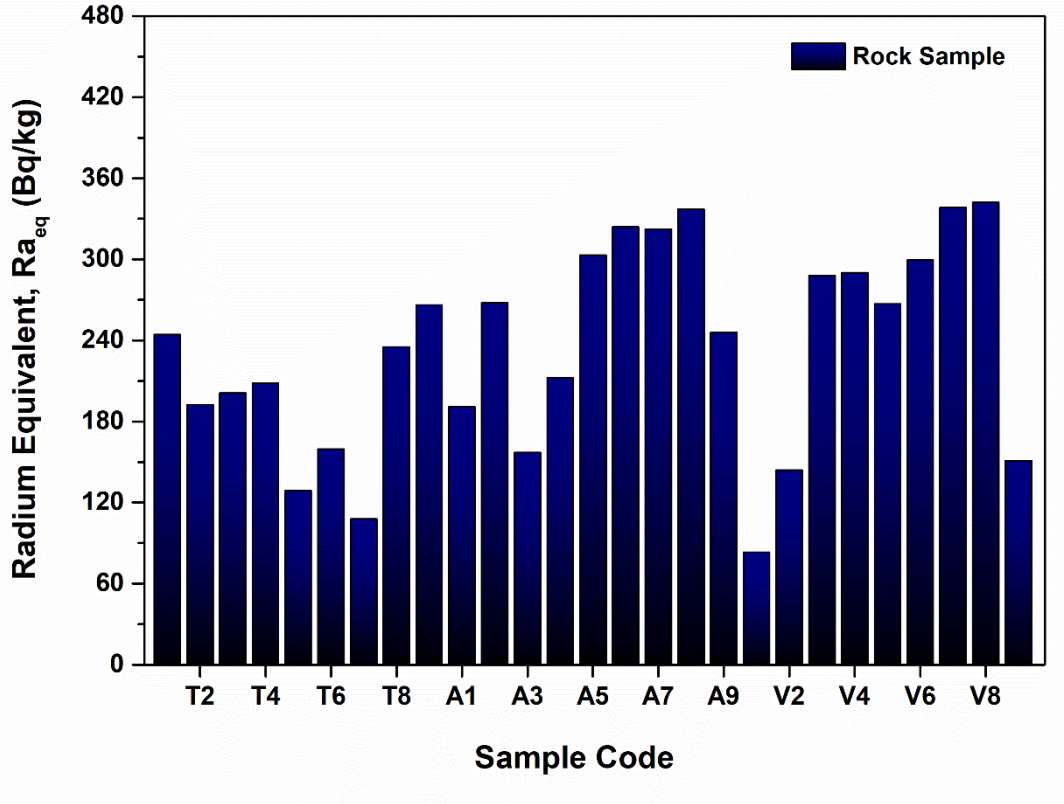

Figure 5.46: Distribution of the Raeq parameter in the study area.

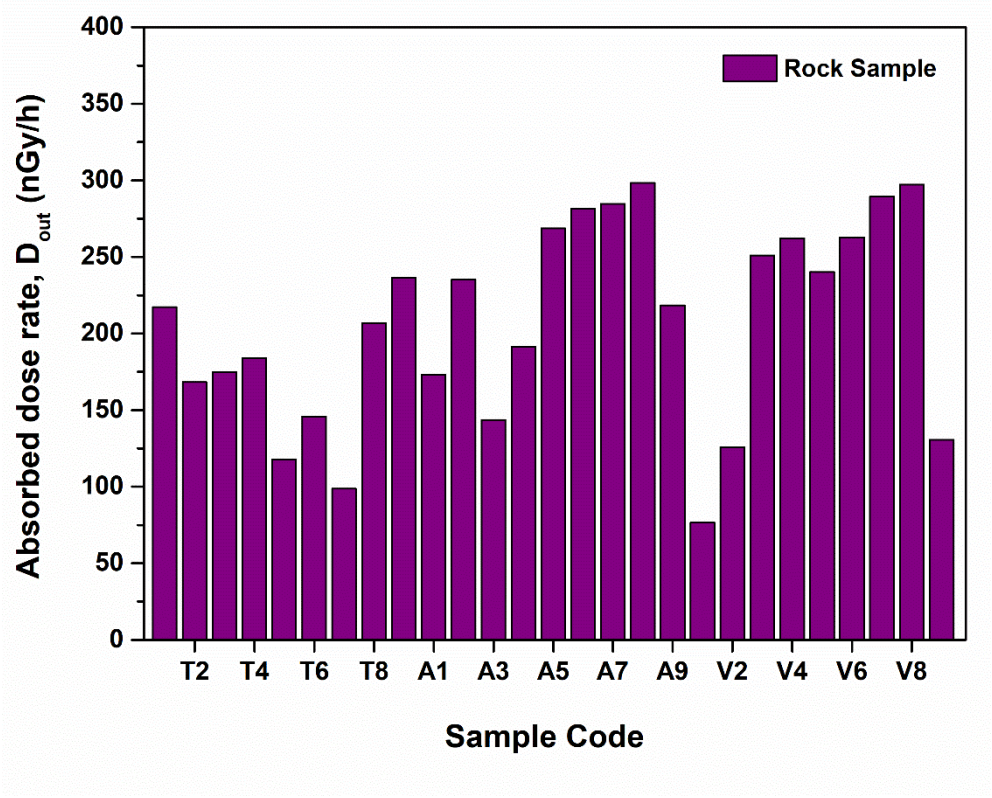

Figure 5.47: Distribution of the D_{out} parameter in the study area.

The correlation between the activity concentrations and absorbed dose rates D_{out} in the soil samples is shown in Figure 5.48 (a-d). Here, the regression was found to be linear and positive. A positive correlation coefficient (R^2) of 0.92, 0.86 and 0.60 between D_{out} and concentrations of ^{226}Ra, ^{232}Th and ^{40}K respectively was observed. Also, the correlation between D_{out} and Ra_{eq} is always prominent ($R^2 = 0.99$).

Figure 5.49 illustrates the distribution of the annual effective dose equivalent (AED) values. The indoor annual effective dose equivalent (AED) values varied from 0.38 to 1.46 $mSvy^{-1}$, with an average of 1.01 $mSvy^{-1}$, which is slightly higher than the global average value of 0.07 $mSvy^{-1}$ [52], [71]. In the case of outdoor annual effective dose equivalent (AED) values varied from 0.09 to 0.37 $mSvy^{-1}$, with an average of 0.25 $mSvy^{-1}$ found to be lower than global average value of 0.40 $mSvy^{-1}$.

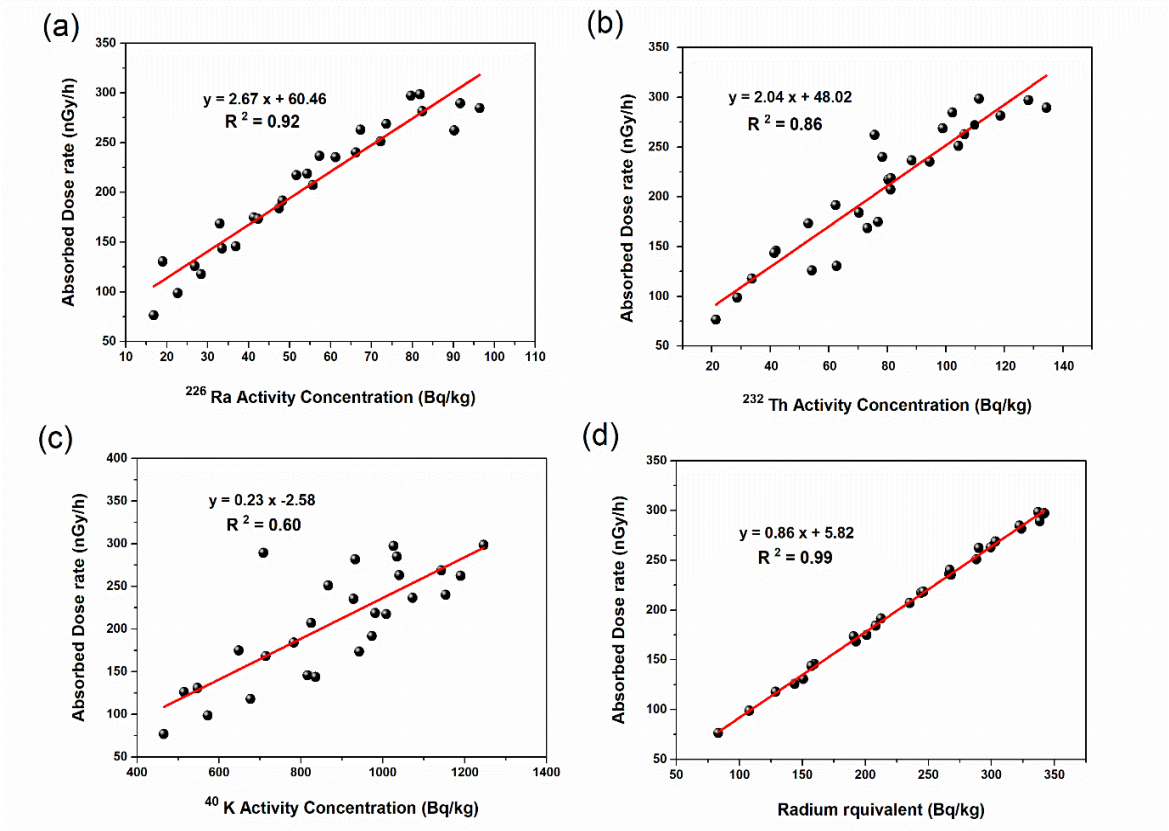

Figure 5.48: The correlation between the activity concentrations and absorbed dose rates.

Figure 5.50 illustrates the distribution of the hazard indices (H_{int} and H_{ext}) in the study area. The calculated internal radiation hazard index (H_{int}) of the soil samples ranged from 0.22 to 0.92, with an average value of 0.63. These values, being less than 1, indicate that according to the report of Radiation Protection [55], there is no significant internal threat if construction materials are made from the rock sample of selected area of Athirappilly waterfalls region. Figure 5.50 illustrates the distribution of the hazard indices (H_{int} and H_{ext}) in the study area. The external hazard index (H_{ext}) due to ^{226}Ra, ^{232}Th, and ^{40}K in the rock sample of the study region ranged from 0.22 to 0.92, with a mean value of 0.63.

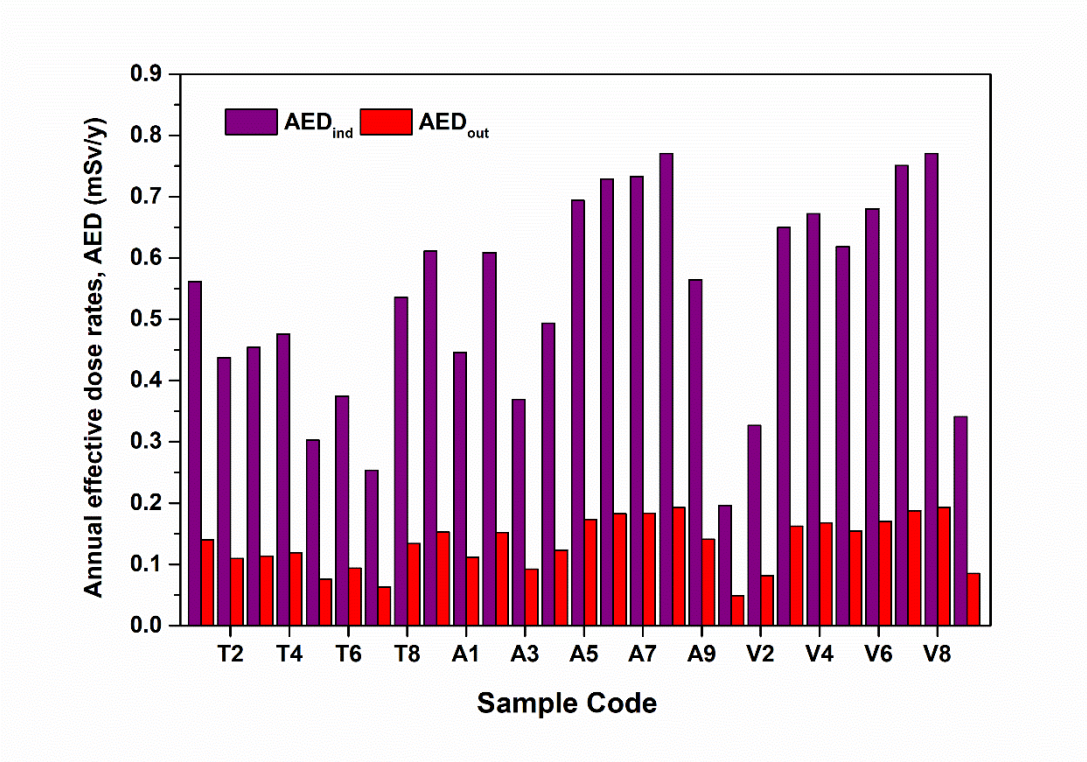

Fgure 5.49: The distribution of the annual effective dose equivalent (AED) values.

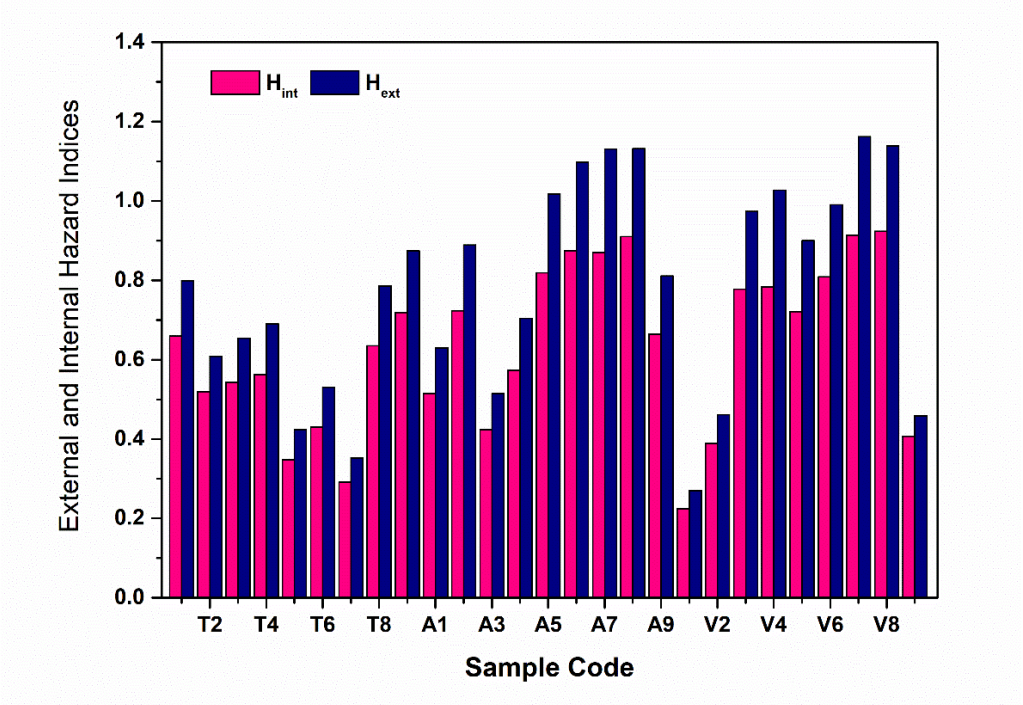

Figure 5.50: The distribution of the hazard indices (H_{int} and H_{ext}) in the study area.

Figure 5.51 illustrates the distribution of the excess lifetime cancer risk (ELCR) in the study area. The indoor excess lifetime cancer risk in the soil ranged from 1.50 $\times 10^{-3}$ to 5.84×10^{-3}, with a mean value of 4.05×10^{-3}. However, the global average value is 1.45 $\times 10^{-3}$, indicating that the cancer risk in the study area is slightly higher than the global average.

The outdoor excess lifetime cancer risk in the soil ranged from 0.37 $\times 10^{-3}$ to 1.46 $\times 10^{-3}$, with a mean value of 1.01 $\times 10^{-3}$. So, comparing with the global average value is 0.29 $\times 10^{-3}$, this indicating that the cancer risk in the study area is slightly higher than the global average[72]. The excess lifetime cancer risk (ELCR) was calculated to assess the potential risk of developing fatal cancer due to exposure in the study regions. The results indicated that the ELCR values exceeded the acceptable limits in these areas, posing significant health risks to the residents.

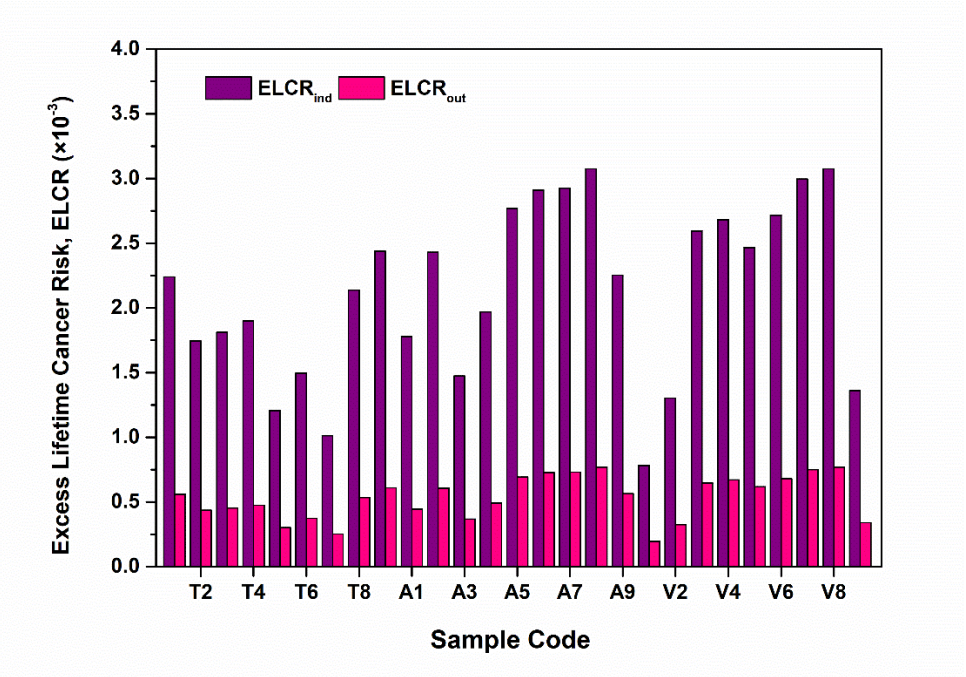

Figure 5.51: The distribution of the excess lifetime cancer risk (ELCR) in the study area.

5.4.6. Mineralogical composition analysis of rock samples by XRD

The results of the XRD analysis of rock samples collected from three locations in the study area (list places) are shown in Figure 5.37 (a-c). The major components identified in all the rock ores include Monazite $(Ce,La,T)PO_4$, Limonite

($FeO(OH).nH_2O$), Zirconium orthosilicate ($ZrSiO_4$), and Zeolite ($NaAlSiO_4$). Additionally, traces of quartz (SiO_2), Titanium dioxide (TiO_2), Chromium oxides (Cr_2O_3), Iron Oxides (Fe_2O_3), Phosphorus oxide (P_2O_5), and calcite ($CaCO_3$) were also detected in the samples. The peaks corresponding to ores observed at different 2θ angles for selected rock samples are illustrated in Figure 5.52 (a-c). Monazite is noteworthy for its composition, which includes light rare earth elements (REE), Thorium, and Uranium. In the stream sediments studied, Monazite mineral grains typically appear as subhedral or euhedral shapes, often flattened or broken, and sometimes displaying pitted surfaces. Zircon, on the other hand, is predominantly found as euhedral to subhedral grains in fine to very fine sizes, typically with a prismatic to elongated shape and exhibiting a notable adamantine luster. The presence of Monazite and Zirconium deposits in these rocks is significant due to their radioactive properties[76]. The Thorium content in Monazite placer deposits varies depending on the type of parent rock; more plutonic parent crystalline rocks tend to have higher Thorium content [46], [47], [49], [56].

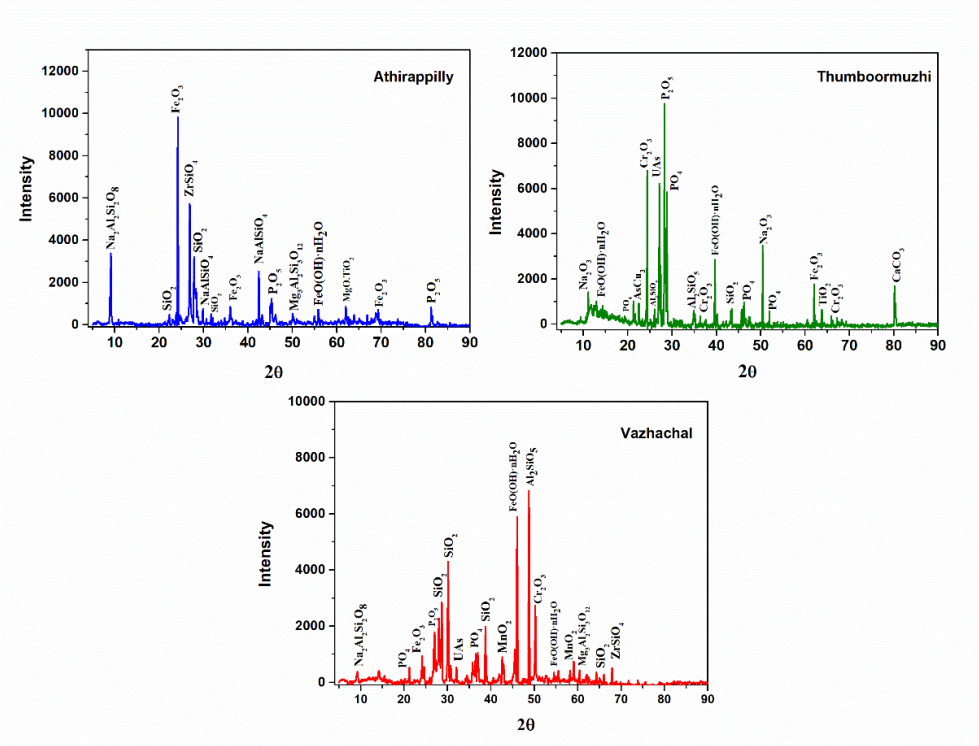

Figure 5.52: XRD spectra of rock samples of Athirappilly region of grain size of ≤ 100µm.

The study reveals that, the enhanced activity of ^{232}Th and ^{226}Ra in the region is due to Monazite, Zirconium orthosilicate ($ZrSiO_4$) and Zeolite ($NaAlSiO_4$) bearing minerals weathered from the rock formations. The radionuclides in the rock samples are directly linked with minerals such as Zircon, Monazite, thorite, uranothorite, iron oxides, and fluorite. Zircon usually contains Uranium and Thorium concentrations ranging from 0.01 to 0.19 and 1 to 2%, respectively [57]. Uranium in iron oxides is first trapped by adsorption. The high Uranium content in the mineralized rock is attributed to the ability of iron oxide in them to adsorb Uranium [58]. The studied locations consist of a variety of rock systems and these rocks contain of varying amount of primordial radionuclides. The obtained data indicates that the major oxides present in the samples are SiO_2, Al_2O_3, MgO, Fe_2O_3, CaO, P_2O_5, K_2O, and TiO_2. The SiO_2 concentration was found to be more than other composites in the rock samples. Al_2O_3 was found to be one of the predominant elements in the samples, with concentrations ranging from 6.72% to 18.71% and averaging 12.42%. This average exceeds the crustal average value of 4.72%, suggesting that a significant portion of this element may have originated from the weathering of silicate-bearing rocks abundant in minerals like feldspar and mica. Additionally, the rocks in the study area are enriched with various oxide forms of elements, indicating that the presence of natural radionuclides with varying concentrations in these rocks can be attributed to these oxide compounds [77].

5.4.7 Pearson correlation analysis

Table 5.17 shows a weak correlation between ^{238}U and ^{232}Th (R = 0.86), a very moderate correlation between ^{238}U and ^{40}K (R^2=0.74), and between ^{232}Th and ^{40}K (R= 0.55). The Pearson correlation analysis is a statistical method used to measure the strength and direction of relationships between radioactive variables. Correlation can be classified into positive and negative types. The correlation coefficient (denoted by "R") ranges from -1 to +1, where a value closer to +1 indicates a strong positive linear relationship between variables. Conversely, a low R value indicates a weak linear relationship, and an R value close to zero suggests no linear relationship[74].

Table 5.17: Correlation matrix between the radionuclides and radiological parameters.

Variables	^{226}Ra	^{232}Th	^{40}K	Ra_{eq}	D_{out}	I_{α}	I_{γ}	AED	ELCR	H_{ext}	H_{int}
^{226}Ra	1										
^{232}Th	0.86	1									
^{40}K	0.74	0.55	1								
Ra_{eq}	0.96	0.95	0.76	1							
D_{out}	0.96	0.94	0.79	0.94	1						
I_{α}	0.92	0.69	0.74	0.92	0.86	1					
I_{γ}	0.94	0.82	0.78	0.94	0.86	0.86	1				
AED	0.91	0.94	0.84	0.76	0.91	0.84	0.86	1			
ELCR	0.93	0.94	0.79	0.81	0.66	0.88	0.88	0.88	1		
H_{ext}	0.96	0.95	0.77	0.86	0.64	0.81	0.81	0.94	0.84	1	
H_{int}	0.97	0.94	0.76	0.87	0.66	0.82	0.78	0.96	0.88	0.91	1

In this study, a strong positive linear correlation coefficient was observed between Uranium (^{238}U) and Thorium (^{232}Th). This correlation suggests that the origin of ^{40}K differs significantly from the origin of the other radionuclides, ^{238}U and ^{232}Th, although they may share similar controlling factors or sources. Additionally, the correlation coefficients (R) of radiological parameters such as Radium equivalent activity, absorbed dose rate, annual effective dose equivalent, internal hazard index, external hazard index, and excess lifetime cancer risk indicate a strong correlation with the activity of ^{238}U in the rocks.

So, this study examines the distribution of radioactive materials in granitoid rocks and their possible origins. Several radiation hazard parameters were assessed, including the dose rate, the annual effective dose, and the excess lifetime cancer risk. Multivariate statistical techniques such as Pearson correlation were employed to analyze the relationship between radionuclides and their associated radiation hazard variables. The findings revealed that the mean activity levels of ^{238}U, ^{232}Th, and ^{40}K in granitoid rocks are 54.74 ± 6.93, 77.90 ± 7.32, and 875.79 ± 21 Bq kg^{-1}, respectively. These levels are below the worldwide average for Uranium (33 Bq kg^{-1}), comparable for Thorium (45 Bq kg^{-1}), and approximately three times higher for Potassium (412 Bq kg^{-1}). The radioactivity in granitoid rocks is primarily due to the presence of Uranium, Thorium, and Potassium. Construction materials derived from most granitoid rocks are unlikely to pose any significant risk to public health.

5.4.8 Elemental concentration of radionuclides and Radiogenic Heat Production (RHP) in Athirappilly region.

The elemental concentrations of ^{238}U in ppm, ^{232}Th in ppm and ^{40}K in % and radiogenic heat production (RHP) in μWm^{-3} of the rock samples collected from Athirappilly, Kerala were calculated and tabulated in Table 5.18 and shown in Figures 5.53, 5.54 and 5.55.

Table 5.18: The elemental concentrations, radiogenic heat production (RHP) and Heat flow (H_f) of the rock samples

Place Name	Place Code	Concentration of radionuclides			RHP (μWm^{-3})	H_f ($\mu W/m^2$)
		^{238}U (ppm)	^{232}Th (ppm)	^{40}K (%)		
Thumboormuzhi	T1	4.18	19.79	3.22	1.02	7.98
	T2	2.67	18.01	2.28	0.79	6.23
	T3	3.34	18.93	2.07	0.87	6.86
	T4	3.84	17.31	2.50	0.90	7.02
	T5	2.30	8.29	2.16	0.51	3.97
	T6	2.98	10.31	2.61	0.64	5.01
	T7	1.84	7.07	1.83	0.42	3.29
	T8	4.51	19.97	2.64	1.03	8.10
	T9	4.64	21.77	3.43	1.12	8.77
Athirappilly Waterfalls	A1	3.43	13.06	3.01	0.77	6.00
	A2	4.96	23.28	2.97	1.17	9.19
	A3	2.71	10.18	2.67	0.61	4.80
	A4	3.91	15.36	3.11	0.87	6.85
	A5	5.96	24.37	3.65	1.32	10.34
	A6	6.67	29.23	2.98	1.49	11.66
	A7	7.81	25.19	3.30	1.50	11.79
	A8	6.62	27.44	3.98	1.47	11.54
	A9	4.39	20.01	3.13	1.04	8.15
Vazhachaal Waterfalls	V1	1.36	5.27	1.49	0.32	2.48
	V2	2.17	13.34	1.64	0.61	4.75
	V3	5.85	25.67	2.77	1.31	10.28
	V4	7.31	18.62	3.80	1.30	10.23
	V5	5.36	19.30	3.69	1.13	8.88
	V6	5.45	26.18	3.32	1.30	10.24
	V7	7.42	33.09	2.26	1.63	12.81
	V8	6.45	31.59	3.28	1.54	12.05
	V9	1.54	15.43	1.75	0.60	4.73

The elemental concentration of Uranium varies from 1.36 to 7.81 ppm with an average of 4.43 ppm. The elemental concentration of ^{232}Th ranged from 5.27 ppm to 33.09 ppm with an average of 19.19 ppm. The elemental concentration of ^{40}K

ranged from 1.49% to 3.98% with an average of 2.81%. Sample collections are mainly done from three Places namely Thumboormuzhi, Athirappilly and Vazhachal region. In Thumboormuzhi zone, the elemental concentration of ^{238}U, ^{232}Th and ^{40}K were observed to be varied from 1.84 to 4.64 ppm, 7.07 to 21.77 ppm and 1.83 to 3.43% respectively. In Athirappilly zone, the elemental concentration of ^{238}U, ^{232}Th and ^{40}K were observed to be varied from 2.71 to 7.81 ppm, 10.18 to 29.33 ppm and 2.67 to 3.98% respectively. In Vazhachal zone, the elemental concentration of ^{238}U, ^{232}Th and ^{40}K were observed to be varied from 1.36 to 7.42 ppm, 5.27 to 33.09 ppm and 1.49 to 3.80% respectively.

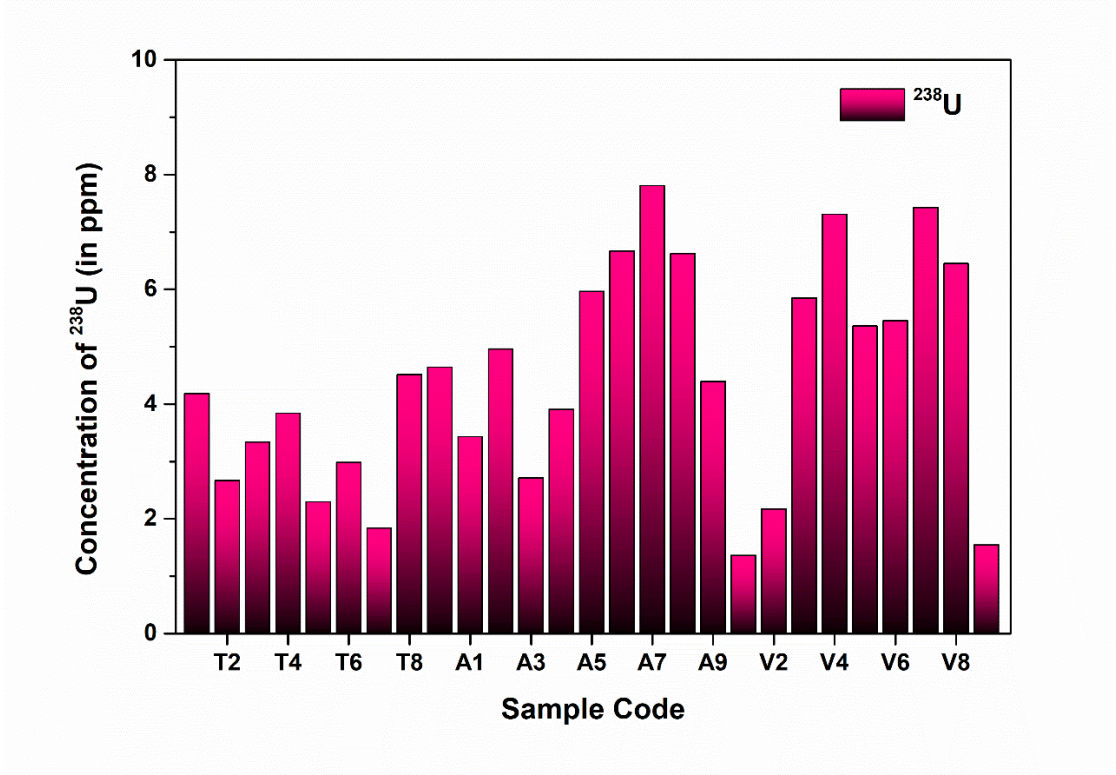

Figure 5.53: The elemental concentrations of ^{238}U (in ppm).

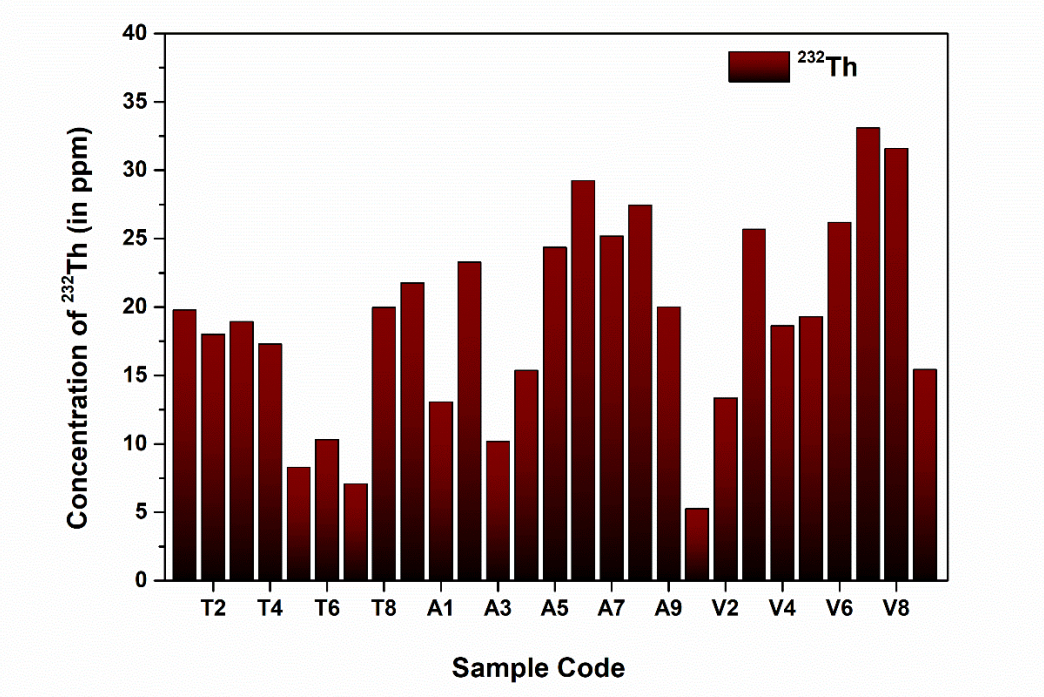

Figure 5.54: The elemental concentrations of ^{232}Th (in ppm).

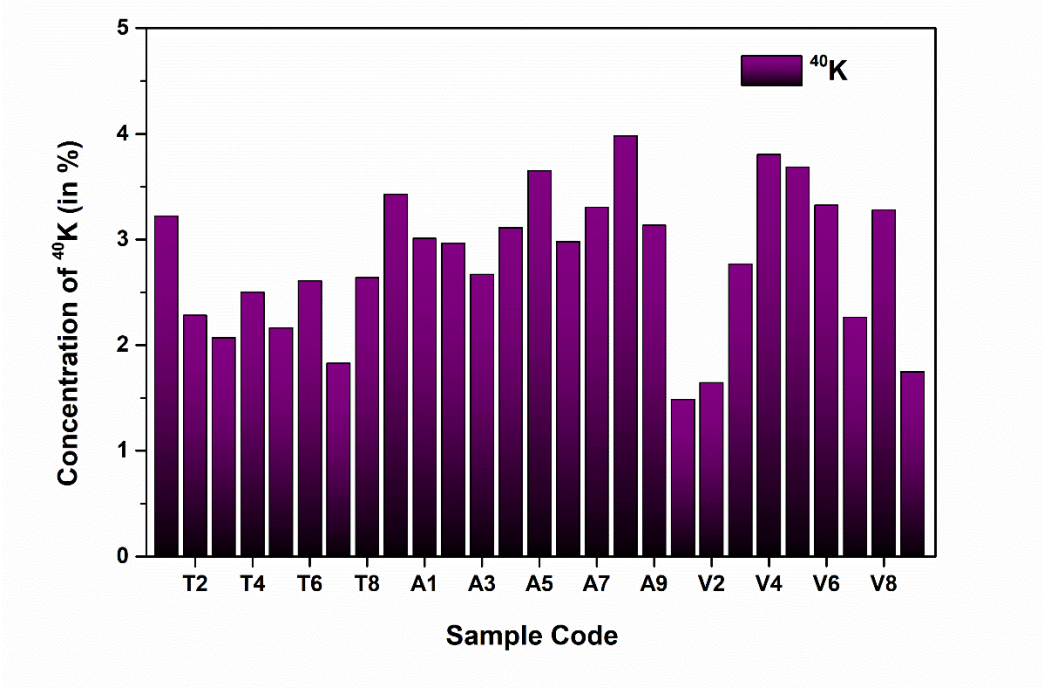

Figure 5.55: The elemental concentrations of ^{40}K (in %).

The radiogenic heat production in the rock samples collected in zone-3 was found to varied from 0.32 to 1.63 μW/m^3 with an average of 1.01 μW/m^3. Figure 5.56 contour representation of the distribution of RHP in the study region.

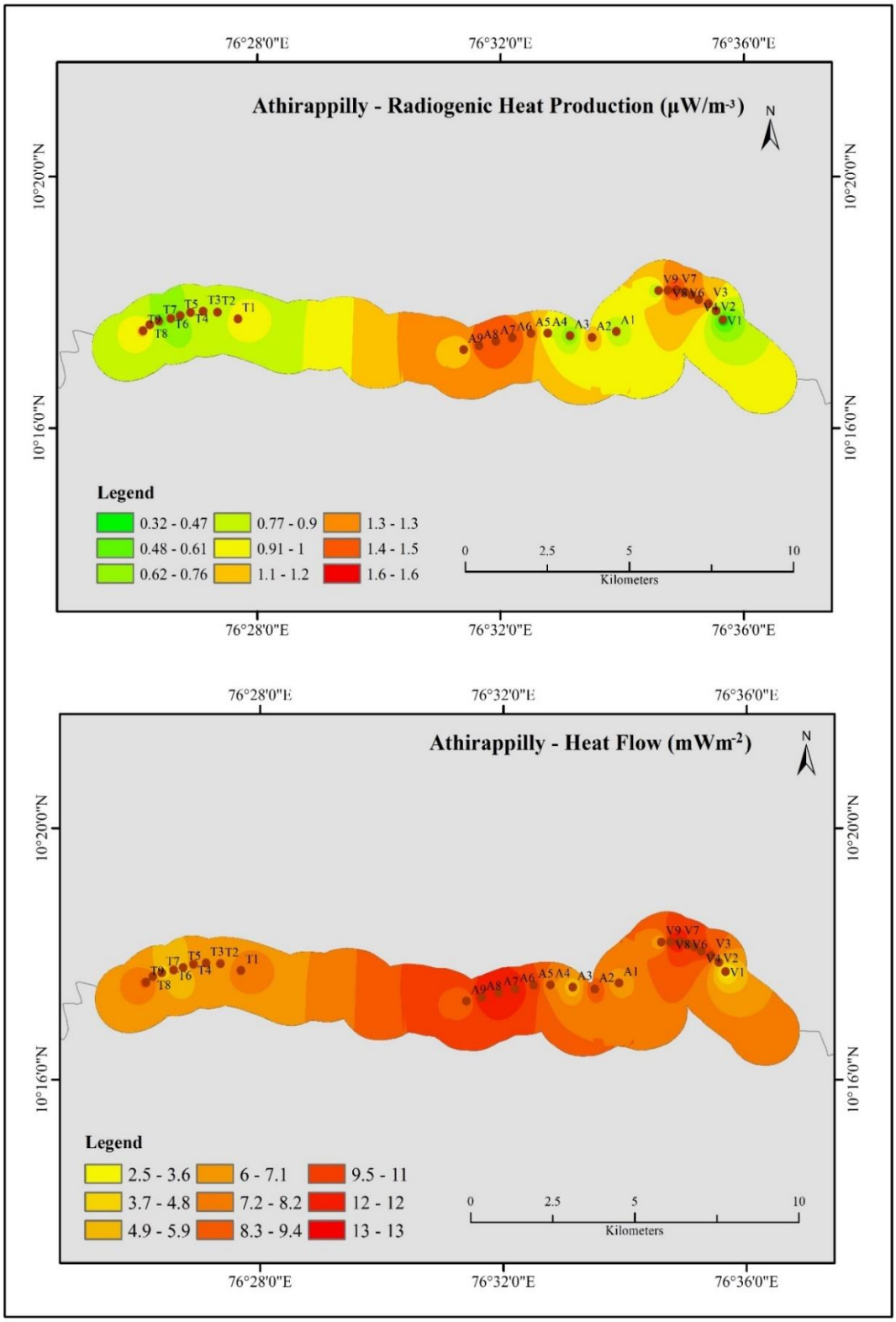

Figure 5.56: The contour representation of Radiogenic heat and Heat flow of the study region.

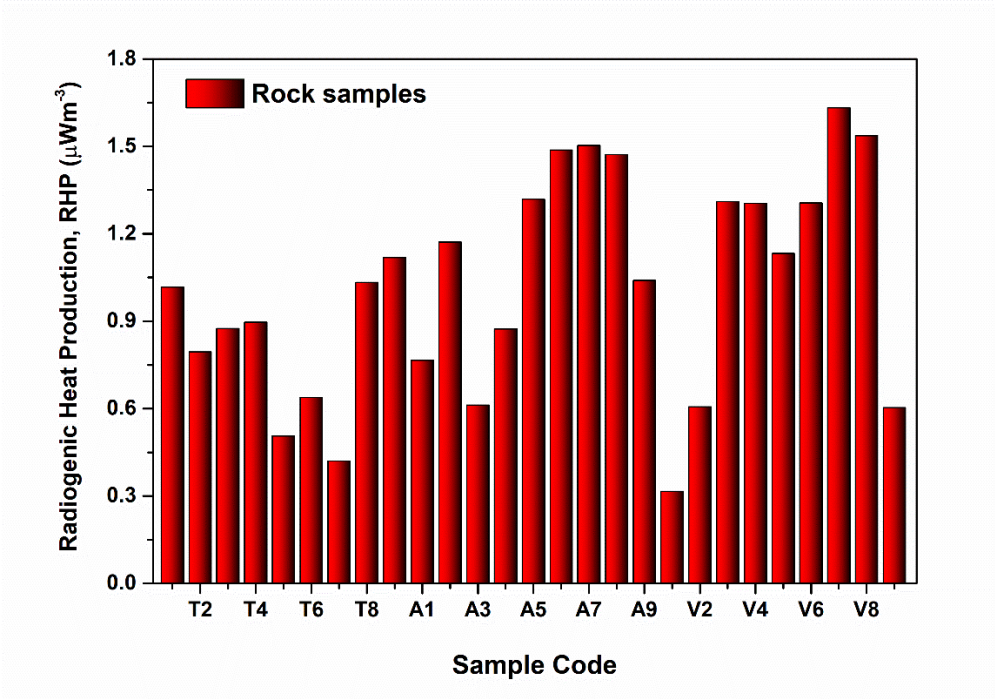

Figure 5.57: Radiogenic heat production in Athirappilly study region.

5.4.9 Correlation between radionuclides and Radiogenic Heat Production (RHP) for studied region.

The RHP weighted mean 0.79 μWm^{-3} compared to the earth's crust mean between 0.8 and 1.2 μWm^{-3} was lower due to significant presence of gneiss rocks and soil in all the studied profiles. In Figure 5.58 (a – b), linear and positive correlations were found. It can be seen that there is a good correlation between ^{232}Th and ^{238}U with correlation coefficient of (R^2 = 0.72). The relation shows a slope of 2.86 with intercept 18.36 ppm. Similarly, Figure 5.58 (b) show a positive moderate correlation coefficient of (R^2 = 0.52) slope of 0.02922 with intercept of 0.1679% while Figure 5.58 (c) has weak correlation of R^2 =0.27 and 0.5435% as slope and intercept, respectively. However, as is argued later in this paper, the most striking fact that there is consistent correlations were observed between ^{238}U and ^{232}Th, and between ^{40}K and ^{238}U with weak correlation coefficients of (R^2 = 0.52) and (R^2 = 0.27), respectively.

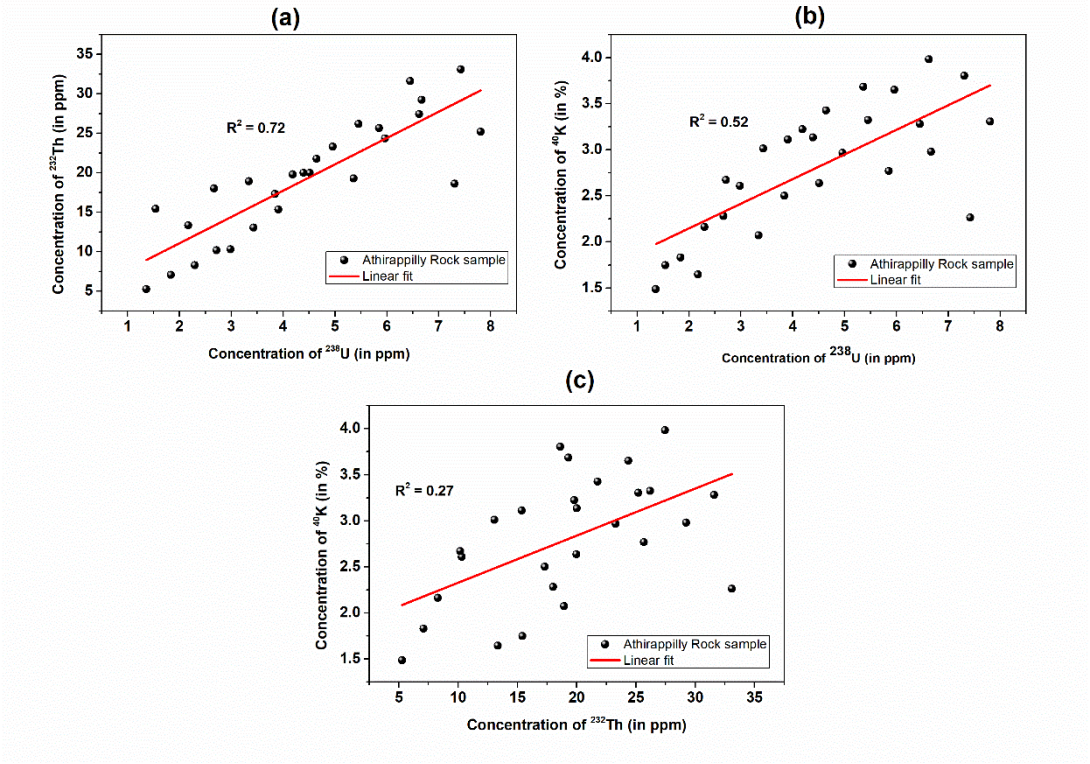

Figure 5.58: Correlation between radionuclides for studied region.

Now figure 5.59 (a-c) shows correlations among radiogenic heat and ^{238}U ^{232}Th, and ^{40}K. From 5.59 (a), it is found that radiogenic heat produced in the study area have a high dependence with ^{238}U concentration ($R^2 = 0.92$). Also, it is observed that, ^{238}Th concentration is the dominant producer of RHP, having $R^2 = 0.93$ and ^{40}K concentration have weak correlation with RHP ($R^2 = 0.48$).

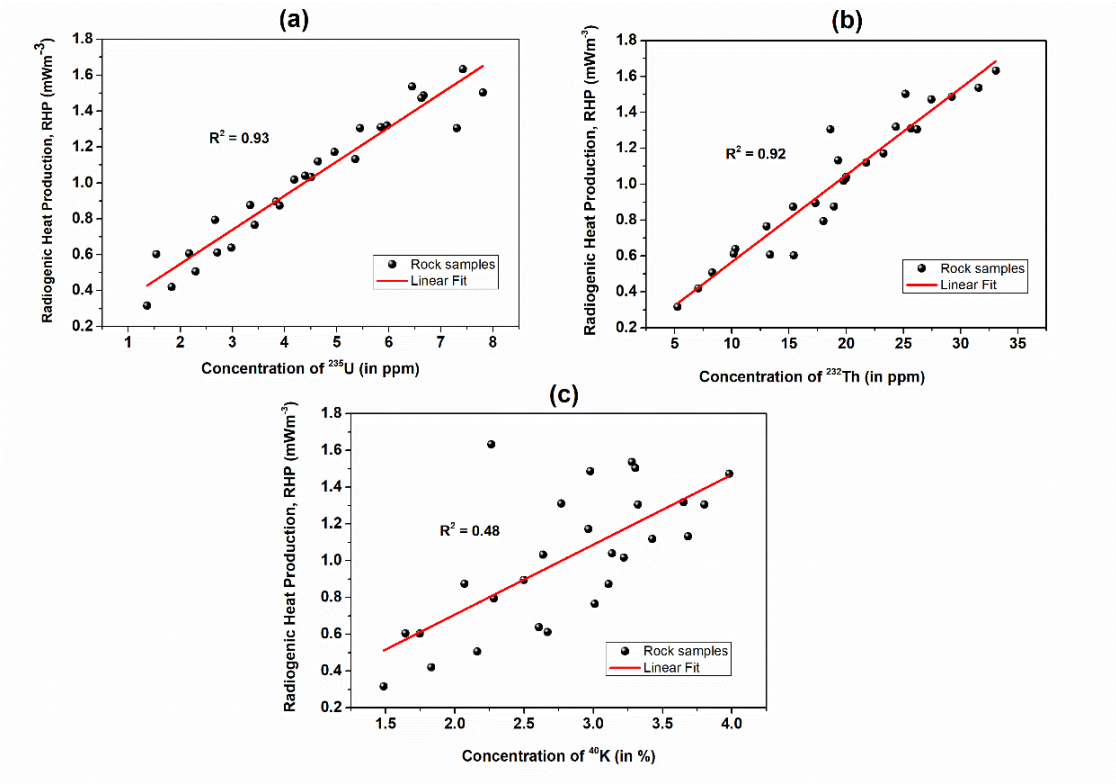

Figure 5.59: Correlation between concentration of radionuclides and Radiogenic Heat Production (RHP) and for studied region.

The H_f in the samples due to the decay of ^{238}U, ^{232}Th and ^{40}K varied from (2.48± 1.0 – 12.81 ± 2.0) mWm^{-2} with average of 7.93± 0.8 mW m^{-2}. This average H_f is less than 21.6 mWm^{-2} reported by Asere and colleagues for quarry sites in Ondo State, Nigeria but less than the global value of 37 mWm^{-2} stated by Turcotte & Schubert for inactive regions[26], [39].

Figure 5.60 illustrates a plot of total RHP and H_f producing a linear distribution segment with strong correlation coefficient of R^2 = 0.99. The linear regression through the data points gives a slope of 16.23 and vertical axis intercept of 0.84 mW m^{-2}.

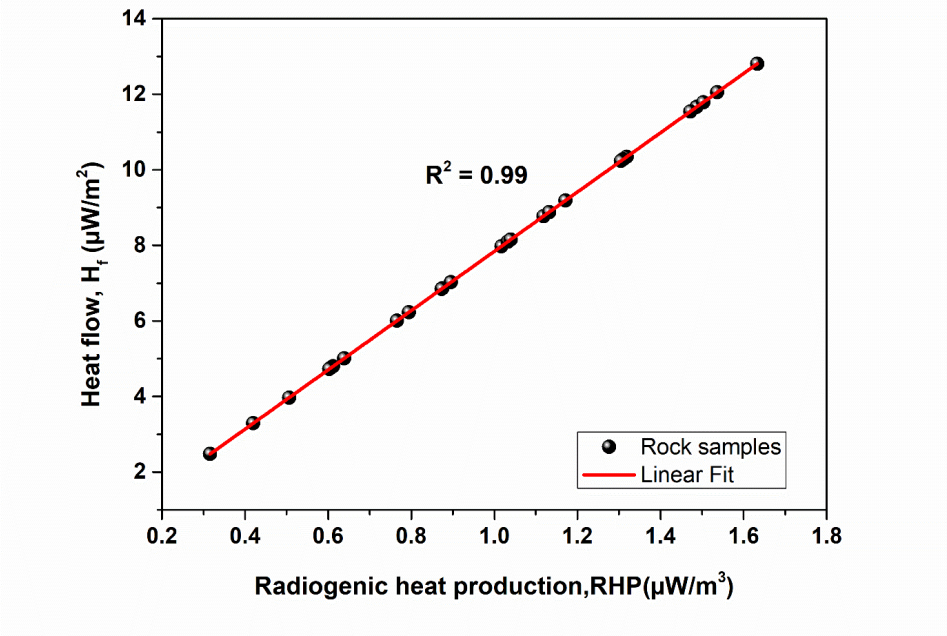

Figure 5.60: Correlation between concentration of heat flow and Radiogenic Heat Production (RHP) and for studied region.

As expected, RHP in the samples produced a significantly greater effect on H_f. The H_f values reflect the high RHP due to decay of ^{238}U, ^{232}Th and ^{40}K in the study area, indicating feasibility for geothermal exploration. Again this agrees with the findings of Turcotte & Schubert for stable continental areas, where the H_f had a very strong correlation with the surface RHP. Hence, this research shows that the study area is in thermally more quiescent regions.

The activity concentration, elemental concentrations of ^{238}U in ppm, ^{232}Th in ppm and ^{40}K in % and radiogenic heat production (RHP) in μWm^{-3} of the rock samples collected from Athirappilly, Kerala were estimated. The mean levels of activity concentrations of ^{226}Ra, ^{232}Th, and ^{40}K were determined to be 54.74, 77.90 and 875.79 Bq/kg respectively. The overall average elemental and activity concentrations of basement rocks are 4.43 ppm, 19.30 ppm and 2.97% for ^{226}Ra, ^{232}Th and ^{40}K, respectively. The observed RHP rates for the studied rocks are in the mean value varied from 0.32 to 1.63 $\mu W/m^3$ with an average of 1.01 $\mu W/m^3$ which is within the world average 0.8–1.2 Wm^{-3}.

5.5. Comparison with Similar Studies

The average activity concentrations of ^{226}Ra, ^{232}Th, and ^{40}K in the present study are compared with the data obtained from similar studies from different parts of the world and is presented in Table 5.19. It is noticed from Table 5.19 that a higher concentration of ^{226}Ra has been found in Egypt, Ghana and Central Nepal. The activity concentration of ^{232}Th has been seen higher in Ghana, Iran and India. In India, higher activity concentration of ^{232}Th has been reported from Karnataka and Tamilnadu which are comparable with the results of the present work. However, the activity concentration of ^{40}K has been seen higher in Brazil, Nigeria, Ghana and Egypt. The results from the present study also show a comparatively higher value.

Table 5.19 Comparison of the activity concentration of ^{226}Ra, ^{232}Th, and ^{40}K in samples of present study with those measured different environs of the world.

Location	^{226}Ra	^{232} Th	^{40} K	Reference
World average	50	50	500	[54]
Bangladesh	60.2	60.8	928	[78]
Brazil	31	73	1648	[57]
China	23	36	891	[79]
Egypt	215	131	822	[80]
Ghana	1.2–40	3.3–117.5	13.5–1510	[81]
Iran	23–93	24–118	462–1190	[82]
Nigeria	47.09	95.02	1118.68	[39]
Pakistan	27.32	50.07	953.1	[83]
Turkey	9.4–27.3	11.7–23.4	275.4–689.2	[81]
Indian average	32	64	400	[54]
Kashmir	37.32	38.57	465.62	[84]
Gujarat	9.1-24.1	3.7-12.7	101.8-264.1	[85]
Himachal Pradesh	31-63	53-78	472 - 630	[86]
Eastern Haryana	41.5 – 54.4	31.4 - 37.9	46.3 - 696	[87]
Punjab	6.37-56.7	24-334	738- 1064	[88]
Jharkhand	6.1-826	8.7-237	291 - 1391	[89]
Andhra Pradesh	20-91	45-365	400-607	[60]
Karnataka	41.08	86.26	869.29	[38]

Karnataka	50.94	79.55	606.20	[57]
Karnataka	BDL- 34.11	79.05	96.72 - 933.68	[90]
Tamilnadu	0.44-50.83	0.21-293.67	233-2091	[68]
Tamilnadu	26.26	53.61	231.93	[51]
Tamilnadu	105.7	13.1	888.8	[91]
Tamilnadu	52	48	840	[67]
Kerala (Wayanad)	66	83	669	[92]
Kerala (Athirappilly)	54.74	77.90	875.79	This Study
Kerala (Thrissur)	16.44-88.33	67.42-174.3	739-1084	This Study
Kerala (NH-66)	19.27-87.47	26.46-132.87	336-1478	This Study

The table highlights the activity concentrations of radionuclides ^{226}Ra, ^{232}Th, and ^{40}K in various regions, including global and local averages. Globally, the average concentrations are 50 Bq/kg for ^{226}Ra, 50 Bq/kg for ^{232}Th and 500 Bq/kg for ^{40}K. Compared to the world average, regions like Brazil exhibit significantly elevated levels, particularly for ^{40}K (1648 Bq/kg) and ^{232}Th (73 Bq/kg). Similarly, Egypt reports much higher ^{226}Ra, (215 Bq/kg) and ^{232}Th, (131 Bq/kg) levels.

In India, regional variations are prominent. For example, Kerala shows a wide range of radionuclide activity. In Wayanad, ^{226}Ra, ^{232}Th, and ^{40}K are reported at 66, 83, and 669 Bq/kg, respectively. The present study recorded ^{226}Ra, ^{232}Th, and ^{40}K levels in Athirappilly as 54.74, 77.90, and 875.79 Bq/kg, respectively, and in Thrissur as 16.44–88.33, 67.42–174.3, and 739–1084 Bq/kg. These values generally surpass the global averages, reflecting Kerala's geogenic characteristics, particularly its monazite-rich coastal sands. Such findings emphasize the importance of localized assessments to evaluate potential radiological health risks.

5.6 Conclusion

In this context, the study of natural radioactivity and gamma attenuation properties of building materials is critically evaluated to ensure the safety and sustainability of construction practices. Building materials, often sourced from natural geological

formations, can contain varying levels of naturally occurring radionuclides such as ^{226}Ra, ^{232}Th and ^{40}K.These radionuclides emit gamma radiation, which can pose health risks to inhabitants if not adequately managed.

Thrissur-Palakkad Highway Region I

In the rock samples from the Thrissur-Palakkad highway region, the average Ra_{eq} activity was found to be 301.57 Bq/kg, below the global limit of 370 Bq/kg. However, the average absorbed dose rate was 138.14 nGy/h, exceeding the world average of 60 nGy/h. Other radiological hazard parameters, such as AEDEout, H_{ext}, H_{int}, Iγ, and Iα, were below the recommended global limits, indicating a radiologically safe environment. Despite this, the average Excess Lifetime Cancer Risk (ELCR) of 0.68×10^{-3} exceeded the permissible limit of 0.29×10^{-3}, suggesting some level of risk. In summary, exposure to natural radionuclides in the studied rock samples does not pose significant health risks to the local population.

In the Thrissur-Palakkad highway region, the observed rates of radiogenic heat production (RHP) for the studied rocks range from 1.44 to 4.96 μWm^{-3}, with an average of 3.34 μWm^{-3}, which exceeds the global average range of 0.8–1.2 μWm^{-3} for such measurements. Notably, charnockite rocks exhibit RHP values above the world crustal average.

NH-66 Highway Region II

Gamma-ray spectrometry was used to measure the concentrations of ^{226}Ra, ^{232}Th and ^{40}K at 24 soil sampling sites along NH-66 in Kerala, spanning 78 km between the Kozhikode and Malappuram districts. On average, the activity concentrations (with standard variation) were found to be 39.88 ± 6.20 $Bqkg^{-1}$ for ^{226}Ra, 61.19 ± 4.32 $Bqkg^{-1}$ for ^{232}Th, and 815.51 ± 18 $Bqkg^{-1}$ for ^{40}K in the soil samples from the study area. The radionuclide activity concentrations in urban soil followed the order $^{40}K > ^{232}Th > ^{226}Ra$ with radiological hazard parameters either equal to or below global averages. Multivariate statistical analysis showed that natural radioactivity had a negligible impact on the soil's physico-chemical properties. All the computed values for the radioactive indices were below the global average thresholds set by radiation monitoring organizations. The overall average elemental and activity

concentrations of basement rocks are 3.53 ppm, 15.95 ppm and 2.61% for ^{226}Ra, ^{232}Th and ^{40}K, respectively. The observed RHP rates for the studied rocks are in the mean value of 0.27 to 1.60 Wm^{-3}, with average of 0.79 Wm^{-3} which is above the world average 0.8–1.2 Wm^{-3}.

Athirappilly Region III

In the Athirappilly region, the distribution, and origins of radioactive materials in granitoid rocks were studied. The mean activity levels of ^{226}Ra, ^{232}Th and ^{40}K were 54.74, 77.90, and 875.79 Bq/kg, respectively. These levels were below the worldwide averages for Uranium and Thorium but higher for Potassium. The radioactivity in these rocks primarily stems from Uranium, Thorium, and Potassium, and construction materials derived from them are unlikely to pose significant health risks. The calculated Radium equivalent indices, Ra_{eq} for the rock samples are found to vary from 83.20 to 342.08 Bq/kg, with a mean value of 233.58 Bq/kg. The mean Radium equivalent activity at all samples was found to be lower than the world limiting value of 370 Bq/kg. The average values of D_{out} due to gamma radiation generated from ^{226}Ra, ^{232}Th, and ^{40}K is 206.73 nGy/h. The elemental concentrations of ^{238}U in ppm, ^{232}Th in ppm and ^{40}K in % and radiogenic heat production (RHP) in μWm^{-3} of the rock samples collected from Athirappilly, Kerala were estimated. The overall average elemental and activity concentrations of basement rocks are 4.43 ppm, 19.30 ppm and 2.97% for ^{226}Ra, ^{232}Th and ^{40}K, respectively. The observed RHP rates for the studied rocks are in the mean value varied from 0.32 to 1.63 $\mu W/m^3$ with an average of 1.01 $\mu W/m^3$ which is within the world average 0.8–1.2 Wm^{-3}.

The overall activity concentrations were found to be highest in the Kuthiran region, followed by the Athirappilly region, both situated at the foothills of the Western Ghats in Kerala, India. These areas predominantly feature the oldest rock units in the region, consisting of thick layers of gneisses and migmatites that have undergone medium to high grade regional metamorphism. The study highlights that while certain regions exhibit elevated levels of natural radioactivity, the associated health risks are generally low, with some exceptions. These findings contribute to safer and

more sustainable construction practices, emphasizing the importance of continuous monitoring and innovation in materials science.

5.7 Reference

[1] Ş. Turhan, "Radiological assessment of urban soil samples in the residents of a central Anatolian volcanic province, Turkey," *Int. J. Environ. Health Res.*, vol. 00, no. 00, pp. 1–14, 2022, doi: 10.1080/09603123.2022.2078797.

[2] Kathren RL, "NORM sources and their origins," *Appl Rad Isot.*, vol. 49, no. 3, pp. 149–168, 1998.

[3] Y. Narayana, P. K. Shetty, and K. Siddappa, "Enrichment of natural radionuclides in Monazite areas of coastal Kerala," *Int. Congr. Ser.*, vol. 1276, pp. 333–334, 2005, doi: 10.1016/j.ics.2004.11.163.

[4] E. Erbek and M. N. Dolmaz, "Investigation of the thermal structure and radiogenic heat production through aeromagnetic data for the southeastern Aegean Sea and western part of Turkey," *Geothermics*, vol. 81, no. April, pp. 113–122, 2019, doi: 10.1016/j.geothermics.2019.04.011.

[5] M. A. Adabanija, O. N. Anie, and M. A. Oladunjoye, "Radioactivity and gamma-ray spectrometry of basement rocks in Okene area, southwestern Nigeria," *NRIAG J. Astron. Geophys.*, vol. 9, no. 1, pp. 71–84, Jan. 2020, doi: 10.1080/20909977.2020.1711695.

[6] M. A. El-Sadek, "Radiospectrometric and magnetic signatures of a gold mine in Egypt," *J. Appl. Geophys.*, vol. 67, no. 1, pp. 34–43, 2009, doi: 10.1016/j.jappgeo.2008.08.012.

[7] R. A. Y. El Qassas, M. Salaheldin, S. M. A. Assran, T. Abdel Fattah, and M. A. Rashed, "Airborne gamma-ray spectrometric data interpretation on Wadi Queih and Wadi Safaga area, Central Eastern Desert, Egypt," *NRIAG J. Astron. Geophys.*, vol. 9, no. 1, pp. 155–167, 2020, doi: 10.1080/20909977.2020.1728893.

[8] S. A. Saqan, M. K. Kullab, and A. M. Ismail, "Radionuclides in hot mineral spring waters in Jordan," *J. Environ. Radioact.*, vol. 52, no. 1, pp. 99–107, 2001, doi: 10.1016/S0265-931X(00)00096-5.

[9] L. Eggeling, A. Genter, T. Kölbel, and W. Münch, "Impact of natural radionuclides on geothermal exploitation in the upper rhine graben," *Geothermics*, vol. 47, pp. 80–88, 2013, doi: 10.1016/j.geothermics.2013.03.002.

[10] R. C. Ramola, M. Yadav, and G. S. Gusain, "Distribution of natural radionuclide along Main Central Thrust in Garhwal Himalaya," *J. Radiat. Res. Appl. Sci.*, vol. 7, no. 4, pp. 614–619, 2014, doi: 10.1016/j.jrras.2014.10.002.

[11] I. Rosianna *et al.*, "Natural radioactivity of laterite and volcanic rock sample for radioactive mineral exploration in mamuju, indonesia," *Geosci.*, vol. 10, no. 9, pp. 1–13, 2020, doi: 10.3390/geosciences10090376.

[12] G. Cinelli *et al.*, "Terrestrial gamma dose rate mapping (Euganean Hills, Italy): comparison between field measurements and HPGe gamma spectrometric data," *Radiat. Eff. Defects Solids*, vol. 175, no. 1–2, pp. 54–67, 2020, doi: 10.1080/10420150.2020.1718131.

[13] A. Innocent, "Evaluation of Naturally Occurring Radionuclide Materials in Soil Samples Collected From Some Mining Sites in Zamfara State, Nigeria," *Br. J. Appl. Sci. Technol.*, vol. 3, no. 4, pp. 684–692, 2013, doi: 10.9734/bjast/2014/3244.

[14] F. Bea, "Residence of REE, Y, Th and U in granites and crustal protoliths; implications for the chemistry of crustal melts," *J. Petrol.*, vol. 37, no. 3, pp. 521–552, 1996, doi: 10.1093/petrology/37.3.521.

[15] İ. Akkurt, K. Gunoglu, O. Gunay, and M. Sarıhan, "Natural radioactivity and radiological damage parameters for soil samples from Cekmekoy-İstanbul," *Arab. J. Geosci.*, vol. 15, no. 1, 2022, doi: 10.1007/s12517-021-09351-x.

[16] N. Maden and E. Akaryali, "A review for genesis of continental arc magmas: U, Th, K and radiogenic heat production data from the Gümüşhane Pluton in the Eastern Pontides (NE Türkiye)," *Tectonophysics*, vol. 664, pp. 225–243, 2015, doi: 10.1016/j.tecto.2015.09.023.

[17] Rybach, "Author Index," *Am. J. Occup. Ther.*, vol. 52, no. 10, pp. 932–935, 1998, doi: 10.5014/ajot.52.10.932.

[18] R. Menon, P. S. Kumar, G. K. Reddy, and R. Srinivasan, "Radiogenic heat production of Late Archaean Bundelkhand granite and some Proterozoic gneisses and granitoids of central India," *Curr. Sci.*, vol. 85, no. 5, pp. 634–638, 2003.

[19] D. Liao, D. Feng, J. Luo, and X. Yun, "Relationship between radiogenic heat production in granitic rocks and emplacement age," *Energy Geosci.*, vol. 4, no. 4, p. 100157, 2023, doi: 10.1016/j.engeos.2023.100157.

[20] C. Jaupart, S. Labrosse, F. Lucazeau, and J. C. Mareschal, "Temperatures, Heat, and Energy in the Mantle of the Earth," *Treatise Geophys. Second Ed.*, vol. 7, pp. 223–270, 2015, doi: 10.1016/B978-0-444-53802-4.00126-3.

[21] N. Podugu, L. Ray, S. P. Singh, and S. Roy, "Heat flow, heat production, and crustal temperatures in the Archaean Bundelkhand craton, north-central India: Implications for thermal regime beneath the Indian shield," *J. Geophys. Res. Solid Earth*, vol. 122, no. 7, pp. 5766–5788, 2017, doi: 10.1002/2017JB014041.

[22] M. L. Gupta and S. R. Sharma, "Heat flow in Rajasthan Craton , North – Western Indian Shield and its Implications," vol. 1, no. 1, pp. 30–34, 2018.

[23] H. Thybo and I. M. Artemieva, "Tectonophysics Moho and magmatic underplating in continental lithosphere," *Tectonophysics*, vol. 609, pp. 605–619, 2013, doi: 10.1016/j.tecto.2013.05.032.

[24] I. M. Artemieva, H. Thybo, K. Jakobsen, K. Nanna, and L. S. K. Nielsen, "PT SC," *Earth-Science Rev.*, 2017, doi: 10.1016/j.earscirev.2017.07.003.

[25] N. I. Christensen, "Seismic velocity structure and composition of the continental crust : A global view," vol. 100, pp. 9761–9788, 1995.

[26] Turcotte D. L. & Schubert G., *2002. Geodynamics , 2nd ed. xv + 456 pp. Cambridge, New York, Melbourne: Cambridge University Press. Price £75.00, US $110.00 (hard covers); £29.95, US $45.00 (paperback). ISBN 0 521 66186 2; 0 521 66624 4 (pb).*, vol. 139, no. 6. 2002.

[27] M. A. S. Youssef and S. T. Elkhodary, "Utilization of airborne gamma-ray spectrometric

data for geological mapping, radioactive mineral exploration and environmental monitoring of southeastern Aswan city, South Eastern Desert, Egypt," *Geophys. J. Int.*, vol. 195, no. 3, pp. 1689–1700, 2013, doi: 10.1093/gji/ggt375.

[28] A. A. S. and O. A. I. D. Ademila O., "Radiometric survey in geological mapping of basement complex area of parts of Southwestern Nigeria," *Vietnam J. Earth Sci.*, vol. 40, no. 3, pp. 288–298, 2018, doi: 10.15625/0866-7187/40/3/12619.

[29] J. Asfahani, M. Aissa, and R. Al-Hent, "Uranium migration in a sedimentological phosphatic environment in Northern Palmyrides, Al-Awabed area, Syria," *Appl. Radiat. Isot.*, vol. 65, no. 9, pp. 1078–1086, 2007, doi: 10.1016/j.apradiso.2007.04.019.

[30] M. A. S. Youssef, "Estimating and interpretation of radioactive heat production using airborne gamma-ray survey data of Gabal Arrubushi area, Central Eastern Desert, Egypt," *J. African Earth Sci.*, vol. 114, pp. 67–73, 2016, doi: 10.1016/j.jafrearsci.2015.10.022.

[31] D. Hasterok, M. Gard, and J. Webb, "On the radiogenic heat production of metamorphic, igneous, and sedimentary rocks," *Geosci. Front.*, vol. 9, no. 6, pp. 1777–1794, 2018, doi: 10.1016/j.gsf.2017.10.012.

[32] M. Elsadek M. Sabra, A. L. Abdeldayem, M. A. S. Youssef, A. A. Masoud, and S. A. Mansour, "Determination of the radiation dose rate and radiogenic heat production of North Gabal Abu Hibban area, central Eastern Desert, Egypt," *NRIAG J. Astron. Geophys.*, vol. 8, no. 1, pp. 103–111, 2019, doi: 10.1080/20909977.2019.1617556.

[33] M. F. Middleton, "Radiogenic heat generation in the Darling Range, Western Australia," *Explor. Geophys.*, vol. 44, no. 3, pp. 206–214, 2013, doi: 10.1071/EG13028.

[34] A. M. Jessop, M. A. Hobart, and J. Sclater, "the World Heat Flow Data Collection - 1975," *Geotherm. Ser.*, vol. 5, no. 5, p. 13, 1976.

[35] P. Chiozzi, P. De Felice, A. Fazio, V. Pasquale, and M. Verdoya, "Laboratory application of NaI(Tl) γ-ray spectrometry to studies of natural radioactivity in geophysics," *Appl. Radiat. Isot.*, vol. 53, no. 1–2, pp. 127–132, 2000, doi: 10.1016/S0969-8043(00)00123-8.

[36] G. Vallinayagam and L. G. Singh, "Radioactive Heat Producing felsic to intermediate volcano- plutonic rocks of Dhiran Area , Malani Igneous Suite , Western India," vol. 4, no. Ii, pp. 68–79, 2011.

[37] L. Ray *et al.*, "High mantle heat flow in a Precambrian granulite province: Evidence from southern India," *J. Geophys. Res. Solid Earth*, vol. 108, no. B2, 2003, doi: 10.1029/2001jb000688.

[38] D. R. Rangaswamy, M. C. Srilatha, C. Ningappa, E. Srinivasa, and J. Sannappa, "Measurement of natural radioactivity and radiation hazards assessment in rock samples of Ramanagara and Tumkur districts, Karnataka, India," *Environ. Earth Sci.*, vol. 75, no. 5, pp. 1–11, 2016, doi: 10.1007/s12665-015-5195-8.

[39] S. O. Asere, and Sedara, "Determination of Natural Radioactivity Concentration and Radiogenic Heat Production in Selected Quarry Sites in Ondo State, Nigeria," *NIPES J. Sci. Technol. Res.*, vol. 2, no. 3, p. 256, Aug. 2020, doi: 10.37933/nipes/2.3.2020.26.

[40] A. S. Akingboye, A. C. Ogunyele, A. T. Jimoh, O. B. Adaramoye, A. O. Adeola, and T.

Ajayi, "Radioactivity, radiogenic heat production and environmental radiation risk of the Basement Complex rocks of Akungba-Akoko, southwestern Nigeria: insights from in situ gamma-ray spectrometry," *Environ. Earth Sci.*, vol. 80, no. 6, pp. 1–24, 2021, doi: 10.1007/s12665-021-09516-7.

[41] O. Kuforijimi and A. Christopher, "Correlation and mapping of geothermal and radioactive heat production from the Anambra Basin, Nigeria," *African J. Environ. Sci. Technol.*, vol. 11, no. 10, pp. 517–531, 2017, doi: 10.5897/ajest2017.2382.

[42] R. U. M. Rao, G. V. Rao, and H. Narain, "Radioactive heat generation and heat flow in the Indian shield," *Earth Planet. Sci. Lett.*, vol. 30, no. 1, pp. 57–64, 1976, doi: 10.1016/0012-821X(76)90008-X.

[43] F. O. Ogunsanwo, J. O. Adepitan, J. D. Ayanda, K. W. Giwa, E. O. Falayi, and A. I. Adejimi, "Radiogenic heat production in crustal quarry rocks of Ogun State, south-western, Nigeria," *Environ. Earth Sci.*, vol. 80, no. 7, pp. 1–15, 2021, doi: 10.1007/s12665-021-09578-7.

[44] K. L. Shrivastava, D. Ram, and V. Gaur, "High heat producing radioactive granites of malani igneous suite at northeast of Jodhpur, northwestern India," *J. Geol. Soc. India*, vol. 89, no. 3, pp. 291–294, 2017, doi: 10.1007/s12594-017-0601-3.

[45] O. Ademila, "Evaluation of Rock Radiation Hazards for Construction Applications in Parts of Southwestern Nigeria," *J. Sci. Res.*, vol. 64, no. 02, pp. 38–49, 2020, doi: 10.37398/jsr.2020.640205.

[46] N. Venunathan, C. S. Kaliprasad, and Y. Narayana, "Natural radioactivity in sediments and river bank soil of Kallada river of Kerala, South India and associated radiological risk," *Radiat. Prot. Dosimetry*, vol. 171, no. 2, pp. 271–276, 2016, doi: 10.1093/rpd/ncw073.

[47] M. M. Prakash, C. S. Kaliprasad, and Y. Narayana, "Studies on natural radioactivity in rocks of Coorg district, Karnataka state, India," *J. Radiat. Res. Appl. Sci.*, vol. 10, no. 2, pp. 128–134, 2017, doi: 10.1016/j.jrras.2017.02.003.

[48] P. V. Divya, C. S. Kaliprasad, Y. Narayana, and V. Prakash, "Distribution of natural radionuclides and assessment of excess lifetime cancer risk along coastal areas of Varkala in Kerala," *J. Radioanal. Nucl. Chem.*, vol. 322, no. 1, pp. 121–127, 2019, doi: 10.1007/s10967-019-06509-6.

[49] V. Vineethkumar, R. Akhil, K. P. Shimod, and V. Prakash, "Geospatial analysis of the source of Monazite deposits and the dynamics of natural radionuclides in the selected coastal environs of Kerala, south west coast of India," *J. Radioanal. Nucl. Chem.*, vol. 326, no. 2, pp. 983–996, 2020, doi: 10.1007/s10967-020-07418-9.

[50] M. Sheela, U. Roselin, and G. Shanthi, "Estimation of radiological parameters of the rock samples from the western ghats in Kerala," Studies in Indian Place Names,vol 40, 18,1245-1249, 2020.

[51] P. K. Manigandan and B. Chandar Shekar, "Measurement of radioactivity in an elevated radiation background area of Western Ghats," *Nucl. Technol. Radiat. Prot.*, vol. 29, no. 2, pp. 128–134, 2014, doi: 10.2298/NTRP1402128M.

[52] UNSCEAR, *Sources, Effects and Risks of Ionizing Radiation*, vol. 120, no. 1. 2008.

[53] M. Tufail, Nasim-Akhtar, Sabiha-Javied, and T. Hamid, "Natural radioactivity hazards

of building bricks fabricated from saline soil of two districts of Pakistan," *J. Radiol. Prot.*, vol. 27, no. 4, pp. 481–492, 2007, doi: 10.1088/0952-4746/27/4/009.

[54] UNSCEAR, *Sources and Effects of Ionizing Radiation, United Nations Scientific Committee on the Effects of Atomic Radiation UNSCEAR 2000 Report to the General Assembly, with Scientific Annexes*, vol. I. 2000.

[55] EC, "Radiation Protection 112: Radiological protection principles concerning the natural radioactivity of building materials," *Eur. Comm.*, pp. 1–16, 1999, [Online]. Available: https://ec.europa.eu/energy/sites/ener/files/documents/112.pdf.

[56] P. Nandakumaran and K. Balakrishnan, "Groundwater quality variations in Precambrian hard rock aquifers: a case study from Kerala, India," *Appl. Water Sci.*, vol. 10, no. 1, pp. 1–13, 2020, doi: 10.1007/s13201-019-1084-8.

[57] E. Srinivasa, D. R. Rangaswamy, and J. Sannappa, "Assessment of radiological hazards and effective dose from natural radioactivity in rock samples of Hassan district, Karnataka, India," *Environ. Earth Sci.*, vol. 78, no. 14, Jul. 2019, doi: 10.1007/s12665-019-8465-z.

[58] P. S. Hameed, G. S. Pillai, and R. Mathiyarasu, "A study on the impact of phosphate fertilizers on the radioactivity profile of cultivated soils in Srirangam (Tamil Nadu, India)," *J. Radiat. Res. Appl. Sci.*, vol. 7, no. 4, pp. 463–471, 2014, doi: 10.1016/j.jrras.2014.08.011.

[59] S. Gulu, A. Districts, A. Olanya, D. Okello, B. Oruru, and A. Kisolo, "Natural Radioactivity Levels and Radiogenic Heat Production in River International Journal of Sciences : Natural Radioactivity Levels and Radiogenic Heat Production in River Sediments from Gulu and Amuru Districts , Northern Uganda," no. August, 2023.

[60] G. V. V Satyanarayana, N. S. Sivakumar, D. Vidyasagar, N. Murali, A. D. P. Rao, and P. V. L. Narayana, "Journal of the Indian Chemical Society Measurement of natural radioactivity and radiation hazard assessment in the soil samples of Visakhapatnam , Andhra Pradesh , India," *J. Indian Chem. Soc.*, vol. 100, no. 1, p. 100856, 2023, doi: 10.1016/j.jics.2022.100856.

[61] P. K. Manigandan and K. K. Natrajan, "Activity Concentrations of Natural Radionuclides in Soils of Rainforest Sites in Western Ghats," *Int. J. Students' Res. Technol. Manag.*, vol. 2, no. 3, pp. 103–108, 2015. doi: 10.18510/ijsrtm.2014.231.

[62] P. K. Shetty, Y. Narayana, and K. M. Rajashekara, "Depth profile study of natural radionuclides in the environment of coastal Kerala," *J. Radioanal. Nucl. Chem.*, vol. 290, no. 1, pp. 159–163, 2011, doi: 10.1007/s10967-011-1173-0.

[63] M. Zubair and Shafiqullah, "Radon Exhalation Rate Study of Sand Samples Collected from Sea Coast of Tirur, Kerala, India Using Track Etch Technique," *Mapan - J. Metrol. Soc. India*, vol. 33, no. 4, pp. 441–448, 2018, doi: 10.1007/s12647-018-0268-2.

[64] G. Skridlaite, B. Baginski, and M. Whitehouse, "Significance of ~ 1.5 Ga Zircon and Monazite ages from charnockites in southern Lithuania and NE Poland," *Gondwana Res.*, vol. 14, no. 4, pp. 663–674, 2008, doi: 10.1016/j.gr.2008.01.009.

[65] A. J. Vishnu C V, "Determination of natural radioactivity, hazard parameters and physico-chemical properties of soils from Palakkad-Thrissur district, Kerala, India,"

Mater. Today Proc., vol. 55, pp. 127–134, 2022, doi: 10.1016/j.matpr.2021.12.548.

[66] M. Ramsiya, A. Joseph, K. P. Eappen, and A. K. Visnuprasad, "Activity concentrations of radionuclides in soil samples along the coastal areas of Kerala, India and the assessment of radiation hazard indices," *J. Radioanal. Nucl. Chem.*, vol. 320, no. 2, pp. 291–298, 2019, doi: 10.1007/s10967-019-06481-1.

[67] B. Jananee, A. Rajalakshmi, V. Thangam, K. M. Bharath, and V. Sathish, "Natural radioactivity in soils of Elephant hills, Tamilnadu, India," *J. Radioanal. Nucl. Chem.*, vol. 329, no. 3, pp. 1261–1268, 2021, doi: 10.1007/s10967-021-07886-7.

[68] M. S. Roselin and G. Shanthi., "Evaluation of Radiation Hazard Indices Due To the Rock Samples of Western Ghats of South Tamilnadu.," *Int. J. Adv. Res.*, vol. 4, no. 12, pp. 486–495, 2016, doi: 10.21474/ijar01/2419.

[69] S. Ramesh, V. Vineethkumar, V. V Sayooj, and V. Prakash, "Investigation on the enrichment of radionuclides in an endosulfan - affected area , Enmakaje Panchayath , Kasargod," pp. 96–101, 2019, doi: 10.4103/rpe.RPE.

[70] J. Yang and Y. Sun, "Natural radioactivity and dose assessment in surface soil from Guangdong, a high background radiation province in China," *J. Radiat. Res. Appl. Sci.*, vol. 15, no. 1, pp. 145–151, 2022, doi: 10.1016/j.jrras.2022.01.019.

[71] R. Ravisankar *et al.*, "Assessments of radioactivity concentration of natural radionuclides and radiological hazard indices in sediment samples from the East coast of Tamilnadu, India with statistical approach," *Mar. Pollut. Bull.*, vol. 97, no. 1–2, pp. 419–430, 2015, doi: 10.1016/j.marpolbul.2015.05.058.

[72] R. S. Mohammed and R. S. Ahmed, "Estimation of excess lifetime cancer risk and radiation hazard indices in southern Iraq," *Environ. Earth Sci.*, vol. 76, no. 7, pp. 1–9, 2017, doi: 10.1007/s12665-017-6616-7.

[73] C. K. S. Kumar *et al.*, "Measurement of ^{226}Ra, ^{232}Th and ^{40}K and the associated radiological hazards in Ponnai river sand , Tamilnadu , India using Gamma-ray spectrometry," 2020, doi: 10.1080/03067319.2020.1796996.

[74] G. Poongodi, A. Chandrasekaran, V. Sathish, S. Karthikayini, A. Tamilarasi, and M. U. Khandaker, "Gamma-ray spectrometric analysis of bore-well rock samples from agricultural area of Tamil Nadu," *Phys. Open*, vol. 17, no. July, p. 100186, 2023, doi: 10.1016/j.physo.2023.100186.

[75] P. K. Manigandan and B. Chandar Shekar, "Risk assessment of radioactivity in soils of forest and grassland ecosystems of the Western Ghats, India," *Radioprotection*, vol. 50, no. 4, pp. 259–264, 2015, doi: 10.1051/radiopro/2015015.

[76] A. E. Abdel Gawad, M. S. Masoud, M. U. Khandaker, and M. Y. Hanfi, "Radiological hazards assessment associated with granitoid rocks in Egypt," *Nucl. Eng. Technol.*, no. January, 2024, doi: 10.1016/j.net.2024.01.032.

[77] A. H. Al-Khawlany, A. R. Khan, and J. M. Pathan, "Determination of Natural Radioactivity Levels and Radiation Hazards for Soil Samples from Aurangabad Maharashtra-India.," *Academia.Edu*, no. Ii, 2018, [Online]. Available: https://www.academia.edu/download/56293446/paper_IJMMS.pdf.

[78] I. Alam, M. N., Chowdhury, M. I., Kamal, M., Ghose, S., M. M. N., Mustafa, M. N., Miah, M. M. H., and Ansary, and M., "The ^{226}Ra, ^{232}Th, ^{40}K activities in beach sand

minerals and beach soils of Cox,s Bazar. Bangladesh," *J. Environ. Radioact.*, vol. 46, pp. 243–250, 1999.

[79] X. Lu and X. Zhang, "Natural radioactivity measurements in rock samples of Cuihua Mountain National Geological Park, China," *Radiat. Prot. Dosimetry*, vol. 128, no. 1, pp. 77–82, 2008, doi: 10.1093/rpd/ncm236.

[80] A. F. Tawfic *et al.*, "Natural radioactivity levels and radiological implications in the high natural radiation area of Wadi El Reddah, Egypt," *J. Radioanal. Nucl. Chem.*, vol. 327, no. 2, pp. 643–652, 2021, doi: 10.1007/s10967-020-07554-2.

[81] N. K. Ahmed, A. Abbady, A. M. El Arabi, R. Michel, A. H. El-Kamel, and A. G. E. Abbady, "Comparative study of the natural radioactivity of some selected rocks from Egypt and Germany," *Indian J. Pure Appl. Phys.*, vol. 44, no. 3, pp. 209–215, 2006.

[82] F. Amini Birami, F. Moore, R. Faghihi, and B. Keshavarzi, "Distribution of natural radionuclides and assessment of the associated radiological hazards in the rock and soil samples from a high-level natural radiation area, Northern Iran," *J. Radioanal. Nucl. Chem.*, vol. 322, no. 3, pp. 2091–2103, 2019, doi: 10.1007/s10967-019-06912-z.

[83] A. A. Qureshi *et al.*, "Study of natural radioactivity in Mansehra granite, Pakistan: Environmental concerns," *Radiat. Prot. Dosimetry*, vol. 158, no. 4, pp. 466–478, 2014, doi: 10.1093/rpd/nct271.

[84] M. Rafique *et al.*, "Evaluation of radiation dose due to naturally occurring radionuclides in rock samples of different origins collected from Azad Kashmir," *Russ. Geol. Geophys.*, vol. 55, no. 9, pp. 1103–1112, 2014, doi: 10.1016/j.rgg.2014.08.005.

[85] A. K. Patra, T. J. Jaison, A. Baburajan, and A. G. Hegde, "Assessment of radiological significance of naturally occurring radionuclides in soil and rock matrices around Kakrapar environment," *Radiat. Prot. Dosimetry*, vol. 131, no. 4, pp. 487–494, 2008, doi: 10.1093/rpd/ncn195.

[86] R. P. Chauhan, P. Chauhan, A. Pundir, S. Kamboj, V. Bansal, and R. S. Saini, "Estimation of dose contribution from ^{226}Ra, ^{232}Th and ^{40}K and radon exhalation rates in soil samples from shivalik foot hills in india," *Radiat. Prot. Dosimetry*, vol. 158, no. 1, pp. 79–86, 2014, doi: 10.1093/rpd/nct190.

[87] R. Daulta, V. K. Garg, and B. Singh, "Natural Radioactivity in Soil, Associated Radiation Exposure and Cancer Risk to Population of Eastern Haryana, India," *J. Geol. Soc. India*, vol. 94, no. 5, pp. 525–532, 2019, doi: 10.1007/s12594-019-1350-2

[88] K. Badhan, R. Mehra, and R. G. Sonkawade, "Natural Radioactivity Measurements in Soils of Jalandhar and Hoshiarpur Districts of Punjab, India," *Int. J. Pure Appl. Phys.*, vol. 13, no. 1, pp. 232–237, 2017, [Online].
Available: http://www.ripublication.com.

[89] R. Prasad, "Radon exhalation and gamma radioactivity levels in soil and radiation hazard assessment in the surrounding area of National Thermal Power Corporation , Dadri," *Radiat. Meas.*, vol. 50, pp. 130–135, 2013,
doi: 10.1016/j.radmeas.2012.09.008.

[90] M. M. Prakash, C. S. Kaliprasad, and Y. Narayana, "Studies on natural radioactivity in rocks of Coorg district, Karnataka state, India," *J. Radiat. Res. Appl. Sci.*, vol. 10, no. 2, pp. 128–134, 2017, doi: 10.1016/j.jrras.2017.02.003.

[91] P. S. Hameed, G. S. Pillai, G. Satheeshkumar, and R. Mathiyarasu, "Measurement of gamma radiation from rocks used as building material in Tiruchirappalli district, Tamil Nadu, India," *J. Radioanal. Nucl. Chem.*, vol. 300, no. 3, pp. 1081–1088, 2014, doi: 10.1007/s10967-014-3033-1.

[92] R. Bhaskaran *et al.*, "Hazard indices and annual effective dose due to terrestrial radioactivity in Northern Kerala, India," *J. Radioanal. Nucl. Chem.*, vol. 314, no. 3, pp. 2171–2179, 2017, doi: 10.1007/s10967-017-5583-5.

CHAPTER 6

RESULTS AND DISCUSSION

Evaluation of gamma radiation shielding properties of concrete reinforced with naturally available additives.

Content	
6.1	*Introduction*
6.2	*Materials and Mixture Design*
6.3	*Results and discussion*
6.4	*Linear- Mass attenuation coefficients*
6.5	*Half Value Layer, Tenth Value Layer and Mean Free Path*
6.6	*Effective atomic number and electron density*
6.7	*Built-up Factors*
6.8	*Fast neutron removal cross section*
6.9	*Conclusion*
6.10	*Reference*

***Abstract**: The production of radiation-protection materials has become a major research focus, particularly through strategies to increase concrete density. These materials are crucial in industrial, medical, and research applications due to their mechanical strength and ease of manufacturing. This study investigated the effects of chemical modifications, including coconut shell powder, Perlite, Vermiculite, and metal oxides of Zirconium and Neodymium, on gamma-ray absorption in concrete. The results showed that higher concentrations of these additives significantly enhanced gamma-ray absorption, indicating their potential for improved radiation protection in concrete materials.*

Concrete samples reinforced with naturally available additives.

6.1 Introduction

The Flora and fauna on the earth are always under the exposure to natural and man-made radiations. Though all the natural radiation cannot be completely shielded out, we can protect ourselves and various instruments from this radiation by using appropriate shielding materials. Generally, the initial level of shielding is given by concrete walls and concrete blocks. It was found that adding certain specific materials to the concrete at the time of preparation can increase the shielding capability [1], [2] .

Evaluating the gamma radiation shielding properties of different oxide-based concretes involves assessing their effectiveness in attenuating gamma rays, which is essential for applications requiring radiation protection. Concrete consisting of Portland cement, sand, aggregates (such as stones and gravel), and water stands as a frequently employed substance in the creation of commercial structures. Presently, standard concrete (with a density around 2.350 g/cm^3) stands out as one of the most widely used materials in radiation shielding. Its popularity can be attributed to an acceptable price, relative freedom in terms of geometry (casting), as well as high material design versatility, which gives it much potential for incorporating a great variety of waste and secondary raw materials [3]–[5]. It is used for radiation protection in radiation therapy facilities, nuclear reactors as well as in military applications [6].To date, many approaches aimed towards improving the radiation shielding properties of concrete have been proposed; including the selection of the proper aggregate type [7]–[9], as well as the proper additives and admixtures. In recent years, special attention has particularly been paid to nanosized admixtures, which lead to far greater improvements in cementitious systems, compared to their micro-sized counterparts [10]–[13]. The beneficial effects of nanoparticles (NPs) are attributable to either their chemical activity, which supports the cement hydration process, or the filling effect, which improves the packing of the material within a matrix as a result of the ultra-fine material size.

Some of the waste materials are used in concrete according to their properties. For instance, fly ash, rice husk, slag, and sludge from the treatment of industrial and

domestic wastewater have been found suitable as partial replacement for cement in concrete [14]. With the rising utilization of radiation like X-rays and gamma rays across diverse domains, ranging from medical purposes to the food industry, safeguarding against their harmful consequences has become an essential concern. Certain oxides, such as those of heavy elements like Lead (Pb), Barium (Ba), Bismuth (Bi), and Gadolinium (Gd), have high atomic numbers and are known for their increased interaction with gamma rays. These interactions include photoelectric absorption and Compton scattering, which result in the reduction of gamma-ray intensity. The heavy elements present in the oxide additives increase the likelihood of gamma rays interacting with the material. Gamma rays can be absorbed by the atoms in the oxides, leading to the release of secondary particles. These secondary particles, in turn, can further interact with the concrete, leading to multiple scattering events. This combination of absorption and scattering leads to a decrease in the energy and intensity of the gamma rays, effectively reducing their penetration through the material. When oxide additives with high atomic numbers are mixed with concrete, the effective atomic number (Z_{eff}) of the resulting material increases. This enhanced Z_{eff} contributes to stronger interactions between the gamma rays and the shielding material, thereby increasing the attenuation of the radiation [15].

In the present study we are investigating the gamma- ray shielding capability of concrete, which we hve prepared by adding naturally occurring materials Perlite, Vermiculate, coconut shell and metal oxides of Zirconium and Neodymium.

Perlite is an amorphous volca nic glass that has a relatively high-water content, typically formed by the hydration of igneous rock called obsidian. It occurs naturally and has the unusual property of greatly expanding when heated sufficiently. It is an industrial mineral and a commercial product useful for its low density after processing. Vermiculite is a hydrous phyllosilicate mineral. Vermiculite is the name of a group of hydrated laminar minerals (Aluminium-iron magnesium silicates) which look like mica. The Coconut shell is a material which can be a substitute for aggregates. The shell of the coconut is mostly used as an ornament and as a source of activated carbon [16]. The powdered shell is also used in the industries of

plastics, glues, and abrasive materials. The use of coconut shells can also help the prevention of pollution of the environment and is also help economically. Sun drying shells are to be used to make sure the decay of biodegradable materials decay before mixing with concrete. It also contributes to sustainable construction.

In this study we have analysed the effect of different material proportions on the gamma radiation transmission properties of concrete using irradiation measurements and Phy/PSD calculations [17]–[19]. Phy/PSD is a database running on a PC and was developed by combining pre-existing databases for interaction processes such as photoelectric absorption, scattering (both coherent and incoherent) and pair production at photon energies from 1 keV to 100 GeV.

6.2 Materials and Mixture Design

To carry out this work, lightweight concrete block were used. These materials are parallelepipeds that are industrially built with 3 main elements: Portland cement, sand and different additives. Ordinary Portland Cement (OPC) conforming to [ASTM C150]. Fine and coarse aggregates are Perlite, Vermiculite, Coconut shell powder (Finely ground coconut shell powder, Neodymium (III) Oxide (Nd_2O_3) and Zirconium dioxide (ZrO_2) (99.98% High-purity micro sized powder). The mix design for ordinary concrete (control) was prepared using a water-to-cement ratio of 0.45 and a cement-to-aggregate ratio of specified ratio of 1:2:4. Concrete mixes were prepared with the addition of 10% and 20% (by weight of cement) of each additive: Perlite, Vermiculite, coconut shell powder, Nd_2O_3, and ZrO_2. For each batch, calculating the weight of each additive as 10% and 20% of the cement weight. Thoroughly mixed the additives with the dry cement before adding water and aggregates. All dry ingredients (cement, additives, fine and coarse aggregates) were dry mixed in a concrete mixer for 2 minutes. Water was added gradually while continuing to mix for an additional 3 minutes until a homogeneous mixture was obtained. The concrete mix was poured into molds of size $10 \times 10 \times 10$ cm³ (in accordance with ASTM C31).

Table 6.1: Details about the concrete sample moulded along with density.

Concrete mix	Sample code	Density ($g/cm^{3.}$)
Ordinary concrete	CS	2.26
Ordinary concrete+10% Coconut shell powder	CSC10	3.14
Ordinary concrete+20% Coconut shell powder	CSC20	3.26
Ordinary concrete+10% Perlite	CSP10	2.86
Ordinary concrete+20% Perlite	CSP20	2.92
Ordinary concrete+10% Vermiculite	CSV10	2.90
Ordinary concrete+20% Vermiculite	CSV20	3.02
Ordinary concrete+10% ZrO_2	CSZ10	3.46
Ordinary concrete+20% ZrO_2	CSZ20	3.52
Ordinary concrete+10% Nd_2O_3	CSN10	3.61
Ordinary concrete+20% Nd_2O_3	CSN20	3.73

The Moulds were vibrated for compaction and then covered with plastic sheets to prevent moisture loss. After 24 hours, the samples were demoulded and cured in a water tank at 23°C for 28 days. The density of the different prepared samples was determined by using standard techniques using the mass and volume of the concrete mix.

6.3 Results and discussion

The present study deals with the determination of the shielding parameters for gamma, neutron, proton and alpha radiation of heavy concrete with Perlite (CSP10 and CSP20), Vermiculite (CSV10 and CSV20), and heavy concrete with metal oxides of Zirconium and Neodymium (CSZ10, CSZ20, CSN10 and CSN20). For gamma attenuation, Figure 6.1 (a) shows moulded concrete samples of size 10 × 10 × 10 cm^3 and Figure 6.1 (b-f) SEM images of the moulded concretes with addition of aggregates (CSC20, CSP20, CSV20, CSN20 and CSZ20 respectively). Table 6.2 presents the chemical content details of the produced samples. XCOM software was used to obtain shielding parameters and further these results were confirmed using the well-known Phy/PSD program.

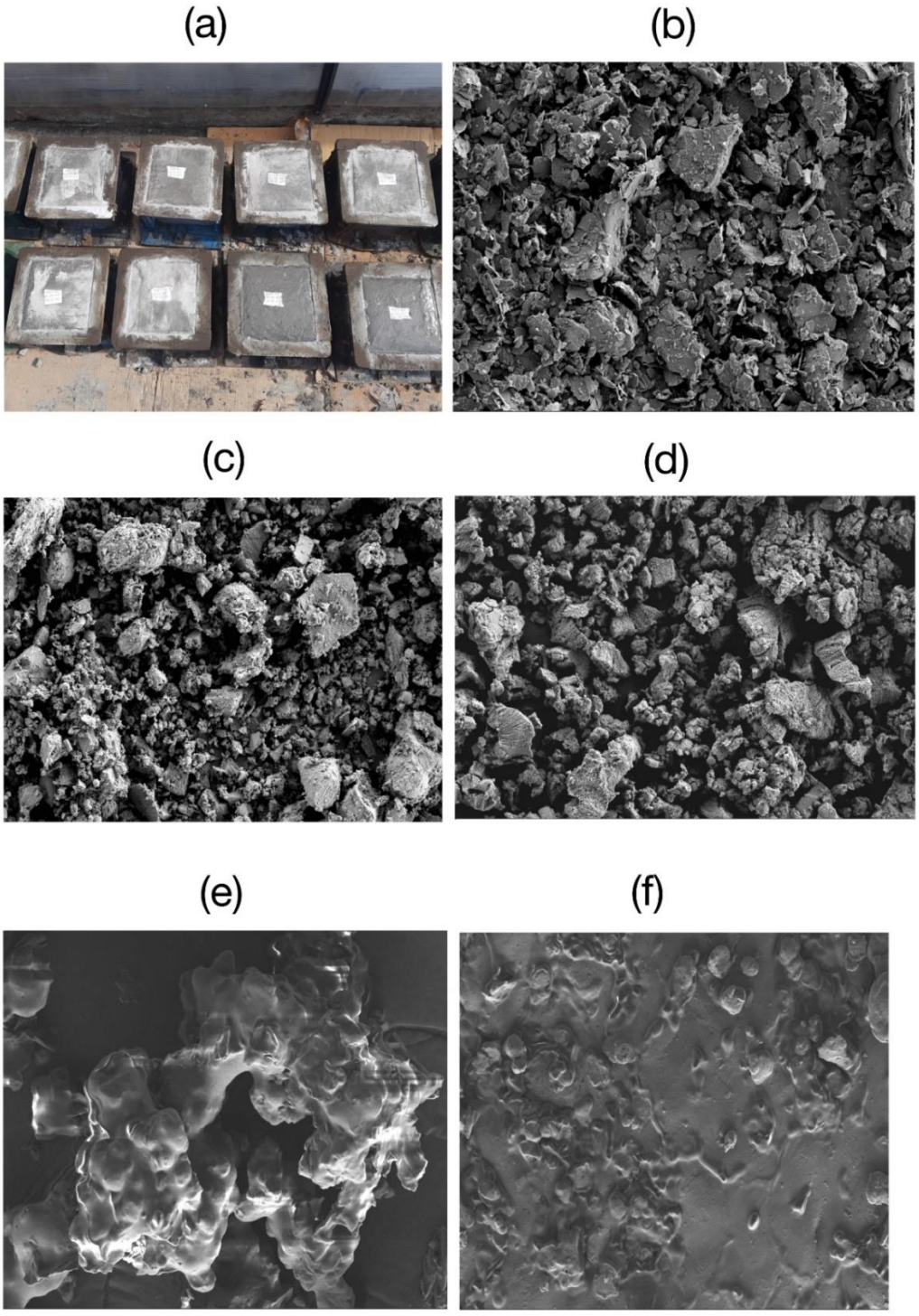

Figure 6.1: Moulded concrete sample of size 10 × 10 × 10 cm³ (a) and SEM images of the moulded concretes with addition of aggregates (b-f).

Table 6.2: Qualitative elemental chemical composition (in wt.%.) of fabricated concretes.

Elements	CaO	SiO_2	Al_2O_3	MgO	Na_2O	K_2O	TiO_2	MnO	Fe_2O_3	Nd_2O_3	ZrO_2
CS	39.27	34.11	12.11	2.52	4.57	1.26	0.98	0.06	5.12	-	-
CSC10	42.36	33.97	12.63	2.01	3.77	0.99	0.72	0.05	4.50	-	-
CSC20	44.57	29.03	12.34	2.40	4.31	1.16	0.86	0.06	5.28	-	-
CSP10	44.57	30.03	11.34	2.40	4.31	1.16	0.86	0.06	5.28	-	-
CSP20	42.00	32.50	11.00	2.53	4.56	1.24	0.95	0.06	5.16	-	-
CSV10	42.69	29.76	12.60	2.46	4.42	1.19	0.88	0.06	5.94	-	-
CSV20	41.52	32.86	12.33	2.18	4.08	1.07	0.78	0.05	5.13	-	-
CSZ10	38.14	30.05	10.7	2.42	3.47	1.21	0.89	0.06	3.05		10.01
CSZ20	34.88	27.67	7.64	2.25	3.2	1.11	0.8	0.05	3.01		19.39
CSN10	38.36	30.95	9.58	2.43	3.84	1.1	0.76	0.05	3.08	9.85	
CSN20	34.81	27.84	7.45	1.82	3.35	1.08	0.65	0.04	3.28	19.68	

Figure 6.2 illustrates the density of the cement pastes, showing variation based on the proportion of additives. The density of the concrete samples ranges from 2.26 to 3.73 g/cm³. Density is crucial not only for photon radiation attenuation but also for minimizing the thickness of the shielding material required.

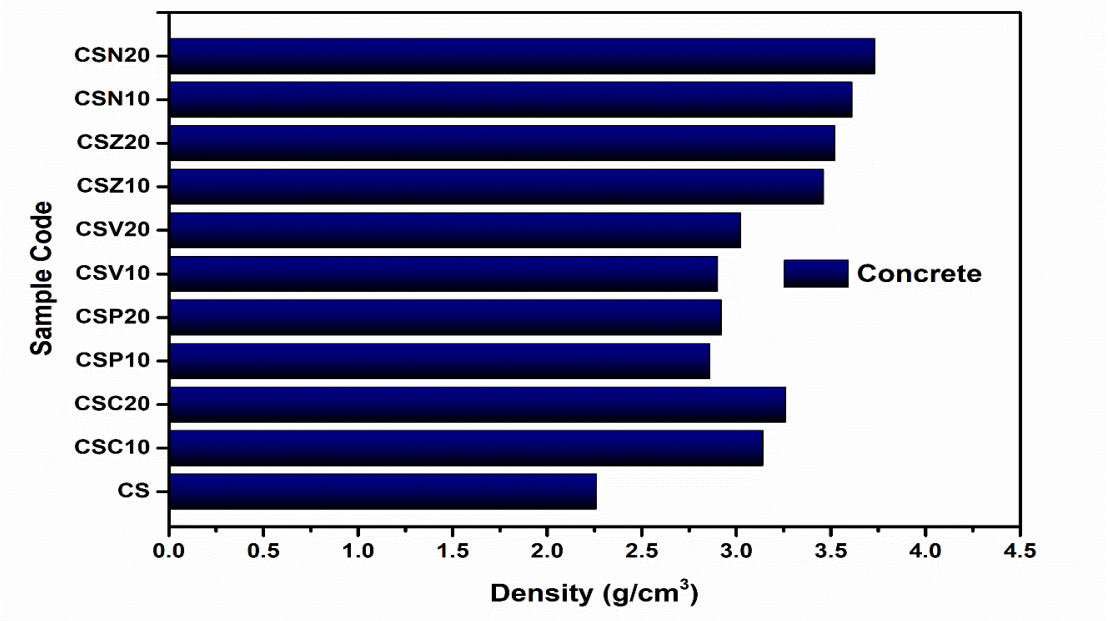

Figure 6.2: Density of moulded concrete samples.

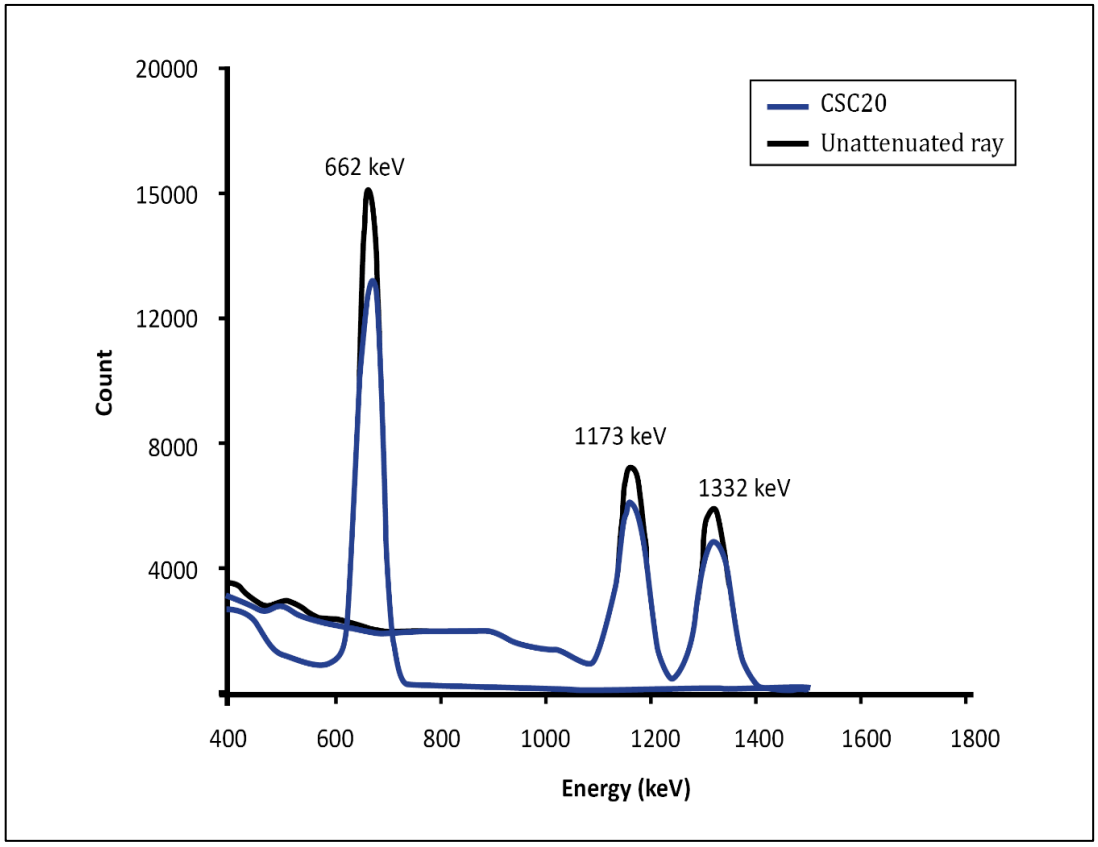

Figure 6.3: The gamma-ray spectrum obtained from CSC20 sample.

Figure 6.3 depicts the spectrum of the CSC20 sample when gamma rays with energies of 662 keV, 1173 keV, and 1333 keV pass through it.

6.4 Linear- Mass attenuation coefficients

The initial step involves experimentally evaluating the radiation attenuation properties of concretes with varying ratios of Perlite, Vermiculite, coconut shell powder, and oxides of Neodymium and Zirconium, alongside theoretically measured linear attenuation coefficients (LAC) for the concrete samples. In Table 6.3, the measured and theoretically estimated Phy-PSD values for the LAC of the concrete with additives for the energies of 0.662, 1.173 and 1.333 MeV were enlisted. The experimentally measured values are important parameter because the authors can estimate other shielding quantities based on the experimental LAC values, so it is useful to test the accuracy of the measured MAC values, and this can be done by compare the measured values with theoretical values generated by Phy-PSD

software. The linear attenuation coefficients experimentally determined and calculated using the Phy-PSD code are given in Table 6.3.

Table 6.3: Experimental and theoretical values of LAC for fabricated concretes.

Sample Code	Linear attenuation Coefficient, μ (cm^{-1})					
	0.662 MeV		1.173 MeV		1.333 MeV	
	Expt.	Phy-PSD	Expt.	Phy-PSD	Expt.	Phy-PSD
CS	0.1699	0.1692	0.1226	0.1224	0.1197	0.1199
CSP10	0.1828	0.1826	0.1294	0.1285	0.1259	0.1254
CSP20	0.1972	0.1979	0.1395	0.1390	0.1362	0.1357
CSV10	0.1769	0.1773	0.1267	0.1239	0.1241	0.1248
CSV20	0.1968	0.1983	0.1370	0.1375	0.1350	0.1345
CSC10	0.1864	0.1871	0.1311	0.1325	0.1287	0.1289
CSC20	0.2007	0.2012	0.1440	0.1438	0.1405	0.1389
CSZ10	0.2089	0.2102	0.1559	0.1549	0.1461	0.1464
CSZ20	0.2027	0.2039	0.1507	0.1502	0.1393	0.1396
CSN10	0.2095	0.2116	0.1531	0.1520	0.1457	0.1452
CSN20	0.2225	0.2233	0.1608	0.1600	0.1534	0.1523

Figure 6.4 shows a graphical representation of the experiental linear attenuation coefficient (LAC) values as a function of the energy for the control concrete and the concretes with different ratios of aggregates. The LAC shows a decrease with energy and the shape of the curve obeys the general equation of Lamberts Beer law, so the change in the LAC with the energy has an exponential decay shape.

To check the dependency of the LAC on the additives, the LAC as a function of eergy at 0.662, 1.173 and 1.333 MeV was plotted (Figure 6.4). Clearly, the LAC shows an increase behaviour while adding aggregates to the concretes.

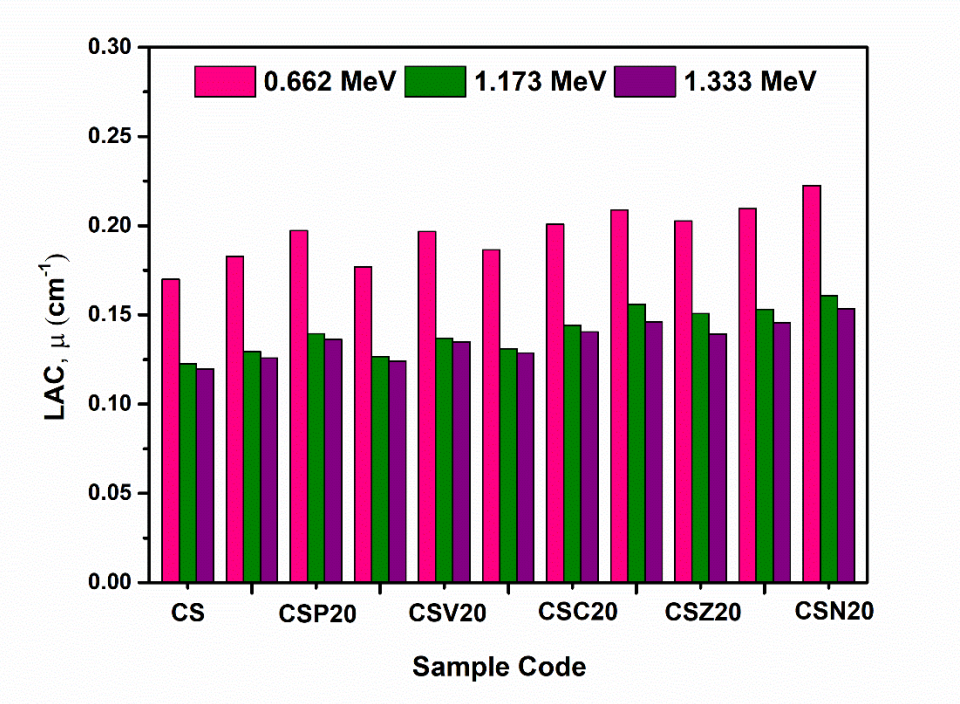

Figure 6.4: The experimental results of LAC for moulded samples in selected energies.

The LAC for pure concrete reduces from 0.169 to 0.119 cm^{-1} over the selected energy range. Also, for the CSP20, it is reduced from 0.197 to 0.136 cm^{-1} over the same energy range and from 0.196 to 0.135 cm^{-1} for CSV20 sample. The coconut shell powder added concrete CSC20 shows reduction of LAC values from 0.201 to 0.141 cm^{-1} 0.662 to 1.333 MeV. This exponential decay in the LAC for the prepared concretes describes the process of reducing the shielding ability rate for these concretes over the selected energy range. On the other hand, the LAC for the metal oxides, ZrO_2 and Nd_2O_3 in concrete is much higher than the LAC for the concretes with Perlite, coconut shell and Vermiculite, especially at low energy. This means that the attenuation competence of these concretes with other concretes. However, Perlite, vermiculite and coconut also have the same ability to block gamma rays.

We have theoretically studied the impact of γ-photon energy on the linear attenuation coefficient (μ) measured values for the investigated concrete samples. Figure 6.5 displays computational results of LAC, depicting a decrease in the μ values with the incoming photon energy in the range 0.01 to 20 MeV.

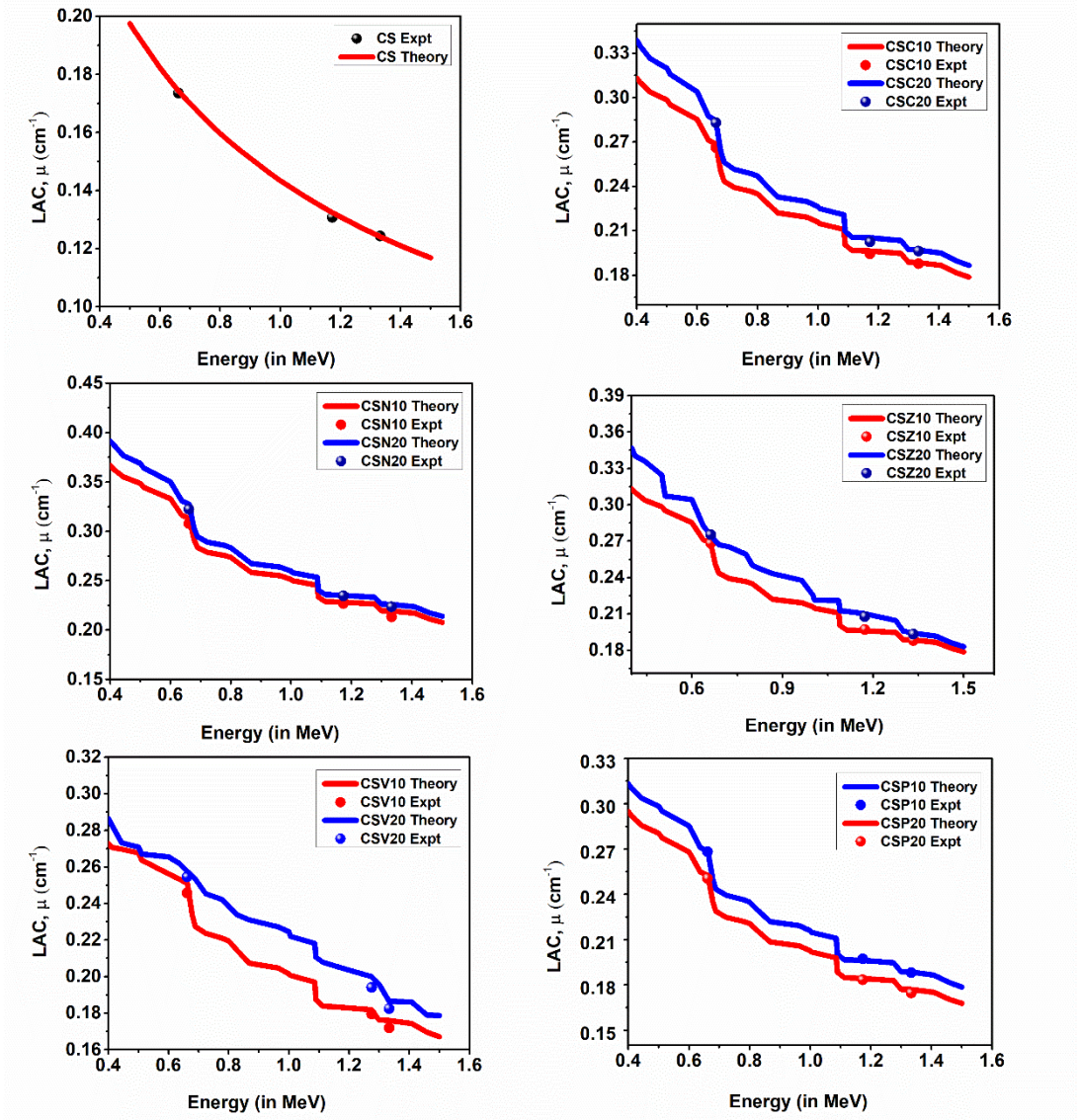

Figure 6.5: Computational and experimental results of LAC of the moulded concretes with respect to energy.

At low energies, the photoelectric effect is the dominant mechanism for the interaction between an incoming photon and the concrete materials. Therefore, the concretes can attenuate the incoming photons and the cross-section of photoelectric effect is proportional inversely to the Energy (σ_{ph} α $E^{-3.5}$). Above 100 keV, the attenuation of photons diminishes due to the second predicated interaction called Compton scattering phenomena. In the Compton scattering interaction, the photons are lessening a part of their energies to eject the electron and the rest of the energy is attenuated inside the concrete materials. Thus, the Compton scattering cross-section

is proportional inversely to the E (σ_{cs} α E^{-1}).

The maximum values of the μ are achieved at a low energy of 0.1 MeV, where it is 0.44, 0.49, 1.51, 3.06, 0.56 and 0.69 cm^{-1} for samples CS, CSV20, CSP20, CSZ20, CSN20 respectively. While the lowest μ values 0.05, 0.06, 0.15, 0.38, 0.07 and 0.064 cm^{-1} are found at high energy of 10 MeV for samples CS, CSV20, CSP20, CSN20 and CSZ20, respectively.

Table 6.4: Experimental and theoretical values of MAC for fabricated concretes.

Sample code	Mass attenuation Coefficient, μ/ρ (cm^2/g)					
	0.662 MeV		1.173 MeV		1.333 MeV	
	Expt.	Phy-PSD	Expt.	Phy-PSD	Expt.	Phy-PSD
CS	0.0751	0.0748	0.0542	0.0541	0.0529	0.0530
CSP10	0.0774	0.0773	0.0548	0.0544	0.0533	0.0531
CSP20	0.0783	0.0786	0.0554	0.0552	0.0541	0.0539
CSV10	0.0761	0.0763	0.0545	0.0533	0.0534	0.0534
CSV20	0.0793	0.0799	0.0552	0.0554	0.0544	0.0542
CSC10	0.0772	0.0775	0.0543	0.0549	0.0533	0.0534
CSC20	0.0783	0.0785	0.0562	0.0561	0.0548	0.0542
CSZ10	0.0785	0.0790	0.0586	0.0582	0.0549	0.0550
CSZ20	0.0803	0.0808	0.0597	0.0595	0.0552	0.0553
CSN10	0.0802	0.0810	0.0586	0.0582	0.0558	0.0556
CSN20	0.0815	0.0818	0.0589	0.0586	0.0562	0.0558

It is seen from Figure 6.6 and Figure 6.7 that experimental and Phy-PSD results of MAC for selected energies are in concordance with each other. 20% Neodymium oxide added cement sample have the highest values of μ/ρ while the lowest values belong to pure concrete sample. It is obvious from Figure 6.7 that the values of μ/ρ depend on both photon energy and chemical composition of samples. Figure 6.7 shows the variation of MAC values of the fabricated concrete samples over the photon energy from 0.01 MeV to 15 MeV and it is evident that MAC depends on incident photon energy and chemical contents of the samples. As sample CSN20, CSN10 and CSC20 have the highest density and higher weight proportion of higher atomic number elements, it has greater values of MAC than its counterparts.

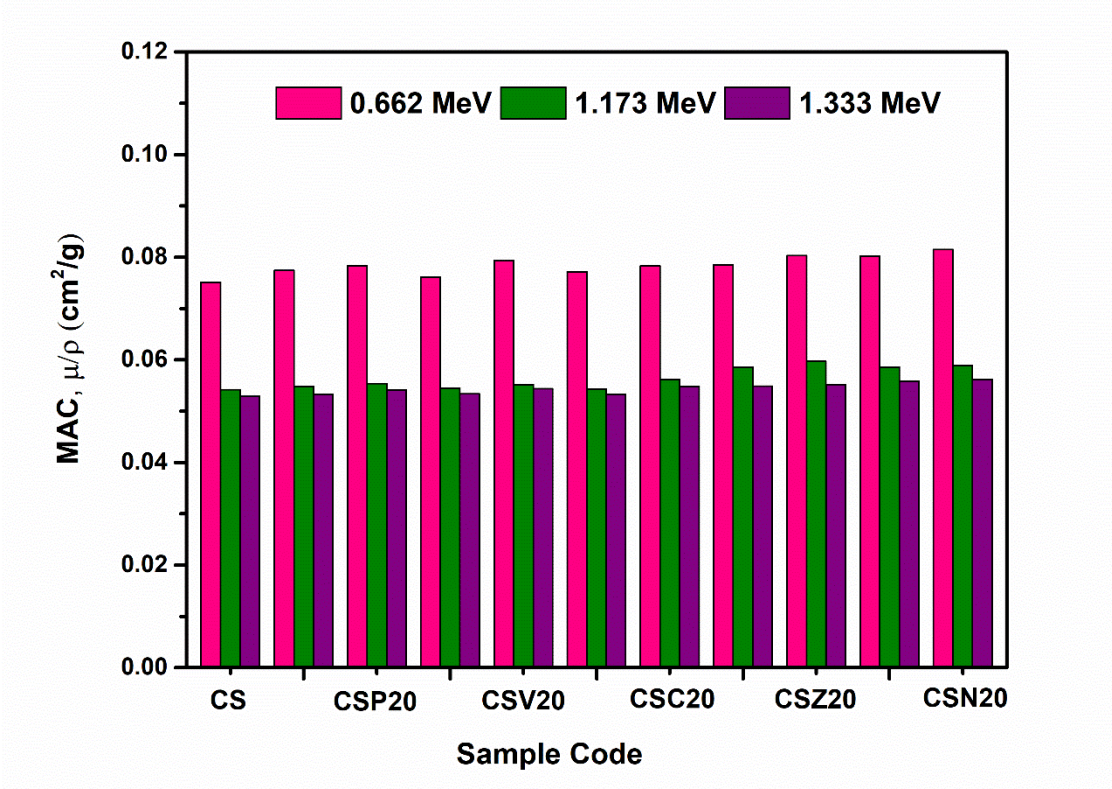

Figure 6.6: The experimental results of MAC for moulded samples in selected energies.

In low energy region, since photoelectric cross section changes proportional with Z^4 and inversely proportional with the incident photon energy as $E^{3.5}$, μ/ρ values of the cement samples were decreased rapidly up to 0.2 MeV. Beyond 0.2 MeV, Compton scattering becomes effective at intermediate energies. μ/ρ values of the cement pastes are almost constant and zero due to the linear dependence of cross-section of Compton scattering with atomic number Z. number elements, it has greater values of MAC than its counterparts. This can further be explained by the reported studies by Chang et al., Kilicoglu and More et al. have emphasized the importance of atomic number and density parameters as the higher the atomic number and density, the greater probability of interaction which results in better attenuation [7], [20], [21].

As the energy increases from 0.015 to 0.1 MeV, there is a sharp decline in MAC values with a peak at 0.04 MeV owing to the photoelectric effect. This trend of variation is in whithin with the results reported by Al-Saadi, A.J. and A.K. Saadon wherein they observed MAC for lead oxide and iron oxide reinforced in silicate

glass samples sharply decreases with an increase of the photon energy from 0.001 to 0.1 MeV with a peak [22].

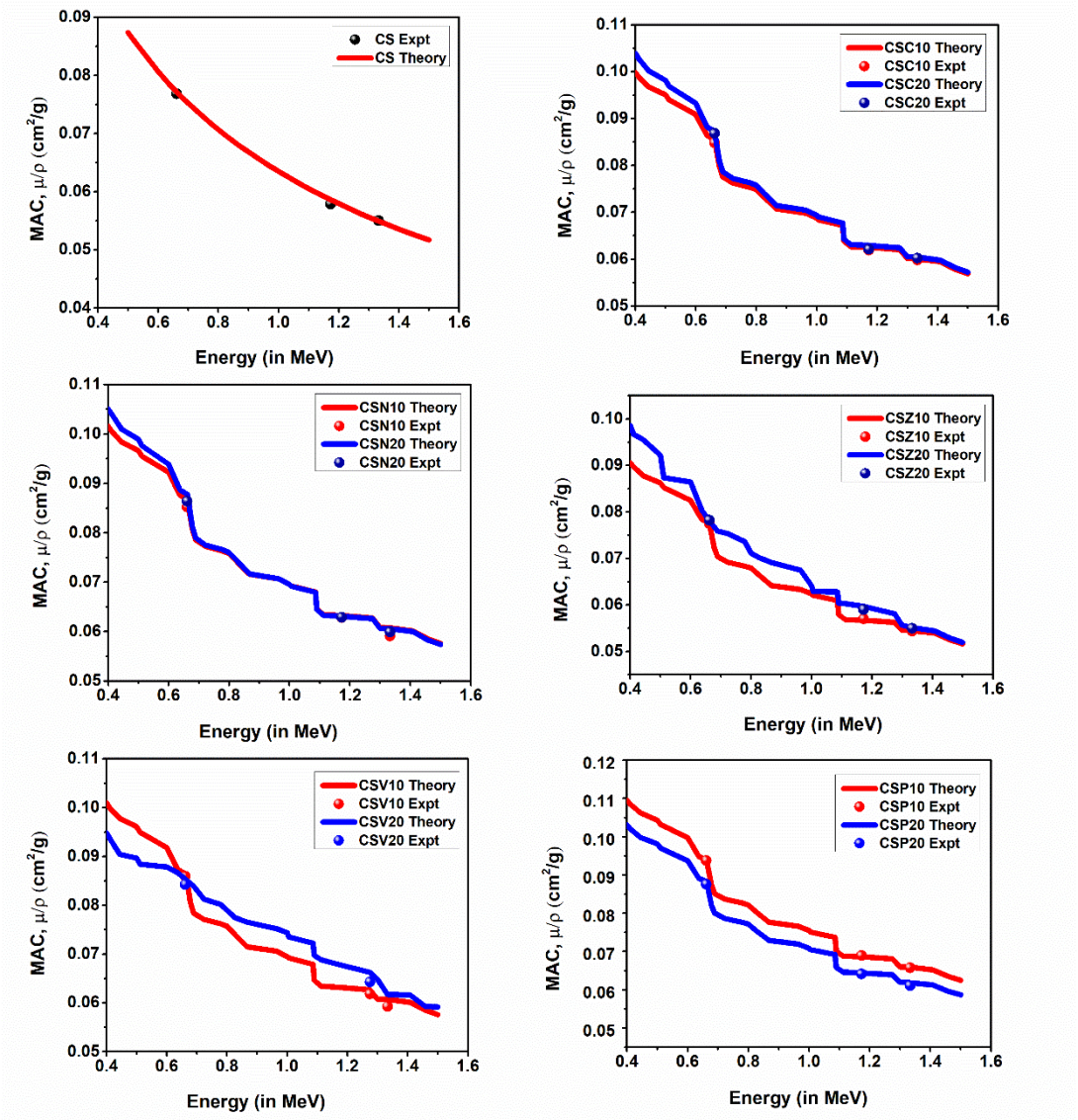

Figure 6.7: Computational and experimental results of MAC by of the moulded concretes with respect to energy.

It was observed that the majority of detected photons had the same energies as the initial gamma-ray photons, accounting for about 10% of the original photon count. This suggests that these photons passed through the concrete specimens without any significant interaction. Additionally, numerous photons with different energies from the initial photons were detected, indicating that most photons interacted with the concrete, resulting in a reduction of their energy. Furthermore, the number of

photons detected with energies matching the initial gamma rays varied among different concrete specimens, correlating with the gamma-ray shielding capacity of the concrete [8]. Specimens with stronger shielding capacities allowed fewer photons with the initial energies to be detected. The data also showed that the number of detected photons decreased sharply with increasing concrete thickness, demonstrating that the thickness of the concrete significantly enhanced its radiation shielding capability.

6.5 Half Value Layer, Tenth Value Layer and Mean Free Path

Table 6.5 shows the variation of half value layer (HVL), tenth value layer (TVL) as a function of incident photon energy.

Table 6.5: Experimental values of HVL and TVL for the selected Energies.

Sample code	Half Value Layer, HVL (cm)					
	0.662 MeV		1.173 MeV		1.333 MeV	
	Expt.	Phy-PSD	Expt.	Phy-PSD	Expt.	Phy-PSD
CS	4.08	4.10	5.65	5.66	5.79	5.78
CSP10	3.13	3.13	4.42	4.45	4.54	4.56
CSP20	3.03	3.02	4.28	4.29	4.38	4.40
CSV10	3.14	3.13	4.38	4.48	4.47	5.55
CSV20	2.90	2.88	4.16	4.15	4.23	4.24
CSC10	2.86	2.85	4.06	4.02	4.14	4.13
CSC20	2.71	2.71	3.78	3.79	3.88	3.92
CSZ10	2.55	2.53	3.41	3.44	3.65	3.64
CSZ20	2.45	2.43	3.29	3.31	3.56	3.56
CSN10	2.39	2.37	3.27	3.30	3.44	3.45
CSN20	2.28	2.27	3.15	3.17	3.31	3.33
	Tenth Value Layer, HVL (cm)					
CS	13.56	13.61	18.78	18.82	19.25	19.21
CSP10	10.40	10.41	14.68	14.79	15.10	15.15
CSP20	10.06	10.02	14.22	14.27	14.56	14.61
CSV10	10.43	10.40	14.57	14.89	14.87	18.45
CSV20	9.63	9.56	13.84	13.79	14.04	14.09
CSC10	9.50	9.46	13.51	13.36	13.76	13.73
CSC20	9.02	9.00	12.57	12.59	12.89	13.03
CSZ10	8.47	8.42	11.35	11.43	12.11	12.09
CSZ20	8.14	8.09	10.95	10.98	11.84	11.82
CSN10	7.95	7.87	10.88	10.96	11.43	11.47
CSN20	7.58	7.55	10.48	10.54	10.99	11.06

These are significant parameters that give the required thicknesses of materials at selected energies and shielding capabilities of materials. These factors have shown the exact contrary trend of variation as that of MAC i.e., increasing one with incident energy. HVL enables us to obtain in an easy way a material's shielding ability. Figure 6.8 represents HVL values versus the incident photon energy and additive content for 0.01-20 MeV photon energies. In contrast to μ/ρ values, HVL values are enhanced as the photon energy increases.

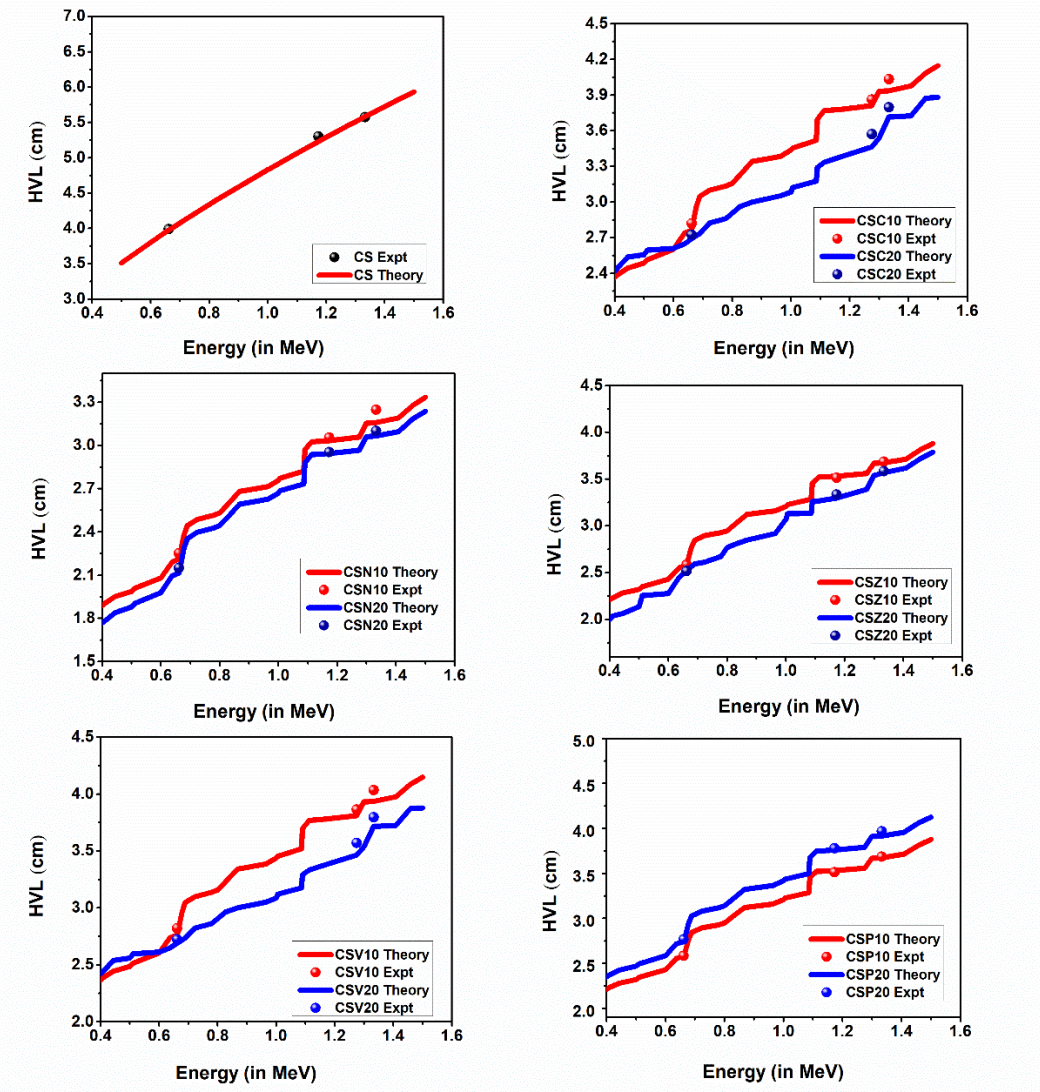

Figure 6.8: Computational and experimental results of HVL of the moulded concretes with respect to energy.

The HVL and TVL values also depend on the density of the sample in inverse proportion. 20% Nd_2O_3 including cement sample (CSN20) have smaller HVL values compared with other samples due to its higher density (3.73 g/cm^3). The photon energy Eγ and density of the examined concrete affect the HVL results. As a result, the materials with the lowest HVL values are considerable and can be used for a variety of shielding purposes. Firstly, values of HVL were raised with increment in photon energy up to 0.075 MeV, then tended to rise slowly and remain stable. At low energies, HVL is less dependent on the content of the material. As the photon energy increases, the HVL values are increased and the HVL values are declined as the additive's ratio in the Portland cement samples increases. The increase in the gamma-photon energy between 0.01 and 10 MeV increases the HVL for developed concretes is between 0.04 and 5.55 cm (for concrete CSN20), 0.01 and 5.77 cm (for concrete CSZ20), 0.003–5.79 cm (for concrete CSC20), 0.01–6.03 cm (for concrete CSV20), and 0.01–5.92 cm (for concrete sample CSP20), respectively.

Variation of TVL of the moulded concretes with respect to energy is shown in Figure 6.9. The Tenth-Value Layer (TVL) is a concept in radiation shielding that refers to the thickness of a material required to reduce the intensity of radiation by a factor of ten. In other words, it is the thickness needed to attenuate the radiation to one-tenth of its original value. This concept is particularly useful for understanding and designing materials and structures for effective radiation protection. TVL refers to the thickness of a specified material that reduces the radiation intensity to 10% of its original value. The TVL depends on the type and energy of the radiation as well as the material's properties, such as its density and atomic composition.

Materials with higher atomic numbers and densities generally have smaller TVLs because they are more effective at attenuating radiation. In designing radiation shielding, multiple layers of different materials might be used to achieve the desired level of attenuation. Materials with lower TVLs are more effective at attenuating radiation and thus require less thickness to achieve the same level of protection.

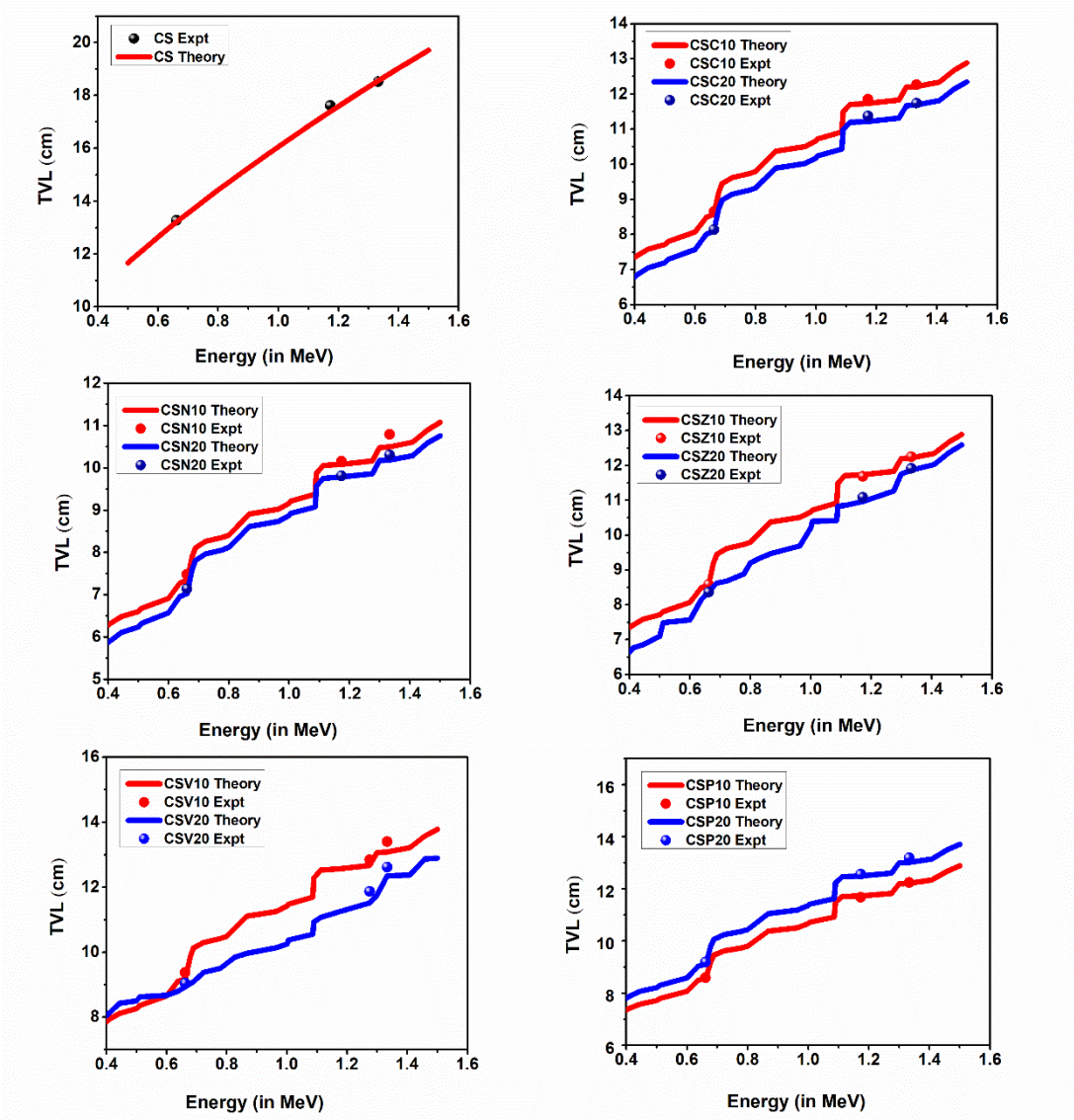

Figure 6.9: Computational and experimental results of TVL of the moulded concretes with respect to energy.

The synthesized concretes' mean free path (λ) was calculated and graphically represented in Figure 6.10. The "λ" factor represents the typical separation between two succeeding collisions of the gamma photon in the concrete. Table 6.6 shows the variation of mean free path as a function of incident photon energy.

Table 6.6: Experimental values of MFP for the selected Energies.

Sample code	Mean Free Path, MFP (cm)					
	0.662 MeV		1.173 MeV		1.333 MeV	
	Expt.	Phy-PSD	Expt.	Phy-PSD	Expt.	Phy-PSD
CS	5.89	5.91	8.16	8.17	8.36	8.34
CSP10	4.51	4.52	6.38	6.42	6.56	6.58
CSP20	4.37	4.35	6.17	6.20	6.32	6.35
CSV10	4.53	4.52	6.32	6.47	6.46	8.01
CSV20	4.18	4.15	6.01	5.99	6.10	6.12
CSC10	4.13	4.11	5.87	5.80	5.98	5.96
CSC20	3.92	3.91	5.46	5.47	5.60	5.66
CSZ10	3.68	3.66	4.93	4.96	5.26	5.25
CSZ20	3.53	3.51	4.75	4.77	5.14	5.13
CSN10	3.45	3.42	4.72	4.76	4.96	4.98
CSN20	3.29	3.28	4.55	4.58	4.77	4.80

The values for concrete with 20% additives can be found to generally increase from 1.9 to 7.8 cm with the increase in photon energy among the incoming photon energies ranging from (81–1408) keV. As a result, gamma photons' capacity to permeate concrete material also increases. The increase in the gamma-photon energy between 0.01 and 10 MeV increases the MFP for developed concretes is between 0.04 and 8.01 cm (for concrete CSN20), 0.01 and 9.23 cm (for concrete CSZ20), 0.003–8.31 cm (for concrete CSC20), 0.01–8.71 cm (for concrete CSV20), and 0.01–8.54 cm (for concrete sample CSP20), respectively.

Among the selected samples, the values of these parameters for CSN20, CSN10, CSZ20 and CSZ10 show better radiation shielding than others in the sample. This can be attributed to the highest density among the studied materials that help to minimize values HVL, TVL, and MFP for CSN20 material that increased the probability of interaction. It is also recognized that although sample CSN20 has a higher density than CSN10, it shows better attenuation capability as CSN20 has more Neodymium constituent.

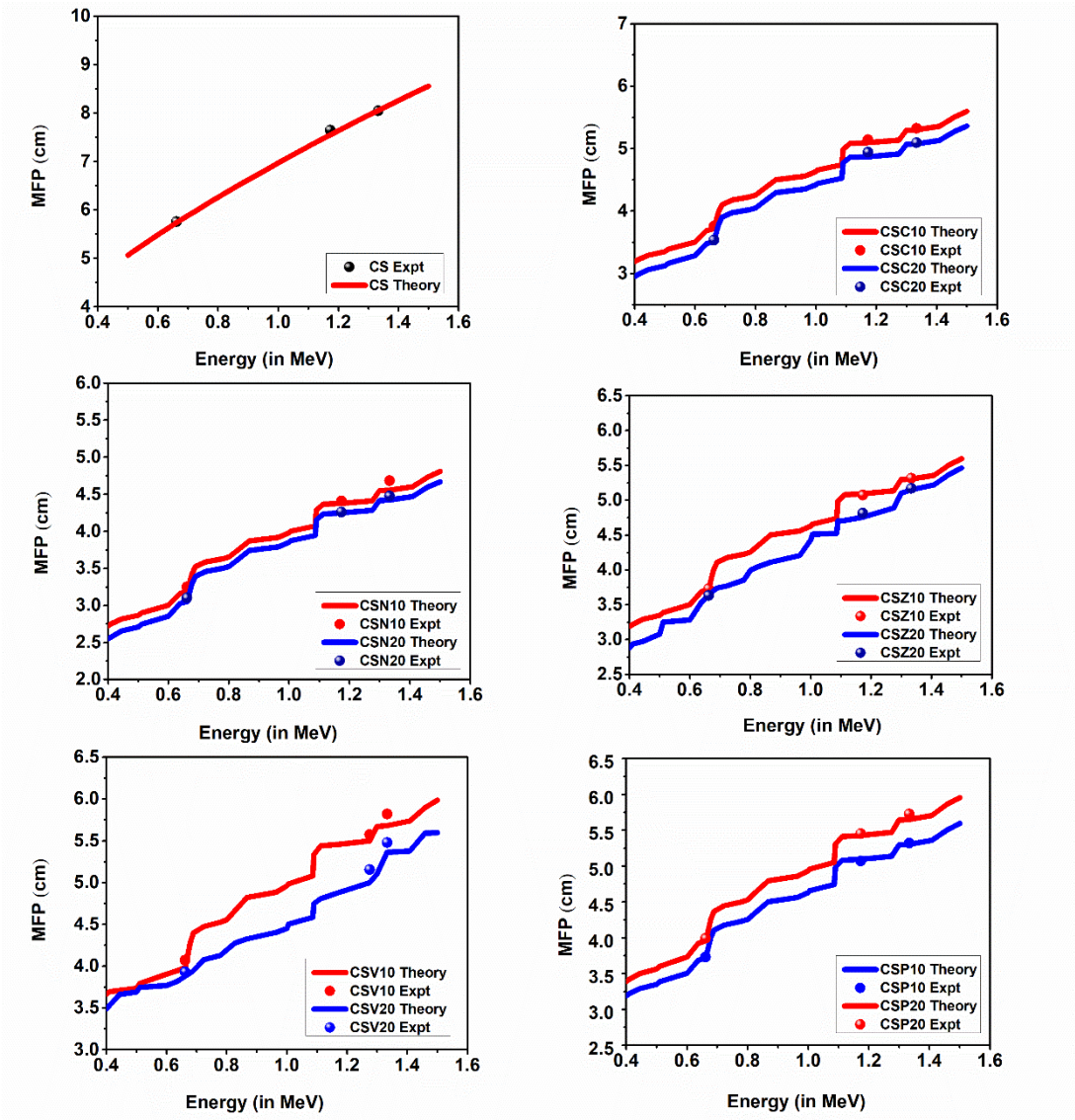

Figure 6.10: Computational and experimental results of MFP of the moulded concretes with respect to energy.

6.6 Effective atomic number and electron density

The effective atomic number (Z_{eff}) was also established to appreciate the efficacy of shielding material attenuation capabilities for the prepared mortars. The probability of photoelectric absorption increases with a high effective atomic number. The mortar sample with the highest concentration of Nd_2O_3 and ZrO_2 showed a steadily increasing linear attenuation coefficient of gamma rays, as shown in Figure 6.11, due to its association with high Z_{eff} values.

The changes of Z_{eff} and N_{eff} with photon energy for the cement paste samples have been indicated in Figure 6.11 and Figure 6.12. For the samples used, different partial photon interaction processes are dominated by Z_{eff}'s variation with photon energy. Z_{eff} values initially decrease slowly, but as mentioned above, sudden increments occur at 0.04 and 0.01 keV due to Ca, Si, Nd and Zr K-shell absorption edges. Z_{eff} starts to increase with photon energy beyond 0.02 MeV and creates a spherical peak in the mid-energy region. According to Figure 6.11, the highest Z_{eff} was for 20% Nd_2O_3 and ZrO_2 added sample since Nd and Zr have higher effective atomic cross section. The Z_{eff} values of the samples at intermediate energies are virtually stable because Compton scattering cross section differs linearly with the Z.

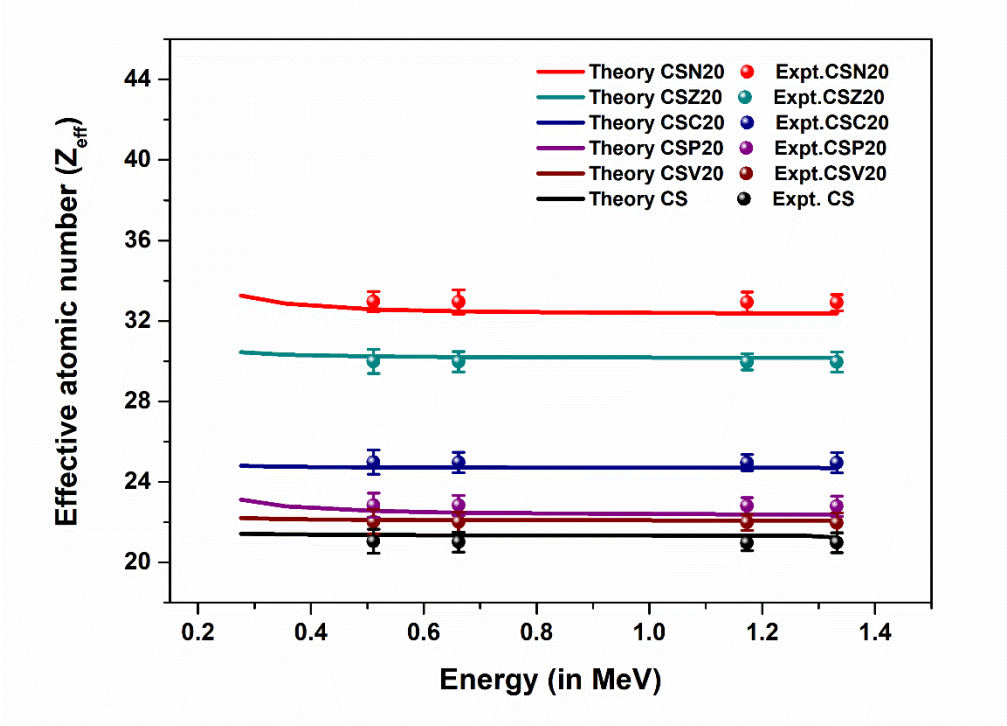

Figure 6.11: Variation of Z_{eff} of the moulded concretes with respect to energy.

For all photon interaction processes, the variation of effective electron density (N_{eff}) in the samples with photon energy is analogous to that of Z_{eff}. Because there is an inverse relationship between N_{eff} and Z_{eff}. The control sample with the lowest effective atomic weight has the highest electron density. The effective electron number N_{eff} results of the investigated concrete samples within the photon energy 0.01 to 20 MeV are computed consistent with (μ_m/σ_e). It is found that there are slight

variations in N_{eff} results for various glass samples wherever a higher result of N_{eff} would indicate an increased probability of photon-electron energy transfer and energy deposition into the concrete. The results of N_{eff} in Figure 6.12 prove that there is an identical photon energy dependence to what was determined for Z_{eff}.

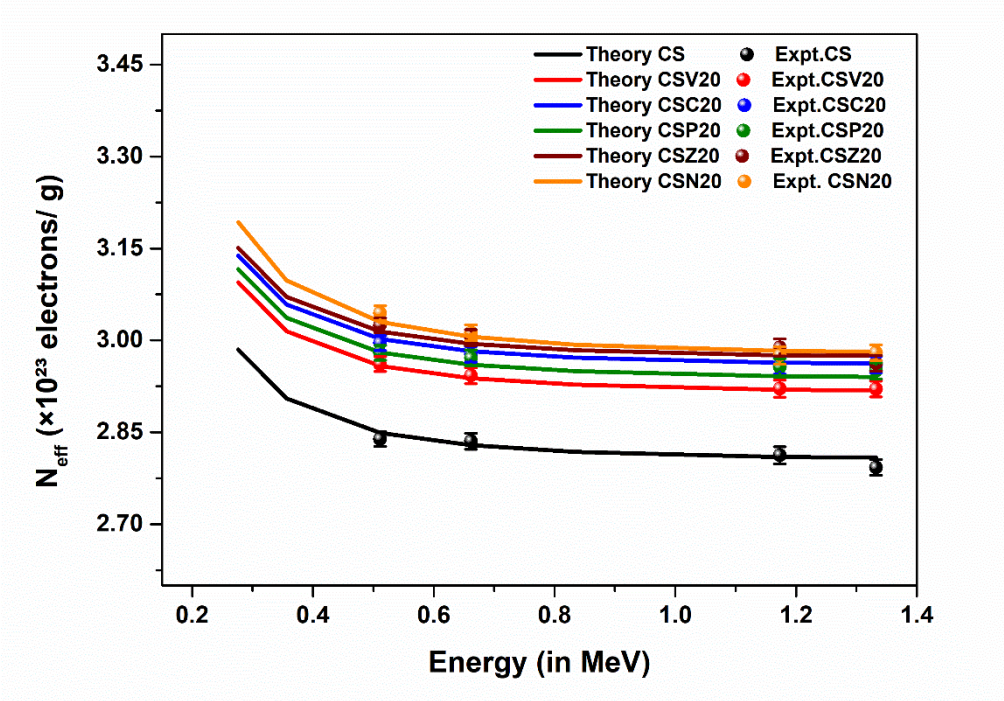

Figure 6.12: Variation of N_{eff} of the moulded concretes with respect to energy.

6.7 Built-up Factors

According to Geometric-Progression fitting method, to find the B values that characterize the photon scattering properties of the materials, the R, Z_{eq} and G-P fitting coefficients must be known.

For materials with low Z_{eq} , there are fewer interactions per unit mass, leading to lower EBAF values. This is because the material is less effective at absorbing and scattering photons. When Z_{eq} increases, the material's ability to absorb and scatter photons increases, leading to higher EBAF values. Higher Z_{eq} materials absorb more energy from incident photons due to increased interaction probabilities.With higher Zeq, the number of scattering events increases, leading to higher EBF values. This results in more exposure from scattered photons, indicating a higher buildup factor.

Table 6.7 and Figure 6.13 provide equivalent atomic numbers (Z_{eq}) of the cement samples with photon energy. It is clear from Figure 6.14 that Zeq values vary between 16-27.

Table 6.7: Equivalent atomic numbers of the pure concrete and 20% additives added composites for various energy values ranging from 0.015 to 15 MeV.

Energy (MeV)	CS	CSC20	CSP20	CSV20	CSZ20	CSN20
0.015	15.11	16.51	16.11	15.52	15.62	16.74
0.02	15.27	16.71	16.29	15.67	17.91	16.95
0.03	15.42	16.93	16.46	15.81	18.31	17.20
0.04	15.52	22.03	16.57	15.90	18.58	17.39
0.05	15.59	22.51	16.65	15.97	18.77	23.21
0.06	15.64	22.86	16.70	16.02	18.92	23.64
0.08	15.70	23.39	16.79	16.09	19.13	24.26
0.1	15.75	23.76	16.84	16.13	19.27	24.69
0.15	15.82	24.36	16.92	16.20	19.50	25.40
0.2	15.86	24.74	16.98	16.23	19.64	25.84
0.3	15.91	25.19	17.03	16.28	19.82	26.38
0.4	15.93	25.47	17.06	16.30	19.92	26.71
0.5	15.95	25.64	17.08	16.32	19.99	26.92
0.6	15.96	25.76	17.08	16.32	20.03	27.07
0.8	15.96	25.87	17.09	16.33	20.06	27.20
1	15.96	25.91	17.09	16.33	20.07	27.23
1.5	14.30	22.16	15.40	14.84	17.35	23.34
2	13.73	18.15	14.72	14.30	15.75	18.71
3	13.55	16.66	14.48	14.11	15.23	16.91
4	13.50	16.32	14.43	14.07	15.11	16.50
5	13.48	16.17	14.40	14.04	15.05	16.32
6	13.47	16.07	14.39	14.03	15.01	16.21
8	13.46	15.97	14.37	14.02	14.97	16.09
10	13.45	15.92	14.36	14.00	14.96	16.03
15	13.44	15.89	14.35	14.00	14.94	15.99

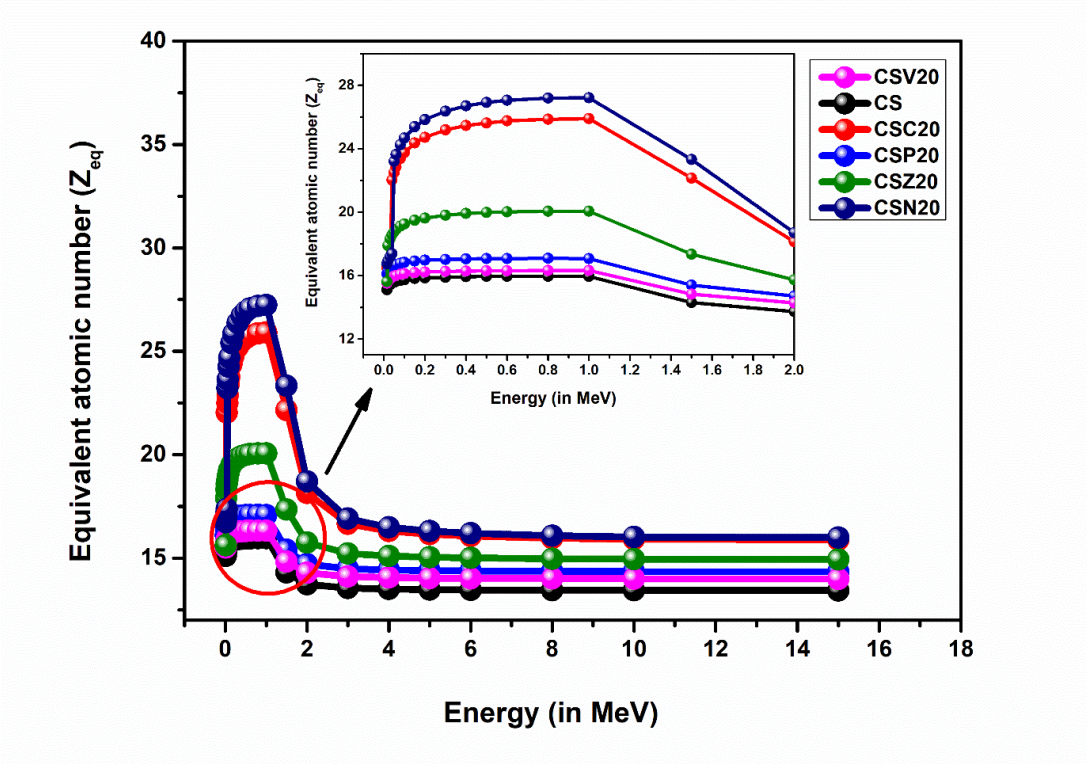

Figure 6.13: Variation of atomic numbers (Z_{eq}) of the cement samples with photon energy.

Like EBAF, materials with low Zeq have fewer scattering events, resulting in lower EBF values. This means there is less buildup of exposure from scattered photons. The Zeq and G-P fitting parameters are manipulated to obtain the energy absorption and exposure build-up factor (EABF and EBF) up to 40 mfp penetration in the 0.015-15 MeV energy range. As shown in Figure 6.14 to Figure 6.16, EABF values are increase with increasing photon energy and reach the maximum value of 0.2-0.3 MeV, and then decrease with the increment of photon energy up to 15 MeV. In this study, these parameters were calculated by using G-P fitting method and the results obtained are tabulated in Tables 6.8 and 6.9 for CSN20 and CSZ20 samples respectively. The five-parameter geometric progression (G-P) fitting method was applied to determine the effective buildup factor (EBF) and effective attenuation buildup factor (EABF) for penetration depths up to 40 mean free paths (mfp) across the energy range from 0.015 MeV to 15 MeV. The EBF of the cement samples indicate minimum values in the low-energy region where photoelectric absorption is dominant. EBF values are raised with increasing photon energy due to Compton

scattering at middle energies. In the high-energy region, where the pair production begins to dominate, the EBF values enter a decreasing curve. Brass doped samples possess the lowest values of EBF while EBF of the control sample, ordinary Portland cement were maximum for all the penetration depths.

Table 6.8 G-P energy absorption and exposure build-up factor parameters of the CSZ20 for various energy values ranging from 0.015 to 15 MeV.

Energy (MeV)	EABF					EBF				
	a	b	c	D	X_k	a	b	c	d	X_k
0.015	0.27	1.02	0.33	-0.15	11.60	0.28	1.02	0.33	-0.21	11.03
0.02	0.16	1.02	0.46	-0.31	30.51	0.25	1.03	0.32	-0.20	19.25
0.03	0.25	1.08	0.35	-0.15	13.17	0.24	1.08	0.36	-0.14	13.13
0.04	0.23	1.17	0.38	-0.13	14.50	0.22	1.16	0.39	-0.12	14.18
0.05	0.22	1.30	0.40	-0.13	14.73	0.21	1.28	0.41	-0.12	14.21
0.06	0.18	1.46	0.47	-0.10	14.85	0.18	1.40	0.49	-0.10	14.36
0.08	0.19	1.95	0.50	-0.09	12.39	0.13	1.63	0.60	-0.07	14.32
0.1	0.13	2.44	0.64	-0.09	13.07	0.08	1.83	0.74	-0.05	14.32
0.15	0.04	3.33	0.90	-0.05	13.42	0.02	2.10	0.98	-0.02	13.69
0.2	0.00	3.49	1.10	-0.03	12.85	-0.02	2.20	1.13	-0.02	12.34
0.3	-0.04	3.17	1.28	-0.01	10.07	-0.04	2.21	1.26	-0.01	10.24
0.4	-0.06	2.85	1.36	0.02	26.70	-0.05	2.17	1.30	-0.01	9.69
0.5	-0.07	2.62	1.38	0.01	17.04	-0.05	2.13	1.30	-0.01	8.83
0.6	-0.06	2.48	1.36	0.02	21.10	-0.06	2.06	1.33	0.01	23.56
0.8	-0.06	2.26	1.34	0.02	16.12	-0.06	1.96	1.32	0.02	18.86
1	-0.06	2.13	1.30	0.02	16.36	-0.06	1.90	1.29	0.02	17.15
1.5	-0.05	1.94	1.23	0.02	14.99	-0.04	1.82	1.21	0.01	16.22
2	-0.03	1.84	1.15	0.01	15.32	-0.03	1.76	1.15	0.01	15.13
3	-0.01	1.69	1.06	0.00	11.44	-0.01	1.66	1.06	0.00	12.65
4	0.01	1.60	0.99	-0.01	12.68	0.01	1.59	1.00	-0.02	14.52
5	0.02	1.52	0.95	-0.03	14.54	0.02	1.52	0.97	-0.02	12.00
6	0.02	1.45	0.95	-0.03	15.58	0.02	1.47	0.96	-0.02	14.29
8	0.04	1.36	0.91	-0.03	11.75	0.03	1.39	0.93	-0.03	13.66
10	0.04	1.30	0.90	-0.04	13.69	0.04	1.33	0.91	-0.03	13.34
15	0.03	1.19	0.93	-0.03	14.48	0.05	1.24	0.88	-0.05	13.08

Table 6.9 G-P energy absorption and exposure build-up factor parameters of the CSN20 for various energy values ranging from 0.015 to 15 MeV.

Energy (MeV)	EABF					EBF				
	a	b	c	D	X_d	a	b	c	d	X_d
0.015	0.24	1.01	0.37	-0.21	18.25	0.25	1.01	0.37	-0.26	17.68
0.02	0.21	1.03	0.38	-0.41	29.58	0.24	1.03	0.33	-0.29	23.47
0.03	0.24	1.09	0.36	-0.14	13.62	0.24	1.09	0.36	-0.14	13.62
0.04	0.21	1.21	0.40	-0.12	14.47	0.21	1.20	0.40	-0.12	14.56
0.05	0.24	1.16	0.36	-0.13	14.32	0.22	1.15	0.38	-0.13	14.07
0.06	0.21	1.25	0.40	-0.13	14.73	0.20	1.22	0.42	-0.11	14.20
0.08	0.18	1.45	0.48	-0.10	15.31	0.17	1.35	0.50	-0.09	14.45
0.1	0.16	1.72	0.52	-0.10	15.19	0.13	1.46	0.59	-0.07	14.15
0.15	0.14	2.50	0.61	-0.11	14.85	0.07	1.70	0.76	-0.05	14.08
0.2	0.08	2.90	0.79	-0.07	13.11	0.03	1.85	0.92	-0.03	13.21
0.3	0.01	3.02	1.02	-0.04	12.51	-0.01	1.96	1.09	-0.02	11.95
0.4	-0.01	2.82	1.14	-0.02	11.81	-0.02	1.97	1.17	-0.01	10.90
0.5	-0.03	2.62	1.20	-0.02	10.72	-0.04	1.95	1.22	-0.01	8.85
0.6	-0.03	2.48	1.22	-0.01	10.44	-0.04	1.93	1.24	-0.01	8.32
0.8	-0.04	2.27	1.23	-0.01	8.51	-0.04	1.88	1.23	-0.01	7.56
1	-0.04	2.13	1.24	0.00	13.62	-0.04	1.83	1.23	0.00	14.40
1.5	-0.04	1.94	1.20	0.01	15.45	-0.04	1.77	1.20	0.01	15.85
2	-0.03	1.83	1.15	0.01	16.23	-0.03	1.75	1.14	0.01	16.13
3	-0.01	1.69	1.06	0.00	12.36	-0.01	1.66	1.06	-0.01	10.87
4	0.01	1.59	0.99	-0.01	12.95	0.01	1.58	1.00	-0.02	10.40
5	0.02	1.51	0.96	-0.03	14.82	0.01	1.51	0.98	-0.02	12.45
6	0.02	1.44	0.95	-0.03	14.93	0.02	1.47	0.96	-0.02	13.49
8	0.03	1.35	0.93	-0.03	13.05	0.03	1.39	0.93	-0.03	13.43
10	0.04	1.29	0.91	-0.04	13.44	0.04	1.32	0.92	-0.03	13.71
15	0.04	1.19	0.92	-0.04	14.24	0.05	1.23	0.90	-0.05	13.24

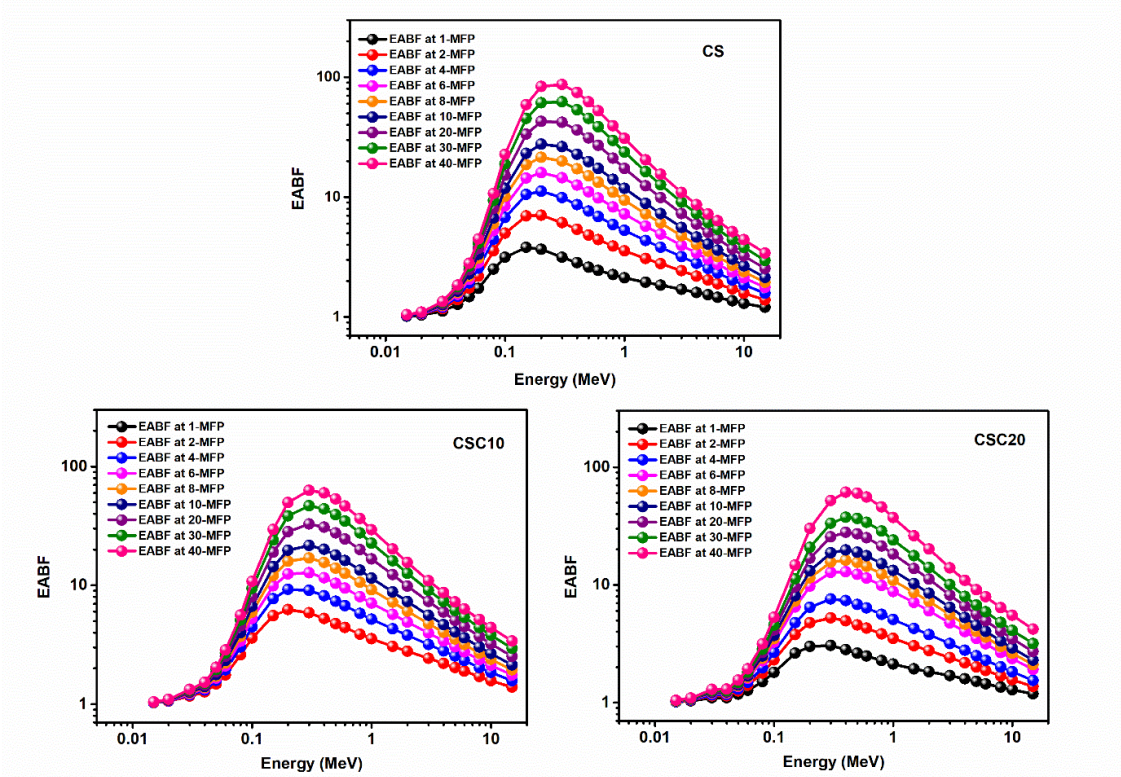

Figure 6.14: Variation of EABF for concrete and concrete modified with coconut shell powder for different mean free path.

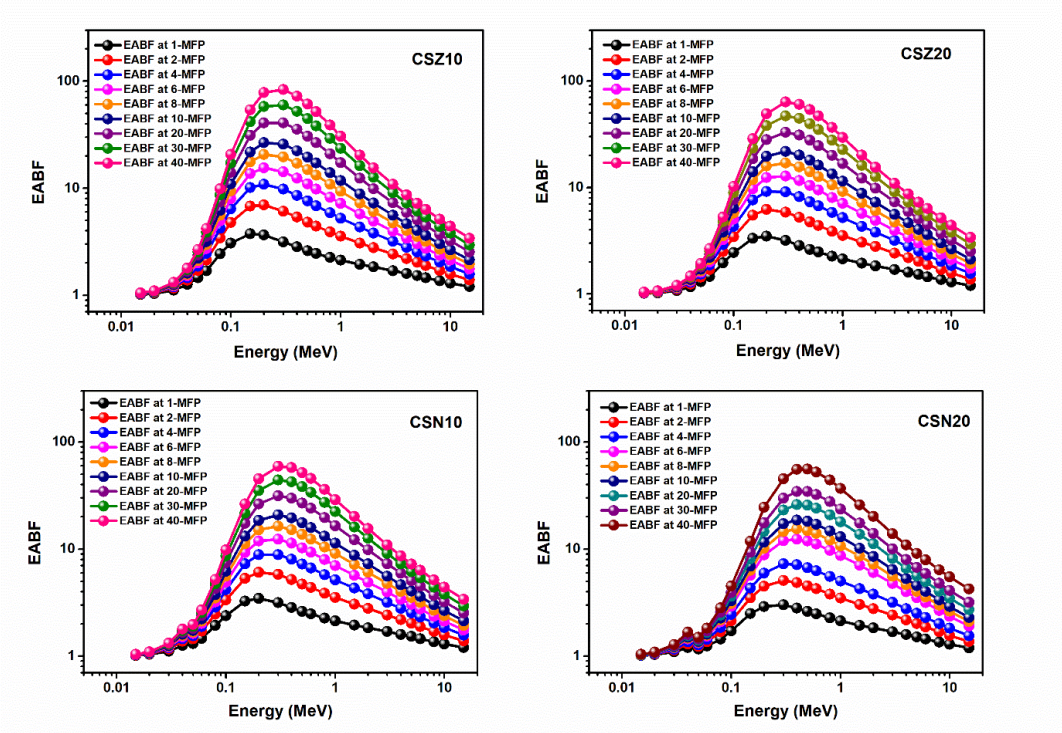

Figure 6.15: Variation of EABF for concrete modified with Zirconium and Neodymium for different mean free path.

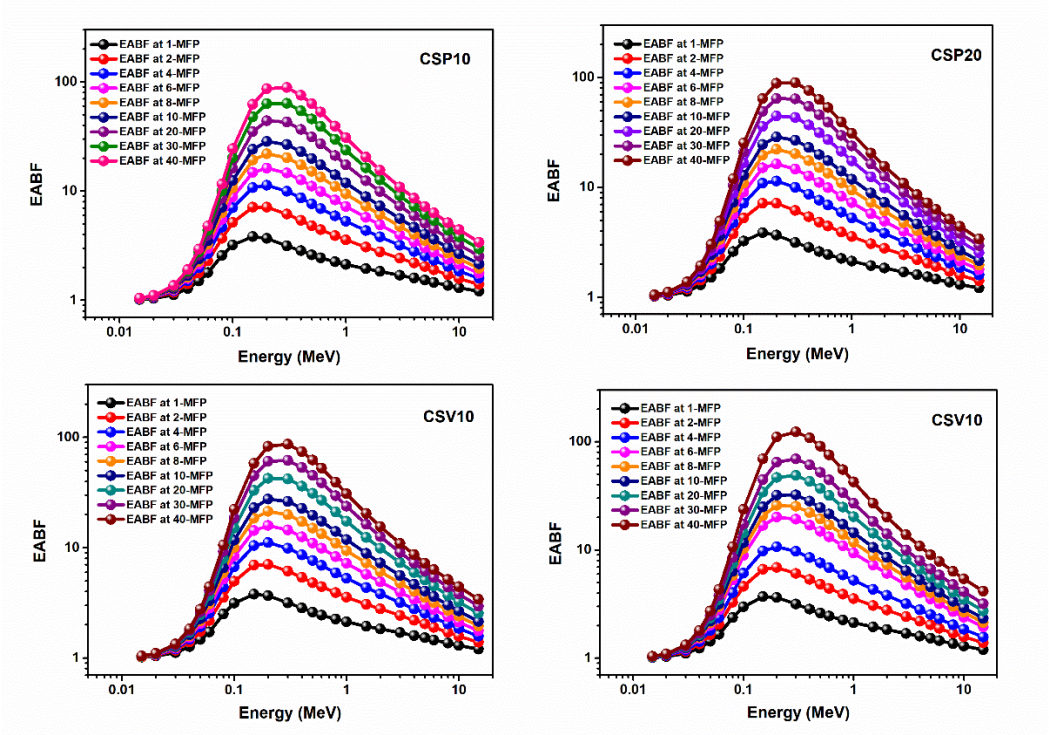

Figure 6.16: Variation of EABF for concrete modified with Perlite and Vermiculite for different mean free path.

Figure 6.17-6.19 shows the EBF values depending on the penetration depth up to 40 mfp for selected energies (0.15, 1.5 and 15 MeV). At 0.15 MeV, which is the low energy region, it yields wide EBF variations for the samples. EBF chiefly depends on chemical composition at 0.15. The CSN20 sample has the lowest EBF. It is also seen that for control samples with low equivalent numbers (Zeq) the values of EBF are larger while the EBF values of brass added samples with higher equivalent numbers are relatively small. At 1.5 MeV, Compton scattering becomes dominant, therefore, the commitment to the composition of the material is reduced. However, for this energy, the doped cements have lower EBF values. EBF values for brass doped cement samples are found to be the highest at 15 MeV, due to the basis of dominance of pair production in this higher energy region. So, the samples with higher Z_{eq} has higher probability to undergo pair-production.

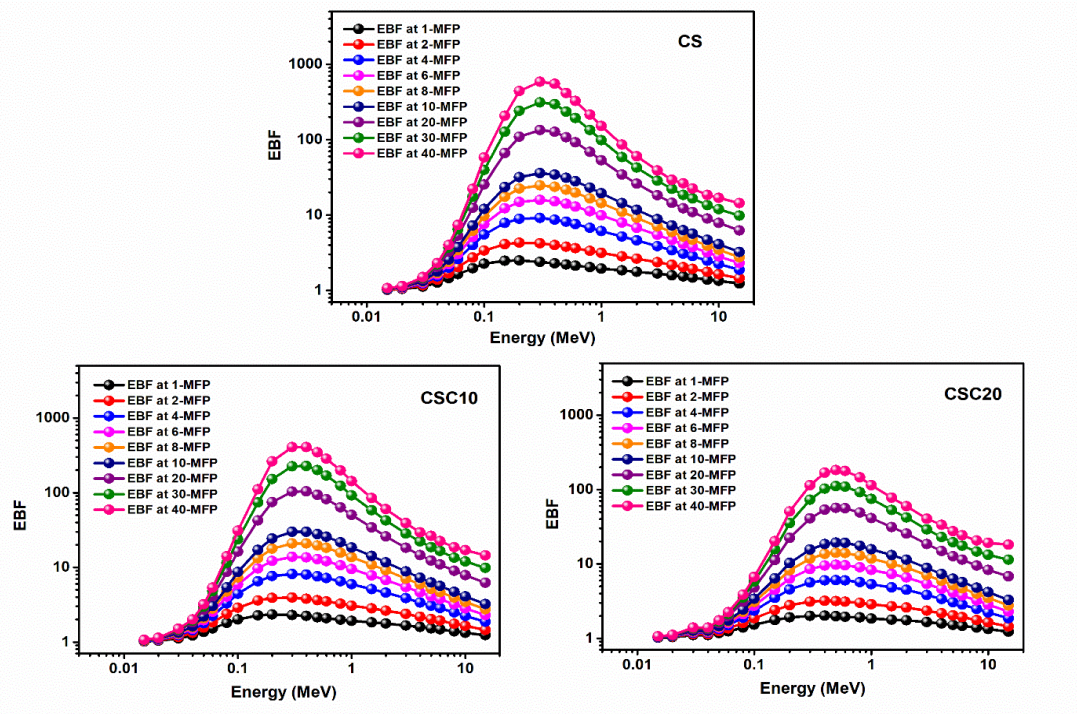

Figure 6.17: Variation of EBF for concrete and concrete modified with coconut shell powder for different mean free path.

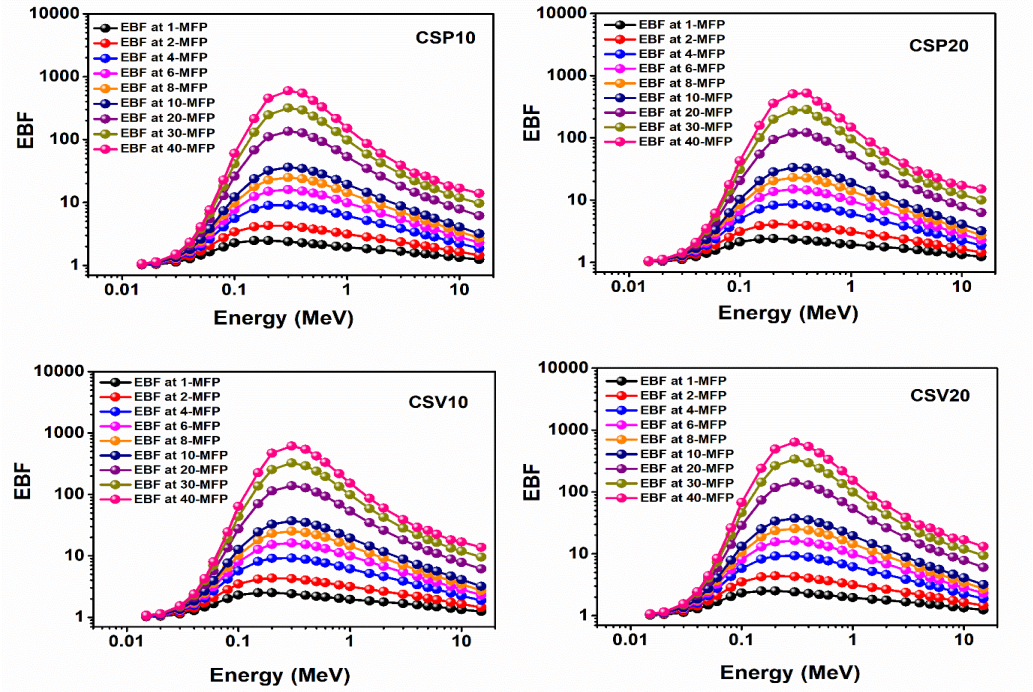

Figure 6.18: Variation of EBF for concrete modified with Perlite and Vermiculite for different mean free path.

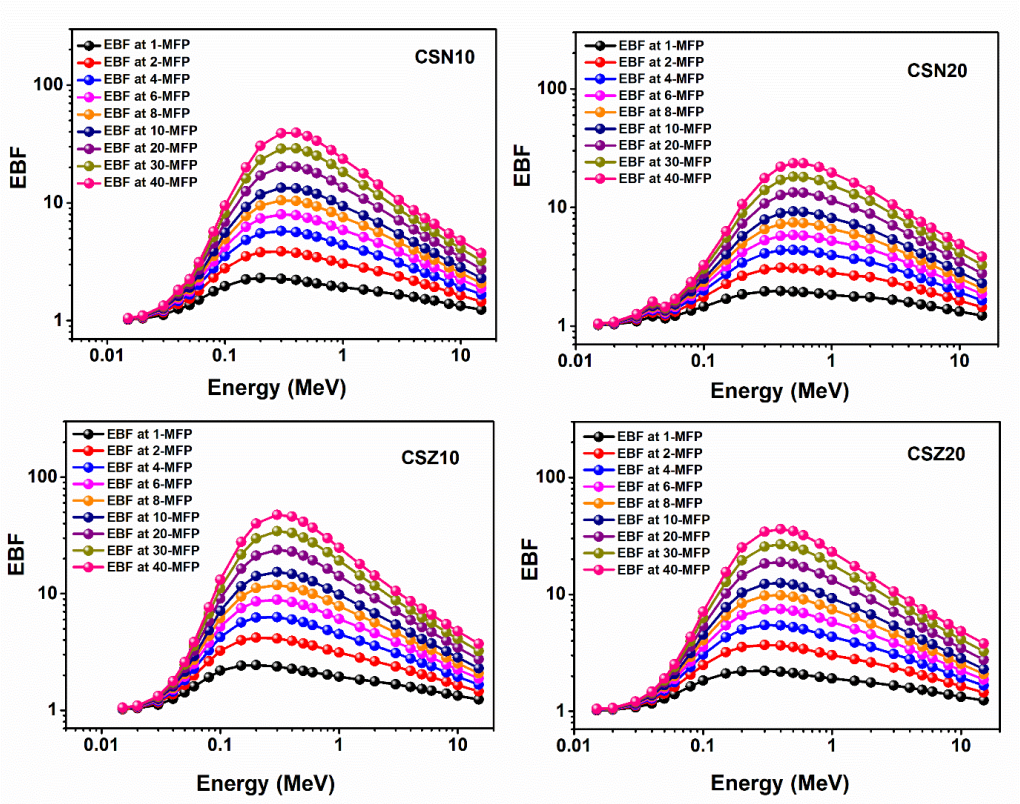

Figure 6.19: Variation of EBF for concrete modified with Zirconium and Neodymium for different mean free path.

6.8 Fast neutron removal cross section

In various applications, materials are exposed to both gamma and neutron radiation. Along with the gamma-ray attenuation parameters, the neutron attenuation capability of these materials has been studied in terms of effective removal cross-section (Σ_R). Figure 6.20 shows effective removal cross-section (Σ_R) values of the concrete samples with density.

The values of Σ_R are 0.126, 0.110, and 0.117 for materials CSZ20, CSN20, and CSC20 respectively. The highest density implies higher values resulting in better neutron attenuation. In this context, sample CSZ20 having a density of 3.52 g/cm^3 which is comparable to densities 3.73 and 3.26 respectively for samples CSN20 and CSC20 has shown enhanced neutron attenuation. Coconut shell powder sample which has greater ability to shield the neutrons. These results are in accordance with the reported results for $BaMnO_3$ doping nickel semiconductor perovskite and gallium germanate-tellurite glasses [17], [23].

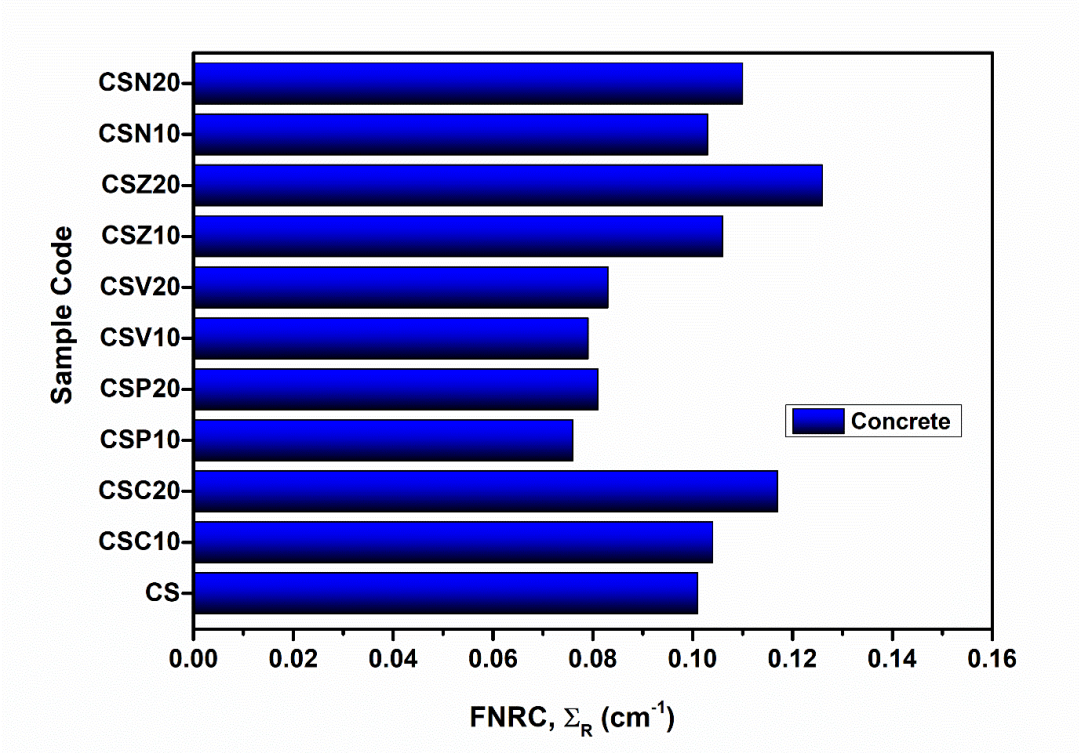

Figure 6.20: Fast effective removal cross-section (Σ_R) values of the concrete samples.

6.9 Conclusion

In recent years, the production of radiation-protection materials has become a major focus of research, particularly through strategies aimed at increasing the density of concrete materials, as documented in the literature. Various factors contribute to this trend, but the mechanical strength, ease of manufacturing, and them highly favourable. These materials play a crucial role in radiation-based industrial, medical, and research applications, enhancing process quality significantly. Moreover, once radioactive elements are safely disposed of, it is essential that recycled products retain their original mechanical properties and corrosion resistance. This prevents increased environmental radioactivity by avoiding contamination of nuclear waste, which remains hazardous for many years, and prevents its interaction with soil. This underscores the importance of developing denser concrete structures that also improve mechanical, thermal, and gamma-ray absorption properties.

This study aimed to investigate the effects of certain chemical modifications in

normal concrete, a well-known coconut shell powder, naturally available minerals Perlite and Vermiculite and metal oxides of Zirconium and Neodymium on gamma-ray absorption. The findings indicated that increasing the density, particularly with a higher concentration of these additives, significantly enhanced the overall gamma-ray absorption characteristics. This suggests that incorporating these kinds of less toxic additives is an effective approach for improving gamma-ray absorption properties, making it a suitable material for applications requiring enhanced radiation protection.

The μ, μ/ρ, Z_{eff} and HVL values which are the significant gamma absorption parameters were obtained theoretically and experimentally for 511, 662, 1173 and 1333 keV photon energies. Study exploring the radiation shielding properties of concrete samples contributes to the existing theoretical and practical literature. Methodologically, the study first calculates the mass attenuation coefficient values by using Phy-PSD software code at 0.015–15 MeV energies. Then, the results derived from Phy-PSD are subject to comparison with Xcom results. The MAC values are used to compute other parameters such as HVL, TVL, MFP, Z_{eff}. Studying concrete samples for gamma protection shows that the Silicon, iron, Aluminium, and Zirconium and Neodymium content is an important factor affecting that feature. Therefore, composites CSN20 and CSZ20 having higher Zirconium and Neodymium with appreciable amount of silicon, Aluminium and iron in its composition with cement shows larger μ/ρ, Z_{eff} lowest EBF, and EABF values. As expected HVL, TVL, and MFP quantities of concrete samples which are subjects of this study are increased as the photon energy increases and decreases because of the contribution of silicon, Aluminium, and iron increases. It is observed that the CSC20 concrete sample has higher Σ_R values than CSP20, CSV20 and CSZ20.

The outcomes indicate that the insertion of these additives positively affects the photon shielding parameters of cement samples. It can be concluded that those cement samples can be evaluated for further gamma protection applications.

6.10 Reference

[1] A. Khanna, S. S. Bhatti, K. J. Singh, and K. S. Thind, "Gamma-ray attenuation coefficients in some heavy metal oxide borate glasses at 662 keV," *Nucl. Instruments Methods Phys. Res. Sect. B Beam Interact. with Mater. Atoms*, vol. 114, no. 3–4, pp. 217–220, 1996, doi: 10.1016/0168-583X(96)00196-6.

[2] I. Akkurt, H. Akyıldırım, B. Mavi, S. Kilincarslan, and C. Basyigit, "Annals of Nuclear Energy Photon attenuation coefficients of concrete includes barite in different rate," *Ann. Nucl. Energy*, vol. 37, no. 7, pp. 910–914, 2010, doi: 10.1016/j.anucene.2010.04.001.

[3] K. G. Mahmoud, M. S. Alqahtani, O. L. Tashlykov, V. S. Semenishchev, and M. Y. Hanfi, "The influence of heavy metallic wastes on the physical properties and gamma-ray shielding performance of ordinary concrete: Experimental evaluations," *Radiat. Phys. Chem.*, vol. 206, no. January, p. 110793, 2023, doi: 10.1016/j.radphyschem.2023.110793.

[4] W. Ramadan, K. Sakr, M. Sayed, N. Maziad, and N. El-Faramawy, "Anisotropic thermal, physical and neutron attenuation studies of borated acrylamide composites," *Radiat. Phys. Chem.*, vol. 172, no. November 2019, p. 108745, 2020, doi: 10.1016/j.radphyschem.2020.108745.

[5] A. Obeid, M. Roumie, M. S. Badawi, and R. Awad, "Evaluation of the Effect of Different Nano-Size of WO_3 on the Structural and Mechanical Properties of HDPE," *J. Inorg. Organomet. Polym. Mater.*, vol. 32, no. 4, pp. 1506–1519, 2022, doi: 10.1007/s10904-021-02219-3.

[6] E. Kavaz, S. R. Armoosh, U. Perişanoğlu, N. Ahmadi, and M. Oltulu, "Gamma-ray shielding effectiveness of the Portland cement pastes doped with brass-copper: An experimental study," *Radiat. Phys. Chem.*, vol. 166, no. October 2019, 2020, doi: 10.1016/j.radphyschem.2019.108526.

[7] O. Kilicoglu, C. V. More, U. Kara, and M. Davraz, "Investigation of the effect of cement type on nuclear shield performance of heavy concrete," *Radiat. Phys. Chem.*, vol. 209, no. November 2022, p. 110954, 2023.
doi: 10.1016/j.radphyschem.2023.110954.

[8] Y. Xia *et al.*, "Value-added recycling of cathode ray tube funnel glass into high-performance radiation shielding concrete," *Resour. Conserv. Recycl.*, vol. 199, no. August, p. 107252, 2023, doi: 10.1016/j.resconrec.2023.107252.

[9] U. Rilwan *et al.*, "Recycling and characterization of bone incorporated with concrete for gamma-radiation shielding applications," *Nucl. Eng. Technol.*, no. February, pp. 1–7, 2024, doi: 10.1016/j.net.2024.02.045.

[10] M. E. Mahmoud, A. M. El-khatib, A. M. Halbas, and R. M. El-sharkawy, "Investigation of physical , mechanical and gamma-ray shielding properties using ceramic tiles incorporated with powdered lead oxide," *Ceram. Int.*, no. March, pp. 1–9, 2020, doi: 10.1016/j.ceramint.2020.03.119.

[11] A. H. Almuqrin, M. I. Sayyed, M. Elsafi, and M. U. Khandaker, "Comparison of radiation shielding ability of Bi_2O_3 micro and nanoparticles for radiation shields," *Radiat. Phys. Chem.*, vol. 200, no. March, p. 110170, 2022.
doi: 10.1016/j.radphyschem.2022.110170.

[12] N. Z. Noor Azman *et al.*, "Effect of Bi_2O_3 particle sizes and addition of starch into Bi_2O_3–PVA composites for X-ray shielding," *Appl. Phys. A Mater. Sci. Process.*, vol. 122, no. 9, pp. 1–9, 2016, doi: 10.1007/s00339-016-0329-8.

[13] M. I. Sayyed, H. Al-Ghamdi, A. H. Almuqrin, S. Yasmin, and M. Elsafi, "A Study on the Gamma Radiation Protection Effectiveness of Nano/Micro-MgO-Reinforced Novel Silicon Rubber for Medical Applications," *Polymers (Basel).*, vol. 14, no. 14, 2022, doi: 10.3390/polym14142867.

[14] S. M. Malkapur *et al.*, "Waste-polymer incorporated concrete mixes for neutron and gamma radiation shielding," *Prog. Nucl. Energy*, vol. 135, no. February, p. 103694, 2021, doi: 10.1016/j.pnucene.2021.103694.

[15] M. El-Desouky, A. Abdelaziz, M. El-Fransawy, and R. El-Sadany, "Gamma Radiation Effect on Normal Weight Concrete, Heavy Weight Concrete, Steel Bars, and Fiber Bars," *Egypt. J. Chem.*, vol. 0, no. 0, pp. 0–0, 2023. doi: 10.21608/ejchem.2022.156089.6756.

[16] C. V Vishnu, A. Joseph, T. A. Sajith, and S. Thomas, "Design of Flexible Gamma-ray Shielding Material Composite of Natural Rubber with Coconut Shell / Clay Powder," vol. 64, pp. 886–887, 2019.

[17] M. Ghozza, "Radiation Attenuation Properties of $BaMnO_3$ Doping Nickel Semiconductor Perovskite Using Phys-X/PSD Software," *Arab J. Nucl. Sci. Appl.*, vol. 0, no. 0, pp. 0–0, 2023, doi: 10.21608/ajnsa.2022.154447.1621.

[18] R. Barman, M. S. Hossain, A. Das, and M. K. Ahmmad Rabby, "Investigation of radiation shielding characteristic features of different wood species," *Radiat. Phys. Chem.*, vol. 192, no. May 2021, 2022, doi: 10.1016/j.radphyschem.2021.109927.

[19] S. Stalin *et al.*, "Influence of Bi_2O_3/WO_3 substitution on the optical, mechanical, chemical durability and gamma-ray shielding properties of lithium-borate glasses," *Ceram. Int.*, vol. 47, no. 4, pp. 5286–5299, 2021. doi: 10.1016/j.ceramint.2020.10.109.

[20] L. Chang *et al.*, "Preparation and characterization of Tungsten/epoxy composites for γ-rays radiation shielding," *Nucl. Instruments Methods Phys. Res. Sect. B Beam Interact. with Mater. Atoms*, vol. 356–357, pp. 88–93, 2015. doi: 10.1016/j.nimb.2015.04.062.

[21] C. More, P. P. Pawar, M. S. Badawi, and A. A. Thabet, "Extensive theoretical study of gamma-ray shielding parameters using epoxy resin-metal chloride mixtures", Nuclear Technology and Radiation Protection, vol. 35, no. October, pp. 138–149, 2020. https://doi.org/10.2298/NTRP2002138M.

[22] A. J. Al-Saadi and A. K. Saadon, "Gamma-ray attenuation coefficients for lead oxide and iron oxide reinforced in silicate glasses as radiation shielding windows," *Ibn Al-Haitham Jour. Pure Appl. Sci*, vol. 27, no. 3, p. 2014, 2014.

[23] Y. S. Rammah, F. I. El-Agawany, A. M. A. El Soad, E. Yousef, and I. A. El-Mesady, "Ionizing radiation attenuation competences of gallium germanate-tellurite glasses utilizing MCNP5 simulation code and Phy-X/PSD program," *Ceram. Int.*, vol. 46, no. 14, pp. 22766–22773, 2020. doi:10.1016/j.ceramint.2020.06.043.

CHAPTER 7
RESULTS AND DISCUSSION

Gamma shielding analysis on Natural Rubber composites fortified with Barium tungstate oxide ($BaWO_4$).

Contents	
7.1	*Introduction*
7.2	*Materials and Methods*
7.3	*Results and discussion*
7.4	*Gamma-ray shielding properties.*
7.5	*Conclusion*
7.6	*Reference*

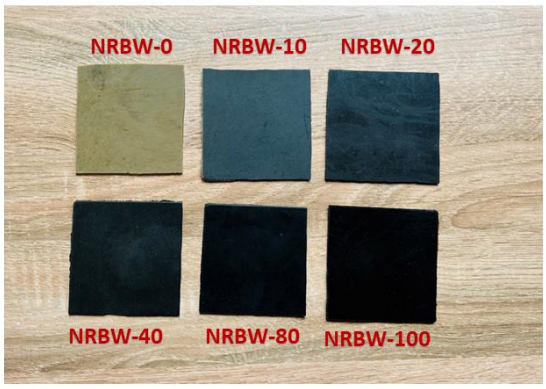

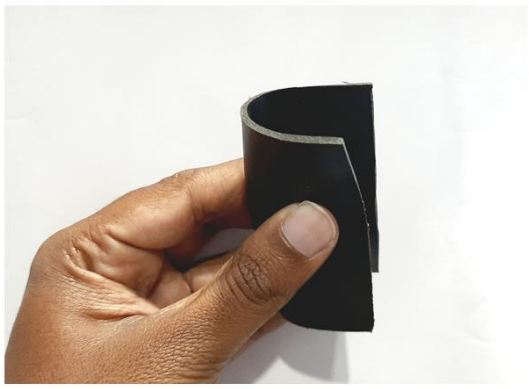

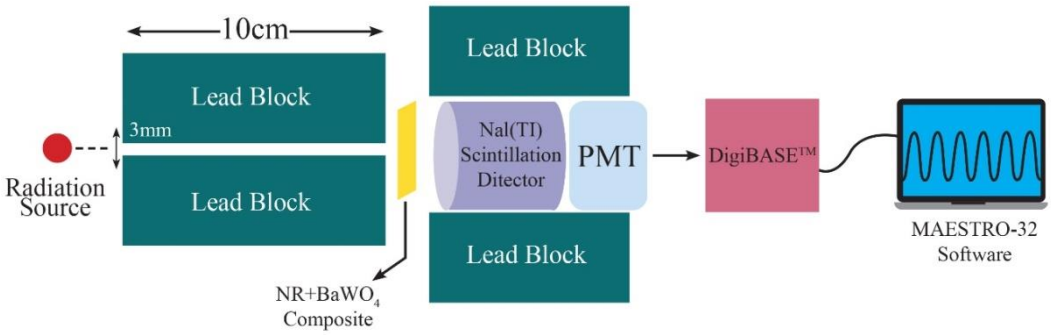

Abstract: *Emission of radiation has significant impacts, and its harmful effects must be minimized. This study investigated the gamma-ray shielding properties of natural rubber composites with varying proportions of Barium Tungstate ($BaWO_4$). Results showed that adding $BaWO_4$ improved gamma radiation shielding, with the highest linear attenuation coefficient (LAC) of 0.307 cm^{-1} at 662 keV for the composite with 100 phr $BaWO_4$. Simulations and theoretical evaluations of shielding parameters confirmed the experimental findings and compared the composites to other materials.*

7.1 Introduction

The development of flexible and lightweight materials capable of providing effective radiation protection for workers and the environment is a highly practical and important area of research. These materials are of utmost importance in creating protective clothing, curtains, and gloves, safeguarding individuals exposed to direct or secondary soft X-rays in diverse applications, such as radiology, radiotherapy, and airport scanning facilities[1], [2]. Individuals in research laboratories who work with gamma rays and other radioactive sources should be well safeguarded as well. Other factors to consider while choosing an efficient shielding material are conformability, cost-effectiveness, weight factor, toxicity, and durability, among others [3].

To minimize the weight of radiation protectors, it is essential to predominantly use shielding materials containing high atomic number elements like lead, Tungsten, Bismuth, and barium, as well as their derivatives. This selection is motivated by the fact that the X-ray attenuation cross-section is directly proportional to the fifth power of the atomic number, especially when considering the dominant role of the photoelectric effect in soft X-ray absorption[1]. By utilizing materials with higher atomic numbers, the effectiveness of X-ray attenuation is significantly enhanced, allowing for lighter and more practical radiation protection solutions [4]. Polymer composites incorporating a blend of high atomic number elements within a hydrogenous polymer matrix, featuring micro or nanoscale characteristics, hold great promise for radiation shielding applications. The combination of high atomic number elements enhances the materials' ability to attenuate radiation effectively, while the hydrogenous polymer matrix contributes to overall flexibility and versatility. These attributes make such polymer composites well-suited for various radiation shielding needs[2], [5], [6]. Numerous radiation-resistant shielding materials have been developed and documented in the literature. In general, the reduction of gamma rays as they pass through a substance can be comprehended by examining the cross-sections of the most probable interactions, which include the photoelectric effect, Compton scattering, and pair production[7]. Lead is frequently employed as a standard material for radiation shielding because of its high atomic number (Z = 82), widespread availability, economic accessibility, and affordability in various forms. Nevertheless, lead does have several drawbacks, such as limited

usage flexibility, chemical instability, mechanical fragility, significant weight, proneness to cracking, and the negative impact on human well-being and the environment caused by its toxicity [8], [9].

It is believed that when compared to micro-filled composites, the use of micro-nanosized fillers can significantly enhance the composites' capacity to absorb and scatter photons due to their uniform distribution throughout the polymer matrix [7], [10]. Metal polymer composites (MPCs) are among the most frequently discussed advanced materials utilized in attenuating gamma radiation in recent years. The MPC is basically a combination of metal filler bonding with a polymer matrix [11]. Improved characteristics of the MPCs are provided because of uniform dispersion of the high Z small sized particles inside the light and flexible polymer matrix. In fact, they meet both advantages, lightweight yet radiation protection effective. Many attempts have been made in order to investigate shielding properties of MPCs in both theoretical and experimental [10], [12]–[14] fields. Most of the literature on the shielding applications of MPCs has been focused on the effect of filler size on attenuating gamma radiation. It is believe that the nanosized filler can effectively increase the ability of composites to absorb and scatter photons because they disperse perfectly uniform within the polymer matrix as compared to micro filled composites [5], [9], [12], [15]–[20].

Natural rubber (NR) or latex with the chemical formula $(C_5H_8)_n$ is an isoprene polymer made of a runny, milky white liquid from a rubber tree (Hevea brasiliensis). NR has good elasticity, high flexibility, and high strength compared to other polymer types. In a previous study, NR demonstrated its ability to attenuate radiation sufficiently more highly than other polymers [21], [22]. It was reported that lightweight, rubber-based radiation shielding materials show better performance than the lead-based shields and the related information is described in the literature[23].

Prior to the fabrication of the samples, a theoretical estimation is required to ensure that the samples are adequately created and yield the expected findings. Because of the aforementioned factors, researchers and radiation shielding material producers estimate the MAC using theoretical approaches. This is a prerequisite for starting the experiment. Currently, various simulation software and codes are commonly

employed to conduct theoretical analyses of the mass attenuation coefficients (MAC). These tools, including WinXCom, Phy-X, Geant4, MCNP, EPICS2017, and others, play a pivotal role in investigating the interactions between radiation and matter [24]–[26]. Researchers and practitioners in the field often choose the most appropriate software tool based on their specific needs and the capabilities of the software. Each of the mentioned tools has its strengths and applications, and they contribute to advancing our understanding of radiation-matter interactions. These simulation software and codes have been instrumental in evaluating the attenuation properties of diverse shielding materials, ranging from glass systems to building materials. Researchers can effortlessly determine the Mass Attenuation Coefficients (MAC) of their samples using these techniques and codes. By comparing the theoretical data with experimental results and confirming their agreement, researchers can proceed to investigate further factors. Mass attenuation coefficient) plays a crucial role in comprehending how ionizing radiation penetrates through matter. It quantifies the likelihood of interaction between incident photons and a unit mass per unit area of the material. The precise definition of μm depends on the specific energy range being considered [27]. In addition to its role in ionizing radiation penetration, μ_m holds significant importance in dosimetry and the study of biological shielding materials. It serves as a crucial parameter for calculating energy deposition and photon penetration. Numerous other radiation parameters, such as total molecular cross section (mol), total atomic cross section (ACS), and total electronic cross section (ECS), can be derived from μm. Furthermore, researchers have focused on estimating the effective atomic number (Z_{eff}) and effective electron number (N_{eff}) due to their crucial role in determining energy absorption, particularly at low energy levels. These estimations have proven valuable in the field of medical diagnosis and therapy [27], [28].

The primary aim of the work is to fabricate and assess the attenuation properties of a natural rubber composite enriched with varying amounts of micro $BAWO_4$ powder. The incorporation of $BaWO_4$ in the composite is particularly intriguing due to the presence of elements with relatively high Z values, specifically Barium (Ba = 56) and Tungsten (W = 74). These properties make $BaWO_4$ a promising candidate for serving as a gamma radiation shielding material [29]. Experimental calculations were performed to determine the radiation shielding parameters, including MAC,

LAC, MFP, HVL, TVL, Z_{eff}, EABF, EBF, and N_{eff}, for all the composite materials. Afterward, these experimental findings were juxtaposed with the theoretical values acquired from the photon cross-section database, utilizing the Phy-X/PSD code. The study's outcomes not only provide a comparative assessment of γ-ray shielding properties for multi-layered products but also suggest encouraging approaches to preserve the mechanical properties of shielding materials with substantial filler contents.

7.2 Materials and Methods

The diagram with a short description of the whole experiment setting was shown in Figure 7.1.

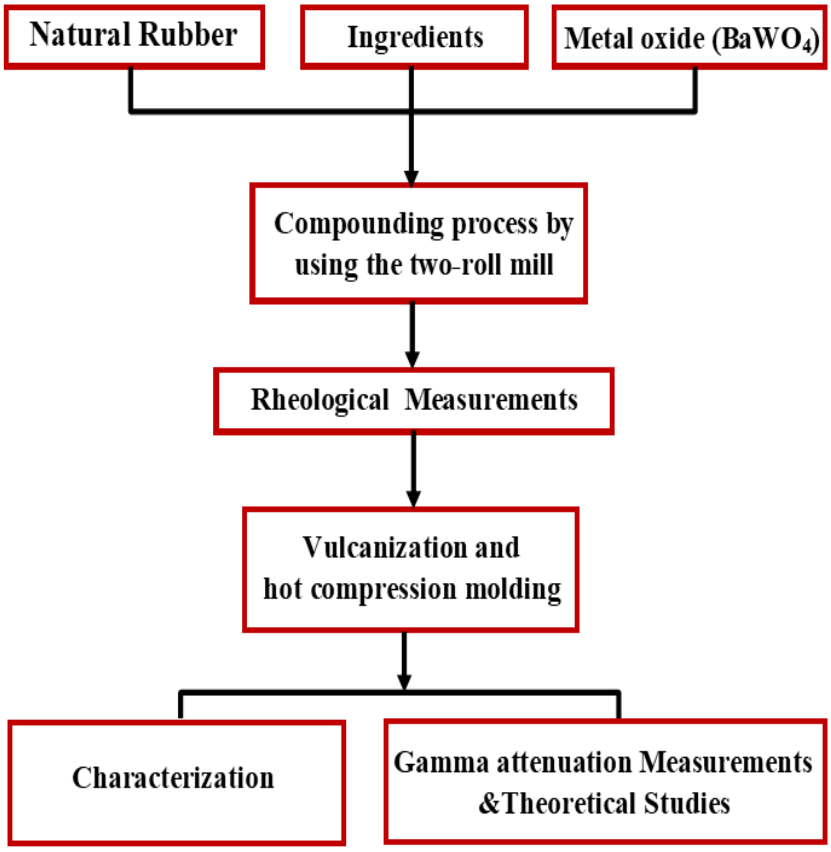

Figure 7.1. Diagram with a short description of the experiment setting.

7.2.1 Preparation of NR composites

Natural rubber (NR, Indian Standard Natural Rubber Grade 5) was used as the main matrix for the present work. The preparation of the composite is known as vulcanization. The various components used in this work, their contents (in phr), function and supplier are given in Table 7.1. The barium tungstate ($BaWO_4$) powder (< 80 μm, 99% purity and density of 5.04g/mol) was purchased from intelligent materials private limited, Mohali, Punjab, India.

The NR composites were prepared using two steps: mastication and compounding. For the mastication step, the NR was masticated on a two-roll mill (Yong Fong Machinery for 10 min. The masticated NR was then compounded with the prepared chemicals and gamma protective fillers for a further 20–25 min. It should be noted that, although the maximum content of metal oxides used in this work was as much as 100 phr, the volumes of these metal oxides were actually less than the NR's volume, due to higher densities of metal oxides shown in Table 7.1, which made mixing possible using a two-roll mill.

Table 7.1: Components of natural rubber (NR) composites, their contents, function, and suppliers.

Material	Content (phr)[a]	Function
Natural Rubber	100	Polymeric Material
Zinc Oxide (ZnO)	5	Activator
Stearic Acid	2.5	Activator
TMQ[b]	1	Accelerator
CBS[c]	1.5	Accelerator
Processing Oil	0-7.5	Lubricant
Sulphur	2.5	Crosslinking agent
Barium Tungstate ($BaWO_4$)	10,20,40,80,100	Shielding Filler

where a: parts per hundred

b: TMQ: 2,2,5 4-Trimethyl-1,2 Dihydroquinoline

c: CBS: N-Cyclohexyl-2-benzothiazole sulfonamide (CBS)

The activator used in the preparation is zinc stearate. It is a mixture of stearic acid and zinc oxide. It has applications as releasing agent and lubricant which can be easily incorporated. And it is insoluble in polar solvents and soluble in aromatic hydrocarbons. The accelerators used are CBS and TMQ mixture. It is a medium fast primary accelerator suitable for NR, IR, SBR, NBR, HR and EPDM. It is effective and safe when used at ordinary temperatures.

Aromatic processing oil is an oil composition which has a kinematic viscosity at 100^0C of from 32 to 50^0C. It is Aromatic grade of rubber process oil, dark in colour. It is a primary aromatic hydrocarbon, blended with carefully selected aromatic extracts. Witprol A-711 is appropriate to be employed in the manufacture of automobile tyres, beltings, mats, shaped rubber components Etc. It is good solvency & is compatible with wide range of rubbers like NR, SBR and PBR. Rubber process oil (RPO) are used during mix of rubber compounds. These help in improving the dispersion of fillers and flow characteristics of the compound during any processing. To each composition curing agent (sulphur), accelerator, activator and processing oil are added. All the chemicals are having commercial grade.

Figure 7.2: HEXA PLAST Two Roll Mill.

These compositions are mixed using two roll mill method for about 20 minutes. It is done in HEXA PLAST Two Roll Mill with fixed speed and friction is laid out for constant working conditions. The machine is available with roll diameters of 150 mm. The temperature between the two rolls are kept constant. The mixing is done at room temperature. It is allowed to settle for about 24 hours.

Figure 7.3: Compression mould hot press.

The material is made into sheets by using compression mould hot press. The machine is by PSPL polyhedron system- Belgaum. 100 g of the sample from each material is taken. It is then placed on mould having dimension 20cm length, 20cm breadth and 0.2 cm thickness. The material is moulded in "hot compression mould". The temperature of the mould is kept at 160 ^{0}C. Once the temperature between the compressor plates is 170^{o}C, place the mould with the material. It is degassed by moving the plate up and down. The pressure is kept at 120 kgm^{-2}. Supply voltage is 415 and 50 Hz AC. It is placed under the mould for a time equal to the cure time of the material. Then the temperature between the plates is lowered to 70^{o}C by

circulating water. Then the moulded sheet is removed from the compressor. The sheets are having the dimension of the mould. These sheets are used for swelling studies, tensile strength, tear strength etc. Corresponding to each specific composition of natural rubber and other components, replicas of four sheets were prepared. This was meant for attenuation studies by varying the total absorber thickness by putting one over the other.

7.2.2. Cure Characteristics Measurements

Cure characteristics were studied using a Monsanto Moving Die Rheometer (MDR 2000) according to ASTM D 2240-93. Samples (5 g) of the respective compounds were tested at the vulcanization temperature (160°C). From the rheometer curves, scorch time (t_s), optimum curing time (t_{90}), maximum torque (M_H) and minimum torque (M_L) were obtained. These data were used to calculate the cure kinetic parameters. To evaluate the ageing resistance of the rubber compounds at high curing temperatures, a defined parameter R_{300} was developed. R_{300} is the percentage of reversion of the rubber compound after 300 s from the time at M_H and was calculated using the following equation:

$$R_{300\%} = [(M_H - M_{300s}) / M_H] \times 100\%$$

Where MH is the maximum torque, M_{300s} is the torque after 300 s from the maximum torque. From the cure data obtained from the rheometer curve, the state of cure (α) can be calculated using the following equation.

$$\alpha = (M_t - M_L) / (M_H - M_L)$$

Where M_L, M_t and M_H are the minimum torque, the torque at the time t and the maximum torque, respectively.

Cure index is calculated using the equation,

$$\text{CRI (Cure rate index)} = 100 / (t_{90} - t_s)$$

7.2.3. Density Measurement

The density of each sample is determined by using density kit with balance. It is based on Archimedes' principle. Contech High Precision Balances incorporate advanced Electro Magnetic Force Compensation (EMFC) technology for offering unmatched accuracy and reliability, coupled with unique ADC circuit with inbuilt temperature compensation to offer a very high stability up to a resolution of 6 million counts. All adjustment parameters are programmable to take care of any minor mismatch of different subassemblies & Balances are configured with these parameters. Density determination Kit consists of density weighing pan assembly, stainless steel base for beaker, glass beaker and optional sinker.

Density is calculated by taking the weight of the sample in air and weight loss in water. The equation is given as

Density (D) = weight in air / weight loss in water.

Figure 7.4: Density kit with balance

7.2.4. Radiation shielding measurements.

A narrow beam geometry was employed to investigate the gamma-ray shielding effects of composites using gamma radiation sources such as ^{241}Am, ^{137}Cs, and ^{60}Co. The measurements were conducted to assess the shielding capabilities of the composites under examination (as illustrated in Figure. 7.5).

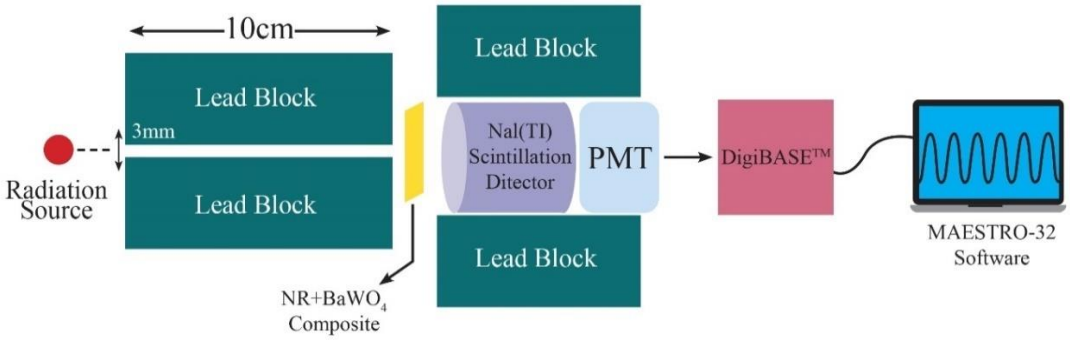

Figure. 7.5: The schematic diagram of the gamma-ray attenuation experimental setup using NaI(Tl) Detector.

In the experimental setup, a thin sheet of NR shielding composite measuring approximately 2 mm thick and 7.5 x 7.5 cm in size was placed between a radiation beam and a 3-inch x 3-inch NaI(TI) scintillation detector. The detector was connected to a 14-pin photomultiplier (PMT) DigiBASE™, which included an integrated bias supply (850 V), preamplifier, and MCA (multi-channel analyzer) MAESTRO-32 software [18]. Vulcanizate samples, sized 15 cm × 15 cm × 0.25 cm, were positioned 50 cm away from the gamma source and 20 cm away from the gamma detector. The sample sets used in this study exhibited different thicknesses, ranging from 0.25 to 1 cm, with increments of 0.25 cm. For each sample with a specific thickness, researchers recorded three independent 5-hour counts, and then calculated the average count (I). Furthermore, they also noted the average count when no samples were present, which served as the initial or reference count (I_0).

7.2.5 Phy-X/PSD software analysis

The manual calculation of photon attenuation parameters for selecting and categorizing materials to be used as shielding can be a challenging and time-consuming task in various technological applications. Therefore, it becomes essential to develop faster, more practical, and accurate methods for calculating all photon attenuation parameters. This aspect is especially vital during the design of novel shielding materials as it enables effective evaluation across the continuous energy spectrum or at specific energies to fulfil the specific requirements of the application[30]. In the realm of radiation protection, this method finds widespread use in assessing and fine-tuning shielding designs for various facilities dealing with

radiation sources. These facilities encompass nuclear power plants, medical centres, research laboratories, and industrial settings, among others. With this software, we can efficiently compute a set of eighteen parameters related to photon attenuation. for any desired energy level[24]. With the simple input of the material's chemical composition, density, and energy values, the software can automatically calculate the photon attenuation parameters for the user [30]. The researchers have introduced the Phy-X/PSD software in this study. This software has been designed to calculate all the mentioned shielding and dosimetry parameters efficiently and accurately. It can perform these calculations in a continuous energy range and also at specific energy values for the developed materials.

7.3 Results and Discussion

7.3.1 Cure characteristics of the sample

The preparation process was meticulously carried out to ensure that the final thickness remained consistent for each specified weight fraction of natural rubber and $BaWO_4$. However, the weight fraction of $BaWO_4$ was varied during the preparation. Vulcanization is a process of heating rubber in the presence of sulphur to improve the rubber's elasticity and strength. Vulcanized rubber results in three-dimensional cross-linking of the chain rubber molecules (polyisoprene) bonded by sulphur atoms [21]. Metal oxide added to NR increases the maximum torque of the composite. Prepared samples, labelled as NRBW-0, NRBW-10, NRBW-20, NRBW-40, NRBW-80 and NRBW-100, depending on the content of Barium Tungsten oxide in phr is shown in Figure 7.6.

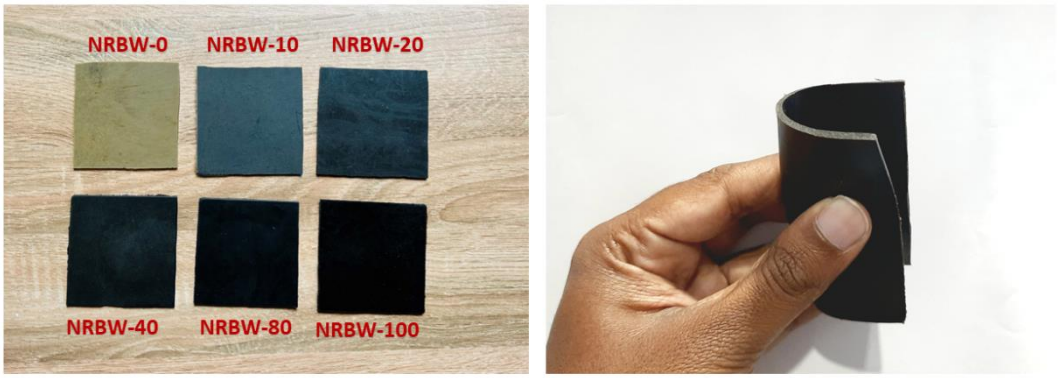

Figure 7.6: The fabricated flexible NR composites with NRBW nanoparticles.

Figure 7.7 depicts the correlation between torque and vulcanization time for metal oxide-NR composites at a temperature of 170 °C. Initially, the torque value decreases as the vulcanization time increases, which is attributed to changes in the compound's viscosity. As the vulcanization progresses, there is a subsequent increase in torque, indicating an acceleration in the vulcanization reaction. This phase corresponds to the curing period during which the cross-linking network in the rubber material undergoes growth [26].

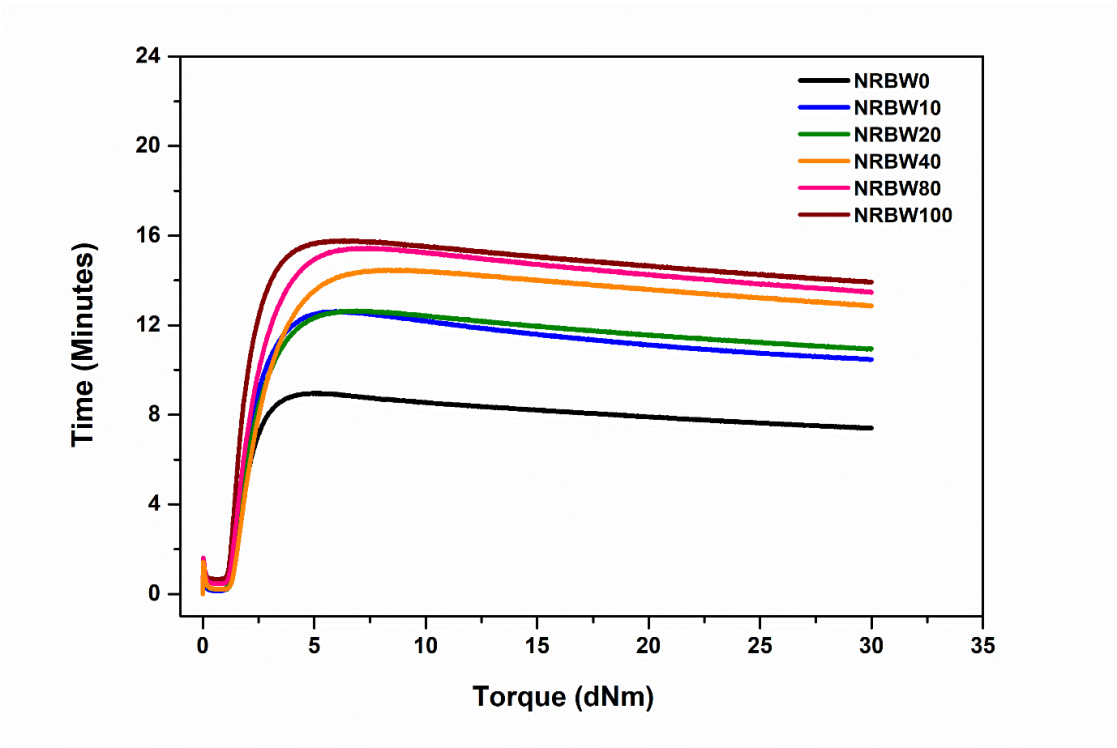

Figure 7.7: The relationship between torque and vulcanization time on metal oxide-NR composites

NRBW-100composite has the highest maximum torque, followed by NRBW-80, NRBW-40, NRBW-20 and NRBW-10 composites. This result implies that the presence of metal oxide in the NR increases the chemical cross-linking of the NR. Lim-Aroon et al., in 2019 reported that metal oxides could act as a co-activator in NR's vulcanization process, which assist in increasing the crosslink density and improving the physical properties (tensile strength and elongation at break) of NR[31]. Cure characteristics of the samples given in Table 7.2.

Table 7.2: Cure characteristics of the samples.

Sample	S'(M_L) (dNm)	S'(M_H) (dNm)	Torque difference (dNm)	T_S (min.)	T_{90} (min.)	CRI (min^{-1}.)
NRBW-0	0.15	8.98	8.83	1.51	2.99	67.5676
NRBW-10	0.13	12.62	12.49	1.40	3.48	48.0769
NRBW-20	0.12	15.27	15.15	1.31	3.21	52.6316
NRBW-40	0.20	12.64	12.44	1.45	3.81	42.3729
NRBW-80	0.21	15.19	14.98	1.41	3.99	38.7597
NRBW-100	0.23	14.48	14.25	1.58	4.52	34.0136

S' (M_L) = Elastic minimum torque (dNm)

S' (M_H) = Elastic maximum torque (dNm)

T_s = Scorch time (min).

T_{90} = Curing time (min).

7.3.2. Chemical Analysis and elemental distribution

The chemical compositions and mass densities of the composite samples were determined using SEM-EDAX analysis, which provides the relative percentages of the basic components for each sample. The results are presented in Table 7.3. Scanning Electron Microscopy (SEM) analysis was utilized to examine the distribution of particulates in both the natural rubber matrix and the natural rubber composites. Increasing the filler content led to distinct morphological differences in the composites. In the natural rubber composite, a fine and even dispersion of particles was observed, but with the incorporation of $BaWO_4$, the uniformity of particle distribution decreased. The increase in the content of $BaWO_4$ led to a higher proportion of the W element, as depicted in Table 7.3.

Table 7.3: The weight fractions of the elements for the samples.

Sample	Density, ρ (g/cm^3)	Elemental composition (%weight.)							
		C	H	O	Zn	S	N	Ba	W
Pure NR	2.765	8.630	50.450	3.540	23.980	7.360	6.040	0.000	0.000
NRBW10	2.904	8.210	46.780	3.250	24.210	6.940	5.650	1.815	3.146
NRBW20	3.124	7.470	42.710	3.010	25.050	6.630	5.200	3.462	6.468
NRBW40	3.226	6.910	39.050	2.860	26.120	5.890	4.160	5.016	9.994
NRBW80	3.342	6.560	35.760	2.740	26.490	5.010	3.460	7.929	12.051
NRBW100	3.418	5.890	31.340	2.610	27.190	4.780	3.040	9.505	15.645

The high density of radiation shielding material gives significant interaction probability for X-rays and gamma rays, resulting in better shielding performance. Figure 7.8 shows the density of prepared composites. The density of NR was 2.765 g/cm^3. When it was implanted with filler material, the density of the composite increased to the range of 2.765 g/cm^3 to 3.418 g/cm^3.

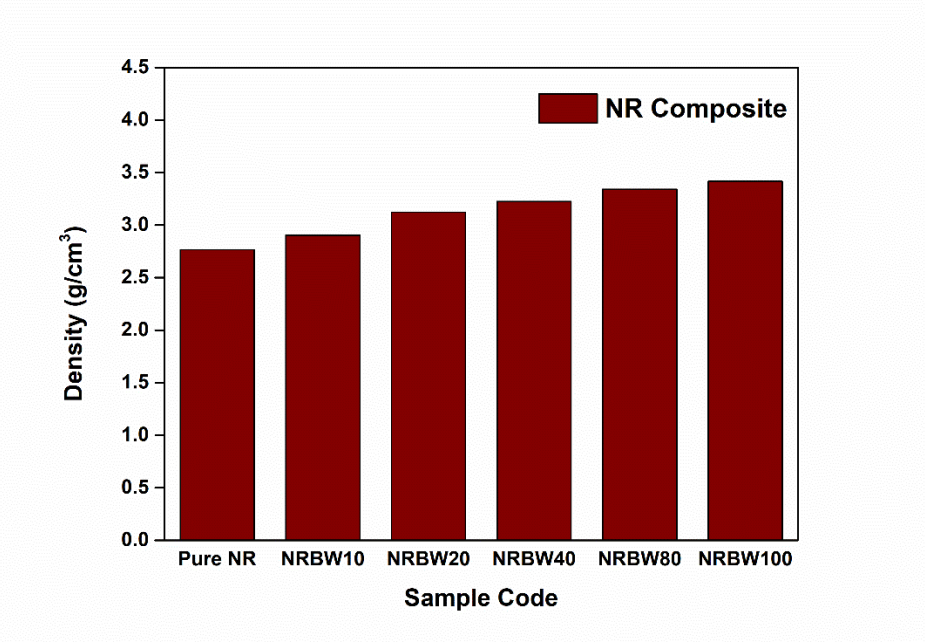

Figure 7.8: Density of the moulded rubber samples.

7.4 Gamma-ray shielding properties.

7.4.1 Linear Attenuation Coefficient

To assess the shielding effectiveness of the polymer composites, the linear attenuation coefficient (LAC) was calculated for samples containing different loadings of micro-sized $BaWO_4$. The linear attenuation coefficient (μ) depends on density and atomic number, but it is independent of the chemical nature or structure of absorber material.

Table 7.4. Experimental, XCOM, and Phy-X values of LAC for NR+$BaWO_4$ composites.

Linear attenuation coefficient, μ (cm^{-1})						
Sample	**Energy (0.059 MeV)**			**Energy (0.662 MeV)**		
	Expt	**XCOM**	**Phy-X**	**Expt**	**XCOM**	**Phy-X**
NRBW-0	1.5819	1.5843	1.6455	0.2107	0.2115	0.2135
NRBW-10	6.2872	6.3098	6.3545	0.2375	0.2393	0.2384
NRBW-20	9.2658	9.2861	9.3376	0.2649	0.2659	0.2668
NRBW-40	11.1826	11.1981	11.2568	0.2803	0.2784	0.2823
NRBW-80	13.3249	13.3874	13.4018	0.2914	0.2934	0.2954
NRBW-100	14.3942	14.4363	14.4728	0.3069	0.3124	0.3090
Sample	**Energy (1.172 MeV)**			**Energy (1.333 MeV)**		
	Expt	**XCOM**	**Phy-X**	**Expt**	**XCOM**	**Phy-X**
NRBW-0	0.1571	0.1598	0.1606	0.1460	0.1488	0.1501
NRBW-10	0.1586	0.1644	0.1673	0.1504	0.1539	0.1545
NRBW-20	0.1743	0.1759	0.1790	0.1624	0.1634	0.1649
NRBW-40	0.1768	0.1800	0.1819	0.1668	0.1681	0.1671
NRBW-80	0.1858	0.1835	0.1872	0.1704	0.1724	0.1711
NRBW-100	0.1846	0.1853	0.1907	0.1736	0.1747	0.1740

The experiments involved four photon energies within the range of 59.5–1333 keV. In general, for all concentrations, the values derived from XCOM and the other Phy-X/PSD software are slightly greater than the experimentally obtained ones. Furthermore, regarding shielding capability, it is evident that at the same concentration and given energy, the composites with added $BaWO_4$ demonstrate superior performance compared to regular composites. Figure 7.9 and 7.10 illustrate the results of the linear attenuation coefficient μ (cm^{-1}) for NR-$BaWO_4$ composites. It is evident that the linear attenuation coefficient of the composites significantly increases with a rise in the $BaWO_4$ filler concentration, whether in the form of micro or nanoparticles, in the polymer matrix. Furthermore, the LAC values decrease more rapidly with increasing photon energy.

The linear attenuation coefficient μ is derived from the slope of the linear relationship between ln (I/Io) and sample thickness x. It represents the product of the number of atoms per cubic centimeter of the shielding material and the probability of photons being scattered or absorbed by the nucleus or electrons within an atom of the shielding material. A higher μ value indicates better shielding performance of the materials. Figure 7.9 illustrates the experimental μ values for gamma radiation across various NR composites. The experiment indicated that μ increased after the NR was filled with metal oxides. The magnitude of μ depends on the metal oxide types used in the following order: NRBW100 > NRBW80 > NRBW40 > NRBW20 > NRBW10 > Pure NR. These results are in line with the literature that μ increases with atomic number (Z) of the element used as filler and with the density of the material. The data presented in

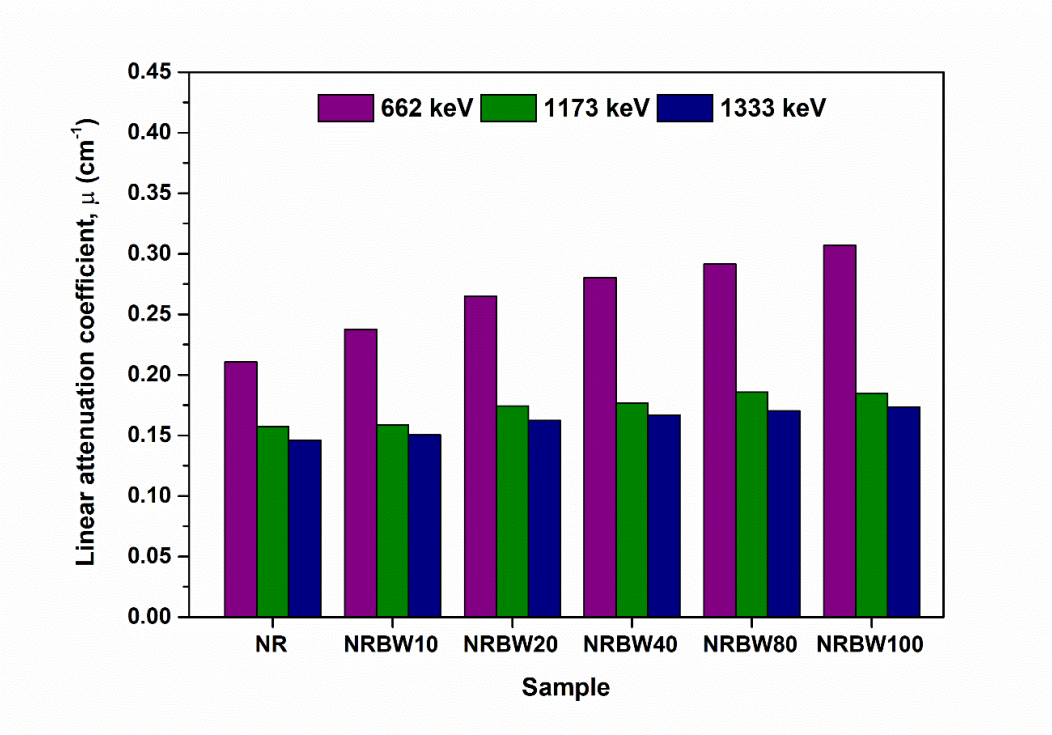

Figure 7.9: The experimental values of the NR composites for 662 keV, 1173 keV, and 1333 keV gamma rays.

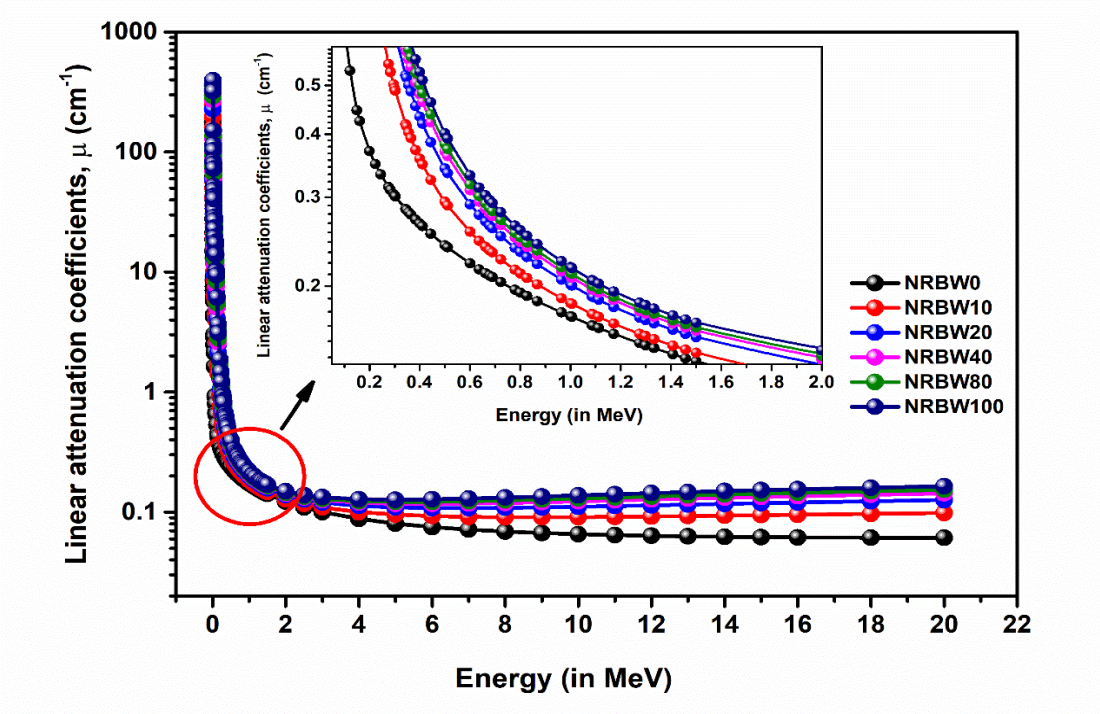

Figure 7.10: The linear attenuation coefficient of the studied NR-BaWO4 composites across a continuous energy range.

Figure 7.10 illustrates an upward trend in theoretical calculation of photon attenuation for samples with higher density values. The LAC value primarily depends weakly on the filler doping ratio, which can be attributed to the increase in the density range of the samples (NRBW-10 = 1.904 to NRBW-100 = 2.418 g/cm^3).

In other words, increasing the material density leads to a reduction in photon transmission through the sample. Consequently, high-density samples can effectively shield gamma photons, making them suitable for practical applications in shielding NR composites. This suggests that high-density samples possess the ability to efficiently absorb gamma rays, making them versatile materials catering to various industrial and health-related demands. A higher value of this factor for a particular sample indicates its superior capability for attenuation [32], [33]. However, at medium and higher energies, Compton scattering's contribution becomes significant compared to photoelectric absorption. As a result, for the same weight fraction of micro particles, the mass attenuation coefficient decreases rapidly. Table 7.5 shows the comparison of linear attenuation coefficient of some rubber composites that are previously reported at 0.66*2* MeV energy of the ^{137}Cs with the present study.

Table 7.5: Comparison of the linear attenuation coefficients between the different rubber shields of gamma-rays at 0.662 MeV.

No	Samples	Density (g/cm^3)	LAC (cm^{-1})	Reference
1	SBR+ TeO_2	2.227	0.172	[34]
2	Waste Rubber+PbO	1.687	0.156	[35]
3	NBR+Pb	-	0.478	[36]
4	EPDM/500-phr W_2O_3	2.742	0.192	[37]
5	EPDM/500-phr Bi_2O_3	2.893	0.246	[37]
6	SR+MgO	1.760	0.198	[38]
7	Pb_3O_4-NR	1.679	0.144	[21]
8	SnO_2-NR	1.623	0.111	[21]
9	Bi_2O_3-NR	1.696	0.127	[21]
10	WO_3-NR	1.684	0.148	[21]
11	NR/NBR/Bi_2O_3	3.741	0.336	[39]
12	NR+$BaWO_4$	3.418	0.306	Present study

As indicated in Table 7.5, the NR+$BaWO_4$ composites developed in this study exhibited comparable linear attenuation coefficient (LAC) values to those reported previously. In particular, the NR+$BaWO_4$ Composite rubber composites with 100-phr $BaWO_4$ had a slightly lower NR/NBR/Bi_2O_3 composites with 45-phr Bi_2O_3 [39].

In earlier studies, rubber-based composites have been explored extensively for radiation shielding due to their flexibility, lightweight nature, and ability to incorporate high atomic number additives. For instance, NR/NBR/Bi_2O_3 demonstrated superior shielding performance with a high density of 3.741 g/cm³ and an LAC of 0.336 cm^{-1}, while EPDM/500-phr Bi_2O_3 exhibited slightly lower values (2.893 g/cm³, LAC 0.246 cm^{-1}). Similarly, EPDM/500-phr WO_3 and SBR+TeO_2 showcased commendable LAC values (0.192 cm^{-1} and 0.172 cm^{-1}, respectively), reflecting their efficiency in gamma-ray attenuation. However, materials such as SnO_2-NR (1.623 g/cm³, LAC 0.111 cm^{-1}) and Bi_2O_3-NR (1.696 g/cm³, LAC 0.127 cm^{-1}) had relatively lower shielding capacities, likely due to their reduced densities or less effective incorporation of heavy-metal oxides. In comparison, the present study's NR+$BaWO_4$ composite stands out with a density of 3.418 g/cm³ and an LAC of 0.306 cm^{-1}. This material combines the flexibility and versatility of rubber with the high atomic number and density of $BaWO_4$, resulting in superior shielding properties that rival or surpass many of the previously studied composites. While materials like NBR+Pb exhibit even higher LAC values (0.478 cm^{-1}), their use is limited due to environmental and toxicity concerns. The NR+$BaWO_4$ composite offers an excellent balance of shielding efficiency, practicality, and environmental safety, making it a promising candidate for applications requiring effective yet sustainable radiation shielding solutions.

7.4.2 Mass Attenuation Coefficient

Table 7.6 presents the total mass attenuation coefficient (μ_m) for the NR and $BaWO_4$ composite, prepared with varying concentrations of $BaWO_4$ (0, 10, 20, 40, 80, and 100 phr). A comparison between the experimental and theoretical values is provided in Table 7.6, revealing a good agreement between the trends of the two sets of μ_m values. It was observed that the μ_m of all NR/$BaWO_4$ samples decreased with

increasing photon energy. This trend indicates the dependency of μ_m on the photon energy.

Table 7.6. Mass attenuation μ/ρ (cm^2/gm) and results for experimental, XCOM, and Phy-X of NR+$BaWO_4$ composites.

Mass attenuation coefficient, μ_m (cm^2/gm)						
Sample	**Energy (0.059 MeV)**			**Energy (0.662 MeV)**		
	Expt	**XCOM**	**Phy-X**	**Expt**	**XCOM**	**Phy-X**
NRBW0	0.5721	0.5730	0.5951	0.0762	0.0765	0.0772
NRBW10	2.165	2.1728	2.1882	0.0818	0.0824	0.0821
NRBW20	2.9660	2.9725	2.9890	0.0848	0.0851	0.0854
NRBW40	3.4664	3.4712	3.4894	0.0869	0.0863	0.0875
NRBW80	3.9871	4.0058	4.0101	0.0872	0.0878	0.0884
NRBW100	4.2113	4.2236	4.2343	0.0898	0.0914	0.0904
Sample	**Energy (1.172 MeV)**			**Energy (1.333 MeV)**		
	Expt	**XCOM**	**Phy-X**	**Expt**	**XCOM**	**Phy-X**
NRBW0	0.0568	0.0578	0.0581	0.0528	0.0538	0.0543
NRBW10	0.0546	0.0566	0.0576	0.0524	0.0530	0.0532
NRBW20	0.0558	0.0563	0.0573	0.0520	0.0523	0.0528
NRBW40	0.0548	0.0558	0.0564	0.0517	0.0521	0.0518
NRBW80	0.0556	0.0549	0.0560	0.0510	0.0516	0.0512
NRBW100	0.0540	0.0542	0.0558	0.0508	0.0511	0.0509

The experiments involved four photon energies within the range of 59.5–1333 keV. This was achieved by dividing the MAC values with the corresponding density of each sample. Notably, the experimental μ_m values of W (183.84 atomic weight) were considerably heavy. To assess the experimental findings, the corresponding theoretical values were obtained using the XCOM and Phy-X/PSD program [40]. As per the fundamental theory, when photons interact with matter, two primary phenomena come into play: the photoelectric effect and Compton scattering. These processes play a crucial role in determining the ability of materials to attenuate gamma-rays. Generally, the probability of the photoelectric effect is directly proportional to Z^3/E^3, where Z denotes the atomic number of the absorbing element, and E represents the energy of the photon. At higher energy levels of gamma-rays, Compton scattering becomes the dominant process (e.g., at 551 keV). High-energy

gamma-rays, when interacting with materials, experience multiple Compton scattering events before the lower-energy scattered photons are eventually absorbed via the photoelectric effect. This distinction in the attenuation process accounts for how materials respond differently to low and high-energy gamma-rays [42].

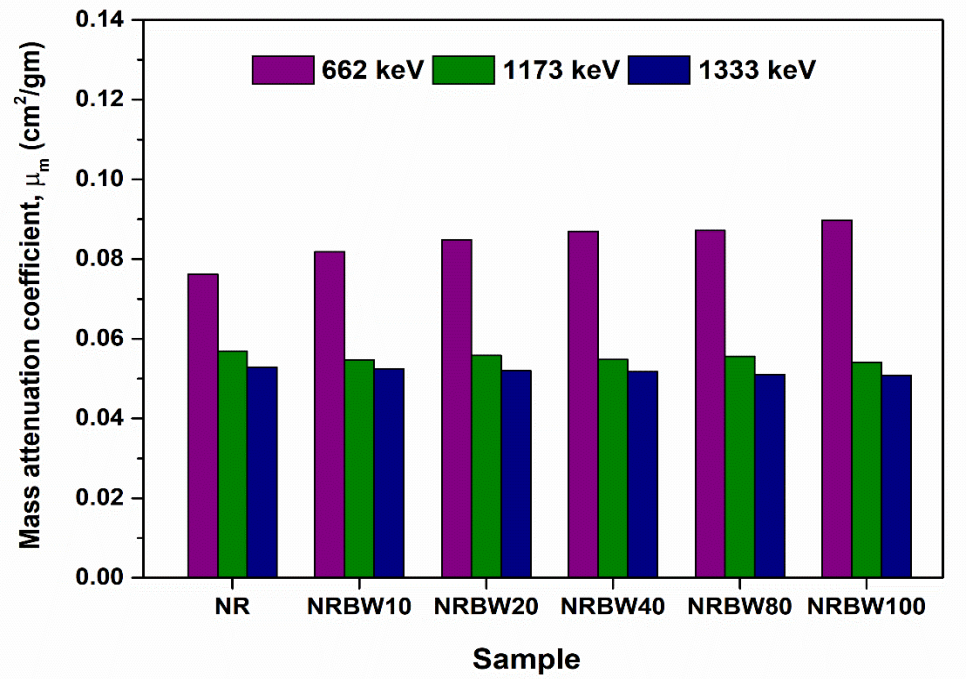

Figure 7.11: The experimental μ_m value of the NR composites for 662 keV, 1173 keV, and 1333 keV gamma rays.

Low-energy gamma-rays can be directly absorbed through the photoelectric effect, while high-energy gamma-rays experience more intricate interactions with matter due to multiple Compton scattering events, making them more challenging to shield effectively. As a result, as the energy of gamma-rays increases, the attenuating properties of materials decrease [42]. At low energies, the composite containing $BaWO_4$ (100 phr) as a dopant exhibits a mass attenuation coefficient (μ/ρ) twice that of the composite with $BaWO_4$ (10 phr) dopant. However, as the energy level increases, this difference diminishes. At higher energy levels, the coefficients become nearly equal for both composites.

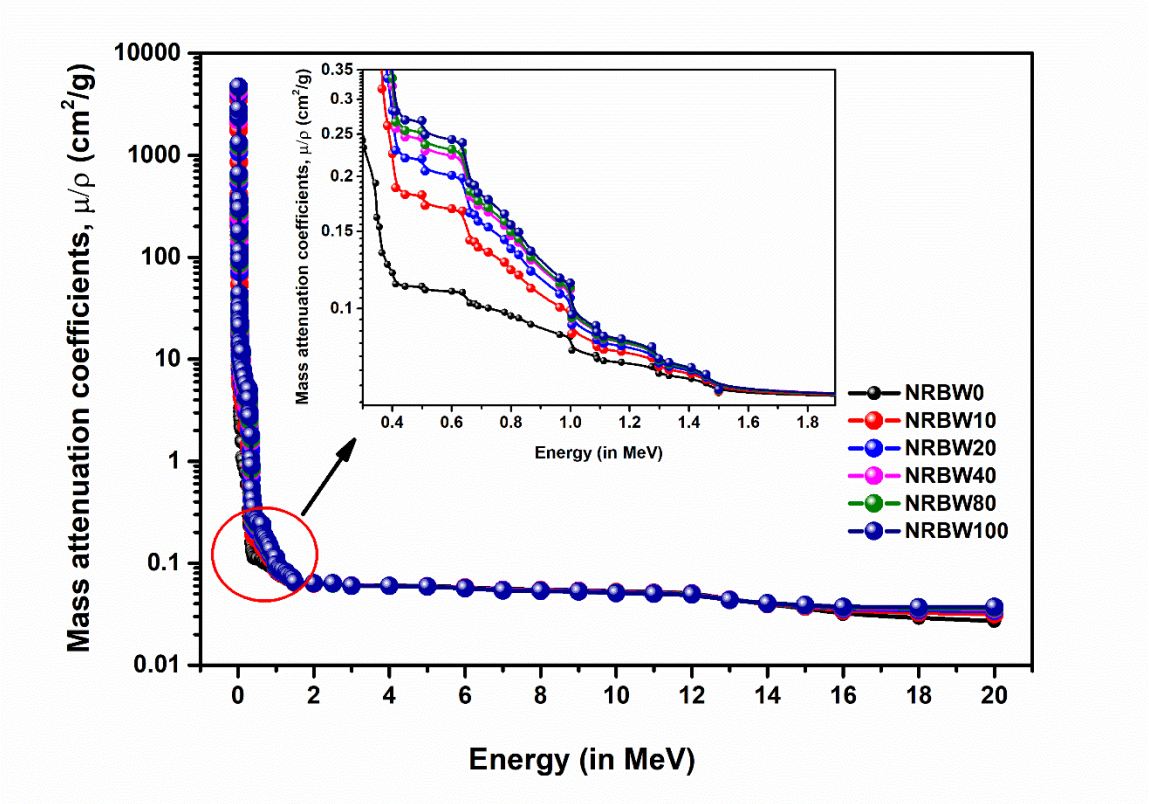

Figure 7.12 : Variation of the mass attenuation coefficient of the investigated NR-$BaWO_4$ composites in the continuous energy region.

The XCOM code employs pre-established elemental tables supplied by the program developers and incorporates the elemental weights of the materials to compute the mass attenuation coefficients (MAC) for suggested radiation shielding attenuators [44]. These coefficients are measured in units of cm^2/g. The program necessitates inputting the desired radiation energy without the requirement to specify the density or thickness of the considered material.

7.4.3 Half-Value Layer (HVL) and Tenth-Value Layer (TVL)

The study also examines the values of Half-Value Layer (HVL), and Tenth-Value Layer (TVL), as they serve as useful indicators of a material's gamma radiation shielding capacity. These parameters are dependent on gamma radiation energy, as shown in the calculations. At higher photon energies, HVL and TVL values increase. This variation can be attributed to the prevalence of distinct photon interaction processes in various energy regions, as discussed previously concerning

mass attenuation coefficients. It is worth noting that lower HVL values are preferred for exceptional gamma-ray shielding materials, as they increase the likelihood of photon interaction with the material [33]. Figure 7.13 demonstrates the dependence of HVL values on photon energy for all samples.

When photon energy is increased to 3 MeV, its values significantly increase. Following that, as the energy is increased up to 10 MeV, the HVL slowly grows. Beyond this energy,10 MeV, HVL behaves in a consistent manner. At a maximum photon energy of 15 MeV, the HVL of all samples increases by nearly 1000 times. Therefore, samples with low density have the greatest HVL value, and vice versa, as high-energy photons will be absorbed by thick sample layers. Otherwise, a sample with a high density has a better chance of absorbing photons than others. TVL as a function of Photon energy provides instant feedback on the size or thickness of the specimen, which can block up to 90% of input photons. The same tendency of HVL is shown in Figure 7.13,7.14,7.15 and 7.15 where the variance of HVL and TVL with density is very small in all energy ranges.

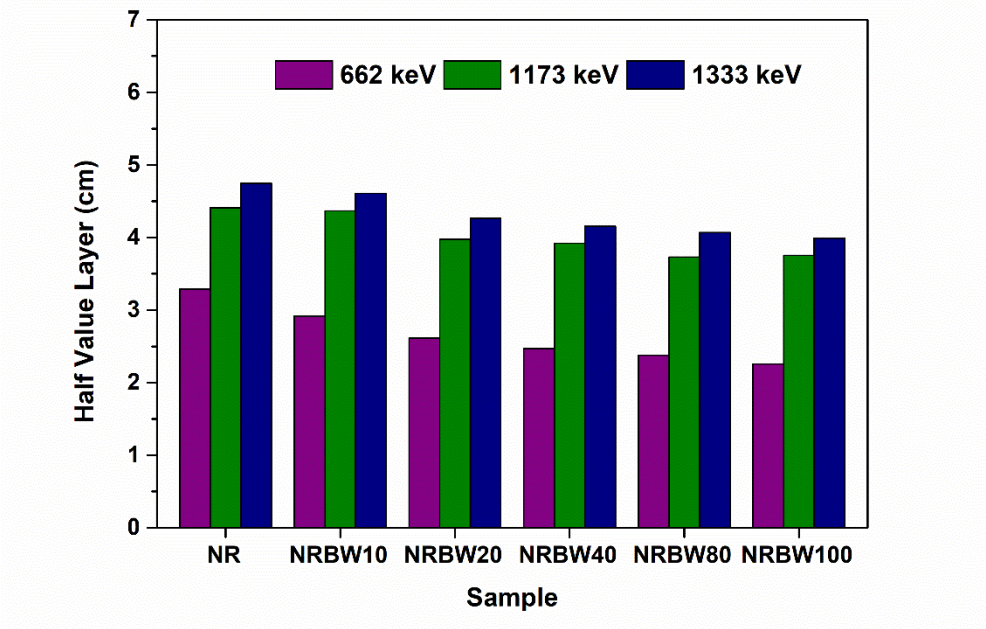

Figure 7.13: The experimental HVL value of the NR composites for 662 keV, 1173 keV, and 1333 keV gamma rays.

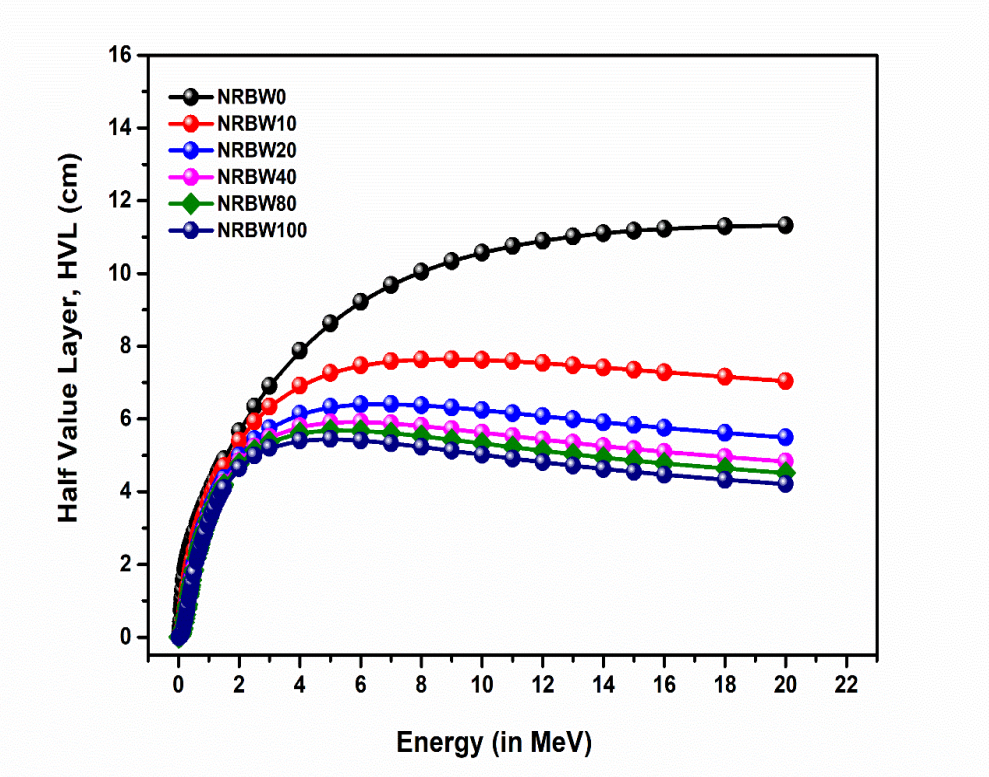

Figure. 7.14: Half value layer (HVL) as a function of photon energy and $BaWO_4$-content of the samples.

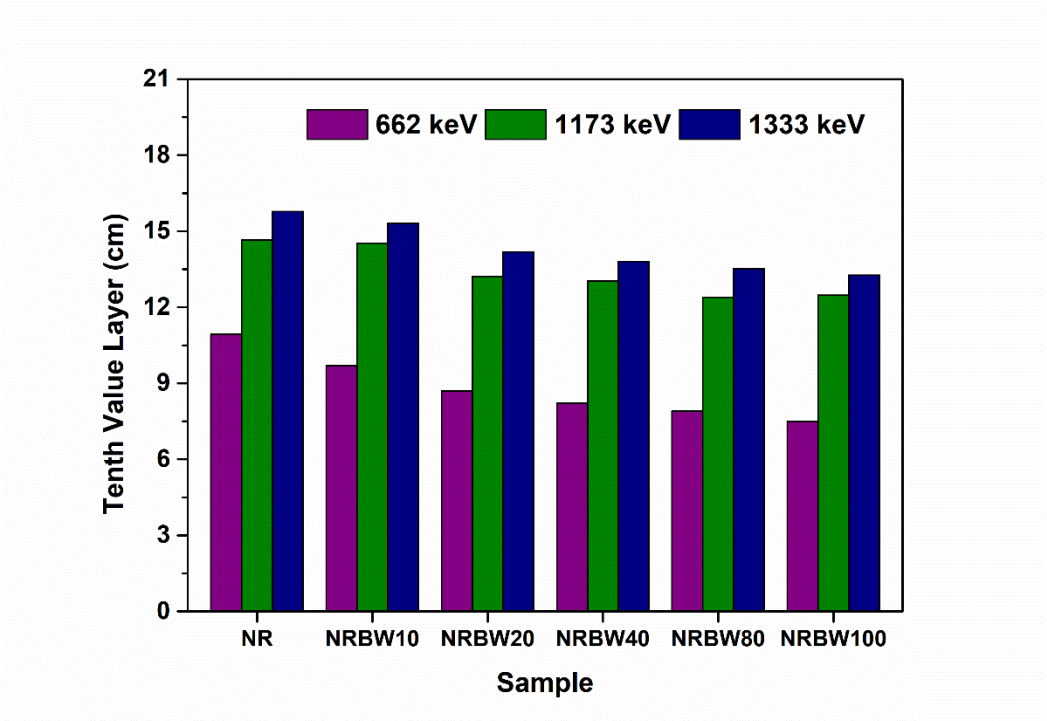

Figure 7.15: The experimental HVL value of the NR composites for 662 keV,

1173 keV, and 1333 keV gamma rays

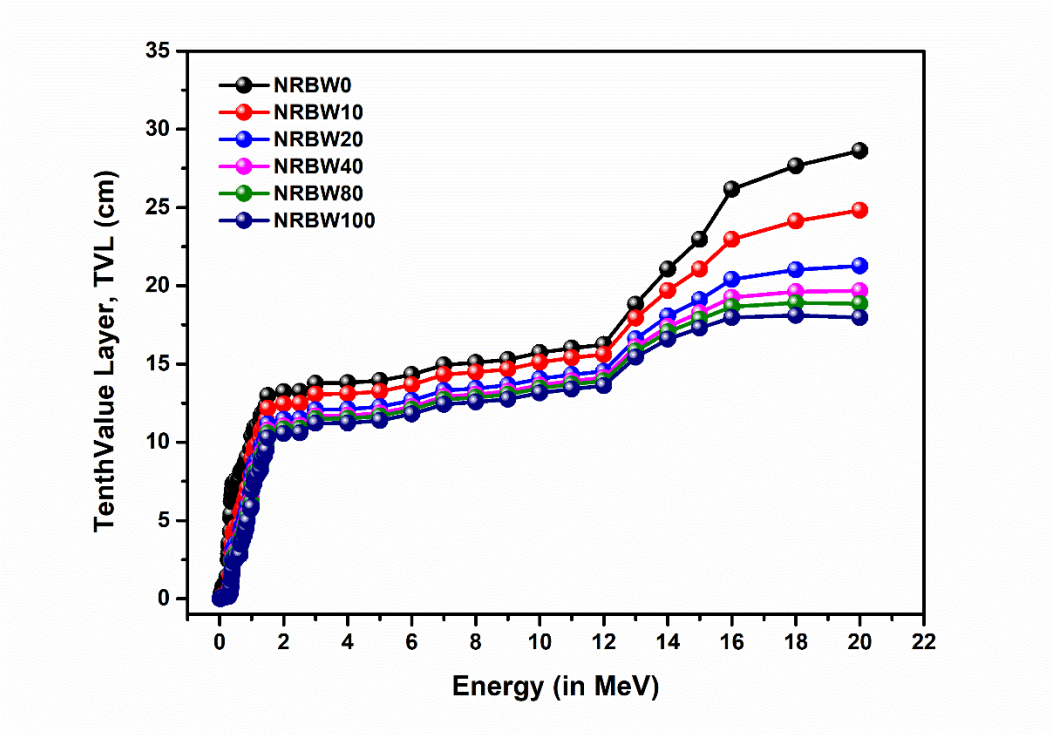

Figure 7.16. Tenth value layer (TVL) as a function of photon energy and $BaWO_4$-content of the samples.

7.4.4 Mean Free Path (MFP)

The Mean Free Path (MFP) can be effortlessly determined by inverting the total linear attenuation coefficient, which represents the average distance between two consecutive photon interactions with the material, leading to a decrease in the intensity of the initial photon beam by a factor of 1/E. Concerning the values of MFP, TVL, and HVL, at any given energy, an increase in the amount of $BaWO_4$ microparticles results in a higher mass attenuation coefficient for the composites, while the MFP, HVL, and TVL values decrease. Furthermore, the results suggest that as the photon energy increases, the shielding performance of the produced samples decreases, which aligns with the expected outcome. Figure 7.17 illustrates the results of the mean free path for NR-$BaWO_4$ composites.

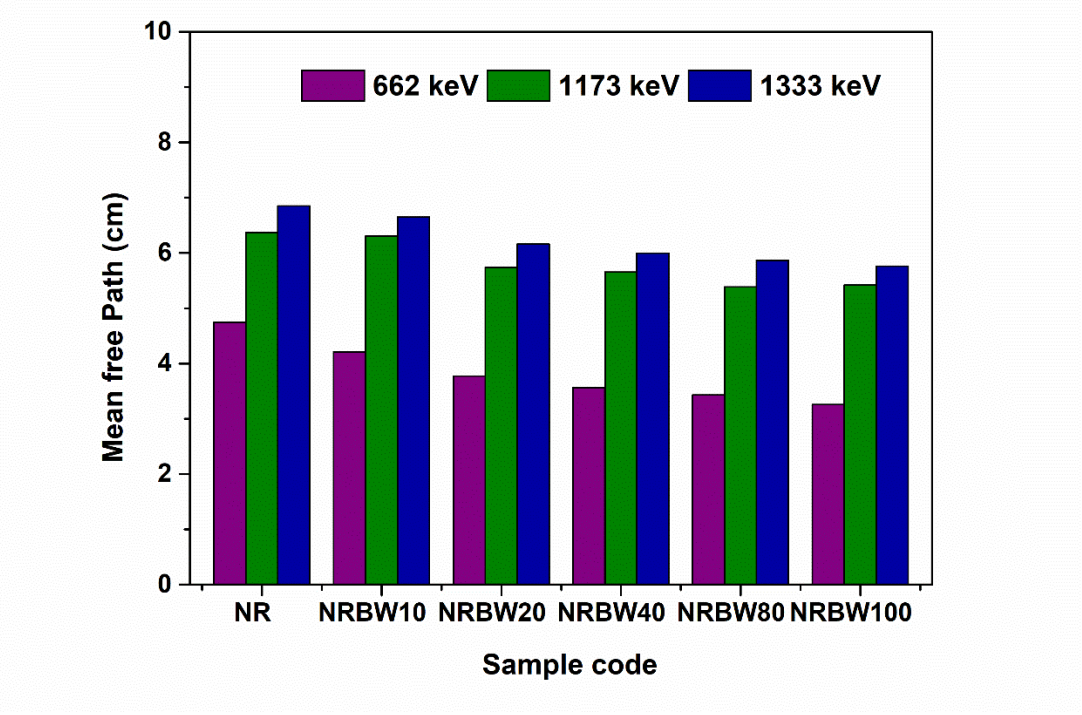

Figure 7.17: The experimental MFP value of the NR composites for 662 keV, 1173 keV, and 1333 keV gamma rays

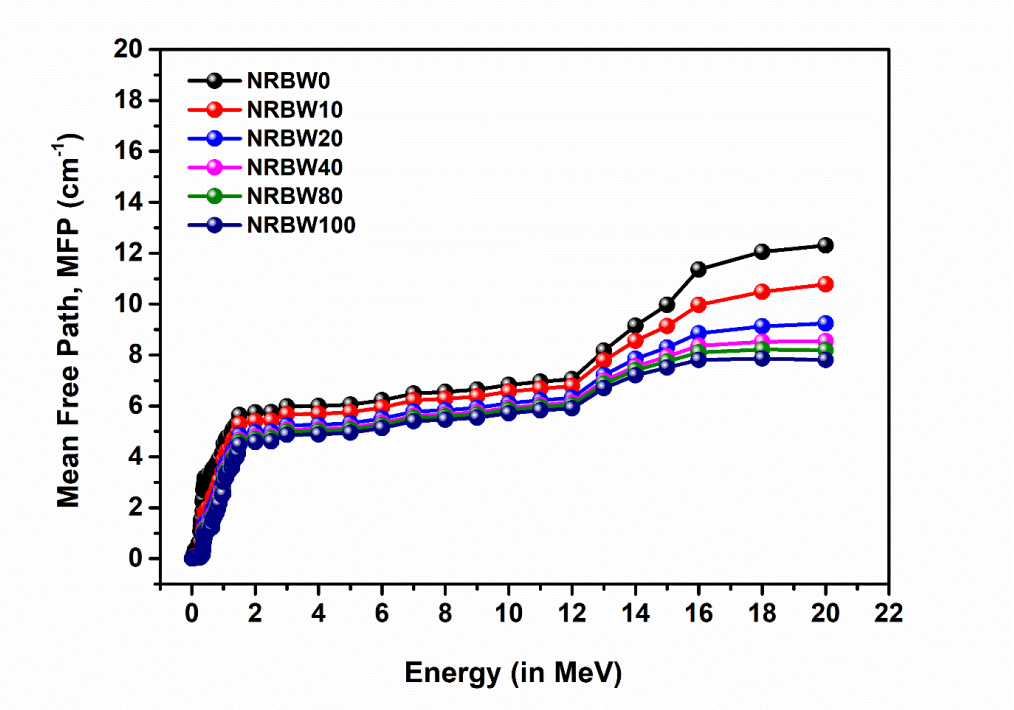

Figure 7.18: Mean free path (MFP) as a function of photon energy and $BaWO_4$-content of the samples.

7.4.5 Atomic Cross-Section (ACS) and Electronic Cross-Section (ECS)

The values of atomic cross section (ACS) and electronic cross section (ECS) for a particular radiation-shielding material offer a concise representation of the probability of radiation interactions per atom or electron within each unit of volume. Similar variations in ACS and ECS behavior have been observed in the present study. Compared to $BaWO_4$ (10 phr) composite, ACS and ECS values for $BaWO_4$ (100 phr) material are higher. From the data, it can be inferred that the increase in $BaWO_4$ content throughout the energy range directly corresponds to the cross-sections, reducing the incident photon energy for all the examined samples. The photoelectric and pair production effect is dominant in low and high energy regions, respectively, in high A samples, while the Compton effect is dominant and energy independent. Figure. 7.19 and 7.20 illustrate the integrated ACS (Atomic Cross-Section) and ECS (Electronic Cross-Section) values, respectively. The higher the number of atoms and electrons in unit volume of a substance, the larger will be the corresponding ACS and ECS of that substance. In terms of radiation shielding, materials with high ACS and ECS are superior. Figures 7.19 and 7.20 indicate that ACS and ECS behave similarly across the whole energy range. ACS and ECS depend on the chemical makeup of the material and the incident photon energy (E_{ph}), which explains the similarities between the behavior of ACS and ECS. The examination of these figures also shows that the sample NRBW100 yields the highest ACS and ECS values, whereas the NRBW10 sample yields the lowest. Furthermore, as E_{Ph} rises, these values drop.

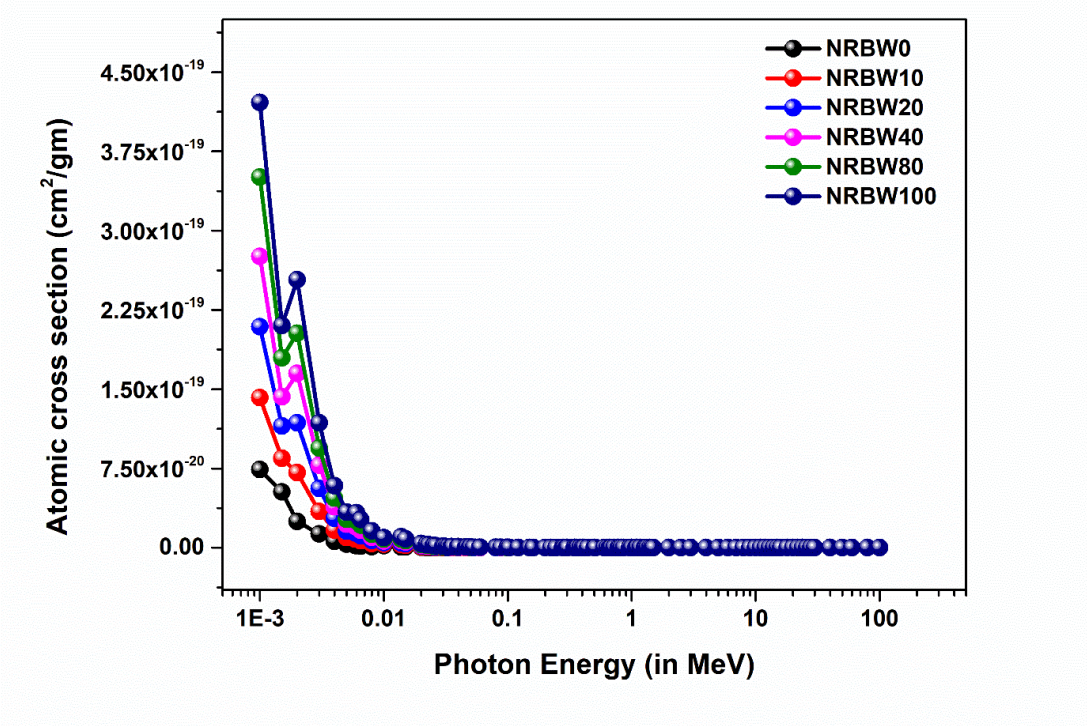

Figure 7.19: Atomic cross section (ACS) as a function of photon energy and $BaWO_4$-content of the samples.

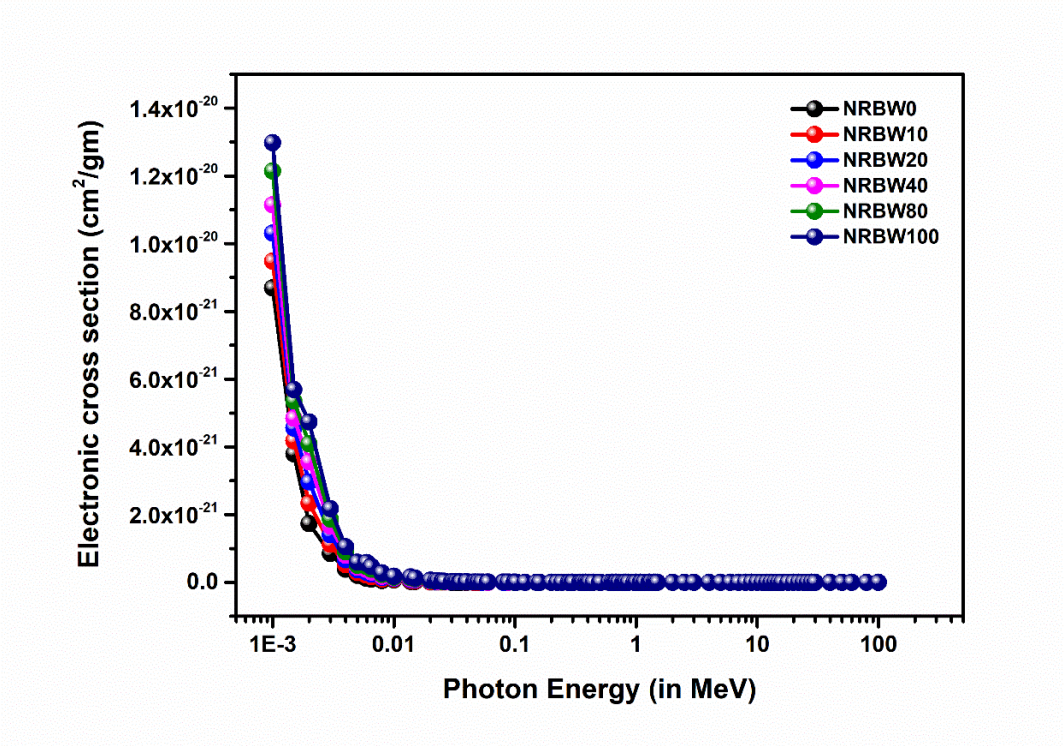

Figure 7.20: Electronic cross section (ECS) as a function of photon energy and $BaWO_4$-content of the samples.

7.4.6 Effective atomic number (Z_{eff}) and Effective electron density (N_{eff})

The atomic cross section depends on the fifth power of atomic number Z of the medium and this relation is valid for gamma-ray energies of few hundreds of keV. Also, the linear attenuation coefficient is N (atomic density) times the atomic cross section. As the atomic density increases with the weight percentage of $BaWO_4$ (below the threshold limit), linear attenuation coefficient also increases correspondingly. As expected, both Z_{eff} and N_{eff} demonstrate a similar pattern, indicating a decrease with the rise in gamma radiation energy across all samples, as depicted in Figures 7.21 and Figure 7.22, respectively. Furthermore, there was a significant difference in Z_{eff} values for $BaWO_4$ (10 phr) and $BaWO_4$ (100 phr), with the values increasing in the sequence of $BaWO_4$ (10 phr) < $BaWO_4$ (20 phr) < $BaWO_4$ (40 phr) < $BaWO_4$ (80 phr) < $BaWO_4$ (100 phr).

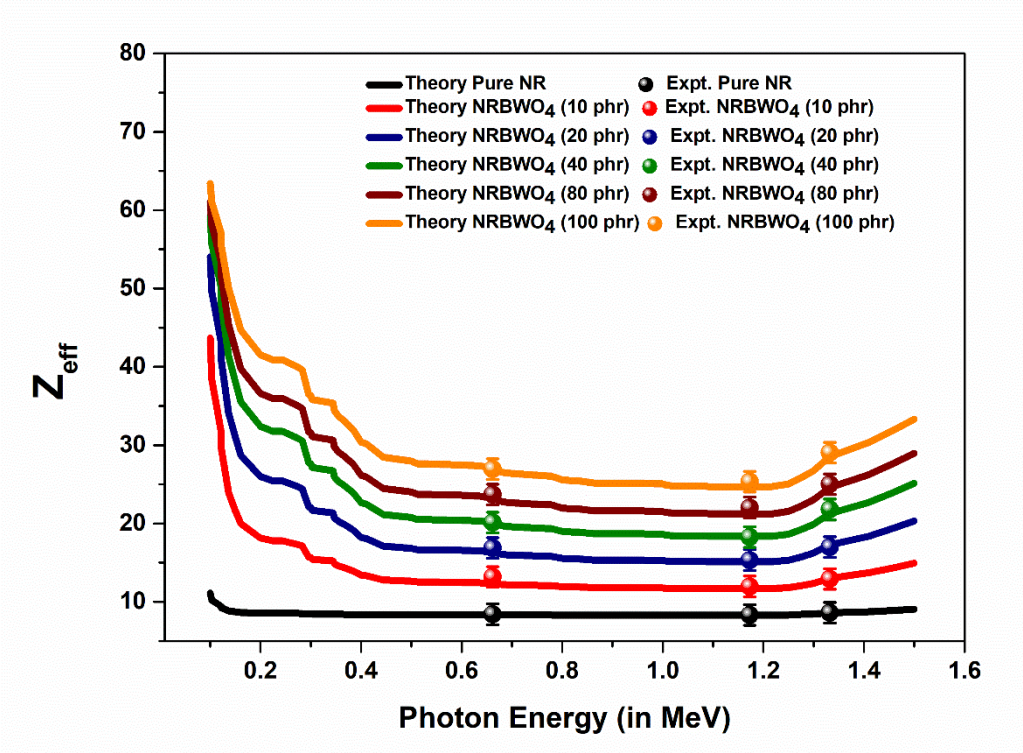

Figure 7.21: Effective atomic number (Z_{eff}) as a function of photon energy and $BaWO_4$-content of the samples (computational study).

Based on the effective atomic number (Z_{eff}) and effective electron density (N_{eff}), $BaWO_4$ (100 phr) exhibits superior radiation attenuation properties. It was observed

that Z_{eff} increases with the rising concentration of $BaWO_4$ and decreases as photon energies increase, following the same trend as μ_m. This behaviour can be attributed to the higher atomic number of $BaWO_4$, which influences the probability of interaction between photons and electrons within the material. The variation of the Z_{eff} for the studied samples in the energy range 0.015–20 MeV is revealed in Figure 7.21, where Z_{eff}'s value decreases as photon energy rises at lower energies; but at intermediate energies, Zeff is nearly constant; and at higher energies, Z_{eff} rises slightly. For NRBW-10, NRBW-20, NRBW-40, NRBW-80 and NRBW-100, the Z_{eff} values at 0.015 MeV are 47.43, 55.91, 61.10, 62.69, and 65.01, respectively. At 15 MeV, the Z_{eff} values are 19.99, 27.59, 33.76, 37.99, and 42.60, respectively for NRBW-10, NRBW-20, NRBW-40, NRBW-80 and NRBW-100. This means that gamma rays have a higher chance of interacting with the $BaWO_4$ in NR sample and a lower chance of penetrating it.

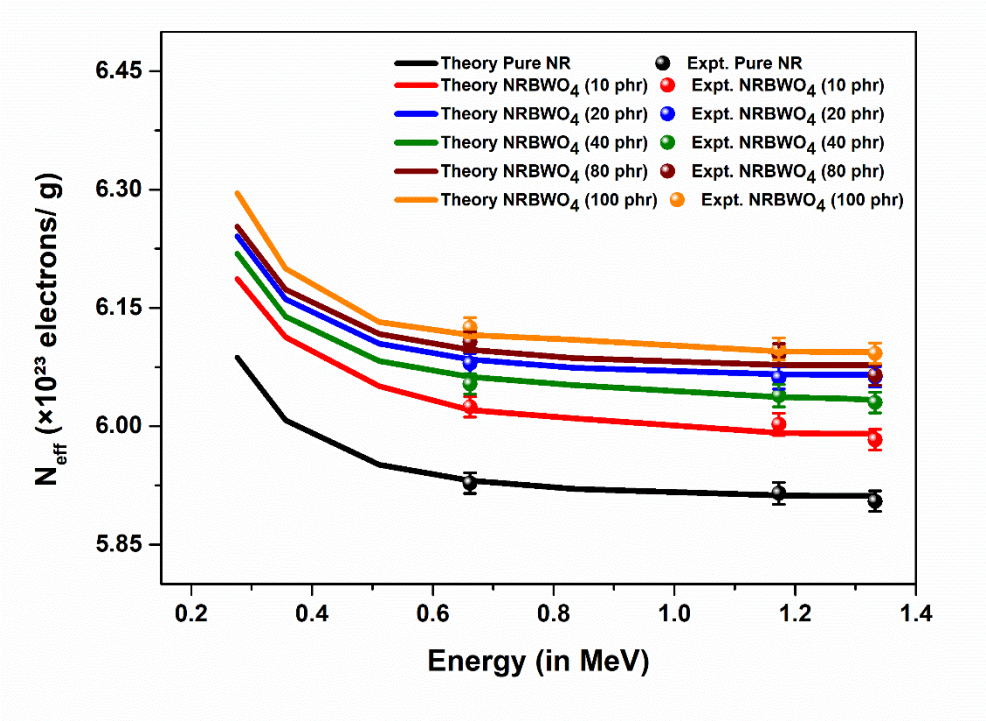

Figure 7.22: Effective electron density (N_{eff}) as a function of photon energy and $BaWO_4$-content of the samples.

The effective electron density (N_{eff}) denotes the quantity of electrons per unit mass present in a material [45]. As the atomic number of elements increases, the electron density of materials significantly decreases [46]. Hence, materials composed of

heavy atoms tend to have lower N_{eff} values, making this parameter unsuitable as a direct shielding indicator. Nevertheless, it does provide valuable characterization of materials within a specific class. Figures 7.22 displays the changes in N_{eff} values concerning photon energy. The results indicate that the composites exhibit approximately 2.67×10^{23} electrons per unit mass. This finding supports the earlier explanation that materials comprising elements with higher atomic numbers tend to have lower electron densities. Furthermore, the expanded N_{eff} graph reveals an inverse relationship between the decreasing order of N_{eff} values for any energy of the composite and the order of MAC, LAC, and Z_{eff} values [46].

7.4.7 Built-up Factors

According to the geometric progression fitting method, determining the B values that describe the photon scattering properties of materials requires knowledge of the R, Z_{eq}, and G-P fitting coefficients. In this study, these parameters were computed using the G-P fitting method, and the outcomes are presented in Tables 7.7 and 7.8 for the BaWO4 (10 phr) and BaWO4 (100 phr) samples, respectively. The effective buildup factor (EBF) and effective attenuation buildup factor (EABF) were determined using the five-parameter geometric progression (G-P) fitting method. This analysis covered penetration depths up to 40 mean free paths (mfp) and spanned energies ranging from 0.015 MeV to 15 MeV[47].

Table 7.7 Geometrical progression (G-P) based parameters of energy absorption build-up factor (EABF) and exposure build-up factor (EBF) for the $BaWO_4$ (10 phr)-blended NR composite at various photon energy values ranging from 0.015 to 15 MeV (computational).

Energy (MeV)	EABF					EBF				
	A	b	c	d	X_k	a	b	c	d	X_k
0.015	0.197	1.023	0.408	-0.091	11.592	0.254	1.024	0.356	-0.173	12.496
0.02	0.184	1.047	0.421	-0.104	16.162	0.178	1.047	0.428	-0.097	16.253
0.03	0.219	1.141	0.390	-0.123	13.874	0.213	1.141	0.394	-0.115	14.406
0.04	0.212	1.209	0.400	-0.117	14.489	0.212	1.205	0.401	-0.119	14.560
0.05	0.206	1.352	0.426	-0.119	14.362	0.199	1.327	0.439	-0.113	14.270
0.06	0.165	1.513	0.503	-0.091	15.337	0.169	1.447	0.505	-0.095	14.351
0.08	0.170	1.496	0.493	-0.095	15.398	0.165	1.383	0.511	-0.091	14.429
0.1	0.156	1.770	0.541	-0.095	15.273	0.130	1.493	0.600	-0.073	14.163

0.15	0.139	2.518	0.618	-0.111	14.806	0.073	1.707	0.767	-0.045	14.070
0.2	0.079	2.897	0.793	-0.071	13.116	0.033	1.845	0.915	-0.033	13.219
0.3	0.017	3.009	1.007	-0.039	12.550	-0.006	1.947	1.078	-0.019	12.017
0.4	-0.011	2.811	1.125	-0.026	11.890	-0.023	1.957	1.166	-0.014	11.025
0.5	-0.027	2.619	1.190	-0.016	10.965	-0.034	1.937	1.213	-0.009	9.162
0.6	-0.032	2.482	1.211	-0.013	10.544	-0.037	1.913	1.229	-0.009	8.395
0.8	-0.035	2.272	1.221	-0.013	8.627	-0.037	1.867	1.228	-0.012	7.336
1	-0.040	2.129	1.225	-0.002	10.673	-0.038	1.824	1.218	-0.003	11.249
1.5	-0.044	1.937	1.214	0.014	15.535	-0.042	1.784	1.207	0.012	15.804
2	-0.034	1.836	1.158	0.010	14.703	-0.032	1.778	1.154	0.009	15.074
3	-0.009	1.706	1.050	-0.001	10.914	-0.011	1.686	1.056	0.001	10.653
4	0.008	1.616	0.984	-0.011	13.115	0.006	1.610	0.992	-0.008	14.681
5	0.019	1.546	0.945	-0.014	12.860	0.016	1.541	0.953	-0.018	14.957
6	0.026	1.489	0.921	-0.027	15.655	0.029	1.498	0.915	-0.024	12.887
8	0.032	1.397	0.900	-0.021	12.300	0.033	1.410	0.898	-0.023	13.041
10	0.038	1.337	0.883	-0.028	13.917	0.041	1.352	0.874	-0.030	13.525
15	0.042	1.240	0.873	-0.034	14.733	0.058	1.264	0.831	-0.049	14.648

Table 7.8 Geometrical progression (G-P) based parameters of energy absorption build-up factor (EABF) and exposure build-up factor (EBF) for the $BaWO_4$(100 phr)-blended NR composite at various photon energy values ranging from 0.015 to 15 MeV (computational).

Energy (MeV)	EABF					EBF				
	a	b	c	d	X_k	a	b	c	d	X_k
0.015	0.220	1.008	0.412	-0.150	11.283	0.307	1.009	0.373	-0.227	9.115
0.02	0.249	1.017	0.367	-0.181	11.467	0.193	1.016	0.432	-0.100	10.905
0.03	0.240	1.050	0.354	-0.155	13.977	0.219	1.051	0.372	-0.157	14.969
0.04	0.242	1.056	0.338	-0.149	15.214	0.247	1.056	0.335	-0.116	11.962
0.05	0.243	1.093	0.347	-0.137	13.867	0.236	1.089	0.361	-0.137	13.615
0.06	0.240	1.143	0.355	-0.144	14.611	0.223	1.128	0.383	-0.125	13.839
0.08	0.474	1.285	0.169	-0.199	14.138	0.607	1.529	0.148	-0.215	14.280
0.1	0.286	1.234	0.314	-0.151	14.993	0.263	1.186	0.344	-0.142	13.780
0.15	0.278	1.527	0.339	-0.157	14.030	0.165	1.274	0.512	-0.086	14.369
0.2	0.306	2.300	0.329	-0.192	13.994	0.166	1.488	0.534	-0.095	14.249
0.3	0.159	2.384	0.559	-0.098	14.059	0.080	1.588	0.733	-0.043	14.489
0.4	0.110	2.642	0.703	-0.089	13.907	0.040	1.696	0.882	-0.034	14.177
0.5	0.073	2.650	0.813	-0.067	13.896	0.020	1.751	0.963	-0.025	14.293
0.6	0.053	2.608	0.872	-0.056	13.755	0.007	1.770	1.009	-0.019	13.954
0.8	0.031	2.472	0.946	-0.043	13.654	-0.005	1.779	1.058	-0.014	14.034

1	0.019	2.345	0.982	-0.035	13.539	-0.010	1.762	1.078	-0.012	13.430
1.5	-0.013	1.942	1.099	-0.014	12.875	-0.031	1.636	1.164	0.002	8.394
2	-0.014	1.838	1.099	-0.009	10.263	-0.021	1.675	1.122	-0.004	9.703
3	-0.001	1.685	1.041	-0.015	12.240	-0.008	1.632	1.064	-0.010	12.515
4	0.016	1.584	0.981	-0.026	12.508	0.007	1.570	1.012	-0.017	12.217
5	0.021	1.498	0.963	-0.032	14.577	0.015	1.508	0.983	-0.023	13.209
6	0.028	1.431	0.945	-0.036	12.875	0.023	1.461	0.960	-0.029	13.316
8	0.033	1.335	0.932	-0.033	12.137	0.033	1.382	0.932	-0.038	13.457
10	0.046	1.282	0.899	-0.048	13.899	0.038	1.318	0.923	-0.042	13.481
15	0.035	1.176	0.943	-0.039	14.483	0.064	1.235	0.868	-0.065	13.738

Table 7.9 and 7.10 provides the values of Z_{eq} and R values for $BaWO_4$ blended natural polymer composite at specific photon energies from 0.015 MeV to 15 MeV. When gamma rays traverse through a material, they undergo various interactions, including scattering and absorption. This can lead to an increase in radiation intensity beyond what would be expected from simple exponential attenuation. The buildup factor becomes crucial in accounting for these multiple interactions. It acknowledges that gamma-ray attenuation is not solely dependent on the material's linear attenuation coefficient (μ) but also on the distance travelled by the gamma rays within the material. By considering the effects of multiple scattering and re-absorption of gamma rays, the buildup factor provides a more accurate representation of the radiation field. For evaluating the build-up factor two important parameters used are the equivalent atomic number Z_{eff} and R. Figures 7.23 and 7.24 are the plots showing the variation of the computationally obtained Zeq with incident photon energy in the range 0.015-15 MeV.

Table 7.9: Equivalent atomic numbers Z_{eq} of the $BaWO_4$ blended natural rubber composites at various photon energy values ranging from 0.015 to 15 MeV (computational).

Equivalent atomic numbers Z_{eq}						
Energy (MeV)	**Pure NR**	**NRBW-10**	**NRBW-20**	**NRBW-40**	**NRBW-80**	**NRBW-100**
0.015	11.67	13.85	15.61	17.03	18.09	19.52
0.02	12.02	14.36	16.20	17.67	18.76	20.16
0.03	12.47	14.99	16.94	18.49	19.61	21.04
0.04	12.75	17.31	20.14	22.29	24.59	26.32
0.05	12.95	17.78	20.69	22.89	25.26	27.02
0.06	13.10	18.13	21.12	23.36	25.75	27.53
0.08	13.31	23.47	28.50	32.31	34.93	37.88
0.1	13.45	24.15	29.31	33.18	35.83	38.80
0.15	13.68	25.21	30.57	34.54	37.19	40.20
0.2	13.82	25.88	31.34	35.37	38.04	41.05
0.3	13.99	26.70	32.27	36.37	39.01	42.04
0.4	14.08	27.20	32.84	36.98	39.61	42.63
0.5	14.12	27.52	33.21	37.35	40.00	43.02
0.6	14.15	27.74	33.45	37.60	40.24	43.27
0.8	14.17	27.94	33.67	37.84	40.49	43.51
1	14.19	28.02	33.77	37.96	40.59	43.63
1.5	8.96	21.42	28.47	33.50	36.70	40.29
2	7.91	13.32	18.59	23.38	27.13	31.41
3	7.69	10.74	13.93	17.07	19.84	23.29
4	7.63	10.20	12.90	15.57	17.99	21.02
5	7.61	9.96	12.47	14.93	17.19	20.04
6	7.59	9.83	12.22	14.55	16.72	19.45
8	7.58	9.69	11.96	14.16	16.23	18.84
10	7.57	9.62	11.83	13.98	16.00	18.55
15	7.55	9.57	11.73	13.83	15.82	18.33

Table 7.10: R parameter values of the $BaWO_4$ doped polymer composites for various energy values ranging from 0.015 to 15 MeV.

R parameter						
Energy (MeV)	**Pure NR**	**NRBW-10**	**NRBW-20**	**NRBW-40**	**NRBW-80**	**NRBW-100**
0.015	0.024	0.013	0.009	0.007	0.006	0.004
0.02	0.055	0.031	0.021	0.016	0.013	0.010
0.03	0.163	0.093	0.063	0.048	0.040	0.032
0.04	0.314	0.135	0.086	0.063	0.046	0.037
0.05	0.469	0.224	0.146	0.109	0.081	0.066
0.06	0.601	0.321	0.219	0.166	0.126	0.103
0.08	0.777	0.318	0.195	0.138	0.111	0.088
0.1	0.869	0.451	0.298	0.219	0.179	0.145
0.15	0.954	0.695	0.540	0.436	0.376	0.318
0.2	0.979	0.823	0.704	0.610	0.551	0.486
0.3	0.993	0.924	0.862	0.804	0.762	0.712
0.4	0.996	0.959	0.922	0.886	0.859	0.824
0.5	0.998	0.974	0.949	0.925	0.906	0.882
0.6	0.998	0.981	0.964	0.946	0.932	0.914
0.8	0.999	0.989	0.978	0.967	0.959	0.947
1	0.999	0.992	0.985	0.977	0.971	0.962
1.5	0.998	0.992	0.987	0.981	0.977	0.971
2	0.990	0.984	0.977	0.970	0.964	0.956
3	0.967	0.954	0.941	0.929	0.918	0.904
4	0.937	0.918	0.899	0.881	0.865	0.845
5	0.905	0.880	0.855	0.832	0.811	0.787
6	0.872	0.841	0.811	0.784	0.760	0.732
8	0.807	0.768	0.731	0.698	0.669	0.637
10	0.747	0.702	0.660	0.623	0.593	0.558
15	0.623	0.570	0.524	0.485	0.454	0.420

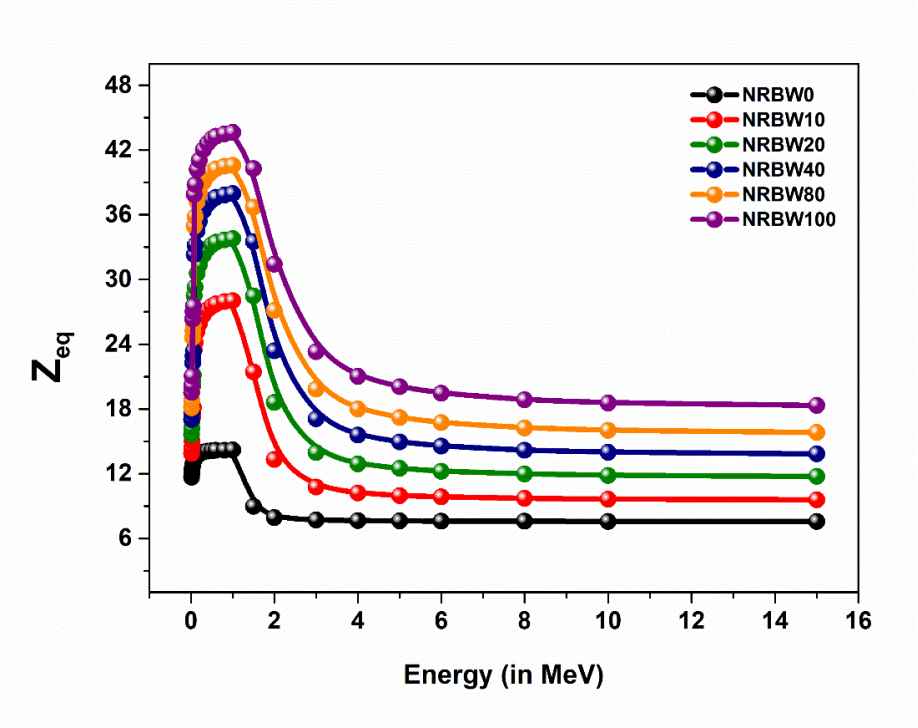

Figure 7.23: Equivalent atomic number (Z_{eq}) as a function of photon energy and $BaWO_4$-content of the samples.

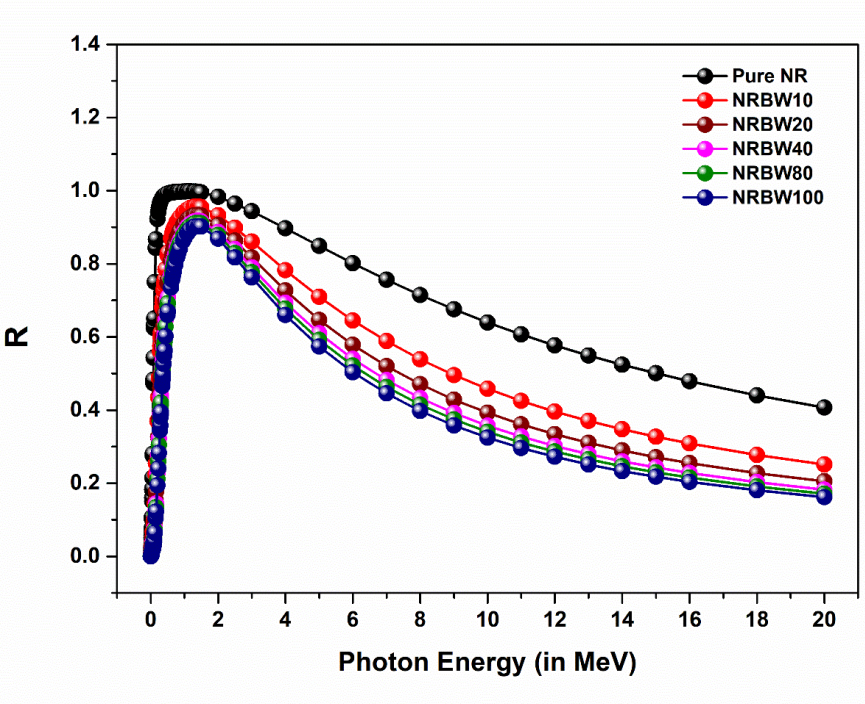

Figure 7.24. R values as a function of photon energy for BaWO4-incorparated NR samples

Figure 7.25 (a-f) shows the variation of the build-up factor EABF values with incident photon energy for $BaWO_4$-blended natural rubber composites (a-NRBW0, b-NRBW10, c-NRBW20, d-NRBW40, e-NRBW80, f-NRBW100), corresponding to the MFP values of 1, 2, 4, 8,10,15, 20 and 40 between 0.015 and 15 MeV energies as similar to previous studies [44], [48].

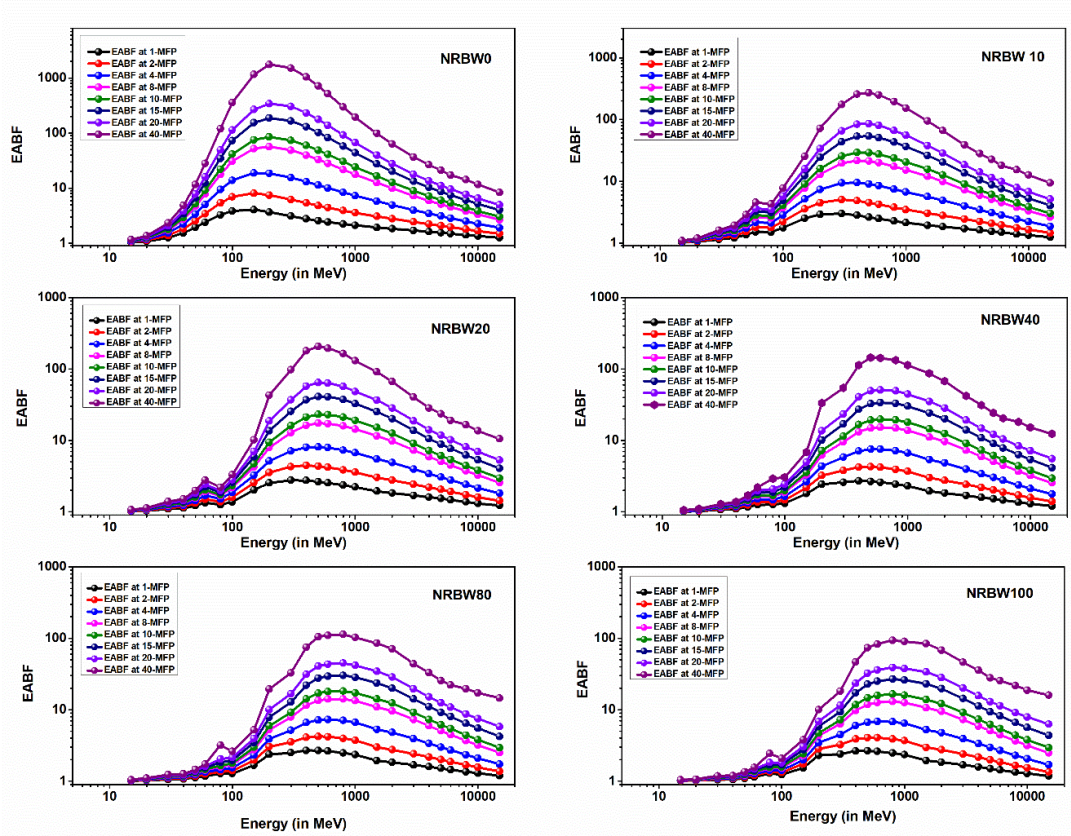

Figure 7.25. Variation of build-up factor EABF with incident photon energy for $BaWO_4$-blended natural rubber composites, corresponding to the MFP values of 1, 2, 4, 8,10,15, 20 and 40 (computational).

Also, Figure 7.26 (a-f) shows the variation of the build-up factor EBF values with incident photon energy for $BaWO_4$-blended natural rubber composites (a-NRBW0, b-NRBW10, c-NRBW20, d-NRBW40, e-NRBW80, f-NRBW100), corresponding to the MFP values of 1, 2, 4, 8,10,15, 20 and 40. Figure 7.26 shows that EBF-values at 40 mfp indicate a peak at 0.8 MeV for $BaWO_4$ (10 phr) (87.19), at 1 MeV $BaWO_4$ (20 phr) (62.19), 1.5 MeV for $BaWO_4$ (40 phr) (56.02) and at 2.0 MeV $BaWO_4$ (80 phr) (52.69). $BaWO_4$ (10 phr) has the highest EBF-EABF values in the medium energies in all penetration-depths.

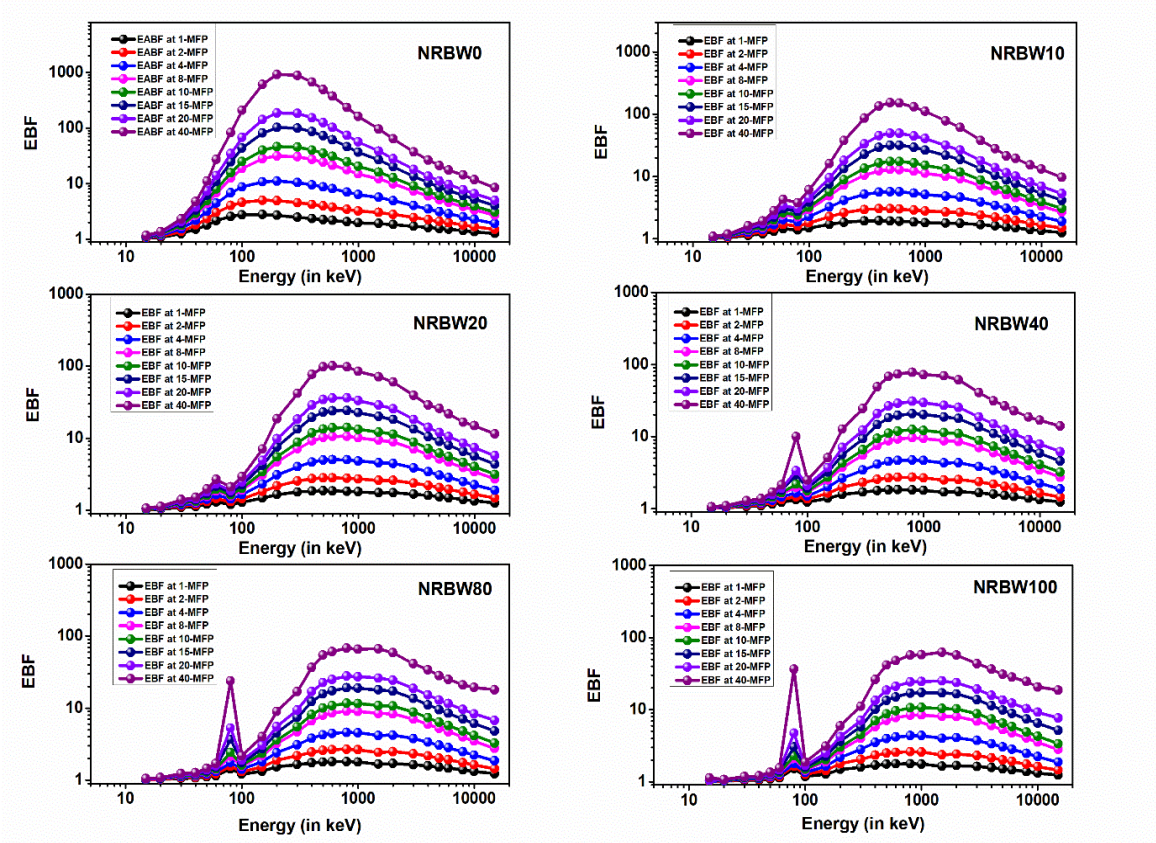

Figure 7.26. Variation of build-up factor EABF with incident photon energy for $BaWO_4$-blended natural rubber composites, corresponding to the MFP values of 1, 2, 4, 8,10,15, 20 and 40 (computational).

The EBF and EABF values have a modest start but show rapid increments with increasing photon energy. Different energy regions, including low, medium, and high levels, are conventionally employed to classify energy levels, with each region having its dominant interactions and effects. In the low-energy region, the photoelectric effect predominates, resulting in an inverse relationship with $E^{3.5}$. The selected composite samples efficiently absorb a large number of low-energy photons, preventing them from reaching outside the source. In the intermediate energy region, Compton scattering becomes the primary interaction process, leading to elevated EBF and EABF values for all the composites. The EBF values of all materials in the Compton scattering region demonstrate an increase in the Gaussian pattern. The significant EBF and EABF values do not solely originate from the mean free path (MFP) but are influenced by various scattering processes. In the high-energy region, the pair production process becomes predominant, causing a decline

in EBF and EABF values with increasing incident photon energy. Among the samples, $BaWO_4$-100 exhibits the highest Z_{eq} value and the lowest EBF and EABF values. Furthermore, Figures 7.25 and 7.26 demonstrate an inverse relationship between EBF, EABF, and Zeq, wherein lower Zeq values correspond to larger EBF and EABF values. This indicates that NRBW-100 is a more effective gamma-ray shielding composite than NRBW-10. For instance, NRBW-10, which has the lowest Zeq among the samples, exhibits the highest values of EABF and EBF at various energy levels.

The most significant EABF and EBF values are observed in the medium energy zone, corresponding to the Compton scattering region. Additionally, at 40 MFP, the build-up factors reached their highest levels. Figure 7.25 illustrates that the EABF values at 40 MFP exhibit a peak at 0.5 MeV for BaWO4 (10 phr) (178.12), at 0.8 MeV for $BaWO_4$ (20 phr) (90.16), at 1.5 MeV for $BaWO_4$ (40 phr) (75.31) and at 2.0 MeV for $BaWO_4$ (80 phr) (69.2).

Figure 7.26 shows that EBF-values at 40 mfp indicate a peak at 0.8 MeV for $BaWO_4$ (10 phr) (87.19), at 1 MeV for $BaWO_4$ (20 phr) (62.19), at 1.5 MeV for $BaWO_4$ (40 phr) (56.02) and at 2.0 MeV for $BaWO_4$ (80 phr) (52.69). $BaWO_4$ (10 phr) has the highest EBF-EABF values in the medium energies at all penetration-depths.

It was observed that there is an increase in the gaussian form in the EBF values of all materials in the Compton scattering region. This situation indicates that the build-up effects are much higher in the intermediate energy region. Additionally, in the transition to the energy region where the pair production event is predominant, the build-up factor tends to decrease again with increasing photon energy and become almost independent of the chemical composition of the materials in the high-energy region.

7.5 Effective Conductivity (C_{eff}) and Fast neutron removal cross-section (FNRCS)

Figure. 7.27 illustrates the alterations in the effective conductivity (C_{eff}) values of the materials analysed in this study across the energy range from 0.015 to 20 MeV.

When photons interact with a material, they induce excitation in the electrons, converting them into free electrons. The fluctuations in the number of these unbound electrons impact the material's electrical conductivity. Materials whose electrical conductivity is influenced by photon density and energy may display modified shielding characteristics. Therefore, understanding this parameter is crucial in assessing how a material behaves in different nuclear applications. The changes of C_{eff} values of the materials examined in this study depending on the photon energy are shown in Figures. 7.27.

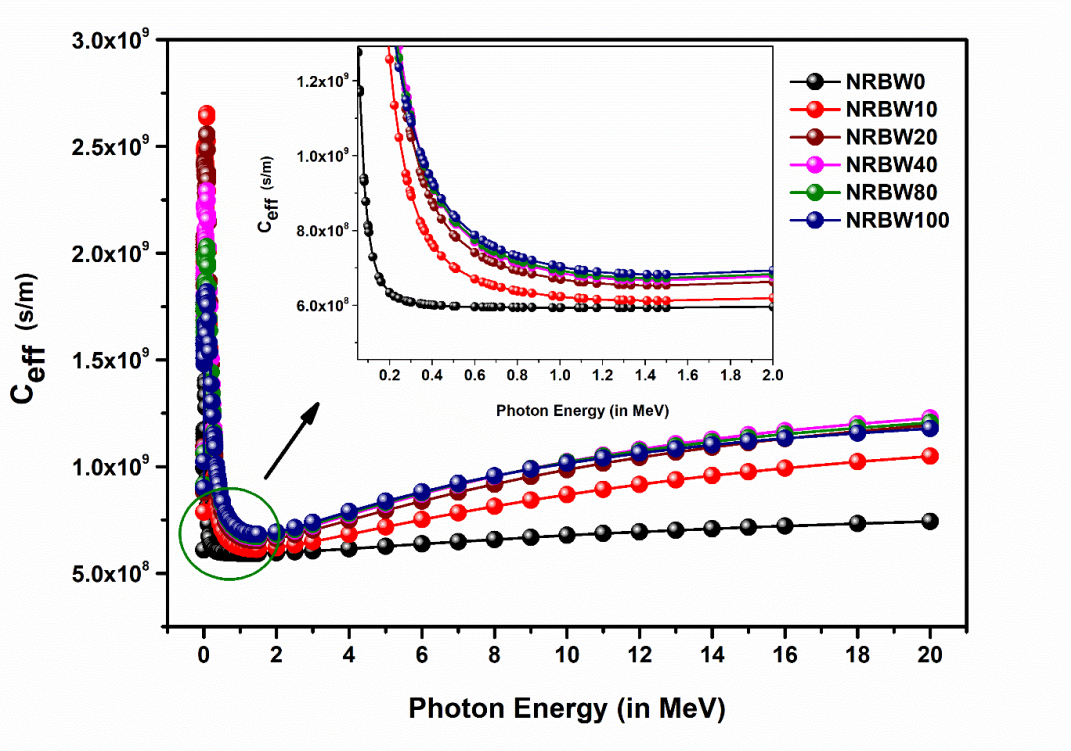

Figure 7.27. Conductivity C_{eff} as a function of photon energy and $BaWO_4$-content of the samples.

The photons coming on the material stimulate the electrons in the materials and convert them into free electrons. The increase or decrease in the number of these un-bonded electrons changes the electrical conductivity of the materials. The material whose electrical conductivity varies according to the photon density and energy can change the shielding characteristic. For this reason, it is very important to know this parameter, which shows how a material maintains its characteristics according to the place of use in nuclear applications. The changes of C_{eff} values of the materials

examined in this study depending on the photon energy are shown in Figures. 7.27.

Figure 7.27 shows in the very low energy range, C_{eff} decreases slightly as the energy values increase. Notably, NRBW-100 consistently exhibited the highest C_{eff} values at each measured photon energy. Despite the fact that C_{eff} and N_{eff} are directly related, C_{eff} values vary with energy differently than N_{eff} due to the varied densities of the examined substances. This finding was previously researched for different alloys [46]. The generation of free electrons is pronounced in the region dominated by photoelectric absorption. In this range, photons have lower energy and longer wavelengths, which increases the likelihood of interactions with electrons in the target material. Because of the increased likelihood, more photons are absorbed by electrons, resulting in more free electrons values. The conductivity of the examined materials are virtually independent of the photon energy in the Compton scattering region. Figure 7.28 clearly shows that Σ_R increases as the density of the composites rises. To evaluate the appropriateness of a material for radiation-shielding purposes, it is crucial to comprehend its capacity to capture high-speed and thermal neutrons.

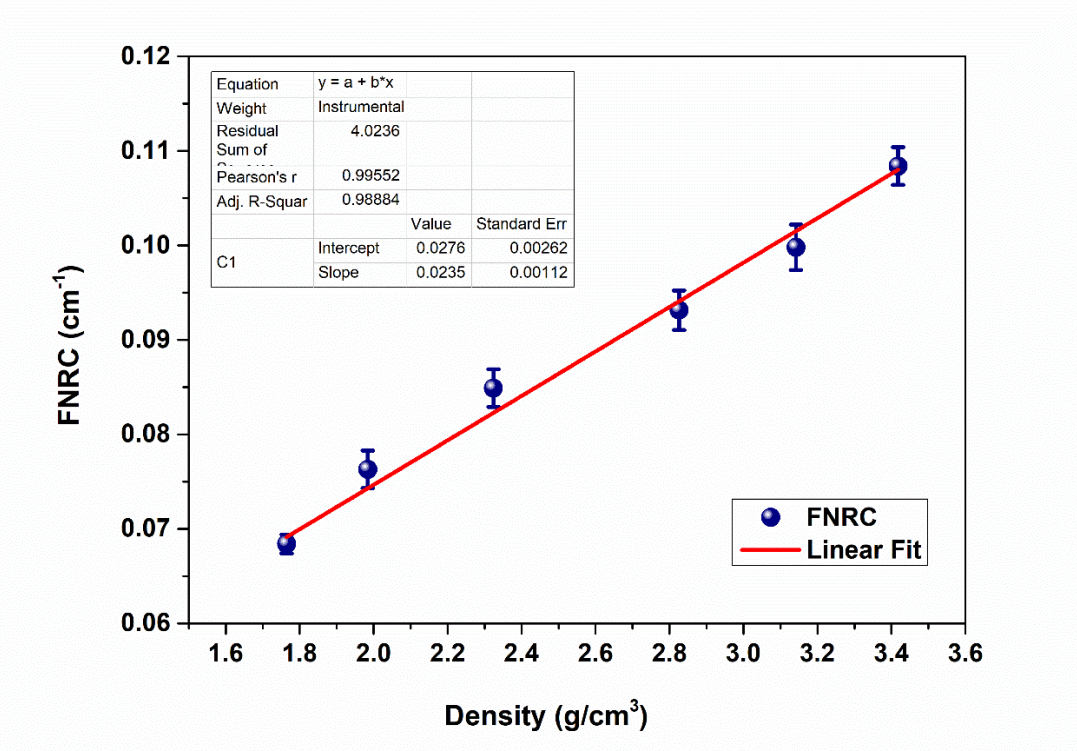

Figure 7.28: Fast neutron removal cross-sections of the investigated sample.

Hence, in the last stage of this study, the fast neutron removal cross-section (FNRCS) values of the examined materials were computed, and the outcomes are illustrated in Figure 7.28. Among the composites, NRBW-100 exhibited the highest ΣR (cm^{-1}) value, while NRBW-10 composite showed the lowest. The findings reveal that incorporating higher amounts of $BaWO_4$ in the natural rubber results in a significant improvement in the overall reduction of gamma-rays, in line with the observed increase in density. This suggests that the inclusion of $BaWO_4$ is an effective method that can be utilized in natural rubber, making it a suitable material for enhancing gamma-ray absorption in relevant situations.

7.6 Conclusion

The room-temperature vulcanization method was successfully employed to produce flexible composites comprising natural rubber (NR), and varying percentages of Tungsten oxide ($BaWO_4$). Increasing the concentration of $BaWO_4$ resulted in higher values for the mass attenuation coefficients (μ_m), effective atomic number (Z_{eff}), and effective electron densities (N_{eff}) of the NR composites. Conversely, these values decreased with the rise in photon energy. The experimental measurements showed good agreement with theoretical calculations from XCOM and simulation results using the Phy-X/PSD software. The main evaluated quantities are, linear attenuation coefficient, mass attenuation coefficient, half-value layer, mean-free path, effective atomic number, effective electron density, equivalent atomic number and build-up factor. The developed composites possess several advantageous characteristics, such as lightweight, ease of processing, non-toxicity, flexibility, and good dispersion properties. Because of these characteristics, they can effectively serve as gamma-ray shielding materials. The composite material is suitable for various applications, including both mobile and stationary radiation shielding purposes. Additionally, it can be used in scenarios where flexible radiation shielding, such as gloves, aprons, shoes, and coats is necessary to protect workers from radiation exposure.

7.7 Reference

[1] G. P. R. Dejangah M, Ghojavand M, Poursalehi R, *Mater. Des.*, vol. 11, no. 20, pp. 5035–5040, 2021, [Online].
Available: https://doi.org/10.1016/j.matdes.2020.109338.

[2] D. Toyen, A. Rittirong, W. Poltabtim, and K. Saenboonruang, "Flexible, lead-free, gamma-shielding materials based on natural rubber/metal oxide composites," *Iran. Polym. J. (English Ed.*, vol. 27, no. 1, pp. 33–41, 2018, doi: 10.1007/s13726-017-0584-3.

[3] C. V Vishnu, A. Joseph, T. A. Sajith, and S. Thomas, "Design of Flexible Gamma-ray Shielding Material Composite of Natural Rubber with Coconut Shell / Clay Powder," vol. 64, pp. 886–887, 2019.

[4] J. D. and K. S. Arkarapol Thumwong, "Comparative X-ray Shielding Properties of Single-Layered and Multi-Layered Bi_2O_3/NR Composites: Simulation and Numerical Studies," Polymers 2022, 14(9), 1788.
https://doi.org/10.3390/polym14091788

[5] S. Jaiyen, A. Phunpueok, and V. Thongpool, "Determination of radiation attenuation coefficients of BaSO4/PVC and BaSO4/PS for X-ray shielding," *J. Phys. Conf. Ser.*, vol. 1380, no. 1, 2019, doi: 10.1088/1742-6596/1380/1/012133.

[6] T. Özdemir, A. Güngör, and A. Reyhancan, "Flexible neutron shielding composite material of EPDM rubber with boron trioxide: Mechanical, thermal investigations and neutron shielding tests," *Radiat. Phys. Chem.*, vol. 131, pp. 7–12, 2017, doi: 10.1016/j.radphyschem.2016.10.012.

[7] H. Alavian, A. Samie, and H. Tavakoli-anbaran, "Experimental and Monte Carlo investigations of gamma-ray transmission and buildup factors for inorganic nanoparticle / epoxy composites," *Radiat. Phys. Chem.*, vol. 174, no. April, p. 108960, 2020, doi: 10.1016/j.radphyschem.2020.108960.

[8] T. Özdemir, A. Güngör, I. K. Akbay, H. Uzun, and Y. Babucçuoglu, "Nano lead oxide and epdm composite for development of polymer based radiation shielding material: Gamma irradiation and attenuation tests," *Radiat. Phys. Chem.*, vol. 144, no. August 2017, pp. 248–255, 2018, doi: 10.1016/j.radphyschem.2017.08.021.

[9] S. Intom *et al.*, "Mechanical and radiation shielding properties of flexible material based on natural rubber/ Bi_2O_3 composites," *Radiat. Phys. Chem.*, p. 108772, 2020, doi: 10.1016/j.radphyschem.2020.108772.

[10] N. Z. Noor Azman *et al.*, "Effect of Bi_2O_3 particle sizes and addition of starch into Bi_2O_3–PVA composites for X-ray shielding," *Appl. Phys. A Mater. Sci. Process.*, vol. 122, no. 9, pp. 1–9, 2016, doi: 10.1007/s00339-016-0329-8.

[11] K. Asaduzzaman *et al.*, "Assessment of natural radioactivity levels and potential radiological risks of common building materials used in bangladeshi dwellings," *PLoS ONE*, vol. 10, no. 10. 2015, doi: 10.1371/journal.pone.0140667.

[12] D. Toyen *et al.*, "Gamma-ray shielding characteristics of flexible silicone Tungsten composites," *Radiat. Phys. Chem.*, vol. 27, no. October 2019, p. 108901, 2020, doi:

10.1016/j.apradiso.2019.108901.

[13] M. R. Ambika *et al.*, "Preparation and characterisation of Isophthalic-Bi_2O_3 polymer composite gamma radiation shields," *Radiat. Phys. Chem.*, vol. 130, no. March 2016, pp. 351–358, 2017, doi: 10.1016/j.radphyschem.2016.09.022.

[14] L. Chang *et al.*, "Preparation and characterization of Tungsten/epoxy composites for γ-rays radiation shielding," *Nucl. Instruments Methods Phys. Res. Sect. B Beam Interact. with Mater. Atoms*, vol. 356–357, pp. 88–93, 2015, doi: 10.1016/j.nimb.2015.04.062.

[15] S. J. Perera, S. M. Egodage, and S. Walpalage, "Enhancement of mechanical properties of natural rubber-clay nanocomposites through incorporation of silanated organoclay into natural rubber latex," *E-Polymers*, vol. 20, no. 1, pp. 144–153, 2020, doi: 10.1515/epoly-2020-0017.

[16] W. Chaiphaksa *et al.*, "Photon, charged particles, and neutron shielding properties of natural rubber/ SnO_2 composites," *Radiat. Phys. Chem.*, vol. 203, p. 110622, Feb. 2023, doi: 10.1016/j.radphyschem.2022.110622.

[17] E. Kalkornsurapranee *et al.*, "Wearable and flexible radiation shielding natural rubber composites: Effect of different radiation shielding fillers," *Radiat. Phys. Chem.*, vol. 179, p. 109261, Feb. 2021,
doi: 10.1016/j.radphyschem.2020.109261.

[18] N. Plangpleng *et al.*, "Flexible gamma-ray shielding based on natural Rubber/$BaSO_4$ nanocomposites," *Radiat. Phys. Chem.*, vol. 199, Oct. 2022.
doi: 10.1016/j.radphyschem.2022.110311.

[19] C. V. More, Z. Alsayed, M. S. Badawi, A. A. Thabet, and P. P. Pawar, *Polymeric composite materials for radiation shielding: a review*, vol. 19, no. 3. Springer International Publishing, 2021.

[20] S. Yonphan *et al.*, "Development of flexible radiation shielding materials from natural Rubber/Sb_2O_3 composites," *Radiat. Phys. Chem.*, vol. 200, no. July, p. 110379, 2022, doi: 10.1016/j.radphyschem.2022.110379.

[21] A. Fisli *et al.*, "Some Metal Oxide-Natural Rubber Composites for Gamma and Low-Energy X-Ray Radiation Shielding," *Atom Indones.*, vol. 49, no. 1, 2023, doi: 10.55981/aij.2023.1213.

[22] R. R. Bhosale, C. V. More, D. K. Gaikwad, P. P. Pawar, and M. N. Rode, "Radiation shielding and gamma-ray attenuation properties of some polymers," *Nucl. Technol. Radiat. Prot.*, vol. 32, no. 3, pp. 288–293, 2017, doi: 10.2298/NTRP1703288B.

[23] P. Limarun, T. Markpin, N. Sombatsompop, E. Wimolmala, and K. Saenboonruang, "Cellular Bi_2O_3/natural rubber composites for light-weight and lead-free gamma-shielding materials and their properties under gamma irradiation," *J. Cell. Plast.*, vol. 58, no. 2, pp. 285–303, 2022, doi: 10.1177/0021955X21997353.

[24] E. Şakar, Ö. F. Özpolat, B. Alım, M. I. Sayyed, and M. Kurudirek, "Phy-X / PSD: Development of a user friendly online software for calculation of parameters relevant to radiation shielding and dosimetry," *Radiat. Phys. Chem.*, vol. 166, no. September 2019, 2020, doi: 10.1016/j.radphyschem.2019.108496.

[25] M. I. Sayyed *et al.*, "Radiation shielding characteristics of selected ceramics using the EPICS2017 library," *Ceram. Int.*, vol. 47, no. 9, pp. 13181–13186, 2021. doi: 10.1016/j.ceramint.2021.01.183.

[26] S. Stalin *et al.*, "Influence of Bi_2O_3/WO_3 substitution on the optical, mechanical, chemical durability and gamma-ray shielding properties of lithium-borate glasses," *Ceram. Int.*, vol. 47, no. 4, pp. 5286–5299, 2021. doi: 10.1016/j.ceramint.2020.10.109.

[27] B. Ahmed, G. B. Shah, A. H. Malik, Aurangzeb, and M. Rizwan, "Gamma-ray shielding characteristics of flexible silicone Tungsten composites," *Appl. Radiat. Isot.*, vol. 155, no. October 2019, p. 108901, 2020. doi: 10.1016/j.apradiso.2019.108901.

[28] M. Kurudirek, M. Aygun, and S. Z. Erzeneoğlu, "Chemical composition, effective atomic number and electron density study of trommel sieve waste (TSW), Portland cement, lime, pointing and their admixtures with TSW in different proportions," *Appl. Radiat. Isot.*, vol. 68, no. 6, pp. 1006–1011, 2010. doi: 10.1016/j.apradiso.2009.12.039.

[29] S. M. Kassem *et al.*, "Novel flexible and lead-free gamma radiation shielding nanocomposites based on LDPE/SBR blend and $BaWO_4/B_2O_3$ heterostructures," *Radiat. Phys. Chem.*, vol. 209, p. 110953, Aug. 2023. doi: 10.1016/J.RADPHYSCHEM.2023.110953.

[30] Y. Al-Hadeethi and M. I. Sayyed, "Radiation attenuation properties of Bi_2O_3–Na_2O–V_2O_5– TiO_2–TeO_2 glass system using Phy-X / PSD software," *Ceram. Int.*, vol. 46, no. 4, pp. 4795–4800, 2020, doi: 10.1016/j.ceramint.2019.10.212.

[31] P. Lim-Aroon, E. Wimolmala, N. Sombatsompop, and K. Saenboonruang, "Manufacturing process and properties of lead-free natural rubber sponge for use in X-ray and gamma-ray shielding applications," *IOP Conf. Ser. Mater. Sci. Eng.*, vol. 526, no. 1, 2019, doi: 10.1088/1757-899X/526/1/012015.

[32] R. Barman, M. S. Hossain, A. Das, and M. K. Ahmmad Rabby, "Investigation of radiation shielding characteristic features of different wood species," *Radiat. Phys. Chem.*, vol. 192, no. May 2021, 2022, doi: 10.1016/j.radphyschem.2021.109927.

[33] V. S. Zali, O. Jahanbakhsh, and I. Ahadzadeh, "Preparation and evaluation of gamma shielding properties of silicon-based composites doped with WO_3 micro- and nanoparticles," *Radiat. Phys. Chem.*, vol. 197, no. April, 2022. doi: 10.1016/j.radphyschem.2022.110150.

[34] M. Elsafi, H. jamal ALasali, A. H. Almuqrin, K. G. Mahmoud, and M. I. Sayyed, "Experimental assessment for the photon shielding features of silicone rubber reinforced by tellurium borate oxides," *Nucl. Eng. Technol.*, vol. 55, no. 6, pp. 2166–2171, 2023, doi: 10.1016/j.net.2023.02.022.

[35] A. M. El-Khatib *et al.*, "Conductive natural and waste rubbers composites-loaded with lead powder as environmental flexible gamma radiation shielding material," *Mater. Res. Express*, vol. 7, no. 10, 2020, doi: 10.1088/2053-1591/abbf9f.

[36] A. Khalaf, M. Hana, I. Hasan, and F. M. Al-jomaily, "Gamma-ray absorption using rubber — lead mixtures as radiation protection shields," pp. 653–659, 2012, doi:

10.1007/s10967-011-1556-2.

[37] W. Poltabtim, E. Wimolmala, and K. Saenboonruang, "Properties of lead-free gamma-ray shielding materials from metal oxide/EPDM rubber composites," *Radiat. Phys. Chem.*, vol. 153, no. August, pp. 1–9, 2018. doi: 10.1016/j.radphyschem.2018.08.036.

[38] M. I. Sayyed, H. Al-Ghamdi, A. H. Almuqrin, S. Yasmin, and M. Elsafi, "A Study on the Gamma Radiation Protection Effectiveness of Nano/Micro-MgO-Reinforced Novel Silicon Rubber for Medical Applications," *Polymers (Basel).*, vol. 14, no. 14, 2022, doi: 10.3390/polym14142867.

[39] O. Aziz, E. Salama, D. E. El-Nashar, and A. Bakry, "Development of Sustainable Radiation-Shielding Blend Using Natural Rubber/NBR, and Bismuth Filler," *Sustainability*, vol. 15, no. 12, p. 9679, 2023, doi: 10.3390/su15129679.

[40] E. E. Saleh *et al.*, "Synthesis and Nuclear Radiation Shielding Ability of Li_2O-ZnO-P_2O_5 Glasses: The Role of Yb_2O_3," *J. Electron. Mater.*, vol. 51, no. 12, pp. 7283–7296, 2022, doi: 10.1007/s11664-022-09979-9.

[41] C. V. Vishnu, A. Joseph, and K. Anju, "Evaluation of the gamma radiation shielding characteristics of epoxy wall paint modified with micro sized Bi_2O_3 and WO_3," *Mater. Today Proc.*, no. xxxx, 2023, doi: 10.1016/j.matpr.2023.03.309.

[42] J. H. Liu *et al.*, "Elevated gamma-rays shielding property in lead-free Bismuth tungstate by nanofabricating structures," *J. Phys. Chem. Solids*, vol. 112, no. July 2017, pp. 185–189, 2018, doi: 10.1016/j.jpcs.2017.09.007.

[43] A. Barabash, D. Barabash, V. Pertsev, and D. Panfilov, "Polymer-Composite Materials for Radiation Protection," *Adv. Intell. Syst. Comput.*, vol. 983, pp. 352–360, 2019, doi: 10.1007/978-3-030-19868-8_36.

[44] O. Kilicoglu *et al.*, "Micro Pb filled polymer composites: Theoretical, experimental and simulation results for γ-ray shielding performance," *Radiat. Phys. Chem.*, vol. 194, no. February, 2022, doi: 10.1016/j.radphyschem.2022.110039.

[45] A. Ardiansyah *et al.*, "Physical , mechanical , optical , and gamma radiation shielding properties of the BaO-based glass system prepared by the melt-quench technique : A review," vol. 210, no. February, 2023.

[46] Ş. Erdem, "Determination of photon-shielding features and build-up factors of nickel – silver alloys," vol. 172, no. February, 2020. doi: 10.1016/j.radphyschem.2020.108778.

[47] M. F. Turhan, "Photon interaction performance of various contrast agents : Theoretical and simulation results," *Appl. Radiat. Isot.*, vol. 177, no. June, p. 109920, 2021, doi: 10.1016/j.apradiso.2021.109920.

[48] O. Kilicoglu, C. V. More, U. Kara, and M. Davraz, "Investigation of the effect of cement type on nuclear shield performance of heavy concrete," *Radiat. Phys. Chem.*, vol. 209, no. November 2022, p. 110954, 2023. doi: 10.1016/j.radphyschem.2023.110954.

CHAPTER 8

RESULTS AND DISCUSSION

Evaluation of the gamma radiation shielding characteristics of Epoxy wall paint modified with micro sized Bi_2O_3 and WO_3.

Contents	
8.1	***Introduction***
8.2	***Fabrication of the samples and determination of their intrinsic charachertiscs***
8.3	***Gamma-ray attenuation in samples.***
8.4	***Conclusion***
8.5	***Reference***

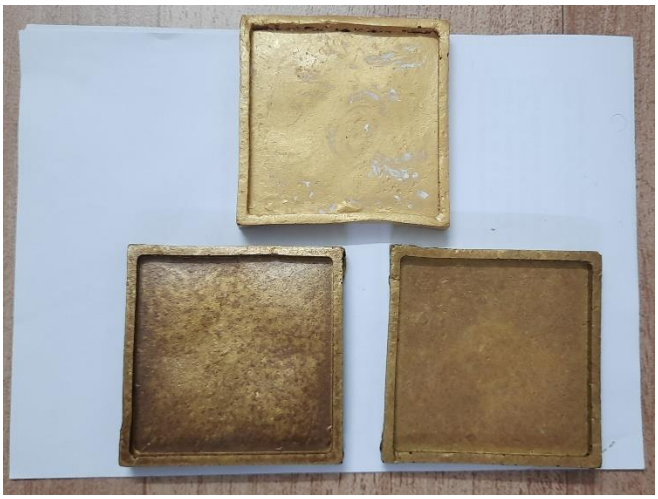

Epoxy wall paint

modified with micro sized Bi_2O_3 and WO_3.

Abstract: *This study examines the effects of micro Bi_2O_3 and WO_3 on the gamma-ray shielding properties of epoxy wall paints, both theoretically and empirically. The mass attenuation coefficients were compared with predictions from the WinXCOM and Phy-X/PSD programs, showing excellent agreement. Results indicate that Bi_2O_3 (20%) wall paint composites effectively reduce photons, suggesting a novel gamma shielding absorber with reduced lead content.*

8.1 Introduction

Gamma radiation shielding makes use of the absorption and attenuation principles. In general, the shielding materials must meet fundamental characteristics such as high density and atomic number, ease of heat dissipation, availability in needed thickness, shielding permanence, multi-use possibilities, and obtainability [1]. Lead-based shielding is widely used because it provides high atomic number, high density and provides shielding with the highest absorption and attenuation [2], [3]. On the other hand, lead shielding is heavy and in general rigid material, making it inconvenient. Sometimes furthermore, due to its toxicity, it can cause both health and environmental problems [4]. As a result of these, efforts are being made to develop shielding materials (devoid of lead) that could eventually be used to swap lead in radiation shielding. [3]–[5]. Many studies on non-lead composites for shielding with reinforcement particles of high atomic numbers such as silicon oxide (SiO_2), iron oxide (Fe_3O_4), Tungsten oxide (WO_3), and Bismuth oxide (Bi_2O_3) have been published[6]–[11].

In this study, we devised a gamma shielding material out of epoxy wall paint (WP) mixed with Bismuth and Tungsten oxides. Wall paints have been found to retain properties such as thermal and chemical stability, a high melting point, resistance to abrasion and scratch resistance, durability, flexibility, ease of cleaning, economy, light weight and non-toxicity[12]. These characteristics make wall paint suitable for use as a shielding material. Photons from gamma and X-ray radiation will scatter before being absorbed by the photoelectric effect. As a result, improved attenuation performance is supposed to be achieved with the effective chemical composition and suitable weight fraction, and also heavy density compound radiation shielding material [13].

Bismuth (Bi, Z = 83) is a transition metal with one of the least thermally conductive nuclei known. Bi_2O_3 is the most important commercial chemical derived from Bismuth[3]. Tungsten (W, Z = 74) is a rare metal found almost entirely in nature as compounds with other elements. Because of its environmental friendliness, ease of fabrication, and low cost, WO_3 has sparked widespread concern.

Furthermore, the mechanical properties of WO_3 are enhanced due to its unique structure, such as its high valence and field strength of W^{+6} [10], [14]. Much recent research has focused on the utilisation of micro and nanosized Bi_2O_3 and WO_3 granules as radiation shielding materials that are environmentally amicable in the fields of glasses, cementitious materials, alloys, and polymers [3], [10], [15]–[17].

The goal of this study is to properly examine the effects of micro Bi_2O_3 and WO_3 on the gamma-ray shielding properties of newly designed epoxy wall paint samples were studied both theoretically and empirically.

8.2 Fabrication of the samples and determination of their intrinsic characteristics.

To develop the composites used in this study, commercial wall paint made of epoxy resin, was used as the polymer matrix and Bi_2O_3 and WO_3 (99% purity, less than 50 μm size and density 8.9 and 7.16 gm/cm^3, respectively) microparticles were used as radiation shield filler materials. Here, the commercial epoxy wall paint and then the particles granules were weighed, carefully before mechanically mixed at the desired weight percentage (0%, 5%, 10%, 15%, and 20%). Subsequently the mixture was moulded in the form of a rectangular shape with a dimension of 8×8× 2.5 cm. This process leads to the polymerization reaction. After that the samples were were annealed at 60^0C in the oven for 24 hours. Later the relative percentage of basic components in the composite's samples determined by FESEM-EDAX analysis.

In this study, our purpose was to investigate the two epoxy samples to investigate radiation shielding abilities as a function of chemical composition and oxide configuration to identify the sample with the most effective radiation shielding properties. Table 8.1 shows the results of summarising the chemical compositions and densities of each sample. Density of each sample was determined by corresponding mass and volume values. Subsequently the mole percentage compositoion of different elements in the sample swere determined by EDAX analysis. As shown in Figure 8.2, samples of wall paint containing varying amounts of Bismuth and Tungsten oxide were prepared and scanned with a scanning electron microscope (FESEM) to measure particle uniformity and dispersion in the matrix.

Prior to the addition of Bi_2O_3 and WO_3, normal paint samples exhibit a crumbly morphology. Following integration, these particles are spread on the paint-corresponding surface of these flakes.

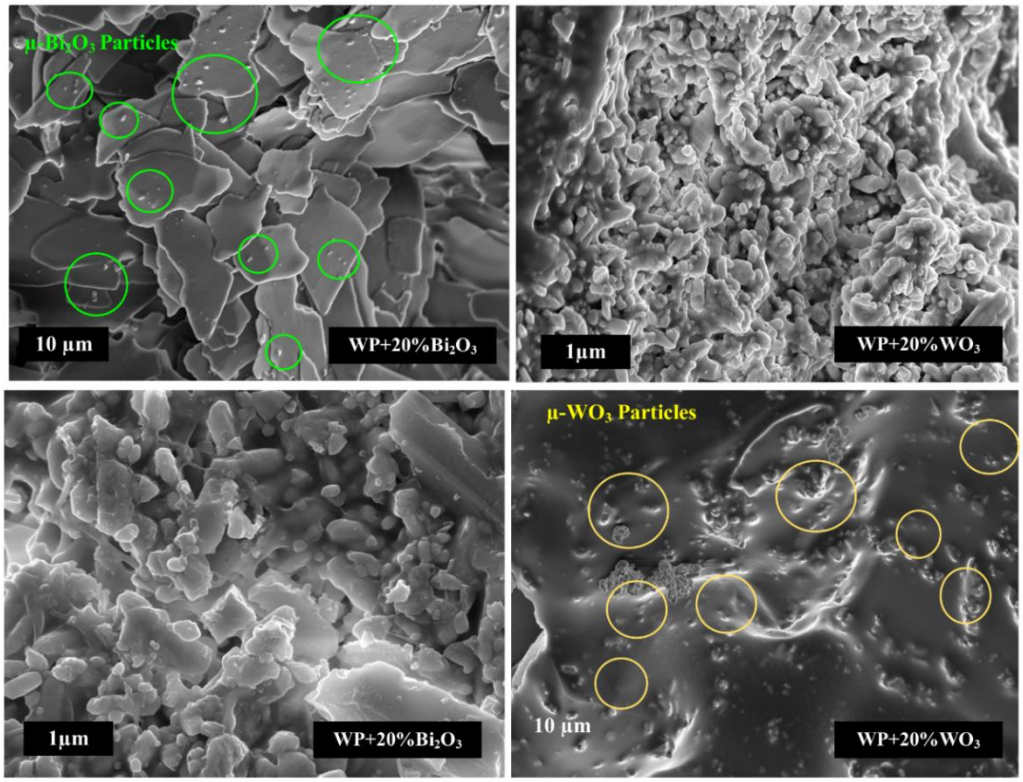

Figure. 8.1: FESEM images of composite with of Bismuth and Tungsten oxides.

Table 8.1 The fabricated samples' nominal compositions and codes.

Sample	Density, ρ (g/cm^3)	Composition (mol%)					
		SiO_2	TiO_2	CaO	ZnO	Bi_2O_3	WO_3
WP (Pure)	1.673	20.94	6.75	48.81	24.43	-	-
WPB1 (WP+5% Bi_2O_3)	2.161	19.95	5.84	47.71	21.84	5.01	-
WPB2 (WP+10% Bi_2O_3)	2.321	19.63	5.37	44.52	21.37	10.02	
WPB3 (WP+15% Bi_2O_3)	2.621	19.01	5.02	42.31	20.32	15.02	
WPB4 (WP+20% Bi_2O_3)	2.934	18.92	4.82	40.83	19.35	20.01	-
WPW1 (WP+5% WO_3)	2.378	20.02	6.35	45.71	22.76	-	5.01
WPW2 (WP+10% WO_3)	2.684	19.47	5.66	42.81	22.66		10.02
WPW3 (WP+15% WO_3)	2.821	19.09	4.07	40.35	21.68		15.02
WPW4 (WP+20% WO_3)	3.097	18.68	3.98	39.35	20.58	-	20.01

8.3. Gamma-ray attenuation in samples.

It is necessary to determine a shielding material's shielding and attenuation aspects in order for it to successfully protect ionising radiations [18]. The radiation shielding characteristics of the prepared samples, such as linear and mass attenuation coefficients, atomic-electronic cross-sections, mean free path, half-value layer, and effective atomic number, of the samples were determined, and validated using theoretical calculations. From the calculated linear attenuation coefficients, other shielding parameters were evaluated experimentally at the gamma-ray photon energies of 0.511 MeV (^{22}Na), 0.662 MeV (^{137}Cs), 1.173 MeV and 1.333 MeV (^{60}Co). For measuring the intensity of radiation, a NaI(Tl) detector (3"×3″) with an energy resolution of 13% at 662 keV was linked to a multichannel analyser (MCA). The geometry of a narrow beam setup was used to test the linear attenuation coefficient, μ (as shown in Figure 8.1). Using specific data collection software, the pulse-height spectrum of NaI (Tl) scintillator was collected and computed the area beneath the photopeaks. for each sample and each energy, the detector was exposed for four hours. This was repeated for five times. The statistical error was estimated to be 5%.

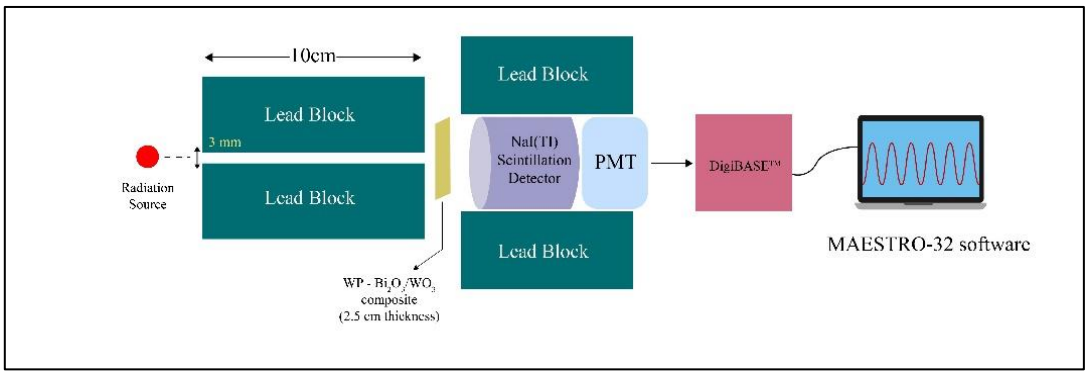

Figure 8.2. Schematic design of radiation shielding experimental setup.

8.3.1. Theoretical prediction of gamma-ray attenuation in samples.

When developing new shielding materials, all photon attenuation parameters must be determined in the continuous energy range or at specific energies [19]. To calculate the shielding parameters in this investigation, we used the online photon shielding and dosimetry Shielding and Dosimetry (Phy-X/PSD) software. This software can calculate eighteen photon attenuation parameters at any energy value [19]–[21]. In this work, Phy-X/PSD data library was utilized to theoeretical prediction of the radiation shielding characteristics of selected systems [8], [20]. The LACs were calculated experimentally and by extracting and interpolating photo atomic data at various discrete photon energy by using the Phy-X/PSD values. Then were compared. The user merely needs to enter the material's chemical composition, density, and energy values, and the software will calculate the photon attenuation parameters [1], [20].

8.3.2 Gamma-ray shielding properties.

Using the attenuation setup described in this section, the property of pure wall paint (WP) and WP with various concentrations of micro Bi_2O_3 and WO_3 to attenuate radiation was achieved experimentally. Following the setup of the -ray spectrometer, the gamma-ray spectra for background radiations was collected for 14400 seconds (four hours). The distance between the γ-ray source and detector was maintained constant at 15 cm during recording gamma-ray spectra. Gamma-ray sources were collimated using a 0.8 cm diameter lead collimator. First, the ^{137}Cs -ray spectra were obtained without any composite. Figure 8.3 depicts this spectrum. Gamma-ray spectra were acquired in the same manner for different energy sources.

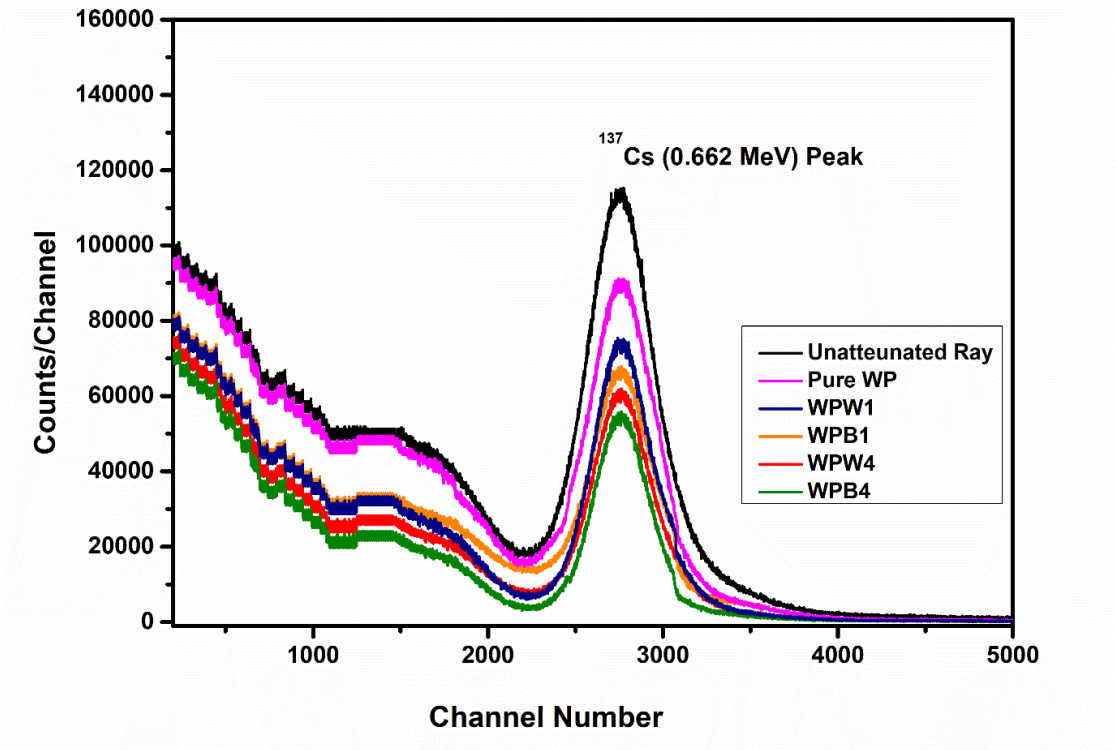

Figure 8.3: Energy spectra of gamma rays obtained from ^{137}Cs source, which attenuated by composites in different concentrations.

8.3.3 Linear attenuation coefficient.

The linear attenuation coefficient is a critical property studied for gamma-ray absorption. It defines how well a material can absorb gamma rays by indicating the material's ability to reduce the intensity of incident photons as they pass through it [26]. The estimated linear attenuation coefficient (LAC) was validated by comparing the measurement results to those acquired by Phy-X/PSD, as shown in Table 8.2.

The linear attenuation coefficient μ was derived from the slope of the linear relationship between ln (I/Io) and sample thickness x. It represents the product of the number of atoms per cubic centimeter of the shielding material and the probability of photons being scattered or absorbed by the nucleus or electrons within an atom of the shielding material. A higher μ value indicates better shielding performance of the materials.

Table 8.2: Theoretically (Phy-X/PSD) computed LAC (cm^{-1}) of the samples with the experimental values recorded at various γ-ray photon energies.

Energy (0.511 MeV)			Energy (0.662 MeV)		
Sample	**Expt**	**Theo.**	**Sample**	**Expt**	**Theo.**
Pure WP	0.1425	0.1412	Pure WP	0.1258	0.1275
WPB1	0.1928	0.1869	WPB1	0.1755	0.1597
WPB2	0.2163	0.2177	WPB2	0.1931	0.1913
WPB3	0.2548	0.2603	WPB3	0.2228	0.2257
WPB4	0.2908	0.2887	WPB4	0.2535	0.2558
WPW1	0.2143	0.2055	WPW1	0.1888	0.2059
WPW2	0.2453	0.2391	WPW2	0.2185	0.2142
WPW3	0.2604	0.2590	WPW3	0.2344	0.2316
WPW4	0.2893	0.2852	WPW4	0.2608	0.2620
Energy (1.173 MeV)			**Energy (1.333 MeV)**		
Sample	**Expt**	**Theo.**	**Sample**	**Expt**	**Theo.**
Pure WP	0.0934	0.0939	Pure WP	0.0900	0.0877
WPB1	0.1223	0.1223	WPB1	0.1154	0.1147
WPB2	0.1325	0.1333	WPB2	0.1253	0.1256
WPB3	0.1523	0.1552	WPB3	0.1436	0.1447
WPB4	0.1743	0.1796	WPB4	0.1617	0.1646
WPW1	0.1334	0.1384	WPW1	0.1253	0.1322
WPW2	0.1508	0.1508	WPW2	0.1423	0.1425
WPW3	0.1588	0.1602	WPW3	0.1504	0.1526
WPW4	0.1747	0.1762	WPW4	0.1685	0.1666

However, the linear attenuation coefficient describes in more detail the fraction of attenuated monoenergetic incoming photon with all the possible interactions including photoelectric effect, and Compton scattering, whether it was completely absorbed by the electrons on the atom's orbit, or half absorbed with the remainder being distributed. Figures 8.4 and 8.5 depict the change in the experimental LAC of the composite of Bi_2O_3 and WO_3 content as a function of gamma-ray photon energy.

Compared with the Bi_2O_3 incorparated samples WO_3 incorparated samples have little more attenuation capability. Figures 8.6 and 8.7 depict the change in the linear attenuation coefficient of the composite of Bi_2O_3 and WO_3 content as a function of various gamma-ray photon energy.

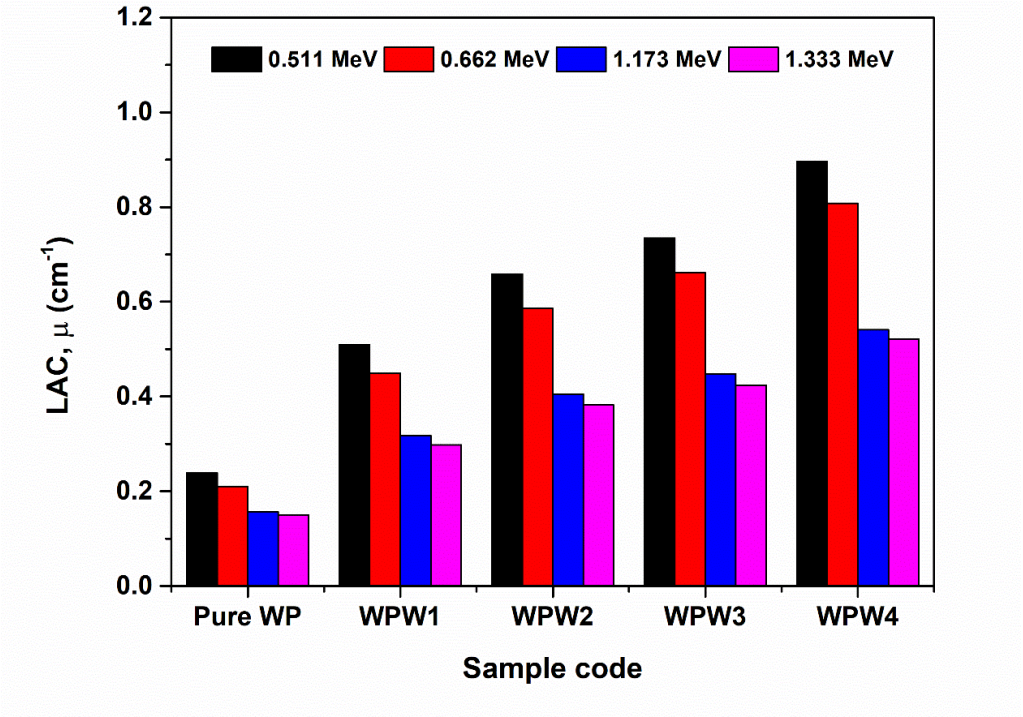

Figure 8.4: The Experimental values of LAC as a function of photon energy for wall paint reinforced with micro WO_3.

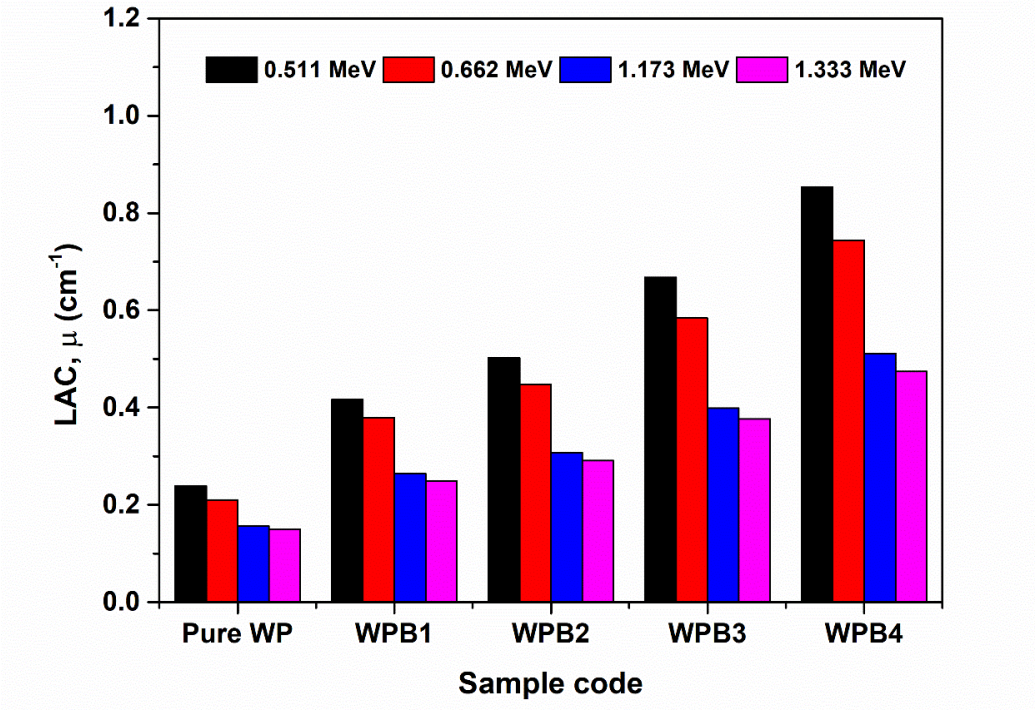

Figure 8.5: The Experimental values of LAC as a function of photon energy for wall paint reinforced with micro Bi_2O_3.

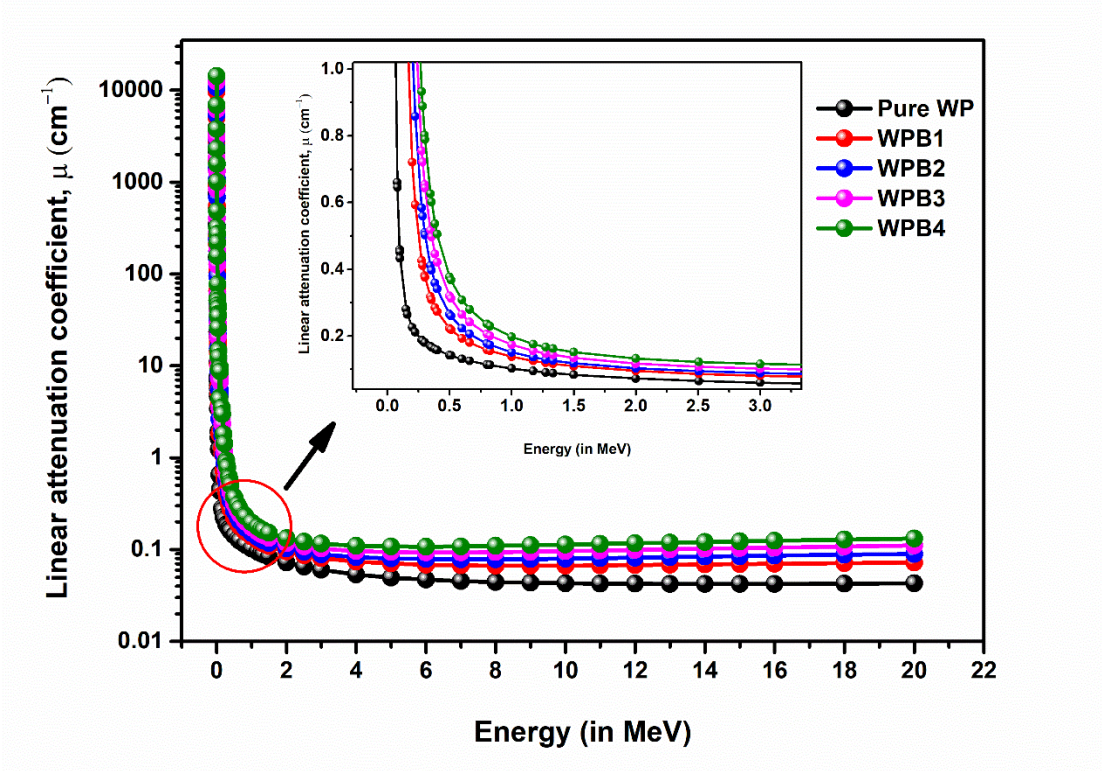

Figure 8.6: The LAC as a function of photon energy for wall paint reinforced with micro Bi_2O_3.

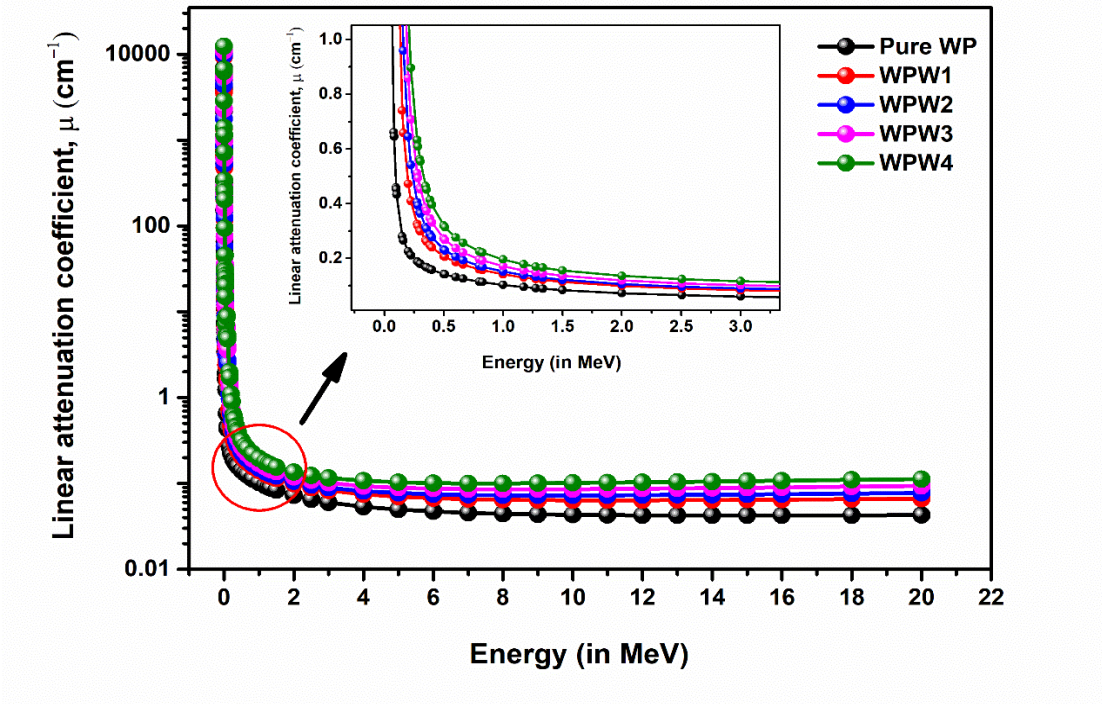

Figure 8.7: The LAC as a function of photon energy for wall paint reinforced with micro WO_3.

8.3.4 Mass attenuation coefficient.

The estimated mass attenuation coefficient (MAC) was validated by comparing the measurement results to those acquired by Phy-X/PSD, as shown in Table 8.3 and Figures 8.8 and 8.9.

Table 8.3: Examination of the theoretically (Phy-X/PSD) computed MAC of the samples with the experimental values recorded at various γ-ray photon energies.

Mass Attenuation Coefficient (MAC) μ/ρ (cm^2/g)					
Energy (0.511 MeV)			**Energy (0.662 MeV)**		
Sample	**Expt**	**Theo.**	**Sample**	**Expt**	**Theo.**
Pure WP	0.0852	0.0844	Pure WP	0.0752	0.762
WPB1	0.0892	0.0865	WPB1	0.0812	0.0739
WPB2	0.0932	0.0938	WPB2	0.0832	0.0824
WPB3	0.0972	0.0993	WPB3	0.0850	0.0861
WPB4	0.0991	0.0984	WPB4	0.0864	0.0872
WPW1	0.0901	0.0864	WPW1	0.0794	0.0866
WPW2	0.0914	0.0891	WPW2	0.0814	0.0798
WPW3	0.0920	0.0918	WPW3	0.0831	0.0821
WPW4	0.0934	0.0921	WPW4	0.0842	0.0846
Energy (1.173 MeV)			**Energy (1.333 MeV)**		
Sample	**Expt**	**Theo.**	**Sample**	**Expt**	**Theo.**
Pure WP	0.0558	0.0561	Pure WP	0.0538	0.0524
WPB1	0.0566	0.0566	WPB1	0.0534	0.0531
WPB2	0.0571	0.0574	WPB2	0.0540	0.0541
WPB3	0.0581	0.0592	WPB3	0.0548	0.0552
WPB4	0.0594	0.0612	WPB4	0.0551	0.0561
WPW1	0.0561	0.0582	WPW1	0.0527	0.0556
WPW2	0.0562	0.0562	WPW2	0.0530	0.0531
WPW3	0.0563	0.0568	WPW3	0.0533	0.0541
WPW4	0.0564	0.0569	WPW4	0.0544	0.0538

Depending on photon intensities, theoretical and experimental data were found to be very consistent. Figures 8.6 and 8.7 depict the change in the experimental values of the mass attenuation coefficient of the composite of Bi_2O_3 and WO_3 content as a function of various gamma-ray photon energy. The mass attenuation coefficient of the samples grew gradually with increasing metal oxide concentrations at decreasing

photon energy. However, when photon energy increases, the samples' mass attenuation coefficient becomes basically saturated and irrespective of filler percentage variation. As per the fundamental premise, photon contact with matter causes the photoelectric effect and Compton scattering, both influence the ability of materials to attenuate gamma rays [2]. Especially, the rate of μ/ρ change has a clear and good association with the specified surface area Bi_2O_3 and WO_3 particles with less energy (0.1 MeV).

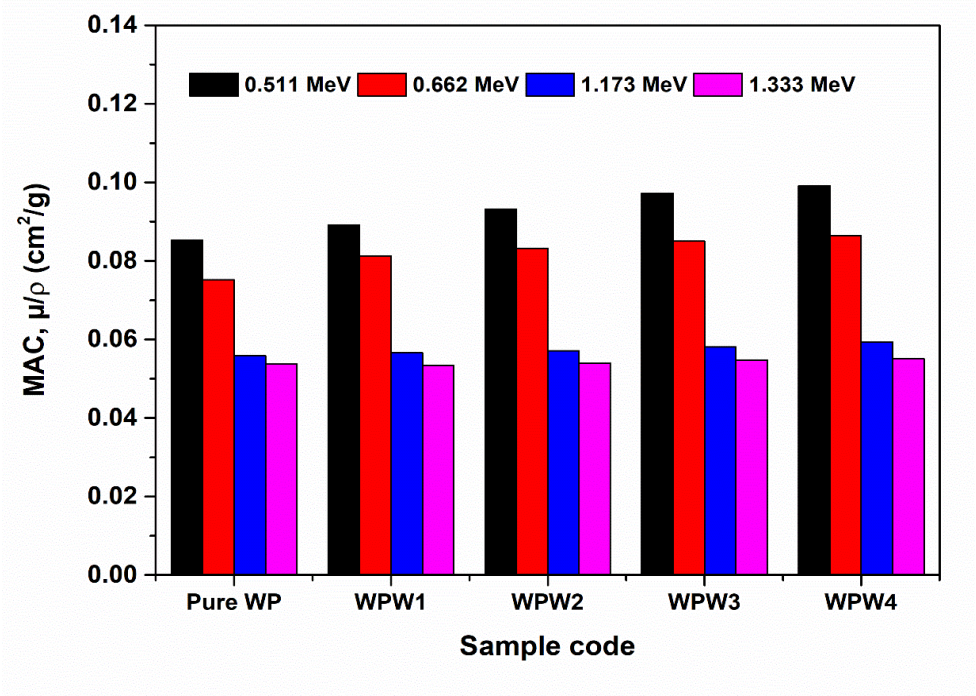

Figure 8.8: The Experimental values of MAC as a function of photon energy for wall paint reinforced with micro WO_3.

Figures 8.10 and 8.11 depict the change in the mass attenuation coefficient of the composite of Bi_2O_3 and WO_3 content as a function of various gamma-ray photon energy for the range of 0.01MeV to 20 MeV.

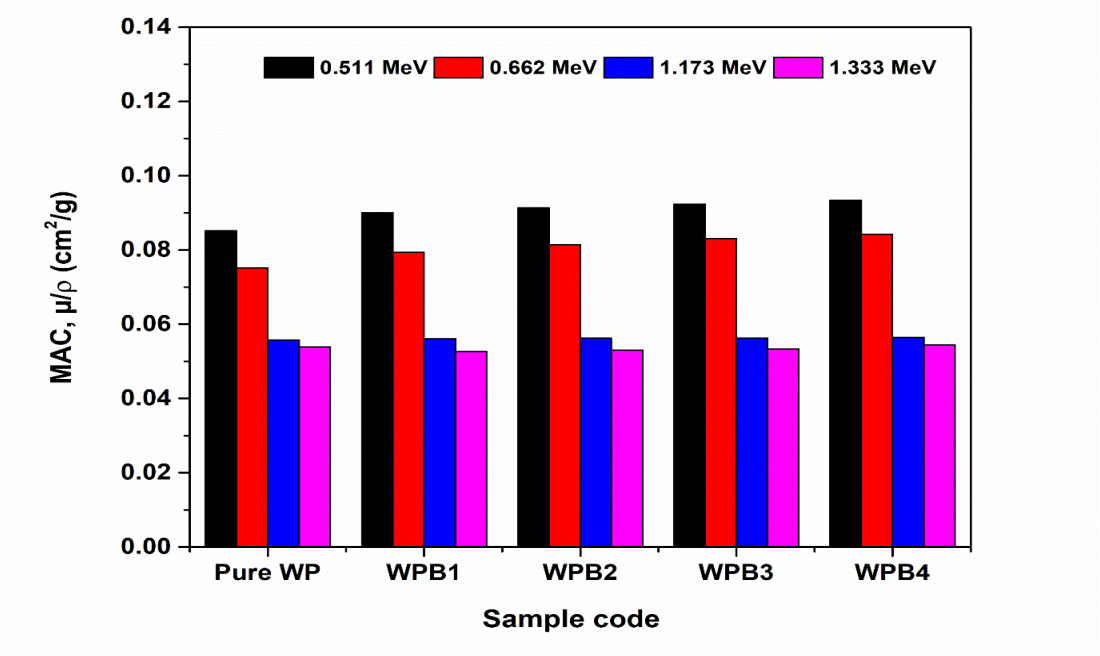

Figure 8.9: The Experimental values of MAC as a function of photon energy for wall paint reinforced with micro Bi_2O_3.

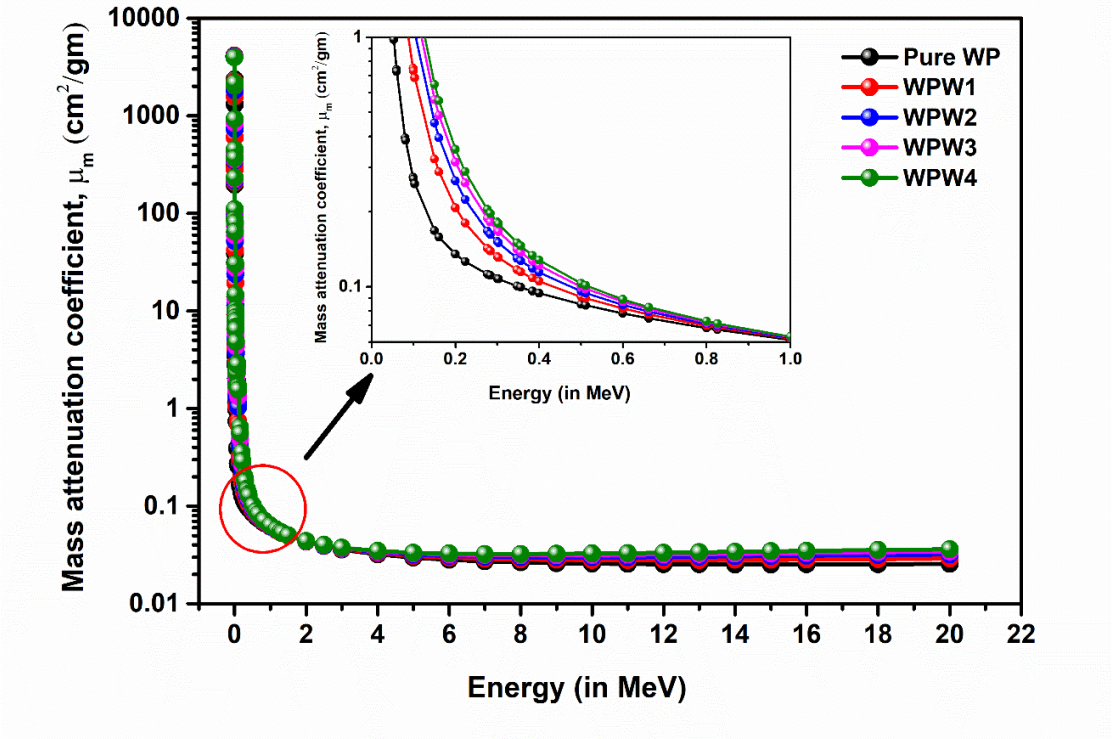

Figure 8.10: The MAC as a function of photon energy for wall paint reinforced with micro WO_3.

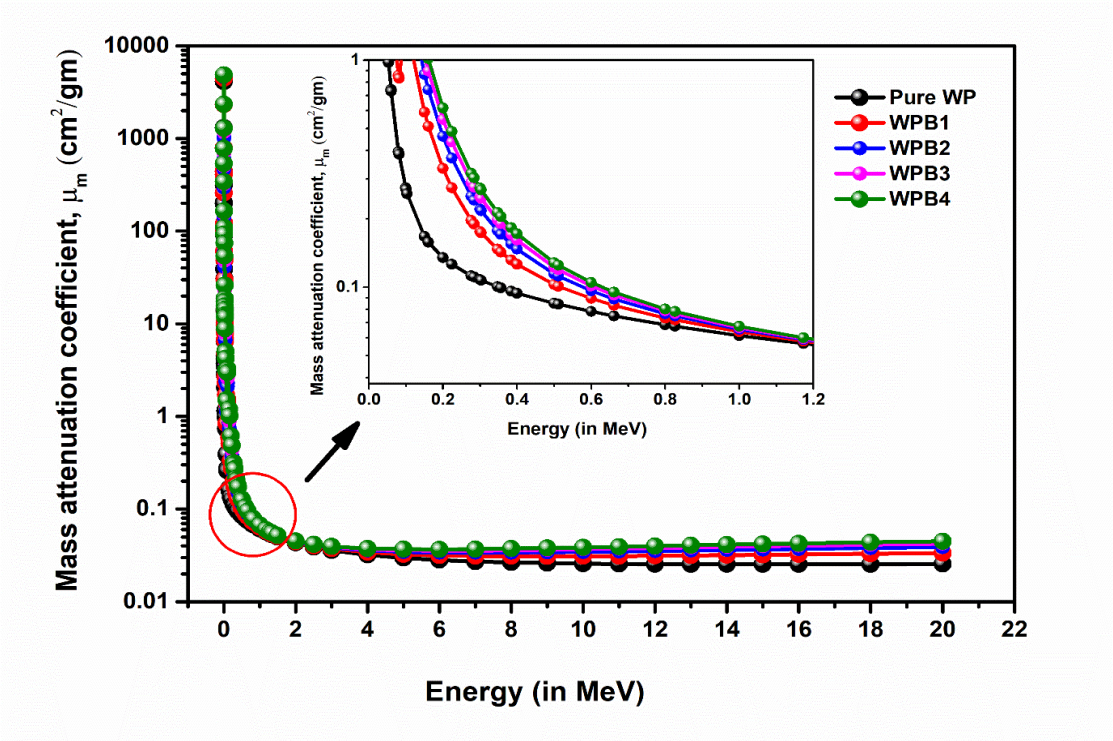

Figure 8.11: The MAC as a function of photon energy for wall paint reinforced with micro Bi_2O_3.

It steadily weakens as the gamma-ray energy increases from 0.511 to 1.333 MeV. That is, at lower gamma-ray energies, the physical properties of composites are more likely to occur. As a result, the surface effects of these filler structures are expected to increase the likelihood of gamma-ray collisions with extranuclear electrons of matter, particularly if photoelectric processes are conceivable. It causes an improvement in the gamma-ray capture cross section [2], [3]. In general, the likelihood of a photoelectric effect is related to Z^3/E^3, where Z is the atomic number of the absorbing element and E is the photon energy. At high gamma-ray energies, Compton scattering dominates (such as 0.551 MeV). At high energies, materials attenuate gamma-rays via Compton scattering a few times, and through the photoelectric effect, the weaker energy scattered photons are finally abs orbed [2], [14], [22].

As an outcome, low energy gamma-rays can be absorbed directly by the photoelectric effect, whereas High energy gamma-rays have more extensive photon interactions with materials and are therefore harder to prevent. When a result, as gamma-ray energy increases, so do sample attenuating properties [2]. Table 8.4

shows the comparison of mass attenuation coefficient of some composites that are previously reported at 0.66*2* MeV energy of the ^{137}Cs with the present study.

Table 8.4: Comparison of the mass attenuation coefficients between the different shields of gamma-rays at 0.662 MeV(^{137}Cs)

No	Samples	Density (g/cm^3)	MAC (cm^2/g)	Reference
1	Lead	11.35	0.0952	[23]
2	Lead Glass System	3.34-5.91	0.0764-0.1061	[11]
3	Nickel-Silver Alloy	8.67-8.73	0.073-0.072	[24]
4	NR+Bi_2O_3	-	0.083-0.096	[25]
5	Hematite-serpentine concrete+µWO_3	-	0.0834	[10]
6	Hematite-serpentine concrete+ µ Bi_2O_3	-	0.0838	[10]
7	PbO-B_2O_3-P_2O_5 Glass+ µWO_3	5.24-6.17	0.0887-0.0889	[14]
8	White cement+ µBi_2O_3	1.48-2.97	0.0779-0.0833	[17]
9	Wallpaint+Bi_2O_3 and WO_3	1.67-3.09	0.0753-0.0864	Present study

In earlier studies, materials like lead (11.35 g/cm^3) demonstrated excellent gamma-ray shielding due to their high density and atomic number, though their heavy weight and toxicity limited practicality. Alternatives such as lead glass systems (3.34–5.91 g/cm^3) offered moderate density and transparency, while nickel-silver alloys (8.67–8.73 g/cm^3) provided good mechanical properties with slightly lower shielding efficiency. Composite materials like hematite-serpentine concrete with µWO_3 or µBi_2O_3 additives showed effective gamma-ray attenuation, though they were primarily suited for large-scale, rigid applications. The present study introduces wall paint with Bi_2O_3 and WO_3 additives (1.67–3.09 g/cm^3), offering comparable shielding efficiency with the added benefits of being lightweight, flexible, and easily applicable on various surfaces. Compared to traditional materials, the wall paint composite combines practical advantages with strong shielding capabilities. With a mass attenuation coefficient (MAC) ranging from 0.0753 to 0.0864 cm^2/g, it rivals composites like µWO_3- and µBi_2O_3-based concretes while addressing issues of weight, cost, and versatility. Unlike lead, which is heavy, costly, and requires careful handling due to toxicity, the paint is inexpensive, inert, and simple to manufacture. Its flexibility makes it ideal for retrofitting, temporary

installations, and environments where rigid materials are impractical, establishing it as a promising alternative for effective radiation shielding.

8.3.5 Half-Value Layer (HVL)

Effective shielding parameters such as HVL (cm), MFP (cm), Z_{eff} and N_{eff} of the samples are theoretically calculated shielding using Phy-X/PSD program codes and compared with experimental results obtained at various gamma-ray photon energies, respectively. Table 8.5 shows the experimental as well as theoretical values of HVL as a function of photon energy for wall paint composites of 5% to 20% micro Bi_2O_3 as well as micro WO_3.

Table 8.5: Theoretically (Phy-X/PSD) computed HVL (cm) of the samples with the experimental values recorded at various γ-ray photon energies.

Half Value Layer, HVL (cm)					
Energy (0.511 MeV)			**Energy (0.662 MeV)**		
Sample	**Expt**	**Theo.**	**Sample**	**Expt**	**Theo.**
Pure WP	4.86	4.91	Pure WP	5.51	5.44
WPB1	3.60	3.71	WPB1	3.95	4.34
WPB2	3.20	3.18	WPB2	3.59	3.62
WPB3	2.72	2.66	WPB3	3.11	3.07
WPB4	2.38	2.40	WPB4	2.73	2.71
WPW1	3.23	3.37	WPW1	3.67	3.37
WPW2	2.82	2.90	WPW2	3.17	3.24
WPW3	2.66	2.68	WPW3	2.96	2.99
WPW4	2.40	2.43	WPW4	2.66	2.64
Energy (1.173 MeV)			**Energy (1.333 MeV)**		
Sample	**Expt**	**Theo.**	**Sample**	**Expt**	**Theo.**
Pure WP	7.42	7.38	Pure WP	7.70	7.91
WPB1	5.67	5.67	WPB1	6.01	6.04
WPB2	5.23	5.20	WPB2	5.53	5.52
WPB3	4.55	4.47	WPB3	4.82	4.79
WPB4	3.98	3.86	WPB4	4.29	4.21
WPW1	5.19	5.01	WPW1	5.53	5.24
WPW2	4.59	4.59	WPW2	4.87	4.86
WPW3	4.36	4.32	WPW3	4.61	4.54
WPW4	3.97	3.93	WPW4	4.11	4.16

Figure 8.12 shows the theoretical HVL values of (in the energy range 0.01 to 20 MeV) wall paint samples reinforced with both micro sized Bi_2O_3 and WO_3.

The demonstrated agreement between experimental and theoretical shielding capabilities strongly supports the developed materials' radiation protection capability [18]. Because the 5%-WO_3 of wall paint sample has the highest HVL, we must use a large amount of micro WO_3 to minimize the sample's dimension. For example, a thickness of 4.013 cm from 20% WO_3 of wall paint sample is needed to attenuate photons with an energy of 662 keV, whereas 20% Bi_2O_3 requires just 2.832 cm. This finding has implications for the design of lead-free radiation shielding composites that are extensible. Thinner, more flexible materials with higher shielding properties can thus replace thicker shielding materials [25].

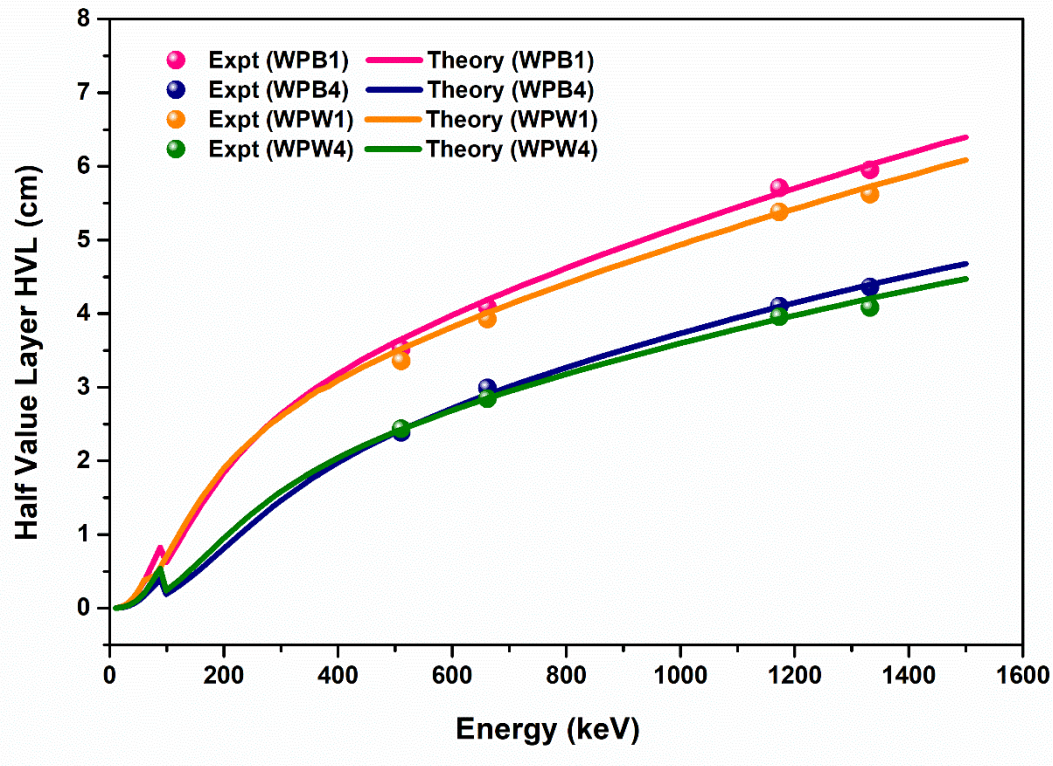

Figure 8.12: The experimental and theoretical values of HVL as a function of photon energy for wall paint reinforced with micro Bi_2O_3 and WO_3.

8.3.6 Mean Free Path (MFP)

The mean free path (MFP) is the average distance travelled by a moving particle (such as an atom, molecule, or photon) between subsequent collisions [14]. From Table 8.6 and Figure 8.13 it is clear that, the MFP values rise as photon energy increases.

Table 8.6: Theoretically (Phy-X/PSD) computed MFP (cm) of the samples with the experimental values recorded at various γ-ray photon energies.

Mean Free Path, MFP (cm)					
Energy (0.511 MeV)			**Energy (0.662 MeV)**		
Sample	**Expt**	**Theo.**	**Sample**	**Expt**	**Theo.**
Pure WP	7.02	7.08	Pure WP	7.95	7.84
WPB1	5.19	5.35	WPB1	5.70	6.26
WPB2	4.62	4.59	WPB2	5.18	5.23
WPB3	3.92	3.84	WPB3	4.49	4.43
WPB4	3.44	3.46	WPB4	3.94	3.91
WPW1	4.67	4.87	WPW1	5.30	4.86
WPW2	4.08	4.18	WPW2	4.58	4.67
WPW3	3.84	3.86	WPW3	4.27	4.32
WPW4	3.46	3.51	WPW4	3.83	3.82
Energy (1.173 MeV)			**Energy (1.333 MeV)**		
Sample	**Expt**	**Theo.**	**Sample**	**Expt**	**Theo.**
Pure WP	10.71	10.65	Pure WP	11.11	11.40
WPB1	8.18	8.18	WPB1	8.67	8.72
WPB2	7.55	7.51	WPB2	7.98	7.96
WPB3	6.57	6.44	WPB3	6.96	6.91
WPB4	5.74	5.57	WPB4	6.18	6.08
WPW1	7.50	7.23	WPW1	7.98	7.56
WPW2	6.63	6.63	WPW2	7.03	7.02
WPW3	6.30	6.24	WPW3	6.65	6.55
WPW4	5.72	5.68	WPW4	5.93	6.00

In the photon energy range 0.01-0.3MeV, the MFP values are exceptionally low (less than one cm). In the energy range of 0.3-6 MeV, the values of MFP in all

samples increases slower than that in the lower energy range. In the higher energy range of photon (E > 10 MeV), the mean free path values are not impacted by photon energy [14].

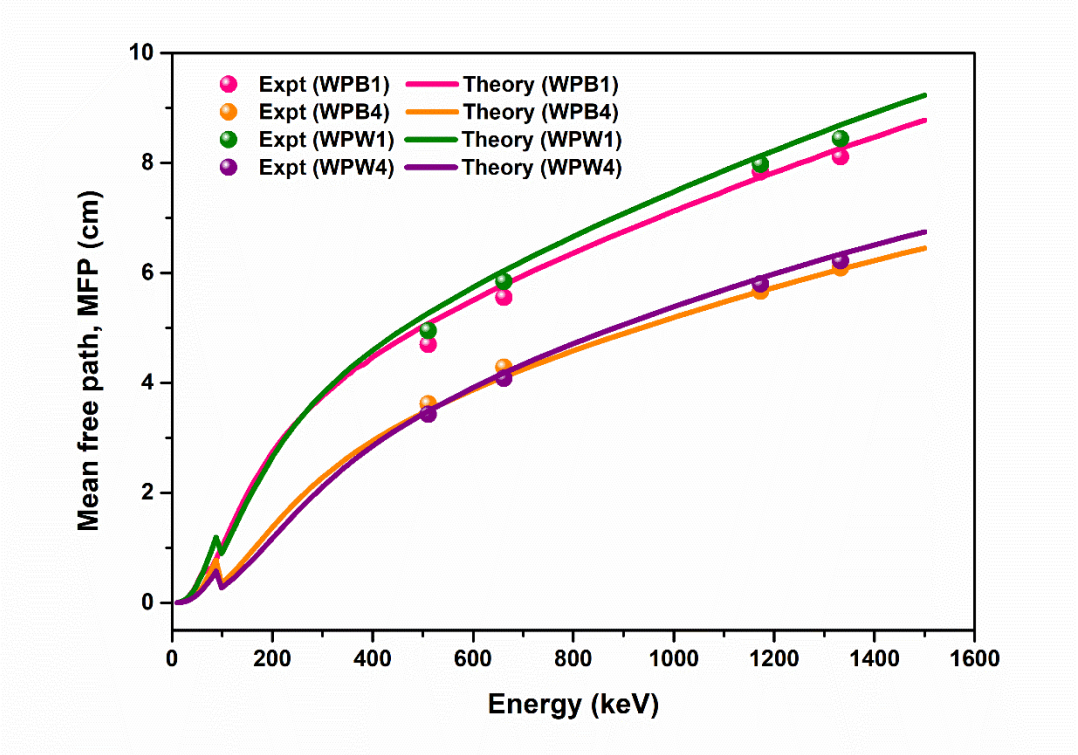

Figure 8.13: MFP as a function of photon energy for wall paint reinforced with micro Bi_2O_3 and WO_3.

8.3.7 Effective atomic number (Z_{eff}) and Effective electron density (N_{eff})

The composites' effective atomic number (Z_{eff}) was estimated. It was discovered that Z_{eff} grows with rising Bi_2O_3 concentration and decreases with increasing photon energies, following the same trend as μ_m, owing to greater atomic number increasing of Bi_2O_3 having an impact on the probability of photon energy interaction with electron in matter [25]. Nonetheless, Z_{eff}'s results are in good accord with the theoretical values. It is seen that the increase of density by adding Bi_2O_3 and WO_3 into the wall paint composite has an effect on the N_{eff} value. The N_{eff} increases in value as Bi_2O_3 increases, implying that the composite has more immersive electrons per unit mass. Furthermore, the N_{eff} results exhibit similarities with μ_m and Z_{eff}. When photon energy is increased, the trend shows that declines dramatically [25].

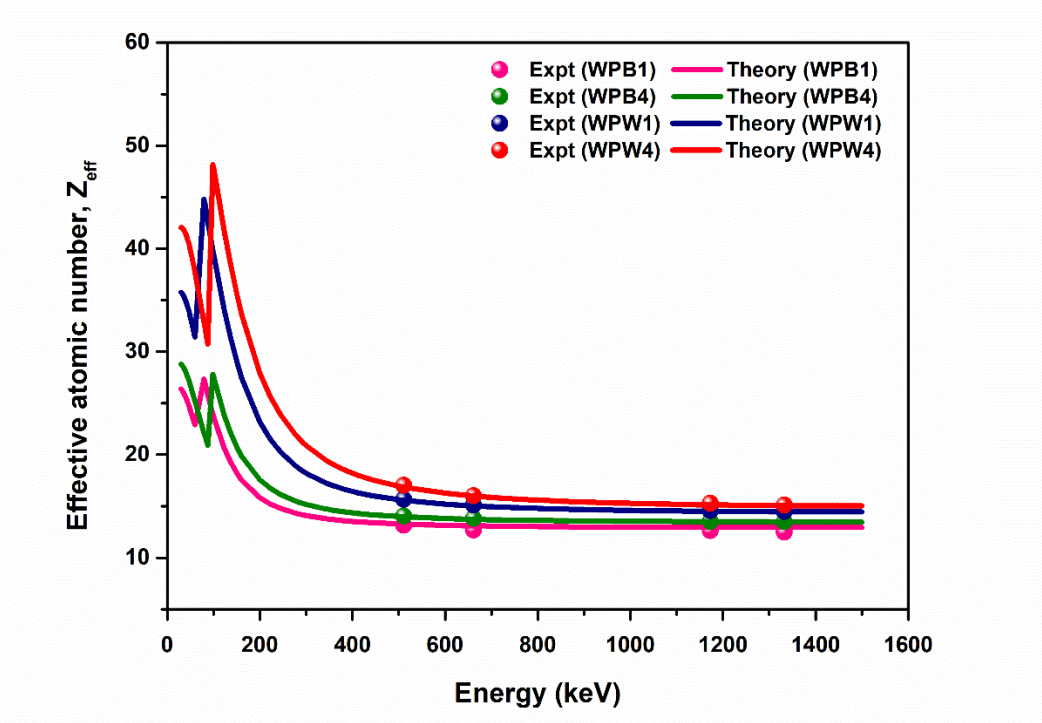

Figure 8.14: Z_{eff} as a function of photon energy for wall paint reinforced with micro Bi_2O_3 and WO_3.

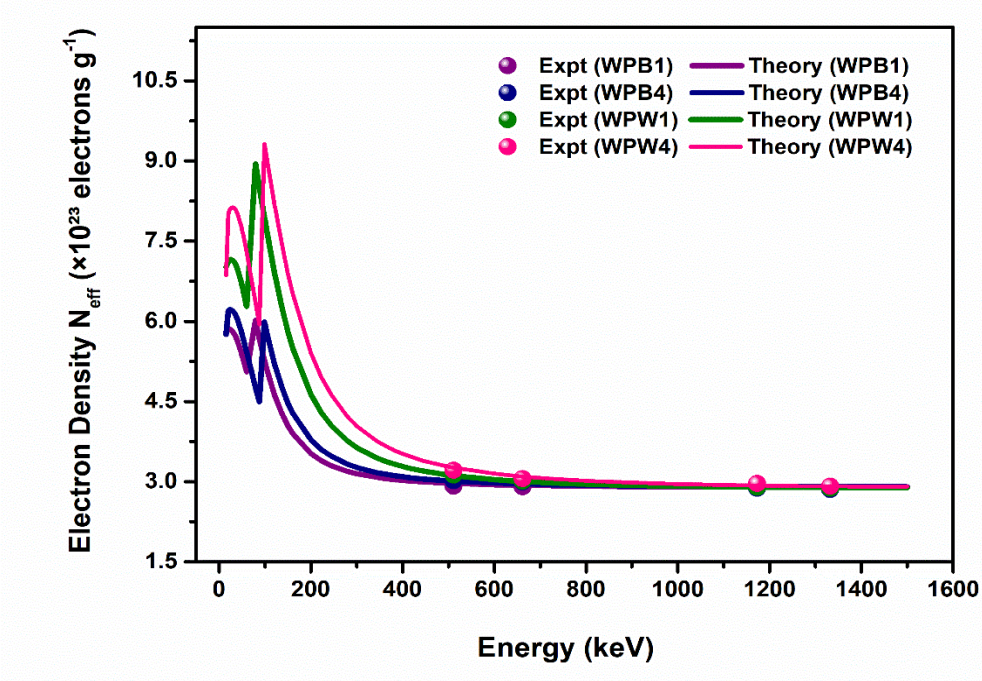

Figure 8.15: N_{eff} as a function of photon energy for wall paint reinforced with micro Bi_2O_3 and WO_3.

8.3.8 Built-up Factors

To evaluate build-up factors, the equivalent atomic number (Z_{eq}) must first be computed. It is computed by employing logarithmic interpolation to interpolate the R values with the R values of adjacent elements. Table 8.7 serves the determined equivalent atomic number (Z_{eq}) for the sampled, displaying the composite material's attributes in terms of equivalent element.

Table 8.7: Equivalent atomic numbers (Z_{eq}) of the composites for numerous gamma-ray energy levels ranging between 0.015 to 15 MeV (by Phy-X/PSD software).

Energy (MeV)	Pure WP	WPW1	WPW2	WPW3	WPW4	WPB1	WPB2	WPB3	WPB4
0.015	19.80	20.75	21.90	22.76	23.33	20.62	21.97	22.81	23.14
0.02	20.05	21.06	22.21	23.09	23.71	21.61	23.47	24.79	25.58
0.03	20.39	21.44	22.62	23.55	24.23	22.06	24.02	25.43	26.32
0.04	20.58	21.69	22.90	23.87	24.59	22.38	24.40	25.86	26.77
0.05	20.71	21.88	23.11	24.12	24.88	22.61	24.69	26.21	27.20
0.1	21.05	27.67	23.30	24.33	37.92	29.85	24.93	26.49	42.38
0.15	21.21	28.51	31.30	34.55	39.22	31.05	25.32	26.96	44.13
0.3	21.38	29.75	31.99	35.32	40.99	32.80	35.32	39.38	46.55
0.4	21.44	30.18	33.06	36.52	41.58	33.41	36.79	41.02	47.34
0.5	21.47	30.46	33.73	37.28	41.98	33.83	37.75	42.07	47.88
0.6	21.49	30.64	34.58	38.20	42.22	34.11	38.91	43.33	48.24
0.8	21.51	30.82	35.11	38.77	42.48	34.38	39.64	44.11	48.63
1	21.52	30.90	35.45	39.14	42.59	34.50	40.12	44.62	48.78
1.5	19.47	27.52	35.67	39.38	39.88	30.99	40.44	44.97	46.27
2	17.96	22.40	35.89	39.62	33.31	24.60	40.80	45.32	39.31
3	17.41	19.95	35.99	39.73	27.26	20.92	40.94	45.49	31.06
4	17.28	19.35	32.87	36.85	25.52	20.04	37.89	42.79	28.37
5	17.21	19.09	26.84	30.45	24.74	19.66	30.90	35.78	27.18
6	17.17	18.94	22.88	25.34	24.28	19.44	25.13	28.57	26.50
8	17.12	18.78	21.87	23.95	23.79	19.23	23.56	26.40	25.80
10	17.10	18.70	21.43	23.34	23.57	19.12	22.89	25.46	25.47
15	17.07	18.64	21.17	22.97	23.40	19.03	22.51	24.92	25.23

It should be highlighted that the Z_{eq} must be between the lowest and highest atomic number of the material[27]. Figure 8.16 and 8.17 shows EBF values for Bi_2O_3 and WO_3 doped composites (5% wt. and 20% wt.) with photon energies of 1, 2, 5, 10, 20

and 40 mfp. The five parameters were calculated by using G-P fitting method and the results obtained are tabulated in Tables 8.8 and 8.9 for WPB4 and WPW4 samples respectively.

Table 8.8 G-P energy absorption and exposure build-up factor parameters of the WPB4 for various energy values ranging from 0.015 to 15 MeV.

Energy (MeV)	EABF					EBF				
	a	b	c	d	X_k	a	b	c	d	X_k
0.015	-0.34	1.01	1.21	0.27	7.08	-0.35	1.01	1.21	0.27	6.11
0.02	0.32	1.01	0.26	-0.30	18.05	0.62	1.01	0.13	-0.63	11.37
0.03	0.25	1.02	0.33	-0.19	16.78	0.19	1.03	0.37	-0.24	24.56
0.04	0.23	1.05	0.36	-0.20	18.79	0.24	1.05	0.33	-0.11	12.83
0.05	0.24	1.09	0.35	-0.14	13.55	0.24	1.08	0.36	-0.14	13.38
0.06	0.24	1.14	0.35	-0.15	14.59	0.23	1.12	0.38	-0.13	13.75
0.08	0.21	1.26	0.40	-0.12	14.51	0.19	1.20	0.45	-0.11	14.06
0.1	0.37	1.21	0.23	-0.19	13.75	0.34	1.19	0.27	-0.17	13.75
0.15	0.34	1.44	0.27	-0.19	14.02	0.21	1.23	0.43	-0.11	14.26
0.2	0.32	1.96	0.30	-0.19	13.98	0.17	1.37	0.51	-0.10	14.45
0.3	0.19	2.08	0.49	-0.11	13.91	0.10	1.47	0.68	-0.05	14.32
0.4	0.14	2.37	0.62	-0.10	13.88	0.06	1.58	0.81	-0.04	14.15
0.5	0.10	2.43	0.73	-0.08	13.88	0.04	1.64	0.89	-0.03	14.11
0.6	0.08	2.44	0.79	-0.07	13.73	0.02	1.67	0.95	-0.02	14.01
0.8	0.05	2.37	0.88	-0.05	13.63	0.01	1.70	1.01	-0.02	14.08
1	0.04	2.27	0.92	-0.04	13.50	0.00	1.69	1.03	-0.02	13.43
1.5	0.00	1.93	1.06	-0.02	13.59	-0.02	1.59	1.14	0.00	11.58
2	0.00	1.85	1.06	-0.02	12.63	-0.02	1.61	1.13	-0.01	12.16
3	0.01	1.69	1.02	-0.03	12.52	0.00	1.60	1.06	-0.02	12.38
4	0.01	1.54	1.01	-0.03	14.06	0.01	1.54	1.02	-0.03	12.93
5	0.02	1.46	0.99	-0.04	14.15	0.01	1.48	1.01	-0.03	13.22
6	0.02	1.39	0.98	-0.04	14.31	0.02	1.43	0.99	-0.04	13.30
8	0.03	1.30	0.96	-0.05	14.01	0.03	1.35	0.97	-0.05	13.61
10	0.04	1.23	0.96	-0.05	14.28	0.04	1.30	0.95	-0.06	13.96
15	0.05	1.15	0.95	-0.05	14.64	0.05	1.20	0.96	-0.06	14.38

Table 8.9 G-P energy absorption and exposure build-up factor parameters of the WPW4 for various energy values ranging from 0.015 to 15 MeV.

Energy (MeV)	EABF					EBF				
	a	b	c	d	X_k	a	b	c	d	X_k
0.015	-0.33	1.01	1.20	0.26	7.14	-0.34	1.01	1.20	0.27	6.14
0.02	0.30	1.01	0.29	-0.26	16.01	0.48	1.01	0.23	-0.45	11.23
0.03	0.25	1.03	0.33	-0.18	17.44	0.20	1.03	0.37	-0.27	25.11
0.04	0.24	1.07	0.34	-0.13	13.91	0.25	1.07	0.34	-0.12	12.09
0.05	0.24	1.12	0.35	-0.14	14.37	0.23	1.12	0.37	-0.13	14.03
0.06	0.22	1.19	0.38	-0.13	14.71	0.21	1.17	0.41	-0.11	14.18
0.08	0.46	1.28	0.18	-0.19	14.15	0.58	1.51	0.16	-0.21	14.26
0.1	0.28	1.24	0.33	-0.15	15.26	0.26	1.19	0.35	-0.14	13.79
0.15	0.27	1.56	0.35	-0.16	14.00	0.16	1.29	0.52	-0.08	14.35
0.2	0.30	2.32	0.35	-0.19	13.96	0.16	1.50	0.55	-0.09	14.21
0.3	0.15	2.41	0.58	-0.09	13.99	0.08	1.60	0.75	-0.04	14.39
0.4	0.10	2.68	0.72	-0.09	13.89	0.04	1.71	0.89	-0.03	14.14
0.5	0.07	2.69	0.83	-0.06	13.90	0.02	1.77	0.98	-0.02	14.32
0.6	0.05	2.64	0.89	-0.05	13.76	0.01	1.79	1.02	-0.02	13.94
0.8	0.03	2.49	0.96	-0.04	13.66	-0.01	1.79	1.07	-0.01	14.03
1	0.02	2.36	0.99	-0.03	13.54	-0.01	1.77	1.09	-0.01	13.43
1.5	-0.01	1.94	1.10	-0.01	12.83	-0.03	1.64	1.16	0.00	8.49
2	-0.01	1.84	1.09	-0.01	10.96	-0.02	1.66	1.12	0.00	10.42
3	0.00	1.68	1.04	-0.02	12.34	0.00	1.62	1.06	-0.01	12.12
4	0.01	1.56	1.00	-0.03	13.95	0.01	1.55	1.03	-0.02	12.93
5	0.02	1.48	0.97	-0.04	14.19	0.01	1.49	1.01	-0.03	13.13
6	0.02	1.40	0.97	-0.04	14.09	0.02	1.45	0.98	-0.03	13.34
8	0.03	1.31	0.95	-0.04	13.59	0.03	1.36	0.97	-0.04	13.62
10	0.04	1.25	0.94	-0.05	14.17	0.04	1.30	0.94	-0.05	13.86
15	0.04	1.15	0.96	-0.05	14.58	0.05	1.21	0.94	-0.06	14.23

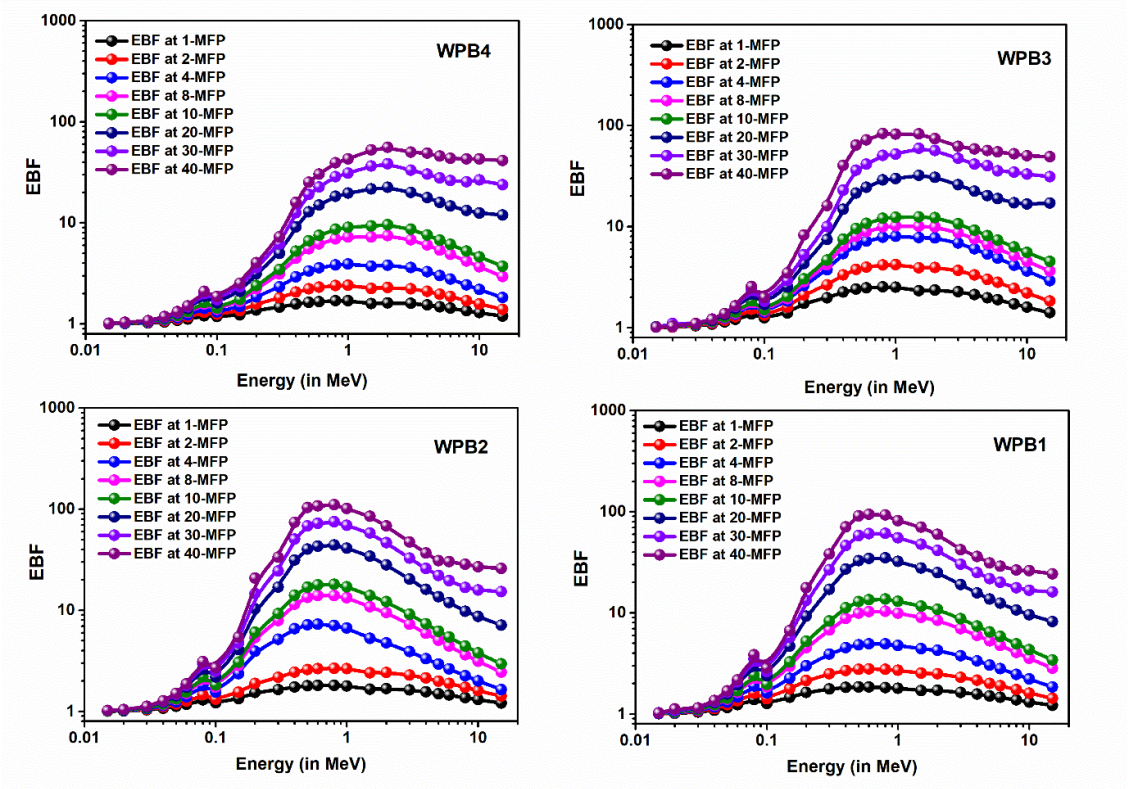

Figure 8.16. Energy build-up factors (EBF) against photon energies at various mean free paths of wall paint composites with 5% to 20% loading of Bi_2O_3.

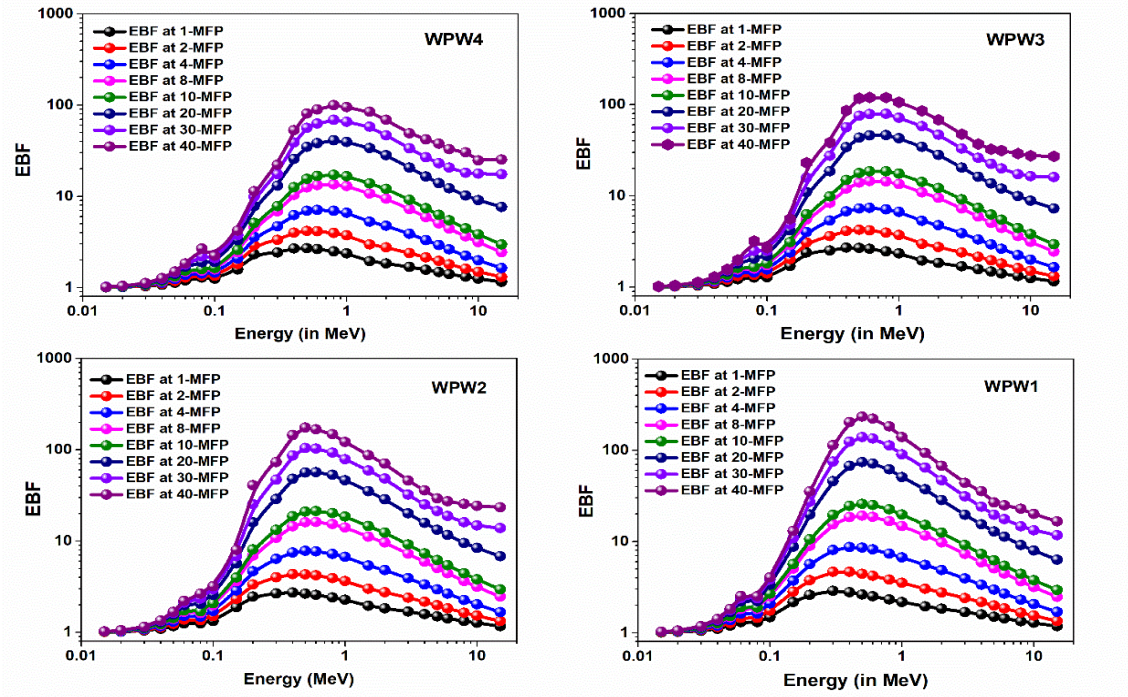

Figure 8.17. Energy build-up factors (EBF) against photon energies at various mean free paths of wall paint composites with 5% to 20% loading of WO_3.

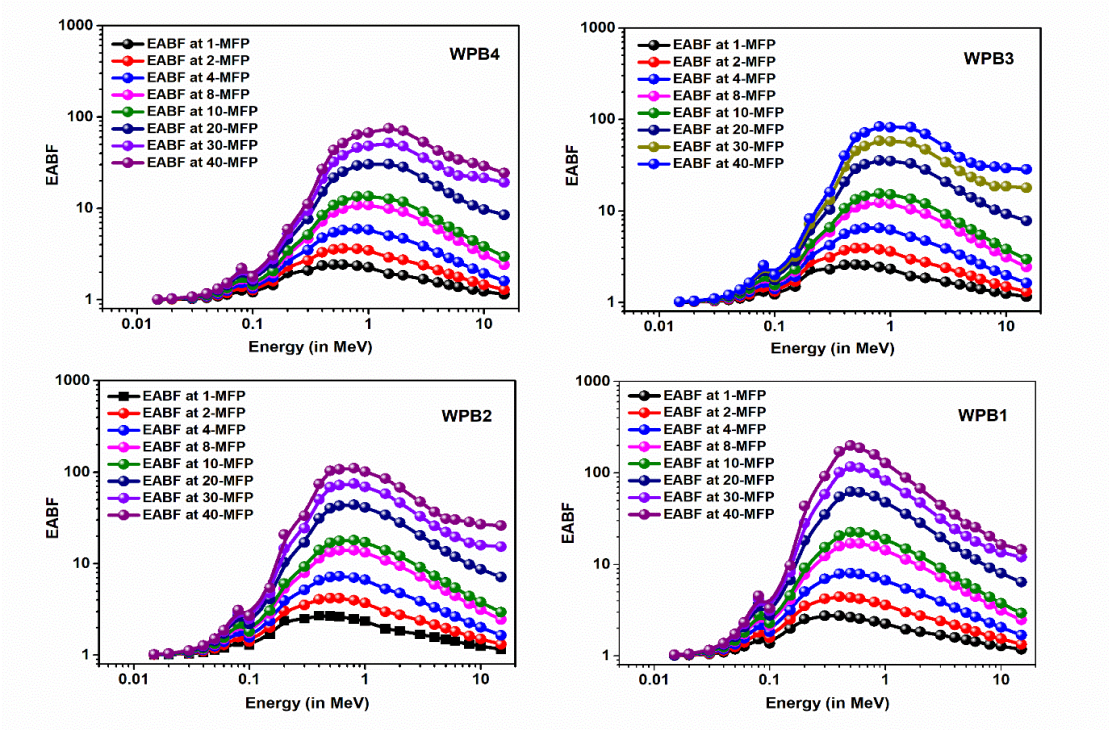

Figure 8.18. Energy absorption build-up factors (EABF) against photon energies at various mean free paths of wall paint composites with 5% to 20% loading of Bi_2O_3.

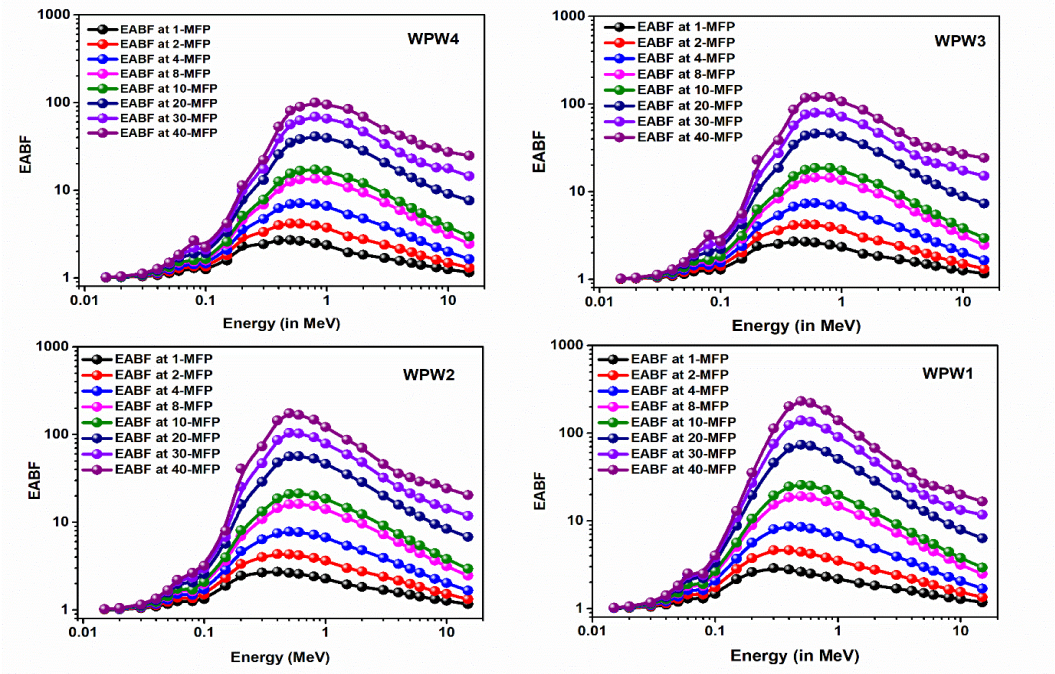

Figure 8.19: Energy absorption build-up factors (EABF) against photon energies at various mean free paths of wall paint composites with 5% to 20% loading of WO_3

The EBF and EABF values are relatively low, but quickly escalate as photon energy grows. Increasing energy levels, as well as low, mid, and high-level energy zones, are frequently used, each with a distinct predominant incident and effects [27]. Figure 16 and 17 shows that for WP with 20%WO_3, EBF-values at 40 mfp imply maximum at 0.5 MeV (99.8), 0.8 MeV (80.6), at 1.5 MeV for (84.4) and at 2.0 MeV (68.7) but in the case of 5% of loading of WO_3, EBF-values at 40 mfp reflect high point at 0.5 MeV (233.1), at 0.8 MeV (183.2), at 1.5 MeV for (93.2) and at 2.0 MeV (67.4). Like EABF, EBF-values maintaining the same trend and was shown in Figures 8.18 and 8.19. WO_3 (20%) has the finest EBF-EABF values in all transmittances, medium energies are used.

In the weak energy domain, the photoelectric effect takes over as the primary incident, arising an inversely proportional effect with $E^{3.5}$[27]. Since the selected composite samples absorb the greatest number of low-energy photons, these photons are not permitted to collect [27], [28]. In the intermediate energy area, Compton scattering becomes dominating, resulting in high EBF and EABF values for all selected composites[27]. Rather than the MFP, these high EBF and EABF values are created by scattering mechanisms. The pair production process is dominant in the high-energy domain, and the EBF and EABF values drop with incident photon energy WO_3 (5%) owns lowest Z_{eq} value and the most EBF and EABF values. Moreover, Z_{eq} is inversely correlated to EBF and EABF, with the lowest Z_{eq} value generating the highest EBF and EABF value. The highest EABF and EBF values are found at varied levels in WO_3 (5 percent) (the sample's lowest Z_{eq}). Similarly, the lowest EABF and EBF values occur at various levels in Bi_2O_3 (20 percent) (which is the greatest Z_{eq} in the sample). That is, Bi_2O_3 (20% with wall paint) is a better gamma-ray shielding composite than WO_3 (20 percent with wall paint). The medium energy zone has the highest EABF and EBF scores (Compton scattering zone). Furthermore, at 40 mfp, build-up factors were at their peak. Finally, for high Z_{eq} composites, the maximum values of EABF and EBF move to higher energies. For example, maximum EABF and EBF values occur at 0.5 MeV for WP+5 percent WO_3 (lowest Z_{eq}), while maximum EABF and EBF values occur at 0.8 MeV for WP+20 percent WO_3 (highest Z_{eq}).

8.3.9 Effective Conductivity (C_{eff}) and Fast neutron removal cross-section (FNRCS)

Figure 8.20 illustrates the variation in effective conductivity (C_{eff}) across all paint samples. There is a significant and rapid decrease observed as photon energy increases, particularly in regions where the photoelectric effect dominates. Conversely, at higher energy levels, C_{eff} shows an increase. Despite these variations, the WPB4 sample exhibited the highest C_{eff} values among all tested samples. Since effective conductivity is related to electron density, an increase in electron density also results in increased conductivity[26].

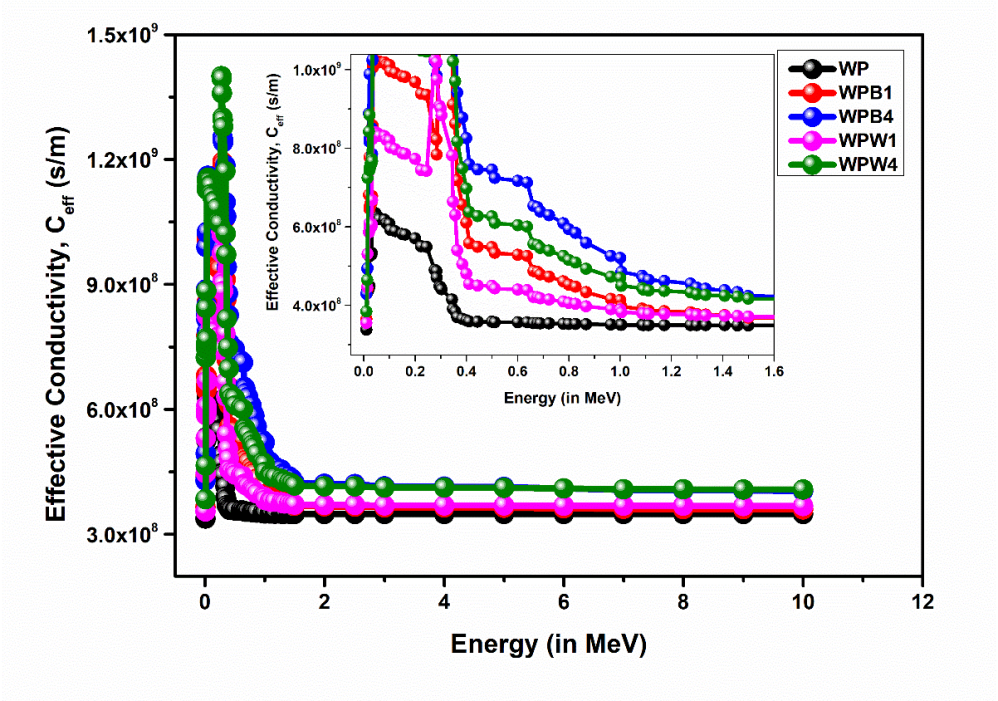

Figure 8.20: The variability in effective conductivity (C_{eff}) in paint samples

For the current wall paint systems, the effective removal cross-section for fast neutron (FRCS: Σ_R) was estimated mathematically and by using Ph-X program as shown in Figure 8.21.

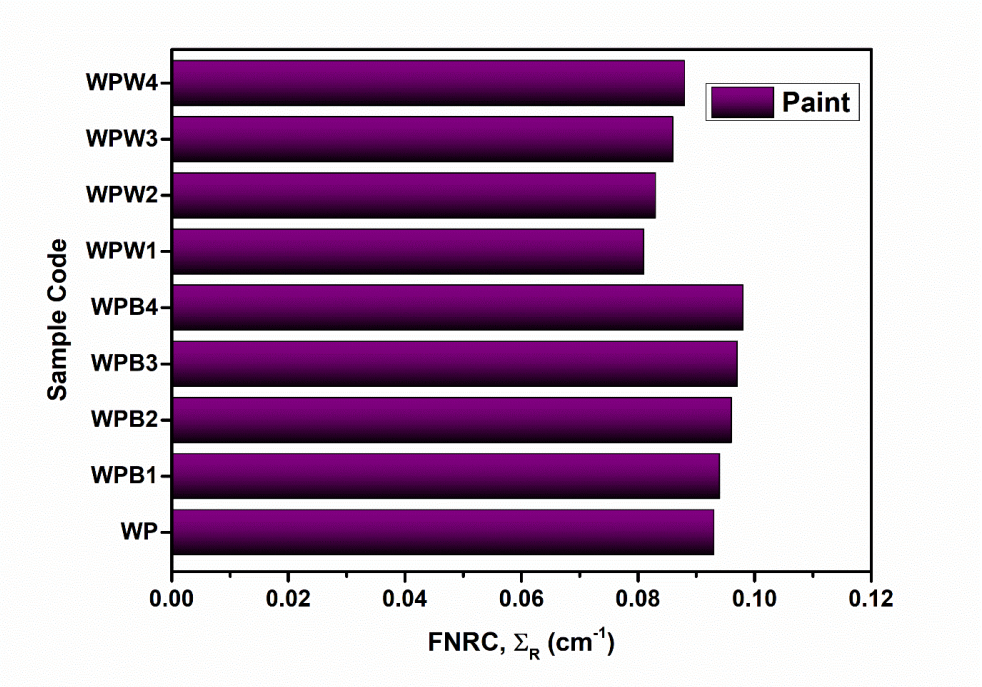

Figure 8.21 The effective removal cross-section values of the fabricated wall paint samples.

It has been established that neutron reactions increase with lighter elements and decrease with higher neutron energies. Moreover, the probability of neutron scattering increases progressively with the number of collisions within wall paint samples. Therefore, it is crucial to assess the capability of new shielding materials to retain neutron energy effectively. Despite the reduction of neutron attenuation values reported with increasing Bi content, the Σ_R of all prepared glasses is better than some standard materials such as water (0.102 cm^{-1}), graphite (0.077 cm^{-1}) and concrete (ordinary = 0.094 cm^{-1} and serpentine = 0.097 cm^{-1}) [29], [30].

8.4 Conclusion

Bi_2O_3 and WO_3 added epoxy wall paints were prepared and subjected for evaluating gamma radiation shielding characteristics. To ensure that the experimental data was consistent, the values of the acquired mass attenuation coefficients were contrasted to those anticipated by the XCOM application, as well as the Phy-X/PSD program for simulation (for the energy range of 0.010 MeV to 15 MeV). There is an excellent concordance between the experimental results and theoretical (XCOM) and

simulation calculations. The parameters investigated are the mass attenuation coefficient, linear attenuation coefficient, HVL, MFP, Z_{eff}, N_{eff}, EBF, and EABF. The results demonstrate that the composites of fabricated materials are efficient at photon reduction, with the foremost material being Bi_2O_3 (20 percent) wall paint-metal oxide-based composite. The assessment of shielding parameters ranging from 0.015 to 15 MeV demonstrates that the attributes of MAC, LAC, Z_{eff}, and N_{eff} rises with the inclusion of Bi_2O_3/WO_3 mol percent and decrease with energy. We propose a novel absorber of gamma shielding, by reducing the quantity of lead in the micro-compounds created as a result of the new material's ability to attenuate photons.

8.5 Reference

[1] I. G. Geidam *et al.*, "Oxide ion polarizabilities and gamma radiation shielding features of TeO_2–B_2O_3–SiO_2 glasses containing Bi_2O_3 using Phy-X/PSD software," *Mater. Today Commun.*, vol. 31, no. January, p. 103472, 2022, doi: 10.1016/j.mtcomm.2022.103472.

[2] J. H. Liu *et al.*, "Elevated gamma-rays shielding property in lead-free Bismuth tungstate by nanofabricating structures," *J. Phys. Chem. Solids*, vol. 112, no. July 2017, pp. 185–189, 2018, doi: 10.1016/j.jpcs.2017.09.007.

[3] A. H. Almuqrin, M. I. Sayyed, M. Elsafi, and M. U. Khandaker, "Comparison of radiation shielding ability of Bi_2O_3 micro and nanoparticles for radiation shields," *Radiat. Phys. Chem.*, vol. 200, no. March, p. 110170, 2022, doi: 10.1016/j.radphyschem.2022.110170.

[4] N. Plangpleng *et al.*, "Flexible gamma-ray shielding based on natural Rubber/$BaSO_4$ nanocomposites," *Radiat. Phys. Chem.*, vol. 199, no. October 2021, p. 110311, 2022, doi: 10.1016/j.radphyschem.2022.110311.

[5] Z. Wu *et al.*, "Gamma radiation shielding properties of WO_3/Bi_2O_3/waterborne polyurethane composites," *J. Korean Phys. Soc.*, vol. 81, no. 3, pp. 199–205, 2022, doi: 10.1007/s40042-022-00503-0.

[6] D. Toyen, A. Rittirong, W. Poltabtim, and K. Saenboonruang, "Flexible, lead-free, gamma-shielding materials based on natural rubber/metal oxide composites," *Iran. Polym. J. (English Ed.*, vol. 27, no. 1, pp. 33–41, 2018, doi: 10.1007/s13726-017-0584-3.

[7] S. N. Yılmaz, İ. K. Akbay, and T. Özdemir, "A metal-ceramic-rubber composite for hybrid gamma and neutron radiation shielding," *Radiat. Phys. Chem.*, vol. 180, no. June 2020, 2021, doi: 10.1016/j.radphyschem.2020.109316.

[8] S. Stalin *et al.*, "Influence of Bi_2O_3/WO_3 substitution on the optical, mechanical, chemical durability and gamma-ray shielding properties of lithium-borate glasses," *Ceram. Int.*, vol. 47, no. 4, pp. 5286–5299, 2021, doi: 10.1016/j.ceramint.2020.10.109.

[9] A. Kozlovskiy, D. B. Borgekov, D. I. Shlimas, and V. Zdorovets, "Study of the efficiency of increasing the Bi_2O_3 concentration on the optical, radiation shielding and strength characteristics of $0.5TeO_2$-$(0.5-x)WO_3$-xBi_2O_3 glasses," *Opt. Mater. (Amst).*, vol. 120, no. May, p. 111494, 2021, doi: 10.1016/j.optmat.2021.111494.

[10] H. O. Tekin, M. I. Sayyed, and S. A. M. Issa, "Gamma radiation shielding properties of the hematite-serpentine concrete blended with WO_3 and Bi_2O_3 micro and nano particles using MCNPX code," *Radiat. Phys. Chem.*, vol. 150, no. April, pp. 95–100, 2018, doi: 10.1016/j.radphyschem.2018.05.002.

[11] R. El-Mallawany, M. I. Sayyed, M. G. Dong, and Y. S. Rammah, "Simulation of radiation shielding properties of glasses contain PbO," *Radiat. Phys. Chem.*, vol. 151, no. June, pp. 239–252, 2018, doi: 10.1016/j.radphyschem.2018.06.035.

[12] M. Movahedi *et al.*, "Novel paint design based on nanopowder to protection against X and gamma rays," *Indian J. Nucl. Med.*, vol. 29, no. 1, pp. 18–21, 2014, doi: 10.4103/0972-3919.125763.

[13] M. Almatari, Y. Koraim, I. H. Saleh, M. I. Sayyed, M. Uddin Khandaker, and M. Elsafi, "Investigation of the photon shielding capability of kaolin clay added with micro and nanoparticles of Bi_2O_3," *Radiat. Phys. Chem.*, vol. 200, no. January, p. 110191, 2022, doi: 10.1016/j.radphyschem.2022.110191.

[14] A. M. A. Mostafa, S. A. M. Issa, and M. I. Sayyed, "Gamma-ray shielding properties of PbO-B_2O_3-P_2O_5 doped with WO_3," *J. Alloys Compd.*, vol. 708, pp. 294–300, 2017, doi: 10.1016/j.jallcom.2017.02.303.

[15] Y. Karabul and O. İçelli, "The assessment of usage of epoxy based micro and nano-structured composites enriched with Bi_2O_3 and WO_3 particles for radiation shielding," *Results Phys.*, vol. 26, 2021, doi: 10.1016/j.rinp.2021.104423.

[16] M. Asgari, H. Afarideh, and H. Ghafoorifard, "Comparison of nano / micro lead , Bismuth and Tungsten on the gamma shielding properties of the fl exible composites against photon in wide energy range (40 keV e 662 keV)," *Nucl. Eng. Technol.*, vol. 53, no. 12, pp. 4142–4149, 2021, doi: 10.1016/j.net.2021.06.022.

[17] S. M. A.-B. andMahmoud T. A. Mona M. Gouda, AhmedM. El-Khatib , Mahmoud I. Abbas, "Gamma Attenuation Features of White Cement Mortars," vol. 16, p. 1580, 2023.

[18] H. Aboud, M. J. R. Aldhuhaibat, and Y. Alajermi, "Gamma radiation shielding traits of B_2O_3–Bi_2O_3–CdO–BaO–PbO glasses," *Radiat. Phys. Chem.*, vol. 191, no. October 2021, p. 109836, 2022, doi: 10.1016/j.radphyschem.2021.109836.

[19] Y. Al-Hadeethi and M. I. Sayyed, "Radiation attenuation properties of Bi_2O_3–Na_2O–V_2O_5– TiO_2–TeO_2 glass system using Phy-X / PSD software," *Ceram. Int.*, vol. 46, no. 4, pp. 4795–4800, 2020, doi: 10.1016/j.ceramint.2019.10.212.

[20] E. Şakar, Ö. F. Özpolat, B. Alım, M. I. Sayyed, and M. Kurudirek, "Phy-X / PSD: Development of a user friendly online software for calculation of parameters relevant to radiation shielding and dosimetry," *Radiat. Phys. Chem.*, vol. 166, no. September 2019, 2020, doi: 10.1016/j.radphyschem.2019.108496.

[21] R. Barman, M. S. Hossain, A. Das, and M. K. Ahmmad Rabby, "Investigation of

radiation shielding characteristic features of different wood species," *Radiat. Phys. Chem.*, vol. 192, no. May 2021, 2022, doi: 10.1016/j.radphyschem.2021.109927.

[22] M. R. Ambika *et al.*, "Preparation and characterisation of Isophthalic-Bi_2O_3 polymer composite gamma radiation shields," *Radiat. Phys. Chem.*, vol. 130, no. March 2016, pp. 351–358, 2017, doi: 10.1016/j.radphyschem.2016.09.022.

[23] A. Khalaf, M. Hana, I. Hasan, and F. M. Al-jomaily, "Gamma-ray absorption using rubber — lead mixtures as radiation protection shields," pp. 653–659, 2012, doi: 10.1007/s10967-011-1556-2.

[24] Ş. Erdem, "Determination of photon-shielding features and build-up factors of nickel – silver alloys," vol. 172, no. February, 2020. doi: 10.1016/j.radphyschem.2020.108778.

[25] S. Intom *et al.*, "Mechanical and radiation shielding properties of flexible material based on natural rubber/ Bi_2O_3 composites," *Radiat. Phys. Chem.*, p. 108772, 2020, doi: 10.1016/j.radphyschem.2020.108772.

[26] G. Almisned *et al.*, "The impact of chemical modifications on gamma-ray attenuation properties of some WO_3-reinforced tellurite glasses," *Open Chem.*, vol. 21, no. 1, 2023, doi: 10.1515/chem-2022-0297.

[27] O. Kilicoglu *et al.*, "Micro Pb filled polymer composites: Theoretical, experimental and simulation results for γ-ray shielding performance," *Radiat. Phys. Chem.*, vol. 194, no. February, 2022, doi: 10.1016/j.radphyschem.2022.110039.

[28] M. I. Sayyed, M. Y. AlZaatreh, M. G. Dong, M. H. M. Zaid, K. A. Matori, and H. O. Tekin, "A comprehensive study of the energy absorption and exposure buildup factors of different bricks for gamma-rays shielding," *Results Phys.*, vol. 7, pp. 2528–2533, 2017, doi: 10.1016/j.rinp.2017.07.028.

[29] Y. S. Alajerami, "Radiation Shielding Properties for NaO–CdO–Bi_2O_3–B_2O_3 Glasses Using XCOM, Phy-X/PSD and Srim Programs," *Glas. Phys. Chem.*, vol. 47, pp. S10–S20, 2021, doi: 10.1134/S1087659621070026.

[30] V. P. Singh and N. M. Badiger, "Shielding Efficiency of Lead Borate and Nickel Borate Glasses for Gamma Rays and Neutrons 1," vol. 41, no. 3, pp. 276–283, 2015, doi: 10.1134/S1087659615030177.

CHAPTER 9
SUMMARY AND CONCLUSION

This PhD thesis, titled "Investigations on the Natural Radioactivity and Gamma Attenuation Properties of Building Materials," aims to systematically evaluate the levels of natural radioactivity in commonly used building materials and to assess their gamma attenuation properties. By understanding these factors, we can better mitigate potential radiological hazards and contribute to the development of safer construction practices. This research not only adds to the existing body of knowledge but also provides practical insights for the construction industry, regulatory bodies, and public health agencies.

In this context, the study of natural radioactivity and gamma attenuation properties of building materials is critically evaluated for ensuring the safety and sustainability of construction practices. Building materials, often sourced from natural geological formations, can contain varying levels of naturally occurring radionuclides such as Uranium-238, Thorium-232, and Potassium-40. These radionuclides emit gamma radiation, which can pose health risks to inhabitants if not adequately managed. In addition, thesis proposed three different composites for gamma-ray shielding applications belongs to rigid concrete based composite system, flexible natural rubber-based system and epoxy-based wall paint for coating applications.

In order to understand natural radioactivity systematic approaches are adopted, three important populated areas in Kerala, India selected for this study. The results obtained from this study and major conclusions are drawn are described here. In rock samples from the Thrissur-Palakkad highway region in Kerala has been assessed. The average Raeq activity was found to be 301.57 Bq/kg, below the global limit of 370 Bq/kg, while the average absorbed dose rate of 138.14 nGy/h exceeded the world average of 59 nGy/h. Other radiological hazard parameters such as AED_{out}, H_{ext}, H_{int}, I_{γ}, and I_{α} were below the recommended global limits, indicating a radiologically safe environment. However, the average Excess Lifetime Cancer Risk

(ELCR) of 0.68 × 10^{-3} exceeded the permissible limit of 0.29 × 10^{-3}, suggesting some level of risk. Overall, the exposure to natural radionuclides in the studied rock samples does not pose significant distress to the local population.

Gamma-ray spectrometry was used to measure the concentrations of ^{226}Ra, ^{232}Th, and ^{40}K at 24 soil sampling sites along NH-66 in Kerala, spanning 78 km between Kozhikode and Malappuram districts. The radionuclide activity concentrations in urban soil followed the order ^{40}K > ^{232}Th > ^{226}Ra, with radiological hazard parameters either equal to or below global averages. Multivariate statistical analysis showed that natural radioactivity had a negligible impact on the soil's physico-chemical properties.

In the Athirappilly region, the distribution, and origins of radioactive materials in granitoid rocks were studied. The mean activity levels of ^{238}U, ^{232}Th, and ^{40}K were 54.74, 77.90, and 875.79 Bq/kg, respectively. These levels were below the worldwide averages for Uranium and Thorium but higher for Potassium. The radioactivity in these rocks primarily stems from Uranium, Thorium, and Potassium, and construction materials derived from them are unlikely to pose significant health risks.

Natural radioactivity in various geological formations arises from radionuclides like ^{238}U, ^{232}Th, and ^{40}K. The radiogenic heat production, and heat flow in samples from the Thrissur-Palakkad highway, NH-66 highway, and Athirappilly regions. Ground radiometric data were collected for geothermal modeling purposes. The average concentrations of ^{226}Ra, ^{232}Th, and ^{40}K were 4.80 ppm, 29.58 ppm, and 2.93%, respectively. The RHP rates for the rocks were higher than the world average, particularly in charnockite rocks. Sites along NH-66. The activity concentrations were 39.88 Bq/kg for ^{226}Ra, 61.19 Bq/kg for ^{232}Th, and 815.51 Bq/kg for ^{40}K, all below global safety thresholds. The average elemental concentrations in basement rocks were 3.53 ppm for ^{226}Ra, 15.95 ppm for ^{232}Th, and 2.61% for ^{40}K, with RHP rates above the world average. In Athirappilly, rock samples showed the average elemental concentrations were 4.43 ppm for ^{226}Ra, 19.30 ppm for ^{232}Th, and 2.97% for ^{40}K, with RHP rates within the world average. The Thrissur-Palakkad highway

region, with its higher RHP rates (3.34 μWm^{-3}) in charnockite rocks, shows significant promise for geothermal energy. For the NH-66 region and Athirappilly region, RHP rates (0.79 μWm^{-3} and 1.01 μWm^{-3} respectively) are within the Earth's crust average ranging between 0.8 and 1.2 μWm^{-3}. These findings emphasize the importance of continuous monitoring and exploration to harness geothermal energy effectively.

Overall, the Kuthiran region had the highest activity concentrations, followed by Athirappilly, both at the foothills of the Western Ghats. The study areas consist of ancient rock units, including various gneisses and migmatites that have undergone significant regional metamorphism.

In this thesis, a fruitful effort was done to synthesis and evaluated the radiation shielding efficiency of various composites. Based on our motivation, synthesis are done at different ways with cost effectively.

Initially, this study examined the impact of chemical modifications in standard concrete using coconut shell powder, Perlite, Vermiculite, and Zirconium and Neodymium oxides on gamma-ray absorption. Results showed that increasing density with these additives significantly improved gamma-ray absorption. This indicates that incorporating these fewer toxic additives effectively enhances radiation protection properties, making the material suitable for applications requiring increased radiation shielding. Gamma absorption parameters such as μ, μ/ρ, Z_{eff}, and HVL were determined both theoretically and experimentally at photon energies of 511, 662, 1173, and 1333 keV. The study calculated mass attenuation coefficients using Phy-PSD software and compared them with Xcom results to compute HVL, TVL, MFP, and Z_{eff} values. The presence of silicon, iron, Aluminium, Zirconium, and Neodymium in concrete significantly influenced its gamma shielding properties. Composites CSN20 and CSZ20, with higher concentrations of Zirconium and Neodymium, showed superior μ/ρ, Z_{eff}, and lower EBF and EABF values. As photon energy increased, HVL, TVL, and MFP quantities also increased, highlighting the contributions of silicon, Aluminium, and iron. The CSC20 concrete sample had higher Σ_R values compared to CSP20,

CSV20, and CSZ20. The outcomes indicate that the insertion of these additives positively affects the photon shielding parameters of cement samples. It can be concluded that those cement samples can be evaluated for further gamma protection applications.

The room-temperature vulcanization method was successfully employed to produce flexible composites comprising natural rubber (NR), $BaWO_4$, and $BaWO_4$ with varying percentages of Tungsten oxide. Increasing the concentration of $BaWO_4$ resulted in higher values for the mass attenuation coefficients (μ_m), effective atomic number (Z_{eff}), and effective electron densities (N_{eff}) of the NR composites. Conversely, these values decreased with the rise in photon energy within the range of 103 keV to 1333 keV. The experimental measurements showed good agreement with theoretical calculations from XCOM and simulation results using the Phy-X/PSD software. The evaluation of the fabricated composites encompassed various parameters, including mass attenuation coefficient, linear attenuation coefficient, Half-Value Layer (HVL), Mean Free Path (MFP), effective atomic number (Z_{eff}), effective electron density (N_{eff}), Z_{eq}, effective buildup factor (EBF), and effective attenuation buildup factor (EABF). The developed composites possess several advantageous characteristics, such as lightweight, ease of processing, non-toxicity, flexibility, and good dispersion properties. Because of these characteristics, these materials can effectively serve as gamma-ray shielding materials. The composite material is suitable for various applications, including both mobile and stationary radiation shielding purposes. Additionally, it can be used in scenarios where flexible radiation shielding, such as gloves, shoes, and coats, is necessary to protect workers from radiation exposure.

Our further efforts were to synthesis a epoxy wall paint composites based metal oxide samples for shielding applications. Epoxy wall paints with added Bi_2O_3 and WO_3 were prepared to evaluate their gamma radiation shielding properties. The mass attenuation coefficients obtained experimentally were compared with predictions from the XCOM application and Phy-X/PSD program simulations (0.010 MeV to 15 MeV range), showing excellent agreement. Parameters such as

mass attenuation coefficient, linear attenuation coefficient, HVL, MFP, Z_{eff}, N_{eff}, EBF, and EABF were examined. The results indicate that Bi_2O_3 (20 percent) wall paint composites are highly effective at photon reduction. Shielding parameters (0.015 to 15 MeV) showed that MAC, LAC, Z_{eff}, and N_{eff} increase with higher Bi_2O_3/WO_3 content and decrease with energy. This suggests a novel gamma shielding absorber, reducing the need for lead in these new materials.

Based on the data obtained in the second part of this study, Table 9.1 compares the linear attenuation coefficients (LAC) and HVL of the different shields to determine which one is the most effective at attenuating gamma rays at 0.662 MeV.

Table 9.1: Comparison of linear attenuation coefficients for different shields in the present study of gamma rays at 0.662 MeV energy.

No	Samples with code	Density (g/cm^3)	LAC (cm^{-1})	HVL (cm)
1	CSZ10	3.461	0.203	3.414
2	CSZ20	3.523	0.208	3.332
3	CSN10	3.612	0.209	3.316
4	CSN20	3.731	0.223	3.108
5	NRBW80	3.342	0.293	2.365
6	NRBW100	3.418	0.306	2.265
7	WPB4	2.934	0.254	2.728
8	WPW4	3.097	0.261	2.655

NRBW100 has the highest LAC value (0.306 cm^{-1}), making it the most effective shield for attenuating gamma rays at 0.662 MeV. Also, NRBW80, with LAC value of 0.293 cm^{-1}, is the second most effective shield. WPB4 and WPW4 also show relatively high LAC values of 0.254 cm^{-1} and 0.261 cm^{-1}, respectively. CSZ10 has the lowest LAC value (0.203 cm^{-1}), indicating the least effectiveness among the samples tested. In summary, while NRBW100 is the best in terms of LAC, WPB4 and WPW4 also provide strong performance with the advantage of being less dense.

Consideration of the specific application requirements (cost, weight, mechanical properties) will help in making the final decision on the best shielding material.

Epoxy-based coatings are identified and evaluated for their effectiveness in gamma ray attenuation because of their unique combination of properties that make them suitable for radiation shielding applications. Epoxy resins are versatile and can be enhanced with additives like heavy metals or high atomic number materials (e.g., tungsten, bismuth) to improve gamma-ray attenuation by increasing density and atomic number. They offer excellent adhesion, durability, and mechanical strength, making them ideal for radiation shielding in environments like nuclear facilities and aerospace. Unlike heavy materials like lead, epoxy coatings with high-density fillers provide a lightweight, cost-effective alternative. They can also be safer and more environmentally friendly. Advancements in nanotechnology further improve their shielding performance using nano-sized fillers. By combining their inherent properties with the ability to be tailored for specific attenuation requirements, epoxy-based coatings are a promising material for radiation shielding in diverse applications

CHAPTER 10
RECOMMENDATIONS

Recommendations for Future Work

- Expanded geographical and material scope: Conduct further investigations across a broader geographic area and include a wider variety of building materials. This would provide a more comprehensive understanding of the regional variations in natural radioactivity in different climatic zones or geological formations.

- Longitudinal Studies and Monitoring: Conduct long duration studies to monitor changes in natural radioactivity over time. This could involve periodic sampling and analysis to assess any fluctuations in radiation levels and their implications for long-term exposure risks. Long duration data would contribute to establishing baseline values and detecting any trends or anomalies.

- Further studies have to be conducted at Pantheeramkavu, near Calicut, for finding out the possible reasons for the enhanced radioactivity observed at this sampling site.

- Advanced Shielding Material Development: Focus on advancing the development of novel gamma-ray shielding materials. Investigate innovative compositions and manufacturing techniques that prioritize not only effectiveness in radiation attenuation but also factors such as cost-effectiveness, sustainability, and ease of application. Explore the integration of nanotechnology or composite materials to enhance shielding capabilities. Kerala, being the state producing the largest amount of natural rubber in our country, there is ample scope for continuing research based on natural rubber based shielding materials.

- ❖ Impact Assessments and Standards: Conduct studies to assess the impact of natural radioactivity and gamma attenuation properties of wall paints on the indoor air quality and occupant health in buildings. Establish or refine standards and guidelines for safe levels of radiation exposure in houses and other establishments. Collaborate with regulatory bodies and industry stakeholders to implement these standards effectively.

- ❖ Interdisciplinary Approaches: Foster interdisciplinary collaborations between radiation physicists, materials scientists, health professionals, and policy makers. This collaborative approach would facilitate the integration of diverse expertise and perspectives to address complex challenges related to natural radioactivity and gamma attenuation in building materials.

- ❖ Public Awareness and Education: Increase public awareness and education initiatives regarding the potential risks associated with natural radioactivity in building materials. Develop educational programmes for architects, engineers, construction professionals, and homeowners to promote informed decision-making and the adoption of radiation-safe practices in building design and maintenance.

By pursuing these avenues through further research and development, the field of radioactivity, both natural and man-made, can be made more beneficial and fearless to the future generations.

APPENDIX

Table A1: Minimum detectable activities (MDA).

Nuclides	Energy (In keV)	MDA (Bq/kg)
^{214}Pb	295.1	1.7
^{222}Ra	186.1	0.3
^{212}Pb	727.3	1.5
^{208}Tl	583.0	0.8
^{214}Bi	609.3	0.5
^{40}K	1460.7	1.3

Minimum detectable activity is calculated by using the equation,

$$\text{MDA} = \frac{1.645\sqrt{BC}}{\gamma \epsilon t m} \text{ (Bq/kg)}$$

where BC is the counts on background.

Table A.2 Represents the energy sources with activity used for the gamma attenuation measurements.

Table A2: Energy sources with activity.

Nuclide	Energy (keV)	Activity (Bq)	Reference Date	Relative Error (%)
Cs-137	662	660	24 Aug, 2021	6
Co-60	1173	1460	24 Aug, 2021	10
Co-60	1333	1460	24 Aug, 2021	10

Figure A1 and A2 shows one of the spectrums produced from the samples from Athirappilly and Kuthiran region.

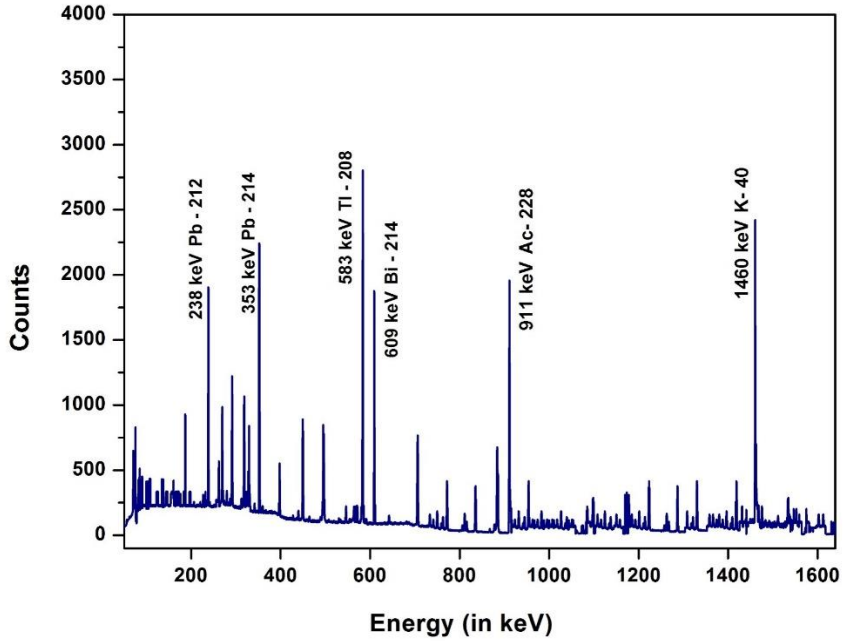

Figure A1: Gamma Energy Spectrum of rock sample from athirappilly (Under this study)

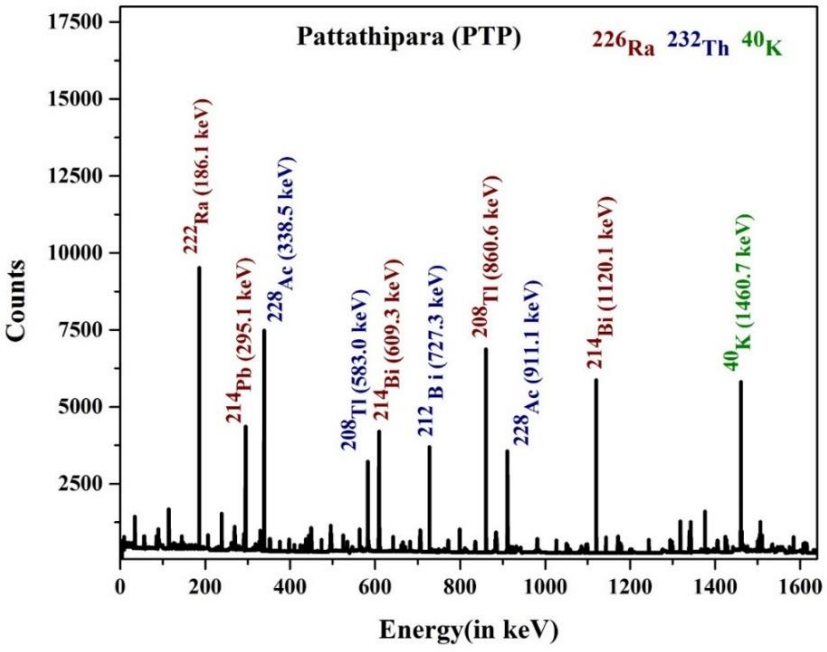

.

Figure A2: Gamma Energy Spectrum of rock sample from Kuthiran (Under this study).